UNDERSTANDING THE NATURE OF THE FAINT RADIO-SOURCE POPULATION



Eleni Vardoulaki

St. Peter's College

A thesis submitted for the degree of

Doctor of Philosophy

at the

University of Oxford

Trinity Term 2009

Declaration

I declare that no part of this thesis has been accepted, or is currently being submitted, for any degree or diploma or certificate or any other qualification in this University or elsewhere. This thesis is the result of my own work unless otherwise stated. Most of the work was carried out in collaboration with Steve Rawlings (University of Oxford).

Part of this thesis has been published in the following refereed journals:

Chapter 2: Vardoulaki, E., Rawlings, S., Simpson, C., Ivison, R. J., Ibar, E., 2008, MNRAS, 387, 505.

Chapter 3: Vardoulaki, E., Rawlings, S., Hill, G. J., Mauch, T., Inskip. K., Riley, J., Brand, K., Croft, S., Willott, C. J., 2009, MNRAS, 401, 1709.

UNDERSTANDING THE NATURE OF THE FAINT RADIO-SOURCE POPULATION

Eleni Vardoulaki

St. Peter's College

Submitted for the Degree of Doctor of Philosophy

Trinity Term 2009

Abstract

This DPhil dissertation presents two new and independent samples of faint radio sources. The first sample is the 37 SXDS radio sources with flux densities at 1.4-GHz above 2 mJy, a spectroscopic completeness of 65% and a median redshift $z_{\rm med} \approx 1.1$. The second sample is the 47 TOOT00 radio sources with flux densities at 151 MHz above 100 mJy, a spectroscopic completeness of 85% and $z_{\rm med} \sim 1.25$. Optical, near- and mid-IR photometry, optical spectroscopy, and radio observations are used in the analysis and comparison of the two samples. The quasar fraction in the TOOT00 radio sources is $0.13 < f_{\rm q} < 0.25$ above the FRI/FRII break in radio luminosity, while use of 24 μm data reveals objects with significant but sometimes obscured accretion and gives quasar-mode fraction of $0.5 \rightarrow 0.9$ above the FRI/FRII break. The FRI/FRII divide seen at $z \lesssim 0.5$ is also observed at $z \sim 1$ for FRII objects in the TOOT00 and SXDS samples, but examples of FRI radio sources above the FRI/FRII break do exist. The total number of the TOOT00 objects and their distribution are consistent with simulations based on extrapolations from previous work, while for the SXDS objects the results are only broadly similar. Based on that comparison, the redshift spikes seen at $z \sim 1.3$ in TOOT00 and at $z \sim 0.65$ & 2.7 in SXDS appear to be significant, and might be due to Large-Scale Structure. A $V/V_{\rm max}$ test suggests the cosmic evolution of the TOOT00 and SXDS samples, is different. The TOOT00 radio sources are 2-times more luminous in host-galaxy starlight than the SXDS radio sources. The almost proportionality between radio luminosity at 1.4 GHz and 24 μm luminosity suggests that $L_{\rm rad}$ traces accretion luminosity and $L_{\rm [OII]} \propto L_{\rm rad}^{0.7}$ may reflect imperfections in the $L_{\rm [OII]}$-accretion luminosity scaling. Mid-IR 24 μm observations in the SXDS sample suggest that 30% of the light from the nucleus is absorbed by the torus and re-emitted in the mid-IR, while ~ 1% of the light is scattered above and below the torus.

Acknowledgements

I would like to dedicate this DPhil thesis to my parents and brother for supporting me mentally and financially during this DPhil.

A huge thanks to my supervisor, Steve Rawlings, for being a great teacher and advisor, and for showing me how to become a proper astronomer.

Finally, I would like to thank all the people, friends and colleagues, that helped me with the DPhil during my time in Oxford.

Contents

1 Introduction **1**

1.1 On a historical note 2

1.2 Different types of AGN and radio sources 3

1.2.1 AGN classification 3

1.2.2 Structural classification of radio sources 5

1.3 The Unified AGN model 7

1.3.1 The central engine 9

1.3.2 Modes of accretion 10

1.3.3 Re-current episodes of AGN activity 11

1.4 Cosmic evolution of the radio-source population 12

1.5 Host galaxies of radio sources 13

1.6 Radio Surveys and connection to other wavebands 14

1.7 Cosmology 18

1.7.1 Observational Cosmology 23

1.8 Chapter description 24

2 The Subaru/*XMM-Newton* Deep Field - II. The 37 brightest radio sources **26**

2.1 Introduction 27

2.2 Data and Observations 30

2.3 Analysis 33

2.3.1 Basic information 33

2.3.2 Photometric redshifts 39

2.3.3 Optical/infrared radio-source classification 42

2.4 Discussion 44

2.4.1 Accretion Indicators 44
2.5 Conclusions 49
2.6 Notes on the 37 brightest SXDS radio sources 51

3 The TexOx-1000 redshift survey of radio sources I: the TOOT00 region 77
3.1 Introduction 77
3.2 Data and observations 81
3.3 Analysis 93
3.3.1 Optical classification and redshifts 93
3.3.2 Radio classification, spectral indices and sizes 95
3.3.3 The FRI/FRII structural divide 99
3.3.4 The quasar fraction 100
3.4 The redshift distribution of TOOT00 101
3.5 Conclusions 106
3.6 Notes on the TOOT00 radio sources 107

4 Investigating Large-Scale Structure in the TOOT00 and SXDF regions 150
4.1 Introduction 151
4.2 Data 152
4.3 Redshift Distributions 153
4.4 Redshift spikes in the TOOT00 and SXDS redshift distributions 154
4.4.1 $V/V_{\rm max}$ test 161
4.5 Conclusions 167
4.6 Results on the probability for redshift spikes in two samples of 100 S^3-SEX simulated sky areas equal to the TOOT00 and SXDS 167

5 The $K-z$ relation and the radio structure of the TOOT00 and the SXDS radio sources 172
5.1 Introduction 173
5.2 The Sample 176
5.3 Analysis 179

5.4 Discussion 186
5.4.1 The $K-z$ diagram 186
5.4.2 Relation of K-band magnitude, radio luminosity and radio structure . . 191
5.5 Comparison of the TOOT00 and the SXDS radio sources with the low-redshift 6dF radio sources 196
5.6 Conclusions 200

6 Accretion indicators and radio structure in the TOOT00 and the SXDS samples of radio sources 201
6.1 Introduction 202
6.2 Analysis 206
6.3 Discussion 207
6.3.1 Correlation of emission-line and radio luminosity 207
6.3.2 Accretion indicators using 24 micron data 213
6.3.3 Radio structures of the TOOT00 and the SXDS radio sources 215
6.4 Conclusions 217

7 Conclusions 220
7.1 The future of radio astronomy 222

D 224
D.1 Statistics 224
D.1.1 Survival analysis statistical package – ASURV 224
D.1.2 Poisson Probability 224
D.1.3 Kolmogorov-Smirnov statistic 225

List of Figures

1.1 Unified AGN model 9

1.2 Hubble diagram at the K-band 13

2.1 Sky positions of the 37 brightest radio sources in the SXDS 30

2.2 Spectroscopic vs photometric redshifts for the SXDS 42

2.3 $\log_{10}(L_{24\mu\mathrm{m}})$ vs redshift z 43

2.4 Blueness versus mid-IR excess for the 37 brightest SXDS radio sources 45

2.5 $\log_{10}(L_{1.4\mathrm{GHz}})$ vs spectral index α 46

2.6 $\log_{10}(L_{1.4\mathrm{GHz}})$ vs largest projected linear size D 48

2.7 Near-IR/radio and optical/radio overlays, optical spectroscopy and SEDs for the SXDS radio sources 58

2.7 sxds_0002 & sxds_0003 59

2.7 sxds_0004 & sxds_0005 60

2.7 sxds_0006 & sxds_0007 61

2.7 sxds_0008 & sxds_0009 62

2.7 sxds_0010 & sxds_0011 63

2.7 sxds_0012 & sxds_0013 64

2.7 sxds_0014 & sxds_0015 65

2.7 sxds_0016 & sxds_0017 66

2.7 sxds_0018 & sxds_0019 67

2.7 sxds_0020 & sxds_0021 68

2.7 sxds_0022 & sxds_0023 69

2.7 sxds_0024 & sxds_0025 70

2.7 sxds_0026 & sxds_0027 71

2.7 sxds_0028 & sxds_0029 72
2.7 sxds_0030 & sxds_0031 73
2.7 sxds_0032 & sxds_0033 74
2.7 sxds_0034 & sxds_0035 75
2.7 sxds_0036 & sxds_0037 76

3.1 Sky area of TOOT00 86
3.2 Spectroscopic vs photometric redshifts for TOOT00 93
3.3 $S_{74\mathrm{MHz}}$ vs $S_{151\mathrm{MHz}}$ 97
3.4 $L_{151\mathrm{MHz}}$ vs α 98
3.5 Radio Luminosity at 151 MHz $L_{151\mathrm{MHz}}$ versus redshift z. 99
3.6 $L_{151\mathrm{MHz}}$ vs D 101
3.7 Histogram of redshift distribution of the TOOT00 objects and the S^3-SEX distribution 102
3.8 Histogram of flux density distribution for the TOOT00 objects 104
3.9 Histogram of the redshift distribution of the TOOT00 objects 105
3.10 Near-IR/radio overlays, optical spectroscopy and SEDs for the TOOT00 radio sources - TOOT00_1140 & TOOT00_1099 126
3.10 TOOT00_1125 & TOOT00_1143 127
3.10 TOOT00_1233 & TOOT00_1022 128
3.10 TOOT00_1204 & TOOT00_1235 129
3.10 TOOT00_1224 & TOOT00_1291 130
3.10 TOOT00_1107 & TOOT00_1180 131
3.10 TOOT00_1027 & TOOT00_1195 132
3.10 TOOT00_1069 & TOOT00_1094 133
3.10 TOOT00_ 1149& TOOT00_1298 134
3.10 TOOT00_1200 & TOOT00_1215 135
3.10 TOOT00_1240 136
3.10 TOOT00_1289 & TOOT00_1072 137
3.10 TOOT00_1134 & TOOT00_1244 138

3.10 TOOT00_1066 & TOOT00_1261 139
3.10 TOOT00_1252 & TOOT00_1214 140
3.10 TOOT00_1152 & TOOT00_1129 141
3.10 TOOT00_1090 & TOOT00_1267 142
3.10 TOOT00_1188 & TOOT00_1196 143
3.10 TOOT00_1173 & TOOT00_1228 144
3.10 TOOT00_1034 & TOOT00_1255 145
3.10 TOOT00_1048 & TOOT00_1029 146
3.10 TOOT00_1115 & TOOT00_1132 147
3.10 TOOT00_1250 & TOOT00_1268 148
3.10 TOOT00_1251 & TOOT00_1203 149

4.1 Histogram of the redshift distribution for TOOT00/SXDS and S^3-SEX simulations 154
4.2 Cumulative distribution of fraction of number of TOOT00 and SXDS objects compared to S^3-SEX 155
4.3 Coordinates of the 100 S^3-SEX simulated fields 158
4.4 Histogram of TOOT00 radio sources at different binning 158
4.5 Histogram of SXDS radio sources at different binning 159
4.6 Histogram of the S^3-SEX simulation scaled to TOOT00 and SXDS sky areas 160
4.7 Comparison of TOOT00 redshift distribution to S^3-SEX simulation using Poisson statistics 160
4.8 Comparison of SXDS redshift distribution to S^3-SEX simulation using Poisson statistics 161
4.9 $V/V_{\rm max}$ vs redshift for the TOOT00 and the SXDS radio sources 162
4.10 $V/V_{\rm max}$ test for the TOOT00 and SXDS radio sources for different radio luminosity intervals 163

5.1 $L_{151\rm MHz}$ versus redshift z for the TOOT00 and the SXDS radio sources . . . 180
5.2 K-correction and passive evolution correction for the K-band versus redshift 181

5.3 $L_{K-\mathrm{Ke}}/L_{K-\mathrm{WKe}}$ and $L_{K-\mathrm{K}}/L_{K-\mathrm{WKe}}$ vs z for the TOOT00 and the SXDS objects 182
5.4 $L_{K-\mathrm{Ke}}$ vs $L_{K-\mathrm{WKe}}$ vs z for the TOOT00 and the SXDS radio sources 183
5.5 The $K-z$ diagram for the TOOT00 and the SXDS radio sources 187
5.6 $K_{\mathrm{Vega}}-K_{\mathrm{W}}$ vs redshift z for the TOOT00 and the SXDS radio sources . . . 188
5.7 $K_{\mathrm{Vega}}-K_{\mathrm{W}}$ histogram for the TOOT00 and the SXDS radio sources 189
5.8 K magnitude vs $L_{K-\mathrm{Ke}}$ and $L_{K-\mathrm{K}}$ in L^*_K units for the TOOT00 and the SXDS radio sources 189
5.9 $L_{K-\mathrm{Ke}}$ vs α and z for the TOOT00 and the SXDS radio sources 190
5.10 $L_{1.4\mathrm{GHz}}$ vs $L_{K-\mathrm{Ke}}$ for the TOOT00 and the SXDS radio sources 193
5.11 $L_{151\mathrm{MHz}}$ vs $L_{K-\mathrm{Ke}}$ for the TOOT00 and SXDS radio sources 194
5.12 Histogram of redshift distribution of the SXDS objects and the S^3-SEX distribution 195
5.13 $L_{1.4\mathrm{GHz}}$ vs z for the TOOT00, the SXDS and the 6dF radio sources 197
5.14 K magnitude vs z for the TOOT00, the SXDS and the 6dF radio sources . . 198
5.15 $L_{K-\mathrm{Ke}}$ vs z and $L_{1.4\mathrm{GHz}}$ vs $L_{K-\mathrm{Ke}}$ for the TOOT00, SXDS and 6dF radio sources 199

6.1 $L_{[\mathrm{OII}]}$ vs $L_{151\mathrm{MHz}}$ and $L_{1.4\mathrm{GHz}}$ for the TOOT00 and SXDS radio sources; optical class 209
6.2 $L_{[\mathrm{OII}]}$ vs $L_{151\mathrm{MHz}}$ and $L_{1.4\mathrm{GHz}}$ for the TOOT00 and SXDS radio sources; radio class 210
6.3 $L_{[\mathrm{OII}]}$ vs $L_{151\mathrm{MHz}}$ and $L_{1.4\mathrm{GHz}}$ for the TOOT00 and SXDS radio sources; radio-optical class 210
6.4 Blueness vs mid-IR excess in the SXDS 215
6.5 $L_{[\mathrm{OII}]}$ vs $L_{24\mu\mathrm{m}}$ for the SXDS radio sources 216
6.6 $L_{1.4\mathrm{GHz}}$ vs $L_{24\mu\mathrm{m}}$ for the SXDS radio sources 217
6.7 Blueness vs $L_{[\mathrm{OII}]-24}$ in the TOOT00 and the SXDS samples 218

List of Tables

2.1 Basic properties of the 37 brightest SXDS radio sources 34

2.1 Basic properties of the 37 brightest SXDS radio sources (cont.) 35

2.2 Observing log for optical spectroscopy of the SXDS radio sources 36

2.2 Observing log for optical spectroscopy of the SXDS radio sources (cont.) 37

2.3 Measured quantities for the 37 SXDS radio sources 38

2.4 Point source depths for SXDF optical, near-infrared and mid-infrared bands. . 39

3.1 Radio properties of the 47 TOOT00 radio sources 87

3.2 Observing log for the TOOT00 optical spectroscopy 88

3.2 Observing log for the TOOT00 optical spectroscopy (cont.) 89

3.3 Spectroscopic and photometric redshifts for TOOT00 90

3.3 Spectroscopic and photometric redshifts for TOOT00 (cont.) 91

3.4 Emission line properties for TOOT00 92

3.5 Optical and near-IR photometry for TOOT00 used in HyperZ 116

3.5 Optical and near-IR photometry for TOOT00 used in HyperZ (cont.) 117

3.6 Detailed optical and near-IR photometry for TOOT00 118

3.6 Detailed optical and near-IR photometry for TOOT00 (cont.) 119

3.6 Detailed optical and near-IR photometry for TOOT00 (cont.) 120

3.6 Detailed optical and near-IR photometry for TOOT00 (cont.) 121

3.6 Detailed optical and near-IR photometry for TOOT00 (cont.) 122

3.6 Detailed optical and near-IR photometry for TOOT00 (cont.) 123

3.6 Detailed optical and near-IR photometry for TOOT00 (cont.) 124

3.6 Detailed optical and near-IR photometry for TOOT00 (cont.) 125

4.1 Probability for redshift spikes in the TOOT00 redshift distribution 157

4.2 Probability for redshift spikes in the SXDS redshift distribution 157
4.3 Basic statistics on the 100 S^3-SEX simulated sky areas 159
4.4 Banded $V/V_{\rm max}$ test for various sub-samples in the TOOT00 sample 164
4.5 Banded $V/V_{\rm max}$ test for various sub-samples in the SXDS sample 164
4.6 Results from the analysis on the 47 TOOT00 radio sources 165
4.7 Results from the analysis on the 37 SXDS radio sources 166
4.8 Minimum probability for redshift spikes in the 100-simulations with sky area equal to TOOT00 compared to the S^3-SEX simulation 168
4.8 Minimum probability for redshift spikes in the 100-simulations with sky area equal to TOOT00 compared to the S^3-SEX simulation (cont.) 169
4.9 Minimum probability for redshift spikes in the 100-simulations with sky area equal to SXDS compared to the S^3-SEX simulation 170
4.9 Minimum probability for redshift spikes for SXDS compared to 100 simulations (cont.) 171

5.1 Basic properties of the 47 TOOT00 radio sources needed for analysis of the $K-z$ diagram 177
5.2 Basic properties of the 37 SXDS radio sources needed for analysis of the $K-z$ diagram 178
5.3 Luminosity at K for the 47 TOOT00 radio sources 184
5.4 Luminosity at K for the 37 SXDS radio sources 185

6.1 Emission-line and radio luminosities for the TOOT00 radio sources 211
6.2 Emission-line and radio luminosities for the SXDS radio sources 212

Chapter 1

Introduction

The goal of this DPhil thesis is to provide a better understanding of the faint extragalactic radio-source population. The tool is studying the properties of faint radio sources in various wavebands (e.g. radio, optical, near- and mid-infrared), their structure, their connection to the unified AGN model and to compare these results with already known facts for radio sources and AGN.

Extragalactic radio sources are considered to be amongst the most spectacular objects in the Universe. They exhibit unique extended structures, which can extend to hundreds of kiloparsecs from a central active object, and they radiate energy over ten times that of normal galaxies. Radio sources are excellent probes of cosmology, since they can be observed at long distances and at various wavebands. Powerful radio sources, such as radio galaxies and quasars, trace the most massive galaxies (e.g. Jarvis et al. 2001a; De Breuck et al. 2002; Willott et al. 2003) and are associated with the most massive black holes (Dunlop et al. 2003; McLure et al. 2004; McLure & Jarvis 2004) in the Universe, at all cosmic epochs. Radio galaxies have been detected up to redshifts of just above five (van Breugel et al. 1999), and quasars up to and beyond redshifts of six (Fan et al. 2003). Furthermore, they have been proven to be excellent probes of the Large-Scale Structure (LSS) because they are mostly associated with massive ellipticals that tend to reside in clusters (e.g. Brand et al. 2003).

1.1 On a historical note

The first attempts in radio astronomy were made by Karl Jansky who in 1933 discovered radio emission from the Milky Way. A few years later, Grobe Reber observed radio emission from our galaxy, but in was not until after the second World War that extragalactic radio astronomy became a significant field of its own. The parallel discovery of extragalactic radio sources and Active Galactic Nuclei (AGN) in the 1940s-50s led to the beginning of a new era of observational techniques, in order to identify radio objects with their optical counterparts. Since then, the field of radio astronomy has grown with new telescopes being built quite frequently.

The discovery of AGN by Carl Seyfert in 1943, and their description as objects that have central regions with peculiar spectra and with notable emission lines as well as their association with supermassive black holes, places AGN among the most interesting natural phenomena in the Universe. Contrary to otherwise normal galaxies, like our own, they produce huge amounts of energy in a small volume ($\ll 1$ pc^{-3}) that can emerge in a broad range of frequencies, from the radio to the γ-rays; in some cases the luminosity per band[1] can be roughly constant across thirteen orders of magnitude in frequency. They also exhibit emission-line, and occasionally absorption-line spectra with line widths that suggest velocities of up to $\sim 3 \times 10^4$ km s^{-1} or ~ 0.1 c; c is the speed of light. Although their nuclei seem to be unresolved in the optical, using radio observations it is possible to reveal extended radio structure. Also, AGN display very strong cosmological evolution, where the most luminous active galaxies were ~ 1000 times more numerous at redshift 2.5 than they are today (e.g. Dunlop & Peacock 1990). Through the years, AGN have been proven a great tool to study interactions of galaxies, clusters of galaxies, the properties of the intergalactic and intracluster medium, and large-scale structure (e.g. Brand et al. 2003).

Since the 1950s, the rapid development of radio astronomy led to the discovery of numerous radio sources, while various surveys with flux-limited samples have shown that the study of radio sources joined with the AGN phenomenon, is one of the fastest increasing fields in astronomy. Combination of radio and optical observations created the need for a common

[1]The luminosity per decade in frequency is $\int_{\nu_1}^{10\nu_1} L_\nu \, \mathrm{d}\nu = [\log_{10}(e)]^{-1} \int L_\nu \, \nu \, \mathrm{d}(\log_{10}(\nu))$, which gives $\sim$ 2.3 νL_ν assuming a flat spectral energy distribution (SED), i.e. $\nu L_\nu \sim \nu^0$. We use this conversion for the SEDs presented in this dissertation.

classification to describe the objects according to structure and other characteristics, like size and brightness. For years, various different objects were being discovered, some of them with common characteristics but some with major differences. The need for individual classification as well as a common classification that would describe and unite them led to the unified AGN model, where objects observed at the optical (e.g. Seyferts, QSOs) are connected to objects observed in the radio (e.g. FRIs, FRIIs; see Section 1.2).

1.2 Different types of AGN and radio sources

1.2.1 AGN classification

An issue in the study of AGN and radio sources is the classification of individual sources. The reason for this is the variety of properties these objects display depending on observing frequencies and viewing angles.

A good review on the individual characteristics of AGN is given by Krolik (1999). The classifications mentioned there depend on optical characteristics such as emission lines and variability, but also radio observations:
1) radio-selected objects include Narrow Line Radio Galaxies (NLRGs), Broad Line Radio Galaxies (BLRGs), Radio Loud Quasars (RLQs); 2) according to their emission-line width, radio-quiet objects are classified as Seyfert 1s, Seyfert 2s, Radio Quiet Quasars (RQQs); 3) extreme objects are classified as Optical Violent Variable objects (OVVs) that display variability in their emitting flux; BL Lac objects that have no emission lines but exhibit variability; and Low-Ionisation Nuclear Emission Regions (LINERs) that occupy the margin of activity.

Briefly, the characteristics of the above classes are:
i) *Seyferts*, that were discovered by Carl Seyfert in 1943, are sub-divided into two main types: Seyfert 1s have broad-emission-line optical spectra whereas Seyfert 2s have narrow; intermediate class objects do exist. All types emit comparable amounts of energy over a wide range of frequencies, but are weak in the radio and have narrow-emission-line spectra. The basic difference between the two types is that Seyfert 1s are pointlike, have broad emission line spectra, and have some variability in their flux output, contrary to Seyfert 2s.
ii) *Quasars*, or as originally stated, quasi-stellar objects, are the 'generic AGNs' and 'radio-

loud' objects. They are pointlike, exhibit a broad spectrum, broad emission (and sometimes absorption) lines, as well as narrow emission lines, and sometimes their energy output is variable and linearly polarised up to a few percent. An object that shows absorption in the optical spectrum is called a 'broad-absorption-line' QSO (BALQSO).

iii) *Broad-line radio galaxies* are a subset of FRII objects (Fanaroff & Riley 1974; see Sec. 1.2.2) that are very energetic in the radio wavebands. They are not pointlike in the optical, their energy output is comparable in the infrared, optical and X-ray bands, they exhibit broad- and narrow-line spectra, but they show weak variability and their flux is rarely polarised.

iv) *Narrow-line radio galaxies* include both FRIs and FRIIs (Fanaroff & Riley 1974; see Sec. 1.2.2). They are not pointilike in the optical (i.e they are associated with obvious galaxies) and have only narrow emission lines in their spectra. They are bright in the radio and show no variability in their flux, while they can be polarised due to scattered quasar light.

v) *BL Lac* objects were first thought to be variable stars in the constellation of Lacerta, but later on they were associated with AGNs since they have many similarities to the other AGN types. They are pointlike, emit similar amounts of energy over a wide range of frequencies, are bright in the radio, and their flux is variable and linearly polarised. The difference from other AGN types is the absence of broad- and narrow-emission lines in their spectra.

vi) *OVVs* show rapid and large amplitude variability in the optical band. They are pointlike in the optical, their energy output is comparable in different bands, have both broad and narrow emission lines, they are bright in the radio and their flux is variable and polarised.

vii) *Blazars* are objects with extremely steep spectrum, and were brought in to unite BL Lacs and OVVs. Their output flux is affected by Doppler boosting, that arises from a relativistic collimated flow that is aligned close to the line of sight to the observer.

viii) *Quasi-stellar objects* (QSOs) are 'radio-quiet' quasars. They are pointlike in the optical, have broad- and narrow-emission-line spectra in a broad range of frequencies, they have weak radio emission (e.g Miller, Rawlings & Saunders 1993), and their energy output is frequently variable. Large populations of absorbed (type-2 QSOs) objects are now known, pinpointed by typically hard X-ray emission (e.g. Norman et al. 2002) or mid-infrared emission (e.g. Martínez-Sansigre et al. 2006).

ix) *LINERs* were discovered in the early 1980s and show weak emission lines, like Seyfert galaxies, but the relative strengths of those lines from low-ionisation stages are rather greater than in Seyfert galaxies. The only AGN feature they exhibit is narrow-emission-line spectra.

1.2.2 Structural classification of radio sources

The first astronomers to give a precise definition to the radio structure of the radio-source population were Fanaroff & Riley (1974), who examined a subsample of sources in the 3CR catalogue that were clearly resolved into two or more components, and sorted the sources in classes based on a purely structural criterion. They designated as class 1 those radio galaxies for which the ratio of the distance between the two brightest hot spots on either side of the nucleus to the overall source size was less than 0.5 and as class 2 those for which the ratio was greater than 0.5. This way, objects defined as FRI and FRII according to these entirely structural criteria were found to be strongly related to their radio luminosity at 178 MHz: the ones above $L_{178\mathrm{MHz}} = 2\times10^{25}$ WHz^{-1}sr^{-1} ($H_0 = 50$ km s^{-1}Mpc^{-1}, $\Omega_\mathrm{M} = 1$ and $\Omega_\Lambda = 0$) being FRII radio sources and the ones below FRI. The main difference in FRI and FRII types, is that in the FRIIs the energy is maintained when it's transferred through the jets to the lobes and then interacts with the surrounding environment of the source (intra-cluster medium), where it produces the hot spots we observe at the 'leading edges' of the source, whereas in the FRI-type radio sources energy is released as a result of jet deceleration due to the object's surrounding environment (Combes et al. 2002; Peacock 1999). Another very important difference of FRIs and FRIIs is that jets are intrinsically less powerful in FRIs (Combes et al. 2002) and there are physical models (e.g. Kaiser & Alexander 1997) explaining why low jet power goes alongside jet disruption. The majority of FRI sources show very complex structure, but in most of them the structure close to the associated galaxy indicates that material has been ejected in opposite directions, as is presumed to occur in most of the powerful double sources in FRII class objects. Away from the centres of the class I sources there is a great diversity of structure - the components often show considerable changes of curvature along their lengths. Distortion of the components to this degree is not found in most of the class II sources, although the low brightness tails of their components are often significantly inclined to the source axis, and

there is evidence of 'backflow' (e.g. Alexander & Leahy 1987) from the hotspots back towards the origin of the jets.

Snellen & Best (2003) talk of a single population scheme for FRI and FRII radio sources where their cosmological evolution is independent of FR class, and instead solely a function of radio power. Furthermore, according to Kaiser & Best (2007b) all sources start out with an FRII-type structure and develop FRI or FRII structure depending on their intermediate environment. In particular, the lobe pressure in sources with weaker jets falls so rapidly that they come into pressure equilibrium with their surroundings while they are still located in the core region. Their jets develop turbulent flows with an FRI-type radio structure. More powerful jets grow beyond the core region before the pressure in their lobes decreases too much, thus they retain their FRII-type radio structure.

The dichotomy between FRI and FRII radio sources is marked by a characteristic radio luminosity, as stated above. Ledlow & Owen (1996) found that the radio luminosity at the break of the FRI/FRII class scales with optical luminosity roughly as $L^2_{\rm opt}$. Traditionally, objects above the break display FRII-type radio structure, while objects below show FRI radio structure. More recent studies have shown, though, that FRI objects above the FRI/FRII break in radio luminosity do exist (e.g. Heywood, Blundell & Rawlings 2007; Vardoulaki et al. 2009). Evidence that the division changes with redshift, meaning that FRI objects can exist above the traditional break luminosity at higher redshifts, suggests a systematic change in the environments of radio sources with cosmic epoch (Heywood, Blundell & Rawlings 2007).

Baum, Zirbel & O'Dea (1995), suggest that the FRI/FRII dichotomy (i.e., the observed differences in the properties of low- and high-power radio sources) is due to qualitative differences in the structural properties of the central engines in these two types of sources. Further discussion is presented in Section 1.3.2.

Although the FR structural division is very straightforward, there are radio sources that fit somewhere in between, since they could fall into one class according to structure while having a luminosity more typical of the other.

Another division according to radio structure is the one appearing in Owen & Laing (1989). In this case we have Classical Double (CD), Twin Jet (TJ) and Fat Double (FD) radio sources:

CDs correspond to FRIIs, TJs to FRIs and FDs to FRI/II division objects. Furthermore, Compact (COM) radio sources correspond to objects that appear unresolved. These divide further to Compact Steep Spectrum (CSS) and GHz-Peaked Spectrum (GPS) radio sources, that are powerful yet compact radio sources whose spectra are generally simple and convex with a peak between 100 MHz and a few GHz (e.g. Stanghellini 2006; Koekemoer et al. 2003). Both types of objects are as powerful as large-scale CD radio galaxies, but are up to several orders of magnitude more compact: CSS sources typically have size scales $\lesssim$ 10-20 kpc, while GPS sources are often $\ll$ 1 kpc.

The extensive study of these objects by astronomers has created the need for a unification scheme, a common physical mechanism that produces all the similar effects observed in these objects. On the other hand it was critical to understand the reason why they exhibit these remarkable differences. The most common idea is that of a 'unified AGN model' in which objects appear different due to different orientations of the source to the observer.

1.3 The Unified AGN model

In early observations the classification of different types of radio sources was dependent on the survey, the flux limit and the statistics involved in the analysis. The need to name every type of radio source according to its structure led to structural classification and the FRI-FRII division. Further investigation of the properties of these sources, such as the emitted radio power and optical emission-line luminosity (e.g. Hine & Longair 1979) made researchers at the time believe that there must be a difference in the accretion ratio of the two major types of radio sources, suggesting a different central AGN and a different immediate environment. In the next years new surveys with lower flux density limits were constructed to solve this mystery and give a better insight to the AGN phenomenon, suggesting a unified AGN model. According to Rawlings & Saunders (1991) there is strong evidence for a common central-engine mechanism in all extragalactic radio sources.

The unified active galactic nuclei (AGN) model consists of a super-massive black hole (SMBH; e.g. Rees 1984) that is surrounded by an optically-thick and geometrically-thin accretion disk, a hot corona and an opaque and obscuring torus of gas and dust (Antonucci

1993) that surrounds the central engine. The accretion disc provides the radiation field that photoioinizes the broad-line region (BLR), located close to the accretion disk, and narrow-line region (NLR), outside the disk and torus region, in the optical and gives rise to the X-ray emission via Compton scattering. The torus, if it is sufficiently optically thick, can prevent a distant observer from seeing events deep in its interior in regions very near to the black hole. The obscuration is likely to be most effective at optical, untraviolet (UV) and soft X-ray wavelengths, with the torus becoming less opaque at both longer and sorter wavelengths. Observations at the mid-infrared, and in particular near 24 μm, target regions of hot dust close to the active nucleus without getting blocked by the torus.

The standard model for AGN proposes that the energy released is produced by the accretion of matter onto a SMBH. The AGN is powered by the conversion of gravitational potential energy into radiation, although the rotational kinetic energy of the SMBH may also serve as an important source of energy (e.g. via the Blandford-Znajek mechanism; Blandford & Znajek 1977). A fraction of the matter is ejected involving a poloidal magnetic field in a jet perpendicular to the accretion disk. The powerful jets, observed commonly in radio-loud AGN, consist of relativistic (shocked) plasma[2] which may extend up to kiloparsec scales (showing typically extended radio lobes), much larger in size than their host galaxies.

AGN unification models presume that depending on the viewing angle of the torus-disk-jet complex the observed galaxy appears as a blazar when the jet points towards the observer; as a Seyfert 1, broad-line radio galaxy or QSO for intermediate angles; or as a Seyfert 2 or a narrow-line radio galaxy when the jet lies in the plane of sky. Jets oriented close to the line of sight have favourable observing conditions due to relativistic boosting. Figure 1.1 presents a view of the unified AGN model, where the orientation effect can be seen. Elitzur (2006) claims that AGN type is a viewing-dependent probability due to the clumpiness of the torus, suggesting that the difference between types 1 and 2 is not surely an issue of orientation but of probability for direct view of the AGN. Based on this scenario, type 1 objects can be viewed even through the torus plane, which would explain objects that are classified as type 1 from their optical spectra that also have type 2 spectra in the mid-infrared (e.g. Alonso-Herrero et al. 2003). Unification schemes suggest that QSOs and FRIIs are the same objects, as are

[2]It is not yet known whether this is an electron-positron plasma or an electron-proton plasma.

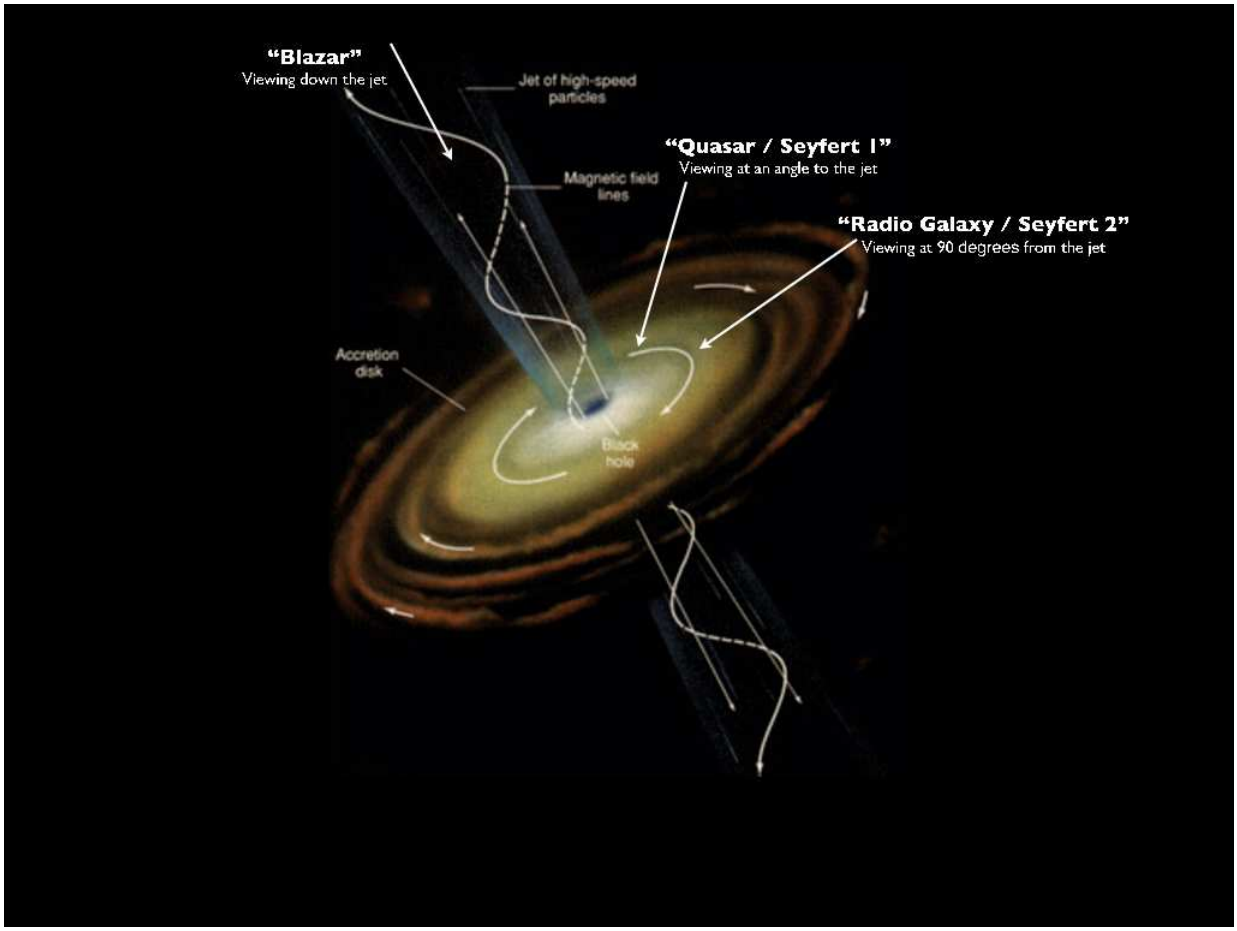

Figure 1.1: A schematic diagram of the geometry essential for unification models (URL: http : //www.southernmaineastronomers.org/).

blazars or BL Lac objects and FRIs.

1.3.1 The central engine

The physical and mathematical structure of a black hole implies that their intrinsic properties are essentially determined by three physical quantities only: mass, spin and accretion rate (e.g. Merloni & Heinz 2008).

BHs can accrete mass both through coalescence with another BH and by accreting cold gas, the latter being the dominant accretion mechanism. The evolution of an active BH is described as a two-stage process of a rapid, Eddington-limited growth up to a peak BH mass, preceded and followed by a much longer quiescent phase with lower Eddington ratios (e.g. Marulli et al. 2008). For a central object with mass $M_{\rm BH}$, the Eddington luminosity is given by $L_{Edd} = 10^{39.1} \times (M/10^8 {\rm M}_\odot)$ W (Shapiro & Teukolsky 1983). The Eddington ratio is defined as $\lambda = L_{\rm bol}/L_{\rm Edd}$, where $L_{\rm bol}$ is the bolometric luminosity of the system. Luminous quasars

tend to have relatively high $\lambda \gtrsim 0.1$ (e.g. McLure & Dunlop 2004; Kollmeier et al. 2006), but some Seyfert galaxies, LINERs, and low-luminosity X-ray and radio AGNs can have $\lambda \lesssim 10^{-2}$, and even as low as $\lambda \sim 10^{-8}$ (e.g. Ho 2002; Soria et al. 2006; Sikora, Stawarz & Lasota 2007). Small & Blandford (1992) talk about quick formation of a BH in newly formed galaxies, with the hole radiating at the Eddington limit. At later epochs, when supply of fuel is no longer plentiful, the holes accrete only intermittently at an average rate that is the same for all quasars.

1.3.2 Modes of accretion

According to Merloni & Heinz (2008), black holes accrete in just three distinct physical states, or 'modes': 1) at low Eddington ratio, only a radiatively inefficient, kinetically dominated mode is allowed; 2) at high Eddington ratio, instead, AGN may display both a purely radiative (radio quiet), and 3) a kinetic (radio loud) mode.

The difference seen in various types of AGN can be attributed to orientation effects explained by the unified AGN model, but not all observed AGN, such as low-power radio-loud AGN (e.g. Ogle, Whysong & Antonucci 2006; Hardcastle et al. 2006), can be explained by orientation based unification schemes (e.g. Barthel 1989; Antonucci 1993). Many authors adopt the idea of different black hole fuelling and triggering mechanisms for low- and high-power AGN. Smolčić et al. (2009) suggest that high- and low-radio-power AGN activity is triggered in different stages during the formation of massive red galaxies. Powerful radio sources ($L_{1.4\mathrm{GHz}} > 5 \times 10^{25}$ W Hz^1) have low stellar masses, are triggered by major mergers of galaxies at high redshift, and show excess mid-IR emission consistent with a hidden radiatively efficient active nucleus. Weak radio AGN occur in the most massive galaxies ($M \gtrsim 10^{11}\mathrm{M}_\odot$, Tasse et al. 2008) already at $z \sim 1$, and they may significantly contribute to the heating of their surrounding medium and thus exhibit gas accretion onto their host galaxies. Kaiser & Best (2007a) proposed that the differences in high-excitation radio galaxies (HERGs) and low-excitation radio galaxies (LERGs) can be explained by the idea of different accretion modes: luminous cold gas accretion in HERGs and radiatively inefficient accretion of hot gas in LERGs (see also Hardcastle, Evans & Croston 2007). Best (2009) supports this line of though, that low-luminosity radio sources are fundamentally distinct objects to high-radio luminosity sources and optically

or X-ray selected AGN, thus suggesting that these are fuelled by a different mechanism. Note that the difference between these two modes of AGN fuelling is distinct from that of the two different radio structural classes of radio-loud AGN (FRI and FRII). The FR-dichotomy is argued to be associated with the environment and evolution of the radio sources (Best 2009).

Best et al. (2006) argue that accretion in FRI objects occurs not only at a smaller rate, but also at lower efficiency than in standard accretion disks. The picture which emerges is that the accretion of hot gas associated with the host galaxy corona represents the dominant process of fuelling for FRI radio galaxies across their full range of radio luminosity, spanning from the faintest level of detectable activity to radio-luminosities marking the transition between FRI and FRII objects. The differences of AGN power across this wide range of luminosities are determined by the available supply of gas, which is closely related to the properties of the hot corona (Balmaverde, Baldi & Capetti 2008).

The mode of accretion in low-luminosity radio-loud AGN is often called 'radio mode' (e.g. Tasse et al. 2008), illustrating the fact that all of the energetic output of these objects is in their radio jets. On the other hand, the 'quasar mode' describes optically/X-ray selected AGN, that may be obscured from direct view at optical/X-ray wavelengths (e.g. Ogle, Whysong & Antonucci 2006). The accretion rate in the 'radio mode' is typically orders of magnitude below the Eddington limit, so that the total mass growth of BHs in the radio relative to the quasar mode is negligible (Marulli et al. 2008).

1.3.3 Re-current episodes of AGN activity

The AGN phenomenon is quite short compared to the age of the Universe, with value of $\sim 1.5 \times 10^7$yr (e.g. Bird et al. 2008), during which time the AGN is active. It is believed that the majority of galaxies have passed through an active phase during their evolutionary history. Such AGN activity is constantly re-triggered (e.g. Best et al. 2006), and plays an important role in balancing the energy losses from hot gas that surrounds massive elliptical galaxies. Cavaliere & Padovani (1989) suggested that objects exhibit re-current episodes of quasar activity, where the luminosity is $L/L_{\rm Edd} \sim 5{\times}10^{-2}$ (for $H_0 = 50$ km s^{-1} Mpc^{-1}). These re-current episodes of quasar activity (i.e. the fraction of the time that the system will be seen as an AGN), is quite small and in the range $\simeq 10^{-4}$-$2{\times}10^{-3}$ (Haehnelt & Rees 1993).

The 'duty cycle', i.e the dimensionless ratio of time active to the sum of time active and dormant, has a value of ~ 0.02 (for $\sim 8 \times 10^8$ yr time-off). The duty cycle is shown to vary in FRI and FRII radio sources, where the ages of FRIs are 5-10 times larger than FRIIs (e.g. Parma et al. 2002).

1.4 Cosmic evolution of the radio-source population

The total of the AGN population was more active in the past (around $z \sim 2$; e.g. Peacock 1999), which can be shown by the source counts. The number density of radio sources is studied by the Radio Luminosity Function (RLF), which can be described as a broken power law or a Schechter luminosity function (Schechter 1976). There is a sharp decline in the number of radio sources at high power, called the RLF break, with a characteristic luminosity of L^*. Objects with radio luminosities above the RLF break are mainly FRII type, while below the break both FRI and FRII type objects can be found (e.g. Willott et al. 2001b). It has been shown (e.g. Dunlop & Peacock 1990; Willott et al. 2001b), that powerful extragalactic radio sources (well above the FRI/FRII break) undergo very strong number density evolution. On the other hand, less powerful sources evolve much less strongly (e.g. Clewley & Jarvis 2004; Mauch & Sadler 2007). These sources dominate the bright ($S_{1.4\mathrm{GHz}} > 1$ Jy) source counts, but at fainter flux densities (< 300 μJy) the counts flatten or possibly turn up, which is usually attributed to the appearance of a population of radio sources which does not contribute significantly at higher flux densities. This new population has been variously explained as being comprised of normal galaxies (Condon 1984), starburst galaxies (Windhorst et al. 1985), and low-luminosity radio galaxies (Wall et al. 1986). More recently (Jarvis & Rawlings 2004; Simpson et al. 2006), it has become clear that also 'radio quiet' quasars make an important contribution to population around ~ 100 μJy.

The RLF of radio galaxies and quasars is very similar up to redshifts $z \sim 2.5$, but there are ~ 100 times more radio-quiet quasars than radio-loud (e.g. Figure 2 of Rawlings 2000). This is probably due to the requirement of a minimum black-hole mass, perhaps linked to conditions necessary to generate SMBHs with large spin, and hence to develop a powerful jet.

Based on the RLF and the lifetimes of quasars of $\sim 10^8$ yr, every massive galaxy with

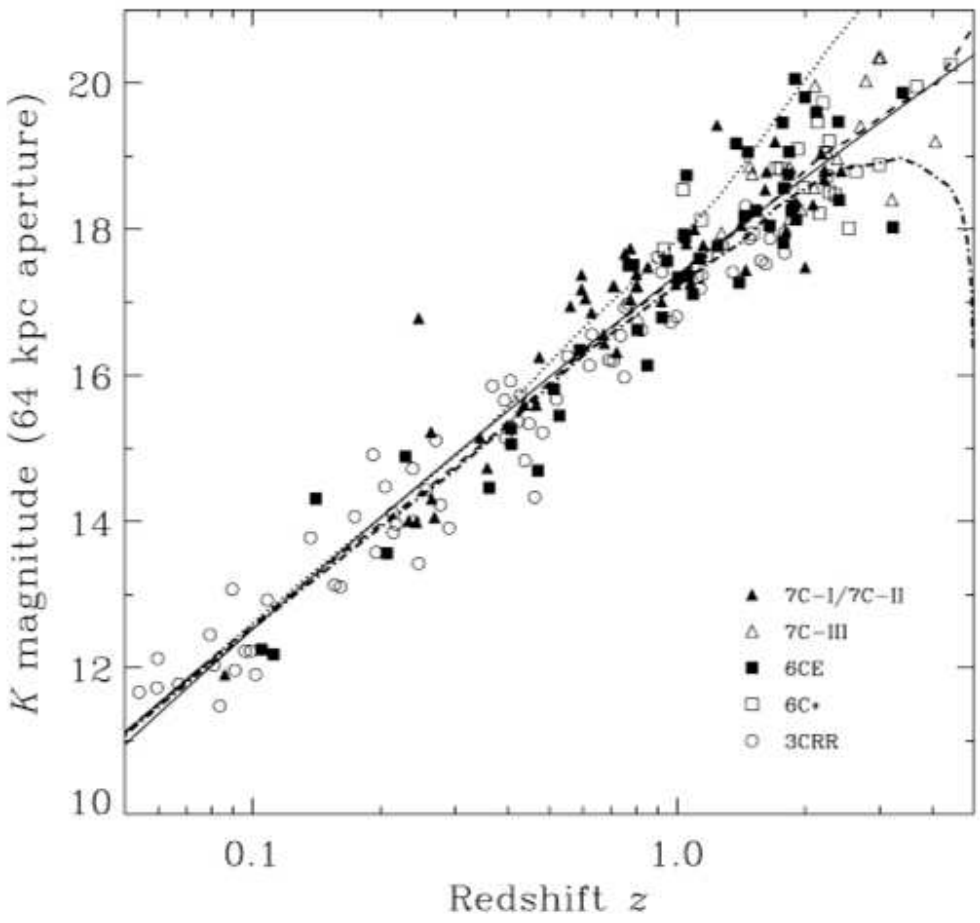

Figure 1.2: Hubble diagram at the K-band (plot from Willott et al. 2003): aperture- and emission-line-corrected K-band magnitude versus redshift z for radio galaxies from the 3CRR, 6CE, 6C* and 7CRS. The solid curve is the best-fitting second-order polynomial relationship between K and $\log_{10}(z)$ for all the data. This is similar to the apparent K magnitude of a galaxy of local luminosity 3 L^*, which forms all of its stars in an instantaneous burst at $z_\mathrm{f} = 10$ (dashed line). A similar model with $z_\mathrm{f} = 5$ (dot-dashed line) predicts that galaxies are much more luminous at $z > 3$. The no-evolution model for a 3 L^* galaxy (dotted) provides a poor fit to the $z > 1$ data.

$L \gtrsim L^*$ was plausibly a quasar at high redshift (e.g. Richstone et al. 1998) and ~ 1 in 100 of such galaxies spent time as a powerful radio source.

1.5 Host galaxies of radio sources

Scenarios of galaxy evolution for giant ellipticals – the only type of galaxy to host powerful radio sources – favour a model of a galaxy that formed all its stars at high redshift (e.g. $z > 5$) and evolved passively till now. This simply means that all the gas available in the galaxy formed the star population at the same time. Studies of radio sources in the near-infrared K-band (e.g. Willott et al. 2003), have shown that the host of radio sources in the 3CRR,

6CE, 6C* and 7CRS surveys agree best with a model of a passively evolving host galaxy, as can be seen in Figure 1.2; a no-evolution model is a poor fit to the $z > 1$ data. Radio sources in the redshift range $0.0 < z < 0.8$ (e.g. 3CRR, 6CE, 7CRS and TexOx-1000 surveys; McLure et al. 2004) are shown to have host luminosities in the range $0.7L^* < L < 10L^*$, with a mean of $3.2 \pm 0.3L^*$. Furthermore, for objects at $z < 1$ it has been shown that the host galaxies of all powerful radio-loud AGN are massive $L > L^*$ ellipticals (e.g. Taylor et al. 1996; McLure et al. 1999; Dunlop et al. 2003).

Hill & Lilly (1991) report of a substantial evolution in the environments of powerful radio sources from $z = 0$ to $z \approx 0.5$. Furthermore, it has been shown that the evolution of the central black hole and its host galaxy are related (e.g. Kormendy & Richstone 1995; Magorrian et al. 1998; Gebhardt et al. 2000; Ferrarese & Merritt 2000). This co-evolution, represented by the connections between galaxy physical properties and SMBH mass, implies that the accretion process in AGN has a powerful influence on galaxy evolution (e.g. Balmaverde, Baldi & Capetti 2008).

Radio sources are found in different environments, depending on their FR class. FRII radio sources reside in normal giant elliptical galaxies with absolute magnitudes near M^* of the Schechter luminosity function, whereas FRIs are often found in e.g D or cD galaxies. Ledlow & Owen (1996) find that both FRIs and FRIIs live in similar environments, but the properties of their host galaxies may strongly influence the structural appearance of the radio sources, at least for those near the division of the two classes. The host galaxies of FRI objects, when compared to those of FRII sources, are more luminous, have higher stellar velocity dispersions, rotate more slowly, have fewer 'disturbed' structures, and tend to be found in regions of high galaxy density.

1.6 Radio Surveys and connection to other wavebands

In search of a better way to determine the evolution of the radio-source population, and to study the RLF, many researchers have defined different redshift surveys using various samples at decreasing flux density limits. The first comprehensive study of the RLF was carried out by Dunlop & Peacock (1990) who used several complete samples selected at 2.7 GHz with flux

density limits between 2.0 and 0.1 Jy. For samples selected at low frequency the benchmark bright survey is the 3CRR survey (Laing, Riley & Longair 1983). Various fainter surveys have followed, like the Parkes Survey at 408 and 2700 MHz, but the most complete in spectroscopic redshifts soon after were the 6CE (Rawlings et al. 2001) and 7CRS samples (Willott et al. 2002).

The need for deeper observations and spectroscopically complete samples of lower radio flux densities that target the population at the RLF break at redshift $z \sim 2$, urged Willott et al. (2001b) to propose a new survey that would improve the results of the 3CRR, 6CE and 7CRS surveys. Thus the TexOx-1000 (TOOT) survey (Hill & Rawlings 2003; Vardoulaki et al. 2006) was designed, which observed radio sources from the 7C survey (Willott et al. 2001b) with a flux density limit of 100 mJy at 151 MHz.

Similar objectives drove the CENSORS survey of radio sources, which is a 1.4-GHz survey of radio sources at a flux density limit of 7.8 mJy (Best et al. 2003; Brookes et al. 2006), even reaching limits of 7.2 mJy (Brookes & Best 2004). The primary goal is to investigate the cosmological evolution of the radio luminosity function. This radio survey, combined with optical and near-IR observations is targeted to explore the nature of the $K - z$ relation and its dependence on the radio luminosity. Results reveal an offset to fainter K-band magnitudes when compared to the $K - z$ relation of Willott et al. (2003), as has also been shown for other samples, like the 6C* (e.g. Cruz et al. 2007).

Radio surveys at multi-radio frequencies include the work of Tasse et al. (2007) that used the low-frequency radio survey of the XMM Large-Scale Structure field (XMM-LSS; Pierre et al. 2004) to study the connection between extragalactic radio-source populations and their environment as traced by X-ray and optical emission. Their radio survey took place using the Giant Meterwave Radio Telescope (GMRT) at frequencies of 240 and 610 MHz, while the same sample was also observed at the Very Large Array (VLA) at 74 MHz (Cohen et al. 2003) and at 325 MHz (Tasse et al. 2006).

Study of the local RLF was obtained with samples of radio sources like the Second Instrumental Data Release of the 6-degree Field Galaxy Survey (6dFGS DR2; Mauch & Sadler 2007). This survey consists of objects with redshift between $0.003 < z < 0.3$, where 60% are fuelled

by star formation and 40% by a AGN powered by a SMBH. Study of the local RLF at 1.4 GHz revealed that radio-loud AGN preferentially inhabit the brightest and hence most massive host galaxies.

In the optical, various recent surveys of QSOs have taken place, in order to put constrains on the upper and lower limits of the QSO luminosity function (LF). Such a survey is the 2-degree Field QSO redshift survey (2QZ; Croom et al. 2004) held in the Anglo-Australian Telescope (AAT). Study of the optical luminosity function of QSOs shows a turn over, peaking at $z \sim$ 2-3, with declining QSO activity at higher redshifts (e.g. Fan et al. 2001), while the two power-law model fits the data well. Another QSO study, with 2dF QSOs at redshifts $0.4 < z < 2.6$ photometrically selected from the Sloan Digital Sky Survey (SDSS; Gunn & Weinberg 1995) on the AAT (2SLAQ; Croom et al. 2009), was designed to prove the faint end of the QSO LF, one magnitude deeper than the 2QZ. This survey reveals a flattening of the QSO LF towards faint absolute magnitudes. Furthermore, they find clear evidence that the number density of faint QSOs peaks at lower redshift ($z < 1$) than bright QSOs, while brighter QSOs peak at $z > 2$.

With the introduction of X-ray telescopes, like Chandra and *XMM-Newton* (Weisskopf et al. 2002 and Watson et al. 2003 respectively), studies of the cosmological evolution of the AGN LF is not just limited to optical observations. X-ray studies suggest of a luminosity dependence of the X-ray LF (XLF), with many authors also including faint objects in their studies (e.g. Aird et al. 2010; Ueda et al. 2003). Silverman et al. (2008) found that at $z > 3$ there is a significant decline in the numbers of AGNs with an evolution rate similar to that found by studies of optically selected QSOs. Two models have been proposed to describe this evolution: a pure luminosity evolution (PLE) parametrization and a luminosity-dependent density evolution model (LDDE). Several authors (e.g. Silverman et al. 2008; La Franca et al. 2005) suggest that the LDDE model describes the AGN XLF the best. In particular, La Franca et al. (2005) found that low-luminosity AGNs ($L_{\rm X} \sim 10^{43}$ erg s^{-1}) peak around redshift $z \sim 0.7$, while high-luminosity AGNs ($L_{\rm X} > 10^{45}$ erg s^{-1}) peak at the higher redshift of $z \sim 2$, agreeing with results based on optical surveys.

Surveys in the near-IR, such as the UKIRT Infrared Deep Sky Survey (UKIDSS; Lawrence

et al. 2007), are designed to provide deeper observations. UKIDSS observations in five filters, ZYJHK covering the wavelength range 0.83 - 2.37 μm, can improve the view of the near-IR sky seen by 2MASS. Amongst the scientific goals, is the better understanding of AGN, while observing optically obscured or distant objects can be easier with deeper near-IR observations.

A breakthrough in observational astronomy was obtained with the Spitzer Space telescope (Lonsdale et al. 2003), which provides observations in the mid-IR enabling us to observe objects obscured by dust in the optical wavebands, like highly obscured AGN (e.g. Ogle, Whysong & Antonucci 2006; Lacy et al. 2004, 2005). SWIRE, the Spitzer Wide-area Infrared Extragalactic legacy survey (Lonsdale et al. 2003) gives observations in the mid-IR over 50 deg^2, 6 regions and 4 bands (3.6 - 8 μm) with the Infrared Array Camera (IRAC; Fazio et al. 1998) and 3 bands (24 - 160 μm) with the Multiwaveband Imaging Photometer (MIPS; Rieke et al. 2004).

Some results from the study of AGN using Spitzer data include the work of Cleary et al. (2007) that studied 3CRR galaxies and quasars at redshifts $0.4 \leq z \leq 1.2$ with the Spitzer Infrared Spectrograph (IRS; Houck et al. 2004) at 15-37 μm and the MIPS at 24, 70 and 160 μm. They found that quasars are more luminous in the mid-IR than galaxies because of a combination of Doppler-boosted synchrotron emission in quasars and extinction in galaxies, both orientation-dependent effects. Spitzer IRS spectroscopy of radio galaxies and quasars enabled the study of the central engines of AGN (Ogle, Antonucci & Whysong 2007).

In the sub-millimetre (sub-mm), recent surveys aim to shed light on sub-mm sources that harbour AGN. An example is the Submillimetre Common-User Bolometer Array (SCUBA) HAlf Degree Extragalactic Survey (SHADES; Mortier et al. 2005), which is a major new blank-field extragalactic sub-mm survey at the James Clerk Maxwell Telescope (JCMT). Some of the goals of the survey were to investigate the population of high-redshift sub-mm galaxies, as well as the clustering properties of submm-selected galaxies in order to determine whether these objects could be progenitors of present-day massive ellipticals (e.g. Mortier et al. 2005). Data from this survey have been combined with multiwavelength observations (e.g from the VLA, Spitzer, UKIRT, XMM-Newton, etc), in order to provide complete photometric redshift information and detailed spectral energy distributions for most of the sub-mm selected sources.

Observations at X-ray wavelengths with *XMM-Newton* (e.g. Watson et al. 2003) proved

helpful since they target the bulk of the objects that contribute to the X-ray background. The soft X-ray sky is dominated by broad-line AGN (since soft X-rays are readily absorbed by gas, and Type-2 AGN are observed though dust and hence gas). The X-ray background has a hard X-ray spectrum and is mainly generated by Type-2 narrow-line AGN (e.g. Page et al. 2007).

1.7 Cosmology

Initially, describing the Universe was done from a qualitative point of view, but as observations grew alongside theories, it has become more quantitative and astronomers have found the need to introduce new parameters and models in order to describe it properly. One of the stronger models to be proposed was the 'cosmological principle', that requires the Universe to be homogeneous and isotropic everywhere but not at every time. Even more strictly, the steady state cosmology of Hoyle (1949) does not allow any changes even with time; one of the uses of quasars is to rule out steady state cosmology since they evolve in this cosmology (Weedman 1968). Observational cosmology is directed towards determining just how large a volume of the Universe must be studied to consider it truly representative of the whole.

In order to describe the properties of the Universe one needs to understand what it is made of and then parametrise it.

The Universe consist of *Baryons*, that are particles made of three quarks, *Electromagnetic Radiation* that pervades the Universe in the form of photons ($E = \mathrm{h}\, v$; h is the Plank constant), *Neutrinos*, weakly interacting particles with a non-zero rest mass (Fukuda et al. 1998), and *Dark matter & dark energy*, the two big questionmarks about the content of our Universe. The effects of dark matter can be seen through observations, like in the light curves of galaxies, but cannot be as yet measured. Furthermore, the observable matter in clusters of galaxies is not enough to create a gravitational field that would hold them together. Hence it is believed unseen dark matter accounts for the remaining mass. Dark energy has been proposed to account for the accelerating expansion of the Universe. It is unknown whether it is constant throughout the Universe or whether it varies in space and time. The properties of dark energy are investigated by observing its effects on the Universe. Dark energy currently makes up $\sim 72\%$ of the energy density of the Universe, while $\sim 23\%$ is dark matter; only 5% is normal matter. The following

discussion closely follows material in Liddle (2004) and Peacock (1999).

There is overwelming observational evidence that the Universe is expanding. Everything is moving away from the observer at velocities measured via the redshift, which is basically the Doppler effect applied to light waves:

$$z = \frac{\lambda_{\rm obs} - \lambda_{\rm em}}{\lambda_{\rm em}}, \tag{1.1}$$

where $\lambda_{\rm obs}$ is the observing wavelength and $\lambda_{\rm em}$ the emitted one. The formula describing the speed with which objects are receding from us is:

$$z = \frac{\upsilon}{c}; \upsilon \ll c, \tag{1.2}$$

or the relativistic version[3]

$$1 + z = \sqrt{\frac{1 + \upsilon/c}{1 - \upsilon/c}}. \tag{1.3}$$

The rate of recession of an object is described by the Hubble law:

$$\vec{v} = H_0 \, \vec{r}. \tag{1.4}$$

which is based on the cosmological principle and does not work very well for very nearby objects that have random motions (e.g. the Milky Way's nearest massive neighbour, M31, is blue-shifted because of gravitational infall in the Local Group). It seems, though, that it describes the average behaviour of galaxies extremely well. H_0 is the Hubble constant that tells us the present expansion of the Universe, and can be parametrised as:

$$H_0 = 100 \; h \text{ km s}^{-1} \text{ Mpc}^{-1}, \tag{1.5}$$

where the value of the parameter h reflects residual uncertainty. Just a few years ago, a controversy raged for the accurate value of H_0, placing it between 50 to 100 km s^{-1} Mpc^{-1}. As better observations came in hand, the Hubble constant took the value of 71 $\pm$ 5% km s^{-1}

[3]This equation does not apply to distant objects since further considerations must be taken into account.

Mpc^{-1} as shown by the Wilkinson Microwave Anisotropy Probe (WMAP; e.g. Nolta et al. 2004). H_0 has units of $[\mathrm{time}]^{-1}$, and gives the Hubble time:

$$H_0^{-1} = 9.77\ h^{-1} \times 10^9 \mathrm{yr}. \tag{1.6}$$

In order to quantify the expansion of the Universe we need the Friedmann equation, which can be crudely understood using pseudo-Newton arguments: in a spherically-symmetric distribution of matter, a particle feels no force at all from the material at greater radii, and the material at smaller radii gives exactly the force which one would get if all the material was concentrated at the central point. The standard form for the Friedmann equation is:

$$\frac{\dot{R}}{R} = \frac{8\pi G}{3}\rho - \frac{kc^2}{R^2}, \tag{1.7}$$

where k is a constant, unchanging with either time or space and has units of $[\mathrm{length}]^{-2}$; c is the speed of light; R is the scale factor that measures the expansion rate of the Universe; and ρ is the mass density of the expanding medium. Furthermore, k is the curvature of the Universe. An expanding Universe has a unique value of k, which is retained throughout its evolution. The expansion of the Universe means that as time goes by objects move further away from each other.

The geometry of the Universe is quantified using its curvature k. For $k > 0$ we have a spherical geometry giving a closed Universe, for $k = 0$ we have a flat geometry and thus a flat Universe, and finally, for $k < 0$ we have a hyperbolic geometry and an open Universe. Results from WMAP have shown that the curvature of space is within 1% of flat.

The Friedmann equation can be re-written as:

$$H^2 = \frac{8\pi G}{3}\rho - \frac{kc^2}{R^2}, \tag{1.8}$$

where H is the Hubble parameter. Introducing the cosmological constant Λ in the Friedmann equation as an extra term gives:

$$H^2 = \frac{8\pi G}{3}\rho - \frac{kc^2}{R^2} + \frac{\Lambda}{3}, \tag{1.9}$$

where Λ has units of [time]$^{-2}$ if we use the assumption $c^2 = 1$. Λ was originally introduced by Einstein in order to balance curvature and get a static Universe; this idea though is rather misguided since such a balance proves to be unstable to small perturbations and could not arise in practice. Nowadays, the cosmological constant is most often discussed in the context of Universes with the flat Euclidean geometry, $k = 0$.

The density parameter is used to specify the density of the Universe. The critical density required to make the Universe flat in the absence of Λ is:

$$\rho_{\rm c}(t) = \frac{3H^2}{8\pi G} \tag{1.10}$$

The dimensionless quantity that describes the density of the Universe compared to its critical density is:

$$\Omega(t) \equiv \frac{\rho}{\rho_{\rm c}} \tag{1.11}$$

The present value of the density parameter is denoted $\Omega_{\rm M}$. Using the above equations (Eqn. 1.10 & 1.11) and Friendmann equation (Eqn. 1.8) one can write:

$$\Omega - 1 = \frac{kc^2}{R^2H^2} \tag{1.12}$$

This notation can be used for every type of matter in the Universe, not only for the total density (e.g $\Omega_{\rm mat}$ or $\Omega_{\rm rad}$). The case $\Omega = 1$ is special, since $k = 0$, and is called a critical-density Universe.

Also useful is to define the density parameter for the cosmological constant as:

$$\Omega_\Lambda = \frac{\Lambda}{3H^2} \tag{1.13}$$

and thus (from Eqn. 1.9, 1.10 & 1.13):

$$\Omega + \Omega_\Lambda - 1 = \frac{kc^2}{R^2H^2}. \tag{1.14}$$

For a flat Universe where $k = 0$, Eqn. 1.14 becomes:

$$\Omega + \Omega_\Lambda = 1 \tag{1.15}$$

The Friedmann equation is often written is the following form using density parameters:

$$\frac{H^2}{H_0^2} = \Omega_{\rm R}\alpha^{-4} + \Omega_{\rm M}\alpha^{-3} + \Omega_{\rm k}\alpha^{-2} + \Omega_\Lambda, \tag{1.16}$$

where α is the normalised scale factor that is defined as $\alpha(t) \equiv R(t)/R_0$, so that $\alpha = 1$ at present; $\Omega_{\rm R}$ is the radiation density today (i.e. when $\alpha = 1$); $\Omega_{\rm M}$ is the matter (dark plus baryonic) density today; Ω_k = 1 - Ω is the spatial curvature density today; and Ω_Λ is the cosmological constant or vacuum density today (e.g. Peacock 1999). For flat $k = 0$ Universe $\sum \Omega_{\rm i} = 1$ at all times. The models normally considered are either matter-dominated with Ω_Λ = 0, or models assuming flat Universe with $k = 0$ and $\Omega_{\rm M} + \Omega_\Lambda = 1$.

Research has shown that the Universe is expanding at a specific rate which is changing with time, given by the Hubble parameter (H). The quantity that quantifies that rate is the deceleration parameter q, where the larger the value the more rapid the deceleration. The deceleration parameter is:

$$q \equiv -\frac{R(t)\ddot{R}(t)}{\dot{R}^2(t)}, \tag{1.17}$$

with q_0 the value today. By using the Friedmann equation, this can be written as:

$$q = \frac{\Omega_{\rm M}}{2} + \Omega_{\rm R} - \Omega_\Lambda. \tag{1.18}$$

The simplest situation is when the Universe is matter dominated, and then one can write:

$$q_0 = \frac{\Omega_{\rm M}}{2}. \tag{1.19}$$

This suggests that a measurement of q_0 gives a value to the total density of matter in the Universe $\Omega_{\rm M}$. Including the cosmological constant Λ gives:

$$q_0 = \frac{\Omega_{\rm M}}{2} - \Omega_\Lambda. \tag{1.20}$$

Futhermore, the deceleration gives us an idea of how large the Universe was when it was younger, and thus measurements of the number of galaxies at large distances could give a measurement for q_0. According to most recent observations (e.g. WMAP or type Iα supernova), q_0 is negative and thus the Universe is accelerating, and corresponds to $\Omega_\Lambda > 1/3$.

The age of the Universe is given by:

$$H_0 t_0 = \frac{2}{3} \frac{1}{\sqrt{1-\Omega_\mathrm{M}}} \sinh^{-1} \left[\sqrt{\frac{1-\Omega_\mathrm{M}}{\Omega_\mathrm{M}}} \right]. \tag{1.21}$$

The most recent measurement for the age of the Universe comes from WMAP, and is 13.73 Gyr to within 1%.

1.7.1 Observational Cosmology

The redshift is defined as the ratio of scale factors at present and at emission $R_0/R \equiv 1+z$, and thus changes with time.

One of the most useful equations in observational cosmology is the one between monochromatic flux density and luminosity. Assuming isotropic emission, then the flux density at the observed frequency ν_0 is:

$$S_\nu(\nu_0) = \frac{L_\nu[(1+z)\nu_0]\ (1+z)}{4\pi D_L^2}, \tag{1.22}$$

where L_ν is the luminosity at the emitted frequency $\nu_0(1+z)$, measured in units of W Hz^{-1}; in the case where the luminosity is emitted into unit solid angle, the factor 4π is not used and the units of L_ν are W Hz^{-1} sr^{-1}. D_L is the luminosity distance measured in parsecs (pc), and is a way of expressing the amount of light received from a distant object; it is not the actual distance to the object, since the geometry of the Universe need not be flat and because the Universe is expanding.

The flux density is often expressed in units of Jansky (Jy), where 1 Jy $\equiv 10^{-26}$ W m^{-2} Hz^{-1}. Instead of the frequency as a measure of bandwidth, one can use wavelength to express the flux density:

$$S_\lambda = \left|\frac{d\nu}{d\lambda}\right| S_\nu = \frac{c}{\lambda^2} S_\nu, \tag{1.23}$$

The luminosity distance is often defined in terms of absolute magnitude M and apparent magnitude m of an object:

$$m = M + 5log_{10}\left(\frac{D_L}{10\mathrm{pc}}\right) - 2.5\log_{10}(1+z) + \mathrm{K}(z) + \mathrm{E}(z), \tag{1.24}$$

where $\mathrm{K}(z)$ is the K-correction, that corrects for the fact that absolute magnitudes in cosmology are affected by a shift of the spectrum in frequency. $\mathrm{E}(z)$ is the evolutionary correction that accounts for changes in the object's colour and luminosity between the time the light was emitted and today; spectrophotometric evolution can be estimated by predicted galaxy spectra as function of time, as for example from stellar synthesis codes like the one in Bruzual & Charlot (1993; 2003). K-corrections allow transforming the observed measurements at a redshift z into a standard measurement at redshift zero. This correction depends on the filter that was used for the observations, the filter used as a rest-frame standard, the shape of the spectral energy distribution (SED) of the galaxy, and the redshift. The K-correction at a given bandpass is given by:

$$\mathrm{K}(z) = -2.5\log_{10}\left(\frac{\int \mathrm{I}(\lambda/1+\mathrm{z})\mathrm{S}(\lambda)\mathrm{d}\lambda}{\int \mathrm{I}(\lambda)\mathrm{S}(\lambda)\mathrm{d}\lambda}\right), \tag{1.25}$$

where $\mathrm{S}(\lambda)$ is the transmission curve of the filter.

The latest values for a ΛCDM cosmological model, as given by the 5-year WMAP results (Dunkley et al. 2009) are $h = 0.719^{+0.026}_{-0.027}$, $\Omega_\mathrm{M} = 0.258 \pm 0.030$ and $\Omega_\Lambda = 0.742 \pm 0.030$. For this DPhil thesis the adopted cosmology is for a low-density, Λ-dominated Universe in which $H_0 = 70$ km s^{-1}Mpc^{-1}, $h = 0.7$, $\Omega_\mathrm{M} = 0.3$ and $\Omega_\Lambda = 0.7$.

1.8 Chapter description

This DPhil thesis studies two samples of radio sources, the SXDS radio sources (Vardoulaki et al. 2008) presented in Chapter 2 and the TOOT00 radio sources (Vardoulaki et al. 2009) in Chapter 3. Further analysis of the two samples together is given in Chapters 4, 5 & 6. In

particular, Chapter 4 is a study of possible redshift spikes in the redshift distributions of the SXDS and TOOT00 radio-sources samples. Chapter 5 shows a near-infrared (K-band) study of these two samples, and presents the $K - z$ diagram as well as comparison with previous surveys; the radio structures of the objects are also discussed. Finally, Chapter 6 studies the accretion indicators and the radio structure in the TOOT00 and the SXDS radio-source samples. Chapter 7 presents the conclusions of the thesis and some brief discussion on future radio telescopes. Appendix A includes notes on the SXDS objects and is attached to Chapter 2. Appendix B includes notes on the TOOT00 objects and is attached to Chapter 3. Appendix C is attached to Chapter 4 and includes extra tables connected to the discussion. Appendix D gives a brief discussion on the statistics used in the analysis and is located after Chapter 7.

This chapter has been published as: Vardoulaki, E., Rawlings, S., Simpson, C., Ivison, R. J., Ibar, E. (2008). 'Radio imaging of the Subaru/XMM-Newton Deep Field -II. The 37 brightest radio sources', MNRAS 387(2), 505-535. [The definitive version of the article is available at http://dx.doi.org/10.1111/j.1365-2966.2008.13246.x via http://www3.interscience.wiley.com].

Chapter 2

The Subaru/*XMM-Newton* Deep Field - II. The 37 brightest radio sources

Abstract

We study the 37 brightest radio sources in the Subaru/*XMM-Newton* Deep Field (SXDF). We have spectroscopic redshifts for 24 of 37 objects and photometric redshifts for the remainder, yielding a median redshift $z_{\rm med}$ for the whole sample of $z_{\rm med} \simeq 1.1$ and a median radio luminosity close to the 'FRI/FRII' luminosity divide. Using mid-IR (Spitzer MIPS 24 μm) data we expect to trace nuclear accretion activity, even if it is obscured at optical wavelengths, unless the obscuring column is extreme. Our results suggest that above the FRI/FRII radio luminosity break most of the radio sources are associated with objects that have excess mid-IR emission, only some of which are broad-line objects, although there is one clear low-accretion-rate object with an FRI radio structure. For extended steep-spectrum radio sources, the fraction of objects with mid-IR excess drops dramatically below the FRI/FRII luminosity break, although there exists at least one high-accretion-rate 'radio-quiet' QSO. We have therefore shown that the strong link between radio luminosity (or radio structure) and accretion properties, well known at $z \sim 0.1$, persists to $z \sim 1$. Investigation of mid-IR and blue excesses shows that they are correlated as predicted by a model in which, when significant accretion exists, a torus of dust absorbs $\sim$30% of the light, and the dust above and below the torus scatters $\gtrsim$1% of the light.

2.1 Introduction

There is growing evidence that all massive galaxies contain a supermassive black hole (SMBH) at their centres (Ferrarese & Merritt 2000; Gebhardt et al. 2000; Magorrian 2006), which implies that these galaxies have all undergone at least one episode of AGN activity. It is believed that this AGN activity is the observational manifestation of feedback processes regulating galaxy and cluster evolution (Best et al. 2005). At low redshifts radio jets emerge from the vicinities of these black holes, where there are indications for a 'duty cycle' for active jet activity that varies from $\sim 0.1 \rightarrow 0.3$ over the 1.4-GHz luminosity range $L_{1.4\mathrm{GHz}} \sim 8 \times 10^{23} \rightarrow 8 \times 10^{21} \mathrm{WHz}^{-1}\mathrm{sr}^{-1}$ – a critical range as it provides a significant fraction ($\sim$25%) of the luminosity density of the population.

Powerful ($L_{1.4\mathrm{GHz}} > 8 \times 10^{23} \mathrm{WHz}^{-1}\mathrm{sr}^{-1}$) radio sources are more common at high ($z \gtrsim 1$) redshifts. They are believed to have central SMBHs with uniformly high accretion rates at the highest radio luminosities and relatively low duty cycles (e.g. Rawlings & Saunders 1991). Low-luminosity radio jets can, however, be associated with high-accretion-rate systems, and these so-called 'radio-quiet' quasars appear to have similar FRI-like radio structures to the low-accretion-rate counterparts of similar radio luminosity objects (e.g. Heywood, Blundell & Rawlings 2007). At low redshift, the most massive ($\gtrsim 10^8 \mathrm{M}_\odot$) SMBHs typically have very low accretion rates with systematically higher average values at $z \gtrsim 2$, the so-called 'quasar epoch' (Yu & Tremaine 2002). These observational results fit in with theoretical ideas that a 'quasar mode' of feedback is prevalent in the distant universe, and that a 'radio mode' of feedback is dominant at low redshift (e.g. Croton et al. 2006).

In the unified model for AGNs (e.g. Antonucci 1993), the central region is surrounded by a dusty torus which absorbs light and re-emits it in the infrared. Above and below the plane of the torus, dust scatters light yielding a blue excess (di Serego Alighieri et al. 1993; Tadhunter et al. 1992; Cimatti et al. 1993; Jannuzi et al. 1995). Such mechanisms make it difficult to observe objects viewed through the torus directly in the optical, UV and soft X-rays. The torus creates anisotropic obscuration of the central regions resulting in two different types of observed objects, type 1 that are viewed face-on and type 2 that are viewed edge-on. Here we use mid-IR observations to search for evidence of accretion in a manner which is far less

dependent on orientation. Note, however, that there are claims that hot-dust emission is mildly anisotropic due to the effects of high optical depths and a toroidal geometry (Granato & Danese 1994).

Through the years, there have been many attempts to classify radio sources according to their observed properties: e.g. their structure, energy output and environment. Fanaroff & Riley (1974) classified radio sources according to their structure by measuring the ratio of distance between the regions of highest surface brightness on opposite sides of the central galaxy or quasar to the total extent of the source up to the lowest brightness contour $R_{\rm FR}$. This way, for FRI radio sources we get $R_{\rm FR} < 0.5$ which makes them edge-darkened, while FRIIs have $R_{\rm FR} > 0.5$ meaning they are edge-brightened. Furthermore, they found a strong correlation of structure with radio luminosity: above $\log_{10}(L_{178\rm MHz}/\rm WHz^{-1}sr^{-1}) \approx 25$ ($H_0 = 50$ km s^{-1}Mpc^{-1}, $\Omega_{\rm M} = 1$ and $\Omega_\Lambda = 0$)[1] lie the FRIIs, and below that the FRIs.

Ledlow & Owen (1996) found that both FRIs and FRIIs live in similar environments, but the properties of their host galaxies may influence the structural appearance of the radio sources, at least for those near the division of the two FR classes. A more refined division of radio sources by structure is the one appearing in Owen & Laing (1989). In this case we have Classical Double (CD), Twin Jet (TJ) and Fat Double (FD) radio sources: CDs correspond to FRIIs, TJs to FRIs and FDs to FRI/FRII division objects. Study of the 3CRR, 6CE, 7CRS and TOOT radio samples at $z \sim 0.5$ (McLure et al. 2004) is consistent with the low-redshift result of Owen & Laing (1989) that FRI (FD & TJ) sources reside in hosts which are on average $\simeq 0.5$ mag brighter than those of classical double/FRII sources of comparable radio luminosity.

Other classification schemes, such as the 'dual-population' model (e.g. Jackson & Wall 2001), divide objects according to nuclear accretion rate following the pioneering study of Hine & Longair (1979). The less radio-luminous population is composed of FRIs and FRIIs with weak or absent narrow emission lines, and the more radio-luminous population of strong narrow-emission-line FRII radio galaxies and broad-line quasars, where the division is at $\log_{10}(L_{178\rm MHz}/\rm WHz^{-1}sr^{-1}) \approx 26$ ($H_0 = 70$ km s^{-1}Mpc^{-1}, $\Omega_{\rm M} = 0.3$ and $\Omega_\Lambda = 0.7$) and corresponds to the Radio Luminosity Function (RLF) break (e.g. Dunlop & Peacock 1990).

[1]This corresponds to $\log_{10}(L_{178\rm MHz}/\rm WHz^{-1}sr^{-1}) \approx 25$ in our adopted cosmology ($H_0 = 70$ km s^{-1}Mpc^{-1}, $\Omega_{\rm M} = 0.3$ and $\Omega_\Lambda = 0.7$) at the typical redshift ($z \simeq 0.1$) of the FRI/FRII division from the Fanaroff & Riley (1974) study.

Best et al. (2003) investigated the dual-population scheme for radio sources using the CENSORS sample, selected from the 1.4 GHz NVSS survey (Condon et al. 1998).

Ogle et al. (2006) studied a sample of FRII narrow-line radio galaxies from the 3CRR survey at redshifts $z < 1$, in order to investigate whether they host hidden quasar nuclei. They found that in most of these radio galaxies, absorption in the mid-IR is present due to dust from a molecular torus. Almost half of their sample of narrow-line FR II radio galaxies is weak at 15 or 30 μm, contrary to single-population unification schemes. They conclude that mid-IR weak radio galaxies may constitute a separate population of jet-dominated sources with low accretion power. In Vardoulaki et al. (2006) we expressed the need to study radio sources in the mid-IR in order to investigate the existence of any hidden accretion activity in low-luminosity radio sources. Spitzer observations at 24 μm are ideal for this task, since they trace warm dust emission which can be obscured only by extreme columns (Ogle et al. 2006).

To address this important issue, we have looked at a complete sample of radio sources in the Subaru/*XMM-Newton* Deep Field (SXDF). The sample studied here is the 37 brightest radio sources from the VLA survey (SXDS) of the SXDF (Simpson et al. 2006) with flux densities greater than 2 mJy at 1.4 GHz. In Section 2.2 we present new data taken on the SXDS radio sources, namely optical and near-infrared imaging and spectroscopy. We also present a cross-correlation with the radio sample of Tasse et al. (2006), who observed this sky region at 325 MHz, as well as GMRT observations at 610 MHz (Section 2.2). Section 2.3 presents the analysis of our sample including K-band/radio overlays (Section 2.3.1), photometric redshift estimation (Section 2.3.2), and the classification of the SXDS-based sample according to optical and infrared data (Section 2.3.3). In Section 2.4 we discuss accretion indicators, based on our optical/infrared radio-source classification. In Section 2.5 we present the conclusions of our study. Finally, in Appendix A (Section 2.6), we describe properties of each radio source individually.

We adopt a radio spectral index $\alpha = 0.8$ ($S_\nu \propto \nu^{-\alpha}$), unless a spectral index could be calculated using the 1.4 GHz, 610 MHz and 325 MHz data. We assume throughout a low-density, Λ-dominated Universe in which $H_0 = 70$ km s^{-1}Mpc^{-1}, $\Omega_{\rm M} = 0.3$ and $\Omega_\Lambda = 0.7$.

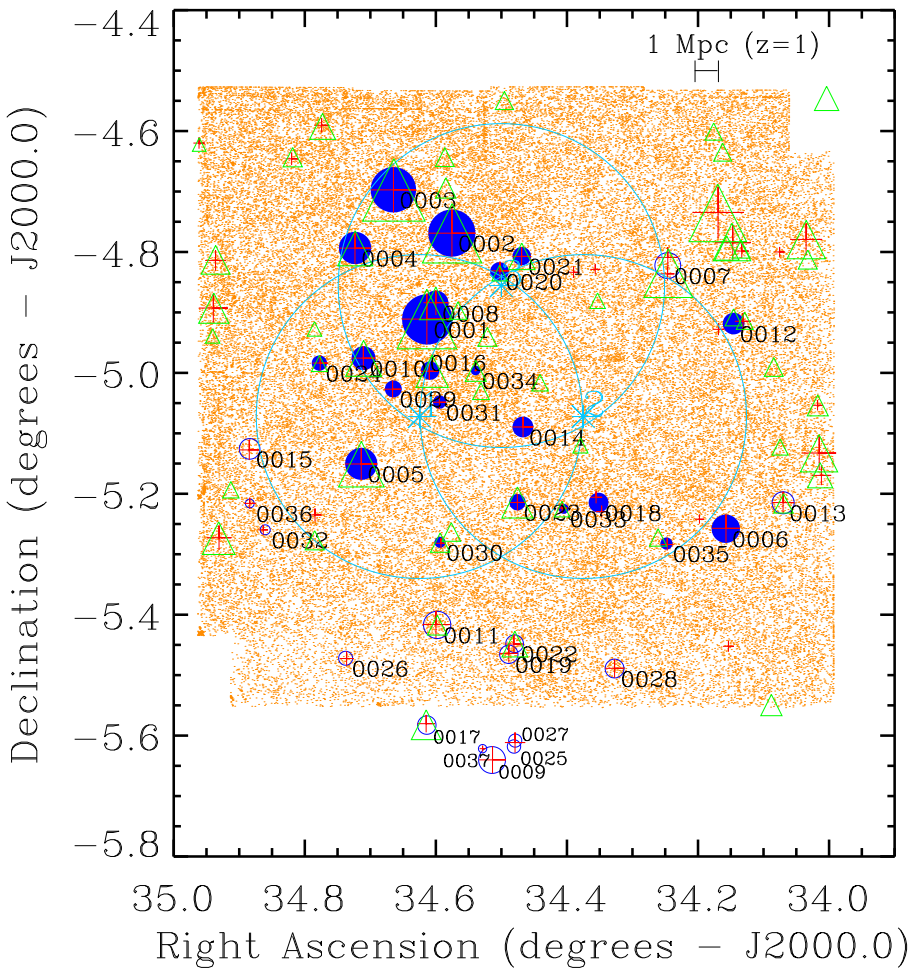

Figure 2.1: Sky positions of the 37 brightest radio sources in the SXDS (blue circles); these are scaled by the logarithm of the integrated flux density at 1.4 GHz from the VLA observations of Simpson et al. (2006) starting at $S_{1.4\mathrm{GHz}} = 2$ mJy. The shaded area shows the UKIDSS-UDS (Lawrence et al. 2007) coverage. Note that sxds_0009, sxds_0017, sxds_0025, sxds_0027 and sxds_0037 lie outside the UDS coverage. Light-blue stars are the VLA A-array pointing positions and big light-blue circles the FWHM points of the primary beam of the VLA primary beam; objects inside these regions have reasonable quality A-array maps and are highlighted with filled blue circles. Green triangles are the 325 MHz sources ($S_{325\mathrm{MHz}} \gtrsim 4$ mJy) in this area (Tasse et al. 2006). Red crosses are NVSS (Condon et al. 1998) sources in the same sky area, again with the symbol size scaled by the logarithm of the NVSS flux density starting at 2 mJy. The 1 Mpc bar shows the proper physical size of a 1 Mpc-long ruler at $z = 1$.

2.2 Data and Observations

Optical and X-ray observations of the SXDF (Figure 2.1) were made within the 1.3 square degree Subaru/*XMM-Newton* Deep Field with Subaru and *XMM-Newton* respectively. A follow-up deep radio imaging survey at 1.4 GHz was conducted with the Very Large Array (VLA) in B and C configurations (Simpson et al. 2006). A-array observations are also available (Ivison et al. 2007). The total radio catalogue, hereafter the SXDS, covers 0.8 deg^2 to a peak flux density limit of 100 μJy at 1.4 GHz.

The Subaru–XMM-Newton Deep Field (SXDF) has excellent multi-wavelength coverage, having been observed in X-rays with the XMM-Newton satellite (Ueda et al. 2008), in the optical $BVRi'z'$ bands with Suprime-Cam on the Subaru telescope (Sekiguchi 2004), in the near infrared J and K bands as part of the UKIRT Infrared Deep Sky Survey Ultra-Deep Survey (UKIDSS - UDS; Lawrence et al. 2007), in all of the Spitzer IRAC (3.6, 4.5, 5.8 and 8.0 μm) and MIPS (24, 70 and 160 μm) bands as part of the Spitzer Wide-area Infra-Red Extragalactic (SWIRE) survey Lonsdale et al. (2003) and at sub-mm wavelengths (450 μm and 850 μm; Mortier et al. 2006 & Aretxaga et al. 2007). The area is large (for such a deep survey), at approximately 1 square degree in the optical and near-infrared, although the coverage varies between the different wavebands. The UDS covers approximately 0.8 deg^2 centred on the SXDF.

We study here the brightest 37 radio sources from the 1.4 GHz SXDS (Simpson et al. 2006); these are named, hereafter, sxds_0001 to sxds_0037 in decreasing order of 1.4-GHz flux density. Table 2.1 gives basic information about our sample, like their radio position, flux density, redshift, optical and radio classification, spectral index, angular size and K (2.2 μm) magnitude (in the AB magnitude system). We adopt the radio structure classification from Owen & Laing (1989), using the VLA data to classify objects as CD, TJ, FD or COM (compact) radio sources. Wherever available, we used the A-array data to determine whether an object has compact hotspots and is therefore a 'CD': in the few cases where this classification is uncertain, because of no available A-array data, we took our best guess based on the appearance of the B-array map and marked the classification with a '?'. Details of the optical classification are presented in Section 2.3.3.

In Table 2.2 we give the result of optical spectroscopy of the SXDS radio sources. We have $\approx$ 65% (24 out of 37) completeness in spectroscopic redshifts, with the spectra shown in Figure 2.7. Table 2.2 summarises spectroscopic observations carried out on the SXDS objects using either the ISIS spectrograph on the WHT telescope, FOCAS on the SUBARU, 2dF or AAOmega on the AAT, VIMOS on the ESO-VLT, SITe1 on the Magellan 2 or DEIMOS on the Keck 2. Calculation of redshifts from VIMOS spectra were done by using the FXCOR cross-correlation task in IRAF with SDSS galaxy templates (Simpson et al. in prep), apart from sxds_0025 where the cross-correlation failed (see Section 2.6 in Appendix A). FOCAS spectra have been corrected for atmospheric absorption. The object sxds_0016 has spectroscopy obtained with the DEep Imaging Multi-Object Spectrograph (DEIMOS) on the Keck 2 telescope (van Breukelen et al. 2007).

Table 2.3 presents the blueness and mid-IR excess, the radio luminosity at 1.4 GHz $L_{1.4\mathrm{GHz}}$,

the luminosity at 24 μm $[\lambda L]_{24\mu\mathrm{m}}$ and basic quantities for the SXDS radio sources used in the analysis (see Section 2.4.1).

Optical and infrared photometric data were used to create SEDs for our objects as shown in Figure 2.7. Thirteen of our objects are not as yet spectroscopically confirmed, so we use photometric redshifts for our analysis (Section 2.3.2). In Figure 2.1 we have shown the sky area occupied by the 37 radio sources in our sample. We are confident that our sample is fairly complete. A NVSS-selected 2-mJy sample in the same area gets 34 of the 37 SXDS sources, and the other four lie just below the formal NVSS 2.3 mJy flux density limit.

In order to calculate spectral indices for our sample we use either the 325 MHz catalogue of Tasse et al. (2006), or the 610 MHz flux densities from Ibar et al. (2009), taking into account the radio-source structure from the A/B-array maps.

Tasse et al. (2006) surveyed the XMM-LSS field (Pierre et al. 2004) in A- and B-array VLA configurations at 325 MHz (see Section 6 of Tasse et al. 2006). To minimise the effect of Doppler-boosted emission, we would ideally have selected our objects at 325 MHz, but this survey was unavailable at the time the selection was made. We have, however, subsequently cross-matched the 325 MHz sample with the whole 1.4 GHz radio catalogue. The resolution of the 325 MHz data is 6.7 arcsec and it has a median 5σ sensitivity of 4 mJy beam^{-1}. Figure 2.1 shows the 325-MHz sources that are in a sky area somewhat larger than our SXDS sample. From our 37-source sample only 22 match with the 325 MHz catalogue. For all of the matching objects we calculate radio spectral indices using the 1.4 GHz and 325 MHz flux densities. Limits on the spectral indices are calculated assuming a $S_{325\mathrm{MHz}} \lesssim 4$ mJy (5σ) limit for the 325 MHz catalogue, although (see Section 2.6 in Appendix A) there are a few cases where this process is unreliable (e.g. sxds_0011 where a steep spectral index is expected from the TJ radio structure of this radio source).

The fact that there are 13 325-MHz objects with reasonably high flux density that match with lower 1.4-GHz flux density objects than our 2 mJy limit is unsurprising, given that $S_{325\mathrm{MHz}} \gtrsim 4$ mJy corresponds to $S_{1.4\mathrm{GHz}} \lesssim 2$ mJy for $\alpha \sim 0.9$ and such steep-spectrum objects exist; their number will be exaggerated by random biases on the 325-MHz flux densities at the limit of the Tasse et al. (2006) survey.

The 610-MHz observations of the SXDF were made with the Giant Metre-wave Radio Telescope (GMRT) in two observing runs: on 2006 February 2–5 and 2006 December 4–9 (details can be found in Ibar et al. 2009). The region was covered with three pointings forming an equilateral triangle with 22-arcmin sides, covering an area of $\sim$0.5 deg^2. Adding both sets of observations, the total integration time per pointing was 11.4 hr.

To calibrate the data, we used 3C 147 or 3C 48 as flux and bandpass calibrators, observed for 20 min at the beginning and end of each track. We also observed 0116−208 or 0240−231 for 7 min every 45 min to be used as phase and amplitude calibrators. The full available bandwidth of 32 MHz was split into two intermediate frequencies (IFs) of 128 channels each, and reduced independently.

For the data reduction we used the Astronomical Image Processing System (AIPS). Standard tasks (e.g. QUACK, TVFLG, UVFLG, SPFLG) were used to flag bad baselines, antennas, initial integrations, and channels that suffered from narrow-band interference. A first rough calibration using CALIB and CLCAL was performed before using the FLGIT task to flag more bad data using a noise-based criterion. The clean data were calibrated again and used to normalise the target using GETJY. Each IF was compressed in chunks of 7 channels (to ensure bandwidth smearing was not a problem) leaving 15 averaged channels which were used for imaging. Each pointing was broken into 37 facets, in order to minimise 3D non-coplanar issues, and imaged using IMAGR.

The GMRT has a large number of antennas in the central region. These dominate the uv coverage and result in a non-Gaussian beam shape. Baselines shorter than 1.5 kλ were omitted from the imaging. We utilised one self-calibration in phase and two in phase and amplitude, averaging both polarisations in these two last passes, in order to obtain the final image facets. These were combined using FLATN, after convolving them to a single, common beam size. The final radio image reaches an r.m.s. of $\sim$ 60 μJy beam^{-1} near the centre of the field, with a synthesised beam of 6.8×5.4 arcsec^2 at position angle of 30 deg. The south-west field, centred at R.A. 2h 18m 44.0s, Dec. -5° $7'$ $20''$ has a considerably larger mean r.m.s. ($\sim 100\mu$Jy) than the other two fields. Also, the noise in the image increases near bright sources, where it can be as high as $\sim$ 300 μJy r.m.s., limiting the detection of nearby sources.

2.3 Analysis

2.3.1 Basic information

In our analysis we use the radio flux densities from Table 2.1 according to the following criteria. In the cases where the NVSS flux density is higher than the SXDS one, and the source is not compact, we use the NVSS flux density for our analysis, since the source may have more structure than the B-configuration VLA observations could reveal. On the other hand, when the NVSS flux density is higher than the SXDS flux density and the source is compact we assume that the NVSS measurement is inaccurate due to confusion by a nearby source (which

Table 2.1: Basic properties of the 37 brightest SXDS radio sources; values in bold are those used in the analysis. **Columns 1, 2 & 3** give the name of the object and its VLA (1.4 GHz) radio position (J2000.0) from Simpson et al. (2006). **Columns 4 & 5** give the integrated flux densities at 1.4 GHz from Simpson et al. (2006) and NVSS respectively; radio sources labelled with 'x' suffer from confusion by a nearby source, which results in a higher NVSS flux density than the SXDS value as seen in objects sxds_0025 and sxds_0027. Objects sxds_0034, sxds_0036 and sxds_0037 are not in the NVSS catalogue since they are fainter than the 2.3 mJy limit of the survey (Condon et al. 1998); their flux densities were measured from the NVSS maps and are labelled with 'n'. **Column 6** gives the 610 MHz flux density in mJy (Ibar et al. 2009); the character 's' shows that the flux densities of each component of the radio source have been added to calculate the whole flux density of the radio sources; '(nif)' means that the object is not inside the field that was observed; values in brackets are inaccurate since they miss part of flux density coming from the source. In **Column 7** we give the 325-MHz flux density from Tasse et al. (2006); values in brackets are not accurate since they miss part of the flux density coming from the source. **Column 8** shows our radio source counterpart optical/IR classification (see Section 2.3.3): 'Q' stands for a quasar, 'OQ' for an obscured quasar, 'G?' for a possible galaxy, 'G' for a secure galaxy, 'SB' for a starburst, 'WQ' for a weak quasar and 'BL' for a BL Lac object. **Column 9** gives the spectroscopic redshift, when available: '?' denotes objects with spectroscopy yielding plausible but insecure redshifts; the symbol '+' indicates clear broad emission lines and 'a' denotes a broad-absorption-line QSO (BALQSO). **Columns 10 & 11** give the photometric redshift calculated with HyperZ using Coleman (CWW) and Bruzual-Charlot (BC) templates respectively; brackets are used to denote unreliable fits. **Column 12** gives the radio spectral index from 1.4 GHz to 610 MHz or from 1.4 GHz to 325 MHz, which are marked with 'm'; we use the 1.4 GHz flux densities in bold for the calculations. Estimated values are in brackets. **Column 13** gives the largest angular size in units of arcsec and **Column 14** gives the radio classification (R Cl) of each object (Owen & Laing 1989): CD stands for classical double; TJ for twin-jet; FD for fat double; and COM for a compact radio source.

we confirmed by inspection of the VLA image); in this case we use the SXDS flux density. Finally, when the SXDS flux density is higher than the NVSS value, and the source has compact radio structure, we assume that the source is time variable; in that case we also use the SXDS flux density for our analysis.

For every SXDS radio source $K-$band UDS images were downloaded from the WFCAM archive (Hambly et al. 2007), with the exception of sxds_0009, sxds_0017, sxds_ 0025, sxds_0027 and sxds_0037 that were not observed by the UDS (Figure 2.1). For these objects we use $z-$band images from Subaru in order to produce overlays of the radio B-array VLA data and imaging, as shown in Figure 2.7. Also in Figure 2.7 we present spectral energy distributions (SEDs) of the objects created as explained in Section 2.3.2.

Table 2.1: (continued)

(1)	(2)	(3)	(4)	(5)	(6)	(7)	(8)	(9)	(10)	(11)	(12)	(13)	(14)
Name	RA (h m s)	Dec (° ′ ″)	$S_{\rm SXDS}$ int (mJy)	$S_{\rm NVSS}$ int (mJy)	$S_{\rm 610MHz}$ int (mJy)	$S_{\rm 325MHz}$ int (mJy)	Optical/IR Type	z_{spec}	z_{phot} CWW	z_{phot} BC	α	θ (arcsec)	R Cl
sxds_0001	02 18 27.32	-04 54 37.29	80.25	**82.5**	194.4	183.5	G	**0.626**	0.618	0.710	1.03	30	TJ
sxds_0002	02 18 18.16	-04 46 07.23	**62.11**	61.8	135.0	180.6	OQ	**1.183**	1.080	1.020	0.93	4.4	CD
sxds_0003	02 18 39.53	-04 41 50.10	50.82	**53.6**	141.3	236.7	OQ	**2.433**	[2.044]	[1.445]	1.17	9	CD
sxds_0004	02 18 53.64	-04 47 35.09	**16.95**	15.1	22.4	21.5	BL	?	[2.126]	**2.270**	0.34	<2	COM
sxds_0005	02 18 51.34	-05 09 00.60	**16.01**	16.7	38.8	53.9	G?	?	1.633	**1.610**	1.07	<2	COM
sxds_0006	02 16 37.86	-05 15 28.15	**12.02**	11.2	7.0	–	G?	–	1.650	**1.882**	-0.65	<2	COM
sxds_0007	02 16 59.02	-04 49 20.53	**9.60**	9.2	43.3^{s}	71.0	G?	**1.325?**	[1.174]	0.980	1.81	123	CD
sxds_0008	02 18 23.99	-04 53 04.10	**9.15**	8.7	16.6	17.5	SB	**0.458**	[0.218]	0.500	0.72	<2	COM
sxds_0009	02 18 03.37	-05 38 25.00	**8.91**	10.5^{x}	(nif)	19.3	Q?	**3.570?**	[3.565]	3.585	0.53$^{\rm m}$	2.5	COM
sxds_0010	02 18 50.55	-04 58 32.00	**8.12**	7.9	17.1	23.0	G?	–	[1.231]	**1.400**	0.90	3.3	COM?
sxds_0011	02 18 23.52	-05 25 00.44	7.95	**10.9**	13.3	5.7	G	**0.647**	0.618	0.695	(0.8)	120	TJ
sxds_0012	02 16 34.99	-04 55 05.61	6.59	**6.9**	15.4	(4.4)	G	**0.865**	0.868	0.770	0.97	120	CD
sxds_0013	02 16 16.82	-05 12 53.47	**6.25**	6.9	6.7	5.4	Q	**2.713**$^{+a}$	[2.922]	[2.475]	0.08	<2	COM
sxds_0014	02 17 52.14	-05 05 21.25	**6.19**	5.7	4.2	–	G?	?	[0.240]	**2.205**	-0.47	<2	COM
sxds_0015	02 19 32.20	-05 07 32.66	**6.10**	6.0	17.0^{s}	–	G	**0.344**	0.386	0.385	1.23	47	FD
sxds_0016	02 18 26.12	-04 59 46.57	**5.95**	4.4	14.1^{s}	16.9	OQ	**1.345?**	1.008	1.082	1.04	45	CD
sxds_0017	02 18 27.57	-05 34 53.77	**4.97**	4.6	(nif)	13.5	Q	**2.583**$^{+a}$	[2.771]	[2.120]	0.68$^{\rm m}$	22	CD?
sxds_0018	02 17 24.38	-05 12 51.68	4.84	**5.7**	13.3	–	G	**0.919**	0.858	0.820	1.02	100	FD
sxds_0019	02 17 57.26	-05 27 55.82	4.83	**5.0**	(nif)	–	G	**0.694**	[2.071]	0.910	(0.8)	52	FD?
sxds_0020	02 18 00.68	-04 49 54.78	4.60	**5.1**	8.5^{s}	3.9	G?	–	[2.553]	**1.135**	0.62	35	FD?
sxds_0021	02 17 52.53	-04 48 23.90	**4.42**	5.0^{x}	9.1	10.2	G?	–	1.728	**1.645**	0.87	<2	COM
sxds_0022	02 17 55.15	-05 26 52.99	**4.36**	4.7^{x}	6.1	9.5	G	**0.248**	0.280	0.290	0.40	<2	COM
sxds_0023	02 17 54.10	-05 12 49.94	**4.20**	4.1	11.3	15.2	G	**0.586**	0.561	0.610	1.19	3	COM
sxds_0024	02 19 06.64	-04 59 00.56	3.61	**3.8**	11.2	4.02	G	**0.516**	0.459	0.500	1.30	45	TJ
sxds_0025	02 17 55.42	-05 37 04.97	**3.23**	5.9^{x}	(nif)	–	WQ?	**0.964?**	[0.019]	[2.465]	(0.4)	<2	COM
sxds_0026	02 18 57.04	-05 28 19.98	3.20	**3.4**	6.4	–	G	**0.450**	0.430	0.445	0.76	10	TJ?
sxds_0027	02 17 54.93	-05 36 29.10	**3.13**	5.9^{x}	(nif)	–	OQ?	?	[0.011]	**1.595**	(0.4)	<2	COM
sxds_0028	02 17 18.59	-05 29 21.02	**2.80**	5.2^{x}	4.1	–	G	**0.627?**	[1.092]	0.895	0.46	<2	COM
sxds_0029	02 18 39.58	-05 01 34.68	**2.72**	4.4^{x}	3.4	–	G?	–	1.272	**1.380**	0.27	<2	COM
sxds_0030	02 18 22.44	-05 16 48.77	**2.56**	2.4	4.6	5.4	G	**0.535**	0.511	0.650	0.71	4	TJ?
sxds_0031	02 18 22.65	-05 02 53.26	2.44	**3.2**	3.9	–	G?	–	1.335	**1.325**	0.24	<2	COM
sxds_0032	02 19 26.48	-05 15 35.00	**2.39**	2.3	7.7^{s}	–	G	–	1.196	**1.010**	1.41	15	FD?
sxds_0033	02 17 37.21	-05 13 27.96	2.37	**2.4**	6.3	3.9	G	**0.647**	0.774	0.790	1.16	18	TJ
sxds_0034	02 18 09.48	-04 59 45.54	**2.31**	1.21^{n}	4.2	6.2	OQ	**1.095**	[1.309]	[1.345]	0.72	<2	COM?
sxds_0035	02 16 59.52	-05 16 55.73	**2.24**	2.9^{x}	1.5	–	G?	–	3.144	**2.715**	-0.48	<2	COM
sxds_0036	02 19 32.15	-05 12 57.26	**2.09**	2.72^{n}	<1.1	–	G	**0.871**	0.857	0.840	<-0.77	<2	COM
sxds_0037	02 18 06.88	-05 37 17.67	**2.07**	1.68^{n}	(nif)	–	G?	–	[0.709]	**1.085**	(0.4)	<2	COM

Table 2.2: Observing log for optical spectroscopy of the SXDS radio sources: **Column 1** gives the name of the object. **Column 2** gives the optical position of the radio sources in RA (h m s) and DEC (° m s). **Column 3** shows the instrument and telescope where spectroscopic observations were conducted; either with ISIS at the WHT (*www.ing.ias.es*), with FOCAS at the SUBARU (*www.subarutelescope.org*), with VIMOS at the ESO-VLT (*www.eso.org/instruments/vimos/*), with 2dF/AAOmega at the AAT (*www.aao.gov.au/AAO/*), with SITe1 at the Magellan 2 (*www.ociw.edu/Magellan*), or with DEIMOS at Keck 2 (*www.keckobservatory.org*). **Column 4** gives the observing date and **Column 5** the spectroscopic redshift (a '?' is added when the redshift not reliable). **Column 6** gives the exposure time; in the case of the WHT we give exposure time for both the ('B') and ('R') parts of the spectrum.

(1)	(2)	(3)	(4)	(5)	(6)
Object	Optical position	Spectrometer/Telescope	Date	$z_{\rm spec}$	Exposure Time (s)
sxds_0001	02 18 27.161	VIMOS/ESO-VLT	26Oct2005	0.626	5400
	-04 54 41.60	ISIS/WHT	26Jul2003	0.625	1x900B, 2x900R
sxds_0002	02 18 18.139	ISIS-WHT	26Jul2003	1.183	1x1800B, 2x900R
	-04 46 07.55				
sxds_0003	02 18 39.559	VIMOS/ESO-VLT	28Oct2005	2.432	5400
	-04 41 49.57	ISIS/WHT	26Jul2003	2.433	1x1800B, 2x900R
sxds_0004	02 18 53.587	AAOMEGA/AAT		?	1800
	-04 47 36.29				
sxds_0005	02 18 51.326	ISIS/WHT	27Jul2003	?	1x1800B, 2x900R
sxds_0006	02 16 37.825				
	-05 15 28.28				
sxds_0007	02 16 59.064	FOCAS/SUBARU	22Dec2003	1.325	1200
	-04 49 20.85				
sxds_0008	02 18 24.005	2dF/AAT	7Dec2002	0.457	1800
	-04 53 05.23	VIMOS/ESO-VLT	26Oct2005	0.458	5400
sxds_0009	02 18 03.420	AAOMEGA/AAT		3.570?	1800
	-05 38 25.43				
sxds_0010	02 18 50.491				
	-04 58 32.31				
sxds_0011	02 18 23.532	2dF/AAT	7Dec2002	0.647	1800
	-05 25 00.69	SITe1/Magellan 2	18Oct2003	0.647	2280
sxds_0012	02 16 34.968	VIMOS/ESO-VLT	8Aug2005	0.865	5400
	-04 55 06.47				
sxds_0013	02 16 16.822	FOCAS/SUBARU	6Oct2003	2.713	1800
	-05 12 53.71				
sxds_0014	02 17 52.118	AAOMEGA/AAT		?	1800
	-05 05 22.23				
sxds_0015	02 19 32.201	2dF/AAT	12Dec2002	0.344	1800
	-05 07 32.67	AAOMEGA/AAT		0.344	1800
sxds_0016	02 18 26.116	DEIMOS/KECK 2	21Dec2006	1.345?	
	-04 59 46.57				
sxds_0017	02 18 27.312	FOCAS/SUBARU	23Dec2003	2.583	1800
	-05 34 57.40				
sxds_0018	02 17 24.415	FOCAS/SUBARU	28Oct2003	0.919	1800
	-05 12 52.63				
sxds_0019	02 17 57.288	FOCAS/SUBARU	20Dec2003	0.694	1800
	-05 27 55.88				
sxds_0020	02 18 00.716				
	-04 49 56.41				
sxds_0021	02 17 52.531				
	-04 48 24.68				
sxds_0022	02 18 18.139	VIMOS/ESO-VLT	2Sep2005	0.248	5400
	-04 46 07.55				
sxds_0023	02 17 54.125	VIMOS/ESO-VLT	8Oct2005	0.586	5400
	-05 12 50.14				
sxds_0024	02 19 06.665	VIMOS/ESO-VLT	10Oct2005	0.516	5400
	-04 59 01.78				

Table 2.2: (continued)

(1)	(2)	(3)	(4)	(5)	(6)
Object	Optical position	Spectrometer/Telescope	Date	$z_{\rm spec}$	Exposure Time (s)
sxds_0025	02 17 55.392	VIMOS/ESO-VLT	7Oct2005	0.936?	5400
	-05 37 05.00				
sxds_0026	02 18 57.046	2dF/AAT	8Dec2002	0.450	1200
	-05 28 19.38	2dF/AAT	10Dec2002	0.450	1200
sxds_0027	02 17 54.943	VIMOS/ESO-VLT	7Oct2005	?	5400
	-05 36 29.80				
sxds_0028	02 17 18.564	FOCAS/Subaru	25Dec2003	0.627?	1200
	-05 29 20.71				
sxds_0029	02 18 39.586				
	-05 01 35.63				
sxds_0030	02 18 22.493	AAOMEGA/AAT	31Aug2006	0.535	1800
	-05 16 48.83				
sxds_0031	02 18 22.620				
	-05 02 53.77				
sxds_0032	02 19 26.484				
	-05 15 34.62				
sxds_0033	02 17 37.198	2dF/AAT	10Dec2002	0.647	1800
	-05 13 29.58	SITe1/Magellan 2	11Mar2005	0.647	2400
sxds_0034	02 18 09.456	FOCAS/SUBARU	18Dec2003	1.095	1200
	-04 59 45.89				
sxds_0035	02 16 59.546				
	-05 16 56.32				
sxds_0036	02 19 32.143	FOCAS/Subaru	20Dec2003	0.871	1200
	-05 12 57.64				
sxds_0037	02 18 06.893				
	-05 37 17.88				

Table 2.3: Measured quantities for the 37 SXDS radio sources:**Column 1** gives the name of the object. **Columns 2 & 3** are the blue excess ($\log_{10}([\nu L]_{4000\mathring{A}\mathrm{rest}}/[\nu L]_{1\mu\mathrm{mrest}})$) and the mid-IR excess ($\log_{10}([\nu L]_{10\mu\mathrm{mrest}}/[\nu L]_{1\mu\mathrm{mrest}})$) respectively. **Columns 4 & 5** give the logarithms of the rest frame luminosity at 1.4 GHz and at 24 μm respectively. **Column 6** is the K_{AB} magnitude from the UDS; the character 'K' denotes point sources at the $K-$band, whereas 'o' denotes point sources in the optical. For sxds_0009, sxds_0017, sxds_0025, sxds_0027 and sxds_0037 we give an estimate of the K magnitude from the SED of the object (see Figure2.1); these values are in brackets.

(1)	(2)	(3)	(4)	(5)	(6)
Object	Blueness	mid-IR excess	$\log_{10}($ $L_{1.4\mathrm{GHz}}/$ $[\mathrm{WHz}^{-1}\mathrm{sr}^{-1}])$	$\log_{10}($ $[\lambda L]_{24\mu\mathrm{m}}/$ [W])	K_{AB} (mag)
sxds_0001	-1.17	< -1.40	25.04	< 36.88	18.49
sxds_0002	-0.60	-0.71	25.57	37.30	19.93
sxds_0003	0.33	< 0.58	26.39	37.98	20.89
sxds_0004	-0.17	0.88	25.38	38.04	21.40^{K}
sxds_0005	-0.32	< 0.04	25.36	< 37.72	20.57
sxds_0006	-1.23	< 0.17	24.62	< 38.16	20.21
sxds_0007	-0.60	< -0.58	25.20	< 37.64	19.68
sxds_0008	-0.21	-0.13	23.14	37.34	18.24
sxds_0009	-0.96	< 0.19	25.61	< 38.51	$(22.52)^{o}$
sxds_0010	-0.76	< -0.39	24.85	< 37.60	21.11
sxds_0011	-0.89	< -1.51	< 24.15	< 36.89	18.07
sxds_0012	-1.01	< -1.31	24.29	< 37.08	19.11
sxds_0013	-0.36	< 0.73	24.96	< 38.25	21.79^{o}
sxds_0014	-3.19	< -2.25	24.51	< 38.33	21.23^{K}
sxds_0015	-0.33	-0.85	23.31	36.66	17.69
sxds_0016	-0.49	< -0.19	24.73	37.86	22.06
sxds_0017	0.30	< 1.07	25.15	< 38.15	$(21.64)^{o}$
sxds_0018	-0.78	< -1.22	24.29	< 37.18	18.88
sxds_0019	-0.54	< -0.57	< 23.88	< 36.97	20.26
sxds_0020	0.06	0.60	24.33	< 37.43	21.22
sxds_0021	-0.09	< 0.54	24.80	< 37.72	21.04
sxds_0022	-0.54	-1.54	22.76	35.87	16.48
sxds_0023	-0.42	< -1.02	23.71	< 36.71	18.97
sxds_0024	-0.82	< -1.63	23.55	< 36.66	17.80
sxds_0025	0.09	< 0.57	< 23.91	< 37.29	(21.60)
sxds_0026	-1.00	< -1.74	23.27	< 36.54	17.65
sxds_0027	-0.39	0.81	< 24.37	38.38	(20.72)
sxds_0028	-0.27	< -0.69	23.45	< 36.84	18.71
sxds_0029	-0.91	< -0.65	24.12	< 37.63	20.62
sxds_0030	-0.85	< -1.23	23.31	< 36.65	18.44
sxds_0031	-0.78	< -0.21	24.15	< 37.58	20.32
sxds_0032	-0.47	< -0.22	24.13	< 37.27	20.51
sxds_0033	-0.23	-1.02	23.57	36.83	18.40
sxds_0034	-0.08	1.00	24.00	38.60	19.75^{Ko}
sxds_0035	-0.80	< 1.50	24.19	< 38.28	21.86
sxds_0036	-1.36	< -1.32	< 23.31	< 37.08	18.71
sxds_0037	-0.92	< -0.52	< 23.83	< 37.40	(20.60)

Table 2.4: Approximate 5-σ point-source depths for the bands used in the SXDF, and, for the Spitzer bands, the flux density limits of the SWIRE catalogues (used as upper limits in the SEDs for undetected objects).

Band	Depth		Catalogue flux limit
	AB mags	μJy	μJy
B	27.5	3.6×10^{-2}	—
V	26.7	7.6×10^{-2}	—
R	26.8	6.9×10^{-2}	—
i'	26.5	9.1×10^{-2}	—
z'	25.5	0.23	—
J	23.5	1.4	—
K	23.5	1.4	—
3.6 μm	22.5	3.7	10
4.5 μm	22.1	5.4	10
5.8 μm	19.7	48	43
8.0 μm	20.0	37.8	40
24 μm	18.0	230	450

2.3.2 Photometric redshifts

We have estimated redshifts for the objects by fitting template spectral energy distributions - SEDs to their observed photometry, using a modified version of the publicly-available[2] HyperZ code, by Bolzonella et al. (2000). HyperZ offers a convenient interface for the provision of photometric bandpass functions, galaxy templates and data, and is well documented. It also has built-in prescriptions for reddening of templates by dust, and for Lyman forest absorption below 912 Å.

For the purposes of galaxy template fitting, we consider only the optical (Subaru), near-infrared (UKIDSS-UDS) and mid-infrared (SWIRE) data. The approximate 5-σ point source depths achieved in each waveband are shown in Table 2.4.

The catalogues contain a variety of adaptive and fixed aperture magnitudes, which have been measured from the image data using SExtractor (Bertin & Arnouts 1996). For the purpose of SED fitting, it was important to select those apertures which provided the most accurate colour information for each object. Whilst the adaptive (such as Kron and isophotal) magnitudes provide a good estimate of the total flux of an object (without the need for an aperture correction to be derived based upon the galaxy's assumed surface brightness distribution and the seeing, as is required to correct a small fixed aperture), the apertures must generally be large, containing areas of low surface brightness which increase the photometric error. Also, an adaptive aperture might be a different size in each measured band and thus sample a different

[2] webast.ast.obs-mip.fr/hyperz/

component of the stellar population, potentially leading to unphysical colours. For these reasons, and because of the problems using adaptive apertures at faint magnitudes (where errors in determining the correct isophotal or Kron radii can exacerbate photometric errors in low signal-to-noise images), we decided to use fixed aperture photometry for our SED fitting.

However, fixed apertures have their own issues to consider. In the ideal situation, we would have a set of images with the same PSF, perfectly registered astrometrically. It would then be possible to extract photometry using apertures placed in exactly the same positions in each image, and we could be confident that, whatever the aperture size, we would be sampling the same fraction of the light from the same regions of each galaxy studied. But this is far from the case when combining data taken with different instruments, under different seeing conditions, as we are doing here. It was undesirable on confusion grounds to degrade the optical and near-IR data to match the large PSF of the Spitzer bands, so we chose the aperture size to minimise the systematic differences in the fraction of the flux measured in each band.

Clearly, there is a trade-off to be made — too large an aperture is vulnerable to confusion and increased background noise, while an aperture which is very small will contain very different fractions of the total flux for images with different PSFs. To investigate this trade off in detail, we looked at the mean difference between aperture magnitudes and the SExtractor MAG_AUTO magnitudes, which uses an adaptive Kron aperture to estimate the total flux. For the smallest diameter-aperture available in all bands (2 arcsec) there were large offsets (of order 0.2–0.3 mags) between the aperture and Kron magnitudes, but most importantly these offsets were very different in the different bands. With the next available aperture diameter (3 arcsec) the mean differences in the aperture and Kron magnitudes were much smaller — less than a tenth of a magnitude. Deeming this an acceptable systematic error, we decided to use 3-arcsec apertures for all photometry.

To combine the catalogues across the optical and infrared bands, we assumed that the closest match between extracted objects, within a search radius of 2 arcsec relative to the radio position (chosen to allow for differences in astrometry between different photometric bands), was the correct association, with the constraint that a catalogue entry was only permitted to match once per band.

We used both empirical and evolving galaxy SEDs in the template fitting. The empirical templates used were the ones supplied with the HyperZ code, which are four typical observed galaxy spectra taken from Coleman, Wu & Weedman (1980; henceforth CWW), extended in the ultraviolet and infrared by matched models (Bruzual & Charlot 1993).

The evolving templates were generated using Galaxev (Bruzual & Charlot 2003; hence-

forth BC[3]), with 14 exponentially decaying star formation rates with e-folding timescales ranging from 0.1 to 30 Gyr, plus an instantaneous burst, a finite burst and a constant star formation rate template, all with solar metallicity and a Salpeter initial mass function for the stars. This is a larger number of BC templates than used by Bolzonella et al. (2000), but our intention was to span the space of possible galaxy types as finely as possible, in the hope that there would always be a template with similar star formation history to any object in the dataset, and that this would then be the best fit.

Both empirical and evolving SEDs were used because parallel work by van Breukelen et al. (2006) seemed to indicate that, while the evolving templates gave slightly more accurate results on spectroscopically identified (and thus also reasonably bright) samples, they more quickly broke down, giving catastrophic redshift estimates, as signal-to-noise was reduced. Catastrophically wrong redshift estimates produced by the two sets of templates are generally different, so agreement between the results obtained with the CWW and BC SEDs is useful to improve confidence that a particular redshift estimate is correct. Where the estimates differ significantly, it is more often the case that the CWW estimate is closer to reality, though this effect is difficult to quantify precisely since catastrophic redshift estimates are a function of the template set, as well as the precise signal-to-noise in each observed band.

Figure 2.7 presents the SEDs constructed for our radio sources; red colour represents the BC templates and black the CWW templates. We decided to use the BC derived value in the case where no spectroscopy is available.

In Figure 2.2 we compare 24 spectroscopic redshifts with the photometric redshifts (Table 2.2); optical spectra of these objects are presented in Figure 2.7. Note that objects significantly deviating from the $z_{\rm spec} = z_{\rm phot}$ line have unclear photometric redshifts (see Table 2.1). Three objects in our sample are classified as quasars (see Section 2.3.3), two of which fall into the $z_{\rm spec} > z_{\rm phot}$ category; the third, sxds_0009, may have a good photometric redshift because the tentative broad-line emission could be scattered light, with the nucleus making an insignificant contribution at the longer wavelengths dominating the calculation of the photometric redshift.

The median redshift for our radio-source sample, including photometric redshifts, is $z = 1.095$. The best fit line for the galaxies 'G' gives an excellent agreement between spectroscopic and photometric redshifts, within the errors. The linear Pearson correlation coefficient is 0.89 and the Spearman correlation coefficient is $\rho = 0.96$ with 99.9% probability for a correlation.

[3]When running HyperZ with the CWW templates, slightly different apertures were used for the magnitudes. An exception is sxds_0016, where magnitudes were measured directly from images and then the BC and CWW templates were fitted to the SED.

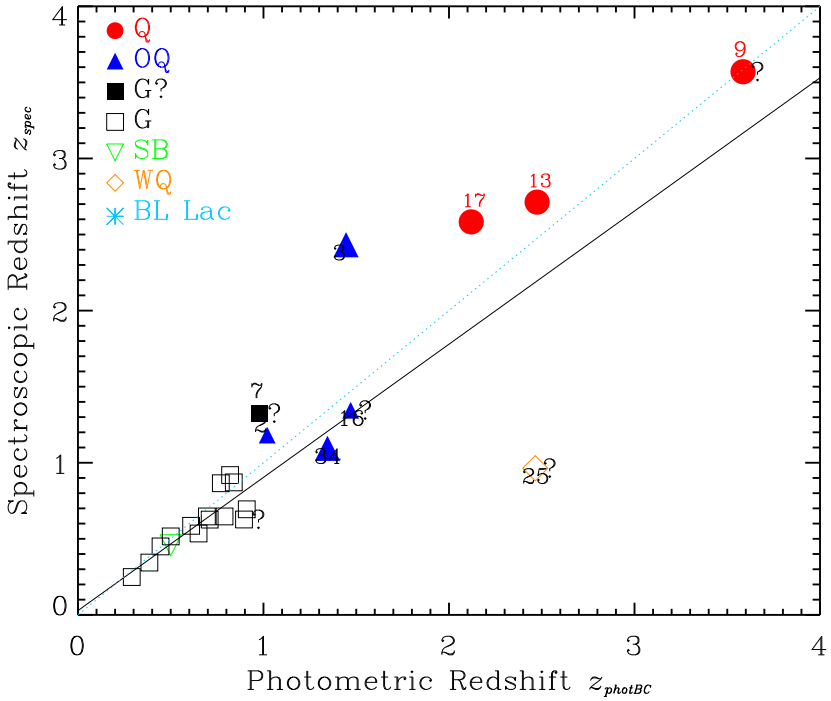

Figure 2.2: Comparison of spectroscopic and photometric (based on BC templates) redshift in the 24 (of 37) cases where both are available. Symbols indicate optical/near-infrared classification as adopted in Section 2.3.3, where filled symbols denote objects with spectroscopic redshifts: red filled circles for quasars 'Q', blue filled triangles for obscured quasars 'OQ', black filled squares for possible galaxies 'G?', black squares for secure galaxies 'G', green upside-down triangles for starbursts 'SB', orange diamonds for weak quasars 'WQ' and light-blue stars for 'BL Lac' objects (note that the 'BL' object is not present due to absence of spectroscopic redshift). The light-blue dotted line corresponds to $z_{\rm spec} = z_{\rm photBC}$. The solid black line fits the 15 galaxies 'G' that have both spectroscopic and photometric redshift: $z_{\rm spec-G} = 0.88 \times z_{\rm photBC-G} - 0.03$. Names in red represent objects with broad-line optical features. Outlying points are labelled with their source number. Objects with uncertain photometric redshifts are plotted with symbols, a factor 1.5 larger than the others.

This makes us confident to use photometric redshifts in the case where no spectroscopy is available. Consequently, we adopt the photometric redshifts in bold-type in Table 2.1.

2.3.3 Optical/infrared radio-source classification

Figure 2.3 shows the rest frame luminosity of the SXDS radio sources at 24 μm versus their redshift. The value of $\log_{10}(L_{24\mu\rm m})$ is calculated using the spectral index measured from the 24 μm data point to the nearest lower-λ detection in the observed frame SED (Figure 2.7).

We use optical/IR observations (Figure 2.3) to classify a radio source as either Quasar 'Q', Obscured Quasar 'OQ', Galaxy? 'G?', Galaxy 'G', Starburst 'SB', Weak Quasar 'WQ' or BL Lac 'BL', as described below. We deem that nuclear accretion is 'significant' in objects that obey $\log_{10}(L_{24\mu\rm m}/[\rm WHz^{-1}sr^{-1}]) > 23.1$ (or $[\lambda L]_{24\mu\rm m} > 10^{37.3}$ W)[4]. This value corresponds

[4]Other authors use slightly different values to separate 'luminous' quasars (and broad-line radio galaxies)

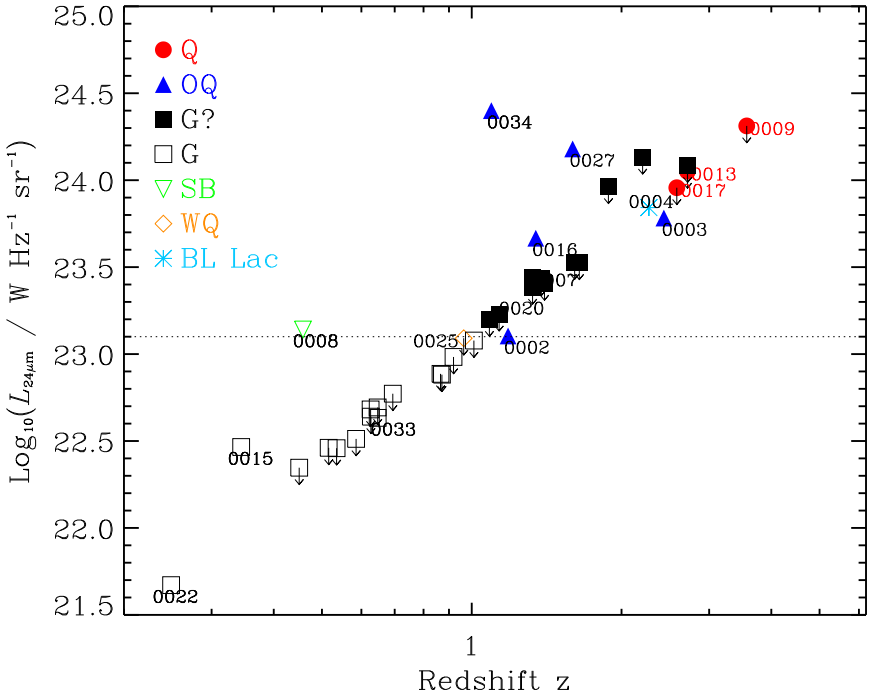

Figure 2.3: Logarithm of the rest-frame Luminosity $L_{24\mu m}$ at 24 μm versus redshift z. Symbols are the same as in Figure 2.2. The dotted line corresponds to $[\lambda L]_{24\mu m} = 10^{-1.8} L_{\rm Edd}$ for a quasar with $M_{\rm BH} \gtrsim 10^8$ M$_\odot$, as discussed in Section 2.3.3. Outlying points are labelled with their source number.

to $[\lambda L]_{24\mu m} \geq 10^{-1.8} L_{Edd}$, a typical lower limit for quasars at $z \sim 1$ (see Figure 2 McLure & Dunlop 2004), for a black hole mass $M_{\rm BH} \geq 10^8 M_\odot$, a typical lower limit for radio sources (McLure et al. 2004); $L_{\rm Edd}$ is the Eddington luminosity $L_{Edd} = 10^{39.1} \times (M/10^8 {\rm M}_\odot){\rm W}$.

We then define the following categories:

i) **Q**: Broad lines in the optical spectrum (3/37 cases). None of these are detected at 24 μm, although their limits are insufficient to rule out significant accretion.

ii) **OQ**: Objects with a 24-μm detection (5/37 cases) and with sufficient L_{24} to represent significant accretion. In all cases we believe that the nucleus seen at 24 μm is obscured optically because the spectra show no broad lines. This class may be incomplete in that some objects in the 'G?' class, as described next, have limits above this critical value.

iii) **G?**: A galaxy that has a 24-μm limit consistent with it lying above the $\log_{10}(L_{24\mu m}/[{\rm WHz^{-1}sr^{-1}}]) = 23.1$ line[5] (11/37 cases).

iv) **G**: All other objects (15/37 cases) without significant accretion, unless they fall into three special categories defined by properties derived from considerations of the optical spectroscopy, the SED and the optical structure: **SB**: evidence from the SED and optical spectra of a

from objects with lower accretion rates (e.g. Ogle et al. 2006 adopt a value of $[\lambda L]_{15\mu m} \sim 10^{36.9}$ W).

[5]Because of the 24 μm flux density limit these objects are the high-redshift (and hence, because of the 1.4-GHz flux density limit) high-$L_{1.4{\rm GHz}}$ sub-set of the objects lacking Spitzer 24 μm detections.

starburst component (1/37 cases; see notes in Section 2.6 in Appendix A); **WQ**: evidence from the SED and optical spectra of a quasar component (see notes in Section 2.6 in Appendix A) but no 24 μm detection (1/37 cases); **BL**: Featureless red continuum and a point source at K (1/37 cases).

Objects labelled as 'Q', 'OQ' and 'G?' include all objects with, or potentially with, significant nuclear accretion, and are represented by filled symbols in Figure 2.4. Note, however, that the definition of 'significant' accretion is somewhat arbitrary as illustrated by the case of the 'WQ' sxds_0025. Some accretion may be necessary in many, or perhaps all FRIs, and especially those near the FRI/FRII divide, if the radio luminosity is assumed to be derived from the Blandford-Znajek mechanism (Cao & Rawlings 2004).

2.4 Discussion

2.4.1 Accretion Indicators

Inspection of the SEDs in Figure 2.7 shows that some of our objects have excess emission at 24 μm above that expected from extrapolation of the stellar populations. This is quantified via a measure of mid-IR excess, $\log_{10}([\nu L]_{10\mu\mathrm{mrest}}/[\nu L]_{1\mu\mathrm{mrest}})$ (Table 2.3). We chose a rest-frame value of 10 μm as our fiducial point as this corresponds to $\sim$ 24 μm in the observed frame for redshifts close to the median redshift of our sample. A comparison of mid-IR excess and blueness is presented in Figure 2.4 where a positive correlation is clear. The generalised Spearman correlation calculated using survival analysis statistics ASURV (Lavalley et al. 1992) is 0.636 with a 99.9% probability for a correlation.

Consider a simple model in which blueness is connected to mid-IR excess through the following equations:

$$[\nu L]_{4000\mathring{\mathrm{A}}\mathrm{rest}} = \mathrm{k}_1 \times [\nu L]_{1\mu\mathrm{mrest}} + \mathrm{k}_2 \times [\nu L]_{10\mu\mathrm{mrest}} \Rightarrow \tag{2.1}$$

$$\log_{10}\left(\frac{[\nu L]_{4000\mathring{\mathrm{A}}\mathrm{rest}}}{[\nu L]_{1\mu\mathrm{mrest}}}\right) = \log_{10}(\mathrm{e}) \times \frac{\mathrm{k}_2}{\mathrm{k}_1} \times \left(\frac{[\nu \mathrm{L}]_{10\mu\mathrm{mrest}}}{[\nu \mathrm{L}]_{1\mu\mathrm{mrest}}}\right) + \log_{10}(\mathrm{k}_1)^6, \tag{2.2}$$

where k_1 encodes the contribution of the stellar population of a passively evolving galaxy formed at high redshift ($z > 5$), and k_2 the mid-IR-excess parameter that we are looking to

[6]Equation 2.2 relies on the $ln(1+x) \approx x$ approximation which is only accurate around and below the knees of the functions plotted in Figure 2.4.

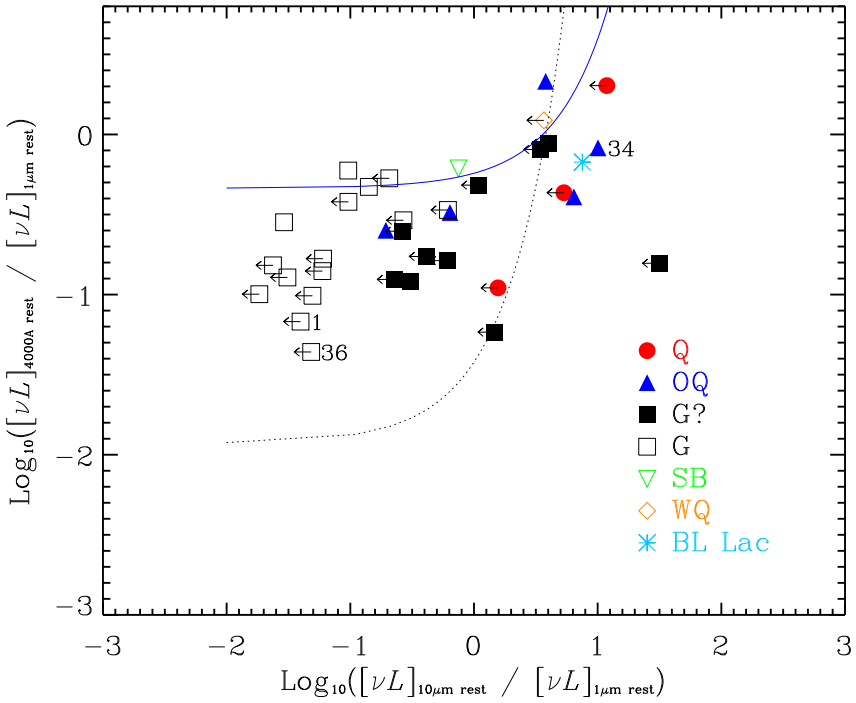

Figure 2.4: Blueness versus mid-IR excess for the 37 brightest SXDS radio sources: Symbols indicate optical/IR classification, as explained in Figure2.2 and Section 2.3.3. Table 2.3 presents measurements of those quantities. The black dotted line corresponds to the best-fit line in the log-linear plane when all objects were treated as detections; the slope and intercept are 0.51 and -1.93 respectively, giving (see Eqn. 2.2) $k_1 \simeq 0.01$ and $k_2 \simeq 0.01$. The blue solid line corresponds to the best-fit line in log-linear plane where objects without detections at 24 μm were treated as limits; the slope and intercept are 0.09 and -0.34 respectively, giving $k_1 \simeq 0.46$ and $k_2 \simeq 0.10$. The Buckley-James method in the survival analysis (ASURV) statistics package (Lavalley et al. 1992) was used in these calculations. 'SB', 'BL', 'Q' and 'WQ' objects were excluded from the fits as explained in Section 2.4.1.

calculate for this sample of radio sources[7]. This model assumes that light from the nucleus with intrinsic optical luminosity L_{opt} is i) absorbed by dust and re-emitted in the mid-IR generating luminosity $[\nu L]_{10\mu\mathrm{mrest}}$ and ii) scattered, generating a contribution to luminosity $[\nu L]_{4000\mathring{\mathrm{A}}\mathrm{rest}}$.

Objects labelled as 'SB', 'BL', 'Q' and 'WQ' have been excluded from the fit since they have SEDs dominated by different physical processes to those assumed in the model described by Eqns 2.1 and 2.2. Without spectropolarimetry it is difficult to determine whether any broad lines are seen as scattered light from the nucleus or they represent a direct view of the nucleus. The 24-μm luminosity versus redshift plane of Figure 2.3 shows that all three broad-line objects, as well as the 'OQ' objects, are consistent with being above or at the limit of $L_{24\mu\mathrm{m}} > 10^{23.1}$ $\mathrm{WHz^{-1}sr^{-1}}$, or $[\lambda L]_{24\mu\mathrm{m}} > 10^{37.3}$ W.

Figure 2.4 shows best-fit lines for two scenarios: 1) all objects were treated as detections

[7]See Chapter 6 for results on a linear-linear fit to Figure 2.4.

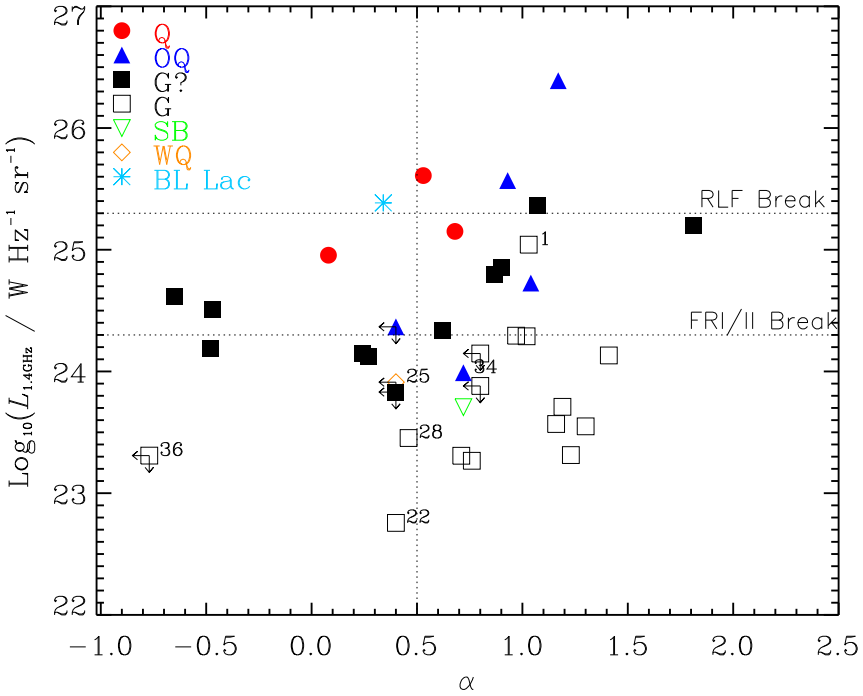

Figure 2.5: Radio Luminosity at 1.4 GHz $\log_{10}(L_{1.4\mathrm{GHz}}/[\mathrm{WHz}^{-1}\mathrm{sr}^{-1}])$ versus the radio spectral index α as in Table 2.1: symbols are the same as in Figure 2.2. The horizontal lines show the RLF and FRI/FRII breaks calculated from the Willott et al. (2003) and the Fanaroff & Riley (1974) values respectively using a typical steep-spectrum spectral index of 0.8. The vertical line at $\alpha = 0.5$ shows the conventional border between steep and flat-spectrum sources. Objects that are discussed in the text (see Section 2.4.1) are labelled with their names.

(black dotted line), and 2) objects are treated as upper limits according to their 24 μm detection (blue solid line). We note that these 'fitted' lines are highly sensitive to the locations in the $\log_{10}([\nu L]_{4000\mathrm{\AA rest}}/[\nu L]_{1\mu\mathrm{mrest}})$ vs $\log_{10}([\nu L]_{10\mu\mathrm{mrest}}/[\nu L]_{1\mu\mathrm{mrest}})$ plane of a small number of objects, and hence are not robust, although they certainly seem to delineate rough bounds to the data. Averaging these results we deduce $k_1 \sim 0.2$ and $k_2 \sim 0.06$, which agrees well with independent evidence for the properties of radio sources as we now argue. The value deduced for k_1 is in line with the expectations of template spectra of galaxies which formed their stars at high redshift. Optical polarisation studies (e.g. Kishimoto et al. 2001) tell us that $[\nu L]_{4000\mathrm{\AA rest}} \gtrsim 0.01[\nu L]_{\mathrm{opt}}$, which is consistent with our value of k_2 given that QSO SED studies suggest $[\nu L]_{10\mu\mathrm{mrest}} \sim 0.3[\nu L]_{\mathrm{opt}}$ (Rowan-Robinson 1995), and $0.06 \times 0.3 \simeq 0.01$. We conclude that whenever nuclear accretion is significant in our sample of radio sources, dust in the torus absorbs 30% of the photons and dust above and below the torus scatters $\gtrsim$1% of the photons.

In previous studies, the quasar fraction has been defined as the number of sources with quasar-like optical features (e.g. optical broad lines) and has a value of $\sim 0.1 \rightarrow 0.4$ over the relevant range of $L_{1.4\mathrm{GHz}}$ (e.g. Willott et al. 2000). We introduce the term 'quasar-mode

fraction' $f_{\rm QM}$ to describe the fraction of objects with 'significant' accretion rates, as determined from the observed 24 μm flux density, to the total number of objects.

In Figure 2.5 we present the radio luminosity at 1.4 GHz of the SXDS radio sources against their radio spectral index α (Table 2.1). A typical flat/steep-spectrum radio spectral index $\alpha = 0.4/0.8$, depending on whether its radio structure is compact/extended, was used in the case where the object was not observed at 610 MHz and is a limit at the 325-MHz catalogue. Note that the median radio luminosity is $L_{1.4\rm GHz} \sim 1.6 \times 10^{24} \rm WHz^{-1}sr^{-1}$, which lies very close to the FRI/FRII luminosity division. Crudely, the SXDS sample is sensitive to objects above this division at $z \gtrsim 1$ and to objects below the FRI/FRII luminosity break at $z \lesssim 1$.

We see from Figure 2.5 that the single 'BL' object has a flat radio spectral index, as expected. It is clear that nearly all the other flat-spectrum objects have significant accretion, although some exceptions do exist, e.g. object sxds_0028 lies close to the boundary of $\alpha = 0.5$ although it has significant errors in the calculation of its spectral index. Object sxds_0022 also lies close to the flat/steep α boundary, which is a typical value if star formation is making a significant contribution to the radio flux density (see notes in Appendix A, Section 2.6). Object sxds_0025 is a 'WQ' with a flat radio spectra index and is expected to be in that region since we believe we are viewing the central region directly (see notes in Appendix A, Section 2.6). The fact that it lies below the limit for 'significant' accretion is consistent with it being a weak quasar. Thus, the only clear exception is sxds_0036, which is a 'G' and there is an uncertainty in the calculation of its spectral index. The only clear region where the quasar-mode fraction is very low, is for steep-spectrum objects below the FRI/FRII break, where $f_{\rm QM} \sim 0.1$.

Figure 2.6[8] shows the radio luminosity at 1.4 GHz versus the projected linear size D. For SXDS sources that are compact we assume a limiting angular size $\theta = 2.0$ arcsec (Simpson et al. 2006). We see that nearly all 'Q', 'OQ' and 'G?' objects of our sample lie above the 'FRI/FRII' luminosity break with the exception of the 'OQ' sxds_0034 (the three 'G?' objects near sxds_0034 lie close to the boundary of significant accretion). Above the FRI/FRII break we find that $f_{\rm QM} \sim 0.5 - 0.9$ (the lower value assumes the 24 μm limits are much higher than the true 24 μm values, whereas the higher value assumes the true values lie just below the limits). The one clear exception in this regime is sxds_0001, which has no evidence of a QSO and a clear Twin-Jet (FRI) radio structure.

The quasar-mode fraction drops dramatically below the FRI/FRII break, and whether or not one excludes some of the compact ($D < 100$ kpc) sources as potentially part of a separate

[8]In the similar figure in Vardoulaki et al. (2006) we used photometric redshifts to estimate values of $L_{1.4\rm GHz}$ used in the plots.

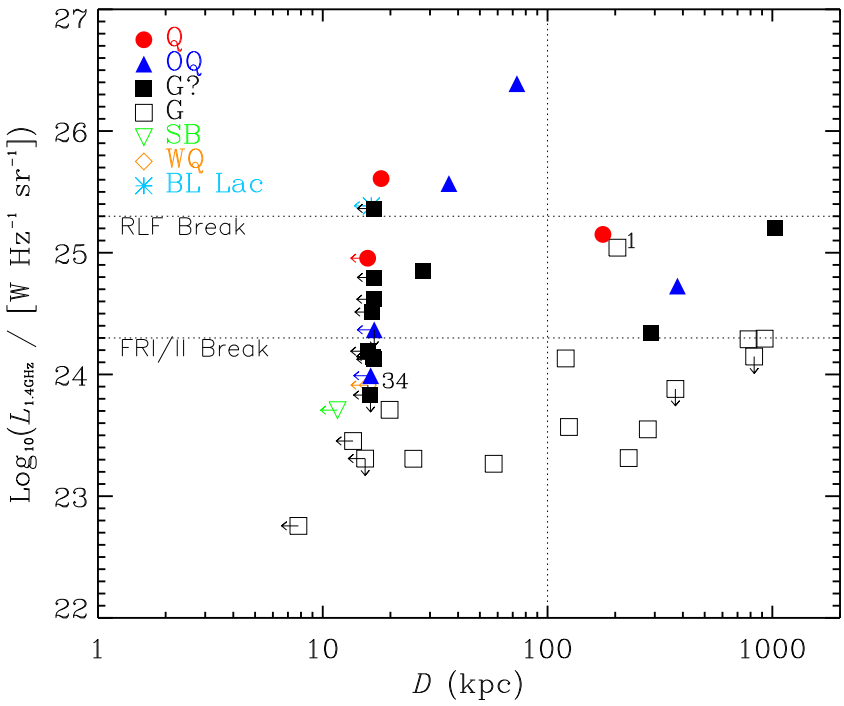

Figure 2.6: Radio Luminosity at 1.4 GHz $\log_{10}(L_{1.4\mathrm{GHz}}/[\mathrm{WHz}^{-1}\mathrm{sr}^{-1}])$ versus largest projected linear size D. Symbols are the same as in Figure 2.2. The horizontal lines show the RLF and FRI/FRII breaks calculated from the Willott et al. (2003) and the Fanaroff & Riley (1974) values respectively using a typical steep-spectrum spectral index of 0.8. Objects that are discussed in the text (see Section 2.4.1) are labelled with their names.

(beamed) population, then $f_{\mathrm{QM}} \lesssim 0.1$ because nearly all objects are galaxies 'G'. The clear counter-example here is sxds_0034, the only 'OQ' below the FRI/FRII break, and potentially an optically-obscured example of unobscured FRI QSOs already studied in this radio luminosity regime (e.g. Sarazin et al. 1999, Blundell & Rawlings 2001). This object is spectroscopically confirmed at redshift $z = 1.095$. An excess of emission at 24 μm places it securely in the 'OQ' classification. This object is not a spectroscopically confirmed quasar but has high-excitation narrow lines in its optical spectrum and is compact both optically and at K; its radio map shows a seemingly unresolved source. This seems to be an optically-obscured 'radio-quiet' quasar in the radio luminosity regime in which most radio sources are thought to have FRI radio structures. Unobscured 'radio-quiet' quasars are known in this regime (see Heywood, Blundell & Rawlings 2007 and references therein), and claims have been made for obscured examples (Martinez-Sansigre et al. 2006). However, as found by the study of Martinez-Sansigre et al. (2006), the surface brightness sensitivity of existing radio data is insufficient to map any extended structure at high redshifts. We also note the presence of broad absorption lines in 2 out of our 3 'Q' category objects. This is a high fraction compared to general QSO samples (e.g. Richards et al. 2003 find this fraction to be between ~ 0.03 and ~ 0.2 for optically

selected samples of quasars).

Both of Figures 2.5 & 2.6 suggest that we have a larger fraction of flat, compact radio sources in our sample since it is selected at higher frequency than low-frequency selected radio samples like the 3CRR, 6CE and 7CRS: 51% ± 7% objects of our sample have $D < 25$ kpc, whereas this fraction is $\sim 25\%$ in 7CRS (e.g. Figure 18 of Blundell, Rawlings & Willott 1999). The quasar-mode fraction is generally high for flat-spectrum objects independent of radio luminosity. Steep-spectrum and extended, presumably FRI-type radio sources (i.e. objects below the FRI/II break at $\alpha > 0.5$) show no signs of significant accretion with just one exception. Cao & Rawlings (2004) studied a sample of 3CR FRI radio sources and found that the $L/L_{\rm Edd}$ ratio in FRI-type radio sources is more than two orders of magnitude less than our limit for significant accretion, which is in line with our findings.

We have discovered that above the FRI/FRII division the quasar-mode fraction is of the order $f_{\rm QM} \sim 1$, where the median redshift of these objects is $z_{\rm med} \sim 1.6$. Below the FRI/FRII break $f_{\rm QM} \rightarrow 0$ for extended steep-spectrum sources, where $z_{\rm med} \sim 0.65$. A key question is whether the presence of significant accretion is linked to the radio luminosity $L_{\rm rad}$ (or radio structure) or to the redshift z. We note that from studies of the 3CR sample (in which the FRI/FRII division is at redshift $z \sim 0.1$ rather that $z \sim 1$, for our sample) that a similar division of mid-IR properties occurs at the same FRI/FRII luminosity division (Ogle et al. 2006). We conclude that it is a luminosity (or structural) effect rather than an epoch effect, and in this paper we have shown that such an effect persists from $z \sim 0.1$ to $z \sim 1$. We will attempt to de-couple the effects of radio luminosity and radio structure in a future paper.

2.5 Conclusions

We have presented a study of the brightest SXDS radio sources with flux density at 1.4 GHz above 2 mJy. Our sample is not as yet spectroscopically complete (24 out of 37 have spectroscopic redshifts), but Figure 2.2 gives us the confidence in the use of photometric redshifts calculated with HyperZ using Bruzual-Charlot templates. The median redshift of the entire sample is $z_{\rm med} \approx 1.1$, which from Figure 2.5 corresponds to objects close to the FRI/FRII division. Optical and infrared imaging, as well as radio observations are in place to give an insight to the type of radio sources at the bright flux density end of the 1.4-GHz SXDS radio survey of the SXDF.

We have classified our radio sources as either quasars ‘Q’, obscured quasars ‘OQ’, possible galaxies ‘G?’, secure galaxies ‘G’, starbursts ‘SB’, weak quasars ‘WQ’ or BL Lac ob-

jects 'BL'. Objects 'Q', 'OQ' and 'G?' have significant nuclear accretion, since they obey $\log_{10}(L_{24\mu\mathrm{m}}/[\mathrm{WHz^{-1}sr^{-1}}]) > 23.1$ (or $[\lambda L]_{24\mu\mathrm{m}} > 10^{37.3}$ W). This value corresponds to $[\lambda L]_{24\mu\mathrm{m}} \geq 10^{-1.8} L_{Edd}$ for a black hole mass $M_{\mathrm{BH}} \geq 10^8 M_{\odot}$.

The 37 brightest radio sources in the SXDS exhibit the following properties:

• Flat-spectrum, presumably mostly Doppler-boosted, radio sources show evidence of accretion in almost all cases, independent of radio luminosity.

• Significant accretion is also nearly ubiquitous above the 'FRI/FRII' luminosity break, i.e. at redshift $z \gtrsim 1$ for objects in our sample. The quasar-mode fraction, defined here as the fraction of objects with significant accretion rates to the total number of objects – and not as the number of sources with quasar-like optical spectra – is $\sim 0.5 \rightarrow 0.9$. There are counter examples like the low-accretion FRI sxds_0001, but they are rare.

• At $z \lesssim 1$ most of the 'FRI'-regime sources have low accretion rates and $f_{\mathrm{QM}} \lesssim 0.1$, but one high-accretion-rate object (sxds_0034) does exist; this is an obscured 'radio-quiet quasar' which may have FRI-like jets.

• The presence of significant accretion is linked to the radio luminosity L_{rad} (or radio structure) of the radio source at $z \sim 1$, just as it is at $z \sim 0.1$.

• Mid-IR excess and blueness are correlated, where the Spearman's generalised $\rho = 0.636$ with a 99.9% probability for a correlation.

• This correlation is consistent with a model in which $\sim 30\%$ of the QSO light is absorbed by a dust torus and $\gtrsim 1\%$ is scattered by dust above and below the torus.

Study of the brightest SXDS radio sources in the mid-IR has revealed that the ratio of objects with significant accretion rates to the total number of objects is high for flat-spectrum radio sources, and for steep-spectrum sources above the FRI/FRII radio luminosity divide. This ratio is much lower for objects below the luminosity corresponding to the FRI/FRII divide. Future work on the brightest SXDS radio sources is likely to involve studies of radio structural properties, host galaxies and other indicators of accretion like emission lines and X-rays.

Appendix A

2.6 Notes on the 37 brightest SXDS radio sources

sxds_0001: The brightest radio source of our sample is a twin-jet (TJ) galaxy at redshift $z = 0.627$. Spectroscopy was obtained both with VIMOS on the VLT and ISIS on the WHT. In the latter case the slit width was 2.5 arcsec and the position angle PA = 320°. This object is resolved at K. The NVSS flux density is higher than the SXDS value (Table 2.1), indicating the existence of diffuse radio structure surrounding the radio source. This is a typical galaxy 'G', according to Section 2.3.3, with a prominent [OII] line in its optical spectrum and no hint of 24-μm emission. The apparent flattening between 610 MHz and 325 MHz maybe due to inaccurate flux density entry in the 325-MHz catalogue.

sxds_0002: This object has a classical double radio structure, as seen in the A-array radio map. It is also an obscured quasar 'OQ', since it has $\log_{10}(L_{24\mu\mathrm{m}}/\mathrm{W}) > 37.3$ and is resolved, and presumably dominated by starlight at K. Optical spectroscopy was obtained at the WHT using a slit with a width of 2.5 arcsec and a PA = 305°. The BRz-radio overlay in Figure 2.7 shows the possibility of merging activity between the radio-source host galaxy and a nearby object.

sxds_0003: This is a classical double radio source since the A-array radio map reveals compact FRII-like hotspots associated with an obscured quasar at redshift 2.433. Spectroscopy was obtained both with VIMOS at the VLT and ISIS at the WHT, where in the latter case, the slit width was 2.5 arcsec and the PA = 313°. The optical spectrum lacks broad emission lines, a result that confirms our classification of this radio sources as 'OQ'. As in sxds_0002, the BRz-radio overlay reveals possible galaxy-galaxy merging activity and it has a 24-μm excess in its SED. The Lyα line in the emission spectrum of this object is spatially extended over ~ 3.4 arcsec $\simeq 25$ kpc.

sxds_0004: A compact flat-spectrum radio source with a SED rising to 24 μm. According to our classification scheme of Section 2.3.3, this is a BL Lac object, which is consistent with it having a flat radio spectral index ($\alpha = 0.164$). The difference between SXDS and NVSS flux densities (Table 2.1) indicates that the radio-source flux density might be time variable. This object was observed using AAOMEGA at the AAT, but we only have a 1-D spectrum available, with one highly questionable emission line at 5900 Å, and this does not give a reliable spectroscopic redshift; we prefer thus the photometric redshift.

sxds_0005: A compact steep-spectrum radio source and a galaxy without a secure spec-

troscopic redshift, since observations with the WHT didn't give a sufficient S/N to measure an accurate redshift (slit width 2.5 arcsec and PA = 310°). The optical spectrum shows a very faint continuum, as expected from its photometry (Simpson et al. 2006) and the fact that the photometric redshift, $z = 1.610$, is in the 'redshift desert' where there is a lack of any strong emission lines.

sxds_0006: A compact radio source that is projected close to a bright star and hence without any entry in the mid-IR Spitzer catalogue. This object has no optical spectroscopy, but we are confident that the photometric redshift is accurate due to a good fit of the template to the SED (Figure 2.7). It has an inverted spectral index, as calculated from the 1.4 GHz and 610 MHz data; the limit at 325 MHz verifies this result.

sxds_0007: A large (123 arcsec) FRII classical double radio galaxy at $z = 1.325$. The NVSS flux density is the sum of the integrated fluxes of the two lobes, which is the same value as the one measured from the NVSS map itself. Both 610 MHz and 325 MHz data suggest a very steep radio spectral index for this source.

sxds_0008: A compact radio source in a $z = 0.458$ blue galaxy. According to our classification of radio sources, this is a starburst 'SB' with a star formation rate $\mathrm{SFR_{FIR}} \sim 100$ $\mathrm{M_{\odot}yr^{-1}}$, calculated from the SED, using a Salpeter IMF and the star formation rate (SFR) relations of Kennicutt (1998). We have a good agreement of spectroscopic and photometric redshifts. From the BRz-radio overlay of Figure 2.7 we see obvious galaxy-galaxy merging activity and a 24-μm excess in its SED. We believe the 24 μm excess is more readily attributable to a starburst than an AGN because the optical spectrum has bright [OII] emission but no corresponding high-excitation lines.

sxds_0009: A compact radio source missing $J-$ and $K-$band data since it lies outside the UDS coverage (Figure 2.1). The weak extensions is the B-array radio map (Figure 2.7) to the east and the south-west are probably artifacts. The high NVSS flux density is due to confusion with a nearby source. This object is probably at $z = 3.570$, which agrees with the photometric redshift (Table 2.1). The photometry of this object in the blue, B = 26.3 mag[9], indicates that the apparent blue tail in the optical spectrum is a spurious feature. This object has a flat radio spectrum and some evidence that a significant fraction of the optical light comes from a point source although there are no broad lines or a 24-μm excess. We classify it as a 'Q?' because of hints of broad wings to the Lyα line and the significant blue continuum, although the limit at 24-μm is insufficient to confirm a QSO-like mid-IR excess.

sxds_0010: A compact radio source and a galaxy 'G'. The HyperZ photometric code gives

[9] ($www.astro.livjm.ac.uk/ \sim cjs/SXDS/radio/$)

a good fit to the SED when we use the BC templates. There are no spectroscopic data available for this source.

sxds_0011: A radio galaxy at $z = 0.647$ with TJ structure. The angular size was measured from the radio overlay from the core to the largest extent of the north-east jet and separately to the south-east radio components, with the two values added together. The 610 MHz flux density was measured around the same area as the 1.4 GHz flux density giving a radio spectral index between these values of 0.62. The NVSS flux density, though, suggests that there is extra emission at large angular sizes. We adopt a typical steep radio spectral index of $\alpha = 0.8$ since steep spectral indices are typical for objects with a FRI radio structure; the spectral index calculated from the SXDS and 325 MHz data suggests an inverted spectral index which is inconsistent with the fact that this is a large twin-jet radio source. We suggest that the 325 MHz data are inaccurate in this case.

sxds_0012: A large FRII galaxy at $z = 0.865$. The 325-MHz catalogue entry includes only part of the source, giving a nonsensical radio spectral index. We use the total 610-MHz flux density from the radio map to calculate the spectral index, whose steep value agrees with the CD radio structure. There are no signs of a QSO nucleus.

sxds_0013:A spectroscopically confirmed quasar at $z = 2.713$ and a point source in the optical. The optical spectrum shows strong absorption features associated with the broad lines. Such broad-absorption-line (BAL) QSOs are rare, but not unknown, in radio-selected samples. The B-array radio image shows a compact source. From the optical overlay of Figure 2.7 it looks like a galaxy is dominant in the $K-$band, since it is not a point source at K, although it is one in the optical. The flat radio spectral index, $\alpha = 0.08$, agrees with the fact that this is a compact radio source.

sxds_0014: This object appears to be red with a rapid drop in its SED from red to blue. In the $K-$band image, although it has a low S/N ratio, the source looks unresolved indicating that the radio source might be compact or there is a hidden quasar nucleus. The limit at 24 μm is insufficient to rule out that this might be an obscured quasar 'OQ'; we define it as a galaxy 'G?' (see Sec 3.3). In Vardoulaki, Rawlings & Simpson (2006) we used 36 radio sources from this sample, accidentally excluding this one; all the subsequent identification numbers have moved downwards in order to include this radio galaxy. The inverted radio spectral index is consistent with the fact that this object has compact radio structure. The tentative emission feature around $\lambda \sim 6000$Å in the optical spectrum of this object cannot provide us with a reliable spectroscopic redshift.

sxds_0015: A possible 'double-double' radio galaxy. Such sources (Schoenmakers et al.

1999) are thought to be jets that have re-started, sometimes (as perhaps in this case) with a change of jet orientation, perhaps due to merging of two supermassive binary black holes (Liu et al. 2003). From the BRz-radio overlay of Figure 2.7 we see evidence of galaxy-galaxy merging in the form of tidal tails (Johnston et al. 2004), and there is also excess emission at 24 μm as can be seen in its SED. We use the radio spectral index calculated between 610 MHz and 1.4 GHz data, which gives a steep value that agrees with the FD radio structure. We don't trust the 325 MHz data since they give a spectral index inconsistent with the radio structure. Although this object is defined as 'G', its detection at 24 μm might indicate it is either a 'SB' or a 'WQ'.

sxds_0016: A classical-double radio source, possibly at $z = 1.345$. Shorter wavelengths in the spectrum are, due to poor resolution, affected by the overlapping spectrum of a nearby object. Photometry of this object was directly measured from images using sxds_0034 as a boot-strap calibrator, since it was not matched with any source within a $2''$ search radius. Using these data we give the photometric redshift in Table 2.1 with an associated uncertainty. According to these measurements, the object has excess emission at 24 μm, which classifies it a 'OQ' according to Section 2.3.3 and Figure 2.3. We use the spectral index calculated between the 610 MHz and 1.4 GHz flux densities, which agrees with the CD radio structure of this object.

sxds_0017:A spectroscopically-confirmed broad-absorption-line quasar at $z = 2.583$, where the Lyα line is heavily absorbed. The spectrum appears peculiar, since the CIV and CIII] lines have narrow cores and a red and blue broad wing respectively. The radio map reveals a prominent hotspot to the north-east; the component to the south-west of the quasar is probably the weak side of an asymmetric double. We use the 325 MHz flux density to calculate a spectral index since it was not observed at 610 MHz.

sxds_0018: A large FD (no compact hotspots in the A-array map) radio galaxy at $z = 0.919$. The radio spectral index is calculated between the 610 MHz and 1.4 GHz data, where the steep value is consistent with the extended FD radio structure. The 325-MHz catalogue entry is probably inaccurate, since plausible extrapolation of the 610 MHz flux density suggests that the object has more flux density at 325 MHz than the limit of that catalogue.

sxds_0019: A FD (no compact hotspots in the A-array map) radio galaxy at $z = 0.694$. It has a very asymmetric radio structure. We assume $\alpha = 0.8$ due to the extended FD radio structure; the inverted spectral index calculated between the 325-MHz and 1.4-GHz data is inconsistent with the radio structure of this object.

sxds_0020: This object has an unusual radio structure that we classify, uncertainly, as

FD. The steep spectral index calculated between 610 MHz and 1.4 GHz is consistent with the extended radio structure. The 325-MHz entry is inaccurate since both the radio structure and the 610-MHz to 1.4-GHz spectral index indicate that it has a steep radio source. There are no spectroscopic data available for this object and the photometric estimate is highly uncertain.

sxds_0021: A radio galaxy 'G' and a compact radio source. The radio structure to the north-west side of the object is probably not associated with the brightest radio source as it has a separate galaxy identification. The photometric redshift is used since there is no spectroscopy available.

sxds_0022: A compact radio source associated with a galaxy at $z = 0.248$; note the spectacular blue arc which is probably a remnant of star formation associated with a galaxy-galaxy interaction. The southern and eastern radio components are probably artifacts. This is possibly a post-starburst galaxy, or an 'E+A', i.e. an elliptical with additional absorption lines (e.g. Hβ in Figure 2.7) in their optical spectra due to stars seen $\sim 10^8$ yr after the starburst has finished (Goto 2007). Star formation might be contributing to the radio emission. There is some evidence for excess emission at 24 μm as well as dramatic tidal tails (Figure 2.1). We classify this radio source as a 'G'.

sxds_0023: A compact radio galaxy at $z = 0.586$. The A-array map reveals a possible double structure, although it might be the base of a FRI-like jet. There is a fairly good agreement between the spectroscopic and photometric redshifts.

sxds_0024: A TJ radio galaxy at $z = 0.516$. The radio spectral index that is calculated between 325 MHz and 1.4 GHz is inconsistent with the TJ radio structure of the source; so we use 610 MHz flux density.

sxds_0025: A compact weak quasar 'WQ' probably at $z = 0.9636$ if the single marginally broad line in the spectrum is MgII (the deconvolved FWHM is ~ 900 kms^{-1}). We are not certain that the [OII]λ2470Å emission line is real, since spectroscopic studies show that this is quite a weak feature (e.g. Serjeant et al. 1998). The photometric redshift is inaccurate due to the absence of $J-$ and $K-$band data (Figure 2.1) and the fact that the optical continuum appears to be dominated by blue QSO light; the rest-frame EW of the putative MgII line is ~ 50 Å and thus within the spread seen in directly viewed quasar nuclei (Francis et al. 1991). The templates used in the HyperZ code cannot provide a proper fit to the SED. The NVSS flux density is higher than expected due to confusion by sxds_0027. This object was not observed at 610 MHz since it is outside the coverage of the survey. We assign a typical flat radio spectral index $\alpha = 0.4$ consistent with the compact radio structure; we do not trust the 325-MHz catalogue to be complete.

sxds_0026: A TJ radio galaxy at $z = 0.450$. The companion galaxy to the west is probably not producing radio emission. According to the radio spectral index calculated between 610 MHz and 1.4 GHz data, this is a steep-spectrum radio source. The fact that the 325-MHz entry is a limit suggests that we should not trust that the 325-MHz catalogue is complete.

sxds_0027: We classify this object as 'OQ' since it has excess emission at 24 μm. We use the photometric redshift since the optical spectrum shows a featureless continuum. The longer-wavelength SED looks more like a BL Lac since it can easily be fitted by a power-law with very steep spectral index $\alpha \sim 2$, and is consistent with the flat continuum in the optical spectrum of this object. The 'tails' in the radio map are probably artifacts, so its compact nature is consistent either with it being a BL Lac object or an 'OQ'. The object is resolved at K which is why we prefer the 'OQ' category. This radio source is not observed at 610 MHz. We assign a typical flat radio spectral index $\alpha = 0.4$ consistent with the compact radio structure; we do not trust the 325-MHz catalogue to be complete at the flux density level appropriate to this source. The NVSS flux density is higher than expected since with the NVSS resolution we can only marginally distinguish this object from the nearby object sxds_0025.

sxds_0028: A compact radio galaxy, probably at $z = 0.627$. The radio map shows a seemingly double source, but in reality there are two radio sources, as there are good optical IDs under both apparent radio lobes. The object under the north-west 'lobe' is sxds_0028, whereas the one under the south-east 'lobe' is sxds_0042 (a compact radio source at redshift $z = 0.382$, which is just below our flux density limit). The flattening of the radio spectral index between 610 MHz and 325 MHz suggests that the 325-MHz catalogue is incomplete; the 325 MHz flux should be higher than the limit of that catalogue.

sxds_0029 A compact radio source that looks unresolved in the $K-$band. Due to absence of spectroscopic data, we use the photometric redshift, which suggests a fairly good fit to the SED (Figure 2.7).

sxds_0030: This probably is a TJ radio galaxy at redshift $z = 0.535$ with the jets swept back forming a narrow-angle tail. There is a fairly good agreement between the photometric and spectroscopic redshifts.

sxds_0031: This is a compact radio galaxy. The radio component to the west is probably not associated with this source as it has its own separate galaxy identification. The fairly good fit of the photometric redshift makes us confident to use it in the absence of spectroscopic data.

sxds_0032: This is probably a FD radio galaxy; no A-array data available to confirm lack of compact hotspots. Without any spectroscopic redshift, the BC templates provide a very good fit to the photometric data and a believable photometric redshift. The 325-MHz

catalogue misses this object. According to the spectral index calculated between the 610 MHz and 1.4 GHz data, this object should have a flux density at 325 MHz that would give a steep spectral index.

sxds_0033: A TJ radio source at $z = 0.647$. It belongs to a small group of galaxies that is interacting and probably merging with a larger group of galaxies (Geach et al. 2007). The feature at 5426 Å in the optical spectrum (Figure 2.7) is CIII] emission from a lensed background object at $z = 1.847$ (see Geach et al. 2007). It is not clear whether the excess emission at 24 μm is associated with the lens or the galaxy. However, the majority of the radio emission probably originates in the lensing source. The steep spectral index calculated between 610 MHz and 1.4 GHz data indicates that the 325 MHz flux density should be higher than the catalogue entry.

sxds_0034: A compact radio source at $z = 1.095$ with a clear QSO component at the wavelengths probed by Spitzer data, a point-like optical structure, and high-excitation narrow lines in its spectrum. It is, most plausibly, a Doppler-boosted object with low extinction and possible time variability. This is the one object with significant accretion that lies below the FRI/FRII break (Figure 2.6), indicating that it is a FRI 'radio-quiet' quasar.

sxds_0035: A compact radio source and a galaxy without spectroscopy or $J-/K-$band data. The HyperZ code fits the 4000 Å break between J and K, which gives a photometric redshift of $z = 2.715$.

sxds_0036: A compact radio source and a galaxy 'G' at $z = 0.871$. The 610 MHz flux density is an upper limit, giving an uncertain measurement for the radio spectral index.

sxds_0037: A compact radio source and a galaxy 'G' that is not observed in the J and K band (Figure 2.1), and which therefore has a tentative photometric redshift. This radio source was outside the coverage of the 610 MHz survey. We use a typical flat radio spectral index $\alpha = 0.4$, consistent with the compact radio structure of this source; we don't trust the 325-MHz catalogue to be complete at this flux density level.

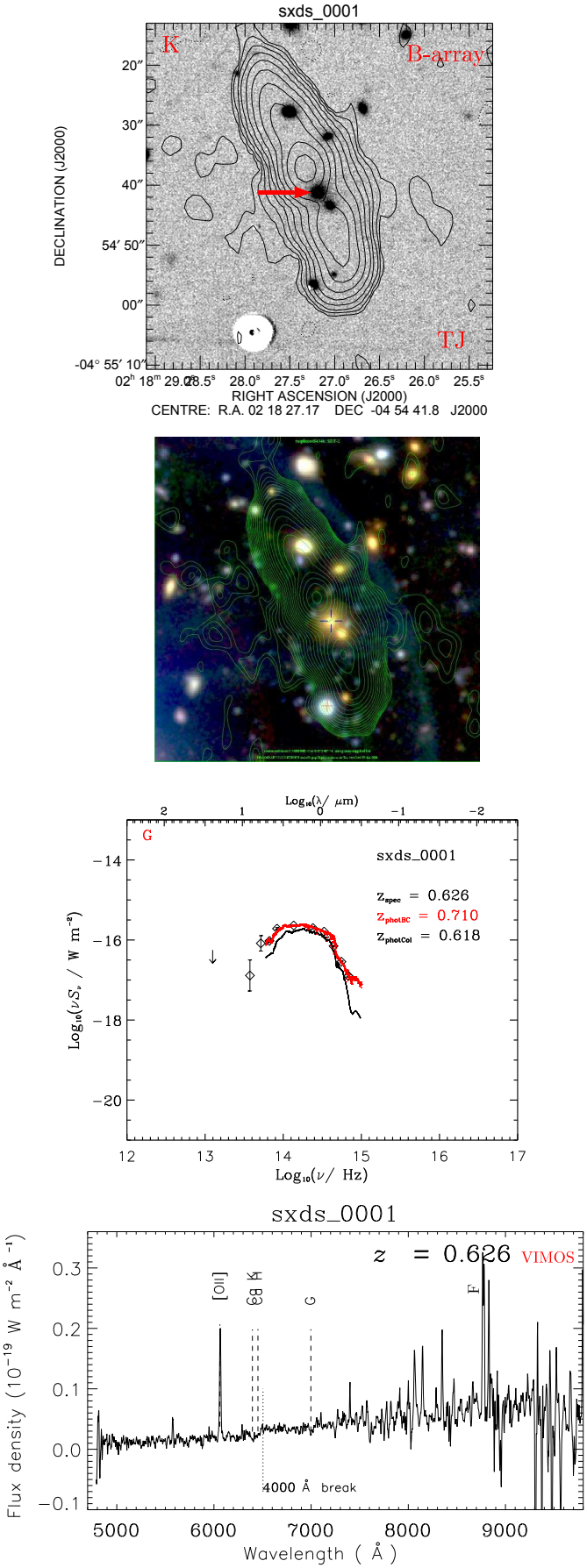

Figure 2.7: ***Top:*** K-band images and overlaid radio contours from the VLA for sxds_0001; either the B/C-array (beam $\simeq 4$ arcsec^2) or the A/B/C-array map (beam $\simeq 1.8$ arcsec^2) is shown, with the image labelled as B or A respectively. For sxds_0009, sxds_0017, sxds_0025, sxds_0027 and sxds_0037 there are no K-band images since these objects are beyond the edge of the UDS survey (see Figure 2.1), so we use z-band images instead. The radio structural classification is shown on the bottom right of the image. ***Second from top:*** Overlays of $B-$, $R-$ and $z-$band images and B-array radio maps from Simpson et al. (2006). In all the overlays, North is up and East is to the left. The contour levels follow: $2^{n_{\rm contour}-1} \times \sigma$, where $\rm n_{contours}$ is the number of contours and σ the noise level. ***Second from bottom:*** Observed frame SEDs of our objects, where we also give the best-fit SEDs, their spectroscopic redshift $z_{\rm spec}$ (where applicable) and their photometric redshift calculated from HyperZ: the red SED is calculated using BC templates and the black with CWW templates (see Section 2.3.2). ***Bottom:*** Optical spectra of 25 of the 37 SXDS radio sources. The character 'A' denotes atmospheric absorption feature, 'S' a featured caused by the dichroic, 'C' a cosmic ray, and 'F' fringing on the CCD. All spectra have been smoothed over 3 pixels. The following AAO/Omega spectra are not flux calibrated: sxds_0004, sxds_0009, sxds_0014, sxds_0030. The spectrum of sxds_0028 is flux calibrated in units of 10^{-19} W m^{-2}Å^{-1}.

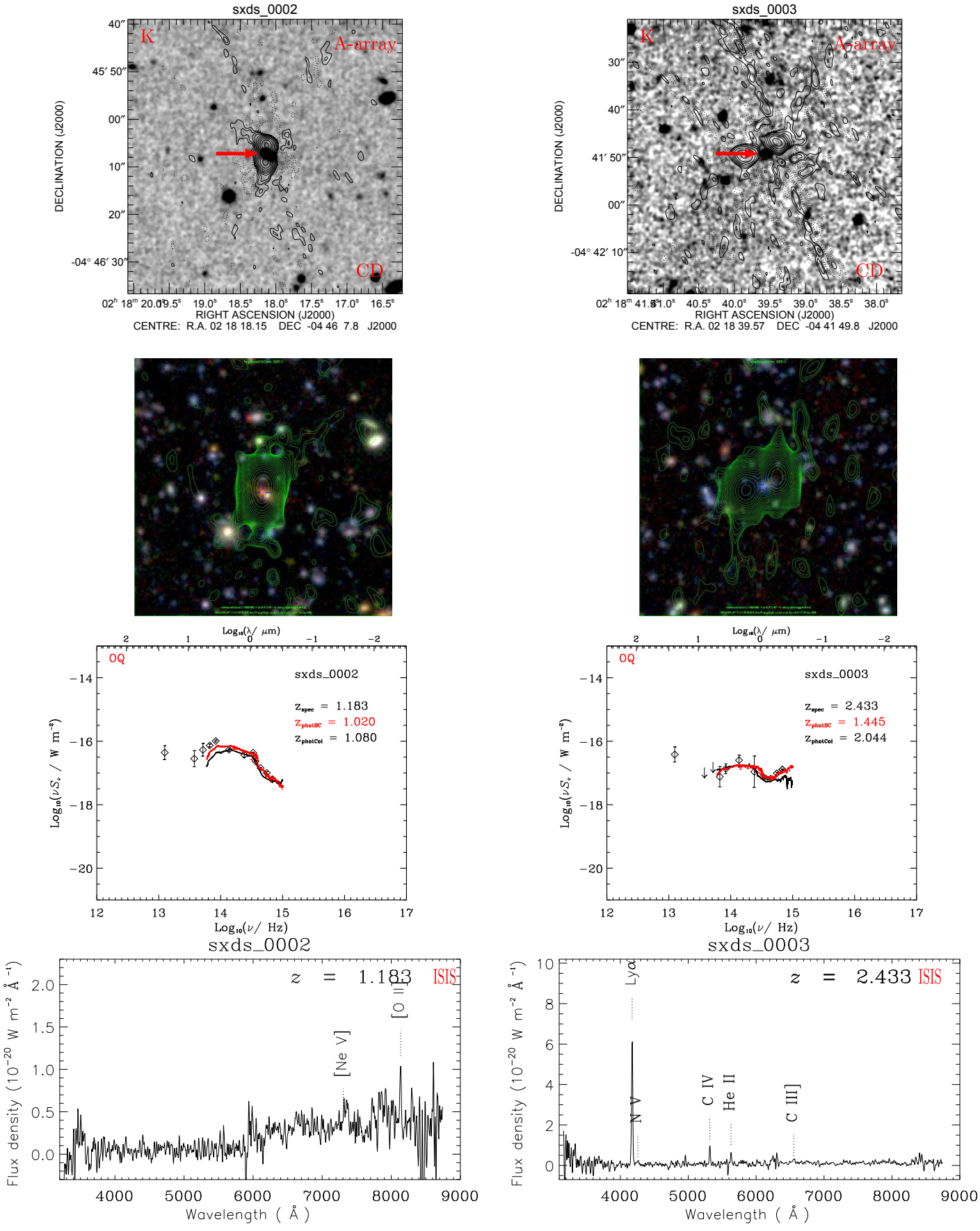

Figure 2.7: (continued)

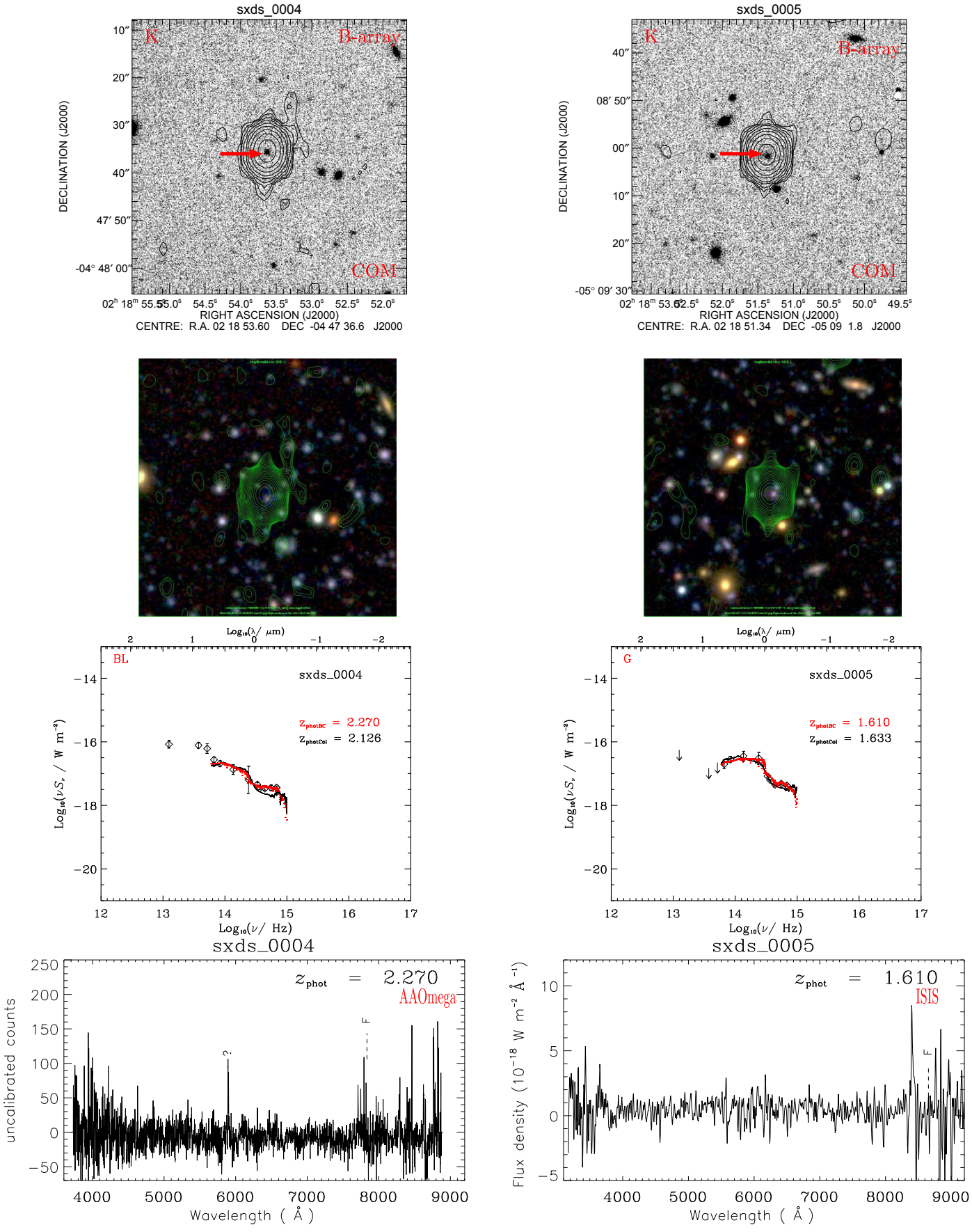

Figure 2.7: (continued)

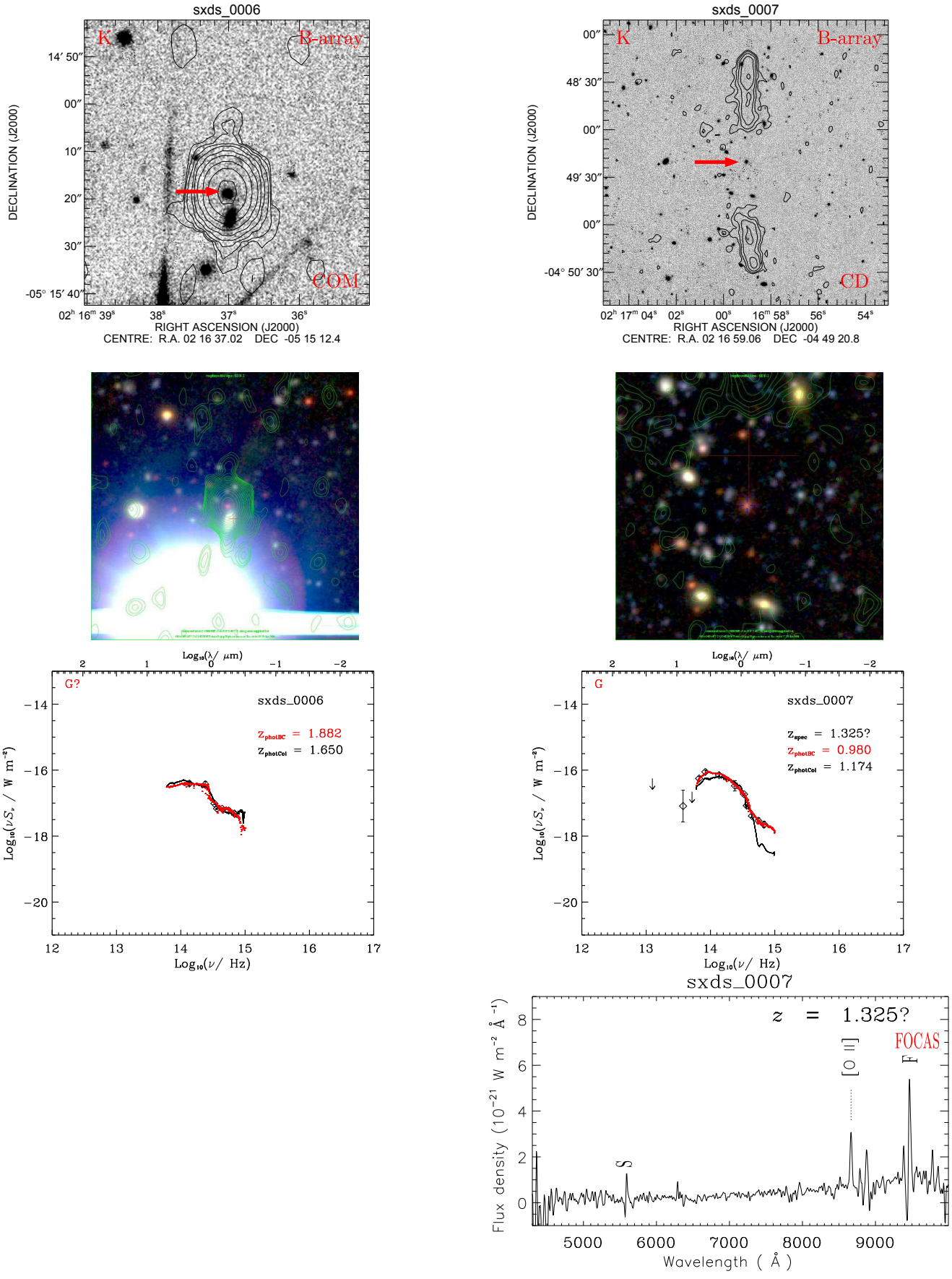

Figure 2.7: (continued)

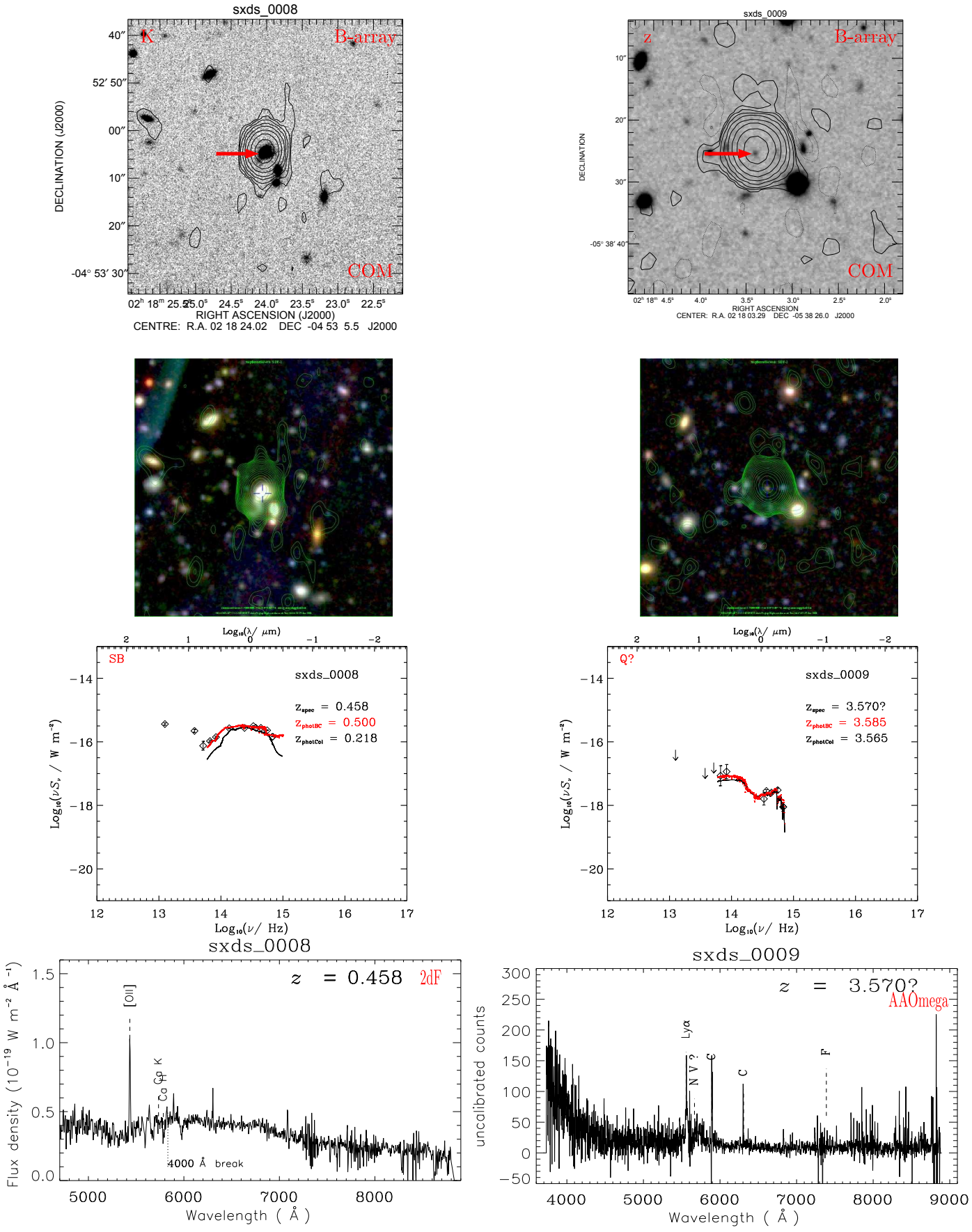

Figure 2.7: (continued)

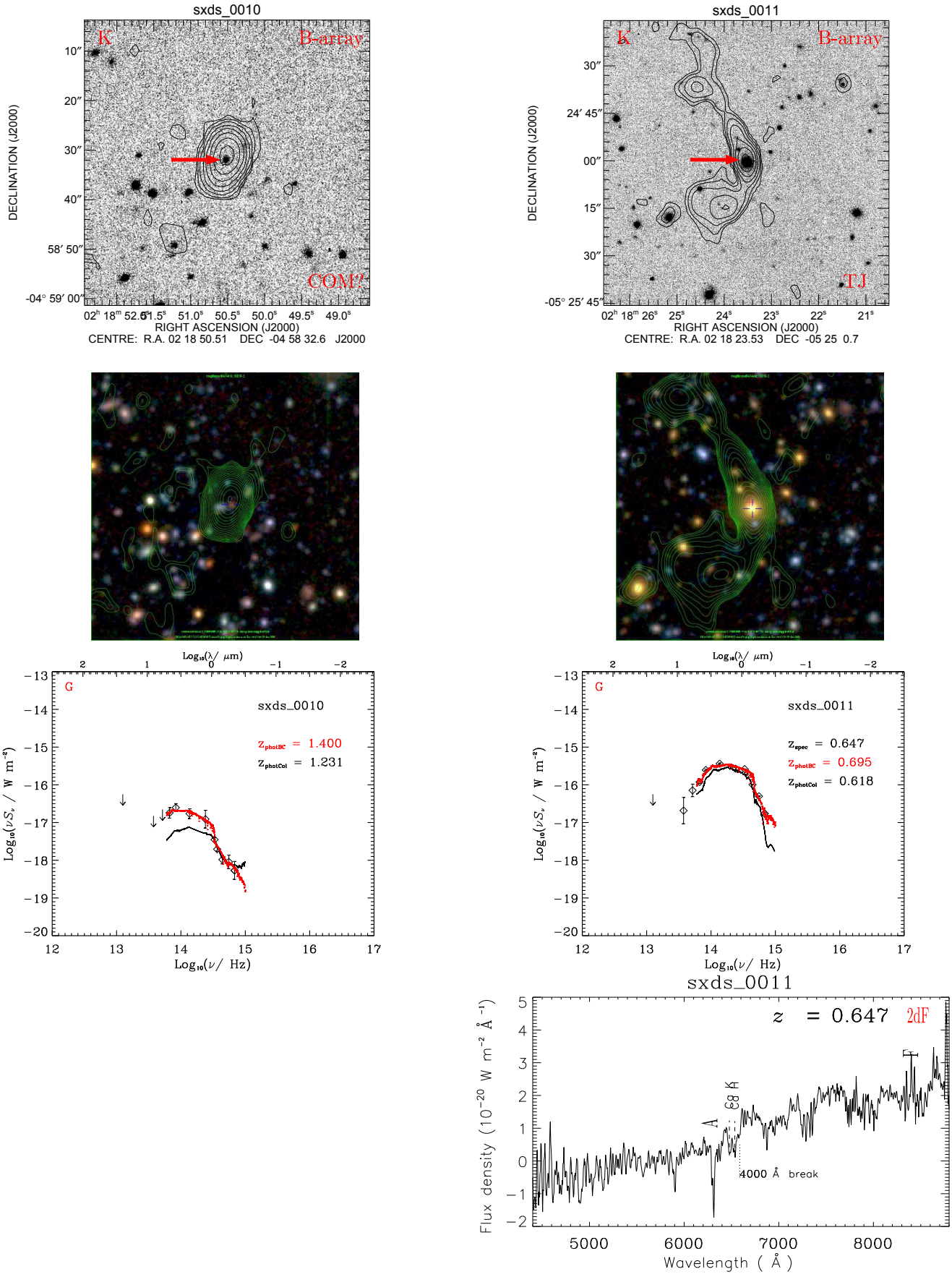

Figure 2.7: (continued)

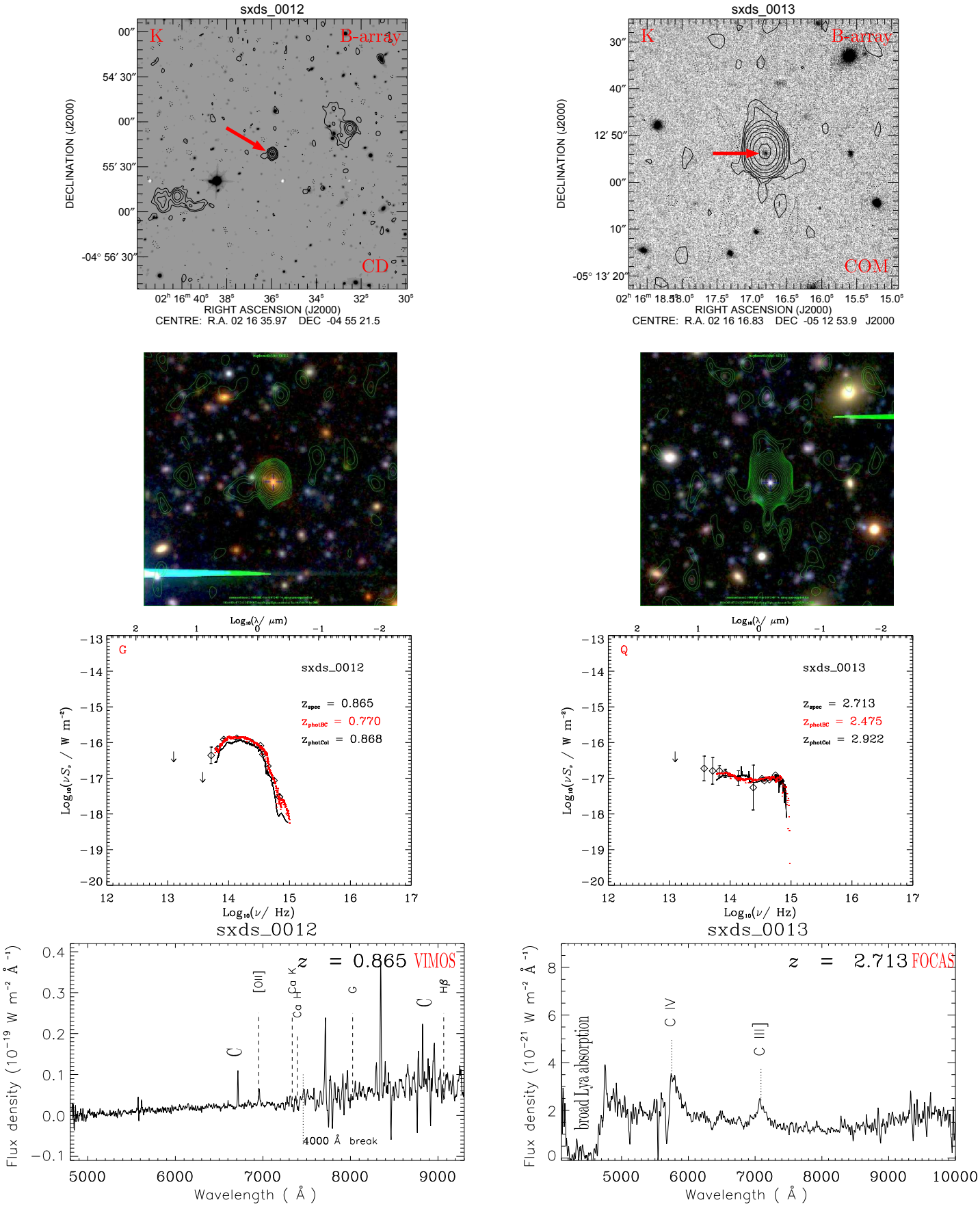

Figure 2.7: (continued)

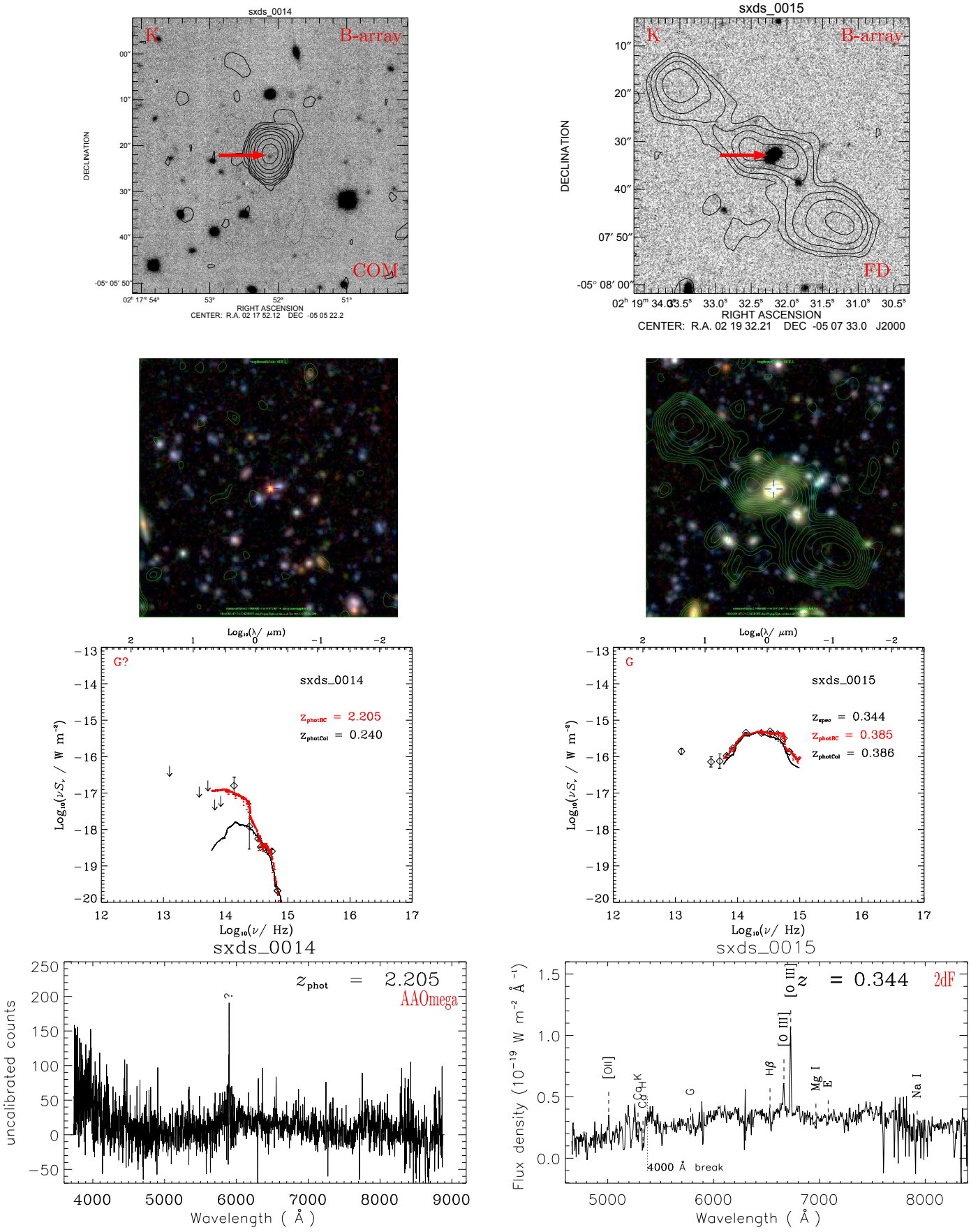

Figure 2.7: (continued)

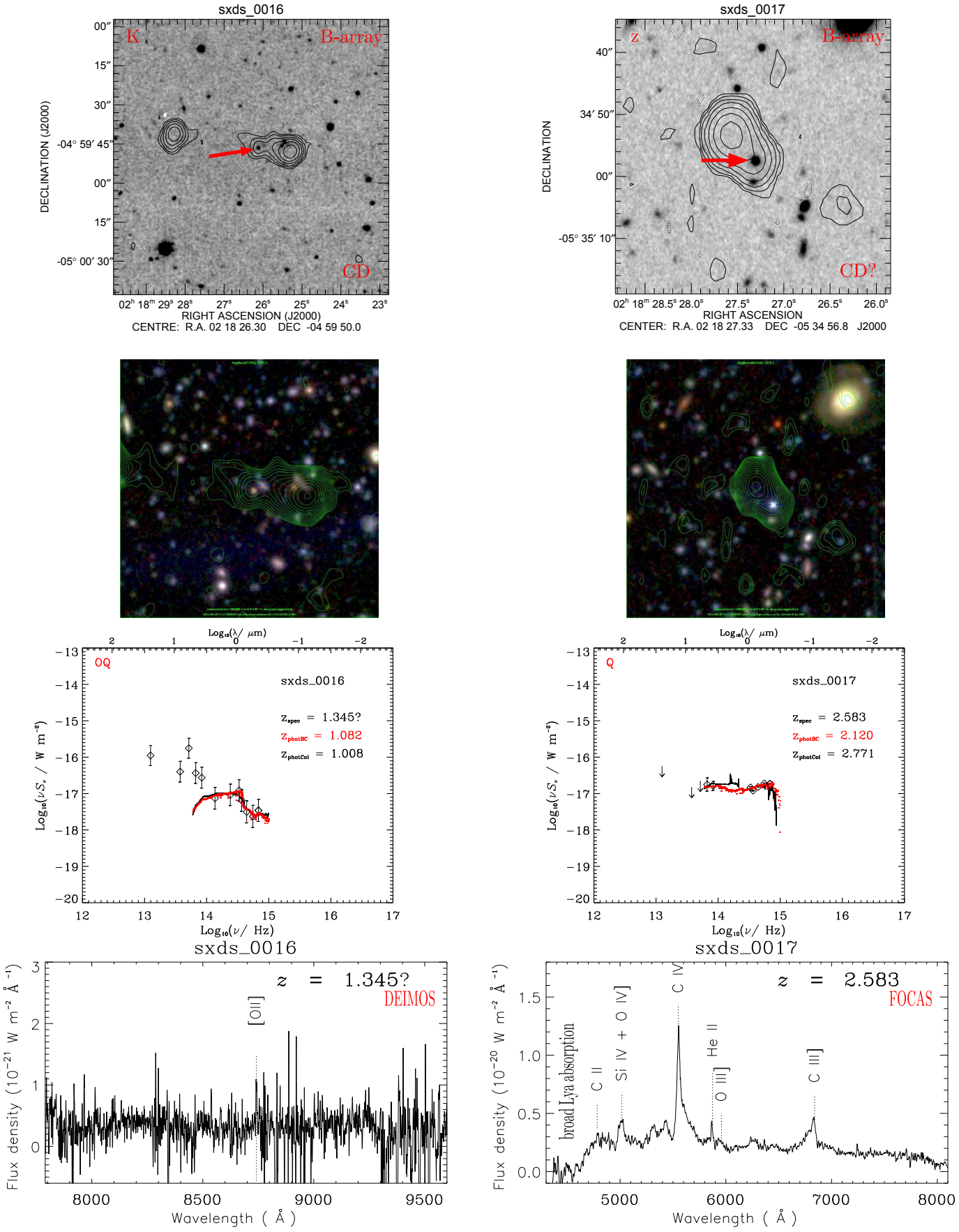

Figure 2.7: (continued)

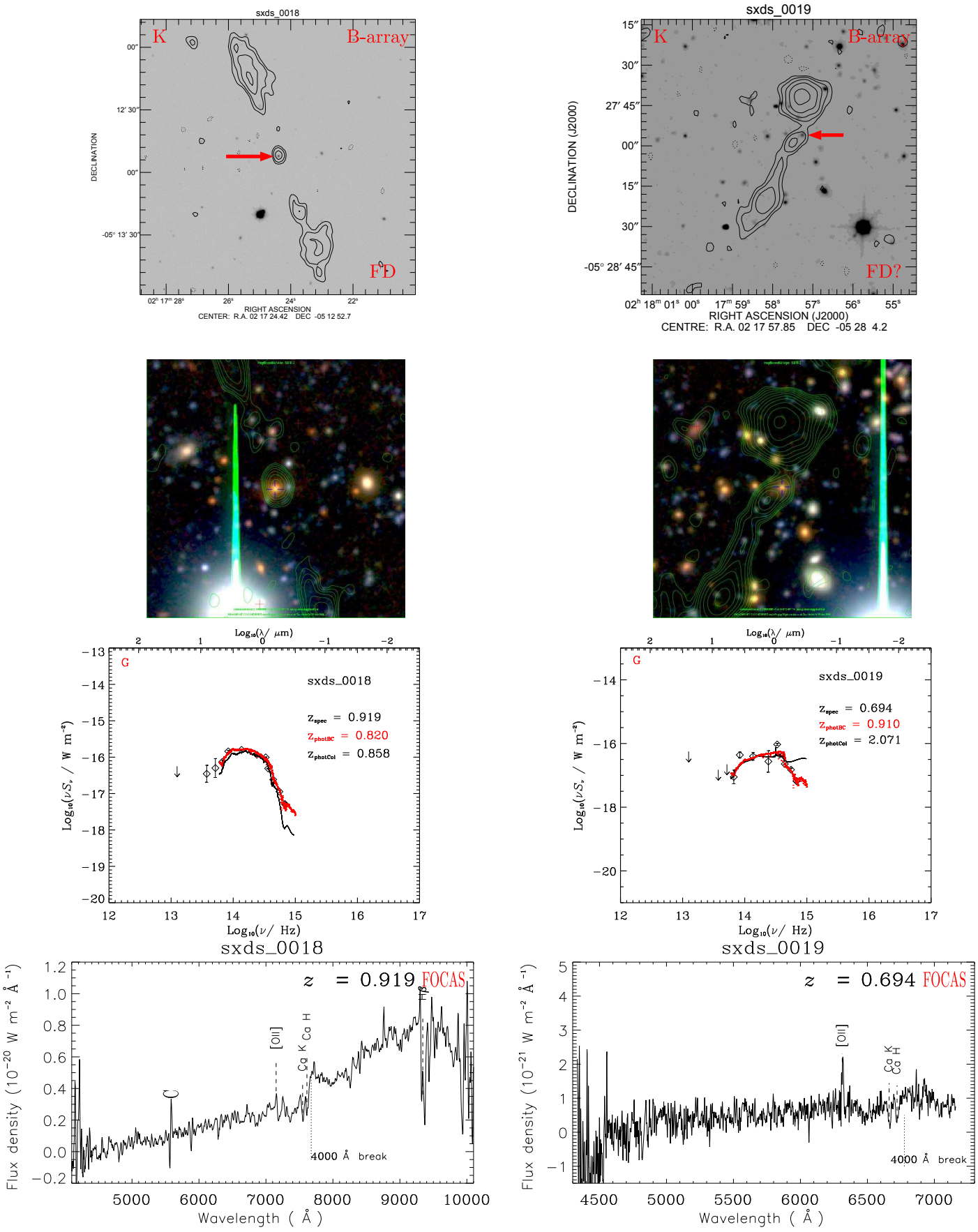

Figure 2.7: (continued)

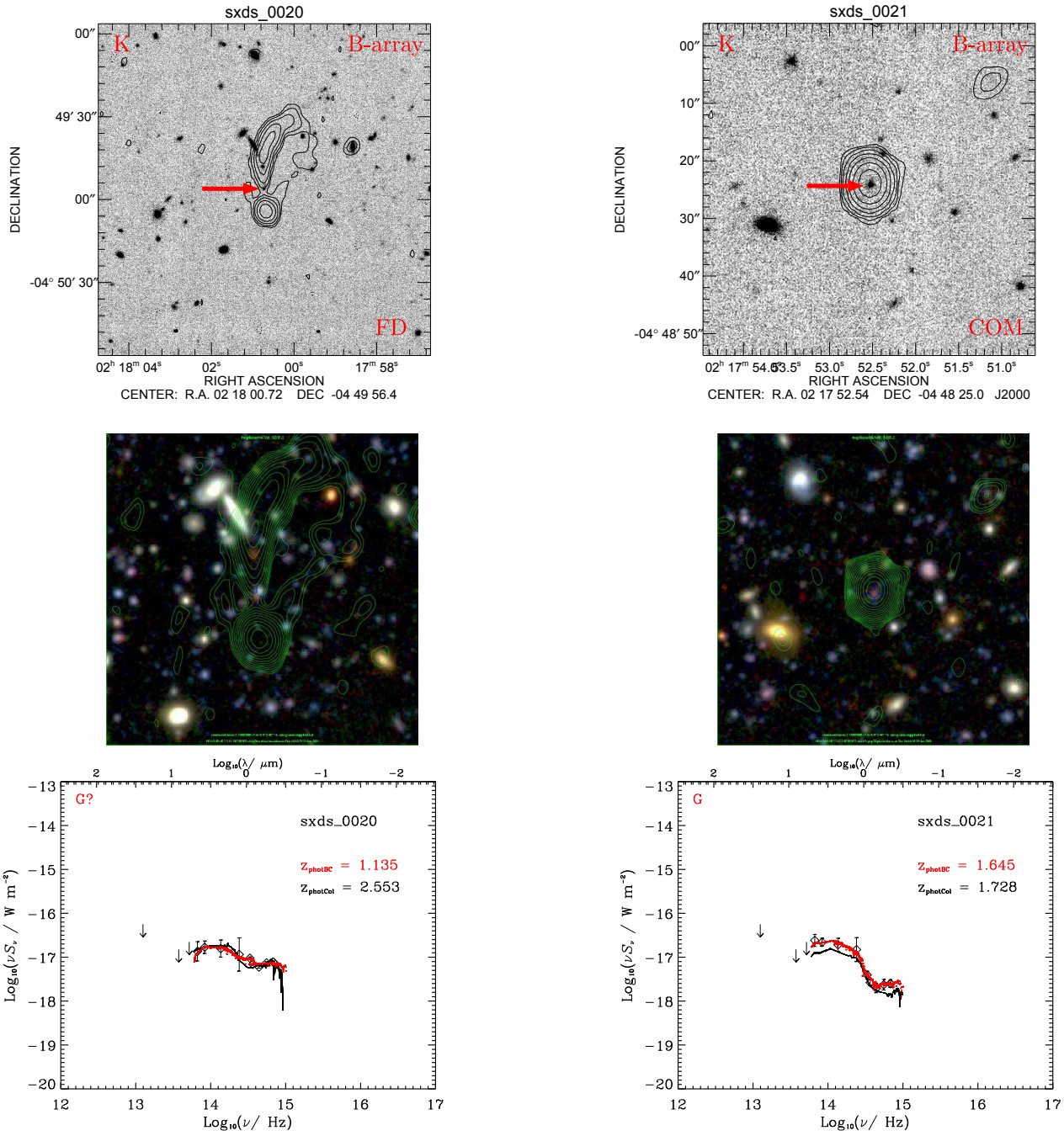

Figure 2.7: (continued)

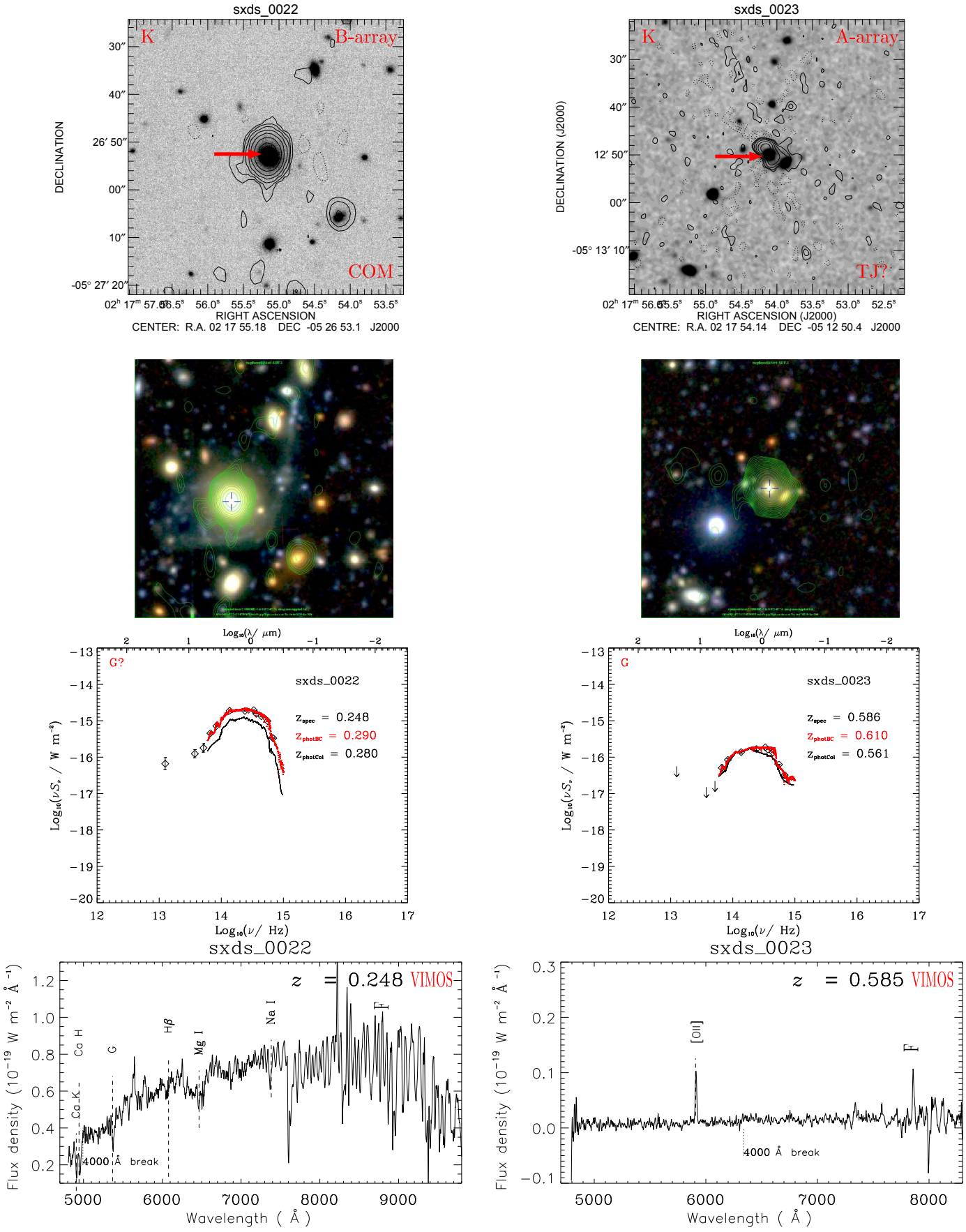

Figure 2.7: (continued)

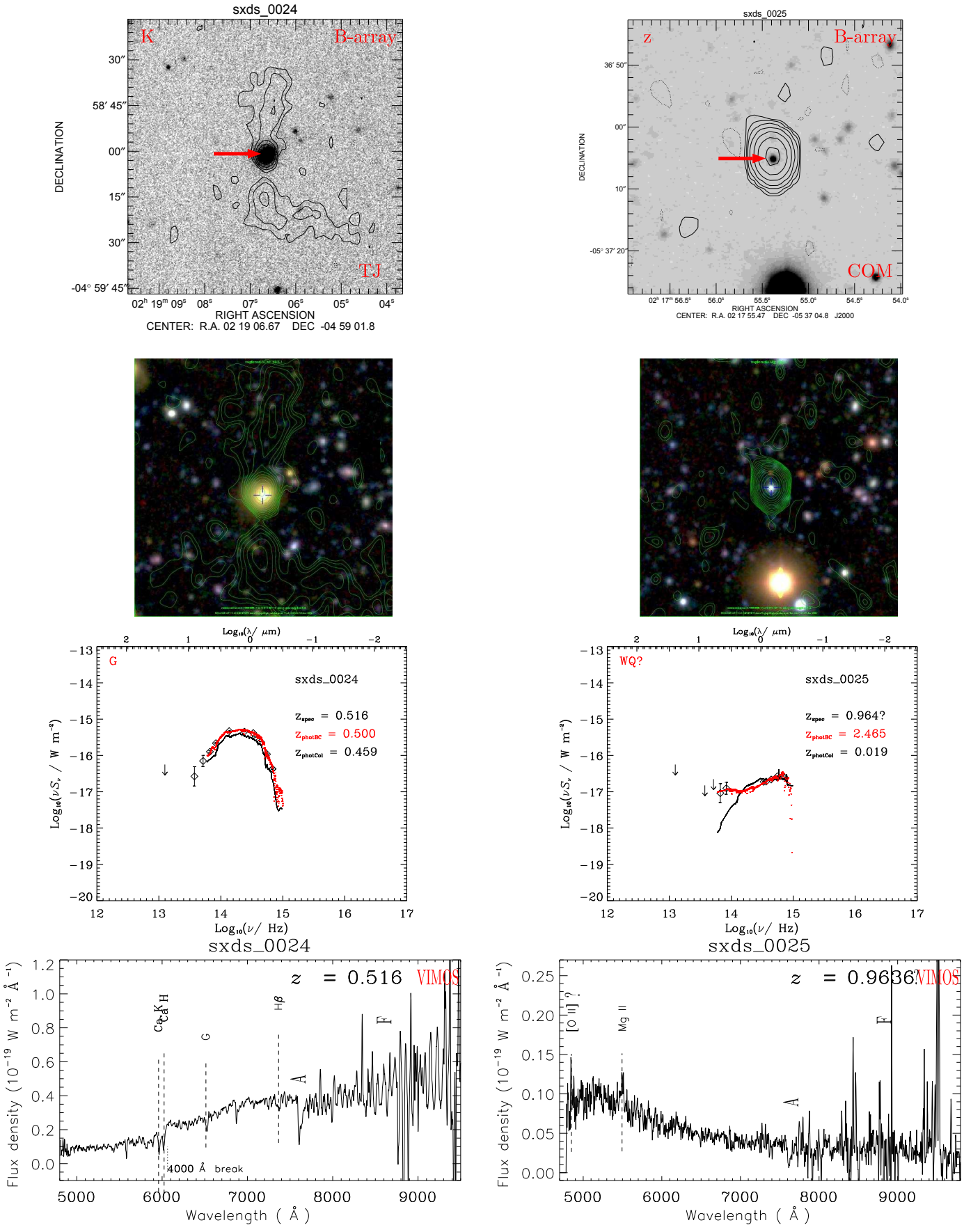

Figure 2.7: (continued)

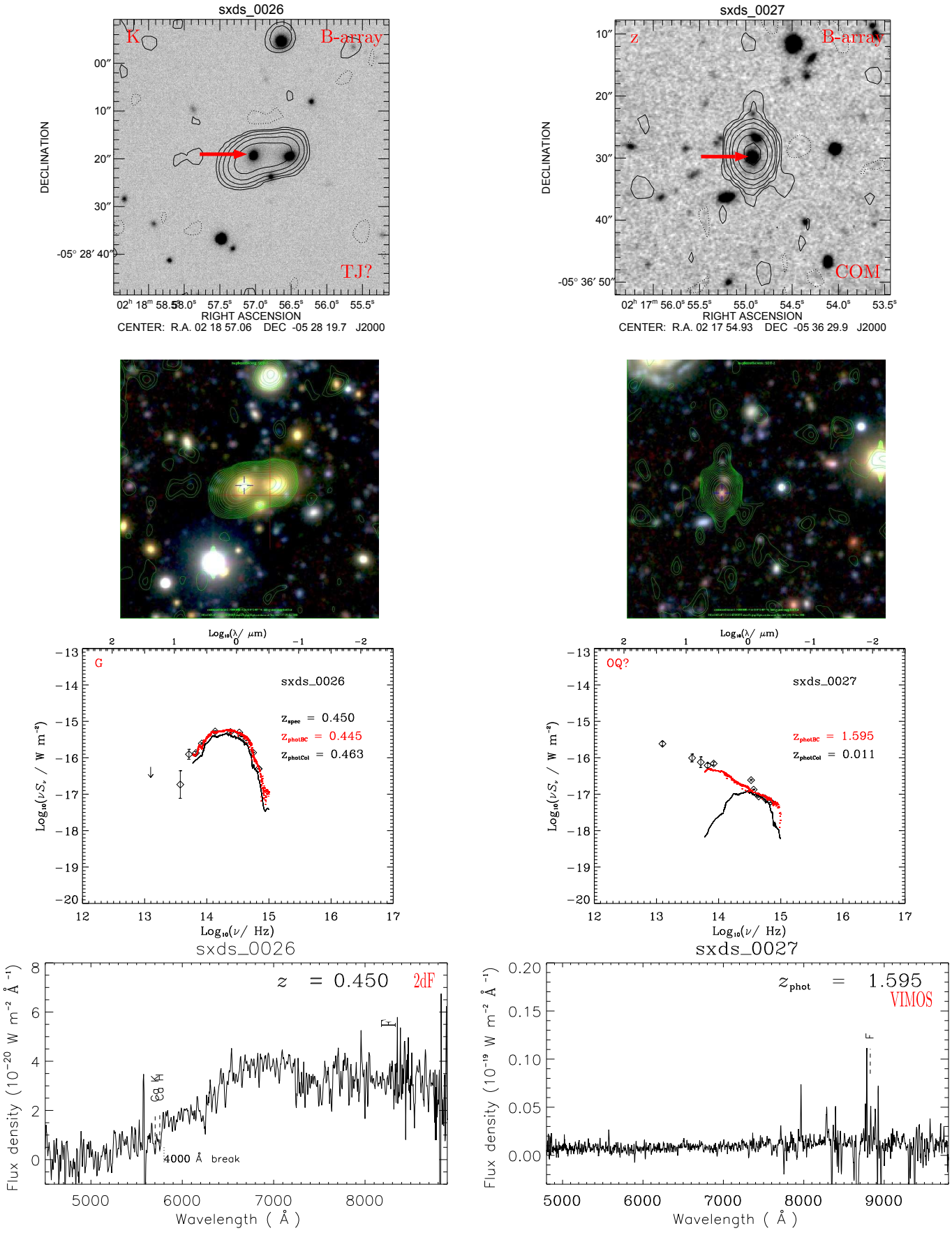

Figure 2.7: (continued)

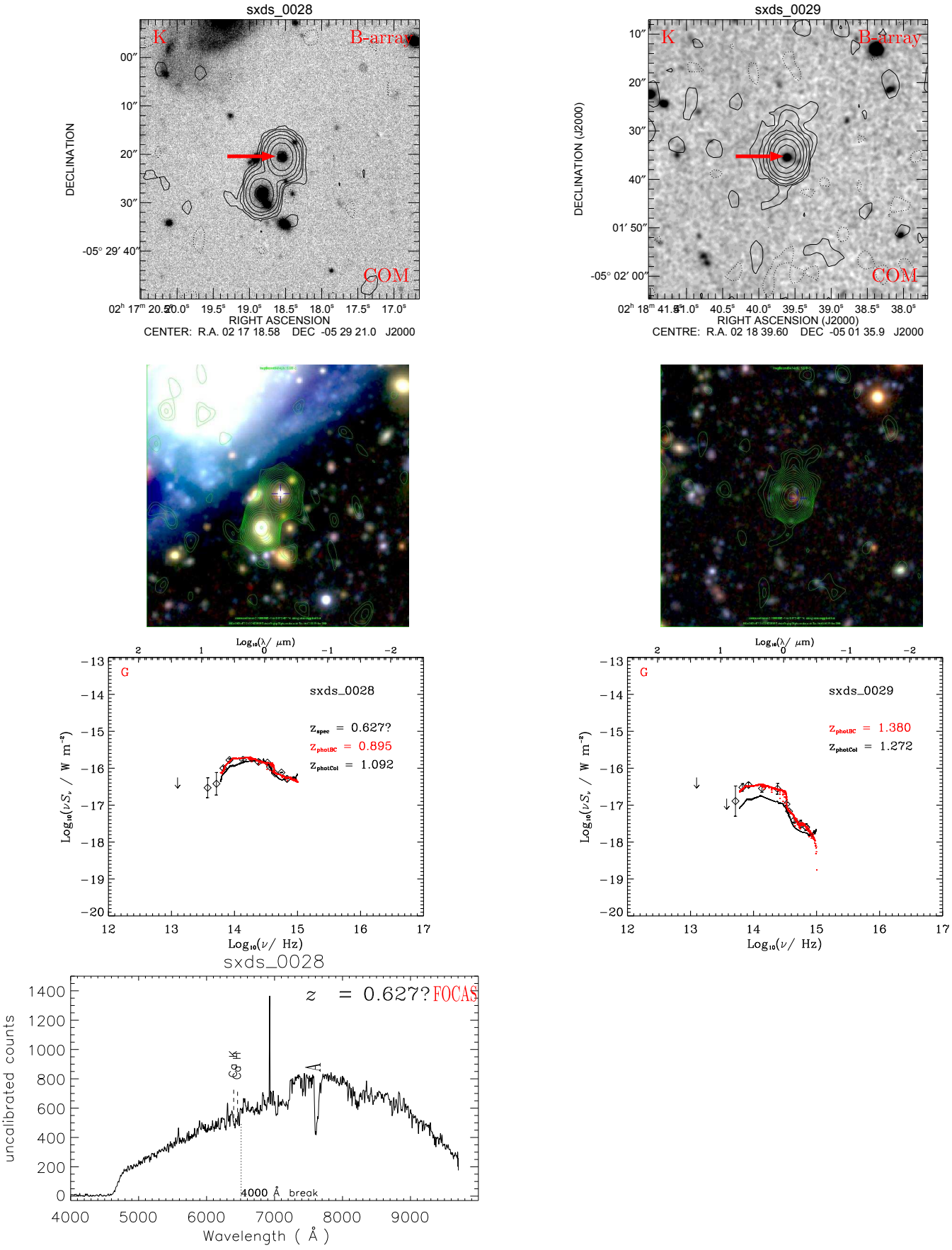

Figure 2.7: (continued)

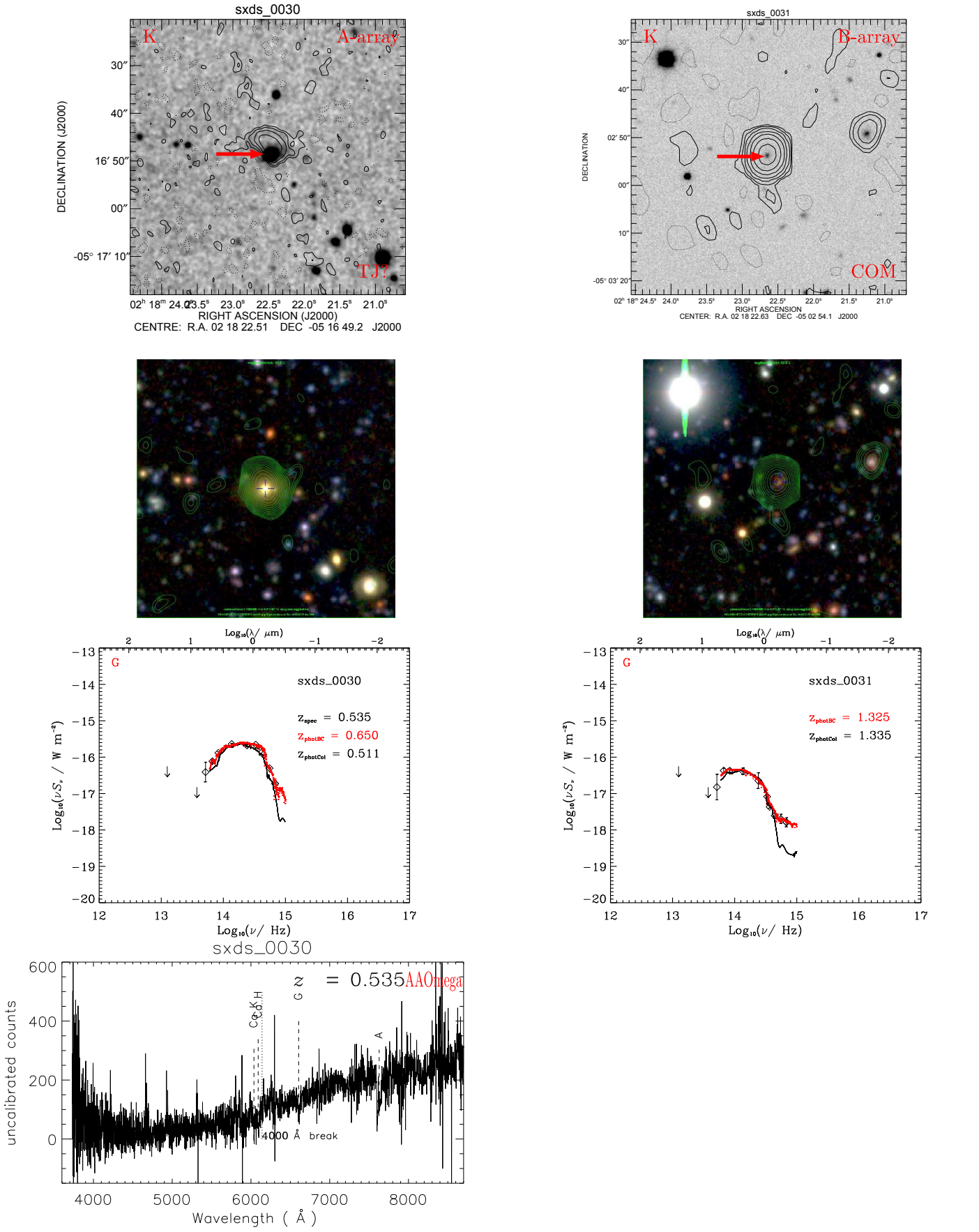

Figure 2.7: (continued)

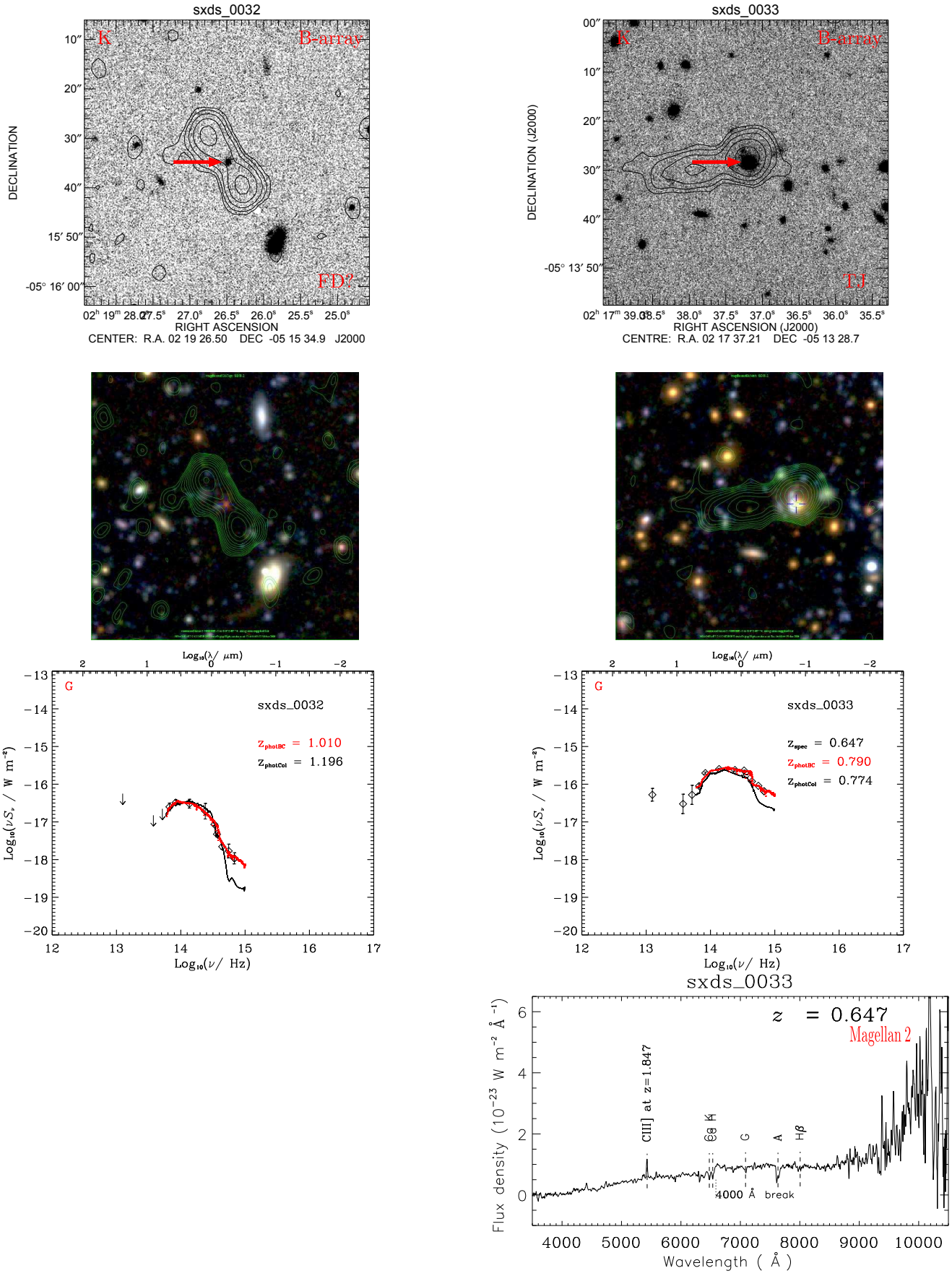

Figure 2.7: (continued)

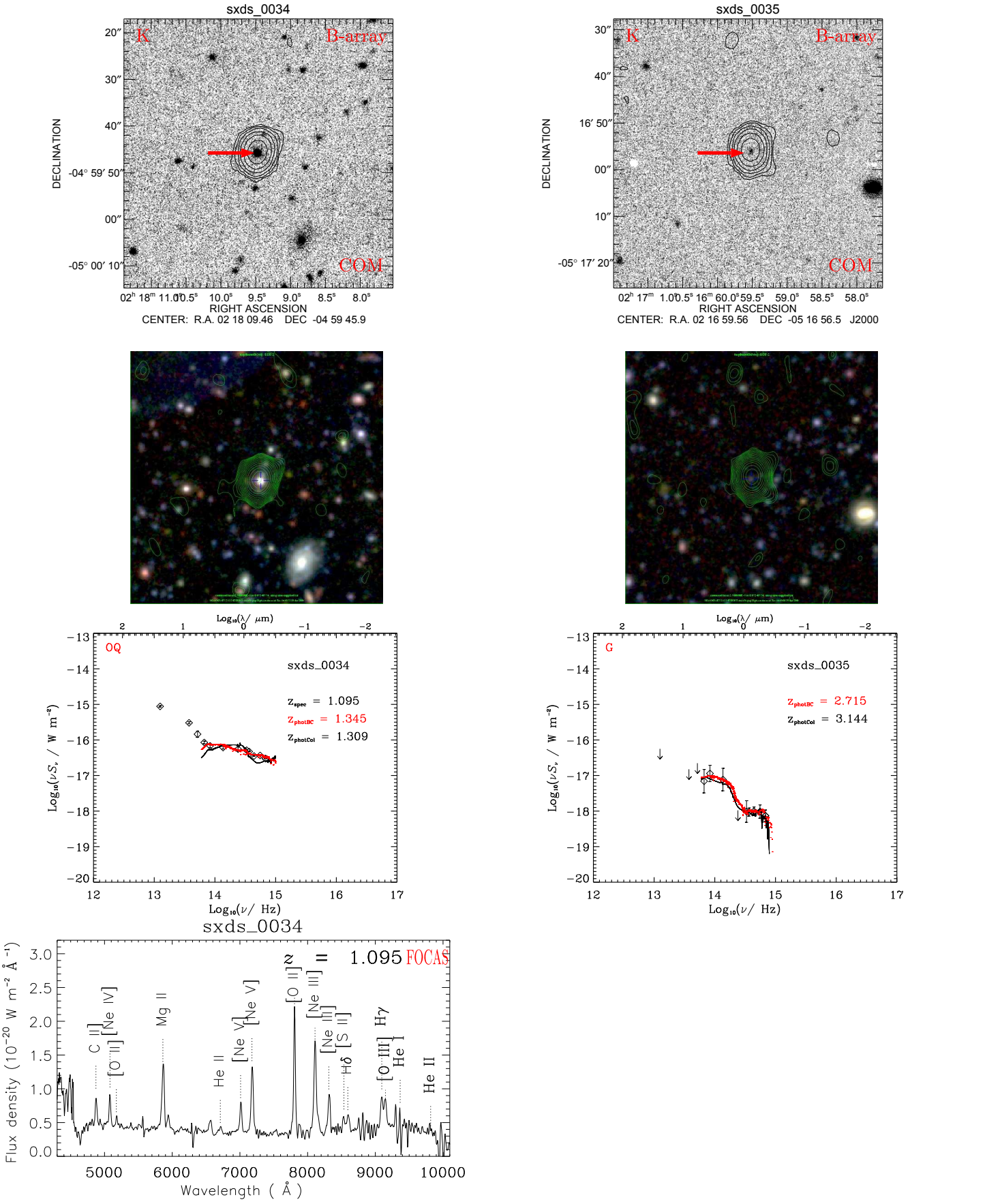

Figure 2.7: (continued)

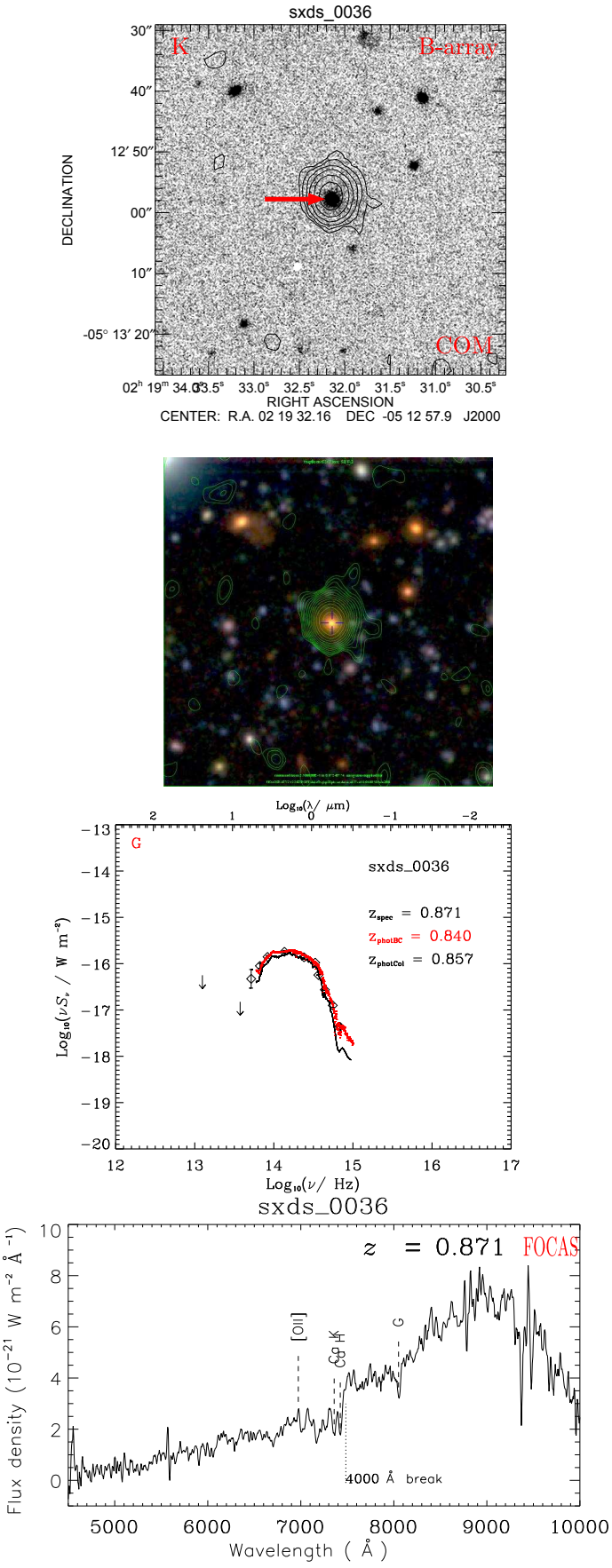

Figure 2.7: (continued)

This chapter has been published as: Vardoulaki, E., Rawlings, S., Hill, G. J., Mauch, T., Inskip. K., Riley, J., Brand, K., Croft, S., Willott, C. J. (2009). 'The TexOx-1000 redshift survey of radio sourcesI: the TOOT00 region', MNRAS 401(3), 1709-1759. [The definitive version of the article is available at http://dx.doi.org/10.1111/j.1365-2966.2009.15810.x via http://www3.interscience.wiley.com].

Chapter 3

The TexOx-1000 redshift survey of radio sources I: the TOOT00 region

Abstract

We present optical spectroscopy, near-infrared (mostly $K-$band) and radio (151-MHz and 1.4-GHz) imaging of the first complete region (TOOT00) of the TexOx-1000 (TOOT) redshift survey of radio sources. The 0.0015-sr ($\sim$ 5 deg^2) TOOT00 region is selected from pointed observations of the Cambridge Low-Frequency Survey Telescope at 151 MHz at a flux density limit of $\simeq$ 100 mJy, $\sim$ 5-times fainter than the 7C Redshift Survey (7CRS), and contains 47 radio sources. We have obtained 40 spectroscopic redshifts ($\sim$ 85% completeness). Adding redshifts estimated for the 7 other cases yields a median redshift $z_{\rm med} \sim 1.25$. We find a significant population of objects with FRI-like radio structures at radio luminosities above both the low-redshift FRI/II break and the break in the radio luminosity function. The redshift distribution and sub-populations of TOOT00 are broadly consistent with extrapolations from the 7CRS/6CE/3CRR datasets underlying the SKADS Simulated Skies Semi-Empirical Extragalactic Database, S^3-SEX.

3.1 Introduction

Radio observations of Active Galactic Nuclei (AGN) reveal some of the complexity of the AGN phenomenon. A central black hole accretes matter through an accretion disk, which along the plane of the disk is hidden by a dusty and gas-rich torus. Radio emission emerges from the immediate vicinity of the black hole through the synchrotron process (e.g. from the base of jets) and potentially other processes like optically thin bremsstrahlung from a slow, dense

disk wind (Blundell & Kuncic 2007). Powerful jets can propagate to large scales and radio telescopes enable the study of these 'radio-loud' objects in detail, which are believed to live from $\lesssim 10^4$ yr for small GHz-peaked sources to $\sim 10^{7-8}$ yr for larger steep-spectrum sources. Best et al. (2005) found that 25% of the most massive galaxies show radio-loud AGN activity, and argued that such AGN activity is constantly re-triggered. Radio sources seem to have a 'duty-cycle', i.e. a recurrent radio-loud AGN activity, which is believed to play an important role in balancing the energy losses from hot gas that surrounds massive elliptical galaxies (Best et al. 2006). This is done by re-heating the cooling gas inside the galaxy halo, in a way that provides a self-regulating feedback mechanism capable of controlling the rate of growth of galaxies (Tabor & Binney 1993). The 'duty-cycle' or, in other words the lifetime of radio sources, differs according to radio-source type.

Fanaroff & Riley (1974) were the first to divide radio sources according to radio structure and radio luminosity: FRIs are bright close to the core whereas FRIIs are edge-brightened radio sources. The radio luminosity divide is at $\log_{10}(L_{178\mathrm{MHz}}/\mathrm{WHz^{-1}sr^{-1}}) \approx 25$ ($H_0 = 50$ km s^{-1}Mpc^{-1}, $\Omega_\mathrm{M} = 1$ and $\Omega_\Lambda = 0$)[1]; above this value lie the FRIIs, and below that the FRIs. Kaiser & Best (2007a, 2007b) suggest that all sources start out with an FRII structure, and the final form they take depends on the host galaxy. On the other hand, Parma et al. (2002) studied a sample of FRI and FRII radio sources with a double-double structure and argued that it is unlikely that many FRIIs evolve to FRIs.

Bird et al. (2008) argue that the average FRII-type (Fanaroff & Riley 1974) radio-source lifetimes are $\sim 1.5 \times 10^7$ yr with a duty cycle[2] ~ 0.02 (for $\sim 8 \times 10^8$ yr time off). Parma et al. (2002) claim that the ages of FRIs are $\sim$ 5-10 times larger than the ages of FRII radio sources, consistent with the Best et al. (2005) inference that massive galaxies are active in either an FRI or FRII phase roughly 25% of the time.

The difference in FRI and FRII radio-source lifetimes may be linked to studies of HI gas as probe of the host environment of these objects. Emonts et al. (2008) studied a sample of nearby FRI radio sources up to redshift of $z \sim 0.04$ and a sample of FRIIs with $z \lesssim 0.06$, and found that different types of radio sources contain different large-scale HI properties; the HI detection rate in FRIIs is significantly higher than the detection rate for the FRI radio galaxies. These findings suggest a different triggering history for different types of radio sources: FRIIs are likely triggered by galaxy mergers and collisions as the large-scale HI is often distributed

[1]This corresponds to $\log_{10}(L_{151\mathrm{MHz}}/\mathrm{WHz^{-1}sr^{-1}}) \approx 25$ in our adopted cosmology ($H_0 = 70$ km s^{-1}Mpc^{-1}, $\Omega_\mathrm{M} = 0.3$ and $\Omega_\Lambda = 0.7$ for an $\alpha \simeq 0.8$ radio source) at the typical redshift ($z \simeq 0.1$) of objects defining the FRI/FRII division of the Fanaroff & Riley (1974) study.

[2]We define duty cycle as the dimensionless ratio of time active to the sum of time active and dormant.

in tail- or bridge-like structures; FRI radio sources are likely fed in other ways, such as steady accretion from a hot IGM.

Radio sources can be observed throughout different cosmic epochs. Studies of radio galaxies and radio-loud quasars (RLQ) can determine the evolution of the radio-source population by defining the Radio Luminosity Function (RLF; e.g. Dunlop & Peacock 1990; Rawlings, Eales & Lacy 2001; Willott et al. 2001b), i.e. the number density of sources per co-moving volume. The sharp decline in the (co-moving) space density of radio sources from epochs corresponding to $z \sim 2.5$ to those corresponding to $z \sim 0$ was inferred from early counts of radio sources by Longair (1966). By combining constraints from radio source counts with surveys of bright high-radio-frequency-selected samples, using spectroscopic and estimated redshifts, Dunlop & Peacock (1990) were the first to map out the cosmic evolution of this population in any detail. They claimed to detect a measurable drop, or redshift-cutoff, in the space density of sources at $z \gtrsim 2.5$. Returning to this problem with virtually-complete spectroscopic redshift information on low-radio-frequency-selected samples, Willott et al. (2001b) measured a RLF in rough agreement with that of Dunlop & Peacock, but differing in important aspects such as a factor ~ 2 lower normalisation at $z \sim 2.5$. Such seemingly subtle differences, attributable largely to biases in the redshift estimates used by Dunlop & Peacock, removed any convincing evidence for the redshift cut-off, a finding in agreement with work focused on the most luminous steep-spectrum radio sources (Jarvis et al. 2001d).

It seems clear, therefore, that spectroscopic redshift surveys of radio sources are of the utmost importance in making robust measurements of the cosmic evolution of the RLF at high redshift. It is also clear that, as emphasised by Willott et al. (2001), the next generation of radio source redshift surveys should be carefully targeted on those objects which make the dominant contribution to the radio luminosity density Π[3]. Evaluated as a function of cosmic time t, $\Pi(t)$ encodes the information needed to estimate crucial physical quantities like the quantity of heat, or entropy, radio sources inject into the inter-galactic medium (Yamada & Fujita 2001; Gopal-Krishna & Wiita 2001; Rawlings 2002). Current estimates of $\Pi(t)$, even at epochs corresponding to the supposedly well-studied redshift range $2 \lesssim z \lesssim 3$, are highly uncertain because they rely on extrapolating from measurements of the most luminous radio sources down a very steep RLF. Robust luminosity density measurements require that space densities are measured for objects much closer to the break in the RLF.

The RLF is often modelled as a broken power law. The break luminosity is close to, but

[3]We define the radio luminosity density by $\Pi = \int\int L_\nu[\mathrm{d}\rho/\mathrm{d}\log_{10} L_\nu]\mathrm{d}(\log_{10} L_\nu)\mathrm{d}\nu$, where $\mathrm{d}\rho/\mathrm{d}\log_{10} L_\nu$ is the co-moving space density (in units of Mpc^{-3}) of radio sources.

above, the dividing line between the two FR structural classes for the large-scale radio structure of these objects. Willott et al. (1998) found that the break in the RLF for radio-loud quasars is at $\log_{10}(L_{151\mathrm{MHz}}/\mathrm{WHz}^{-1}\mathrm{sr}^{-1}) \lesssim 27$[4] ($H_0 = 50$ km s^{-1}Mpc^{-1}, $\Omega_\mathrm{M} = 1$ and $\Omega_\Lambda = 0$), while there is no evidence for a decline in the co-moving space density of RLQs at higher redshift than the peak of the RLF at $z \sim 2$. This is important for radio galaxies, since from unified AGN schemes RLQs and radio galaxies are the same objects where the apparent difference in their properties is a result of the orientation of the radio jets (e.g. Antonucci 1993).

Surveys such as the 3CRR, 6CE and 7CRS (Laing, Riley & Longair 1983; Rawlings, Eales & Lacy 2001 and Willott et al. 2003, respectively) were designed in order to study complete, down to a certain flux density limit, spectroscopic samples of radio sources. The goal was to study the RLF. However, at $z > 2$ these surveys are not deep enough to make a good estimate of the density of radio sources close to the RLF break. In order to target the radio-source population responsible for the bulk of the cosmic heating, one needs to study a deeper low-radio-frequency-selected sample around redshift $z \sim 2$. Willott et al. (2001b) suggested a new study that would target a large sample (~ 1000) of radio sources selected from the 7CRS survey at a flux density limit of 100 mJy at 151 MHz.

The TexOx-1000 (TOOT; Hill & Rawlings 2003) survey is the realisation of a hypothetical survey proposed by Willott et al. (2001). The primary aim of the TOOT survey is to measure spectroscopic redshifts for ≈ 1000 radio sources from a low-frequency-selected sample reaching a flux-density limit $S_{151} \sim 0.1$ Jy over several separate sky patches totalling ~ 0.03 sr (see Tables 1 & 2 of Hill & Rawlings 2003, for details on the TOOT regions and status of the survey). Another objective of the TOOT survey was to target radio sources at redshift $z \sim 2$ where the density of the radio source population is at its maximum (e.g. Rawlings 2003).

In this chapter we study the 00^h targeted sky area of the TexOx-1000, hereafter TOOT00, which includes 47 radio sources with a flux density limit of $\simeq 100$ mJy at 151 MHz. In Section 3.2 we present the 151 MHz and 1.4 GHz radio imaging and optical spectroscopic and near-infrared (mostly $K-$band) imaging data on the TOOT00 sample. In Section 3.3 we present a basic analysis on the TOOT00 sample: a comparison of spectroscopic and photometric redshifts in Section 3.3.1; an analysis of radio spectral indices in Section 3.3.2; an investigation of relationships between radio structure, radio luminosity and redshift in Section 3.3.3; and a discussion of the quasar fraction in Section 3.3.4. In Section 3.4 we present the redshift distribution of the TOOT00 sample (Figure 3.7) and compare it to simulations of the radio sky

[4]This corresponds to $\log_{10}(L_{151\mathrm{MHz}}/\mathrm{WHz}^{-1}\mathrm{sr}^{-1}) \approx 26$ in our adopted cosmology ($H_0 = 70$ km s^{-1}Mpc^{-1}, $\Omega_\mathrm{M} = 0.3$ and $\Omega_\Lambda = 0.7$ for an $\alpha \simeq 0.8$ radio source) at the typical redshift ($z \simeq 1$) of the 3CRR/6CR/7CRS datasets.

from the SKADS Simulated Skies Semi-Empirical Extragalactic Database (S^3-SEX; Wilman et al. 2008). In Section 3.5 we make some concluding remarks. In Appendix B in Section 3.6 we present notes on each object, photometry in the optical and near-IR, as well as a figure with near-IR/radio overlays, optical spectroscopy and Spectral Energy Distributions (SEDs) for the 47 TOOT00 objects.

We use J2000.0 positions and the convention for all spectral indices, α, that flux density $S_\nu \propto \nu^{-\alpha}$, where ν is the observing frequency. We assume throughout a low-density, Λ-dominated Universe in which $H_0 = 70$ km s^{-1}Mpc^{-1}, $\Omega_{\rm M} = 0.3$ and $\Omega_\Lambda = 0.7$.

3.2 Data and observations

The 7C radio source survey was performed using the Cambridge Low Frequency Synthesis Telescope (CLFST) operating at 151 MHz with a resolution of 70×70 cosec(Dec) arcsec^2. General principles of its operation are described by Rees (1990). The instrument was used to survey about one hundred fields north of declination 30 degrees and well away from the galactic plane. The rms noise and hence the limiting flux density of the survey varies both within any one field and between different fields owing to beam distortion, primary beam and ionospheric effects. Some data on individual fields and groups of fields have been published in various papers (see Riley, Waldram & Riley 1999 and references therein). The construction of a final unified catalogue is described in Hales et al. (2007) and is available via the 7C website[5]. The final 7C catalogue lists 43683 sources over an area of about 1.7 sr.

The TOOT00 radio-source sample was selected from the 7C survey to include sources with peak flux densities above $\simeq$ 100 mJy at 151 MHz; the final lower limit was 95 mJy. The area studied is illustrated in Figure 3.1; 56 sources lie in this area. All of the TOOT00 objects were observed with the VLA, in A and B configurations at 1.4 GHz, where 11 pointings were used to cover the TOOT00 area (Figure 3.1). The A-array observations were performed on 12 August 1999 and the B-array on 25 June 2002. To avoid excessive bandwidth smearing these observations were made using seven 3.125-MHz channels centred on 1.370 GHz plus seven 3.125-MHz channels centred on 1.444 GHz. Following standard reduction procedures in AIPS we synthesised maps of all our objects using both separate and combined A- and B-array visibilities. In this paper we present B-array images of the TOOT00 radio sources (Figure 3.10 in Appendix B), unless the A-array maps reveal important information about the radio structure.

[5] *http://www.mrao.cam.ac.uk/surveys/7C*

In the final sample selection all sources with flux densities $S_{151\mathrm{MHz}} > 220$ mJy were included, as well as a sub-set of sources with 95 mJy $< S_{151\mathrm{MHz}} \leq 220$ mJy, close enough to the VLA pointing centres to have good maps in the VLA A-array observations. The 9 sources excluded are characterised as 'off-edge' objects and are typically ~ 30 arcmin away from the centre of the positions where the VLA was pointed. These are faint enough that no reasonable map could be made. Note that this introduces a selection bias against fainter radio sources in the TOOT00 survey. The final TOOT00 sample includes 47 radio sources.

The sky area of TOOT00 was measured using a Monte-Carlo approach: random numbers were generated, uniform in RA and with a $\sin\theta$ distribution in Dec, within a rectangle enclosing the 56 original TOOT00 sources. We tested whether the randomly selected points lay within 35.7 arcmin (see Figure 3.1) of any of the 11 VLA pointing positions. The ratio of points passing this test to the total number of random points (0.68) was multiplied by the sky area of the rectangle. The result is 0.0015 sr or ~ 5.0 deg^2.

Table 3.1 gives the basic radio data on the 47 TOOT00 radio sources. The flux densities used subsequently are shown in bold, and were chosen according to the following criteria: (i) if the integrated flux density has a significantly larger value than the peak flux density and is not the result of confusion, we use the former and (ii) in the case of a compact radio source we always use the peak flux density. The radio spectral indices $\alpha_{151\mathrm{MHz}}^{1.4\mathrm{GHz}}$ were calculated using the 1.4 GHz (NRAO/VLA Sky Survey - NVSS; Condon et al. 1998) and 151 MHz (7C) flux densities for the TOOT00 sources. We also obtained 74 MHz flux densities for 12 out of 47 TOOT00 radio sources from the VLA Low-frequency Sky Survey (VLSS; Cohen et al. 2007). The VLSS has a resolution of 80 arcsec (FWHM), a noise level of ≈ 0.1 Jy beam^{-1} and a typical catalogue point-source detection limit of 0.7 Jy beam^{-1}; the 74 MHz maps are available for searching for fainter sources. The angular sizes of the TOOT00 sources were measured from the VLA (A or B configuration) images. We use our VLA data and the Owen & Laing (1989) radio-source classification to place our objects in four categories: Classical Double (CD), Fat Double (FD), Twin Jet (TJ) and Compact (COM) radio sources. CDs correspond to FRIIs where there is at least one bright hotspot at the ends of the structure in both high- and low-resolution radio maps; FDs represent FRI/II division objects, where the radio structure is more diffuse on the high resolution radio maps than in the case of CDs, and no compact hotspot-like features are visible in the A-array radio map; TJs are FRI type radio sources which are brightest near the centre of the sources; COM radio sources don't show any evidence of extended radio emission on $\gtrsim$ 5-arcsec scales.

Optical spectroscopic observations were undertaken with the ISIS spectrometer on the

William Herschel Telescope (WHT[6]) in August 2000, 2004, 2006 and 2009 (see Table 3.2); TOOT00_1134 was observed with the Marcario Low Resolution Spectrograph (LRS) on the Hobby-Eberly Telescope (HET[7]; Hill et al. 1998). All ISIS observations used the R158R and R158B gratings with the beam split using the 5400-Å dichroic; the R158B grating was used for the blue arm, providing 1.62 Å/pixel and 0.2 arcsec/pixel scales with the EEV12 detector. For the August 2000 observing run the R158R grating was used with the TEK4 detector on the red arm, which gave 2.90 Å/pixel and 0.36 arcsec/pixel scales. For the August 2004 and August 2006 observing runs the red MARCONI detector was used, which provides similar intrinsic spatial and spectral scales to the blue EEV12 detector. For the August 2009 observing run the EEV12 was used alongside the REDPLUS detector: after 3×2 (spectral $\times$ spatial) binning in the blue, and 3×1 binning in the red, this gave $\approx$ 5Å/pixel and $\approx$ 0.44/0.22 (blue/red) arcsec/pixel scales. The LRS was used with a 2-arcsec-wide slit and 300 l/mm grism giving a resolution of 16.7 Å and coverage of 4150 to 10100 Å. Observations and data analysis followed the standard methods described by Rawlings, Eales & Lacy (2001). We offset from nearby bright stars to either optical or radio positions, choosing the position angle (PA) of the slit either on the basis of encompassing companion optical objects or to line up with the radio axis. All the targets were observed below an air mass of 1.2, and all but two were observed below an air mass of 1.1. All the data presented here were taken in photometric conditions with the seeing close to 1 arcsec. In most cases spectral features, emission lines and/or spectral breaks were detected, and the reduced 1D spectra are presented in Figure 3.10. For cosmetic purposes, most of the spectra have been smoothed by replacing the value of each spectral bin by the average of the values in the bin and its two neighbours. All measurements from the spectra were made prior to this process, and the results are tabulated in Table 3.4.

Multi-colour optical images from the INT Wide Field Camera data were obtained as part of the Oxford-Dartmouth 30-Degrees (ODT) survey (see MacDonald et al. 2004). The ODT survey is a multi-band imaging survey, with limiting depths (5σ, $2''$ aperture Vega magnitudes) of $U = 25.3$, $B = 26.2$, $V = 25.7$, $R = 25.4$, $i' = 24.6$, $Z = 21.9$ and $K = 18.5$. In the case where ODT data were unavailable, estimates of the photometry were made from the optical spectrum of the object when available.

Near-IR imaging in the $K-$band was obtained at the United Kingdom Infrared Telescope

[6]The WHT is operated by the Isaac Newton Group of Telescopes (ING), at the Roque de Los Muchachos Observatory in La Palma, Spain.

[7]The Marcario Low Resolution Spectrograph is a joint project of the Hobby - Eberly Telescope partnership and the Instituto de Astronomia de la Universidad Nacional Autonoma de Mexico. The Hobby - Eberly Telescope is operated by McDonald Observatory on behalf of The University of Texas at Austin, the Pennsylvania State University, Stanford University, Ludwig-Maximilians-Universitaet Muenchen, and Georg-August-Universitaet Goettingen.

UKIRT[8] by using either UIST (Howatt et al. 2004) in January 2003 or UFTI (the UKIRT Fast–Track Imager; Roche et al. 2002) in July 2000, December 2000, January 2001 and 2002 and September 2004 with typical exposures of $\sim$ 9-18 min. Further infrared observations of a $z \sim 1$ TOOT00 sub-sample were carried out at the UKIRT in 2003 with UIST and in 2004 with UFTI; we term this the 'Inskip' sub-sample. UIST is a 1–5 μm imager-spectrometer with a 1024×1024 InSb array. The instrument is designed to switch quickly and accurately between imaging and spectroscopic modes. We used the imaging mode, where two plate scales are available, 0.12 arcsec / pixel or 0.06 arcsec / pixel, giving fields of view of 2×2 or 1×1 arcmin^2. UFTI is a 1–2.5 μm camera with a 1024×1024 HgCdTe array and a plate scale of 0.091 arcsec / pixel, which gives a field of view of 92 arcsec. Each object in the 'Inskip' sub-sample was observed in the J, H and K infrared wavebands. The K-band observations were generally of $\sim$ 2 hours duration in total. J-band observations were typically 18-63 minutes, and H-band observations typically 18-72 minutes (depending on source redshift). Table 3.5 (see Appendix B) shows the photometric data used to calculate photometric redshifts, and Table 3.6 shows complete photometry on each object.

All near-IR observations used a nine-point jitter pattern, with offsets of roughly 10 arcsec between each 1 minute exposure. The observational data were dark subtracted, and masked for bad pixels. A first-pass sky flat-field image was created from groups of roughly 60–100 consecutive frames of data, which were combined and median filtered. This accounted for the majority of the pixel-to-pixel variations of the chip, but some larger-scale illumination gradients remained, due to the changing position of the telescope through the course of the night. Smaller blocks of 9–18 first-pass flat-fielded images were similarly combined to create residual sky flat-field images, allowing us to remove the remaining variations. The first-pass flat-fielded data were used to generate masks for any bright objects in the images, and a repeat of the whole process allowed the data to be cleanly flat-fielded without any contamination from stars or galaxies.

The flat-fielded data for each source were sky-subtracted and combined using the IRAF package DIMSUM, creating a final mosaiced image of approximately[9] 115×115 arcsec^2, which was flux calibrated using observations of UKIRT faint standard stars. Astrometry corrections were performed to the finalised near-IR images using the package KARMA. Photometry was carried out within apertures ranging from 3 to 9 arcsec in diameter, using the IRAF routine APPHOT and a single sky annulus. All sources have been corrected for galactic extinction using

[8]The United Kingdom Infrared Telescope is operated by the Joint Astronomy Centre on behalf of the Science and Technology Facilities Council of the U.K.

[9]The highest signal-to-noise level is restricted to the central 70×70 arcsec^2.

the $E(B-V)$ for the Milky Way from the NASA Extragalactic Database (NED) and the parametrised galactic extinction law of Howarth (1983).

Optical and near-infrared photometric data were used to create SEDs for our objects as shown in Figure 3.10 (in Appendix B). Seven of our objects do not as yet have spectroscopically-confirmed redshifts. Table 3.3 summarises the results on the spectroscopic and photometric redshifts, as well as the K magnitude of each object and whether or not the IDs look resolved in the $K-$band. It also gives the Optical (see Section 3.3.1) and Radio-Optical (see Section 3.4) classification of the TOOT00 radio sources.

Table 3.4 presents the measured observed FWHM (in km/s) and EW (in Å) of each line, the radio luminosity at 151 MHz $L_{151\mathrm{MHz}}$ and the flux of the $[\mathrm{OII}]_{\lambda 3727}$ emission line, since it is the most frequently observed line in the optical in quasars and radio galaxies. In the case where the [OII] line was not present, we measured another narrow line (e.g. $[\mathrm{OIII}]_{\lambda 5007}$), or any narrow-line profile of the Lyα, $[\mathrm{CIV}]_{\lambda 1549}$, [CIII] or MgII emission lines. For objects without emission lines in the optical spectrum, a rough estimate of a limit on the [OII] line flux was made as follows: i) for galaxies, i.e. in the case the continuum is clearly strong and stellar, we took a limit of ~ 10 Å which corresponds roughly to lines clearly detectable in a typical spectrum of $z \sim 0.5$ ellipticals, observed with moderate S/N ratio; ii) for fainter objects in which the origin of the continuum is unclear, we supply as a limit the flux of the brightest, but probably spurious, line-like feature in the spectrum adjacent to the estimated location (given the photometric redshift) of the brightest expected narrow line.

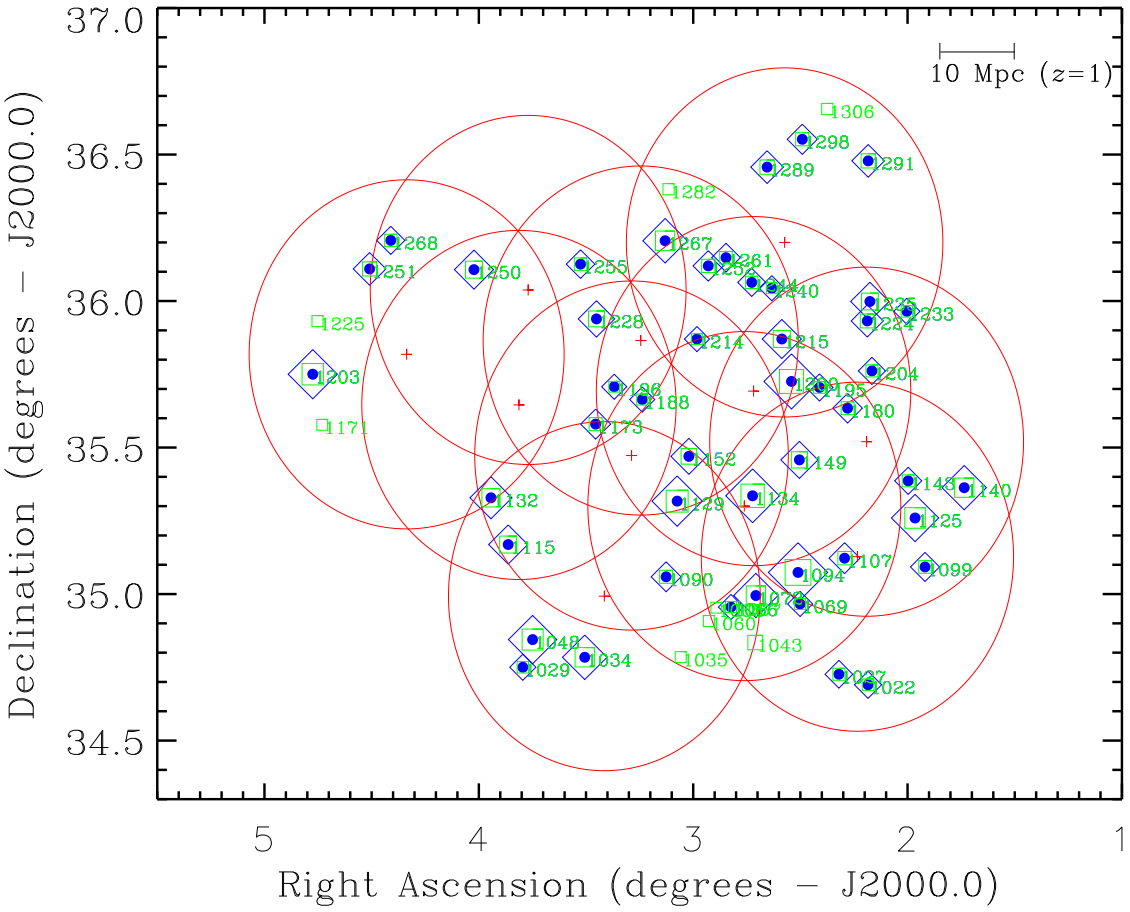

Figure 3.1: Sky area of the TOOT00 region with the bar showing the angle corresponding to a proper distance of 10 Mpc observed at redshift $z = 1$. Symbols: blue diamonds show the 47 TOOT00 radio sources, where their size is proportional to the base-10 logarithm of the 1.4-GHz flux density of each object; objects detected in the 74-MHz VLSS survey (Cohen et al. 2007) are indicated with a solid blue circle. Green boxes represent the 56 objects of the 7C sample in the same sky area with $S_{151\mathrm{MHz}} > 95$ mJy; their size is proportional to the base-10 logarithm of the 151-MHz flux density of each object. The 11 A-array 1.4-GHz VLA pointings are shown as red crosses '+', where the circles around them have a radius of 35.7 arcmin in order to include all the TOOT00 objects, and corresponding roughly to the 32-arcmin-diameter primary beam of the VLA. The 9 'off-edge' objects described in Sec. 3.2 are: TOOT00_1306 at 00 11 50.33 +36 39 19.34 with $S_{151\mathrm{MHz}} = 0.11$ Jy, TOOT00_1043 at 00 13 12.77 +34 50 04.78 with $S_{151\mathrm{MHz}} = 0.21$ Jy, TOOT00_1067 at 00 13 42.51 +34 57 22.04 with $S_{151\mathrm{MHz}} = 0.10$ Jy, TOOT00_1065 at 00 14 06.90 +34 57 12.28 with $S_{151\mathrm{MHz}} = 0.097$ Jy, TOTO00_1060 at 00 14 16.62 +34 54 28.83 with $S_{151\mathrm{MHz}} = 0.10$ Jy, TOOT00_1035 at 00 14 53.67 +34 47 04.59 with $S_{151\mathrm{MHz}} = 0.10$ Jy, TOOT00_1282 at 00 15 28.61 +36 22 53.84 with $S_{151\mathrm{MHz}} = 0.11$ Jy, TOOT00_1171 at 00 23 15.84 +35 34 39.66 with $S_{151\mathrm{MHz}} = 0.098$ Jy, TOOT00_1225 at 00 23 28.63 +35 55 52.86 with $S_{151\mathrm{MHz}} = 0.10$ Jy.

Table 3.1: Radio properties of the 47 TOOT00 radio sources; values in bold are those used in the analysis. **Columns 1, 2 & 3** give the name of the object and its 151-MHz radio position from the 7C survey (J2000.0). **Column 4** gives the angular size of the radio source (A- or B-array in line with Figure 3.10; the characters 'os' denote that the measurement was made from the core to the extent of an one-sided structure). **Columns 5 & 6** give the peak flux density and integrated flux density per beam at 151 MHz respectively. **Column 7** gives the signal-to-noise (S/N) ratio at 151 MHz. **Column 8** gives the flux density at 1.4 GHz as was measured from the B-array VLA maps using IMSTAT task in AIPS; the symbol '+' indicates that the flux density is the sum of two components. **Columns 9 & 10** give the flux density at 1.4 GHz taken from the NVSS survey; the symbol '+' indicates that the flux of each component was measured separately and then added together. **Columns 11 & 12** give the peak flux density and integrated flux density per beam at 74 MHz from the VLSS survey; objects that have flux densities below $\simeq 0.3$ Jy are marked as 2σ limits. Flux densities measured directly from the VLSS maps using the IMSTAT task in AIPS are marked with an 'm'. **Columns 13 & 14** give the spectral index of each object calculated from 1.4 GHz to 151 MHz and 151 MHz to 74 MHz respectively. Fluxes in bold have been used to calculate the spectral index, making use of the NVSS flux density for each one of the radio sources. **Column 15** gives the radio classification (R Cl) of each object (Owen & Laing, 1989): CD stands for classical double, TJ for twin-jet, FD for fat double and COM for a compact radio source.

(1)	(2)	(3)	(4)	(5)	(6)	(7)	(8)	(9)	(10)	(11)	(12)	(13)	(14)	(15)
Name	RA	Dec	θ (arcsec)	S_{151} peak (Jy)	S_{151} integ (Jy)	S/N 151 MHz	$S_{1.4\mathrm{GHz}}$ integ (mJy)	$S_{1.4\mathrm{NVSS}}$ peak (mJy)	$S_{1.4\mathrm{NVSS}}$ integ (mJy)	S_{74} peak (Jy)	S_{74} integ (Jy)	$\alpha_{151}^{1.4}$	α_{74}^{151}	R Cl
TOOT00_1140	00 08 30.81	+35 21 46.98	18	**0.58**	0.53	24.1	92.5	**109.5**	121.1	–	**0.58**^{m}	0.75	0.0	FD
TOOT00_1099	00 09 22.76	+35 05 32.99	$<12^{\mathrm{os}}$	0.14	**0.17**	6.5	16.7	**17.90**	17.90	–	$<$ **0.22**^{m}	1.01	$<$ 0.36	TJ?
TOOT00_1125	00 09 37.58	+35 15 34.76	96	**0.76**	0.76	32.3	86.9	66.10	**93.50**	**1.09**	1.09	0.94	0.40	CD
TOOT00_1143	00 09 47.92	+35 23 11.27	18	**0.12**	0.22	6.1	34.6	**6.400**	9.400	–	$<$ **0.21**^{m}	1.32	$<$ 0.78	FD
TOOT00_1233	00 09 54.04	+35 57 53.41	<6	**0.11**	0.09	4.5	54.1	**51.20**	51.20	–	$<$ **0.20**^{m}	0.34	$<$ 0.84	COM?
TOOT00_1022	00 10 37.58	+34 41 25.24	<7	**0.12**	0.15	6.4	15.5	**15.60**	15.60	–	**0.33**^{m}	0.92	1.42	COM
TOOT00_1204	00 10 40.70	+35 45 41.40	17	**0.12**	0.12	6.1	15.2	19.90	**31.30**	–	$<$ **0.23**^{m}	0.60	$<$ 0.91	FD
TOOT00_1235	00 10 45.45	+35 59 54.58	<6	**0.34**	0.34	20.2	101.9	**99.30**	99.30	–	$<$ **0.24**^{m}	0.55	$<$ -0.49	COM?
TOOT00_1224	00 10 48.54	+35 55 55.46	<6	**0.19**	0.24	11.1	31.2	**32.60**	32.60	–	$<$ **0.20**^{m}	0.79	$<$ 0.07	COM
TOOT00_1291	00 10 51.82	+36 28 42.19	63	**0.20**	0.20	9.7	25.5	23.50	**31.60**	–	$<$ **0.22**^{m}	0.83	$<$ 0.13	CD?
TOOT00_1107	00 11 13.06	+35 07 20.77	25	**0.17**	0.17	9.6	5.71	**5.700**	5.700	–	$<$ **0.16**^{m}	1.52	$<$ -0.09	TJ
TOOT00_1180	00 11 13.21	+35 38 03.49	15	**0.15**	0.11	7.8	16.0	**15.80**	15.80	–	$<$ **0.16**^{m}	1.01	$<$ 0.09	CD?
TOOT00_1027	00 11 17.57	+34 43 34.64	<6	**0.13**	0.11	6.3	656.8	**664.3**	664.3	–	$<$ **0.22**^{m}	-0.73	$<$ 0.74	COM
TOOT00_1195	00 11 52.55	+35 42 18.51	49	**0.12**	0.10	4.8	10.0	10.70	**15.10**	–	$<$ **0.26**^{m}	0.93	$<$ 1.08	CD
TOOT00_1069	00 12 12.51	+34 57 58.20	10	**0.10**	0.09	2.8	3.89	**3.600**	3.600	–	$<$ **0.17**^{m}	1.49	$<$ 0.74	COM?
TOOT00_1094	00 12 16.36	+35 04 25.82	<7	**2.30**	2.21	56.3	242.8	**248.0**	248.0	**3.37**	3.37	1.00	0.54	COM
TOOT00_1149	00 12 17.97	+35 27 28.60	26	**0.30**	0.27	12.7	17.3	27.70	**29.50**	–	**0.26**^{m}	1.04	-0.20	TJ
TOOT00_1298	00 12 24.25	+36 33 07.32	16	**0.16**	0.14	7.0	29.1	27.70	**30.40**	–	**0.40**^{m}	0.75	1.28	TJ
TOOT00_1200	00 12 31.33	+35 43 32.28	27	1.56	**1.59**	51.6	260.7	226.3	**272.4**	**2.60**	2.60	0.79	0.69	CD
TOOT00_1215	00 12 46.06	+35 52 13.70	15	**0.36**	0.35	14.4	38.3	39.80	**42.80**	**0.64**	0.64	0.96	0.81	TJ?
TOOT00_1240	00 13 01.62	+36 02 37.55	209	0.10	**0.13**	4.0	5.9	5.6	**7.4**$^{+}$	–	$<$ **0.21**^{m}	1.29	$<$ 0.67	CD
TOOT00_1289	00 13 12.32	+36 27 25.61	15	**0.20**	0.17	11.3	21.0	19.80	**21.80**	–	**0.41**^{m}	1.00	1.01	CD
TOOT00_1072	00 13 13.26	+34 59 42.15	27	**0.58**	0.55	21.9	102.6	97.80	**111.1**	**0.89**	0.89	0.74	0.60	CD
TOOT00_1134	00 13 21.09	+35 20 07.22	50	**1.37**	1.43	38.5	**119.2**	203.2	237.4	**2.38**	2.75	0.87	0.77	TJ
TOOT00_1244	00 13 29.58	+36 03 49.06	<6	**0.13**	0.10	6.4	32.3	**32.40**	32.40	–	**0.40**^{m}	0.62	1.58	COM
TOOT00_1066	00 13 46.90	+34 57 20.69	19	**0.10**	0.19	2.7	14.8	**14.40**	14.40	–	$<$ **0.18**^{m}	0.87	$<$ 0.82	CD
TOOT00_1261	00 14 06.19	+36 08 52.85	5	**0.14**	0.20	6.2	14.5	**14.20**	14.20	–	$<$ **0.14**^{m}	1.03	$<$ 0.00	CD
TOOT00_1252	00 14 30.42	+36 07 11.83	52os	**0.16**	0.13	7.7	19.3	**18.00**	18.00	–	$<$ **0.19**^{m}	0.98	$<$ 0.24	CD?
TOOT00_1214	00 14 43.35	+35 52 12.64	15os	**0.10**	0.14	4.7	9.4	**11.30**	11.30	–	$<$ **0.19**^{m}	0.98	$<$ 0.90	CD?
TOOT00_1152	00 14 49.99	+35 28 11.78	30	**0.27**	0.24	10.6	35.3	33.80	**38.30**	–	$<$ **0.19**^{m}	0.88	$<$ -0.49	CD
TOOT00_1129	00 15 04.41	+35 19 01.79	15	**1.01**	1.16	44.5	161.5	144.6	**156.6**	**1.45**	1.45	0.84	0.51	CD
TOOT00_1090	00 15 16.66	+35 03 32.07	59	0.16	**0.20**	5.8	19.5	25.70	**27.90**	–	$<$ **0.24**^{m}	0.88	$<$ 0.25	FD
TOOT00_1267	00 15 31.30	+36 12 20.82	10	**0.59**	0.52	25.5	93.9	**99.50**	99.50	**0.83**	1.45	0.80	0.48	CD
TOOT00_1188	00 15 56.42	+35 39 50.04	17	**0.10**	0.11	4.7	13.6	**14.70**	14.70	–	$<$ **0.15**^{m}	0.86	$<$ 0.57	CD
TOOT00_1196	00 16 35.57	+35 42 26.83	–	**0.10**	0.11	4.4	–	–	$<$ **0.9**	–	–	$>$ 2.11	–	FD?
TOOT00_1173	00 16 59.60	+35 34 47.92	41	**0.16**	0.15	7.4	16.6	23.90	**28.80**	–	**0.28**^{m}	0.77	0.78	TJ
TOOT00_1228	00 17 03.05	+35 56 20.54	<4	**0.28**	0.25	10.5	80.1	**79.10**	79.10	–	$<$ **0.16**^{m}	0.57	$<$ -0.78	COM
TOOT00_1034	00 17 04.49	+34 47 03.22	45	0.59	**0.61**	27.6	122.6	129.6	**140.5**	**0.80**	1.45	0.66	0.38	TJ
TOOT00_1255	00 17 27.53	+36 07 33.39	8	**0.14**	0.13	8.3	32.3	**33.80**	33.80	–	**0.29**^{m}	0.64	1.02	CD?
TOOT00_1048	00 18 16.36	+34 50 40.53	7	**0.84**	0.86	38.4	103.4	**104.1**	104.1	**1.18**	1.18	0.94	0.48	CD
TOOT00_1029	00 18 28.43	+34 45 00.55	<5	**0.11**	0.11	5.0	20.5	**24.10**	24.10	–	$<$ **0.21**^{m}	0.68	$<$ 0.91	COM?
TOOT00_1115	00 18 54.19	+35 10 08.54	8	**0.36**	0.32	14.7	55.5	**56.10**	56.10	–	**0.25**^{m}	0.83	-0.51	TJ?
TOOT00_1132	00 19 20.03	+35 19 42.63	4	**0.47**	0.42	18.5	89.3	**88.30**	88.30	–	**0.62**^{m}	0.75	0.39	TJ?
TOOT00_1250	00 19 55.00	+36 06 25.82	25os	**0.36**	0.41	18.3	48.9	**54.00**	54.00	**0.51**	0.51	0.85	0.49	CD?
TOOT00_1268	00 21 51.92	+36 12 25.39	8	**0.13**	0.11	6.7	58.5	**61.20**	61.20	–	$<$ **0.30**^{m}	0.34	$<$ 1.17	COM
TOOT00_1251	00 22 19.64	+36 06 34.89	25	0.20	**0.21**	11.1	20.2	17.30	**19.60**	–	**0.30**^{m}	1.06	0.50	CD
TOOT00_1203	00 23 32.00	+35 45 00.84	5	0.91	**1.06**	38.9	153.2	**164.6**	164.6	**1.07**	1.07	0.84	0.01	CD?

Table 3.2: Observing log for the optical spectroscopy: In **Column 1** we give the name of the object. **Column 2** gives the observing date. **Column 3** gives the coordinates where the slit was centred. **Column 4** gives the exposure time (in seconds) in the blue 'B' and the red 'R' part of the WHT ISIS spectrum; 'LRS' denotes spectroscopy taken with the HET. **Columns 5 & 6** give the width and the position angle of the long axis of the slit respectively.

(1)	(2)	(3)	(4)	(5)	(6)
Object	Date	Position (J2000)	Exposures Time (s)	Slit Width (arcsec)	PA (°)
TOOT00_1140	28Aug2000	00 08 30.81 +35 21 47.9	(1x1450B, 1x600R + 1x900R)	1.5	278
TOOT00_1099	28Aug2000	00 09 23.73 +35 05 05.5	(1x1400B, 1x450R + 1x900R)	1.5	111
TOOT00_1125	28Aug2000	00 09 36.62 +35 15 43.4	(1x740B, 1x600R)	1.5	122
TOOT00_1143	31Aug2000	00 09 46.89 +35 23 45.2	(1x1000B, 1x600R + 1x900R)	1.5	80
TOOT00_1233	30Aug2000	00 09 53.26 +35 58 23.1	(1x600B, 1x250R + 1x300R)	1.5	160
TOOT00_1022	31Aug2000	00 10 37.69 +34 41 22.6	(1x1800B, 2x900R)	1.5	9
	19Aug2006	00 10 37.69 +34 41 22.8	(1x1800B, 2x900R)	2.0	140
TOOT00_1204	29Aug2000	00 10 40.53 +35 45 48.6	(1x1000B, 1x600R + 1x900R)	1.5	112
TOOT00_1235	29Aug2000	00 10 45.54 +35 59 51.7	(1x1100B, 1x450R + 1x600R)	1.5	272
TOOT00_1224	29Aug2000	00 10 48.80 +35 55 48.6	(1x1800B, 2x900R)	1.5	269
	20Aug2006	00 10 48.80 +35 55 48.6	(1x1800B, 2x900R)	2.5	28
TOOT00_1291	30Aug2000	00 10 52.97 +35 28 26.9	(1x1800B, 1x600R + 1x1200R)	1.5	125
	18Jul2004	00 10 52.97 +36 28 26.9	(1x1800B + 1x655B, 1x655R + 2x900R)	2.5	54
TOOT00_1107	14Jul2004	00 11 12.90 +35 07 19.9	(1x600B + 1x1200B + 1x1800B, 4x900R)	1.5	95
TOOT00_1180	29Aug2000	00 11 12.92 +35 37 59.8	(1x1800B, 2x900R)	1.5	160
TOOT00_1027	30Aug2000	00 11 17.00 +34 43 33.7	(1x1800B, 2x900R)	1.5	255
	13Jul2004	00 11 17.57 +34 43 33.7	(1x1200B + 2x1800B, 1x450 + 4x900R)	2.0	255
TOOT00_1195	31Aug2000	00 11 52.40 +35 42 19.2	(1x1800B, 1x600R + 1x1200R)	2.0	96
TOOT00_1069	15Jul2004	00 12 12.58 +34 58 30.9	(1x1800B, 1x450R + 1x600R)	4.0	0
TOOT00_1094	29Aug2000	00 12 16.30 +35 04 23.7	(1x1800B, 2x900R)	2.0	235
TOOT00_1149	28Aug2000	00 12 18.01 +35 27 29.1	(1x300B, 1x300R)	2.0	109
TOOT00_1298	28Aug2000	00 12 24.30 +36 33 10.2	(1x1100B, 1x565R + 1x600R)	2.0	90
TOOT00_1200	29Aug2000	00 12 31.21 +35 43 33.2	(1x1800B, 2x900R)	2.0	143
TOOT00_1215	30Aug2000	00 12 45.89 +35 52 20.5	(1x1800B, 2x900R)	1.5	95
TOOT00_1240	31Aug2000	00 13 05.91 +36 01 47.4	(1x500B + 1x142B, 1x300R+ 1x159R + 1x142R)	2.5	100
			(1x650B, 1x300R + 1x350R)	1.5	100
	15Jul2004	00 13 01.44 +36 02 12.0	(1x1100B, 1x450R + 1x600R)	2.0	19
	19Aug2009	00 13 05.33 +36 01 50.7	(1x1800B, 2x900R)	2.5	100
TOOT00_1289	31Aug2000	00 13 12.32 +36 27 16.3	(1x1800B, 2x900R)	2.0	75
TOOT00_1072	31Aug2000	00 13 13.32 +34 59 40.8	(1x1200B, 2x600R)	2.5	35
TOOT00_1134	17Oct2003	00 13 30.63 +35 20 52.7	(2x1200LRS)	2.0	126
TOOT00_1244	30Aug2000	00 13 29.91 +36 03 51.4	(1x1700B, 1x600R + 1x900R)	1.4	85
TOOT00_1066	31Aug2000	00 13 48.27 +34 56 57.7	(1x1800B, 1x600R + 1x1200R)	2.5	127
TOOT00_1261	30Aug2000	00 14 06.53 +36 08 28.1	(1x110B, 1x450R + 1x600R)	2.0	145
TOOT00_1252	28Aug2000	00 14 28.80 +36 06 52.2	(1x1800B, 2x900R)	2.5	109
	17Jul2004	00 14 30.57 +36 06 44.8	(1x1800B, 2x900R)	1.0	265
TOOT00_1214	28Aug2000	00 14 43.70 +35 52 04.2	(1x1800B, 2x900R)	2.0	116
TOOT00_1152	30Aug2000	00 14 49.61 +35 28 09.6	(1x1300B + 1x1800B, 1x300R + 3x900R)	3.0	65
TOOT00_1129	30Aug2000	00 15 04.40 +35 18 56.5	(1x1800B, 2x900R)	3.0	113
TOOT00_1090	31Aug2000	00 15 16.02 +35 03 26.5	(1x300B, 1x300R)	1.5	87
TOOT00_1267	31Aug2000	00 15 30.89 +36 12 14.4	(1x1800B, 2x900R)	2.0	40
TOOT00_1188	31Aug2000	00 15 56.58 +35 39 49.2	(1x1800B, 2x900R)	2.0	136
TOOT00_1196	16Jul2004	00 16 35.73 +35 42 23.0	(1x1800B, 2x900R)	1.5	256
TOOT00_1173	30Aug2000	00 16 59.54 +35 34 36.0	(1x1100B, 1x450R + 1x600R)	1.5	80
TOOT00_1228	30Aug2000	00 17 03.03 +35 56 18.1	(1x1500B, 1x600R + 1x900R)	1.5	103
	18Jul2004	00 17 03.11 +35 56 18.1	(1x1800B, 2x900R)	2.0	243
TOOT00_1034	30Aug2000	00 17 04.27 +34 46 59.1	(1x1800B, 1x600R + 1x1200R)	2.0	123
	16Jul2004	00 17 04.16 +34 46 59.8	(1x1800B, 2x900R)	2.0	111

Table 3.2: (continued)

(1)	(2)	(3)	(4)	(5)	(6)
Object	Date	Position (J2000)	Exposures Time (s)	Slit Width (arcsec)	PA (°)
TOOT00_1255	30Aug2000	00 17 28.32 +36 07 26.5	(1x1500B, 1x600R + 1x900R)	2.0	156
TOOT00_1048	31Aug2000	00 18 16.28 +34 50 35.5	(1x1800B, 2x900R)	1.5	28
	18Jul2004	00 18 16.37 +34 50 36.6	(1x1800B, 2x900R)	2.5	28
TOOT00_1029	30Aug2000	00 18 28.06 +34 44 49.2	(1x1450B, 1x450R + 1x900R)	2.0	123
TOOT00_1115	28Aug2000	00 18 53.88 +35 10 11.8	(1x1500B, 1x600R + 1x800R)	2.0	90
TOOT00_1132	30Aug2000	00 19 20.11 +35 19 35.8	(1x300B, 1x300R)	1.5	87
TOOT00_1250	30Aug2000	00 19 54.45 +36 06 20.4	(1x399B + 1x591B + 1x859B, 1x300R + 1x600R)	2.0	90
TOOT00_1268	29Aug2000	00 21 52.00 +36 12 18.2	(1x1300B, 2x600R)	1.5	57
TOOT00_1251	29Aug2000	00 22 19.42 +36 06 36.4	(1x1800B, 1x600R + 1x1200R)	2.0	10
TOOT00_1203	29Aug2000	00 23 31.63 +35 45 04.3	(1x1000B, 2x600R)	2.5	90
	30Aug2000	00 23 31.61 +35 45 02.6	(1x1200B, 2x600R)	1.5	0

Table 3.3: Spectroscopic and photometric redshifts: **Column 1** gives the name of the object and **Columns 2 & 3** give the RA and Dec of the near-IR K-band identification of each radio source respectively. **Column 4** gives the optical classification (OpCl) of the radio source, where 'G' stands for a galaxy and 'Q' for a quasar; 'a' denotes a broad-absorption-line QSO (BALQSO). **Column 5** presents the radio-optical classification (R-OpCl): FRIIs correspond to CD objects; FRIs to FD and TJ; Q-F corresponds to quasars with flat radio spectral index ('F' denotes flat radio spectral index $\alpha_{151\mathrm{MHz}}^{1.4\mathrm{GHz}} \lesssim 0.5$; a '?' denotes α close to 0.5); CSS-Q corresponds to quasars with compact radio structure; FRII-Q denotes a quasar that has FRII radio structure; CSS denotes a compact steep spectrum radio source. **Column 6** gives the spectroscopic redshift as measured from the spectra (Figure 3.10); a '?' denotes uncertainty or a featureless continuum. **Column 7** gives the photometric redshift calculated from HyperZ using BC templates (see Section 3.3.1); redshifts corresponding to secondary best-fit templates are marked with '2nd'. Values in brackets are deemed uncertain because there is no clear step change in flux associated with the 4000-Å break in the SED (see Figure 3.10). **Column 8** gives redshifts estimated from the $K-z$ relation of Willott et al. (2003) as described in Section 3.3.1. **Column 9** gives the K magnitude of each object in the Vega system, measured with 4-arcsec (or 3-arcsec in case of confusion) diameter aperture from the centre of its infrared position, denoted as '(4)' (or '(3)'); in the absence of such a measurement we use the one measured from the ODT survey (MacDonald et al. 2004), marked with an (O). The symbol 'p' is used in the case where the object is a point source at K; applicable for magnitudes $K < 18$ as a $\sim 10\sigma$ signal-to-noise ratio is necessary to clarify whether or not an object is a point source at K. The symbol '$*$' denotes data from the 'Inskip' near-IR sample (see Section 3.2).

(1)	(2)	(3)	(4)	(5)	(6)	(7)	(8)	(9)
Name	RA	DEC	OpCl	R-OpCl	z_{spec}	z_{photBC}	$z_{\mathrm{photK-z}}$	K (mag)
TOOT00_1140	00 08 30.8	+35 21 48.1	G	FRI	**0.911?**	1.155	0.821	17.0 (4)
TOOT00_1099	00 09 23.7	+35 05 05.5	G	FRI?	**1.397?**	0.470	0.646	16.5 (4*)
TOOT00_1125	00 09 36.6	+35 15 43.1	Q	FRII-Q	**1.916**	[2.540]	0.424	15.6 (4p)
TOOT00_1143	00 09 46.9	+35 23 44.8	G	FRI	**0.438**	0.370	0.505	16.0 (3)
TOOT00_1233	00 09 53.2	+35 58 23.4	Q[a]	Q-F	**1.244**	[2.255]	0.355	15.3 (4p)
TOOT00_1022	00 10 37.7	+34 41 23.1	G	CSS	?	[2.790]	**2.872**	19.4 (4)
TOOT00_1204	00 10 40.6	+35 45 48.3	G	FRI	**0.6395**	0.600	0.574	16.3 (4)
TOOT00_1235	00 10 45.5	+35 59 51.3	Q	Q-F?	**0.743**	1.720	0.833	17.0 (4*p)
TOOT00_1224	00 10 48.8	+35 55 49.0	G	CSS		[3.050]	**3.438**	19.7 (4*)
TOOT00_1291	00 10 51.4	+36 28 29.7	G	FRII?	?	[1.580]	**0.917**	17.3 (4)
TOOT00_1107	00 11 12.3	+35 07 20.6	G	FRI	**0.300**	2.615 (0.415)[2nd]	1.426	18.1 (4)
TOOT00_1180	00 11 12.9	+35 38 00.1	G?	FRII?	**1.810**	1.345	1.624	18.3 (4)
TOOT00_1027	00 11 17.0	+34 43 33.8	G	CSS	**0.890**	0.655	3.015	19.5 (4)
TOOT00_1195	00 11 52.4	+35 42 20.0	G	FRII	?	[2.290]	**1.418**	18.1 (4*)
TOOT00_1069	00 12 12.6	+34 58 30.9	Q	CSS-Q	**2.300**	[0.050] (2.036)[2nd]	4.840	> 20.3 (4)
TOOT00_1094	00 12 16.3	+35 04 23.4	G	CSS	**1.516?**	1.690	1.616	18.3 (4)
TOOT00_1149	00 12 18.0	+35 27 29.2	G	FRI	**0.260**	0.150	0.257	14.6 (O)
TOOT00_1298	00 12 24.2	+36 33 10.5	G	FRI	**1.287?**	[5.000] (1.491)[2nd]	0.985	17.3 (4)
TOOT00_1200	00 12 31.3	+35 43 33.2	G?	FRII	**0.691**	0.775	1.031	17.4 (4)
TOOT00_1215	00 12 45.9	+35 52 19.1	G	FRI?	**0.278**	1.740	0.306	15.0 (O)
TOOT00_1240	00 13 05.3	+36 01 51.0	G?	FRII	**2.543?**	[4.990]	2.185	18.9 (4)
TOOT00_1289	00 13 12.2	+36 27 16.1	G	FRII	**1.784?**	[1.255]	1.227	17.8 (4)
TOOT00_1072	00 13 13.3	+34 59 40.8	G	FRII	**0.577**	0.715	0.441	15.7 (4)
TOOT00_1134	00 13 21.2	+35 20 07.6	G	FRI	**0.311**	0.365	0.259	14.6 (4)
TOOT00_1244	00 13 30.1	+36 03 51.0	Q	Q-F?	**1.358**	[0.440] (1.590)[2nd]	2.081	18.8 (Op)
TOOT00_1066	00 13 48.3	+34 56 57.6	G	FRII	**0.926?**	1.395	1.382	18.0 (4*)
TOOT00_1261	00 14 06.6	+36 08 27.1	Q?	FRII-Q?	**2.544**	1.940 (2.696)[2nd]	2.365	19.0 (4)
TOOT00_1252	00 14 30.2	+36 06 43.4	G	FRII?	?	[1.670]	**3.229**	> 19.6 (4)
TOOT00_1214	00 14 43.6	+35 52 05.3	Q?	FRII-Q?	**3.081**	[2.360]	1.882	18.6 (3)
TOOT00_1152	00 14 49.7	+35 28 11.1	G	FRII	?	[0.275]	**3.310**	19.6 (4)
TOOT00_1129	00 15 04.3	+35 18 56.9	Q?	FRII-Q?	**1.860**	[2.905]	4.508	20.2 (4)
TOOT00_1090	00 15 15.9	+35 03 27.7	G	FRI	**0.201**	0.290	0.253	14.6 (4)
TOOT00_1267	00 15 31.0	+36 12 16.5	G?	FRII	**0.968**	1.160	0.873	17.1 (4*)
TOOT00_1188	00 15 56.3	+35 39 52.1	G?	FRII	**1.417**	0.945	1.650	18.3 (4)
TOOT00_1196	00 16 35.7	+35 42 22.8	G?	FRII?	?	[1.030]	**1.662**	18.4 (4)
TOOT00_1173	00 16 59.5	+35 34 35.9	G	FRI	**0.332**	0.300	0.367	15.3 (4)
TOOT00_1228	00 17 03.0	+35 56 18.4	G	CSS	**1.135?**	0.100	1.658	18.4 (4)
TOOT00_1034	00 17 04.8	+34 46 56.5	G	FRI	**0.580**	0.695	0.523	16.1 (4)
TOOT00_1255	00 17 28.2	+36 07 27.2	G	FRII?	**0.582**	0.730	0.750	16.8 (4*)

Table 3.3: (continued)

(1)	(2)	(3)	(4)	(5)	(6)	(7)	(8)	(9)
Name	RA	DEC	OpCl	R-OpCl	$z_{\rm spec}$	$z_{\rm photBC}$	$z_{\rm photK-z}$	K (mag)
TOOT00_1048	00 18 16.5	+34 50 36.2	G?	FRII	**1.943**	[0.945]	1.074	17.5 (4p)
TOOT00_1029	00 18 28.0	+34 44 49.5	G	CSS	**0.737**	0.835	0.472	15.9 (4)
TOOT00_1115	00 18 53.9	+35 10 11.4	G	FRI?	**0.416**	0.450	0.470	15.9 (4)
TOOT00_1132	00 19 20.1	+35 19 36.2	G	FRI?	**0.183**	0.155	0.312	15.0 (4)
TOOT00_1250	00 19 54.4	+36 06 22.2	Q	FRII?	**1.350**	2.310	1.346	18.0 (4p)
TOOT00_1268	00 21 52.0	+36 12 18.4	Q?	Q-F	**2.015**	[0.880]	1.142	17.6 (4p)
TOOT00_1251	00 22 19.0	+36 06 29.6	G?	FRII	**2.490**	[1.050]	2.408	19.1 (4)
TOOT00_1203	00 23 31.6	+35 45 04.2	G	FRII?	**1.397**	1.195	1.010	17.4 (4*)

Table 3.4: Emission line properties: **Column 1** gives the name of the object. **Columns 2 & 3** give the measured (observed) values of the equivalent width (EW in Å) and the FWHM (in km/s) of the most prominent emission line in the optical spectrum. **Column 4** gives the flux of the $[OII]_{3727}$ emission line, S_{line} in units of 10^{-19} Wm^{-2}, as measured from the spectrum of each object; in the case where the [OII] line is not present we use the brightest available line as shown; 'n' denotes measurement of a narrow line profile at FWHM using a Gaussian fit; a '—' is used when no spectroscopy is available. **Column 5** gives the emission line used in the calculations. **Column 6** gives the base-10 logarithm of the rest-frame luminosity at 151 MHz, which is used in Figures 3.4, 3.5 & 3.6.

(1)	(2)	(3)	(4)	(5)	(6)
Name	EW (Å)	FWHM (km/s)	$S_{\rm line}$ (10^{-19} W m^{-2})	Emission Line	$\log_{10}($ $L_{151\rm MHz}$/ [WHz^{-1}sr^{-1}])
TOOT00_1140			< 0.20	[OII]	26.21
TOOT00_1099	98	416	9.10	[OII]	26.21
TOOT00_1125	169	5253	70.0	Ly$\alpha^{\rm n}$	27.17
TOOT00_1143			< 0.52	[OII]	24.87
TOOT00_1233	17	1374	4.20	CIII]	25.66
TOOT00_1022			< 3.65	Lyα	26.77
TOOT00_1204	21	388	1.20	[OII]	25.14
TOOT00_1235	30	524	21.4	[OII]	25.72
TOOT00_1224			—		27.07
TOOT00_1291			< 0.91	[OII]	25.78
TOOT00_1107	15	198	0.31	[OII]	24.65
TOOT00_1180	98	434	2.30	Ly$\alpha^{\rm n}$	26.44
TOOT00_1027	22	954	0.22	[OII]	25.13
TOOT00_1195			< 0.20	[OII]	26.05
TOOT00_1069	1296	10870	1.30	Ly$\alpha^{\rm n}$	26.76
TOOT00_1094	290	1402	0.65	MgII	27.43
TOOT00_1149			< 2.05	[OII]	24.70
TOOT00_1298	27	574	1.11	[OII]	26.00
TOOT00_1200	198	738	5.70	[OII]	26.38
TOOT00_1215	23	743	2.70	[OII]	24.84
TOOT00_1240	145	1239	5.64	Lyα	26.89
TOOT00_1289	74	160	1.43	MgII	26.54
TOOT00_1072			< 0.68	[OII]	25.75
TOOT00_1134			< 1.79	[OII]	25.52
TOOT00_1244	336	4526	10.0	CIV$^{\rm n}$	25.92
TOOT00_1066	142	1342	1.14	[OII]	25.50
TOOT00_1261	606	4755	3.60	Ly$\alpha^{\rm n}$	26.78
TOOT00_1252					27.06
TOOT00_1214	444	2055	1.40	Ly$\alpha^{\rm n}$	26.80
TOOT00_1152			< 0.83	Lyα	27.24
TOOT00_1129	277	1185	31.2	Ly$\alpha^{\rm n}$	27.21
TOOT00_1090	12	2453	7.00	[OII]	24.26
TOOT00_1267	1324	104	0.94	[OII]	26.30
TOOT00_1188	113	1102	1.80	[OII]	25.94
TOOT00_1196			< 0.21	MgII	26.64
TOOT00_1173	17	2127	5.00	[OII]	24.64
TOOT00_1228	42	381	1.35	[OII]	26.06
TOOT00_1034	5	1004	0.37	[OII]	25.76
TOOT00_1255	28	361	0.52	[OII]	25.12
TOOT00_1048	454	1744	0.68	Ly$\alpha^{\rm n}$	27.23
TOOT00_1029	25	658	0.60	[OII]	25.26
TOOT00_1115	111	813	3.37	[OII]	25.22
TOOT00_1132	47	680	10.9	[OII]	24.53
TOOT00_1250	141	3865	0.75	CIII]$^{\rm n}$	26.44
TOOT00_1268	401	1285	6.30	Ly$\alpha^{\rm n}$	26.17
TOOT00_1251	225	933	0.14	Ly$\alpha^{\rm n}$	26.95
TOOT00_1203	134	649	35.8	[OII]	26.94

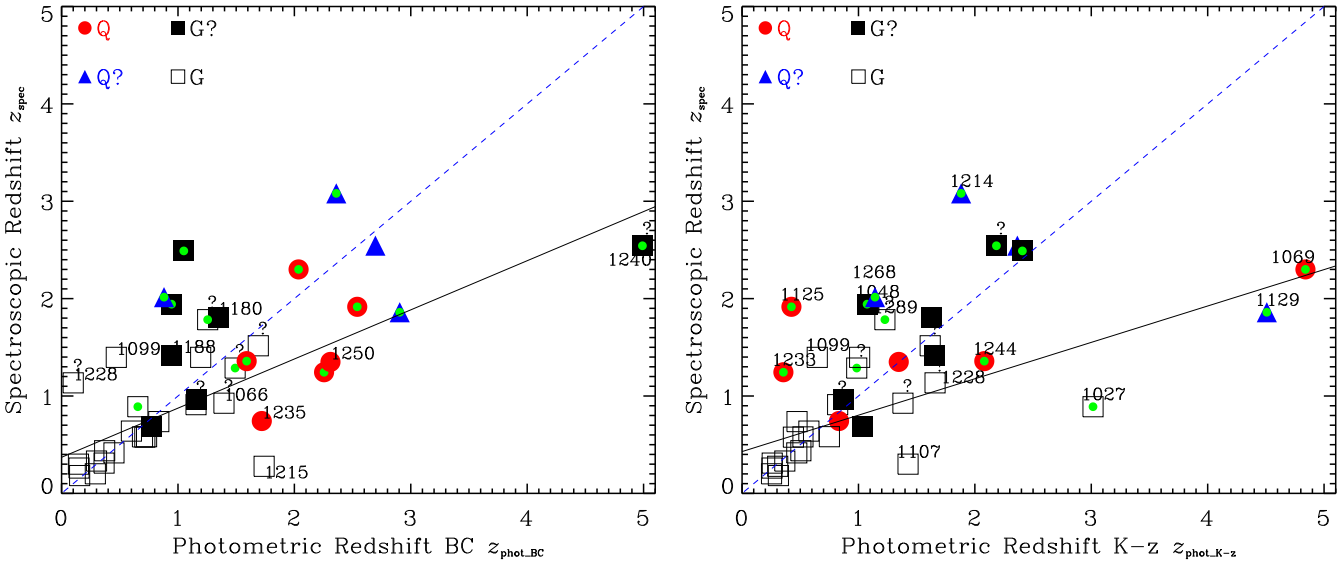

Figure 3.2: **a) Left**: Spectroscopic versus photometric redshift calculated from HyperZ. Symbols indicate optical classification as explained in Section 3.3.1: filled circles for quasars 'Q', blue filled triangles for possible quasars 'Q?', black filled squares for possible galaxies 'G?', and black squares for secure galaxies 'G'. The black solid line is the best fit line for G objects in the $z_{\rm spec}$ vs $z_{\rm photBC}$ correlation, and was calculated using the LINFIT function in IDL, where the objects without spectroscopic redshifts were not included in the calculation: $z_{\rm spec} = 0.50 \times z_{\rm photBC} + 0.37$; the linear Pearson correlation is 0.548 and the Spearman correlation is 0.568 with a 99.53% probability for a correlation. Objects with uncertain photometric redshift are marked with a filled green circle; the character '?' denotes objects with an uncertain spectroscopic redshift. Sources that fall off the dashed blue $z_{\rm spec} = z_{\rm phot}$ line, and do not have an uncertain photometric redshift, are marked with their name. The 7 objects without spectroscopic redshift have been omitted. **b) Right**: Spectroscopic versus photometric redshift calculated using the $K_{\rm W} - z$ relation. Symbols are the same as in figure **a** on the left. The black solid line is the best fit line for G objects in the $z_{\rm spec}$ vs $z_{\rm photK-z}$ correlation, and was calculated as stated above: $z_{\rm spec} = 0.37 \times z_{\rm photK-z} + 0.43$, where the linear Pearson correlation is 0.514 and the Spearman correlation is 0.762 with a 99.99% probability for a correlation. The character '?' denotes objects with an uncertain spectroscopic redshift; objects with uncertain photometric redshift from the HyperZ code are marked with a filled green circle. Sources with $|z_{\rm spec} - z_{\rm phot}| > 0.5$ are marked with their name. Again, the 7 objects without spectroscopic redshift have been omitted. The generalised Spearman correlation coefficient is calculated using survival analysis statistics ASURV (Lavalley et al. 1992).

3.3 Analysis

3.3.1 Optical classification and redshifts

The optical spectroscopy of the 47 TOOT00 radio sources provided 40 out of 47 redshifts. For the other 7 objects there was either a lack of emission lines, or the spectrum was totally blank. Thus the TOOT00 radio-source sample is 85% spectroscopically complete. Using the results

of the spectroscopy, and in combination with individual characteristics for each of them, we classify the 47 TOOT00 radio sources according to the following optical criteria:
i) **Q**: Objects with definite broad lines in their optical spectrum (6/47); all of them have blue SEDs and all apart from one (TOOT00_1069) are point sources at K.
ii) **Q?**: Objects without definite broad lines in the optical spectrum, but that are either point sources at K, or there is a clear hint of broad lines in the optical spectrum, or both (4/47); all objects have a blue SED.
iii) **G?**: Evidence from the optical spectrum that at least one high-excitation (see e.g. Jackson & Rawlings 1997) narrow emission line exists (8/47).
iv) **G**: All the objects that don't fall in the previous categories (29/47); all cases are resolved at K.

One of the TOOT00 'Q' objects, TOOT00_1233, is possibly a broad-absorption-line QSO (BALQSO; see notes on objects in Appendix B), as shown in Figure 3.10.

We calculate photometric redshifts $z_{\rm photBC}$ with the HyperZ photometric code (Bolzonella et al. 2000) using photometry from $U-$band (> 3600 Å) to the $K-$band (2.2 μm) and Bruzual-Charlot (Bruzual & Charlot 2003; BC) templates. In nearly all cases we let reddening (Calzetti et al. 2000) be a free parameter (see notes on objects in Appendix B for a few exceptions), but the derived values of A_V were typically small. Results are shown in Table 3.3. In many cases we put the value obtained in square brackets, as the probability density function for the redshift is not sharply peaked, typically because the SED is not galaxy-like or is too sparsely sampled above the putative 4000 Å break.

In Figure 3.2a we present a comparison of spectroscopic and photometric redshifts. The Q and Q? type objects fall off the correlation line, which is unsurprising because all but two of them have a highly uncertain photometric redshift due, presumably, to significant contributions to their SEDs from non-stellar light causing the galaxy HyperZ templates to be inappropriate; the exception is TOOT00_1244 for which the spectroscopic and photometric $z_{\rm photBC}$ have similar values. The 'G' type objects with high $z_{\rm spec}/z_{\rm photBC}$ typically fall off the correlation, because they have a highly uncertain $z_{\rm photBC}$; the exceptions being TOOT00_1099 and TOOT00_1228, although the latter has an uncertain spectroscopic redshift. In TOOT00_1215 the disagreement between spectroscopic and photometric HyperZ redshift probably reflects the fact that more photometric points are needed for an accurate fit of the BC template. In Figure 3.2b we see that quasars tend to have lower photometric redshifts than their spectroscopic ones, with the exception of TOOT00_1069, presumably because their K-band light is contaminated by non-

stellar emission. Objects TOOT00_1027, TOOT00_1107, TOOT00_1129, TOOT00_1069 are all seemingly intrinsically faint objects in the near-IR K-band, which yields the high $z_{\rm photK-z}$ value (see Willott et al. 2003).

Due to a ∼85% (40 out of 47 objects) spectroscopic completeness we only need to use photometric redshifts for 7 out of the 47 objects. For these 7 objects we use a photometric redshift calculated from the $K-z$ relation of Willott et al. (2003; hereafter $K_{\rm W}-z$ relation). The $K_{\rm W}-z$ fits the 3CRR, 6CE and 7CRS data sets, where the K magnitude is aperture and emission line corrected:

$$K_W = 17.37 + 4.53 \times (\log_{10} z) - 0.31 \times (\log_{10} z)^2, \tag{3.1}$$

where K is the $K-$band magnitude and z the redshift.

When using the $K_{\rm W}-z$ relation we kept in mind that the K magnitude of our sample is not emission-line or aperture corrected. This means that the $K_{\rm W}-z$ relation may give a slightly incorrect estimate for the photometric redshift of our objects. We believe, though, that these errors are negligible for our sample. According to Willott et al. (1999), one expects the line flux to scale with radio flux density at K-band, so the line contamination of the K-band magnitude should be small in TOOT. Additionally, we chose not to perform aperture or emission line corrections in our K magnitude for the following reasons: (i) above redshift $z > 0.6$ aperture corrections are ~ 0.05 mag (Eales et al. 1997); (ii) most of the objects have K-band magnitude measured in the same aperture, apart from some exceptions due to confusion by a nearby object (see Table 3.1 and Appendix B) and any corrections would be highly dependent on the assumed light spatial profile which is uncertain. In our analysis, whenever we use the redshift calculated from the $K_{\rm W}-z$, it is only for objects at high redshift $z > 0.9$, where line and aperture corrections, although uncertain, are probably small.

3.3.2 Radio classification, spectral indices and sizes

Figure 3.10 (see Appendix B) presents near-IR/radio overlays for all the TOOT00 objects, where either the A- or B-array VLA maps were used. Another classification we use is based on their radio structure, as shown in Table 3.1. In the same figure we also present optical spectra and SEDs that were constructed from the photometric data (Table 3.5 in Appendix B), where the best fit BC templates are shown. In the cases where optical photometry was unavailable from the ODT, the optical magnitude was estimated directly from the spectrum; a mean value of the continuum was used to estimate the flux density in each optical band where the fluxes

measured were approximately corrected for systematic errors due to light losses from the slit. This value is approximately 25% for a 1.5-arcsec wide slit; we chose to use a value calculated for each object of $\sim$ 10% to 40% dependent on the slit width (see Table 3.2). The errors on the magnitudes (see Table 3.5 in Appendix B) are taken to be equal to the percentage errors estimated for light losses from the slit.

In Figure 3.3 we present the $S_{74\mathrm{MHz}}$ versus $S_{151\mathrm{MHz}}$ diagram. The VLSS catalogue provides flux densities for 12 (out of 47) TOOT00 radio sources. Direct measurements from the 74-MHz maps were made for a further 11 TOOT00 objects that were not included in the VLSS catalogue, but appeared to be detected in the 74 MHz maps; the measurements were performed using the IMSTAT package in AIPS. For the other 24 TOOT00 objects, a 2σ detection was adopted as an upper limit (see Table 3.1). The median spectral index calculated between 74 and 151 MHz including the limits is $\alpha_{74\mathrm{MHz}}^{151\mathrm{MHz}} \sim 0.5$. This confirms, as expected, that the average low-frequency radio spectra approach the $\alpha \sim 0.5$ value expected in emission from un-aged electron populations at the low rest-frame frequency of $\sim$ 200 MHz (using the median redshift $z \sim 1.25$ of the sample; see Section 3.4). The fact that we have almost the same amount of limits above and below $\alpha = 0.5$ is re-assuring. The overplotted lines in Figure 3.3 indicate that the TOOT00 radio sources not detected at 74 MHz are mainly faint enough sources at 151 MHz that with any reasonable radio spectral index they would fall close to the limit of the VLSS survey. In Figure 3.3, we label three cases (TOOT00_1022, TOOT00_1244 & TOOT00_1298) which, in Table 3.1, have $\alpha_{74\mathrm{MHz}}^{151\mathrm{MHz}} > 1.2$. In all of these cases the signal-to-noise ratio is ≤ 7 at 151 MHz and ≤ 4 at 74 MHz meaning much lower true values of $\alpha_{74\mathrm{MHz}}^{151\mathrm{MHz}}$ are within the errors.

In Figure 3.4 we present the radio luminosity at 151 MHz versus the radio spectral index of our objects, calculated using the 1.4-GHz and 151-MHz flux densities presented in Table 3.1. The median spectral index is $\alpha_{151\mathrm{MHz}}^{1.4\mathrm{GHz}} = 0.86$. In Vardoulaki et al. (2008) we have shown that for a 1.4-GHz selected study of radio sources (SXDS) roughly 10 times fainter at 151 MHz than TOOT00 (see Figure 3.5), the fraction of flat-spectrum objects is higher. Some important differences between the TOOT00 and SXDS radio-source samples can be attributed to the lower radio-frequency selection of TOOT00 radio sources. One such difference is that there seem to be quite a few objects in the SXDS[10] with flat radio spectral index (i.e. $\alpha < 0.5$). The fraction of SXDS objects with $\alpha < 0.5$ is 35 $\pm$ 6% (13 out of 37), while $\sim$ 11 $\pm$ 3% (4 out of 37) have an inverted radio spectral index (i.e. $\alpha < 0$). In the TOOT00 sample, only 3 radio sources ($\sim$ 6 $\pm$ 3%) have a flat radio spectral index, and only one (2 $\pm$ 1%) of them (TOOT00_1027),

[10]The radio spectral indices for the SXDS sources were calculated using 1.4 GHz and 610 MHz (or 325 MHz) data, whereas for the TOOT00 we use 1.4 GHz and 151 MHz flux densities; note that is close enough for a rough comparison of the samples.

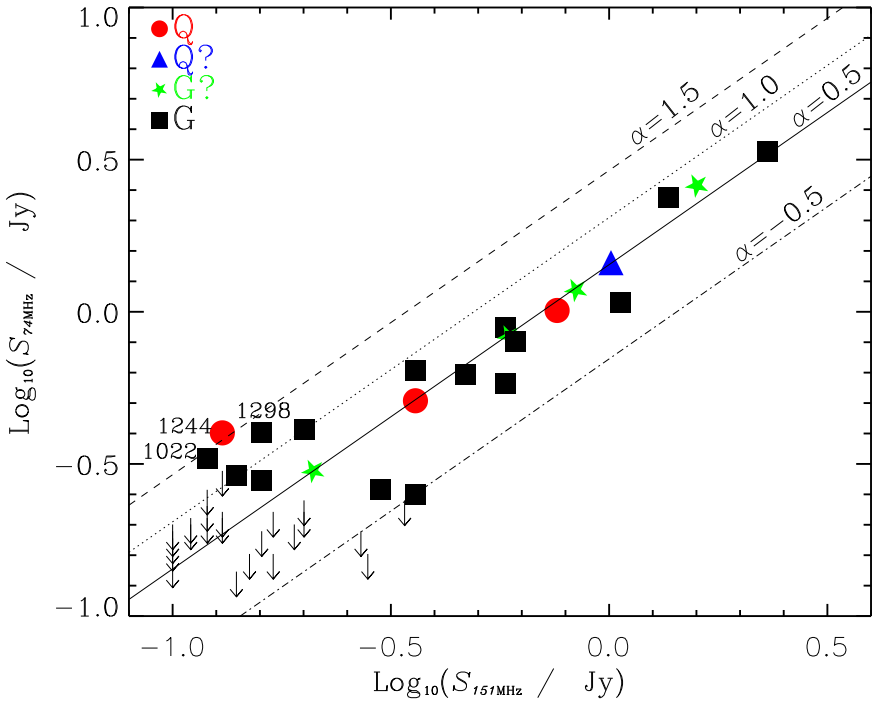

Figure 3.3: Flux density at 74 MHz $S_{74\mathrm{MHz}}$ versus flux density at 151 MHz $S_{151\mathrm{MHz}}$. Symbols: red circles denote quasars 'Q', blue triangles denote possible quasars 'Q?', green stars stand for possible galaxies 'G?', and black squares for secure galaxies 'G'. 12 objects were detected by the VLSS and plotted with their symbol. Another 11 have flux densities at 74 MHz measured directly from the VLSS map (see Table 3.1). Thus, 23 out of 47 TOOT00 objects are detected both at 74 and 151 MHz. The other 24 objects, that have no measurement at 74 MHz, are indicated as 2σ upper limits and plotted with black arrows. The solid black line is for $\alpha = 0.5$, the dotted black line for $\alpha = 1.0$, the dashed black line for $\alpha = 1.5$ and the dotted-dashed line for α = -0.5.

a possible gigahertz-peaked spectrum (GPS) object, has an inverted radio spectral index (see Table 3.1). The other two flat-spectrum objects, TOOT00_1233 and TOOT00_1268, are Q and Q? objects respectively. TOOT00_1235 & TOOT00_1244 have radio spectral indices α close to 0.5 and are probably core-jet objects (e.g. Augusto et al. 1998). These radio sources are usually moderately-flat-spectrum sources ($\alpha \sim 0.5$ corresponds to freshly injected electrons) often with double-sided kpc-scale jet-like structures. Both these objects with $\alpha \sim 0.5$ have linear projected sizes $D \sim 100$ kpc, as can be seen in Figure 3.6–a. The observed core-jet radio structure is probably caused by interactions with the intergalactic medium and projection effects (Paragi et al. 2000). The outlier, TOOT00_1196, is either an unusual source or a spurious 7C detection (see Appendix B).

Figure 3.5 presents the radio luminosity at 151 MHz versus redshift for the TOOT00. The flux density limits of various radio surveys are shown: 3C, 6CE, 7CRS (12.4 Jy, 2.0 Jy and 0.5 Jy respectively; Willott et al. 2001), TOOT00 (0.1 Jy), and SXDS ($\simeq$ 0.01 Jy at 151 MHz[11];

[11] A typical steep spectrum radio spectral index $\alpha = 0.8$ was used to convert from the 2 mJy flux density limit at 1.4 GHz to 151 MHz.

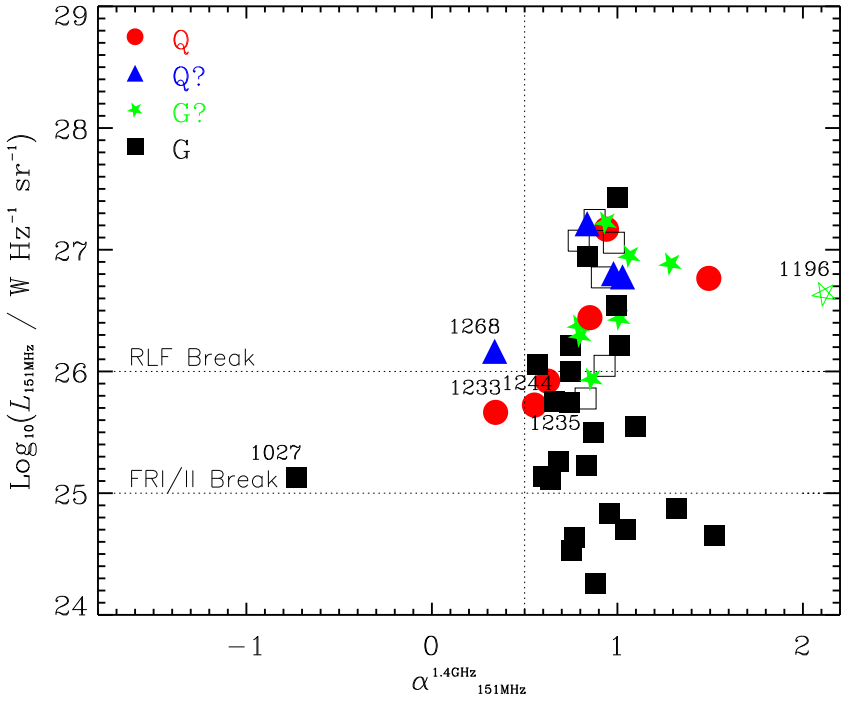

Figure 3.4: Radio Luminosity at 151 MHz $L_{151\mathrm{MHz}}$ versus the radio spectral index α. Symbols are the same as in Figure 3.3; filled symbols denote objects with spectroscopic redshifts and open symbols represent objects with photometric redshifts. The horizontal lines show the RLF and FRI/FRII breaks calculated from the Willott et al. (2003) and the Fanaroff & Riley (1974) values respectively using a typical steep-spectrum radio spectral index of 0.8. The vertical line at $\alpha = 0.5$ shows the conventional border between steep and flat-spectrum sources.

Vardoulaki et al. 2008). We note that 3 out of 4 objects above redshift $z = 3$ are galaxies with photometric redshifts derived from the $K_{\mathrm{W}} - z$ relation (see Section 3.4). The 3 galaxies with photometric redshift $z > 3$ are, TOOT00_1224, TOTO00_1252 & TOOT00_1152 and are very faint at K. According to Willott et al. (2003), the objects in the 7CRS are ≈ 0.3 mag fainter than the ones in the 3CRS and 6CE. Since the $K_{\mathrm{W}} - z$ relation fits all three datasets, it will over-predict the redshift of radio-faint objects[12]. Thus, if we re-calculate the redshift using that correction of 0.3 mag for TOOT00_1224, TOOT00_1252 & TOOT00_1152, then we get redshifts $z = 2.900$, $z = 3.810$ and $z = 2.747$ respectively; only TOOT00_1252 still has a photometric redshift $z_{\mathrm{photK-z}} > 3$.

The angular size θ of the TOOT00 objects is presented in Table 3.1. This value was measured from the radio maps, A- or B-array, depending on the object (see notes on the objects in Appendix B). In cases where the radio structure was compact in the B-array map but there was evidence of extended structure in the A-array data, the latter was used to measure θ. In cases where the radio source had an one-sided structure, θ was measured from

[12]The fact that we are using the $K(z)$ to calculate redshifts, and not the $z(K)$ is also likely to over-predict the estimated z's at higher redshifts.

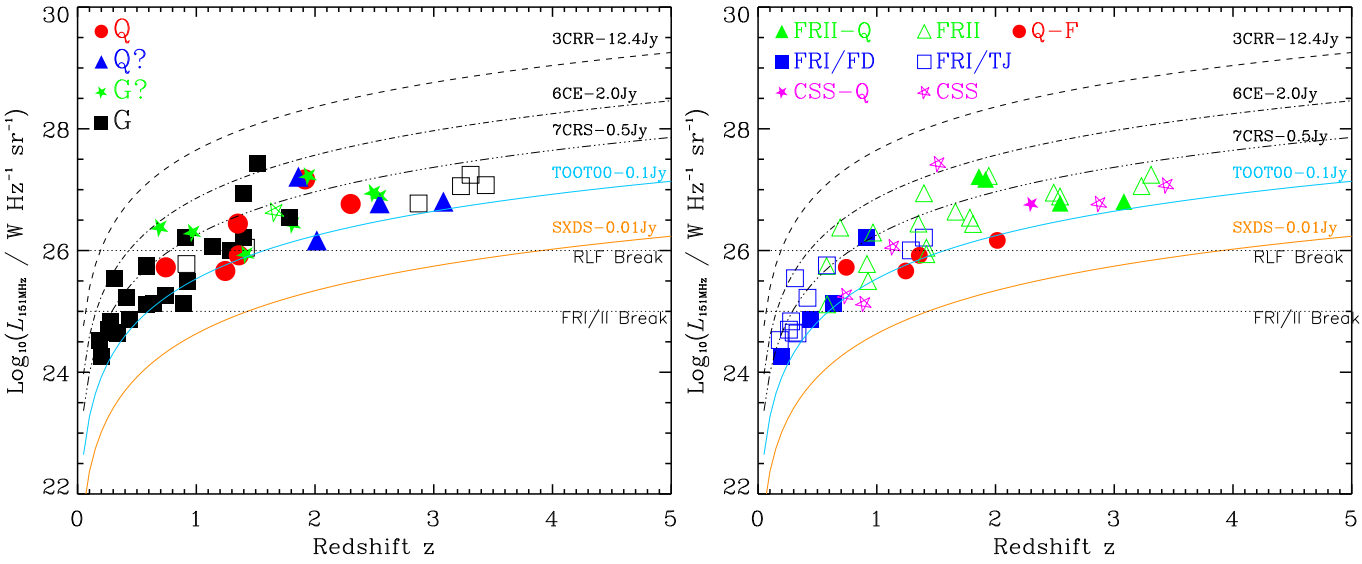

Figure 3.5: Radio Luminosity at 151 MHz $L_{151\mathrm{MHz}}$ versus redshift z for the TOOT00 sample. **a) Left**: Symbols are the same as in Figure 3.3; filled symbols represent objects with spectroscopic redshift and open symbols denote objects with photometric redshift. **b) Right**: Symbols denote radio-optical classification: green filled triangles denote FRII-Q objects; green open triangles denote FRIIs; blue filled boxes denote FD type FRIs; blue open boxes denote TJ type FRIs; red filled circles denote Q-F objects; purple filled stars denote CSS-Q objects; purple open stars denote CSS objects; a '?' denotes uncertainty in the radio-optical classification as stated in Table 3.3. In both plots, the horizontal lines show the RLF and FRI/FRII breaks calculated from the Willott et al. (2003) and the Fanaroff & Riley (1974) values respectively using a typical steep-spectrum index of 0.8. The flux density limits of 3C, 6CE, 7CRS (Willott et al. 2001), TOOT00 and SXDS (Vardoulaki et al. 2008) samples are shown ($\alpha = 0.8$ was used to convert to 151 MHz flux density).

the core to the centre of that lobe. Lastly, in the case where the source presented a complex radio structure (e.g. TOOT00_1107; see Figure 3.10 in Appendix B), the distance from the core to each lobe was measured and then added together. The angular size θ was used in the calculation of the linear projected size D, which is plotted against the radio luminosity at 151 MHz in Figures 3.6–a & 3.6–b.

3.3.3 The FRI/FRII structural divide

The structure of radio sources at low redshifts is directly connected to their radio luminosity, where objects with $\log_{10}(L_{151\mathrm{MHz}}/\mathrm{WHz}^{-1}\mathrm{sr}^{1}) \lesssim 25$ are FRI type radio sources and those above that value are FRIIs (Fanaroff & Riley 1974). Another classification used in Table 3.1 is based on the Owen & Laing (1989) radio classification according to radio structure (see Section 3.1); in that way we classify the TOOT00 radio sources as CDs, FDs, TJs and COM. Finally, we classify the TOOT00 objects based on both radio and optical data, as presented in Table 3.3: FRIIs correspond to CD objects; FRIs to FD and TJ; Q-F corresponds to quasars with flat

radio spectral index ($\alpha \lesssim 0.5$; a '?' denotes α close to 0.5); CSS-Q corresponds to quasars with compact radio structure; FRII-Q denotes a quasar that has FRII radio structure; CSS denotes a compact steep spectrum radio source.

In Figure 3.6–a we present the radio luminosity at 151 MHz $L_{151\mathrm{MHz}}$ versus largest projected linear size D, where we make use of the radio-optical classification (FRI, FRII, Q-F, CSS; see also Figure 3.5–b). Our aim is to investigate whether there is a significant number of FRI objects above the FRI/II and RLF break in radio luminosity. TOOT00 objects with radio luminosities at the FRI/II break are at redshift $z \sim 0.5$, while the ones with $L_{151\mathrm{MHz}} = L_{\mathrm{RLFbreak}}$ are at redshift $z \sim 1.5$ as can be seen in Figure 3.5. FRII type radio sources occupy the area above the FRI/II break, as is expected. It is interesting, however, that we find 7 FRI type (5 TJs and 2 FDs) radio sources above the FRI/II break with 3 out of 7 of the FRIs also above the RLF break. Although there is an uncertainty in the TJ radio structure of several cases, e.g. TOOT00_1099 and TOOT00_1115 (see Table 3.1 and Figure 3.10), we seem able to conclude robustly that there is some cosmic evolution between $z \sim 0$ and $z \sim 1$ in the FRI/II divide as has been commented on previously by Heywood, Blundell & Rawlings (2007).

3.3.4 The quasar fraction

Figure 3.6–b shows the radio luminosity at 151 MHz versus the largest projected linear size D. The quasar fraction to the total number of objects, is $f_{\mathrm{q}} = 0.25$ (10 out of 40 objects) above the FRI/FRII break (we include Q and Q? type objects as quasars in this calculation; $f_{\mathrm{q}} = 0.13$ if we include only Q objects). Above the RLF break the quasar fraction is 0.27 (7 out of 26 objects); the quasar fraction drops to 0.12 if we exclude the Q? objects. Such values agree with previous studies (e.g. Willott et al. 2000) where the quasar fraction is $\sim 0.1 \rightarrow 0.4$ over the relevant range of radio luminosity $10^{25}\mathrm{WHz}^{-1}\mathrm{sr}^{-1} \lesssim L_{151\mathrm{MHz}} \lesssim 10^{27}\mathrm{WHz}^{-1}\mathrm{sr}^{-1}$.

Below the FRI/FRII break, the quasar fraction is $f_{\mathrm{q}} = 0$, which also agrees with previous studies. These values increase if one studies objects using 24 μm emission as an indicator of quasar activity, as has been done by Vardoulaki et al. (2008) on the SXDS radio-source sample. This is because hot dust emission at 24 μm is much harder to hide than optical broad lines which can be extinguished by small amounts of dust. The 'quasar-mode fraction' f_{QM}, i.e. the fraction of objects with 'significant' accretion rates, as determined from the observed 24 μm flux density, to the total number of objects, was found to be $\sim 0.5 \rightarrow 0.9$ above the FRI/FRII break and $f_{\mathrm{QM}} \lesssim 0.1$ below it; some high-accretion-rate objects do exist at low radio luminosities. There are no 24 μm data available in the TOOT00 region on which to make a study of f_{QM} in the TOOT00 sample.

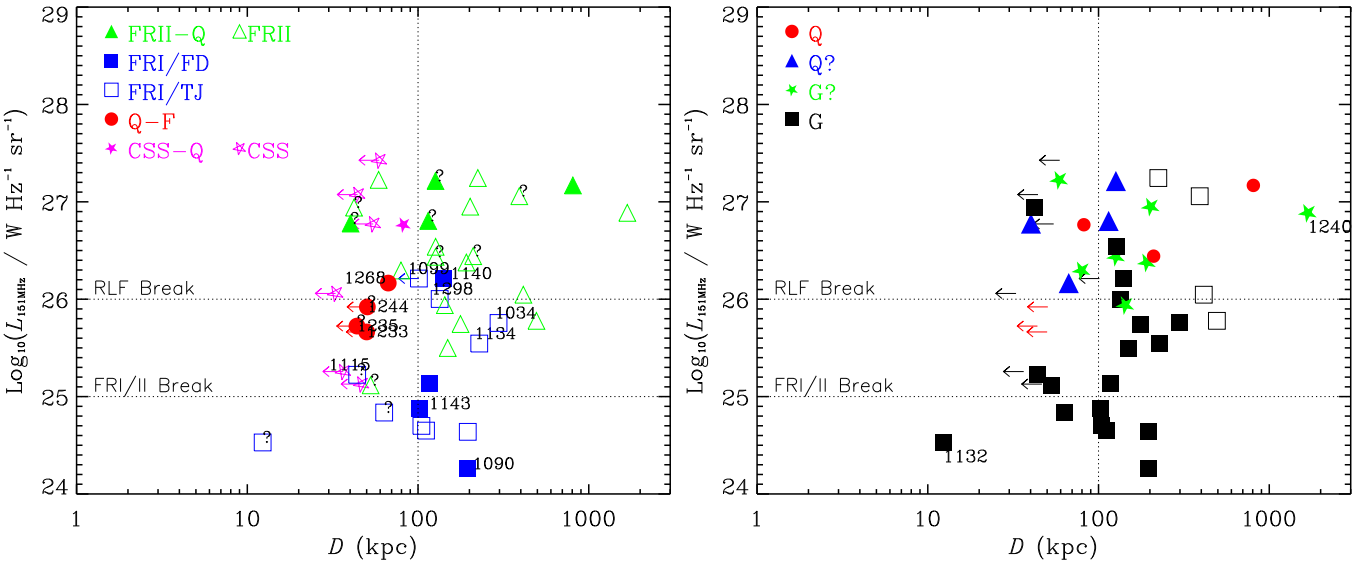

Figure 3.6: Radio Luminosity at 151 MHz $L_{151\mathrm{MHz}}$ versus the largest projected linear size D. **a) Left:** Symbols denote radio-optical classification as in Figure 3.5; a '?' denotes uncertainty in the radio-optical classification as stated in Table 3.3. The horizontal lines show the RLF and FRI/FRII breaks calculated from the Willott et al. (2003) and the Fanaroff & Riley (1974) values respectively using a typical steep-spectrum radio spectral index of 0.8. Objects marked with their name are discussed in the text. **b) Right:** Symbols denote optical classification and are the same as in Figure 3.3; filled symbols represent objects with spectroscopic redshifts and open symbols denote objects with photometric redshifts. The horizontal lines show the RLF and FRI/FRII breaks calculated from the Willott et al. (2003) and the Fanaroff & Riley (1974) values respectively using a typical steep-spectrum radio spectral index of 0.8. Note that TOOT00_1196 is not plotted since we cannot measure an angular size from the radio maps (see notes on the object in Appendix B).

3.4 The redshift distribution of TOOT00

Figure 3.7a presents the redshift distribution of the 47 TOOT00 radio sources, with a binning of dz = 0.05. The median spectroscopic redshift is $z_{\mathrm{spec}} = 1.135$, whereas the median redshift including the photometric redshifts is $z_{\mathrm{med}} = 1.287$. This value is larger than the median redshift of the 6CE and 7CRS radio source surveys (Rawlings, Eales & Lacy 2001; Willott et al. 2003) of $z \sim 1.1$, but we have to take into account that the high-redshift objects of our sample tend to have uncertain photometric redshifts (see Section 3.3.1). If the $K_{\mathrm{W}} - z$ photometric redshifts are re-calculated for an increase of Δm = 0.3 mag in all magnitudes (i.e. assuming a similar offset from the mean $K_{\mathrm{W}} - z$ relation for TOOT00 objects and 7CRS objects), then the median redshift drops to $z_{\mathrm{med}} = 1.244$; we adopt $z_{\mathrm{med}} \sim 1.25$. We note that only TOOT00_1252 could plausibly be at $z \gtrsim 3.5$.

A comparison of the TOOT00 radio-source distribution to any other distribution involves correcting for the 9 objects that were excluded from the original sample and for objects that are missing since the 7C data have significant incompleteness approaching the $S_{151\mathrm{MHz}} = 100$

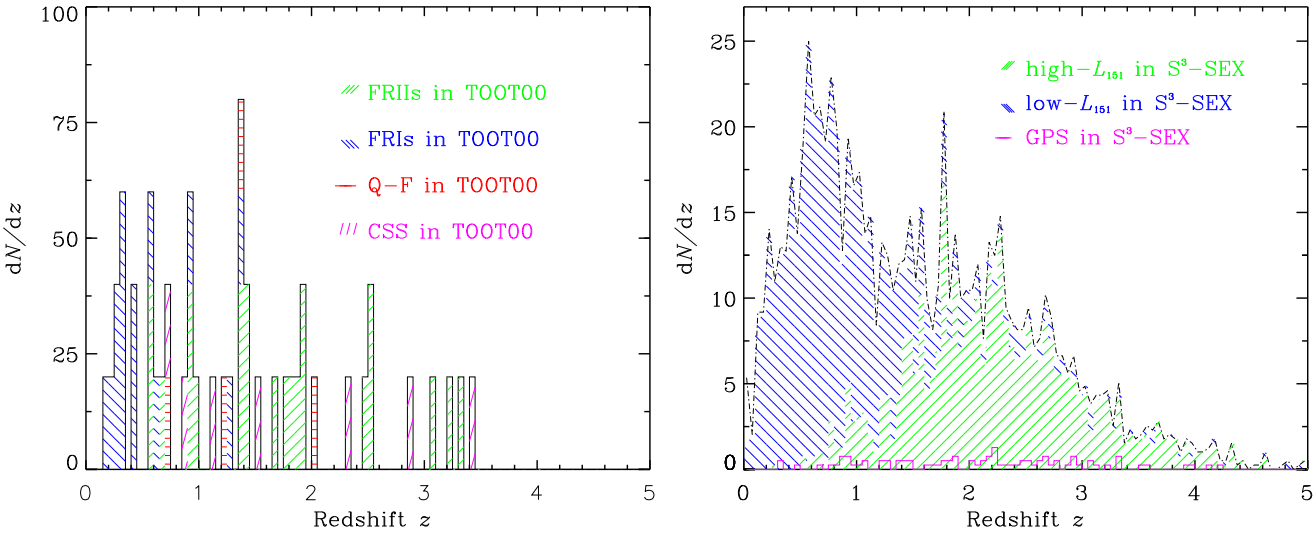

Figure 3.7: **a) Left:** Histogram of the redshift distribution for the 47 TOOT00 radio sources according to radio/optical class (see Table 3.3). The binning on the redshift axis is dz = 0.05. The green colour represents FRIIs, blue represents FRIs, red represents flat-spectrum quasars (Q-F) and purple represents CSS objects; the black histogram shows the TOOT00 distribution. FRIIs correspond to CD radio sources, FRIs to FD and TJ, Q-F to quasars with flat radio spectral index, Q-F? to quasars with α close to the critical value 0.5 ($0.5 < \alpha^{1.4\mathrm{GHz}}_{151\mathrm{MHz}} < 0.7$), Compact Steep Spectrum (CSS) to objects with steep radio spectral index ($\alpha > 0.7$) and compact radio structure, and CSS-Q to quasars associated with a compact steep spectrum ($\alpha > 0.7$) object. **b) Right:** Model predictions from the S^3-SEX simulation (Wilman et al. 2008) for an area of 0.1212 sr, which is scaled down to the TOOT00 area of 0.0015 sr. The binning on the redshift axis is dz = 0.05. Objects are marked according to their radio source classification as stated in Wilman et al. (2008); blue denotes high-L_{151} objects, green denotes low-L_{151} objects and purple stands for GPS sources in the S^3-SEX simulation; RQQ and normal galaxies are not presented for clarity.

mJy flux density limit (see Figure 8 of McGilchrist et al. 1990). The weighting factors needed to correct the sensitivity variations across the TOOT00 7C data area not available, so we can only approximately compare our source counts to those in 7C.

We compare the distribution of the TOOT00 radio sources to a simulation obtained from the SKADS Simulated Skies Semi-Empirical Extragalactic Database S^3-SEX (Wilman et al. 2008). This is a set of simulations of the radio sky suitable for planning science with the proposed Square Kilometre Array (SKA) radio telescope (Wilman et al. 2008), that are constructed to match results from the 3CRR, 6CE and 7CRS redshift surveys, as well as radio source counts. This simulation of the extragalactic radio continuum sky allows for large-scale structure in the cosmological distribution of radio sources, and the types included in the simulations are radio-quiet AGN, radio-loud AGN of 'FRI' and 'FRII' classes and star-forming galaxies. Core-jet radio sources are not explicitly included in the simulation. Furthermore, these 'FR classes' are determined directly by the radio luminosity[13] and not the radio structure of the objects

[13]In S^3-SEX (Wilman et al. 2008), the integration limits for the radio luminosity function of the FRI

(see Wilman et al. 2008). Due to these imperfections, and the fact that our radio-optical classification of the TOOT00 radio sources is structural (see Section 3.3.2), we will name the 'FRI class' in S^3-SEX as the low-L_{151} sub-population and the 'FRII class' as the high-L_{151} sub-population of radio sources. The simulation covers a sky area of 20×20 deg^2 or 0.1212 sr, out to a cosmological redshift of $z = 20$, and down to flux density limit of 10 nJy at 151 MHz, 610 MHz, 1.4 GHz, 4.86 GHz and 18 GHz.

We searched for objects in the S^3-SEX database with simulated 151 MHz total flux density greater than 100 mJy. We found 3139 radio sources above the flux density limit after rejecting those whose core components lay outside the 20×20 deg^2 area of the simulation. The total flux densities of multiple component radio sources (i.e. FRIs and FRIIs) were determined by summing together all of the individual components of each source, including the few components which were outside the 20×20 deg^2 area. Using this full list of radio sources we then constructed 100 circular sub-fields with the same area as TOOT00, namely 0.0015 sr (radius 1.27 deg.) centred at random positions within the simulation. The mean number of objects y from these 100-simulations is <y> = 40.1 with a standard deviation, dominated by Poisson errors and the effects of large-scale structure, $\sigma_{\rm y} = 8.82$.

The flux density scale of TOOT00 was bootstrapped from 6C, so should be accurate at the ± 10% level. This is supported by Figure 3.3, which shows that the sources detected at both 74 MHz and 151 MHz have spectral indices ~ 0.5, as expected at low frequencies where the spectral index should reflect the injected, i.e. un-aged, power-law index of the underlying distribution in electron energies (e.g. Alexander & Leahy 1987).

There has been no quantitative estimate of the incompletenesses and Eddington bias (e.g. Teerikorpi 2004) in the lower flux density bins of the TOOT00 7C data, which are extremely important effects given the low signal-to-noise thresholds adopted in the catalogue (see Table 3.1). The raw TOOT00 7C source counts are significantly higher than those inferred in the 7C survey of McGilchrist et al. (1990), largely because of lower significance sources. At the $S_{151\rm MHz} \simeq 100$ mJy level, corrections for incompleteness and Eddington bias are highly uncertain. Most of the TOOT00 radio sources, apart from 9 (see Table 3.1) and the 9 'off-edge' objects, have a signal-to-noise ratio ~ 5.5, a criterion similar to that adopted by McGilchrist et al. (1990); note that there is only one possible spurious source in our final list (TOOT00_1196; see Appendix B) as we have securely detected all bar this one source with the VLA. We find 56 sources in 5.0 deg^2 in the TOOT00 region. The source counts in the TOOT00 7C region using

radio sources are $20.0 \lesssim \log_{10}(L_{151\rm MHz/WHz^{-1}sr^{-1}}) \lesssim 28.0$ and those of the FRII radio sources are $25.5 \lesssim \log_{10}(L_{151\rm MHz/WHz^{-1}sr^{-1}}) \lesssim 30.5$.

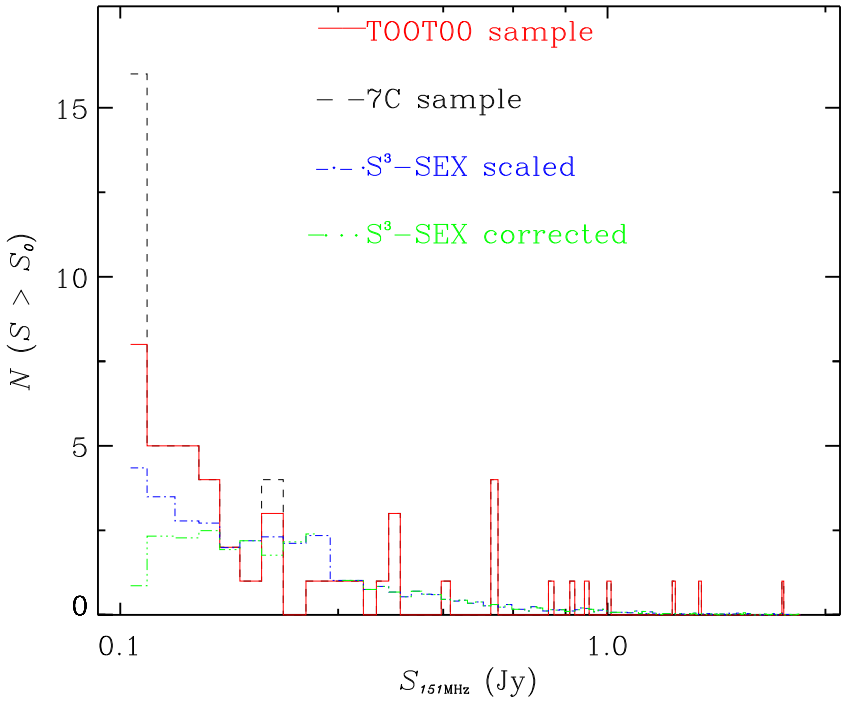

Figure 3.8: Histogram of the flux density distribution for objects in the TOOT00 sky area with flux density $S \gtrsim 100$ mJy at 151 MHz. The black dashed line shows the 56 sources in the 7C sample that lie inside the area marked by the red circles in Figure 3.1. The red solid line indicates the 47 TOOT00 radio sources. The blue dotted-dashed histogram is the S^3-SEX simulation scaled down to 0.0015 sr. This includes ~ 40 objects. The green 3-dotted-dashed line presents the S^3-SEX simulation scaled down to 0.0015 sr in which the lower bins ($S_{151\mathrm{MHz}} <$ 0.25 Jy) are weighted according to Table 5 of the McGilchrist et al. (1990), plus an additional correction takes into account the missing 7C objects in TOOT00. The final number of objects in the scaled and corrected S^3-SEX simulation is ~ 33.

only $> 5.5\ \sigma$ detections are 24.7 ± 1.6, and thus within the errors of the corrected McGilchrist et al. source counts.

Figure 3.8 presents the number of objects in the TOOT00 sample compared to the 7C objects in the same sky area that have flux density limits above 100 mJy at 151 MHz. This histogram shows that 47 out of the 56 objects from the 7C that have $S_{151\mathrm{MHz}} \gtrsim 100$ mJy are included in TOOT00 sample. Figure 3.8 shows that almost all the difference is confined to the lowest (95 mJy $< S_{151\mathrm{MHz}} <$ 115 mJy) bin for reasons explained in Section 3.2 and caption to Figure 3.1.

In Figure 3.8 we also plot the flux density distribution from the S^3-SEX simulation scaled down to the 0.0015-sr sky area of the TOOT00 sample. We note that the S^3-SEX simulation, with or without corrections similar to the McGilchrist et al. (1990) work, significantly under-predicts the 7C objects in the TOOT00 area in the lowest flux density bins (95 mJy $< S_{151\mathrm{MHz}} <$ 115 mJy).

We suspect that the Eddington bias in the 7C sample (which includes sources extracted

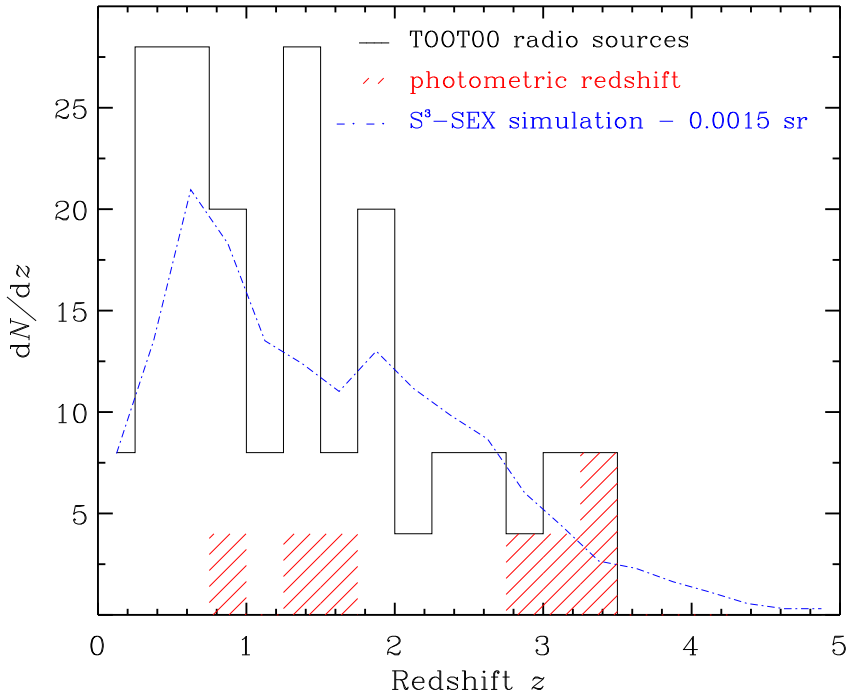

Figure 3.9: Histogram of the redshift distribution for the 47 TOOT00 radio sources with median $z_{\rm med} = 1.287$ (85% spectroscopic and 17% photometric redshifts, black & red lines respectively). The binning on the redshift axis is $\mathrm{d}z = 0.25$. We overplot model predictions from the S^3-SEX simulation for an area of 0.1212 sr, which is scaled down to an area of 0.0015 sr (blue dotted-dashed line) to match the TOOT00 sky area, and includes ~ 40 objects.

from the 7C maps with signal-to-noise ratios as low as ~ 3; see Table 3.1) causes the spike in the lowest-$S_{151\rm MHz}$ bin, meaning that the exclusion of faint 'off-edge' sources (Section 3.2) in the construction of the TOOT00 survey, brings the flux density distribution closer in line between data and simulation. Modelling of the Eddington bias would be possible, given a known source count significantly deeper than the 7C survey, but this will only become available with the advent of LOFAR (e.g. Röttgering 2007).

We hereafter assume that the TOOT00 sample is close to the true distribution (i.e. the one in the TOOT00 area in the limit of infinite signal-to-noise ratio in the low-frequency survey data). We compare this to the S^3-SEX distribution in flux density and other properties without any, in any case highly uncertain, corrections for incompleteness and Eddington bias. With these assumptions, there is a reasonable agreement between the 47 TOOT00 radio sources and the 40 ± 8.8 objects expected from the simulation (the standard deviation is a combination of Poisson errors and genuine field-to-field variations due to the large scale structure enclosed in the S^3-SEX simulation).

In Figure 3.9 we compare the measured TOOT00 redshift distribution and that predicted by the S^3-SEX simulation. We calculated the two-sided Kolmogorov-Smirnov (K-S test) statistic

and associated probability to investigate whether data and simulation are consistent (Press et al. 1993). The maximum deviation between the cumulative distribution of the data and simulation is ~ 0.12 and the significance level of the K-S test is $\sim 44.46\%$. This result suggests that the real TOOT00 and simulated S^3-SEX samples are consistent.

As a further note on the radio-source population, Figure 3.7 demonstrates that there is a broad agreement between the TOOT00 radio/optical classes of the TOOT00 data and the S^3-SEX simulation, allowing for known limitations in the simulation. In the TOOT00 sample (Figure 3.7a) we have 47 objects: 22 FRIIs, 14 FRIs, 4 Q-Fs and 7 CSS radio sources; one of the CSS objects is in fact a GPS radio source. The distribution on the right of Figure 3.7 shows the S^3-SEX simulation, scaled down to 0.0015 sr, which includes ~ 40 objects: ~ 18 high-L_{151} objects, ~ 21 low-L_{151} objects, ~ 0.1 RQQs and ~ 0.2 normal galaxies and ~ 1 GPS; the normal galaxies and RQQs are not plotted in this figure for clarity.

3.5 Conclusions

In this chapter we presented optical spectroscopy and optical and near-IR imaging on the 47 TOOT00 radio-source sample from a survey covering 0.0015 sr. We have 85% spectroscopic completeness and we estimate photometric redshifts for the rest of the sample using the photometric redshift code HyperZ or the $K_{\rm W} - z$ relation from Willott et al. (2003). The key points of our analysis are:

• The median redshift for the whole sample is $z_{\rm med} \sim 1.25$. This value is slightly higher than the $z \sim 1.1$ of the 6CE and 7CRS surveys.
• The fraction of 'naked' quasars is $0.13 < f_{\rm q} < 0.25$ above the FRI/FRII break in the 151-MHz radio luminosity and below that break, the quasar fraction drops towards zero. These are similar results to the 3CRR, 6CE, 7CRS redshift surveys.
• The total number of TOOT00 objects and their distribution are consistent with a simulated distribution of radio sources from the SKADS Simulated Skies Semi-Empirical Extragalactic Database (S^3-SEX), simulations extrapolated from the 3CRR/6CE/7CRS datasets.
• The radio structures of the TOOT00 sample are broadly in line with those in the S^3-SEX sample with small exceptions, like the lack of core-jet sources in the simulation.
• There is observational evidence from TOOT00 that the 'FRI/II' structural divide depends on cosmic epoch. We conclude that there must be some cosmic evolution between redshifts $z = 0$ and $z = 1$. It is interesting that the S^3-SEX 'FRIs' (or low-L_{151} sub-population) include

objects in-between the classic FRI/II break and the RLF, which in real samples include some CD sources as well as the FD sources counted as FRI in this study.

• The low fraction of flat-spectrum objects in TOOT00 of 6% can be attributed to the low-frequency selection of the radio sample. The TOOT00 radio-source sample also includes 2 core-jet objects with radio spectral indices $\alpha \sim 0.5$.

Appendix B

3.6 Notes on the TOOT00 radio sources

TOOT00_1140 is a galaxy 'G' and is resolved in the K-band. This FD radio source (the two components are not compact in the A-array map) is at a spectroscopic redshift $z = 0.911$. The NVSS data suggest the presence of diffuse radio emission that is absent in the A/B-array maps. Due to lack of ODT optical photometry, we measure the optical magnitudes directly from the spectrum, as explained in Section 3.3. The photometric redshift from HyperZ seems to be a good fit to the data (see Figure 3.10), although it does not agree perfectly with the spectroscopic one.

TOOT00_1099 is a possible TJ radio source, and a galaxy resolved in the near-infrared K-band. The optical spectrum reveals only one clear emission line at 8937Å, which is extended over ~ 5 arcsec ≈ 43 kpc. We believe that this is $[\mathrm{OII}]_{\lambda 3727}$ and not $[\mathrm{OIII}]_{\lambda 5007}$, since the weaker of that doublet, $[\mathrm{OIII}]_{\lambda 4959}$, does not appear in the spectrum. The [OII] emission line suggests a redshift $z = 1.397$. We are not concerned that other strong lines, like [CII], are not visible, since they fall near strong sky lines in the blue part of the spectrum. No other expected weak lines can be identified in the spectrum. The photometric redshift values estimated from HyperZ and the $K_{\mathrm{W}} - z$ differ from the spectroscopic value implying an under-luminous galaxy in which the 4000 Å break has not been securely identified in the SED.

TOOT00_1125 is a spectroscopically confirmed quasar at redshift $z = 1.916$, which is unresolved in the K-band. The B-array radio map reveals a CD radio source. The photometric redshift from HyperZ does not agree with the spectroscopic, and the $K_{\mathrm{W}} - z$ relation underestimates the photometric redshift, presumably, in both cases, because of a non-stellar contribution to the K-band.

TOOT00_1143 is a FD radio galaxy (the hot spots at the A-array radio map are not compact) at redshift $z = 0.438$, and is resolved in the K-band. We use the peak flux density at 151 MHz and 1.4 GHz in our analysis, since we believe the integrated flux density is affected by

confusion as indicated by a NVSS map of the area. There is a fairly good agreement between spectroscopic and photometric redshifts.

TOOT00_1233 is a quasar at redshift $z = 0.438$ with a flat radio spectral index, and probably a COM radio source. A comparison of the VLA B-array and NVSS flux densities suggests time variability. This is possibly a broad-absorption-line QSO (BALQSO), although the fact that the blue and red spectra were joined where the MgII line is, causes some concern regarding this classification. The offset between the tentative 6000 Å absorption and the MgII resonance line indicates a speed of ≈ 0.1c of the outflow, which is not unreasonable. The BC galaxy templates obviously provide a very poor fit to the photometric data, since the SED is flat, as expected in an unobscured quasar.

TOOT00_1022 is a COM radio source. The optical spectrum taken on August 2000 (PA = 9°) is completely blank and not presented here. The optical spectrum taken on August 2006 (PA = 140°) shows a featureless faint continuum down to 4000 Å, putting a limit on the redshift of $\lesssim 3.4$. HyperZ provides a poor fit to the photometric data; more photometric points are needed in the near-infrared to estimate a more accurate photometric redshift. We use the $K_{\rm W} - z$ redshift for this object.

TOOT00_1204 is a FD radio galaxy at $z = 0.6395$. The high value of the NVSS flux density is not due to confusion, since there are no nearby radio sources in a 2-arcmin radius; a significant amount of flux is invisible in the A- and B-array data. Due to the absence of ODT optical photometry we measure the optical flux directly from the spectrum (see Section 3.3.2). There is a fairly good agreement between spectroscopic and photometric redshifts.

TOOT00_1235 is a spectroscopically confirmed quasar and probably a COM radio source. In Figure 3.10 we present the A-array VLA map, where the radio structure looks stretched along one axis; this is an artifact caused by bandwidth smearing due to the position of the radio source at the edge of the VLA primary beam (see Figure 3.1). We classify this quasar as a Q-F?, since the value of α is close to 0.5, which also suggests that this is a core-jet radio source. There is a fairly good agreement between spectroscopic and $z_{K_{\rm W}-z}$ redshifts, contrary to the $z_{\rm BC}$ one; this result is expected since the BC templates do not fit a quasar SED well.

TOOT00_1224 is a compact radio source; the A-array map is bandwidth smeared since the object is at the edge of the VLA primary beam (see Figure 3.1). Two optical spectra taken at different PAs and with different slit widths (Table 3.2) are completely blank. As the photometric redshift indicates, this is probably due to the faintness of the object. We use the $z_{K_{\rm W}-z}$ redshift for our calculations since the photometric $z_{\rm BC}$ redshift is highly uncertain. As can be seen from Figure 3.10, the optical magnitudes from ODT are 'bright', but yet the

spectrum is invisible. This can be explained by the fact that in spectroscopy the optical slit only captures a part of the light from the object, while in photometry more of the light gets observed due to the bigger apertures. The optical photometry goes down to $\sim$ 4000 Å, which puts a limit on the redshift of the object of $\lesssim 3.4$.

TOOT00_1291 is a CD? radio source, since the eastern hotspot is compact in the A-array radio map. The optical spectrum is blank, so we use HyperZ to calculate a photometric redshift. The BC templates do not fit the data well; more near-IR photometric points are needed for a more accurate fit. We use the photometric redshift calculated from the $K_{\rm W} - z$ relation for the analysis.

TOOT00_1107 is a TJ radio galaxy at $z = 0.300$. The radio map shows a very diffuse source. From the radio overlay in Figure 3.10 we notice that the extended radio structure is bent backwards as expected if the source of the jets is moving with respect to an intra-cluster medium. We present the secondary best-fit photometric redshift from HyperZ, since that value is closer to the spectroscopic redshift; no reddening law was used to calculate the photometric redshift. The $z_{K_{\rm W}-z}$ does not agree with either spectroscopic or photometric redshifts, implying an intrinsically faint host galaxy. Note that the object's ID might be either of the two objects seen in Figure 3.10. There is a possibility that the real ID is the K object aligned with the radio source, which would give a fainter K magnitude, $K = 18.6$ mag. Since there is only a very faint hint of continuum in the red part of the optical spectrum, the photometric redshift from the $K_{\rm W} - z$ relation would be $z_{K_{\rm W}-z} = 1.87$, which would make it a high redshift FRI radio source.

TOOT00_1180 is probably a rather one-sided CD radio source and a reddened quasar at $z = 1.810$, since the expected broad emission lines (like Lyα and CIV) appear to be narrow in the spectrum of Figure 3.10. We present the A-array radio map since it reveals the extended structure of the radio source; the radio structure is not bandwidth smeared since the source is close to the VLA pointing position.

TOOT00_1027 is a compact radio source at $z = 0.890$, a point source at K and a possible GPS object, since it has an inverted radio spectral index. This spectral turnover might be caused by synchrotron self-absorption (e.g. Snellen et al. 2000) or free-free absorption (e.g. Sawada-Satoh et al. 2000). Apparent extended radio components in the maps of this source are almost certainly artifacts due to imperfect calibration. The photometric redshift calculated from the $K_{\rm W} - z$ is very high compared to the other two redshifts, implying a faint host galaxy. This agrees with the findings of Snellen (2008) that GPS radio sources correspond to fainter hosts than other radio sources.

TOOT00_1195 is a CD radio source with prominent hot spots at the end of the radio structure. The optical spectrum shows only a faint continuum without clear emission lines or any break. HyperZ provides a very poor fit to the data. We use $z_{K_{\rm W}-z}$ in the analysis.

TOOT00_1069 is a possible COM (or marginally extended) radio source and a spectroscopically confirmed quasar at $z = 2.300$ with prominent broad emission lines. Obtaining this redshift was a triumph of 'blind spectroscopy' (Rawlings, Eales & Warren 1990) as a wide (4-arcsec) slit was placed North-South in an attempt to cover all plausible radio components. The A-array radio map is bandwidth smeared, which is not helpful in making a reliable radio classification. We classify it as a compact-steep-spectrum quasar (CSS-Q), as indicated by the steep radio spectral index, $\alpha^{1.4{\rm GHz}}_{151{\rm MHz}} = 1.49$, and the optical spectrum of a quasar (see Figure 3.10). Both photometric redshifts are unrealistic as expected if the SED is dominated by non-stellar emission. We assign an upper limit to the K magnitude, since the signal-to-noise ratio is not high enough to distinguish any associated K object from the background noise.

TOOT00_1094 is a compact radio source with faint continuum and a probable emission line at 7040 Å in the red part of the optical spectrum. The photometric redshifts suggest that this emission line could be MgII, giving a redshift $z = 1.516$. The photometric redshift fit from HyperZ could be improved if more photometric points between I and K were available.

TOOT00_1149 has a TJ radio structure. This radio galaxy is at $z = 0.260$, where spectroscopic and photometric redshifts seem to be in excellent agreement. We don't have a K-band image from UKIRT for this object, so we use the K image from the ODT survey.

TOOT00_1298 is a TJ radio source probably at $z = 1.287$ from likely [OII] and associated red continua in the spectrum. We do not trust the photometric redshift estimated from HyperZ, since only three photometric points were used in the fit. The $z_{K_{\rm W}-z}$ value is slightly different from the spectroscopic and photometric redshift.

TOOT00_1200 is a CD radio source with prominent hot spots at both ends of the radio structure, that are visible in both B- and A-array VLA maps. The optical spectrum has a plethora of narrow emission lines, placing the object at redshift $z = 0.691$. There is a blue excess in the SED.

TOOT00_1215 is a galaxy at $z = 0.278$ with a compact radio component coincident with the galaxy and radio emission slightly elongated to the west; hence we classify it as TJ?. The value of the photometric redshift from the $K_{\rm W} - z$ is very close the spectroscopic one. The redshift calculated from HyperZ has a much higher value, probably because more photometric points are needed for an accurate fit; no reddening law was used to estimate $z_{\rm BC}$. We don't have a K-band image from UKIRT for this object, so we use the K image from the ODT

survey.

TOOT00_1240 is a large CD radio source ~ 2.5 arcmin long, possibly at spectroscopic redshift $z = 2.543$?. We have to note that such a big radio source is rather rare at a high redshift. The exposure times used in the first attempt at spectroscopy (August 2000) of this object were accidentally far too short to detect it. The fact that the K position of the object is close to a spectroscopically confirmed M-star (RA: 00 13 05.2 & Dec: +36 01 48.1; marked with 'M' in Figure 3.10) also makes it hard to get a photometric redshift. We managed to get a spectrum of the M-star and the bright galaxy south-west of the object ID, marked with 'G' in Figure 3.10, at $z = 0.191$. In August 2004 we targeted the object north of the west radio lobe with an associated compact radio component (see Figure 3.10) which is a galaxy at $z = 0.556$. The blue spectrum from the August 2009 observing run has continuum emission blueward of 4290 Å, but, as this becomes increasingly contaminated by leakage from the M-star at redder wavelengths, it is hard to assess the colour of the object. We show in Figure 3.10 only the blue-arm spectrum in which there are possible Lyα and NV$_{\lambda\lambda 1240}$ lines. Along the slit we measured a redshift of $z = 0.193$ for a galaxy close to the western hotspot at RA: 00 13 01.36 & Dec: +36 01 57.04. The $K-$band image of this area excludes the area where the east lobe is located. In Figure 3.10 we present the $K-$band/radio B-array overlay. Below it, we give a DSS image of the area, where the double radio structure is clearly visible. The photometric redshift from HyperZ is not reliable: more photometric points are needed to provide a better fit to the SED. The value of photometric redshift from the $K_{\rm W} - z$ relation ($z_{K_{\rm W}-z} = 2.185$) is close to the tentative spectroscopic redshift.

TOOT00_1289 is CD radio source, since the radio hot spots do not disappear in the A-array VLA map. The optical spectrum indicates a possible redshift of $z = 1.784$ although, if true, there are no hints of Lyα at the expected location. The photometric redshift from HyperZ is highly uncertain; more photometric points are needed for an accurate fit.

TOOT00_1072 is a giant elliptical galaxy with a CD radio structure, since the compact hot spots are also visible in the A-array map, and a clear absorption spectrum, suggesting a spectroscopic redshift $z = 0.577$. We have fairly good agreement between photometric and spectroscopic redshifts, and the best-fit BC template fits the photometric data points well.

TOOT00_1134 is a radio galaxy at $z = 0.311$. The photometric redshift from HyperZ is a good fit to the data and agrees with the spectroscopic value; no reddening law was used in the calculations. The integrated radio flux densities include a contribution from a separate radio source to the south-east (as indicated by a NVSS map of the area); this second object is associated with a galaxy that, from its SED, may well be in the same cluster. We use the

peak flux densities at 74 MHz, 151 MHz for our analysis. For the 1.4-GHz flux density we use the value measured from the B-array VLA map using the package AIPS: we use a box around the radio source, excluding the radio source to the south-east of the object.

TOOT00_1244 is a spectroscopically confirmed quasar at $z = 1.358$ and a compact radio source. We classify it as a Q-F?, since the radio spectral index has a value close to 0.5, which also suggests this may be a core-jet radio source. The photometric redshift is not reliable, as is expected if its blue SED is dominated by non-stellar emission. We don't have a K-band image from UKIRT for this object, so we use the K image from the ODT survey.

TOOT00_1066 is a FD radio source, since the double radio structure seen in Figure 3.10 disappears in the A-array radio map. The spectroscopic redshift is probably $z = 0.926$, although different from the photometric redshifts. We use the peak flux densities at 151 MHz and 1.4 GHz, due to confusion as indicated by a NVSS map of the area.

TOOT00_1261 is a spectroscopically confirmed quasar that appears to be reddened, since the expected broad emission lines, like Lyα and CIV, are broad only in their wings. The A-array radio map reveals a CD radio structure. The apparent offset between the K and radio positions (Figure 3.10) is within the uncertainty of the astrometry. The SED secondary best-fit is surprisingly, and presumably fortuitously, good considering the BC templates are not expected to fit quasar SEDs very well. We use the peak flux densities at 151 MHz and 1.4 GHz, due to confusion as indicated by the NVSS map of the area.

TOOT00_1252 is a possibly one-sided radio source; we classify it as CD?. The west 'lobe' is ~ 45 arcsec from the 'core' which may be a true core plus a short eastern lobe ($S_{1.4\mathrm{GHzint}} = 18.9$mJy and $S_{1.4\mathrm{GHzpeak}} = 14.4$ mJy). The K detection is $2.7''$ South-West of the peak radio position. We assign an upper limit to the K magnitude measured from the K-band image, since the signal-to-noise ratio is not high enough in order to distinguish any K object from the background. The optical spectrum taken on August 2000 (at PA = 109°) is blank in the blue and shows signs of continuum in the red. The spectrum taken on July 2004 (at PA = 265°) is completely blank, with confidence in correct pointing as the slit was pointed in a way to observe as many objects as possible along the slit. Deeper observations could provide a reliable optical spectrum and an accurate optical position for the object. The HyperZ fit gives only a lower limit to the photometric redshift since only upper limits are used in the calculations; more photometric points are needed to improve the fit. We use the photometric redshift from the $K_{\mathrm{W}} - z$ relation, since the photometric redshift from HyperZ is unreliable.

TOOT00_1214 is a one-sided radio source classified as CD?. It is a point source at K and a seemingly reddened quasar at $z = 3.081$. In the optical spectrum we can see evidence of a

Lyα absorption system below 5000 Å. There is a very poor agreement between photometric and spectroscopic redshifts, as expected for a quasar SED. We use the peak flux densities at 151 MHz and 1.4 GHz, due to confusion as indicated by a NVSS map of the area.

TOOT00_1152 is a CD radio source with prominent hot spots at both ends of the radio structure, that do not disappear in the A-array map. The object most likely associated with the radio structure gives a weak featureless faint optical continuum in the spectroscopy, which puts a limit on the redshift of the object of $\lesssim 3$; the fact that z_{K-z} is above redshift 3 is explained in Section 3.3.2. We use the $K_{\rm W} - z$ redshift for our calculations since the formal output of the HyperZ code is clearly a very poor fit.

TOOT00_1129 is a CD radio source, since the hot spots do not disappear in the A-array map, and a possible reddened quasar, as indicated by the narrow Lyα and CIV lines. Neither of the two photometric redshifts agree with the spectroscopic value, as expected if non-stellar (e.g. dust scattered light from the obscured quasar) light is dominating the SED. The formal output of the HyperZ code is clearly a very poor fit.

TOOT00_1090 is a FD radio source, as can be seen by the diffuse radio structure in Figure 3.10. This galaxy is at redshift $z = 0.201$. There is a very good agreement between spectroscopic and photometric redshifts.

TOOT00_1267 is a CD radio source, since the radio hot spots are present in both the A- and B-array radio maps. The optical spectrum places this object at redshift $z = 0.968$. There is a fairly good agreement between photometric and spectroscopic redshifts.

TOOT00_1188 is a CD radio source (the radio hot spots do not disappear in the A-array map) with a spectroscopic redshift $z = 1.417$. The HyperZ fit is fairly good; more near-IR photometric points are needed for a more accurate fit. The redshift calculated from the $K_{\rm W} - z$ relation is slightly higher than the spectroscopic value.

TOOT00_1196 is the only object in the sample that may be a spurious 7C radio source. Its unusual properties means that if it is real it is a very diffuse 'FD?' radio source since there is no bright radio core nor a bright hot spot near the 7C radio position, as can be seen by the B-array map presented in Figure 3.10. Due to this fact, we cannot measure the angular size of the radio source. Any radio emission is probably associated with the galaxy shown in Figure 3.10, close to the 7C radio position. Since any radio source in the B-array map has a flux density below the detection limit, we use a 2σ detection from the NVSS, recalling that the rms noise of the NVSS is 0.45 mJy beam^{-1}. This gives a very steep radio spectral index of > 2.1. The object is not detected at 74 MHz, marginally surprising given a predicted detection at $\sim 4.5\sigma$. We cannot rule out the possibility that the 4.4σ 7C detection is spurious. Assuming

the source is real and the galaxy ID shown in Figure 3.10, optical photometry provides only R- and I-band images, while it was not observed in the B-band, so the HyperZ fit is uncertain. The optical spectrum is blank in the blue, but shows a featureless continuum in the red with no clear lines. This object is classified as a possible galaxy G?, and we use the redshift calculated from the $K_{\rm W} - z$ for our analysis.

TOOT00_1173 is a TJ radio source at $z = 0.332$, with diffuse radio structure. The HyperZ fit is good and there is a good agreement between photometric and spectroscopic redshifts.

TOOT00_1228 is a COM radio source probably at redshift $z = 1.135$, and a point source at K. There is poor agreement between spectroscopic and photometric redshifts.

TOOT00_1034 is TJ radio source at $z = 0.580$, where the east radio emission is very diffuse. The photometric redshift agrees with the spectroscopic one, although more photometric points could improve the HyperZ estimate.

TOOT00_1255 is probably a CD radio source since the hot spots do not disappear in the A-array radio map. Here we present the B-array map (see Figure 3.10). This galaxy is at redshift $z = 0.582$, which does not agree well with the photometric redshift. The one estimated from the $K_{\rm W} - z$ relation has a higher value, presumably because it is an unusually underluminous galaxy.

TOOT00_1048 is a CD radio source since the radio hot spots do not disappear in the A-array map, with a secure redshift $z = 1.943$. The optical spectrum indicates a reddened quasar and it is unresolved in the K-band. The ID in the K is 0.6 arcsec away from the centre of the classical double radio structure, which is within the uncertainty of the astrometry and the radio position. We classify it as a G?. We do not trust the photometric redshift from HyperZ since we have only four photometric points for the calculation.

TOOT00_1029 is probably a COM radio source; the A-array map is bandwidth smeared and isn't presented here. The redshift estimated from HyperZ is close to the spectroscopic redshift; no reddening law was used in that calculation. The $z_{\rm K-z}$ estimate does not agree with the spectroscopic redshift.

TOOT00_1115 is probably a TJ radio source, since both A- and B-array radio maps are extended; here we present the A-array map. McLure et al. (2004) classify this object as a low-excitation-galaxy LEG (see Jackson & Rawlings 1997). The optical spectrum gives a secure redshift $z = 0.416$, and there is very good agreement with the photometric redshift.

TOOT00_1132 is possibly a TJ? radio source and a galaxy at $z = 0.183$. There is a fairly good agreement between the spectroscopic and photometric $z_{\rm BC}$ redshifts, although the $z_{\rm K-z}$ value is slightly higher.

TOOT00_1250 is a spectroscopically confirmed quasar at $z = 1.350$, with broad emission lines in the optical spectrum. The A- & B-array radio maps reveal a CD? radio structure; the A-array map shows clearly that both hot spots are compact (see Figure 3.10). The object is unresolved in the K-band. The value estimated from HyperZ disagrees with the spectroscopic and the $z_{\mathrm{K-z}}$ redshifts due to a poor fit to too few photometric data points.

TOOT00_1268 is a COM radio source at redshift $z = 2.015$, and it might be a reddened quasar. We classify it as a G? optically and a Q-F in the radio for a quasars with a flat radio spectral index. The A-array radio map is bandwidth smeared at the source position; we do not present here. The fact that there is no visible sign of a 4000 Å break spectroscopically and that the SED is relatively flat, makes it hard to estimate an accurate photometric redshift.

TOOT00_1251 is a CD radio source at $z = 2.490$, since the radio hotspots do not disappear in the A-array map. The Lyα line is obvious in the 2D optical spectrum. We do not trust the photometric redshift from HyperZ due to large errors on the photometry. The $z_{K_{\mathrm{W}}-z}$ value agrees with the tentative spectroscopic value.

TOOT00_1203 is a small CD? radio source at redshift $z = 1.397$. The photometric redshifts are slightly lower than the spectroscopic value. More photometric points could improve the HyperZ fit.

Table 3.5: Optical and near-IR photometry for the 47 TOOT00 radio sources that was used to calculate photometric redshifts with HyperZ: U, B, V, R and I, $2''$ Vega magnitudes are from the ODT survey (MacDonald et al. 2004) or they are measured from the spectra of each object (Figure 3.10) due to lack of imaging; $K-$ photometry was obtained by UKIRT; J^*, H^* and K^* magnitudes are provided by K. Inskip (complete photometry in five different apertures is shown in Table 3.6); errors on the magnitudes are in brackets below the values. **Column 1** shows the name of the TOOT00 object. In **Columns 2-6** we give $U-$, $B-$, $V-$, $R-$, $I-$band magnitude respectively; the character 's' shows measurement from the spectrum of each object; the character 'o' denotes ODT data. The errors on the magnitudes are shown below each magnitude value. **Columns 7 & 8** show photometry from the 'Inskip' catalogue on the J^*- and H^*-band, respectively, where they were measured with a $4''$ diameter aperture. **Column 9** presents $K-$band photometry from UKIRT measured with a $4''$ diameter aperture or the one from the 'Inskip' catalogue (see Section 3.2) marked with an '*'; the character 'o' denotes the value is provided by the ODT. Note: In the HyperZ photometric redshift calculation, all errors less than 10% on the near-IR magnitudes were taken as 10%.

(1)	(2)	(3)	(4)	(5)	(6)	(7)	(8)	(9)
Object	U (mag)	B (mag)	V (mag)	R (mag)	I (mag)	J^* (mag)	H^* (mag)	K (mag)
TOOT00_1140			25.2^s	22.8^s	21.0^s	18.8	18.0	17.0*
			(0.38)	(0.38)	(0.38)	(0.08)	(0.06)	(0.04)
TOOT00_1099	23.3^s	23.2^s	22.1^s	21.1^s	20.2^s	18.6	17.5	16.5*
	(0.38)	(0.38)	(0.38)	(0.38)	(0.38)	(0.07)	(0.04)	(0.04)
TOOT00_1125	17.6^s	18.0^s	17.6^s	17.4^s	17.0^s			15.6
	(0.38)	(0.38)	(0.38)	(0.38)	(0.38)			(0.01)
TOOT00_1143	23.0^s	22.8^s	21.3^s	20.1^s	19.2^s			16.0
	(0.38)	(0.38)	(0.38)	(0.38)	(0.38)			(0.01)
TOOT00_1233	18.9^s	19.1^s	18.6^s	18.3^s	17.8^s			15.3
	(0.38)	(0.38)	(0.38)	(0.38)	(0.38)			(0.01)
TOOT00_1022	25.7^s	>26.2^s	25.3^s	24.4^s	>24.6^s			19.4
	(0.23)	(0.23)	(0.23)	(0.23)	(0.23)			(0.19)
TOOT00_1204	22.1^s	23.0^s	21.7^s	20.6^s	19.6^s			16.3
	(0.38)	(0.38)	(0.38)	(0.38)	(0.38)			(0.01)
TOOT00_1235	20.9^s	21.9^s	21.6^s	21.3^s	20.4^s	18.8	17.8	17.0*
	(0.38)	(0.38)	(0.38)	(0.38)	(0.38)	(0.09)	(0.05)	(0.04)
TOOT00_1224		25.8^o	23.9^o	24.1^o	24.0^o	22.0	20.9	19.7*
		(0.35)	(0.14)	(0.25)	(0.45)	(0.51)	(0.29)	(0.23)
TOOT00_1291	24.6^s	23.9^s	22.7^s	22.1^s	21.3^s			17.3
	(0.11)	(0.11)	(0.11)	(0.11)	(0.11)			(0.02)
TOOT00_1107	23.9^s	23.1^s	21.4^s	20.8^s	20.3^s			18.1
	(0.38)	(0.38)	(0.38)	(0.38)	(0.38)			(0.06)
TOOT00_1180	23.6^s	23.9^s	23.7^s	23.0^s	22.4^s			18.3
	(0.38)	(0.38)	(0.38)	(0.38)	(0.38)			(0.08)
TOOT00_1027		>26.2^s	24.2^s	23.2^s	21.7^s			19.5
		(0.23)	(0.23)	(0.23)	(0.23)			(0.24)
TOOT00_1195				24.6^s	>24.6^s	19.5	18.9	18.1*
				(0.23)	(0.23)	(0.12)	(0.10)	(0.08)
TOOT00_1069	22.8^s	23.3^s	22.3^s	22.9^s	24.0^s			> 20.3
	(0.08)	(0.08)	(0.08)	(0.08)	(0.08)			(1.09)
TOOT00_1094	26.1^s	25.8^s	24.7^s	23.6^s	23.0^s			18.3
	(0.23)	(0.23)	(0.23)	(0.23)	(0.23)			(0.13)
TOOT00_1149	21.0^s	20.8^s	19.0^s	18.4^s	17.5^s			14.6^o
	(0.23)	(0.23)	(0.23)	(0.23)	(0.23)			(0.01)
TOOT00_1298				24.4^s	21.1^s			17.3
				(0.23)	(0.23)			(0.04)
TOOT00_1200	21.6^s	22.9^s	22.3^s	21.6^s	20.5^s			17.4
	(0.23)	(0.23)	(0.23)	(0.23)	(0.23)			(0.04)
TOOT00_1215	22.6^s	21.7^s	20.0^s	19.3^s	18.7^s			15.0^o
	(0.38)	(0.38)	(0.38)	(0.38)	(0.38)			(0.01)
TOOT00_1240		22.2	21.7					18.9
		(0.11)	(0.11)					(0.35)
TOOT00_1289	24.8^s	>26.2^s	23.3^s	24.1^s				17.8
	(0.23)	(0.23)	(0.23)	(0.23)				(0.10)
TOOT00_1072		23.3^s	21.6^s	20.4^s	19.0^s			15.7
		(0.11)	(0.11)	(0.11)	(0.11)			(0.02)
TOOT00_1134		21.3^s	19.5^s	18.5^s	17.8^s			14.6
		(0.23)	(0.23)	(0.23)	(0.23)			(0.01)

Table 3.5: (continued)

(1)	(2)	(3)	(4)	(5)	(6)	(7)	(8)	(9)
Object	U (mag)	B (mag)	V (mag)	R (mag)	I (mag)	J^* (mag)	H^* (mag)	K (mag)
TOOT00_1244	19.9^s	20.9^s	20.7^s	20.3^s	20.1^s			18.8
	(0.42)	(0.42)	(0.42)	(0.42)	(0.42)			(0.46)
TOOT00_1066				24.5^s	22.2^s	19.8	18.7	18.0*
				(0.11)	(0.11)	(0.13)	(0.08)	(0.07)
TOOT00_1066		25.3^o	24.6^o	23.6^o	22.5^o	19.8	18.7	18.0*
(HyperZ)		(0.29)	(0.05)	(0.05)	(0.05)	(0.13)	(0.08)	(0.07)
TOOT00_1261	22.5^s	22.4^s	21.9^s	21.9^s	21.6^s			19.0
	(0.23)	(0.23)	(0.23)	(0.23)	(0.23)			(0.06)
TOOT00_1252				$> 25.4^s$	$> 24.6^s$			> 19.6
				(0.50)	(0.50)			(0.44)
TOOT00_1214	22.9^s	23.5^s	22.7^s	22.0^s	22.0^s			18.6
(HyperZ)	(0.23)	(0.23)	(0.23)	(0.23)	(0.23)			(0.03)
TOOT00_1214	23.0^o	24.5^o	23.3^o	22.9^o	22.1^o			18.6
	(0.06)	(0.15)	(0.07)	(0.08)	(0.09)			(0.03)
TOOT00_1152	24.0^s	25.7^s	25.4^s					19.6
	(0.02)	(0.02)	(0.02)					(0.80)
TOOT00_1129	24.4^s	24.2^s	24.0^s	23.6^s	23.8^s			20.2
	(0.02)	(0.02)	(0.02)	(0.02)	(0.02)			(1.13)
TOOT00_1090	20.3^s	20.0^s	18.3^s	17.7^s	16.9^s			14.5
	(0.38)	(0.38)	(0.38)	(0.38)	(0.38)			(0.01)
TOOT00_1267	23.5^s	24.6^s	24.0^s	23.0^s	21.7^s	19.0	18.2	17.1*
	(0.23)	(0.23)	(0.23)	(0.23)	(0.23)	(0.09)	(0.06)	(0.05)
TOOT00_1188	23.2^s	23.9^s	23.5^s	22.8^s	22.7^s			18.3
	(0.23)	(0.23)	(0.23)	(0.23)	(0.23)			(0.01)
TOOT00_1196				24.1^o	22.4^o			18.4
				(0.20)	(0.12)			(0.11)
TOOT00_1173		21.7^s	20.2^s	19.1^s	18.3^s			15.3
		(0.38)	(0.38)	(0.38)	(0.38)			(0.02)
TOOT00_1228	24.1^s	24.1^s	22.5^s	21.8^s	21.0^s			18.4
	(0.23)	(0.23)	(0.23)	(0.23)	(0.23)			(0.13)
TOOT00_1034	25.1^s	24.7^s	21.6^s	20.4^s	19.4^s			16.1
	(0.23)	(0.23)	(0.23)	(0.23)	(0.23)			(0.03)
TOOT00_1255	23.3^s	24.6^s	22.8^s	21.4^s	20.3^s	18.6	17.6	16.8*
(HyperZ)	(0.23)	(0.23)	(0.23)	(0.23)	(0.23)	(0.07)	(0.05)	(0.05)
TOOT00_1255		24.6^o	22.6^o	21.5^o	20.5^o	18.6	17.6	16.8*
		(0.18)	(0.05)	(0.02)	(0.02)	(0.07)	(0.05)	(0.05)
TOOT00_1048	24.1^s	25.2^s	24.1^s					17.5
	(0.11)	(0.11)	(0.11)					(0.16)
TOOT00_1029	23.8^s	24.7^s	23.2^s	21.8^s	20.1^s	18.4	17.6	15.9*
	(0.23)	(0.23)	(0.23)	(0.23)	(0.23)	(0.07)	(0.04)	(0.02)
TOOT00_1115	22.6^s	23.0^s	21.6^s	20.3^s	19.5^s			15.9
	(0.23)	(0.23)	(0.23)	(0.23)	(0.23)			(0.02)
TOOT00_1132	20.0^s	20.3^s	18.8^s	18.3^s	17.6^s			15.0
	(0.38)	(0.38)	(0.38)	(0.38)	(0.38)			(0.01)
TOOT00_1250	23.7^s	22.7^s	22.5^s	22.0^s	22.0^s			18.0
(HyperZ)	(0.23)	(0.23)	(0.23)	(0.23)	(0.23)			(0.14)
TOOT00_1250		22.9^o	22.5^o	21.9^o	22.4^o			18.0
		(0.04)	(0.04)	(0.03)	(0.12)			(0.14)
TOOT00_1268	23.1^s	23.8^s	23.7^s	22.4^s	21.0^s			17.6
	(0.38)	(0.38)	(0.38)	(0.38)	(0.38)			(0.11)
TOOT00_1251	$<25.3^s$	26.0^s	$<25.7^s$	23.5^s	22.8^s			19.1
	(0.23)	(0.23)	(0.23)	(0.23)	(0.23)			(1.30)
TOOT00_1203				22.4^s	20.8^s	18.9	18.3	17.4*
				(0.38)	(0.38)	(0.09)	(0.07)	(0.05)

Table 3.6: Optical and near-IR photometry for the 47 TOOT00 radio sources; errors are in brackets below the values. **Column 1** shows the name of the TOOT00 object. **Column 2** gives the photometric band, where for the $K-$band from UKIRT we also provide the observing date; the J^*-, H^*- and K^*-band data are from the Inksip catalogue; the character 'o' denotes data from the ODT. **Column 3** gives the near-IR position of the object (RA in h m s & Dec in ° ′ ″; J2000.0). **Columns 4-8** present the photometry in different diameter aperture measurements, 3″, 4″, 5″, 8″ and 9″ respectively, for near-IR data only. Note that for the optical photometry (see MacDonald et al. 2004) the magnitudes given are not measured in a 3-arcsec diameter aperture, but are given in the same column due to lack of space.

(1)	(2)	(3)	(4)	(5)	(6)	(7)	(8)
Object	Band	near-IR Position (J2000)	3″mag (3″ error)	4″mag (4″ error)	5″mag (5″ error)	8″mag (8″ error)	9″mag (9″ error)
TOOT00_1140	K-UFTI	00 08 30.8 +35 21 48.1	17.1	17.0	16.9	16.8	16.7
	25Jul2000		(0.02)	(0.02)	(0.03)	(0.04)	(0.05)
	J^*		18.9	18.8	18.8	18.6	18.7
			(0.09)	(0.08)	(0.09)	(0.10)	(0.12)
	H^*		18.0	18.0	17.9	17.8	17.8
			(0.06)	(0.06)	(0.06)	(0.08)	(0.09)
	K^*		17.0	17.0	16.9	16.7	16.7
			(0.04)	(0.04)	(0.04)	(0.04)	(0.04)
TOOT00_1099	K-UFTI	00 09 23.7 +35 05 05.5	16.7	16.6	16.5	16.5	16.4
	25Jul2000		(0.01)	(0.02)	(0.02)	(0.03)	(0.04)
	$J03^*$		18.7	18.6	18.5	18.5	18.6
			(0.08)	(0.08)	(0.08)	(0.10)	(0.12)
	$J04^*$		18.8	18.6	18.5	18.4	18.4
			(0.08)	(0.07)	(0.07)	(0.08)	(0.08)
	$H03^*$		17.7	17.5	17.4	17.4	17.3
			(0.04)	(0.04)	(0.04)	(0.05)	(0.05)
	$H04^*$		17.7	17.5	17.4	17.4	17.4
			(0.05)	(0.04)	(0.04)	(0.05)	(0.06)
	K^*		16.7	16.5	16.5	16.4	16.4
			(0.04)	(0.04)	(0.04)	(0.04)	(0.04)
TOOT00_1125	K-UFTI	00 09 36.6 +35 15 43.1	15.7	15.6	15.6	15.5	15.5
	27Jul2000		(0.01)	(0.01)	(0.01)	(0.01)	(0.02)
TOOT00_1143	K-UFTI	00 09 46.9 +35 23 44.8	16.0	[15.8]	[15.7]	[15.5]	[15.5]
	27Jul2000		(0.01)	(0.01)	(0.01)	(0.02)	(0.02)
TOOT00_1233	K-UFTI	00 09 53.2 +35 58 23.4	15.4	15.3	15.2	15.1	15.1
	25Jul2000		(0.01)	(0.01)	(0.01)	(0.01)	(0.01)
TOOT00_1022	K-UFTI	00 10 37.7 +34 41 23.1	19.0	19.4	19.6	20.0	20.0
	25Jul2000		(0.10)	(0.19)	(0.31)	(0.81)	(0.94)
TOOT00_1204	K-UFTI	00 10 40.6 +35 45 48.3	16.4	16.3	16.2	16.1	16.1
	25Jul2000		(0.01)	(0.01)	(0.01)	(0.02)	(0.03)
TOOT00_1235	K-UFTI	00 10 45.5 +35 59 51.3	17.0	16.9	16.8	16.8	16.8
	25Jul2000		(0.02)	(0.02)	(0.02)	(0.04)	(0.05)
	J^*		19.0	18.8	18.8	18.6	18.6
			(0.09)	(0.09)	(0.09)	(0.10)	(0.11)
	H^*		18.0	17.8	17.8	17.6	17.6
			(0.05)	(0.05)	(0.05)	(0.07)	(0.07)
	K^*		17.1	17.0	17.0	16.8	16.8
			(0.05)	(0.04)	(0.04)	(0.04)	(0.05)
TOOT00_1224	B^o	00 10 48.87 +35 55 51.5	25.8				
			(0.35)				
	V^o	00 10 49.24 +35 55 51.2	23.9				
			(0.14)				
	R^o	00 10 49.16 +35 55 51.4	24.1				
			(0.25)				
	I^o	00 10 49.00 +35 55 51.3	24.0				
			(0.45)				
	K-UFTI	00 10 48.8 +35 55 49.0	(too faint to measure)				
	25Jul2000						
	K-UFTI	00 10 48.8 +35 55 49.0	19.8	19.5	19.4	19.9	20.1
	8Sept2004		(0.12)	(0.13)	(0.14)	(0.41)	(0.56)

Table 3.6: (continued)

(1)	(2)	(3)	(4)	(5)	(6)	(7)	(8)
Object	Band	near-IR Position (J2000)	3″mag (3″ error)	4″mag (4″ error)	5″mag (5″ error)	8″mag (8″ error)	9″mag (9″ error)
TOOT00_1224	$J03^*$		22.4	22.2	21.5	21.4	21.2
			(0.79)	(0.88)	(0.63)	(1.05)	(1.01)
	$J04^*$		22.1	22.0	22.6	22.7	21.6
			(0.46)	(0.51)	(1.00)	(1.98)	(0.90)
	$H03^*$		21.0	20.5	20.1	19.6	19.5
			(0.33)	(0.29)	(0.27)	(0.32)	(0.33)
	$H04^*$		21.1	20.9	20.6	20.7	20.8
			(0.27)	(0.29)	(0.28)	(0.58)	(0.76)
	K^*		19.8	19.7	19.5	19.4	19.5
			(0.21)	(0.23)	(0.23)	(0.39)	(0.51)
TOOT00_1291	K-UIST	00 10 51.4 +36 28 29.7	17.4	17.3	17.3	17.2	17.2
	26Jan2003		(0.02)	(0.02)	(0.02)	(0.04)	(0.05)
	K-UFTI	00 10 51.4 +36 28 29.6	17.3	17.2	17.0	17.2	17.2
	15Sep2004		(0.03)	(0.04)	(0.04)	(0.10)	(0.10)
TOOT00_1107	B^o	00 11 12.22 +35 07 21.0	26.7				
			(1.21)				
	V^o	00 11 12.45 +35 07 20.6	23.9				
			(0.24)				
	R^o	00 11 12.47 +35 07 20.8	23.4				
			(0.14)				
	I^o	00 11 12.40 +35 07 20.2	22.6				
			(0.12)				
	K-UFTI	00 11 12.30 +35 07 20.6	18.3	18.1	18.0	18.1	18.0
	25Jul2000		(0.05)	(0.06)	(0.07)	(0.13)	(0.14)
TOOT00_1180	B^o	00 11 12.94 +35 38 0.3	23.5				
			(0.09)				
	V^o	00 11 12.94 +35 38 0.3	23.5				
			(0.09)				
	R^o	00 11 12.89 +35 38 0.9	23.3				
			(0.11)				
	I^o	00 11 12.90 +35 37 59.9	18.1				
			(0.16)				
	K^o	00 11 12.97 +35 38 0.2	18.1				
			(0.12)				
	K-UFTI	00 11 12.90 +35 38 0.1	18.4	18.3	18.3	18.5	18.6
	27Jul2000		(0.06)	(0.08)	(0.10)	(0.23)	(0.30)
TOOT00_1027	K-UFTI	00 11 17.0 +34 43 33.8	19.5	19.5	19.8	19.6	19.4
	27Jul2000		(0.18)	(0.24)	(0.42)	(0.61)	(0.61)
TOOT00_1195	B^o	00 11 52.68 +35 42 20.6	25.4				
			(0.24)				
	V^o	00 11 52.62 +35 42 19.1	25.5				
			(0.58)				
	R^o	00 11 52.35 +35 42 20.8	23.2				
			(0.10)				
	I^o	00 11 52.35 +35 42 20.2	22.1				
			(0.07)				
	K^o	00 11 52.37 +35 42 20.5	18.5				
			(0.32)				
	K-UFTI	00 11 52.40 +35 42 20.0	18.4	18.3	18.3	18.2	18.2
	27Jul2000		(0.06)	(0.08)	(0.11)	(0.17)	(0.20)
	$J03^*$		20.1	20.0	19.9	19.9	20.0
			(0.18)	(0.19)	(0.20)	(0.31)	(0.38)
	$J04^*$		19.7	19.5	19.4	19.1	19.0
			(0.12)	(0.12)	(0.12)	(0.13)	(0.14)
	H^*		19.1	18.9	18.7	18.4	18.3
			(0.10)	(0.10)	(0.11)	(0.14)	(0.15)
	K^*		18.2	18.1	18.0	17.9	17.9
			(0.08)	(0.08)	(0.08)	(0.11)	(0.12)

Table 3.6: (continued)

(1)	(2)	(3)	(4)	(5)	(6)	(7)	(8)
Object	Band	near-IR Position (J2000)	3″mag (3″ error)	4″mag (4″ error)	5″mag (5″ error)	8″mag (8″ error)	9″mag (9″ error)
TOOT00_1069	B^o	00 12 12.91 +34 58 30.4	26.2 (0.76)				
	V^o	00 12 13.11 +34 58 32.9	24.9 (0.30)				
	R^o	00 12 12.92 +34 58 29.8	24.4 (0.24)				
	I^o	00 12 11.95 +34 58 31.9	22.5 (0.30)				
	K^o	00 12 13.83 +34 58 31.6	18.7 (0.41)				
	K-UIST 26Jan2003	00 12 12.58 +34 58 30.9		> 20.3			
	K-UFTI 15Sep2004	00 12 12.58 + 34 58 30.9		> 19.2 (object at edge of image - unreliable value)			
TOOT00_1094	B^o	00 12 16.60 +35 04 25.8	25.8 (0.53)				
	V^o	00 12 16.56 +35 04 25.6	25.4 (0.47)				
	R^o	00 12 16.53 +35 04 23.3	24.9 (0.62)				
	I^o	00 12 16.42 +35 04 22.5	22.3 (0.26)				
	K-UIST 26Jan2003	00 12 16.3 +35 04 23.4		> 20.6			
	K-UFTI 15Sep2004	00 12 16.3 +35 04 23.4	18.6 (0.13)	18.2 (0.13)	17.8 (0.11)	17.5 (0.15)	17.6 (0.19)
TOOT00_1149	B^o	00 12 17.99 +35 27 29.4	21.1 (0.01)				
	V^o	00 12 18.00 +35 27 29.0	19.5 (0.01)				
	R^o	00 12 18.06 +35 27 29.1	18.6 (0.01)				
	I^o	00 12 17.98 +35 27 29.2	18.1 (0.01)				
	K^o	00 12 18.01 +35 27 29.1	14.6 (0.01)				
TOOT00_1298	K-UFTI 27Jul2000	00 12 24.20 +35 33 10.5	17.3 (0.03)	17.3 (0.04)	17.2 (0.04)	17.2 (0.08)	17.1 (0.09)
TOOT00_1200	U^o	00 12 31.19 +35 43 33.0	22.4 (0.03)				
	B^o	00 12 31.21 +35 43 33.2	22.7 (0.02)				
	V^o	00 12 31.25 +35 43 33.3	22.0 (0.02)				
	R^o	00 12 31.22 +35 43 33.6	21.3 (0.02)				
	I^o	00 12 31.20 +35 43 33.0	20.4 (0.01)				
	K-UFTI 27Jul2000	00 12 31.3 +35 43 33.2	17.5 (0.03)	17.4 (0.04)	17.4 (0.05)	17.4 (0.08)	17.4 (0.10)
TOOT00_1215	U^o	00 12 45.95 +35 52 19.2	21.8 (0.03)				
	V^o	00 12 45.92 +35 52 19.7	19.6 (0.01)				
	R^o	00 12 45.89 +35 52 19.4	18.7 (0.01)				
	I^o	00 12 45.92 +35 52 19.5	18.2 (0.01)				
	K^o	00 12 45.92 +35 52 19.1	15.0 (0.01)				

Table 3.6: (continued)

(1)	(2)	(3)	(4)	(5)	(6)	(7)	(8)
Object	Band	near-IR Position (J2000)	3″mag (3″ error)	4″mag (4″ error)	5″mag (5″ error)	8″mag (8″ error)	9″mag (9″ error)
TOOT00_1240	K-UIST 26Jan2003	00 13 05.30 +36 01 51.0	18.8 (0.25)	18.9 (0.35)	18.6 (0.34)	[15.6] (0.04)	[15.6] (0.04)
TOOT00_1289	K-UFTI 14Sep2004	00 13 12.2 +36 27 16.1	18.1 (0.05)	17.8 (0.05)	17.8 (0.06)	17.8 (0.11)	17.7 (0.11)
TOOT00_1072	B^{o}	00 13 13.35 +34 59 41.6	23.4 (0.05)				
	V^{o}	00 13 13.28 +34 59 41.0	21.5 (0.01)				
	R^{o}	00 13 13.35 +34 59 41.3	20.3 (0.01)				
	I^{o}	00 13 13.25 +34 59 41.3	19.1 (0.01)				
	K^{o}	00 13 13.35 +34 59 40.9	15.7 (0.04)				
	K-UFTI 14Jan2001	00 13 13.3 +34 59 40.8	15.9 (0.02)	15.7 (0.02)	15.6 (0.02)	15.4 (0.03)	15.3 (0.04)
TOOT00_1134	B^{o}	00 13 21.21 +35 20 08.2	21.3 (0.01)				
	V^{o}	00 13 21.17 +35 20 07.6	19.7 (0.01)				
	R^{o}	00 13 21.09 +35 20 10.5	18.9 (0.01)				
	I^{o}	00 13 21.00 +35 20 10.2	18.3 (0.01)				
	K^{o}	00 13 21.15 +35 20 08.6	14.2 (0.01)				
	K-UFTI 25Jul2000	00 13 21.2 +35 20 07.6	14.9 (0.01)	14.6 (0.01)	[14.4] (0.01)	[13.9] (0.01)	[13.8] (0.01)
TOOT00_1244	U^{o}	00 13 30.11 +36 03 49.7	20.2 (0.01)				
	V^{o}	00 13 30.07 +36 03 50.3	20.7 (0.01)				
	R^{o}	00 13 30.05 +36 03 50.0	20.3 (0.01)				
	I^{o}	00 13 30.06 +36 03 50.2	20.1 (0.02)				
	K^{o}	00 13 30.11 +36 03 51.0	18.8 (0.46)				
TOOT00_1066	B^{o}	00 13 48.34 +34 56 57.9	25.3 (0.29)				
	V^{o}	00 13 48.31 +34 56 58.1	26.0 (0.83)				
	R^{o}	00 13 48.36 +34 56 58.3	23.3 (0.09)				

Table 3.6: (continued)

(1)	(2)	(3)	(4)	(5)	(6)	(7)	(8)
Object	Band	near-IR Position (J2000)	3″mag (3″ error)	4″mag (4″ error)	5″mag (5″ error)	8″mag (8″ error)	9″mag (9″ error)
TOOT00_1066	I^o	00 13 48.27 +34 56 58.3	21.9 (0.18)				
	K^o	00 13 48.23 +34 56 57.8	18.9 (0.36)				
	K-UIST 26Jan2003	00 13 48.3 +34 56 57.6	17.9 (0.06)	17.7 (0.07)	17.7 (0.09)	18.2 (0.23)	18.5 (0.36)
	$J03^*$		19.9 (0.14)	19.8 (0.15)	19.7 (0.14)	19.3 (0.15)	19.3 (0.17)
	$J04^*$		20.0 (0.14)	19.8 (0.13)	19.7 (0.13)	19.3 (0.14)	19.3 (0.15)
	$H03^*$		19.0 (0.09)	18.8 (0.09)	18.7 (0.10)	18.5 (0.12)	18.4 (0.13)
	$H04^*$		19.0 (0.08)	18.7 (0.08)	18.6 (0.08)	18.3 (0.08)	18.3 (0.09)
	K^*		18.1 (0.07)	18.0 (0.07)	17.9 (0.07)	17.7 (0.07)	17.6 (0.07)
TOOT00_1261	U^o	00 14 6.64 +36 08 26.9	22.3 (0.04)				
	V^o	00 14 6.60 +36 08 26.9	22.7 (0.05)				
	R^o	00 14 6.59 +36 08 26.5	23.0 (0.11)				
	I^o	00 14 6.60 +36 08 26.8	22.1 (0.09)				
	K-UFTI 13Jan2002	00 14 6.6 +36 08 27.3	19.3 (0.05)	19.0 (0.06)	19.0 (0.07)	18.9 (0.12)	18.8 (0.13)
TOOT00_1252	K-UFTI 14Sep2004	00 14 30.6 +36 06 44.4		> 19.6			
TOOT00_1214	U^o	00 14 43.51 +35 52 05.0	23.0 (0.06)				
	B^o	00 14 43.53 +35 52 05.4	24.5 (0.15)				
	V^o	00 14 43.54 +35 52 05.4	23.3 (0.07)				
	R^o	00 14 43.53 +35 52 05.7	22.9 (0.08)				
	I^o	00 14 43.53 +35 52 05.9	22.1 (0.09)				
	K-UFTI 08Jan2002	00 14 43.6 +35 52 05.4	18.6 (0.03)	[18.3] (0.03)	[18.1] (0.03)	[17.9] (0.05)	[17.9] (0.06)
TOOT00_1152	U^o	00 14 49.09 +35 28 7.4	25.3 (0.97)				
	B^o	00 14 49.88 +35 28 11.6	25.7 (0.43)				
	V^o	00 14 49.10 +35 28 7.2	26.3 (1.16)				
	R^o	00 14 49.10 +35 28 7.4	25.0 (0.40)				
	I^o	00 14 49.49 +35 28 9.2	24.2 (1.51)				
	K^o	00 14 49.08 +35 28 7.2	21.1 (3.19)				
	K-UIST 26Jan2003	00 14 49.7 +35 28 11.1	19.6 (0.6)	19.6 (0.8)	21.2 (4.3)		

Table 3.6: (continued)

(1)	(2)	(3)	(4)	(5)	(6)	(7)	(8)
Object	Band	near-IR Position (J2000)	3″mag (3″ error)	4″mag (4″ error)	5″mag (5″ error)	8″mag (8″ error)	9″mag (9″ error)
TOOT00_1129	U^o	00 15 4.32 +35 19 1.1	22.7 (0.11)				
	B^o	00 15 4.33 +35 19 1.1	23.4 (0.07)				
	V^o	00 15 4.33 +35 19 1.1	23.0 (0.06)				
	R^o	00 15 4.37 +35 19 1.4	22.7 (0.04)				
	I^o	00 15 4.34 +35 19 1.4	22.7 (0.13)				
	K^o	00 15 4.30 +35 19 0.9	18.5 (0.50)				
	K-UIST 27Jan2003	00 15 4.3 +35 18 56.7	20.2 (0.85)	20.2 (1.13)	21.9 (7.10)		
TOOT00_1090	R^o	00 15 16.00 +35 03 28.0	17.9 (0.01)				
	I^o	00 15 15.91 +35 03 27.9	17.4 (0.01)				
	K-UFTI 28Dec2000	00 15 15.9 +35 03 27.7	14.7 (0.01)	14.6 (0.01)	14.4 (0.01)	14.2 (0.01)	14.2 (0.01)
TOOT00_1267	K-UIST 27Jan2003	00 15 31.0 +36 12 16.5	17.6 (0.08)	17.5 (0.09)	17.5 (0.11)	17.5 (0.21)	17.7 (0.29)
	$J03^*$		19.3 (0.12)	19.2 (0.12)	19.0 (0.11)	19.1 (0.15)	19.1 (0.18)
	$J04^*$		19.1 (0.09)	19.0 (0.09)	18.9 (0.09)	18.8 (0.12)	18.9 (0.13)
	H^*		18.3 (0.07)	18.2 (0.06)	18.1 (0.07)	18.1 (0.09)	18.0 (0.10)
	K^*		17.3 (0.05)	17.1 (0.05)	17.1 (0.05)	16.9 (0.05)	16.9 (0.05)
TOOT00_1188	U^o	00 15 56.37 +35 39 49.8	26.3 (1.37)				
	B^o	00 15 56.33 +35 39 51.8	23.5 (0.06)				
	V^o	00 15 56.34 +35 39 52.4	23.2 (0.08)				
	R^o	00 15 56.39 +35 39 52.2	22.5 (0.05)				
	I^o	00 15 56.32 +35 39 52.2	21.9 (0.08)				
	K^o	00 15 56.36 +35 39 51.8	18.0 (0.19)				
	K-UIST 27Jan2003	00 15 56.33 +35 39 52.1	18.1 (0.12)	18.3 (0.20)	18.9 (0.42)		
TOOT00_1196	R^o	00 16 36.76 +35 42 23.1	24.1 (0.2)				
	I^o	00 16 36.76 +35 41 23.1	22.4 (0.12)				
	K-UIST 27Jan2003	00 16 35.74 +35 42 22.9	18.5 (0.09)	18.4 (0.11)	18.3 (0.13)	18.9 (0.37)	19.3 (0.65)
	K-UFTI 15Sep2004	00 16 35.71 +35 42 22.8	17.4 (0.04)	17.4 (0.06)	17.3 (0.07)	17.1 (0.10)	16.9 (0.10)

Table 3.6: (continued)

(1)	(2)	(3)	(4)	(5)	(6)	(7)	(8)
Object	Band	near-IR Position (J2000)	3″mag (3″ error)	4″mag (4″ error)	5″mag (5″ error)	8″mag (8″ error)	9″mag (9″ error)
TOOT00_1173	U^o	00 16 59.49 +35 34 36.2	22.6 (0.09)				
	B^o	00 16 59.54 +35 34 35.6	21.6 (0.02)				
	V^o	00 16 59.52 +35 34 36.0	20.4 (0.01)				
	R^o	00 16 59.55 +35 34 36.3	19.4 (0.01)				
	I^o	00 16 59.53 +35 34 36.3	18.7 (0.01)				
	K-UFTI 14Jan2001	00 16 59.5 +35 34 35.9	15.6 (0.02)	15.3 (0.02)	15.2 (0.02)	15.1 (0.04)	15.1 (0.04)
TOOT00_1228	V^o	00 17 2.99 +35 56 19.0	25.4 (0.57)				
	K^o	00 17 2.79 +35 56 19.9	19.3 (1.49)				
	K-UFTI 14Jan2001	00 17 3.00 +35 56 18.4	18.5 (0.10)	18.5 (0.13)	18.5 (0.18)	18.3 (0.28)	18.6 (0.41)
TOOT00_1034	R^o	00 17 4.87 +34 46 57.2	20.4 (0.01)				
	I^o	00 17 4.79 +34 46 57.1	19.5 (0.01)				
	K-UIST 27Jan2003	00 17 4.8 +34 46 56.5	16.2 (0.03)	16.1 (0.03)	15.9 (0.03)	15.8 (0.05)	15.8 (0.06)
TOOT00_1255	B^o	00 17 28.30 +36 7 27.3	24.6 (0.18)				
	V^o	00 17 28.29 +36 7 27.8	22.6 (0.05)				
	R^o	00 17 28.23 +36 7 27.7	21.5 (0.02)				
	I^o	00 17 28.23 +36 7 27.8	20.5 (0.02)				
	K-UFTI 08Jan2001	00 17 28.2 +36 07 27.2	17.5 (0.03)	17.4 (0.04)	17.3 (0.04)	[16.7] (0.05)	[16.7] (0.05)
	$J03^*$		18.9 (0.10)	18.7 (0.09)	18.5 (0.09)	18.2 (0.09)	17.8 (0.07)
	$J04^*$		18.8 (0.08)	18.6 (0.07)	18.5 (0.07)	18.0 (0.07)	17.7 (0.06)
	H^*		17.8 (0.05)	17.6 (0.05)	17.5 (0.05)	17.1 (0.05)	16.7 (0.04)
	K^*		17.0 (0.05)	16.8 (0.05)	16.7 (0.05)	16.5 (0.05)	16.3 (0.05)
TOOT00_1048	K-UIST 27Jan2003	00 18 16.5 +34 50 36.2	18.0 (0.19)	17.5 (0.16)	17.4 (0.18)	17.2 (0.27)	17.2 (0.33)
TOOT00_1029	K-UFTI 28Dec2000	00 18 28.0 +34 44 49.5	16.0 (0.02)	15.9 (0.02)	15.8 (0.02)	15.4 (0.03)	[15.4] (0.03)
	J^*		18.6 (0.08)	18.4 (0.07)	18.3 (0.07)	18.1 (0.08)	18.1 (0.09)
	H^*		17.7 (0.05)	17.6 (0.04)	17.5 (0.04)	17.4 (0.06)	17.5 (0.06)
	K_a^*		16.8 (0.04)	16.6 (0.03)	16.5 (0.03)	16.4 (0.04)	16.4 (0.04)
	K_b^*		16.8 (0.04)	16.6 (0.04)	16.5 (0.04)	16.4 (0.04)	16.4 (0.04)
TOOT00_1115	K-UFTI 28Dec2000	00 18 53.9 +35 10 11.4	16.0 (0.02)	15.9 (0.02)	15.7 (0.02)	15.4 (0.03)	15.4 (0.03)
TOOT00_1132	K-UFTI 14Jan2001	00 19 20.1 +35 19 36.2	15.1 (0.01)	15.0 (0.01)	14.9 (0.01)	14.8 (0.02)	14.8 (0.03)

Table 3.6: (continued)

(1)	(2)	(3)	(4)	(5)	(6)	(7)	(8)
Object	Band	near-IR Position (J2000)	3″mag (3″ error)	4″mag (4″ error)	5″mag (5″ error)	8″mag (8″ error)	9″mag (9″ error)
TOOT00_1250	B^{o}	00 19 54.43 +36 06 21.7	22.9 (0.04)				
	V^{o}	00 19 54.40 +36 06 22.2	22.5 (0.04)				
	R^{o}	00 19 54.34 +36 06 22.3	21.9 (0.03)				
	I^{o}	00 19 54.33 +36 06 22.4	22.4 (0.12)				
	K-UFTI 28Dec2000	00 19 54.4 +36 06 22.2	18.2 (0.13)	18.0 (0.14)	17.8 (0.16)	18.5 (0.50)	18.4 (0.57)
TOOT00_1268	K-UIST 27Jan2003	00 21 52.0 +36 12 18.4	17.6 (0.08)	17.6 (0.11)	17.5 (0.12)	17.5 (0.21)	[17.4] (0.21)
TOOT00_1251	K-UFTI 28Dec2000	00 22 19.0 +36 06 29.6	17.85 (0.32)	19.1 (1.30)			
TOOT00_1203	K-UFTI 14Jan2001	00 23 31.6 +35 45 04.2	17.6 (0.04)	17.4 (0.05)	17.0 (0.05)	[15.7] (0.02)	[15.7] (0.03)
	J^{*}		19.2 (0.10)	18.9 (0.09)	18.4 (0.07)	16.8 (0.04)	16.8 (0.04)
	H^{*}		18.5 (0.07)	18.3 (0.07)	17.8 (0.06)	16.3 (0.03)	16.2 (0.03)
	K^{*}		17.6 (0.06)	17.4 (0.05)	17.1 (0.05)	15.8 (0.03)	15.8 (0.03)

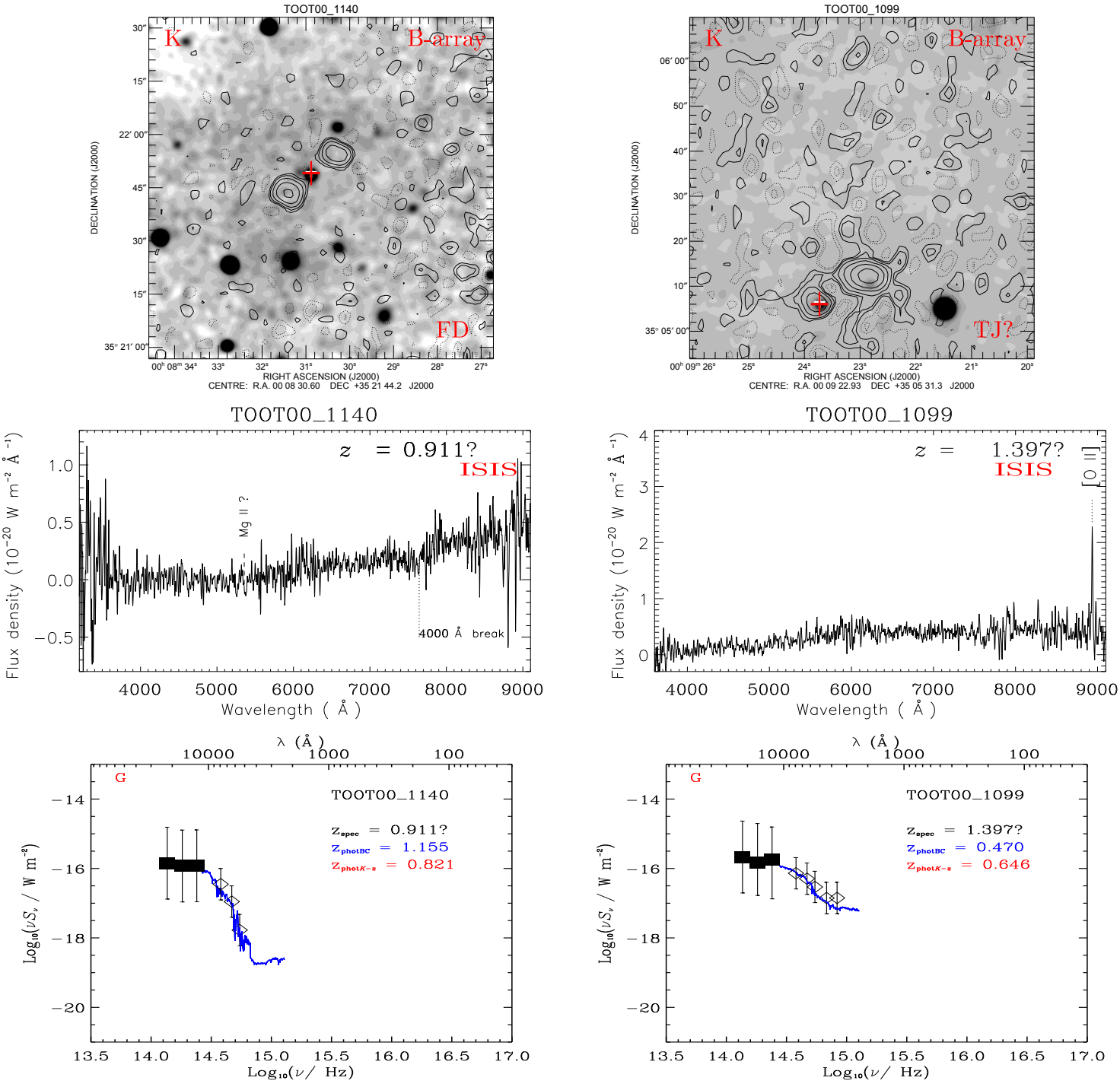

Figure 3.10: At the **top** of each panel we present the K-band images and overlaid radio contours from the VLA (B- or A-array as stated). The contour levels follow: $2^{n_{\rm contour}-1} \times \sigma$, where $n_{\rm contour}$ is the number of contours and σ the noise level. A white/red cross indicates the position of the assumed near-ID. In the **middle** we give the optical spectrum of the object, as described in Section 3.2. The blue and red part of each spectrum have been combined at $\sim$ 6000 Å. We haven't corrected for atmospheric absorption, which is labelled as 'A' in the spectrum; 'S' denotes a sky line; 'F' denotes fringing; and 'C' a cosmic ray effect. At the **bottom** we give the SED and the results from the HyperZ fit on the photometric data. Symbols: filled squares denote photometric points, whereas open diamonds denote that the fluxes were estimated from the optical spectra. Note: for object TOOT00_1240 we also provide a zoomed-in $K-$band/radio overlay and a DSS/radio overlay. The positions of an M-star and a galaxy G ($z = 0.191$) close to the position of TOOT00_1240 are marked with an 'M' and a 'G' respectively. For TOOT00_1252 both A- and B-array radio maps are presented; the K position is not marked since it is a limit at K. The red arrow in the K-band/B-array overlay in TOOT00_1196 shows the 7C radio position.

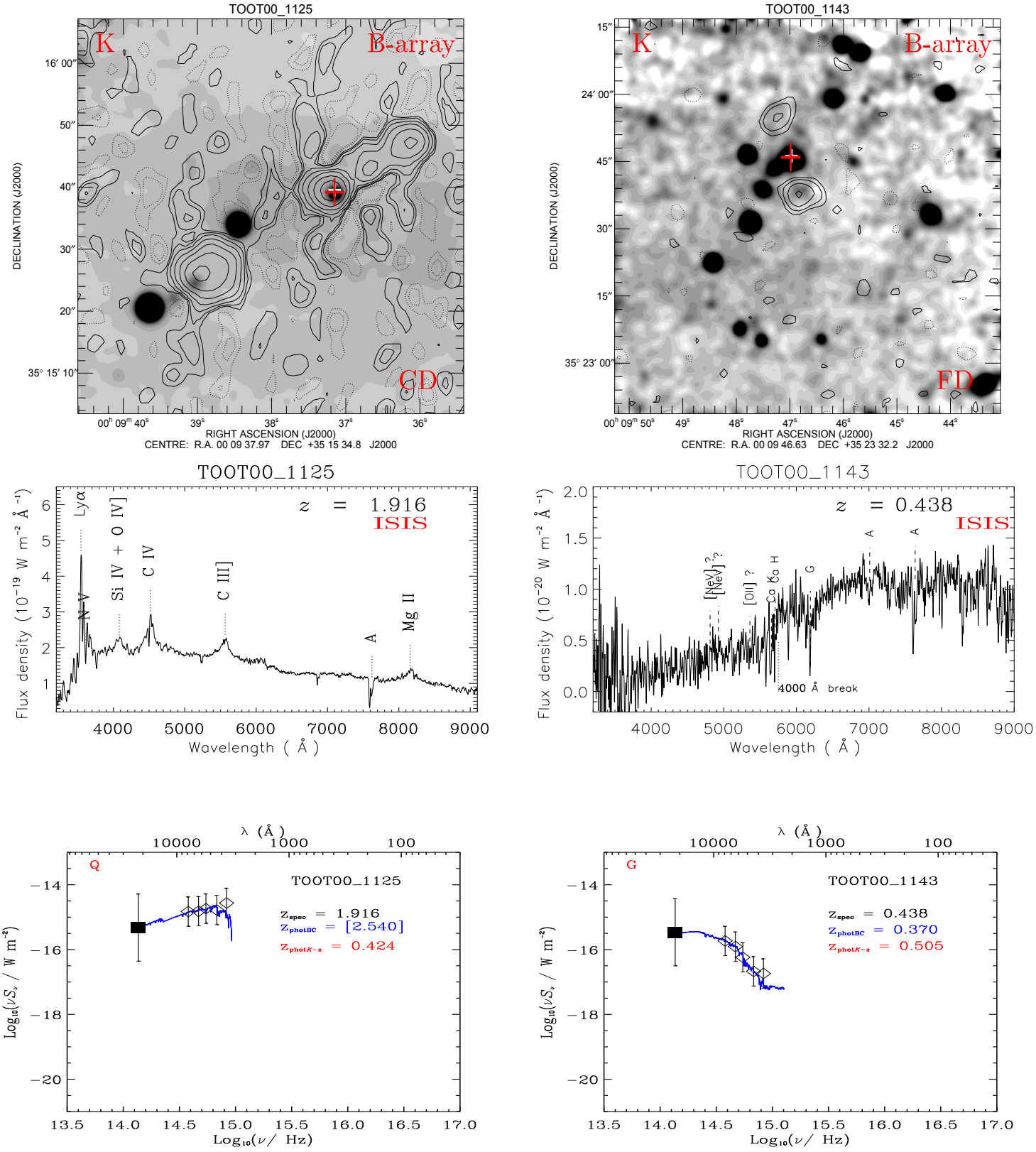

Figure 3.10: (continued)

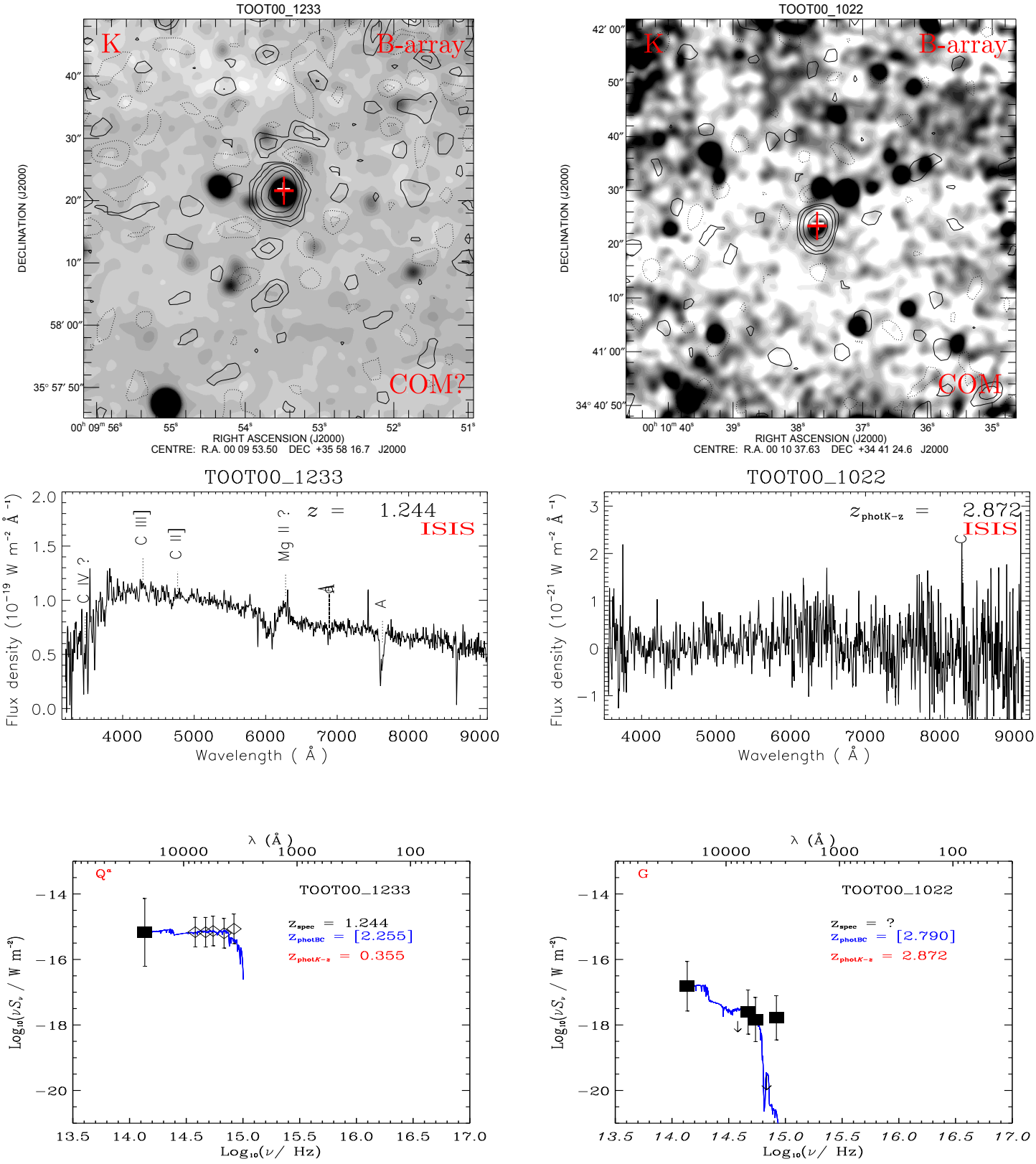

Figure 3.10: (continued)

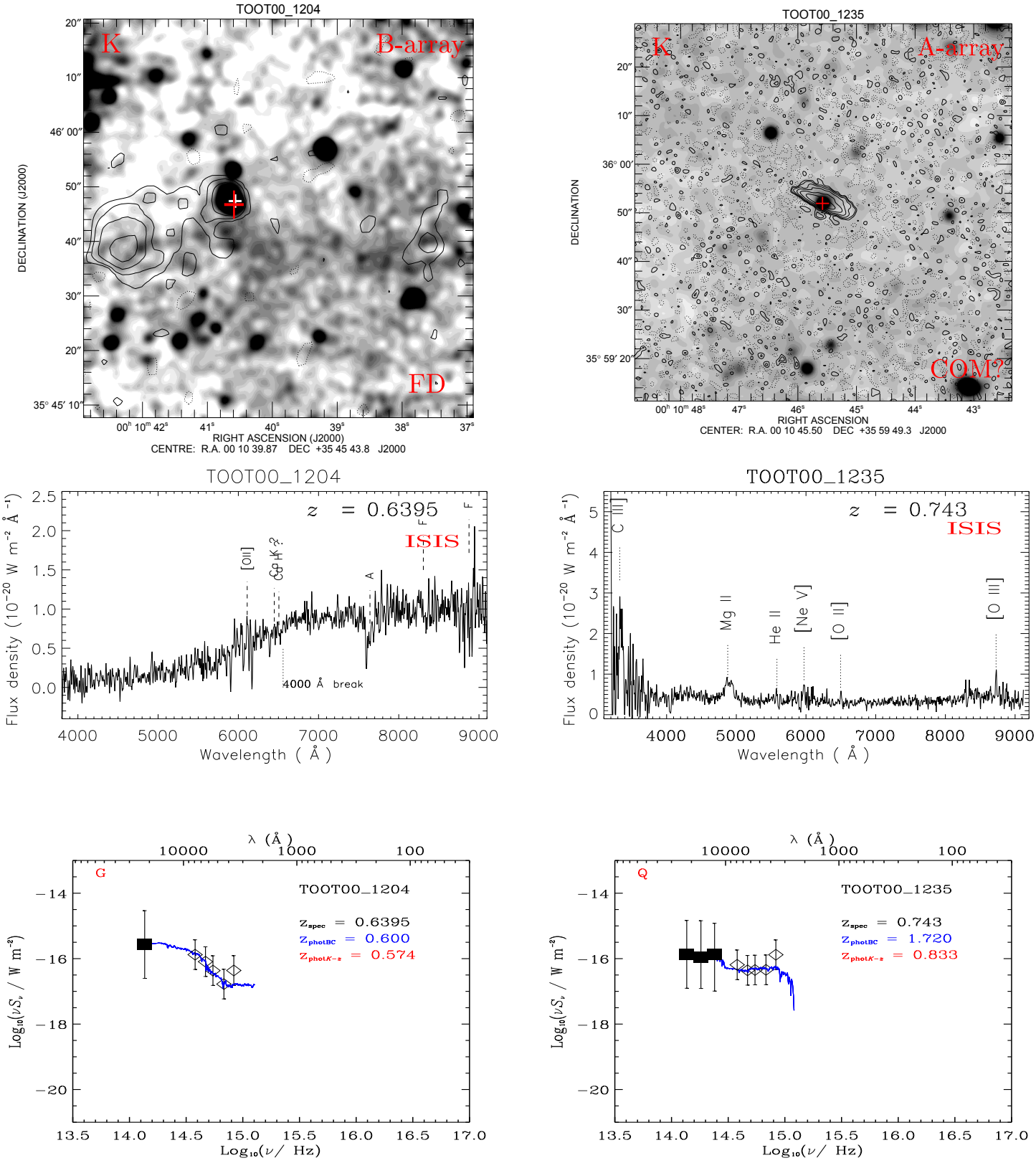

Figure 3.10: (continued)

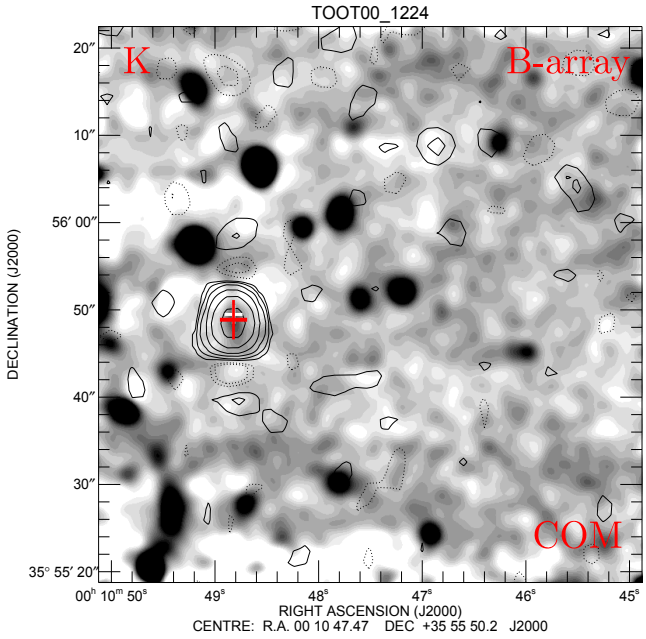

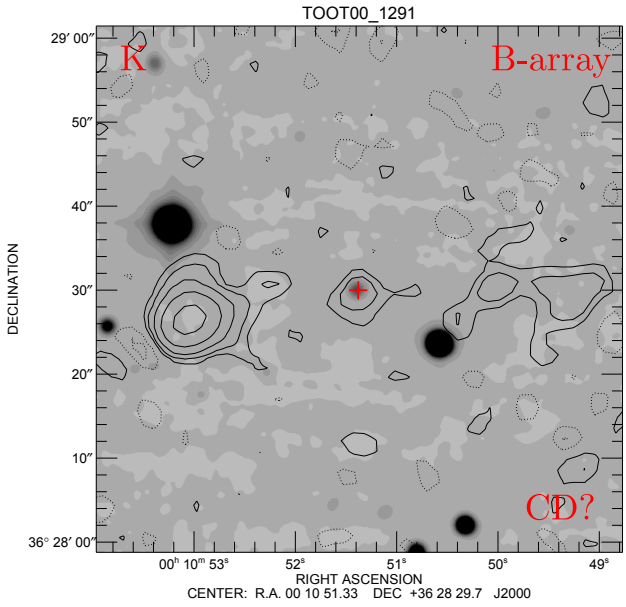

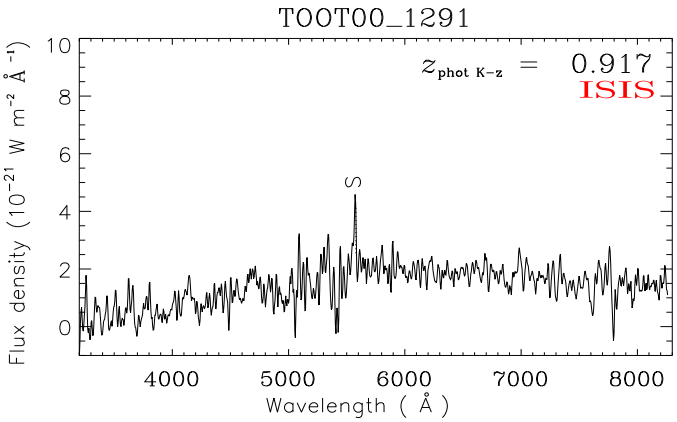

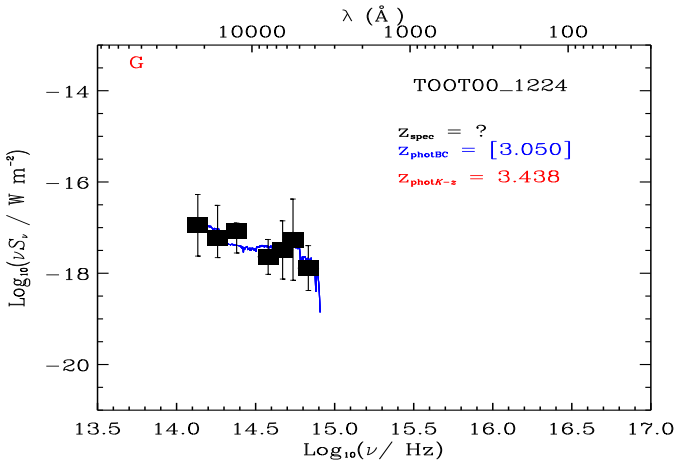

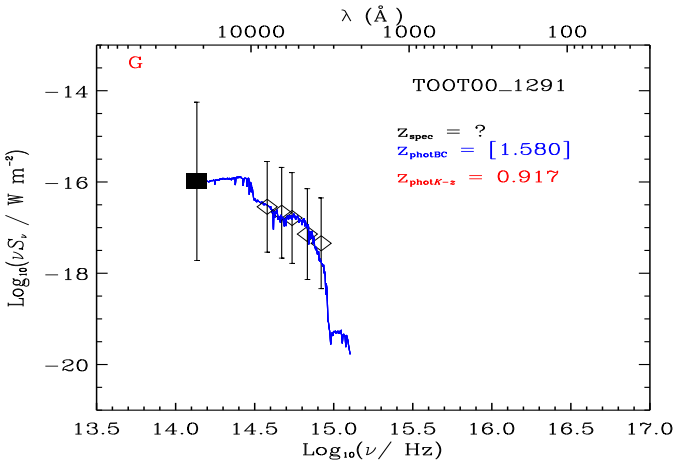

Figure 3.10: (continued)

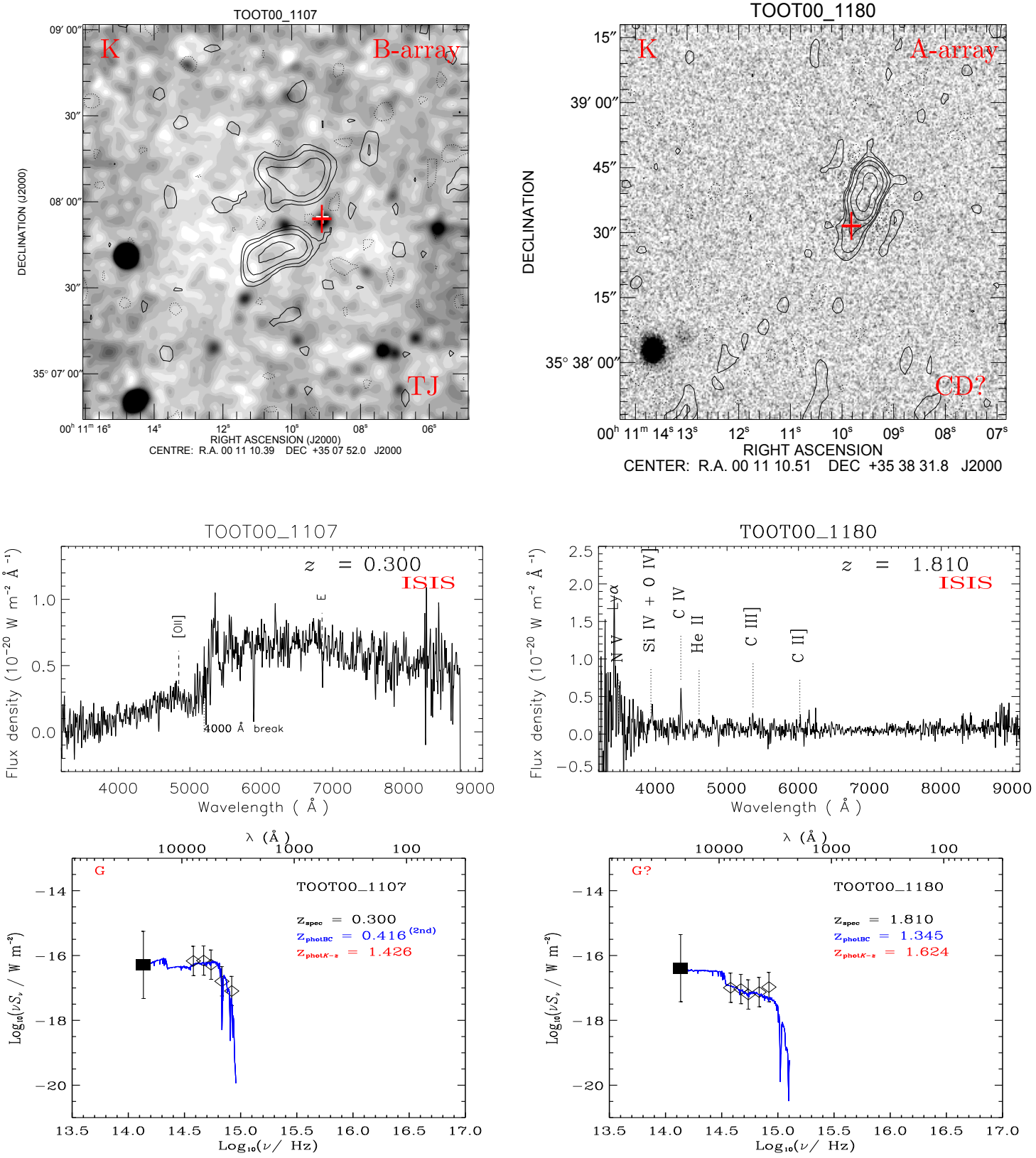

Figure 3.10: (continued)

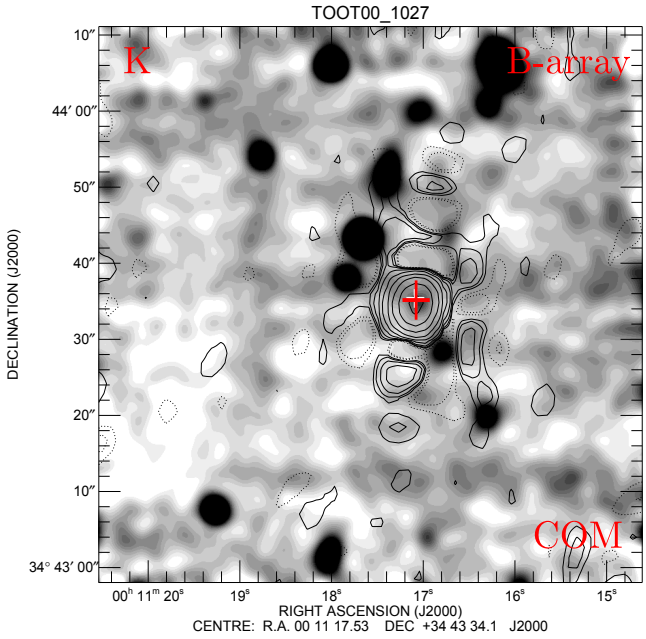

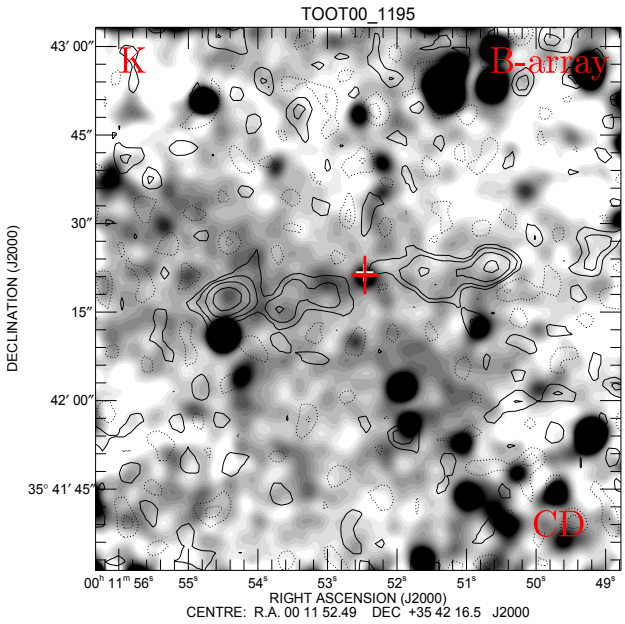

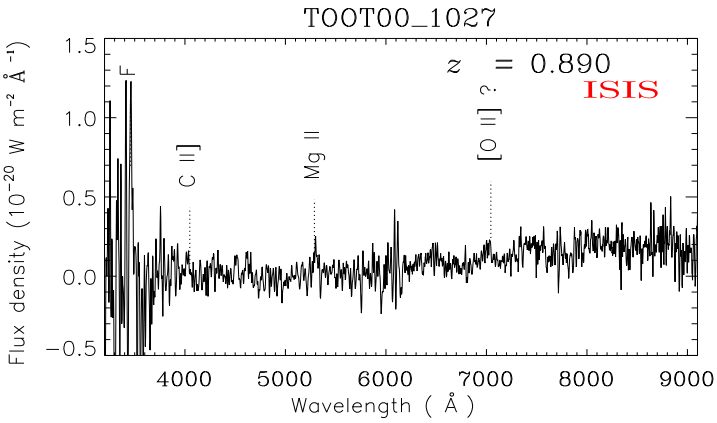

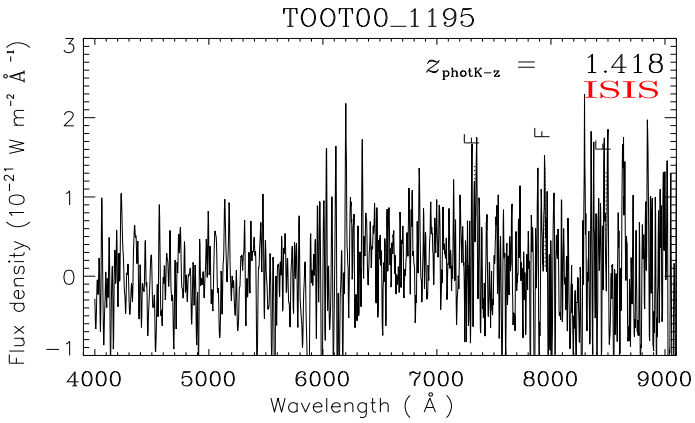

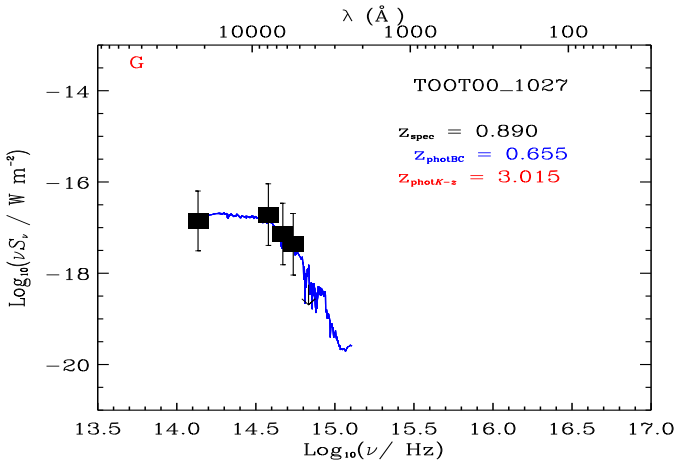

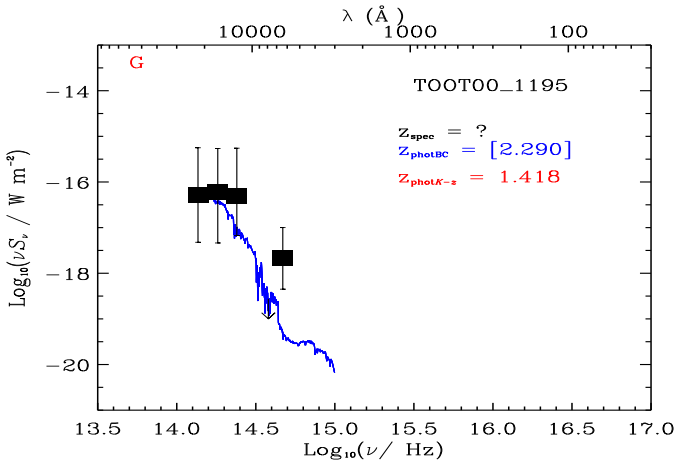

Figure 3.10: (continued)

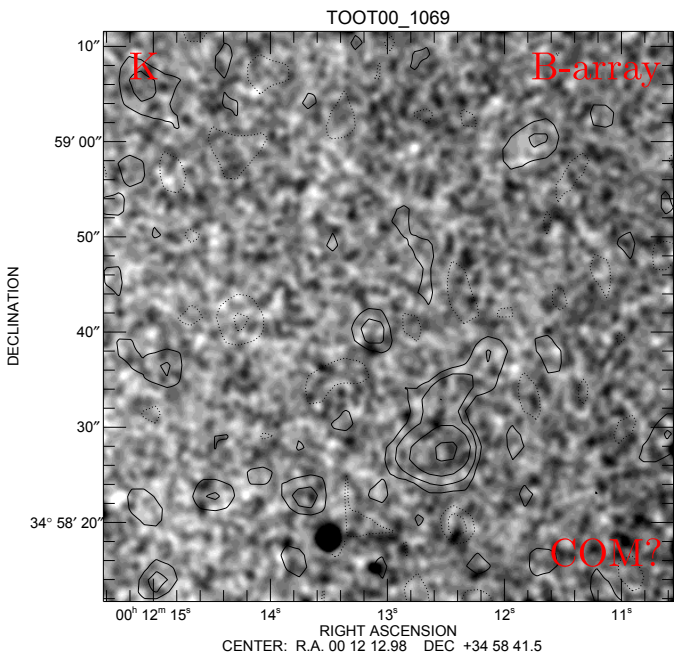

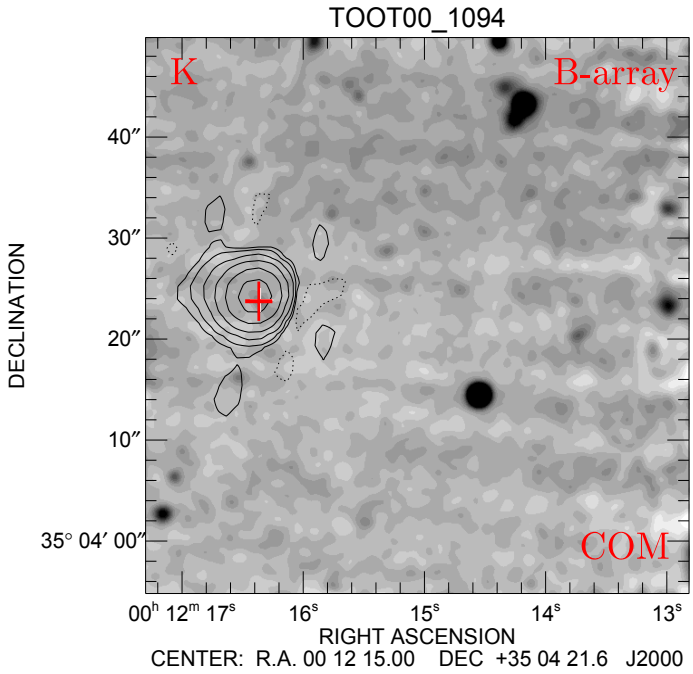

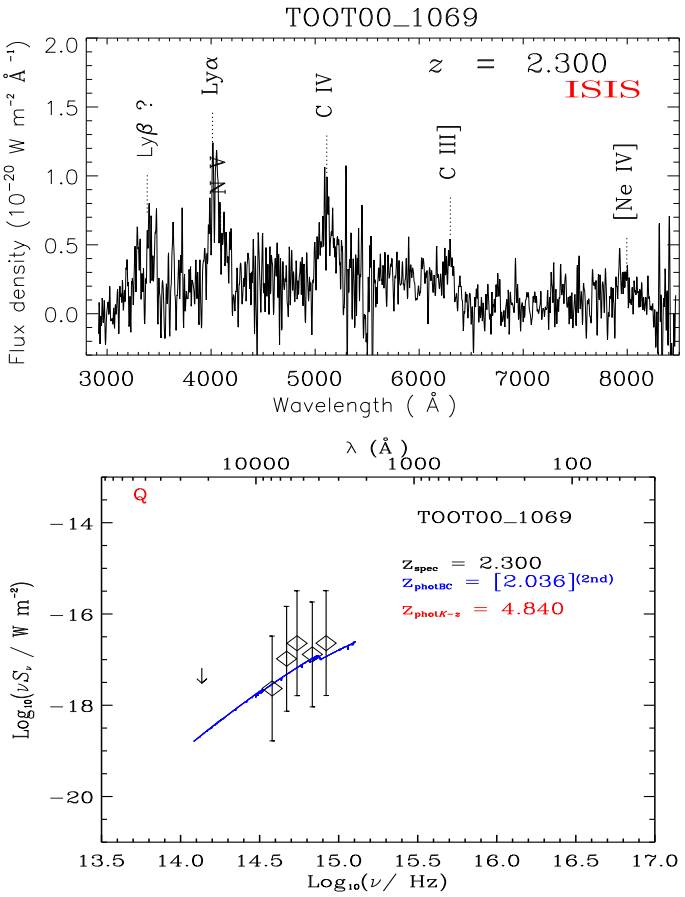

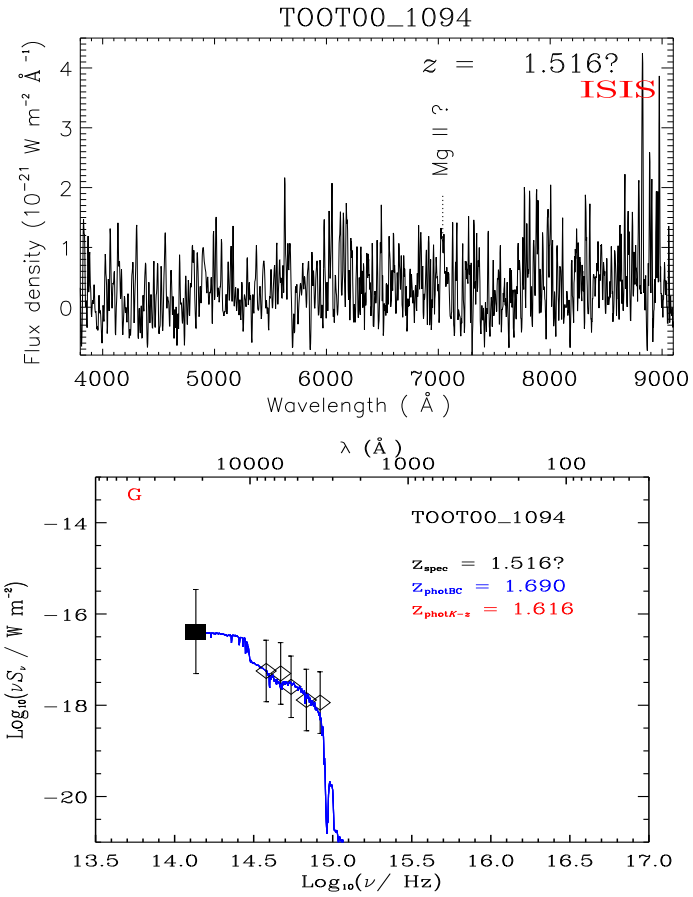

Figure 3.10: (continued)

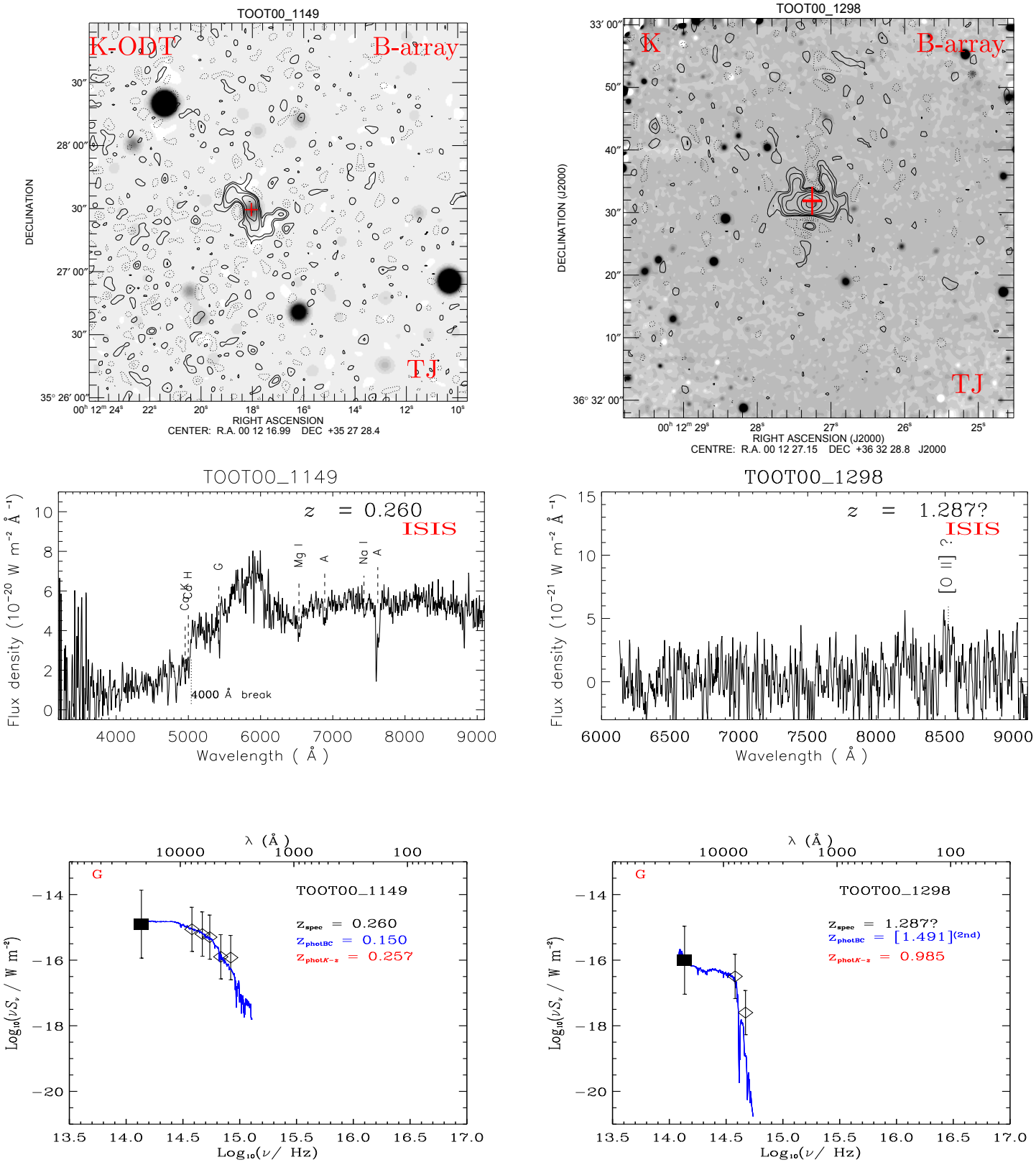

Figure 3.10: (continued)

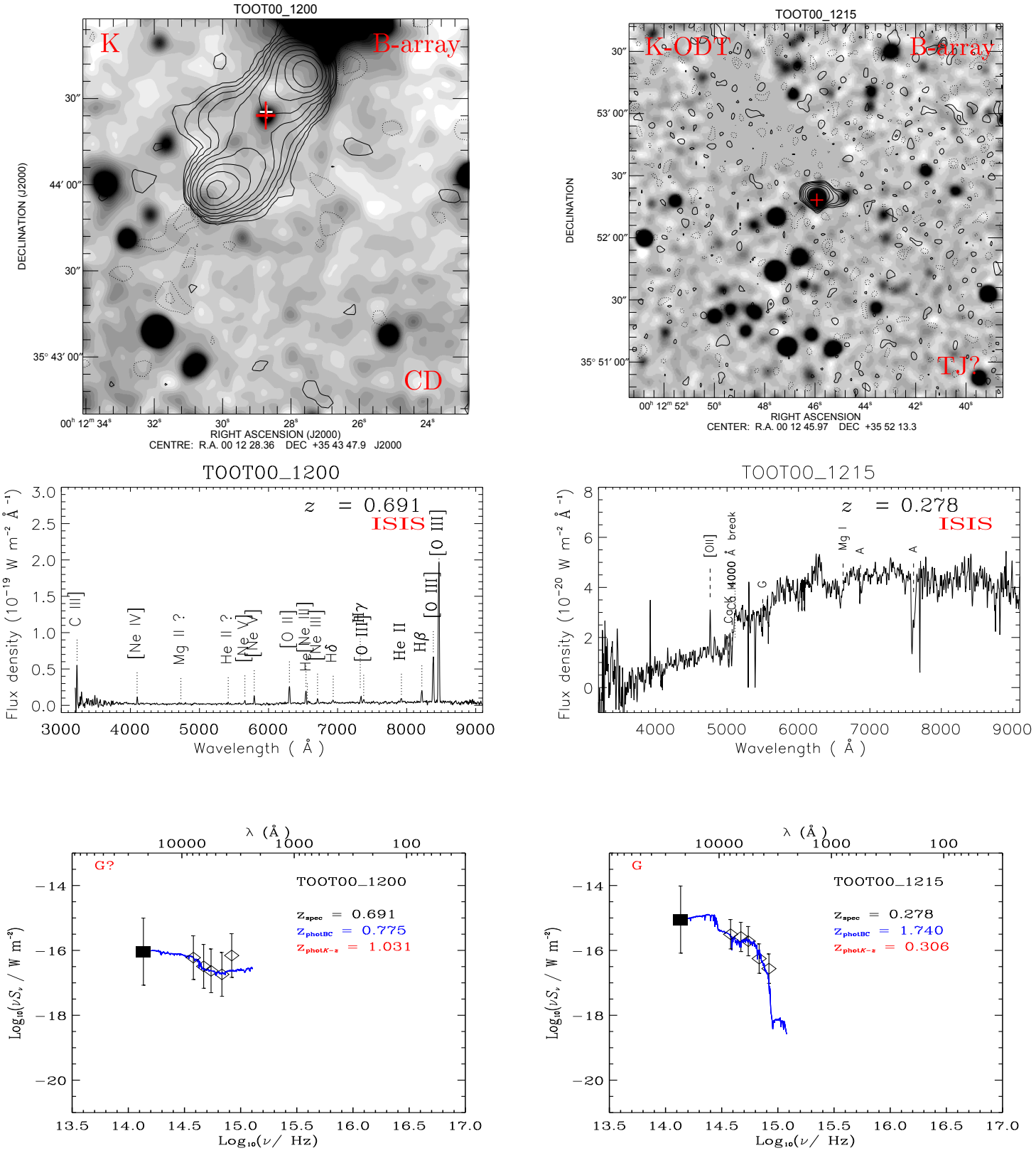

Figure 3.10: (continued)

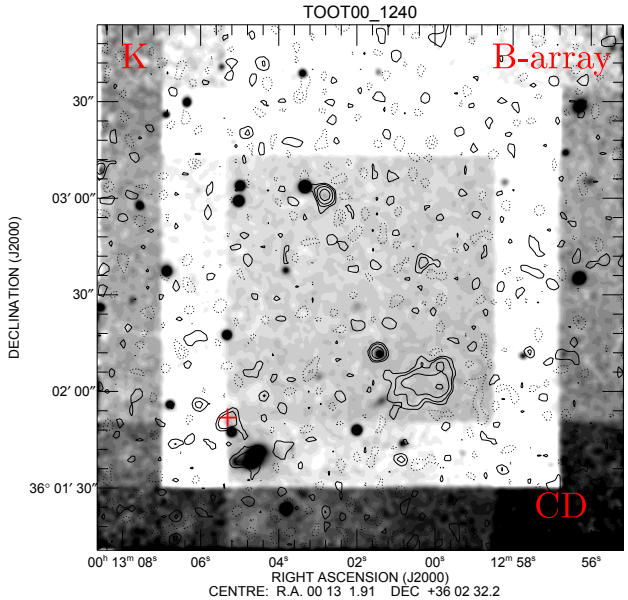

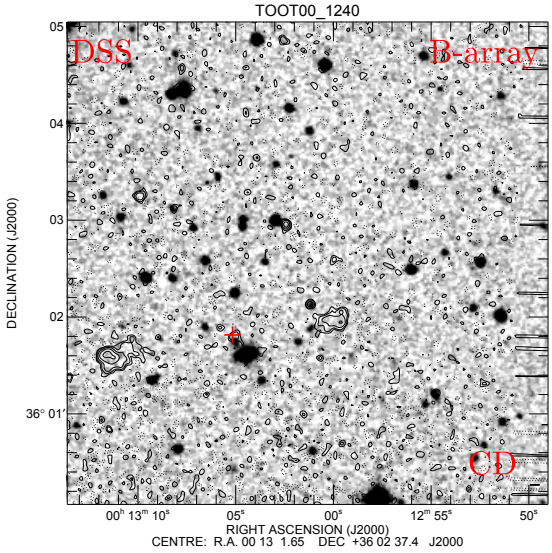

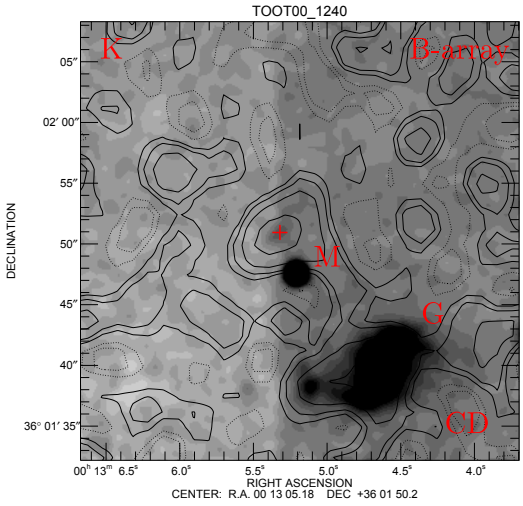

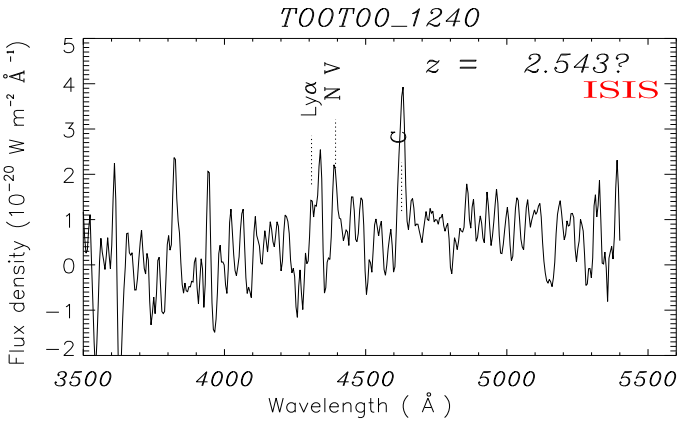

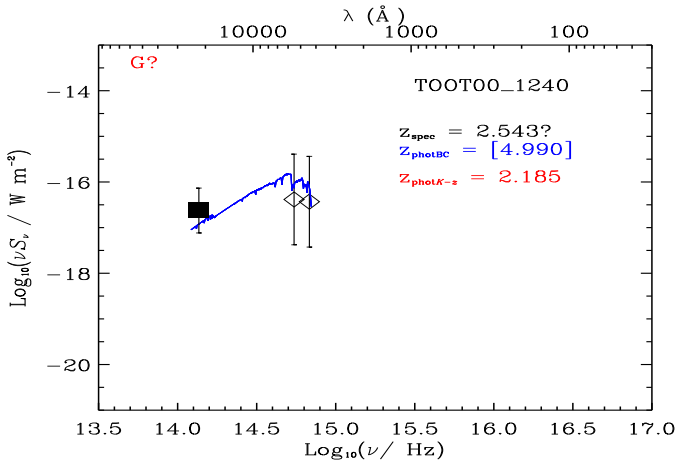

Figure 3.10: (continued)

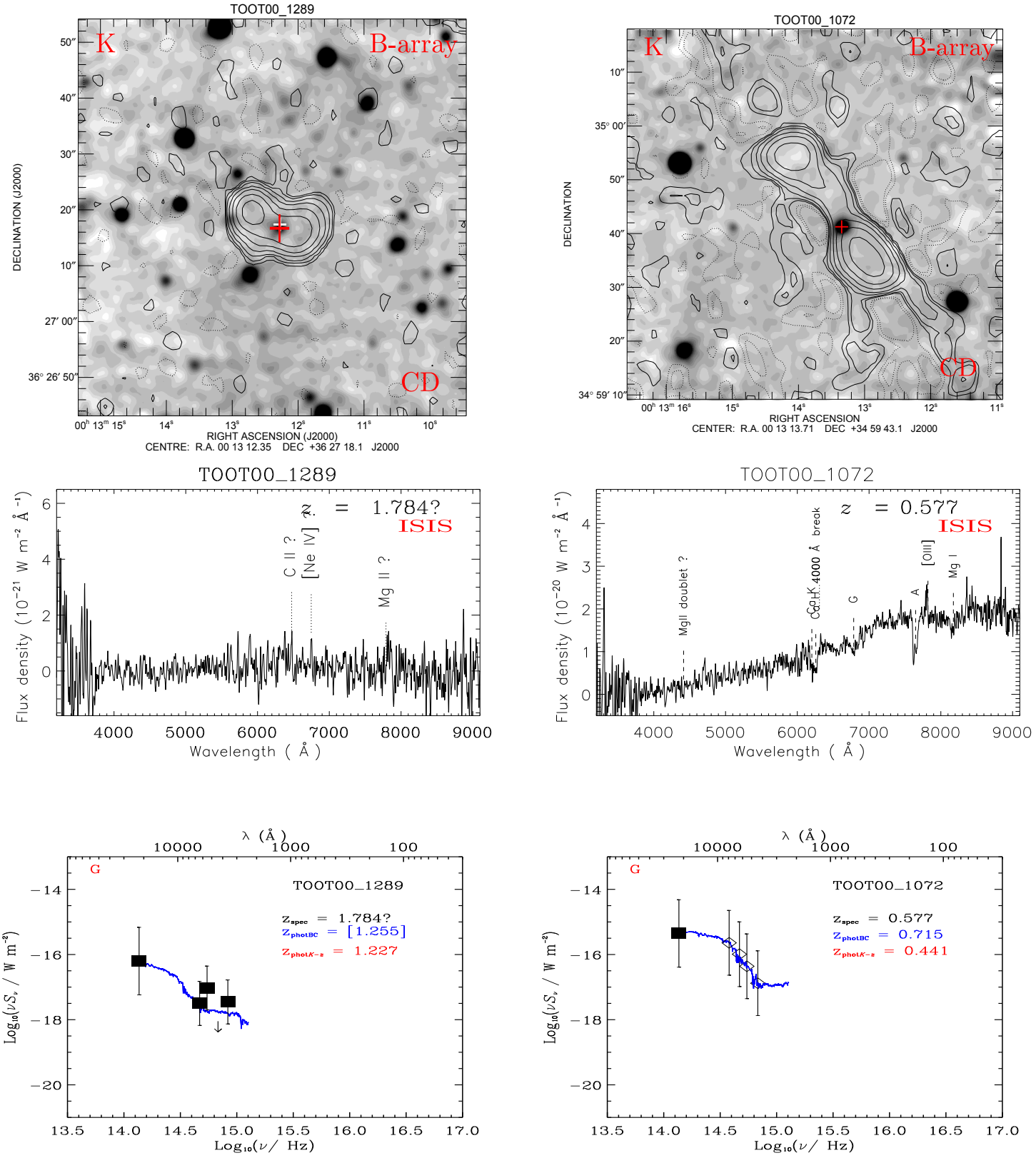

Figure 3.10: (continued)

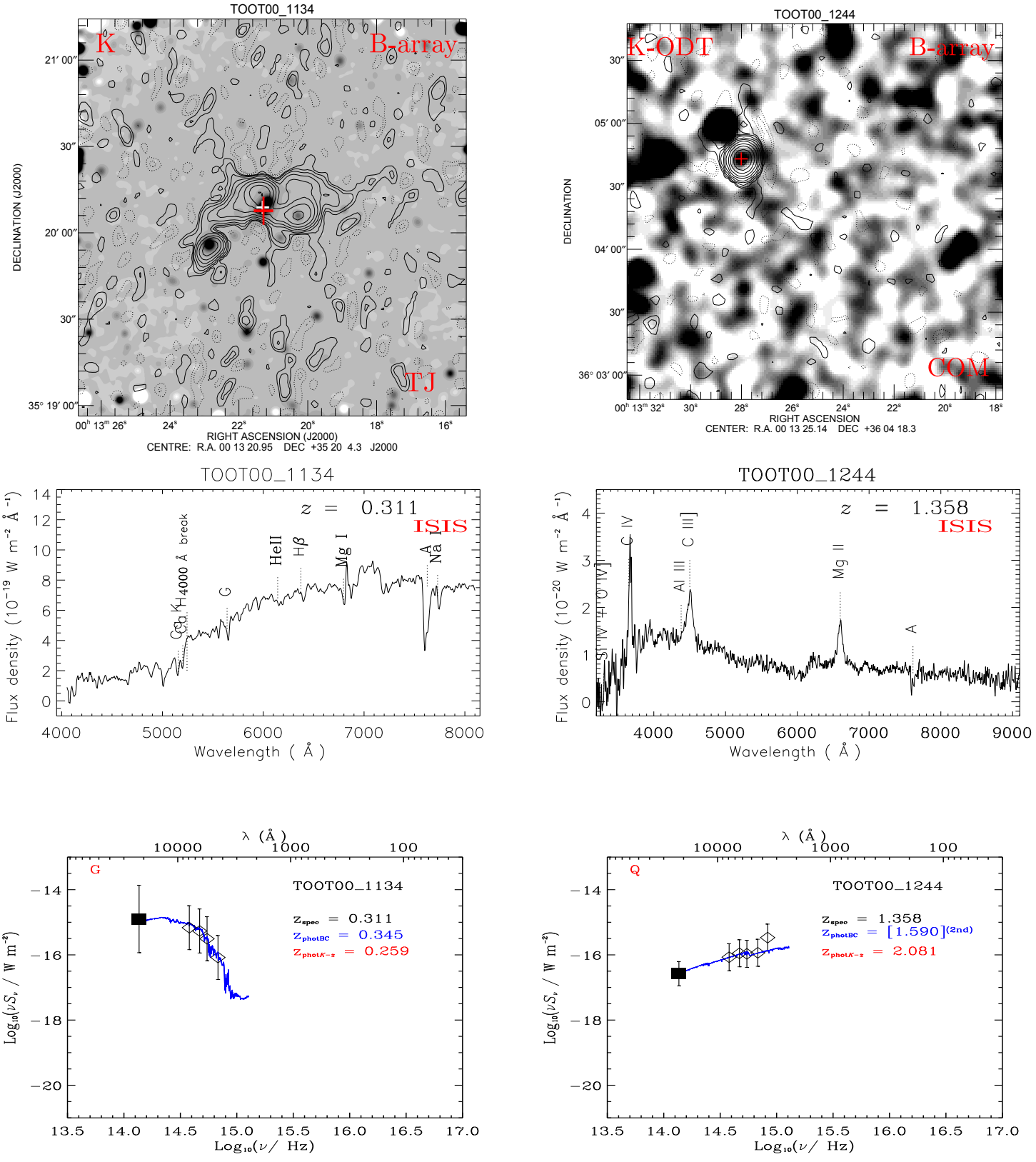

Figure 3.10: (continued)

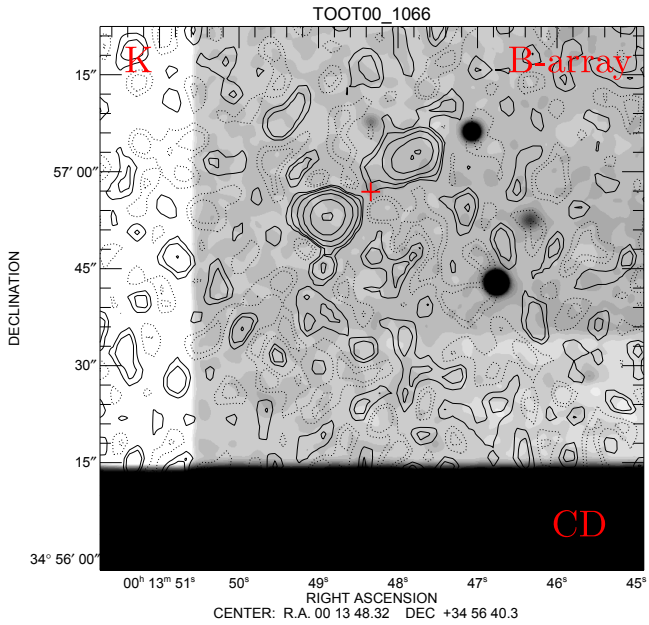

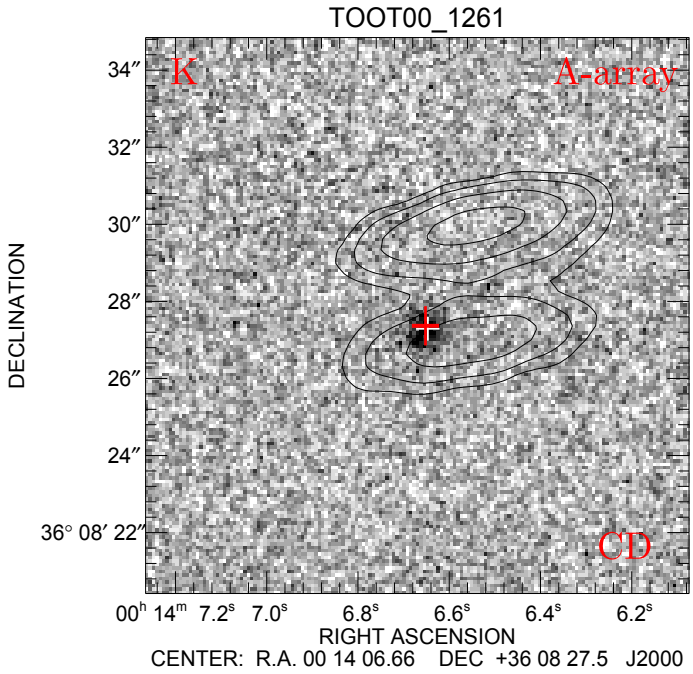

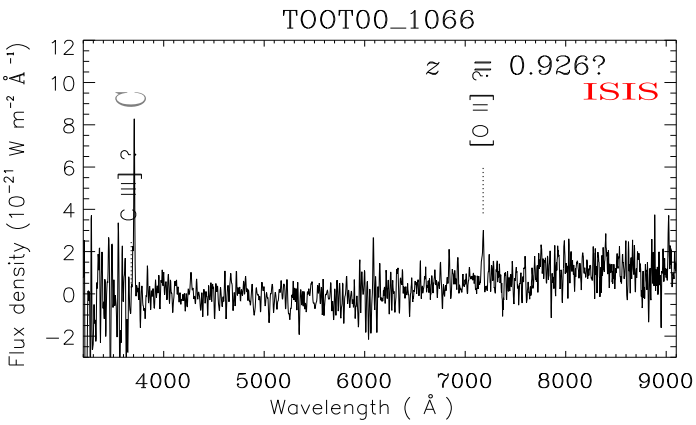

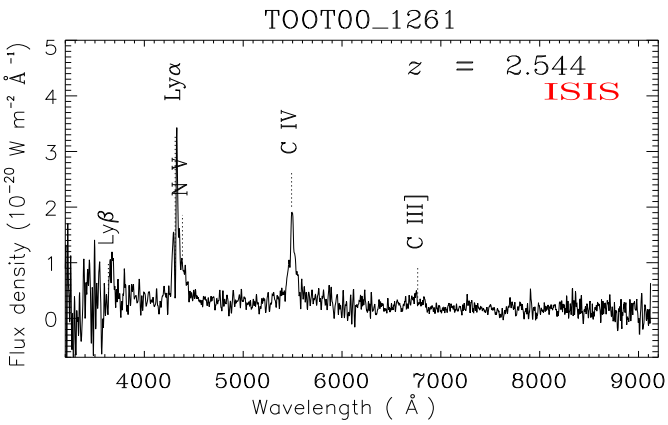

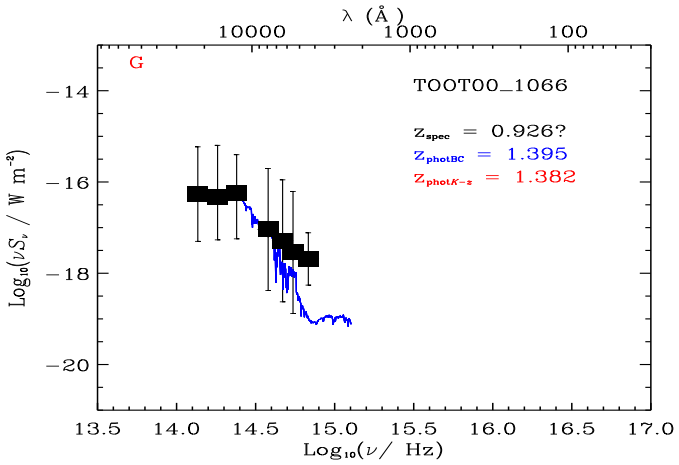

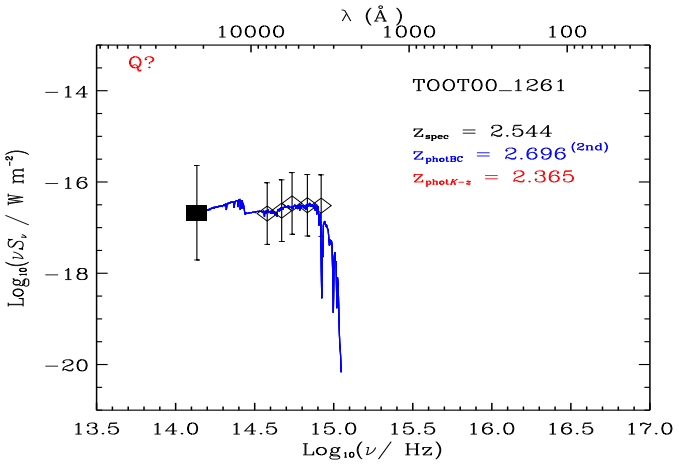

Figure 3.10: (continued)

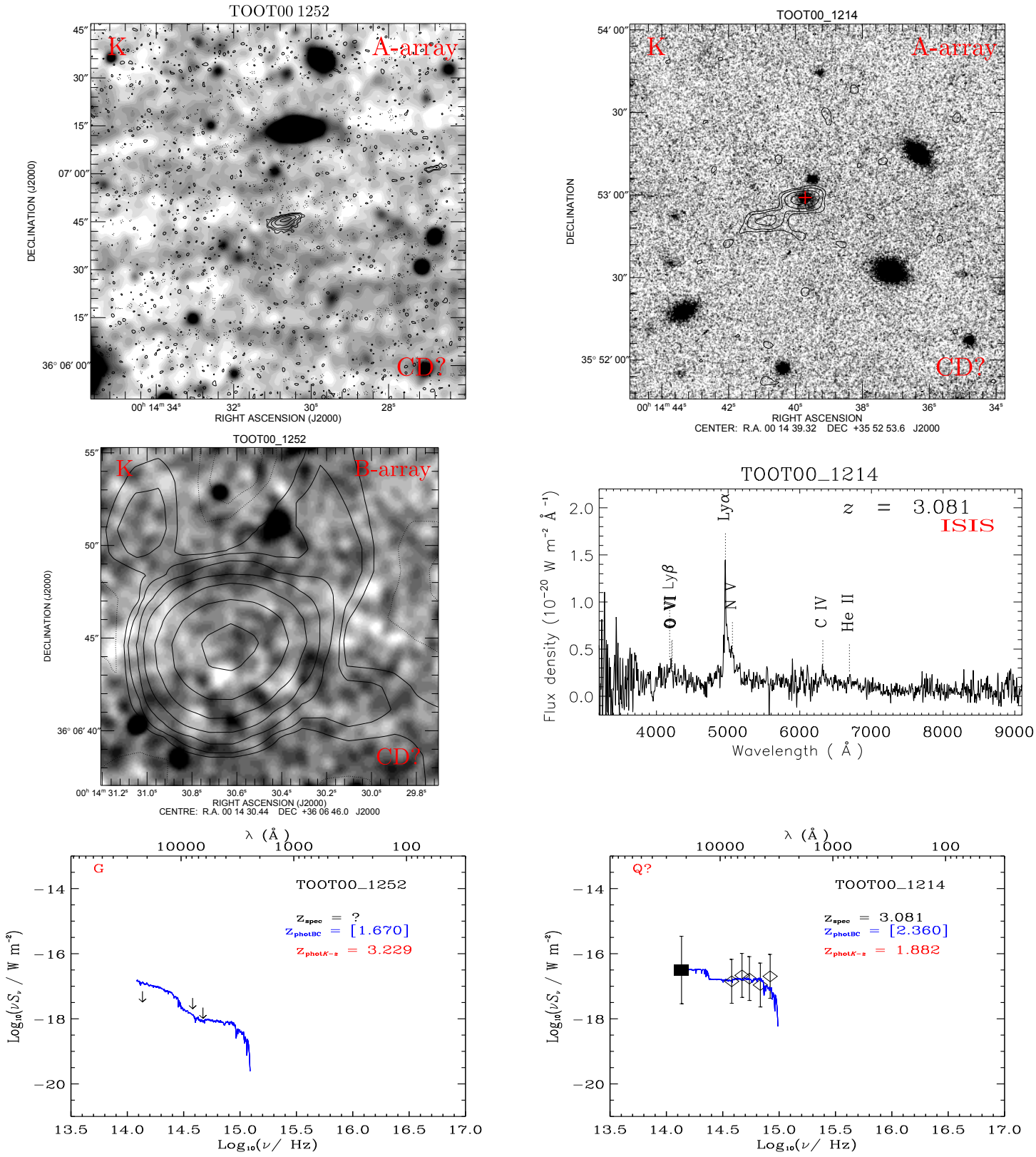

Figure 3.10: (continued)

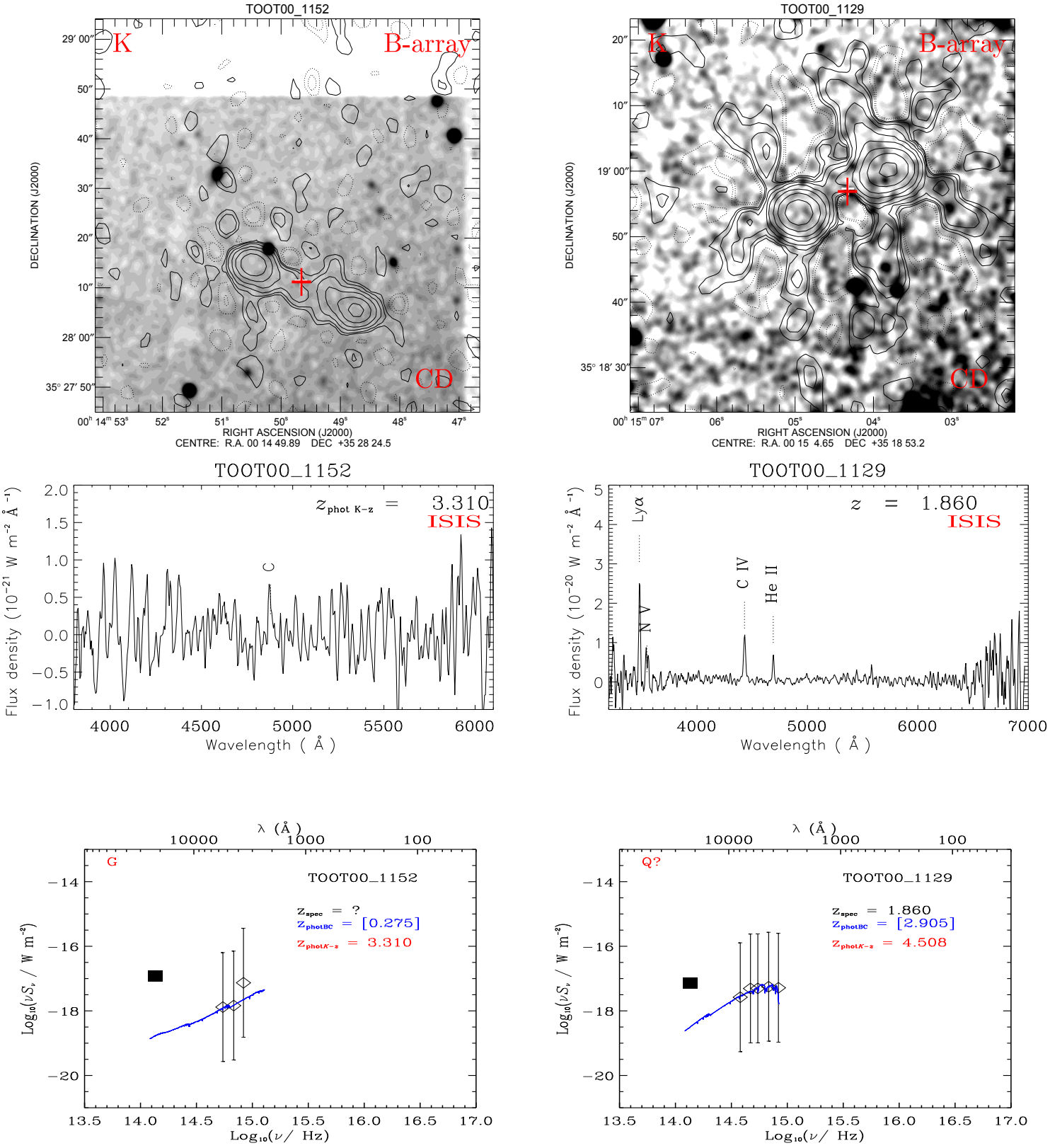

Figure 3.10: (continued)

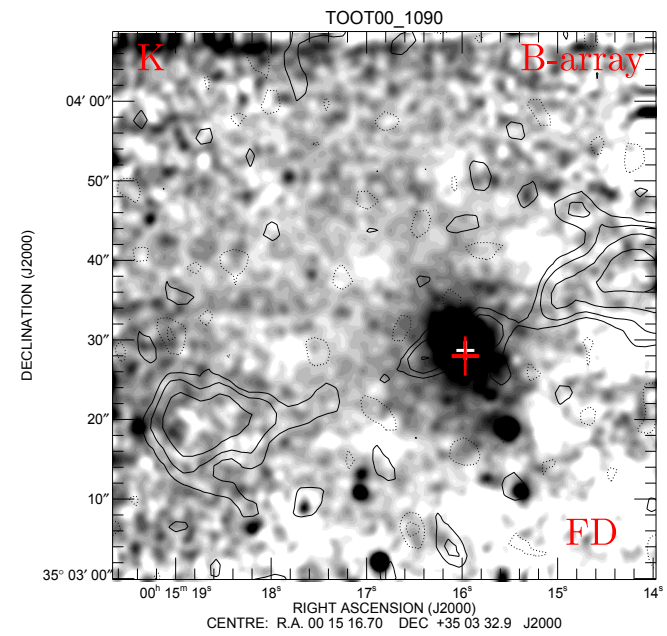

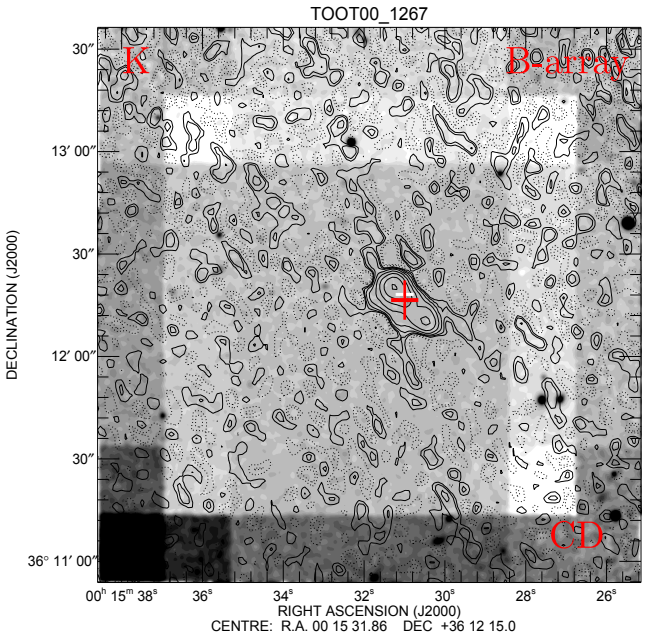

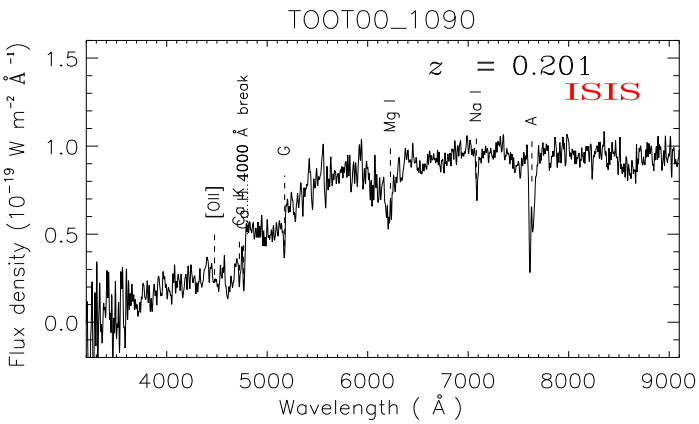

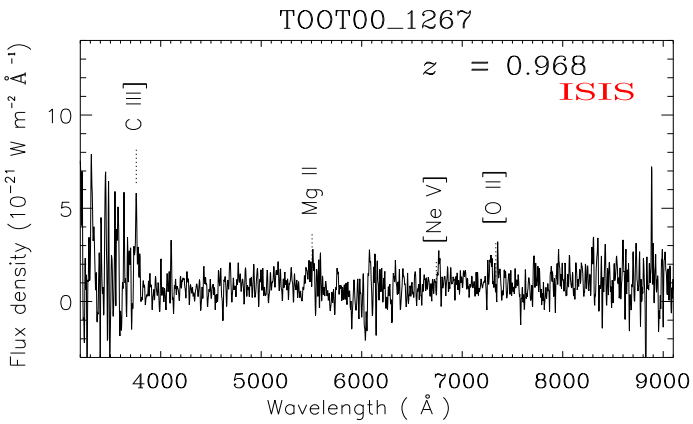

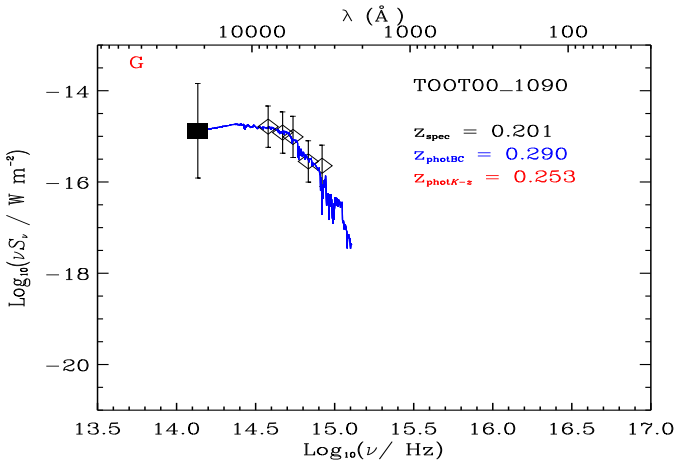

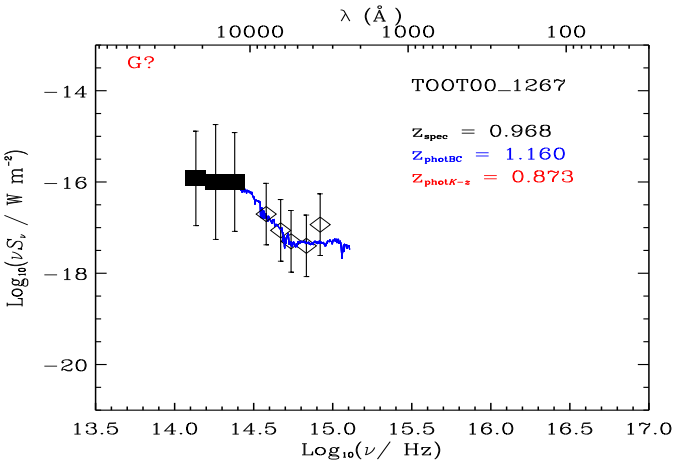

Figure 3.10: (continued)

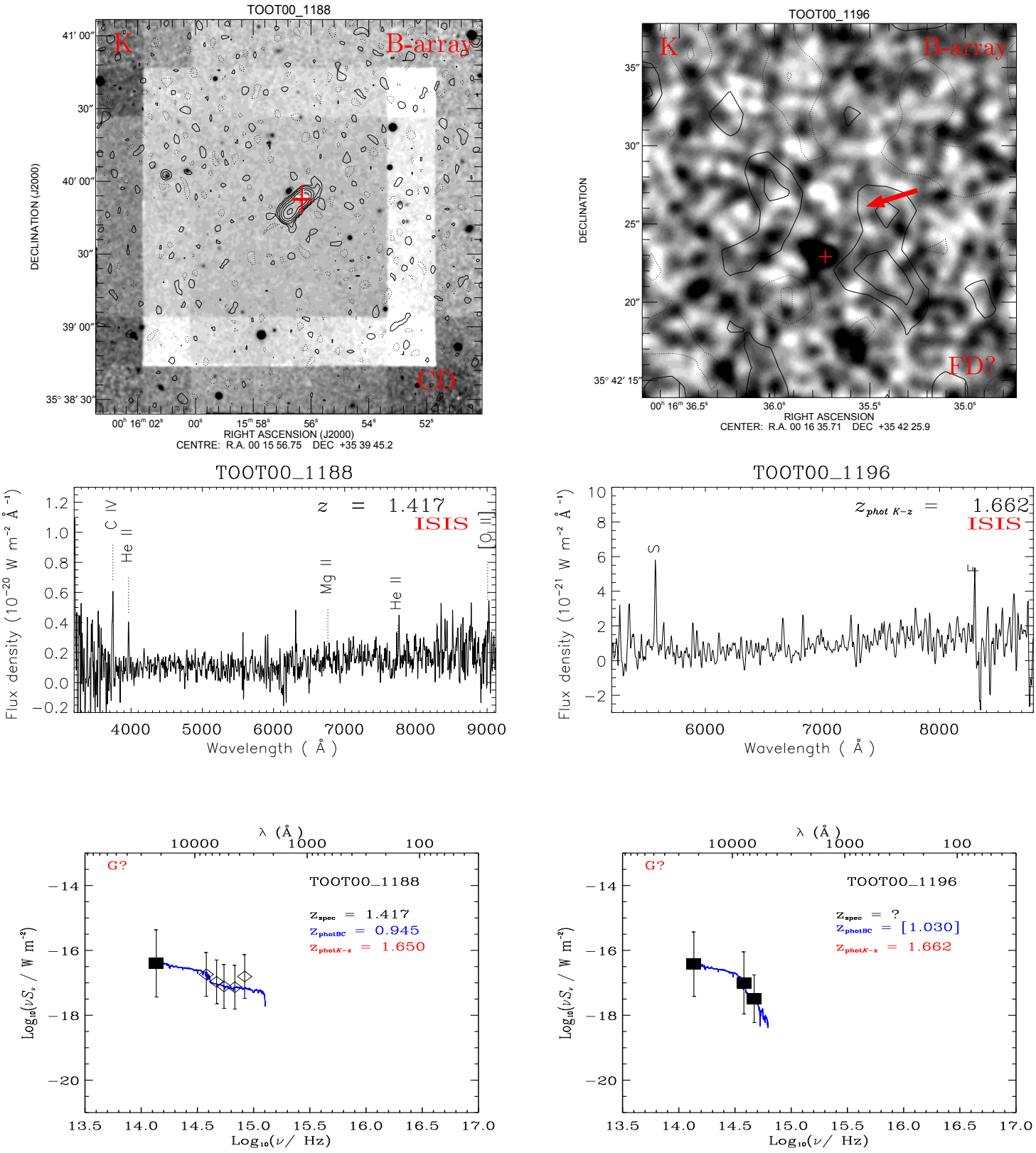

Figure 3.10: (continued)

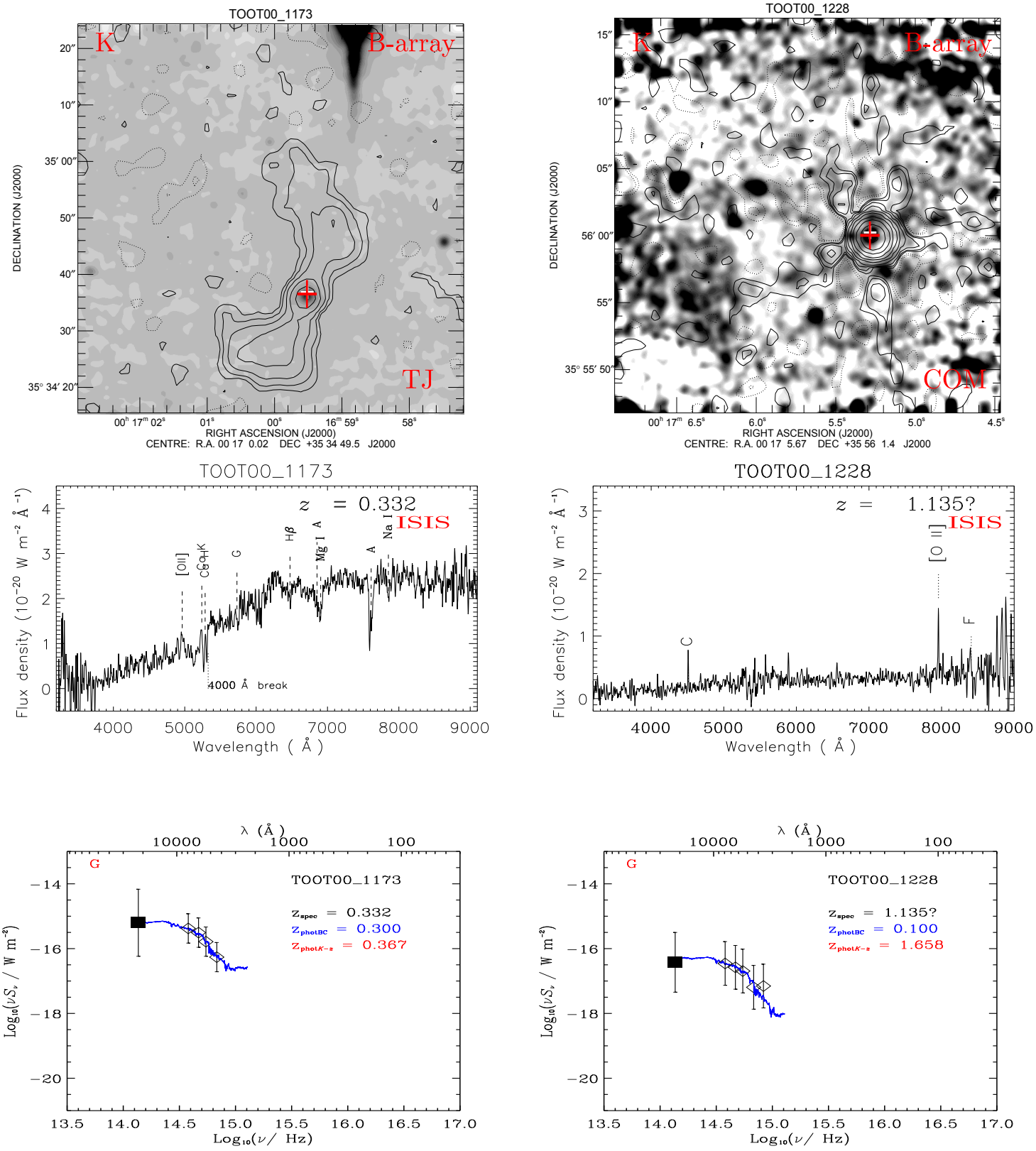

Figure 3.10: (continued)

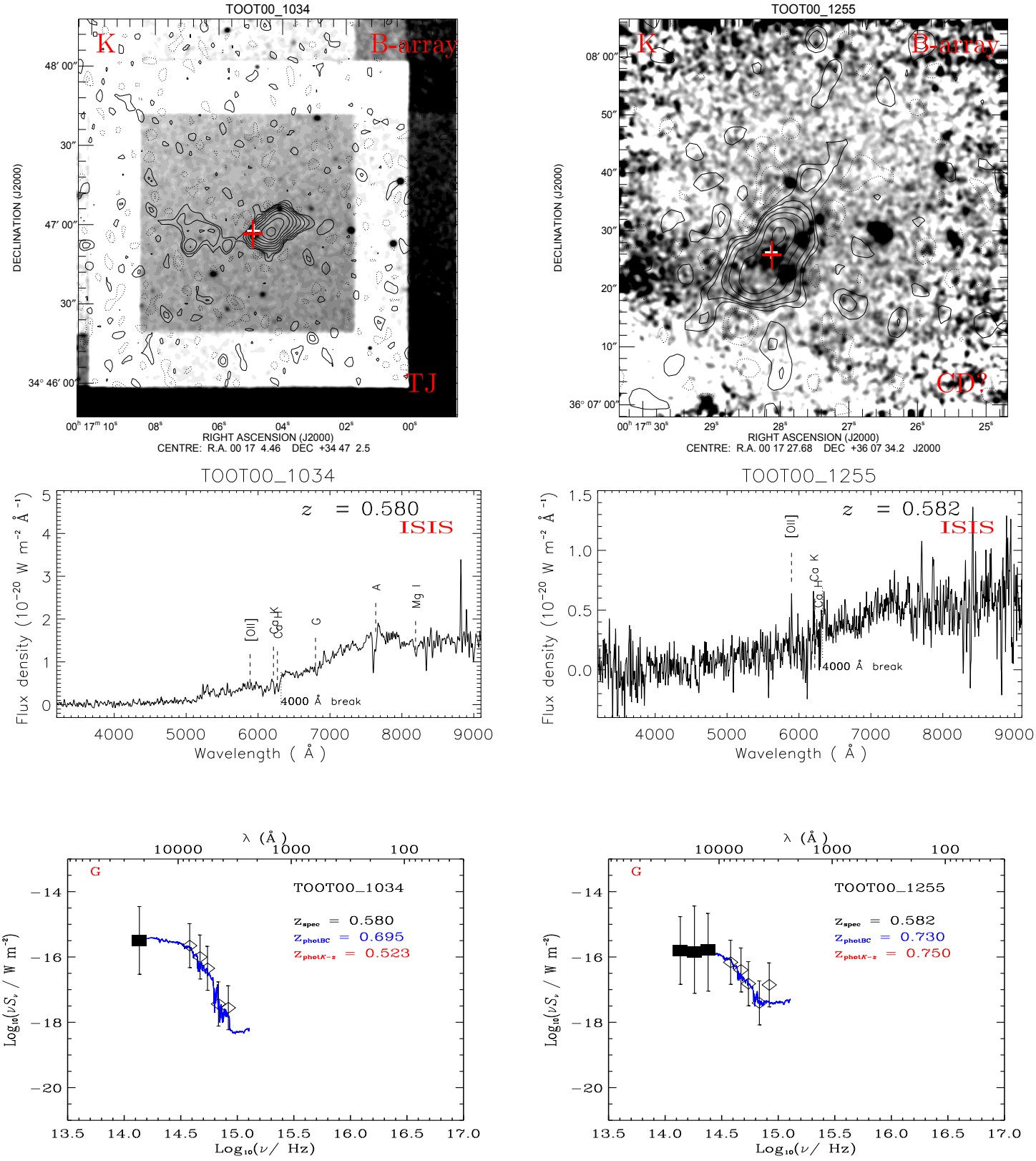

Figure 3.10: (continued)

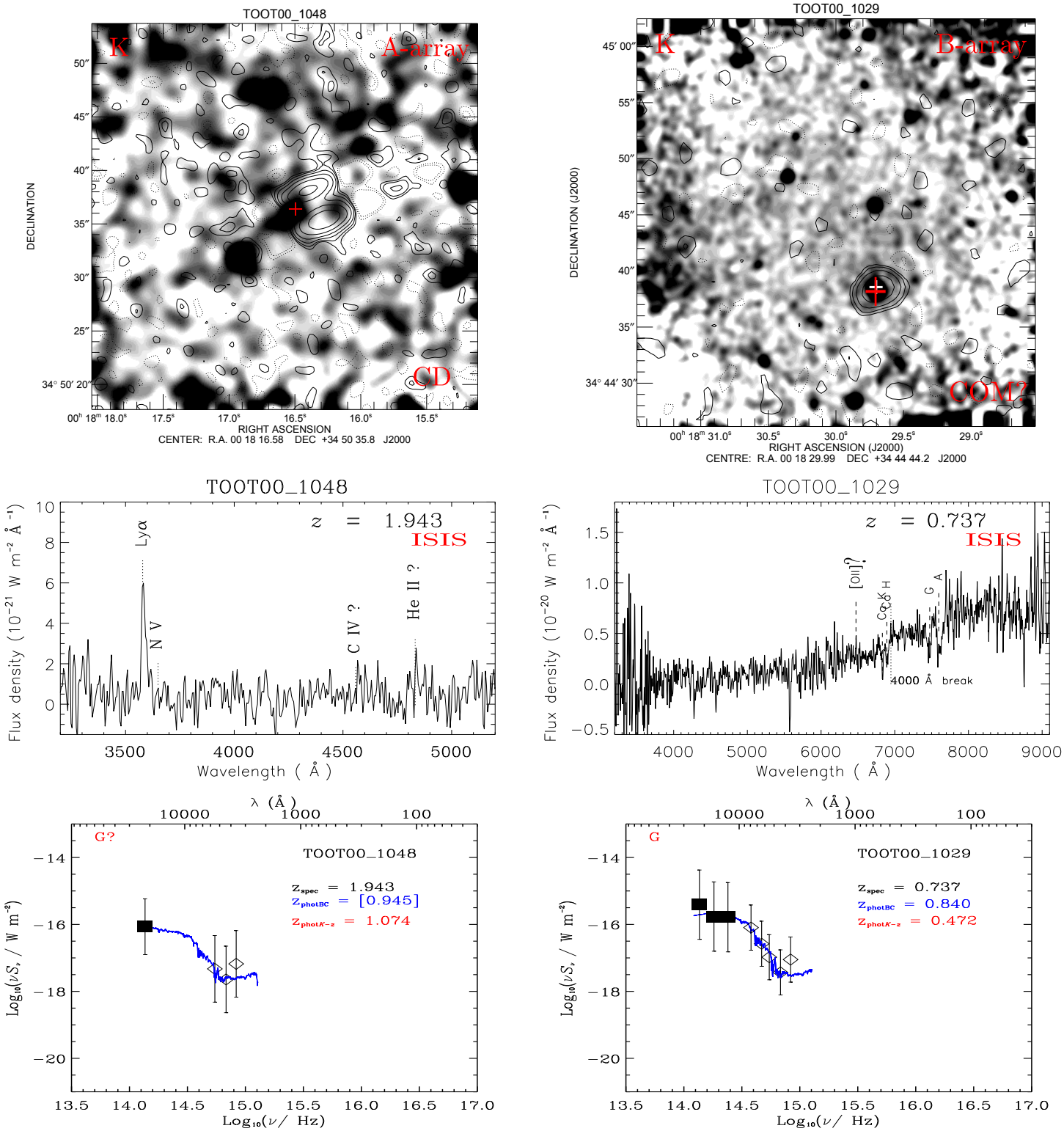

Figure 3.10: (continued)

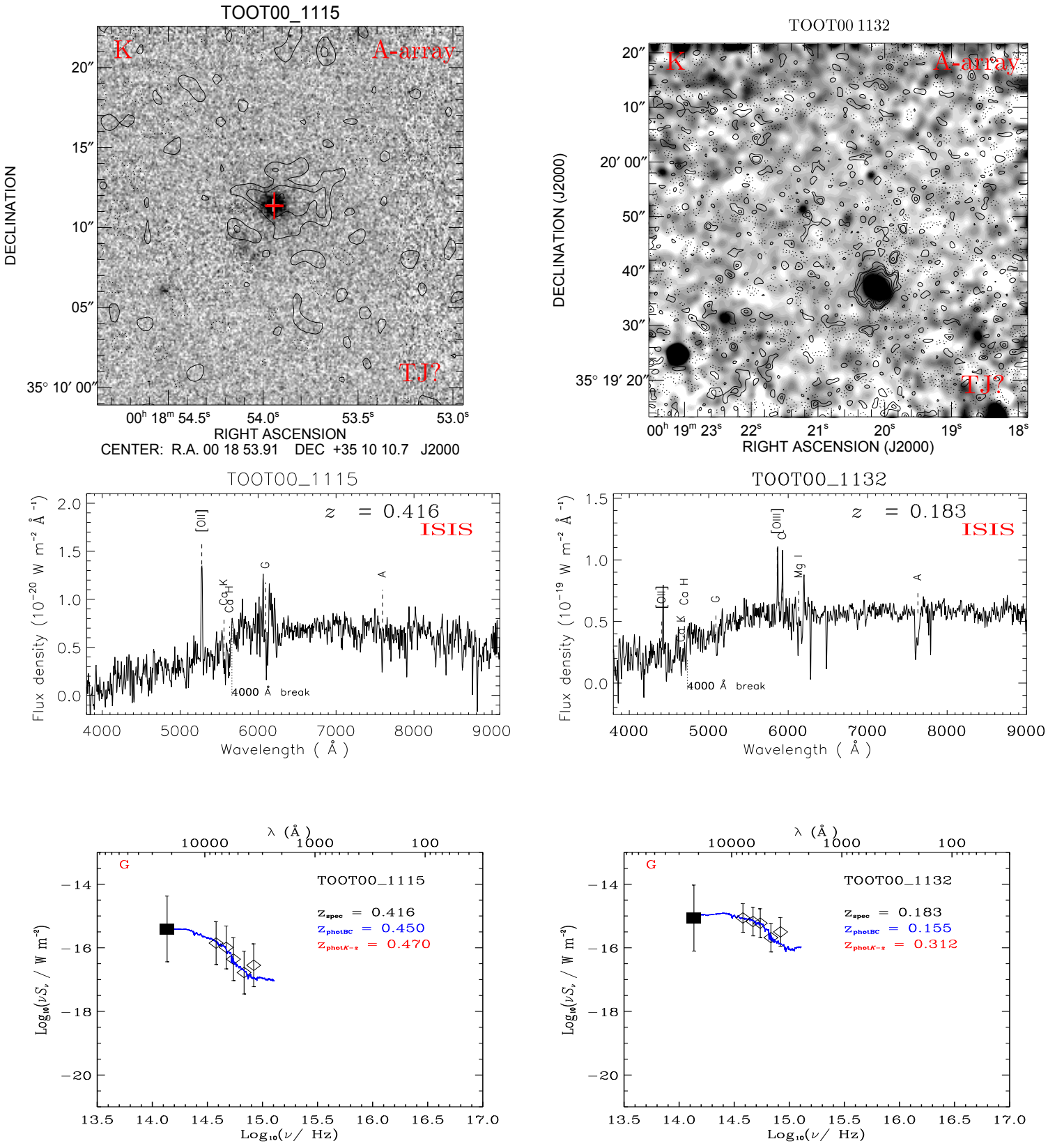

Figure 3.10: (continued)

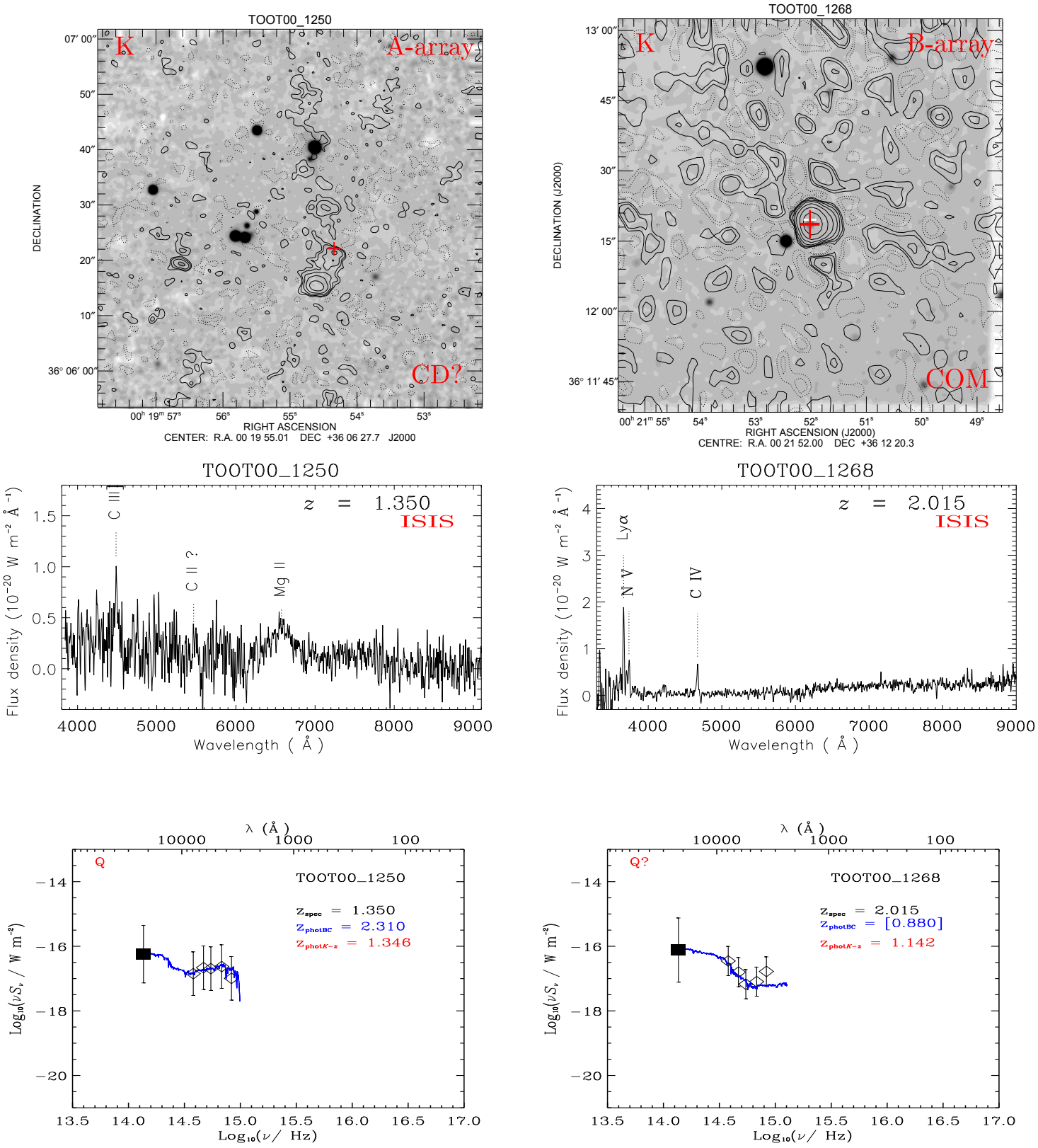

Figure 3.10: (continued)

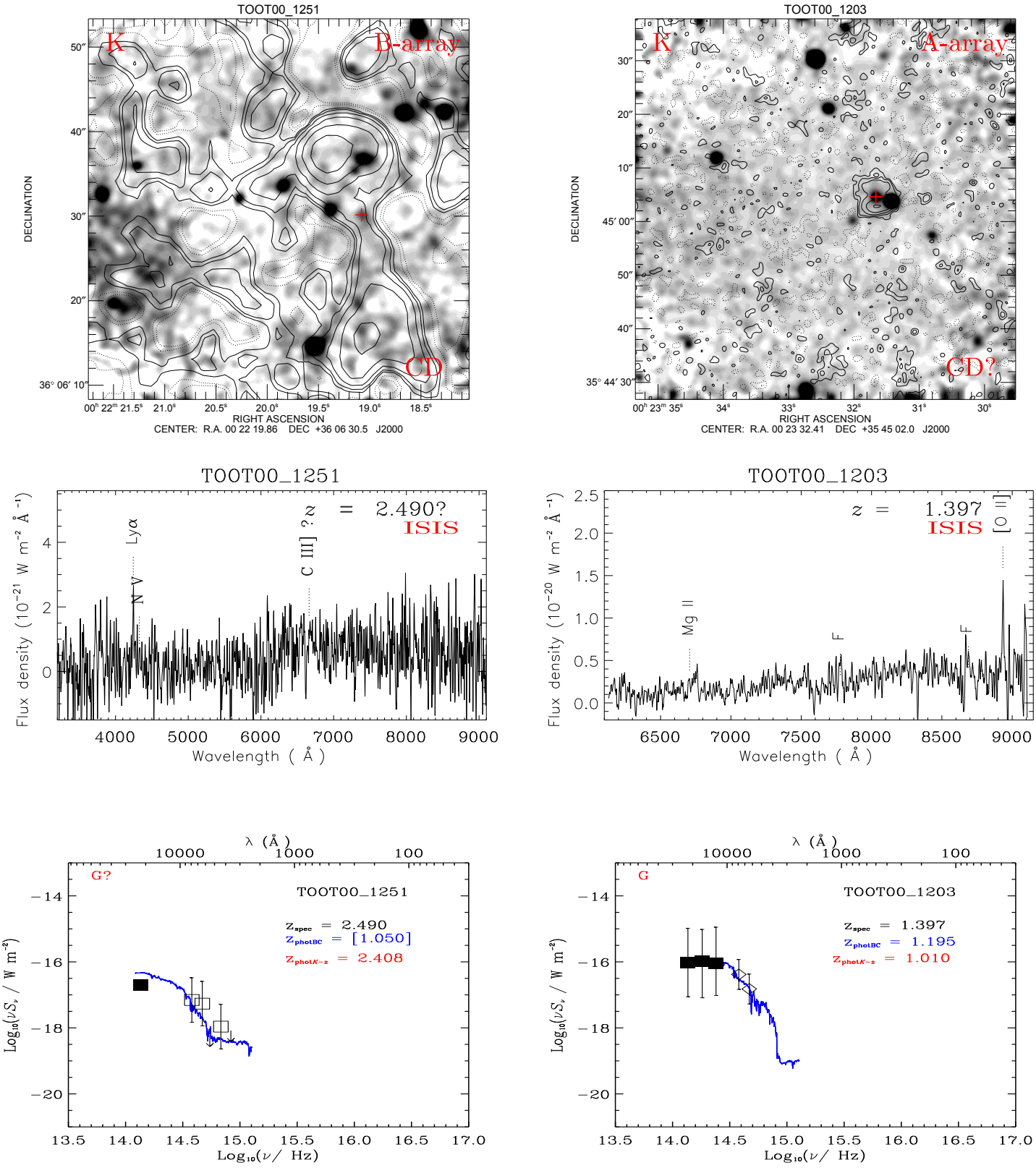

Figure 3.10: (continued)

Chapter 4

Investigating Large-Scale Structure in the TOOT00 and SXDF regions

Abstract

This chapter presents and analyses the redshift distributions of the two radio-source samples described in Chapters 2 & 3 with the specific aim of looking for evidence of the influence of large-scale structures. The first one includes the 47 TOOT00 radio sources (Chapter 3) with flux density $S_{151\mathrm{MHz}} \gtrsim 100$ mJy, occupying a ~ 0.0015-sr sky area. The second consists of the 37 brighter than 2 mJy at 1.4 GHz SXDS radio sources (Chapter 2) inside a ~ 0.0002-sr sky area. Both samples are compared to a semi-empirical simulation, S^3-SEX, of the extragalactic radio continuum sky suitable for aiding the design of next generation radio interferometers such as the Square Kilometer Array (SKA). This simulation, when scaled to the sky areas of the TOOT00 and the SXDS samples, predicts a redshift distribution very similar to the TOOT00, and broadly similar to the SXDS. Comparison of two samples of 100-simulated independent sky areas from the S^3-SEX equal to the TOOT00 and the SXDS sky areas and with appropriate simulated flux density limits, respectively, gives evidence for a redshift spike due to Large-Scale Structure at $z \sim 1.3$ for TOOT00 and $z \sim 0.65$ & 2.7 for the SXDS sample. Furthermore, use of V/V_{max} test shows that the space distribution of the TOOT00 radio sources reveals that they show cosmological evolution with redshift, which is not the case for the SXDS objects that seem to evolve less rapidly.

4.1 Introduction

The existence of Large-Scale Structures (LSS) tells us something important about the initial conditions of the big bang, and about the physical processes that have operated subsequently since they are the consequence of the gravitational amplification of the initial density fluctuations in the early Universe (e.g. Hawkins et al. 2003). The LSS has been observed in redshift galaxy surveys on the local Universe (e.g. 6dF Galaxy Survey - 6dFGS; Jones et al. 2004) and in the high redshift Universe from quasar surveys (e.g. 2dF QSO Redshift survey - 2QZ, Croom et al. 2004; da Angela et al. 2008). In the search for clusters of galaxies and large structures like superclusters, radio sources have been proven to be excellent probes of the LSS because they are mostly associated with massive ellipticals that tend to reside in galaxy clusters (e.g. Brand et al. 2003).

The high luminosity of radio galaxies and quasars makes them detectable out to large, cosmological distances ($z > 4$) and, consequently, useful in studying clustering out to high redshift. It has been shown that radio galaxies are actually more strongly clustered than are local optical galaxies (e.g. Cress et al. 1996).

From the theoretical point of view, modelling of the space distribution of galaxies, and in particular of radio sources, has been of interest for many years and has resulted in semi-empirical models that attempt to model the spatial clustering of radio sources instead of simply placing them on the sky with a uniform random distribution and with some smooth distributions in redshift. One such model is the simulation that was developed under the European SKA Design Study (SKADS) initiative and referred to collectively as SKADS Simulated Skies (S^3 – Wilman et al. 2008). This simulation of the extragalactic radio continuum sky gives an emphasis on the modelling of large-scale cosmological distribution of radio sources. The semi-empirical model S^3-SEX has simulated sources generated by sampling the observed (or extrapolated) radio continuum luminosity functions and covers ~ 100 times more sky area than the semi-analytical models (S^3-SAX – Obreschkow et al. 2009).

The uniformity, or not, of the space distribution of radio sources can be measured by the $V/V_{\rm max}$ test (Rowan-Robinson 1968; Schmidt 1968). This is the ratio of the volume enclosed at the redshift of the object to the maximum volume that would be enclosed at the maximum redshift at which the object would be detectable. The expected mean value for the $V/V_{\rm max}$ quantity is 0.5 if there is no cosmic evolution (e.g. Kembhavi & Narlikar 1999). A value higher than 0.5 suggests that the comoving density effectively increases towards higher redshift, independent of the exact pattern of evolution and conversely for values significantly below 0.5.

The $V/V_{\rm max}$ test allows the inspection of a sample for possible evolution even when the sample size is small. It is necessary, though, for the sample to be complete, as otherwise the values of $V/V_{\rm max}$ will be biased. In fact, $V/V_{\rm max}$ is often used to investigate how complete samples are.

Schmidt (1968) found that quasars are not uniformly distributed in space. This result indicates that the effective density of the sample increases with increasing distance (i.e. redshift), which suggests evolution. Furthermore, from studies of the radio-selected 3CR sample, Laing et al. (1978) found that high-luminosity radio galaxies evolve with cosmological epoch in a manner similar to quasars. Such work has been excluded to fainter radio samples by Dunlop & Peacock (1990), Willott et al. (2000) and Jarvis et al. (2001d).

Here we study the redshift distribution of the TOOT00 (Vardoulaki et al. 2009) and the SXDS (Vardoulaki et al. 2008) radio sources. The goal is to investigate whether any observed redshift spikes are evidence of a clustering signal, or if they are related to Poisson fluctuations in a random distribution; we discriminate between these possibilities by calculating the probability spikes given a random distribution. Section 4.2 presents basic information about these two samples, as well as details on the S^3-SEX simulation (Wilman et al. 2008) used in the analysis. In Section 4.3 we present the redshift distributions of the TOOT00 and the SXDS samples, and a comparison with 100 almost independent S^3-SEX simulations of the same sky area. Section 4.4 presents the probability for redshift spikes in the two distributions and a $V/V_{\rm max}$ test for both TOOT00 and SXDS samples. Section 4.5 presents the conclusions of this study. Additional tables used in the analysis are given in Appendix C in Section 4.6.

We use J2000.0 positions and the convention for all spectral indices, α, that flux density $S_\nu \propto \nu^{-\alpha}$, where ν is the observing frequency. A low-density, Λ-dominated Universe in which $H_0 = 70$ km s^{-1}Mpc^{-1}, $\Omega_{\rm M} = 0.3$ and $\Omega_\Lambda = 0.7$ is assumed throughout.

4.2 Data

The two datasets used in the analysis are i) the 47 TOOT00 radio sources with a flux density limit of 95 mJy at 151 MHz centred at RA: $00^{\rm h}$ 11^m Dec: $+35^{\rm o}$ $35''$ (see Chapter 3) and ii) the 37 SXDS radio sources with flux density limit of 2 mJy at 1.4 GHz centred at RA: $2^{\rm h}$ 17^m Dec: -5$^{\rm o}$ $10''$ (see Chapter 2). The TOOT00 sky area is ~ 0.0015 sr and the median redshift is $z_{\rm med} \simeq 1.25$, whereas the SXDS sky area is ~ 0.0002 sr with a median redshift $z_{\rm med} \simeq 1.1$.

Both radio-source samples have optical spectroscopic and optical/near-IR photometric data, as described in Section 3.2 for the TOOT00 and Section 2.2 for the SXDS objects. Tables 4.6 & 4.7 present some of the quantities used in the analysis. Note that the optical classification of

the SXDS radio sources presented in Table 2.1 (Section 2.3) used in the analysis, and modified to match the TOOT00 optical classification in the following way: Q SXDS objects correspond to Q in TOOT00; OQ, WQ and BL SXDS objects correspond to Q? in TOOT00; G? and SB objects in SXDS correspond to G? in TOOT00; and G objects are common to both samples.

Table 4.6 in Section 4.4 presents the radio classification in FR-type (Fanaroff & Riley 1974), with additional classes for compact sources, for the TOOT00 radio sources based on Table 3.3 (see Section 3.4 in Chapter 3). Furthermore, the SXDS radio sources are classified according to FR-type, as presented in Table 4.7 in Section 4.4 (see also Table 2.1 for radio classification on the SXDS radio sources): CDs are labelled as FRIIs; FDs and TJs are labelled as FRIs; COM with flat radio spectral index are labelled as COM-F; COM with steep radio spectral index are labelled as CSS; and quasars with flat radio spectral index are labelled as Q-F.

Here, the TOOT00 and SXDS redshift distributions are compared to the Semi-Empirical Extragalactic Database simulation S^3-SEX obtained from the SKADS Simulated Skies S^3 (Wilman et al 2008). The simulation covers a sky area of 20×20 deg^2, or 0.1212 sr, out to a cosmological redshift of $z = 20$, and down to flux density limit of 10 nJy at 151 MHz, 610 MHz, 1.4 GHz, 4.86 GHz and 18 GHz.

4.3 Redshift Distributions

Figure 4.1 presents the redshift distribution of the 47 TOOT00 (on the left) and the 37 SXDS (on the right) radio sources respectively. For comparison, the S^3-SEX simulation scaled down to the sky areas of the two samples, 0.0015 and 0.0002 sr, respectively, is also shown. Note that the radio selection criteria (e.g. frequency and flux density limit) have been consistently applied.

A Kolmogorov-Smirnov (K-S[1]; Press et al. 1993) test between the TOOT00 and the appropriate comparison S^3-SEX redshift distributions shows that the maximum deviation between the two cumulative distributions is 0.12 with a significance level of 44.46%. This suggests that the distributions are statistically similar. The results of the K-S test between the SXDS and the appropriate comparison S^3-SEX redshift distributions gives a maximum deviation of 0.15 with a significance level of 31.24%, suggesting the two distributions are broadly similar. The cumulative distributions between data and simulation can be seen in Figure 4.2–a for the TOOT00 and Figure 4.2–b for the SXDS.

These results suggest that the TOOT00 redshift distribution looks similar to the S^3-SEX

[1]The K-S test was calculated using the KSTWO task in IDL.

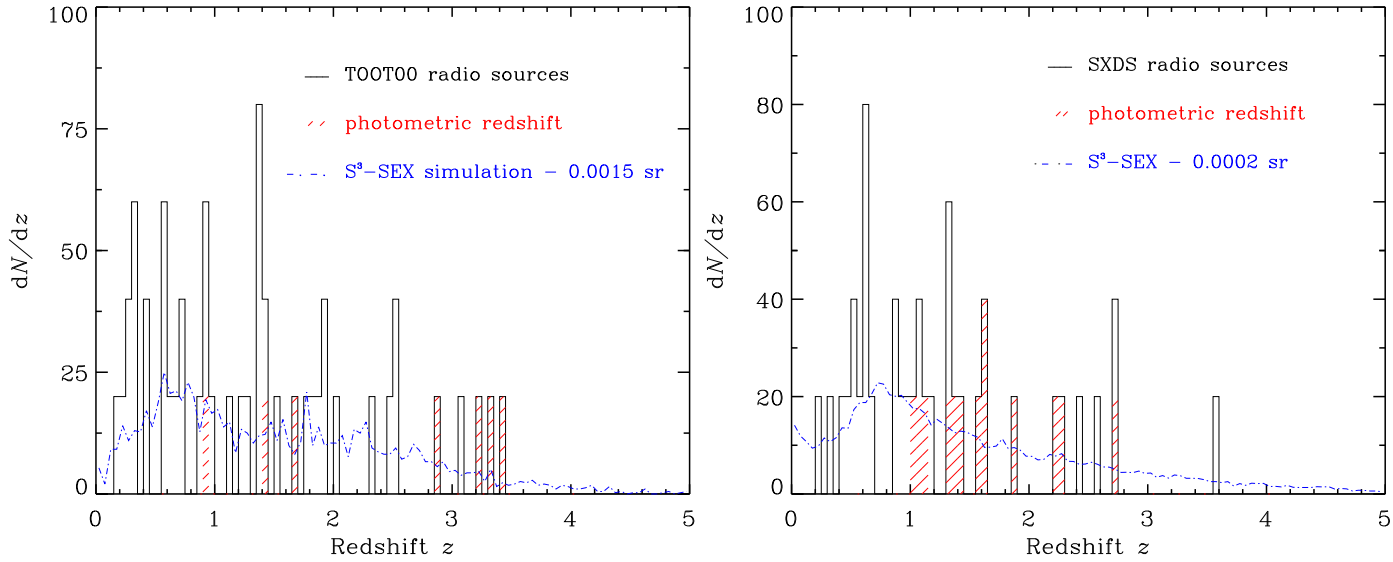

Figure 4.1: **a) Left**: Histogram of the redshift distribution for the 47 TOOT00 radio sources with median redshift $z_{\rm med} \sim 1.25$ (85% spectroscopic and 15% photometric redshifts, black & red hatched lines respectively). The binning on the redshift axis is $\mathrm{d}z = 0.05$ or $\mathrm{d}v \sim$ 15,000 km/s (100 redshift bins). The blue dotted-dashed line shows model predictions from the S^3-SEX simulation for an area of 0.1212 sr and $S_{151\rm MHz} \gtrsim 100$ mJy, which is scaled down to an area of 0.0015 sr to match the TOOT00 sky area, and includes ~ 40 simulated objects. **b) Right**: Histogram of the redshift distribution for the 37 SXDS radio sources with median redshift $z_{\rm med} \simeq 1.1$ (65% spectroscopic and 35% photometric redshifts, black & red hatched lines respectively). Binning on the redshift axis is $\mathrm{d}z = 0.05$ or $\mathrm{d}v \sim 15{,}000$ km/s (100 redshift bins). The blue dotted-dashed line shows model predictions from the S^3-SEX simulation for an area of 0.1212 sr and $S_{1.4\rm GHz} \gtrsim 2$ mJy, which is scaled down to an area of ~ 0.0002 sr to match the SXDS sky area and includes ~ 39 simulated objects with flux density at 1.4 GHz above 2 mJy.

simulation, but the SXDS redshift distribution is only broadly similar to the S^3-SEX simulation. There is marginal evidence that the extrapolation inherent in S^3-SEX underpredicts the high-z tail in samples selected at frequencies and flux-density limits similar to SXDS. This is not entirely surprising as S^3-SEX was built around low-frequency-selected redshift surveys and source counts; it is expected to be less accurate at higher frequencies.

4.4 Redshift spikes in the TOOT00 and SXDS redshift distributions

Based on Figure 4.1, the apparent redshift spikes (e.g. at $z \sim 0.3$ & 1.3 in the TOOT00 sample and at $z \sim 0.6$, 1.3 & 2.7 in the SXDS sample) are investigated in order to quantify their significance using a method similar to Brand et al. (2003). This is performed by calculating the probability, using Poisson statistics[2] (see also Appendix D), that the number of objects per

[2]The Poisson probability is given by $f(k;\lambda) = \lambda^k e^{-\lambda}/k!$, where e is the base of the natural logarithm ($e = 2.71828...$); k is the number of occurrences of an event - the probability of which is given by the function; $k!$ is

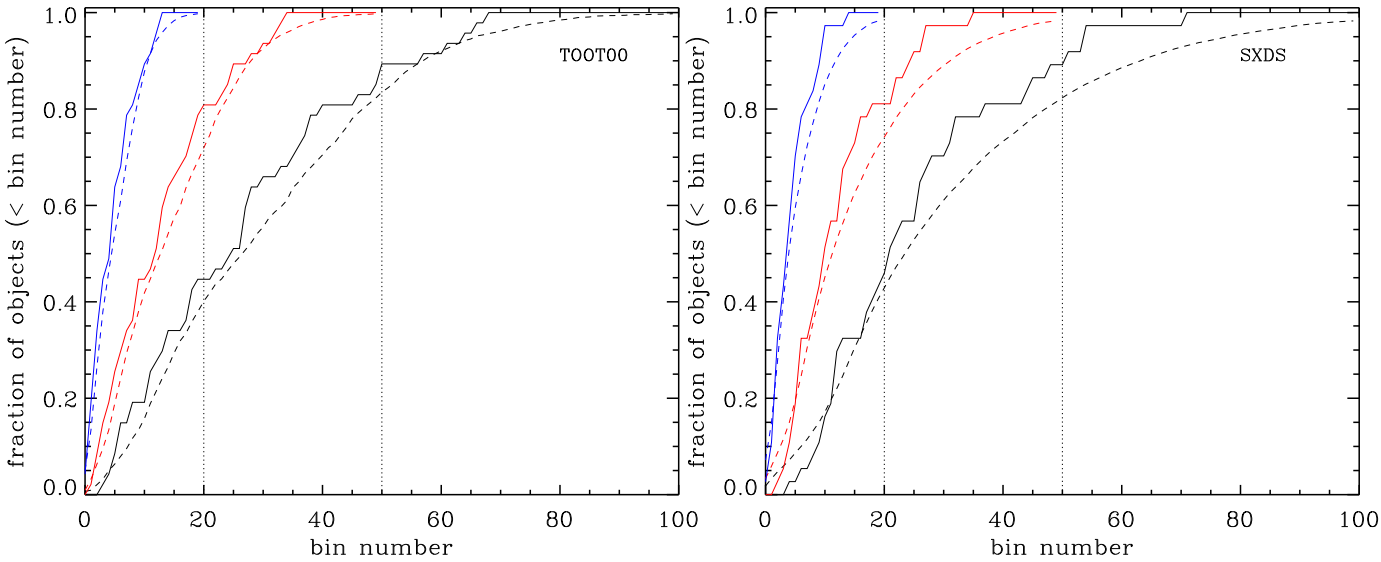

Figure 4.2: Cumulative distribution of the fraction of number of TOOT00 (**a-Left**) and (**b-Right**) SXDS objects compared to S^3-SEX simulation. Black colour denotes binning on the redshift axis of dz = 0.05 or dv $\sim$ 15,000 km/s (100 redshift bins), the red colour denotes binning of dz = 0.1 or dv $\sim$ 30,000 km/s (50 redshift bins) and the blue colour denotes binning of dz = 0.25 or dv $\sim$ 75,000 km/s (20 redshift bins). The solid lines denote TOOT00 or SXDS objects, and dashed lines show the S^3-SEX simulation. The horizontal dotted lines show the 20- and 50-bin redshift-range.

redshift bin is smaller than the observations given the simulation (if the number of objects in the simulation is less than those in the data) or the number of objects per redshift bin is larger than the observation given the simulation (if the number of objects in the simulation is larger than those in the observations). In Figures 4.4 & 4.5 we present the number of TOOT00 and SXDS objects respectively versus redshift (the redshift distribution using only spectroscopic redshifts is also shown on the left), where the binning of the data in redshift is dz = 0.05 or dv[3] = 15,000 km/s (100 redshift bins), dz = 0.1 or dv $\sim$ 30,000 km/s (50 redshift bins) and dz = 0.25 or dv $\sim$ 75,000 km/s (20 redshift bins). Figure 4.6 presents the redshift distribution of the entire ($\sim$ 400 deg^2) S^3-SEX simulation scaled down to the TOOT00 (left graph) and the SXDS (right graph) sky areas, for 100, 50 and 20 redshift bins. Any redshift spikes are diluted by the large cosmic volume simulated, but some regional signals (e.g. at $z \sim 1.8$) are related to known structures, due to LSS, in the S^3-SEX simulation (Wilman et al. 2008).

The probability that there is a significant redshift spike in the distribution of the TOOT00 and the SXDS radio sources is presented in Figures 4.7 & 4.8, respectively. The probability is also calculated only for objects with spectroscopic redshifts (Figures 4.7–a & 4.8–a), in order

the factorial of k; and λ is a positive real number, equal to the expected number of occurrences during the given interval.

[3]dv is calculated by assuming $\Delta z \sim \Delta v$/c, where c is the speed of light. This equation is only an approximation of the cosmological redshift at high redshifts, that takes into account the expansion of the Universe.

to show the effect the photometric redshifts have on the probability of finding redshift spikes. The probability for redshift spikes in four redshift intervals are presented in Tables 4.1 & 4.2 for the TOOT00 and SXDS samples respectively. In both cases the probability is plotted for different binning intervals (100, 50 and 20 redshift bins).

The key point is that the mean expected number of objects is smooth in z, so we are looking for significant spikes that are LSS. In 100 bins, the probability would have to be $\lesssim 1\%$ for a spike to be obvious, in 50 bins the probability would be $\lesssim 2\%$ and in 20 bins $\lesssim 5\%$. Based on these considerations and Figure 4.7 & Table 4.1, the only the redshift spike at $z \sim 1.3$ seem to be significant in the TOOT00 sample. The two objects in that redshift bin have a velocity difference of 2,400 km/s, suggesting they are not in the same group or cluster. Their spatial separation on the sky ($\sim$ 48 Mpc), suggests that they might be members of a supercluster (Brand et al. 2003). We conclude, thus, that the $z \sim 1.3$ redshift spike is possibly real and due to large-scale structure. The other redshift spikes are probably not significant, since the probability is greater than the minimum required value in the smaller redshift bins.

From Figure 4.8–a and Table 4.2 it can be seen that the $z \sim 0.45$, 0.65, 0.9, 1.3 & 2.7 spikes are prominent in the SXDS sample, but the photometric redshifts contribute more to the neighbour redshift bins as seen in Figure 4.8–b. We believe that only the redshift spikes at $z \sim 0.65$ & 2.7 might be significant, since the probability (Table 4.2) of them being significant is much less that 0.01. At $z \sim 0.65$ there are two objects (sxds_0001 & sxds_0028) with a velocity difference of 300 km/s, but these objects are $\approx$ 36 Mpc away from each other. Similarly, at $z \sim$ 2.7, there are two objects (sxds_0009 & sxds_0035) with velocity difference of 600 km/s, but they are $\sim$ 13 Mpc away from each other. For both cases, the velocity information suggests that they could be in the same group or cluster, but their spatial distance suggests they are too far away from each other for this to be the case. Nevertheless, we believe that they might be tracing large-scale structure (e.g. Brand et al. 2003). From Table 4.2 we conclude that none of the other redshift spikes are real.

If more spectroscopic redshifts were available in the SXDS sample, the result might favour the possible redshift spikes shown. As a further check we investigate these redshift spikes by calculating the probability whether they are significant or not. For that we use two samples of 100-simulated, randomly selected, areas from S^3-SEX simulation that are 'almost independent' to each other, and are equal to the TOOT00 and the SXDS sky areas respectively, at the relevant frequency and flux density limit of each survey. The 100-simulated sky areas are not completely independent but there is some overlap in some of them, as can be seen in Figure 4.3. Table 4.3 presents basic statistics on the 100-simulated sky areas. In Chapter 3 it was shown

Table 4.1: Probability for redshift spikes in the TOOT00 redshift distribution. The minimum probability for three redshift bins (100, 50 and 20) is shown, as well as the probability calculated only for objects with spectroscopic redshifts. There is a minimum of 2 objects per redshift interval presented. Note: for binning of dz = 0.25, the redshift range shown in each column is adjusted to the bin-size.

Redshift bins	0.28< z <0.33 Prob	0.55< z <0.60 Prob	0.90< z <0.95 Prob	1.325< z <1.375 Prob	1.38< z <1.43 Prob	2.52< z <2.57 Prob
100	0.004	0.038	0.017	0.0003	0.024	0.012
$z_{\rm spec}$	0.004	0.038	0.074	0.0003	0.125	0.012
50	0.038	0.017	0.775	0.005	0.005	0.051
$z_{\rm spec}$	0.038	0.179	0.775	0.005	0.005	0.051
20	0.022	0.159	0.310	0.010	0.014	0.825
$z_{\rm spec}$	0.022	0.159	0.689	0.038	0.038	0.825

Table 4.2: Probability for redshift spikes in the SXDS redshift distribution. The minimum probability for three redshift bins (100, 50 and 20) is shown, as well as the probability calculated only for objects with spectroscopic redshifts. There is a minimum of 2 objects per redshift interval presented. Note: for binning of dz = 0.25, the redshift range shown in each column is adjusted to the bin-size.

Redshift bins	0.425< z <0.475 Prob	0.625< z <0.675 Prob	0.85< z <0.90 Prob	1.30< z <1.35 Prob	2.70< z <2.75 Prob
100	0.148	0.002	0.080	0.005	0.002
$z_{\rm spec}$	0.148	0.002	0.080	0.031	0.027
50	0.155	0.015	0.853	0.010	0.012
$z_{\rm spec}$	0.155	0.015	0.853	0.143	0.083
20	0.808	0.062	0.746	0.118	0.058
$z_{\rm spec}$	0.808	0.062	0.746	0.761	0.176

that the mean number of objects predicted by the S^3-SEX simulation in a 0.0015-sr sky area is $\sim 40 \pm 9$, which is within the errors of the observed number (47) of the TOOT00 sample. Similarly, the simulated mean number of objects in a 0.0002-sr sky area is $\sim 39 \pm 6$, which is in agreement with the number of sources (37) in the SXDS sky area.

Tables 4.8 & 4.9 in Appendix C (Section 4.6) present the minimum probability for redshift spikes for 100 almost independent S^3-SEX simulated areas (see Figure 4.3) equal to the TOOT00 and the SXDS sky areas respectively at a binning of 100, 50 and 20 redshift bins. The fact that we get some extremely small probabilities (e.g. $\sim 10^{-15}$) for redshift spikes can be explained by clustering in the simulation. For example, field 57 in Figure 4.3–a has a redshift spike at $z = 1.475$ with 23 objects, and field 67 in Figure 4.3–b, that has a redshift spike at $z = 1.575$ with 10 objects. Finding such redshift spikes in simulations is not unusual, since super-clusters of galaxies ~ 100 Mpc across have been found in real surveys (e.g. Brand et al.

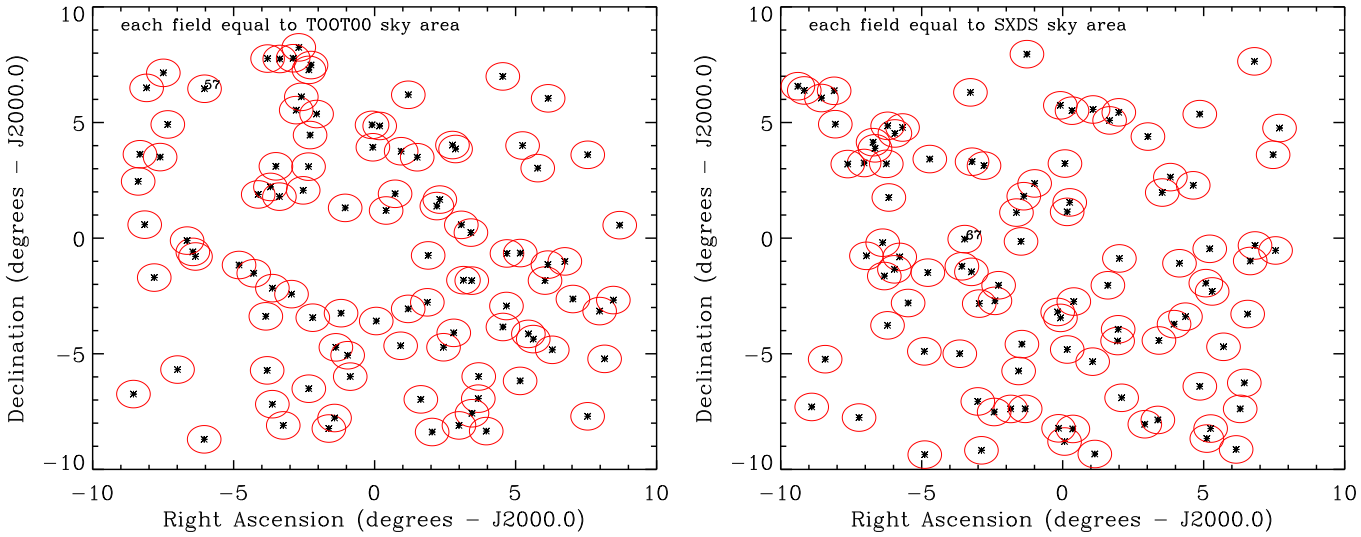

Figure 4.3: Coordinates of the 100 S^3-SEX simulated, randomly-selected, fields. **a) Left:** Coordinates of the 100-simulated sky areas equal to the TOOT00 sky area. **b) Right:** Coordinates of the 100-simulated sky areas equal to the SXDS sky area.

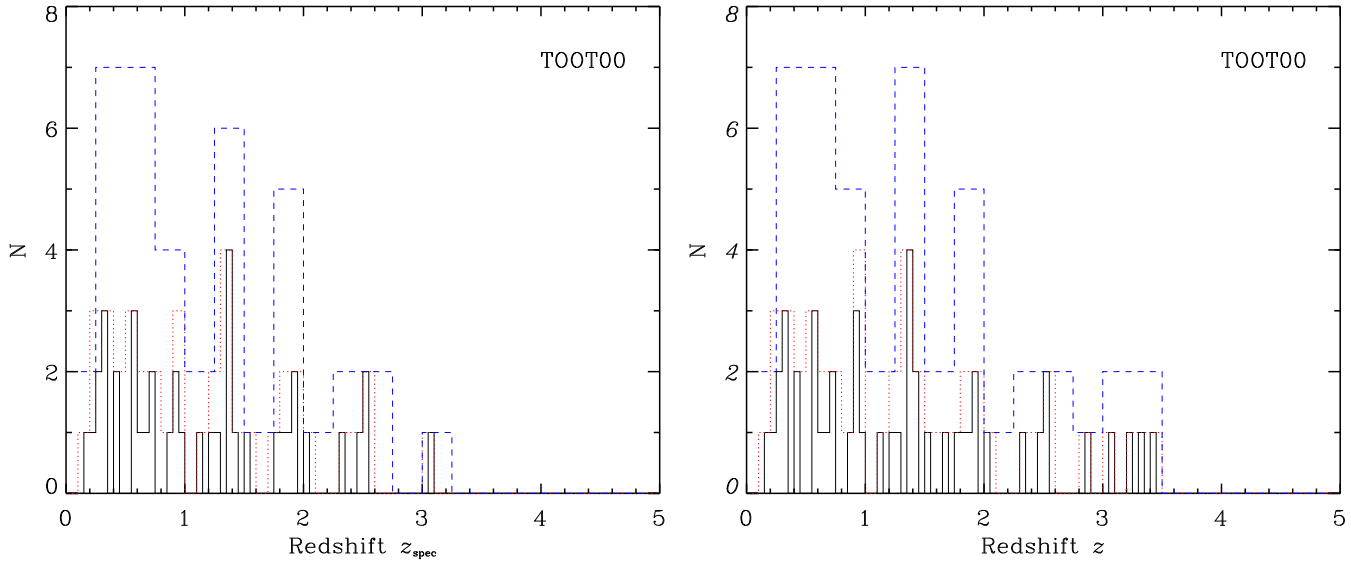

Figure 4.4: Histogram of redshift distribution of the TOOT00 radio sources. **a) Left**: Histogram of the 40 TOOT00 objects with spectroscopic redshift. **b) Right**: Histogram of the 47 TOOT00 radio sources including the photometric redshifts. In both graphs, the black solid line shows binning on the redshift axis of dz = 0.05 (100 redshift bins), the red dotted line denotes binning of dz = 0.1 (50 redshift bins) and the blue dashed line denotes binning of dz = 0.25 (20 redshift bins).

2003). In the TOOT00 sample, the probability of finding a redshift spike at $z \sim 1.3$ in 100 redshift bins, on the assumption of no clustering, is 0.0003 (Table 4.1). Table 4.8 shows that $\sim 55\%$ of the 100-simulated areas have probability equal to or greater than this value showing that clustering can generate such spikes. Similarly, in the SXDS sample the probability of finding a redshift spike at $z \sim 0.65$ in 100 redshift bins, on the assumption of no clustering, is 0.002 (Table 4.2). From Table 4.9 it can be seen that $\sim 1\%$ of the 100-simulated areas have

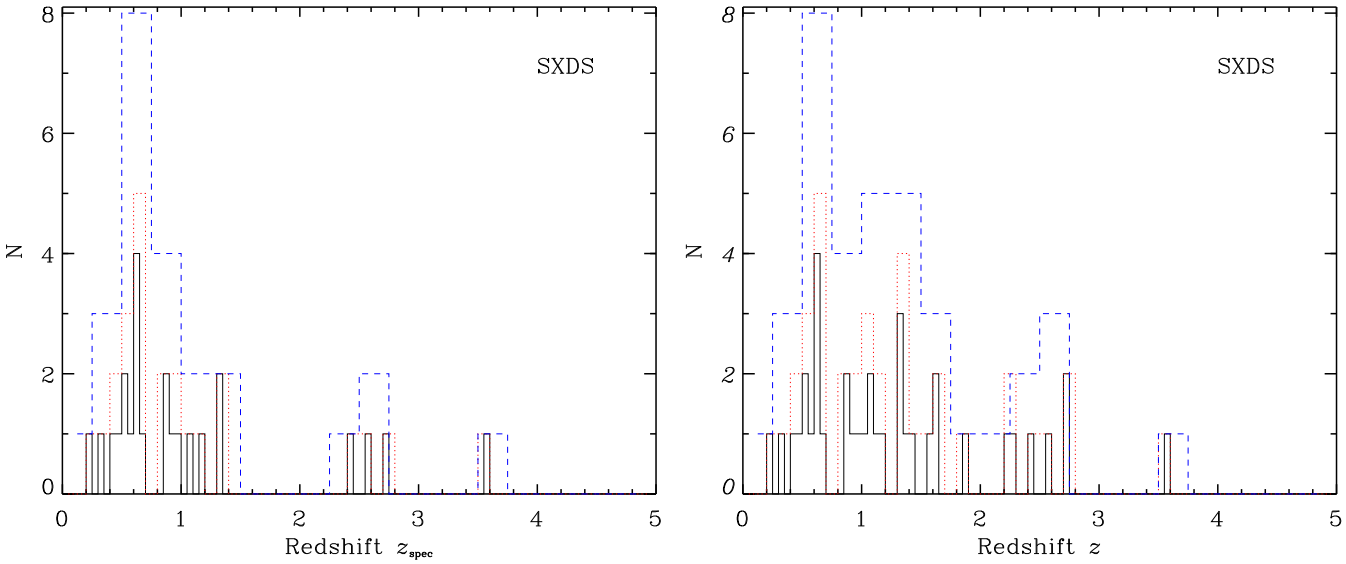

Figure 4.5: Histogram of redshift distribution of the SXDS radio sources. **a) Left**: Histogram of the 24 SXDS objects with spectroscopic redshift. **b) Right**: Histogram of the 37 SXDS radio sources including photometric redshifts. In both graphs, the black solid line shows binning on the redshift axis of dz = 0.05 (100 redshift bins), the red dotted line denotes binning of dz = 0.1 (50 redshift bins) and the blue dashed line denotes binning of dz = 0.25 (20 redshift bins).

Table 4.3: Basic statistics on the 100 S^3-SEX simulated sky areas equal to the TOOT00 and the SXDS sky areas and with appropriate frequency and flux density selection criteria. **Column 1** shows the sample the 100 S^3-SEX simulations are compared to. **Column 2** gives the TOOT00 or the SXDS sky area in steradians, that the 100-simulated sky areas are equal to. **Columns 3 & 4** give the minimum and maximum number of objects in the simulations. **Column 5** gives the median number of objects in the 100 S^3-SEX simulations. **Column 6** gives the mean number of objects in the 100 sky areas, and **Column 7** gives the standard deviation.

Name	SKY AREA ($\times 10^{-3}$ sr)	min $N_{\rm obj}$	max $N_{\rm obj}$	median $N_{\rm obj}$	mean $N_{\rm obj}$	STDEV
S^3-SEX/TOOT00	1.5	28	76	39.0	40.1	8.82
S^3-SEX/SXDS	0.2	24	58	39.0	38.9	5.86

spikes of probability equal or greater than this value, hinting that perhaps the simulation has too much clustering related to the real Universe (see Wilman et al. 2008 for discussion on the limitations of the simulation). These results verify the fact that the real data look like the simulation with clustering. We note that we haven't intercepted any large overdensities, i.e. superclusters, in our two real data samples.

These results add to the above result that in the TOOT00 radio-source sample the redshift spike at $z \sim 1.3$ might be significant, while in the SXDS sample the $z \sim 0.65$ & 2.7 redshift spikes are significant. Note that high-redshift peaks in SXDS may only be significant because the extrapolation of the high-redshift population is inaccurate[4]. The fact that the photometric

[4]At lower flux densities simulations are less accurate, since that requires larger extrapolations.

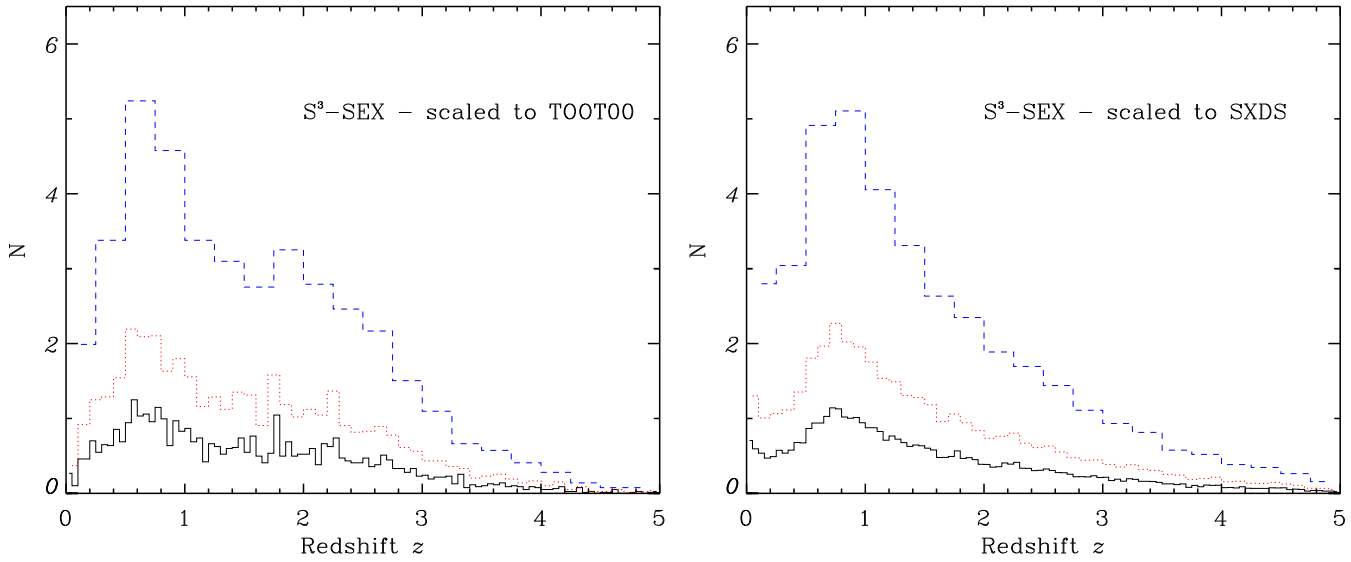

Figure 4.6: Histogram of redshift distribution of the S^3-SEX simulation. **a) Left**: Histogram of the S^3-SEX simulation scaled down to the TOOT00 sky area of 0.0015 sr and for a flux density limit of 100 mJy at 151 MHz. **b) Right**: Histogram of the S^3-SEX simulation scaled down to the SXDS sky area of 0.0002 sr and for a flux density limit of 2 mJy at 1.4 GHz. In both graphs, the black solid line shows binning on the redshift axis of dz = 0.05 (100 redshift bins), the red dotted line denotes binning of dz = 0.1 (50 redshift bins) and the blue dashed line denotes binning of dz = 0.25 (20 redshift bins).

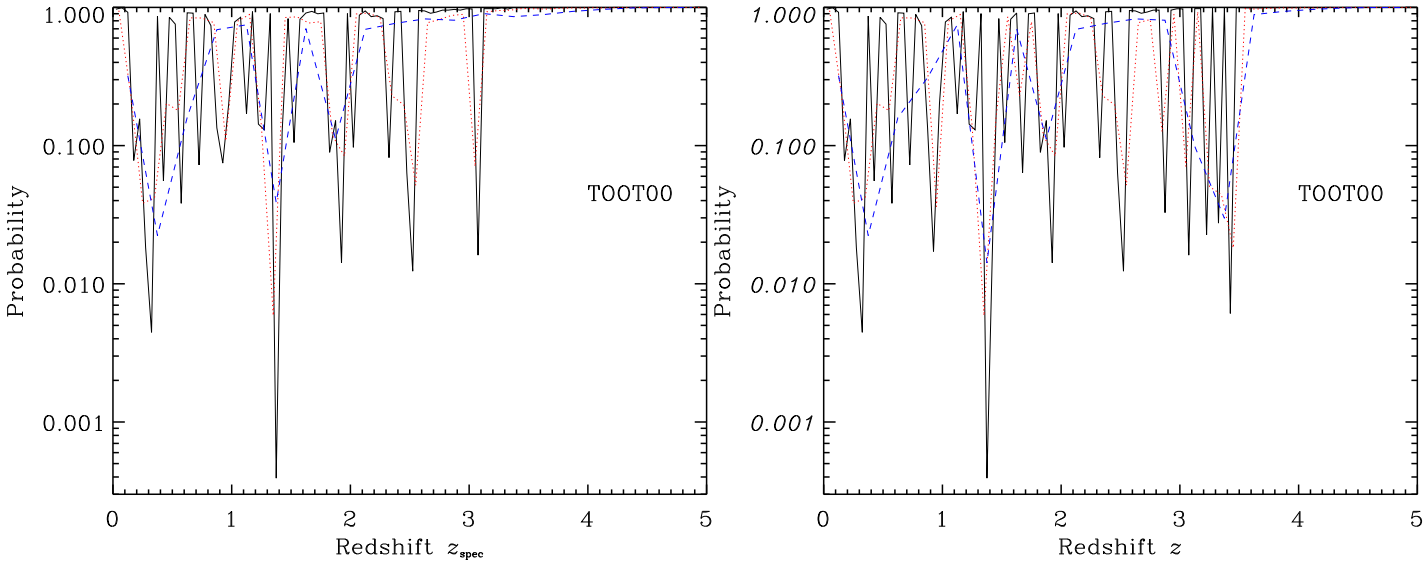

Figure 4.7: Comparison of the TOOT00 redshift distribution to the S^3-SEX simulation using Poisson statistics: The graphs show the probability that the number of objects per redshift bin is smaller than the observations given the simulation (if the number of objects in the data is less than the those in the simulation) or the number of objects per redshift bin is larger than the observations given the simulation (if the number of objects is the data is larger the those in the simulation). **a) Left**: Only the 40 objects with spectroscopic redshifts are taken into account. **b) Right**: All 47 objects are taken into account. In both plots, the black solid line shows binning on the redshift axis of dz = 0.05, the red dotted line denotes binning of dz = 0.1 and the blue dashed line denotes binning of dz = 0.25.

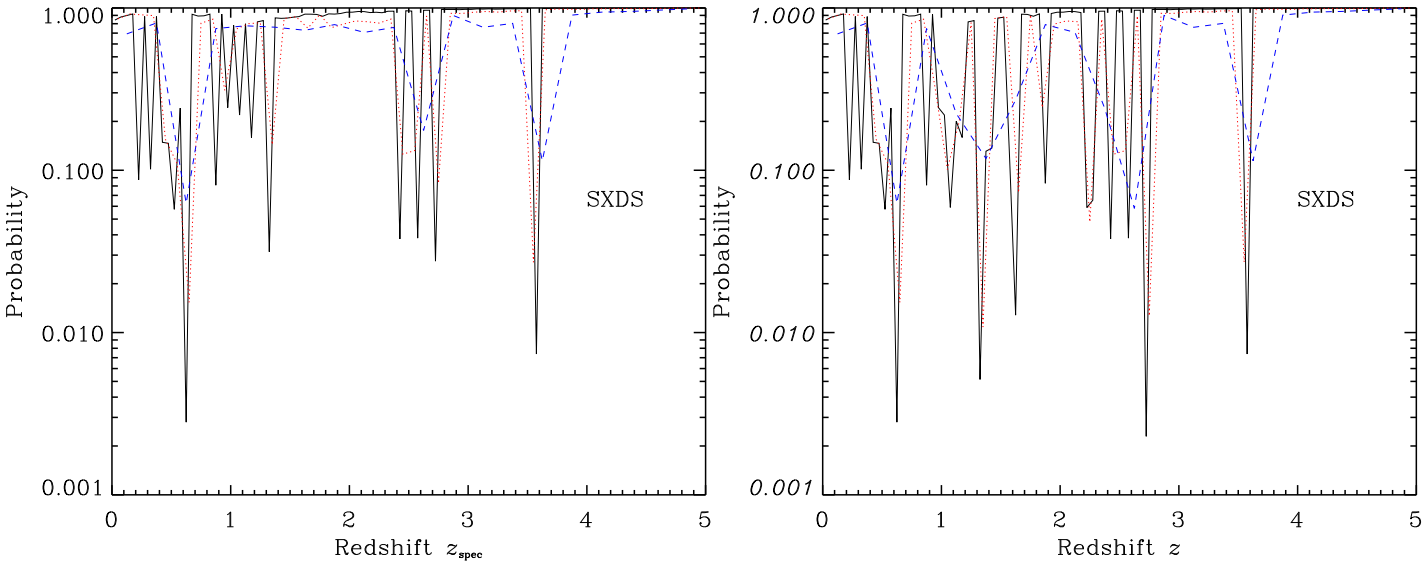

Figure 4.8: Comparison of the SXDS redshift distribution to the S^3-SEX simulation using Poisson statistics: The graphs show the probability that the number of objects per redshift bin is smaller than the observations given the simulation (if the number of objects in the data is less than the those in the simulation) or the number of objects per redshift bin is larger than the observations given the simulation (if the number of objects is the data is larger the those in the simulation). **a) Left**: Only the 24 objects with spectroscopic redshifts are taken into account. **b) Right**: All the 37 objects are taken into account. In both plots, the black solid line shows binning on the redshift axis of dz = 0.05, the red dotted line denotes binning of dz = 0.1 and the blue dashed line denotes binning of dz = 0.25.

redshifts alter the outcome of Figure 4.8 implies that the significance of the redshift spikes might change if the photometric redshifts get replaced by the spectroscopic ones, particularly in the SXDS sample.

4.4.1 $V/V_{\rm max}$ test

A $V/V_{\rm max}$ test is performed on both TOOT00 and SXDS radio-source samples in order to investigate the possibility of comoving density evolution with distance. The comoving volume V for a flat Universe is given by (e.g. Peacock 1999):

$$V(z) = \frac{4\pi}{3}\left(\frac{c}{H_0}\int_0^z \frac{dz'}{\sqrt{((1+z)^2(1+\Omega_0 z) - z(2+z)\Omega_\Lambda)}}\right)^3, \qquad (4.1)$$

where the adopted cosmology (see Section 4.1) was used in the calculations.

For both samples we calculated the volume V included by each object at the redshift of the source, and the maximum volume $V_{\rm max}$ it would occupy given a maximum redshift at the flux density limit of each sample (100 mJy at 151 MHz for the TOOT00 and 2 mJy at 1.4 GHz for the SXDS)[5]. The mean $V/V_{\rm max}$ value for a uniform distribution and standard error for a set of

[5]Both V and $V_{\rm max}$, were calculated using the radio spectral indices of each source as in Tables 4.6 & 4.7.

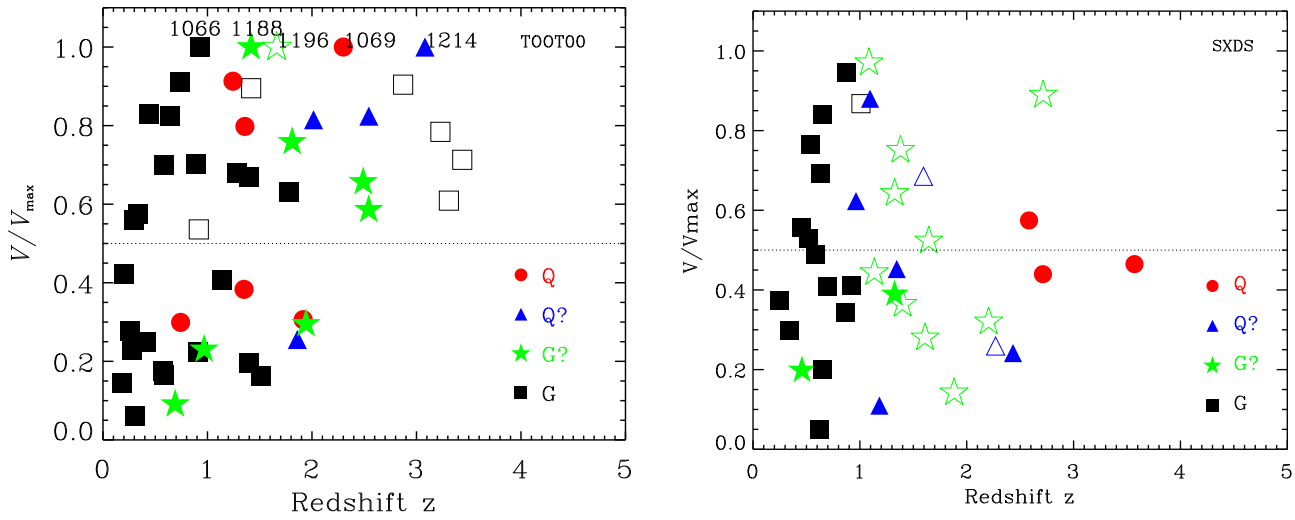

Figure 4.9: $V/V_{\rm max}$ test for the 47 TOOT00 (**a-Left**) and the 37 SXDS (**b-Right**) radio sources. Symbols indicate optical classification: red circles stand for Q, blue triangles denote Q?, green stars denote G? and black squares denote G radio sources; filled symbols denote objects with spectroscopic redshift and open symbols stand for objects with photometric redshift. The horizontal line denotes a mean $< V/V_{\rm max} > = 0.5$ for a uniform distribution. The spectral indices of each source (see Table 4.6 & Table 4.7 for the TOOT00 and SXDS respectively) were used in the calculation of $z_{\rm max}$.

n observations is (e.g. Peacock 1999):

$$\left\langle \frac{V}{V_{\rm max}} \right\rangle = 0.5 \pm (12n)^{-1/2}. \tag{4.2}$$

Figure 4.9–a presents the $V/V_{\rm max}$ test for the TOOT00 radio sources. The mean value is 0.6 ± 0.04, where for the quasars $< V/V_{\rm max} > = 0.66 \pm 0.09$ ($\sim 0.60 \pm 0.12$ if we include only Q objects) and for galaxies $< V/V_{\rm max} > = 0.54 \pm 0.05$ ($\sim 0.55 \pm 0.05$ if we include only G objects). These results indicate that for the TOOT00 objects $< V/V_{\rm max} > \approx 0.6$, while for quasars only $< V/V_{\rm max} > \approx 0.7$, suggesting evolution.

The $V/V_{\rm max}$ test for the SXDS sample is shown in Figure 4.9–b. The mean $< V/V_{\rm max} > \simeq 0.50 \pm 0.05$, where for quasars $< V/V_{\rm max} > = 0.47 \pm 0.09$ (0.49 ± 0.17 when excluding Q? objects) and for galaxies $< V/V_{\rm max} > = 0.51 \pm 0.06$ (0.52 ± 0.07 when excluding G? objects). These values suggest that the SXDS sample has $< V/V_{\rm max} > \approx 0.5$ and thus shows no evolution.

Tables 4.4 & 4.5 present a banded $V/V_{\rm max}$ test (e.g. Willott et al. 2001b) for the TOOT00 and SXDS objects, respectively, in different redshift intervals and radio-luminosity range. The banded $V/V_{\rm max}$ test, is a generalised $V/V_{\rm max}$ test which calculates the mean $V/V_{\rm max}$ restricting the analysis to $z > z_0$ at several values of z_0, hence the evolution below z_0 is masked out of the analysis. Thus the value to calculate is:

$$\frac{V - V_0}{V_{\rm max} - V_0}, \tag{4.3}$$

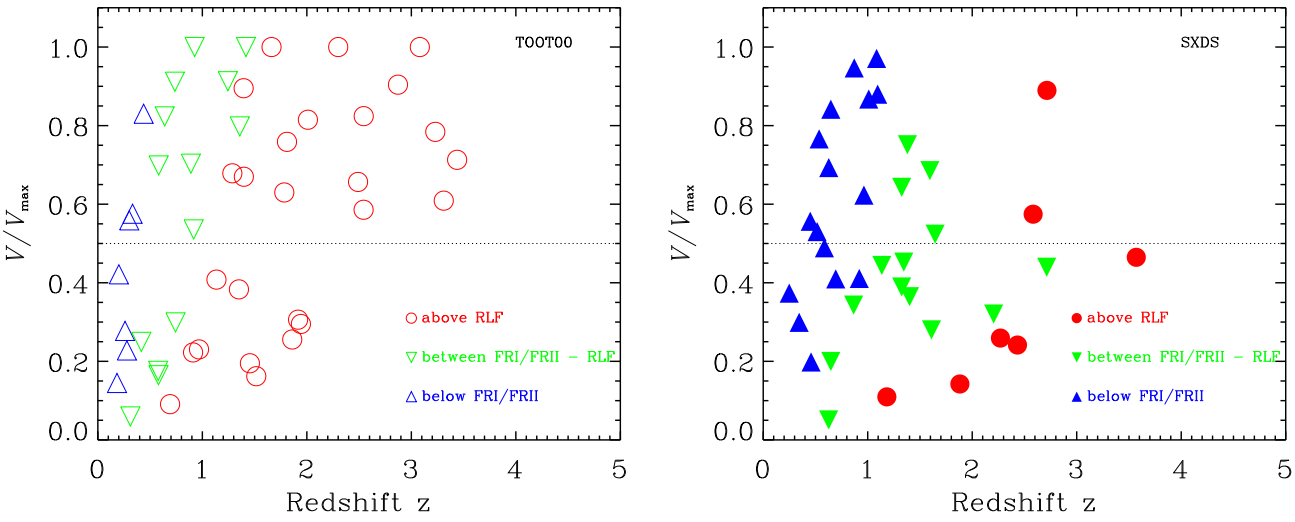

Figure 4.10: (**a) Left**) $V/V_{\rm max}$ test for the TOOT00. Symbols: red circles denote objects with radio luminosity above the RLF break at 151 MHz ($\log_{10}(L_{151\rm MHz}/[\rm WHz^{-1}sr^{-1}])$ = 26.0); blue triangles denote radio sources below the FRI/FRII divide at 151 MHz ($\log_{10}(L_{151\rm MHz}/[\rm WHz^{-1}sr^{-1}])$ = 25.0); green upside-down triangles denote objects between the RLF break and FRI/FRII divide in radio luminosity at 151 MHz. (**Right**) $V/V_{\rm max}$ test for the SXDS objects. Symbols: red circles denote objects with radio luminosity above the RLF break at 1.4 GHz ($\log_{10}(L_{1.4\rm GHz}/[\rm WHz^{-1}sr^{-1}])$ = 25.3); blue triangles denote radio sources below the FRI/FRII divide at 1.4 GHz ($\log_{10}(L_{1.4\rm GHz}/[\rm WHz^{-1}sr^{-1}])$ = 24.3); green upside-down triangles denote objects between the RLF break and FRI/FRII divide in radio luminosity at 1.4 GHz. In both plots, the dotted horizontal line shows the $V/V_{\rm max}$ = 0.5 value of no evolution with distance.

where V_0 is the volume enclosed at redshift z_0.

The main difference between TOOT00 and SXDS samples seen in Tables 4.4 & 4.5, also illustrated in Figure 4.10, is that objects above the FRI/FRII break in the TOOT00 sample have $< V/V_{\rm max} > \approx 0.6$ suggesting they evolve with distance, while this is not the case for the SXDS objects in the same radio luminosity range. Furthermore, the TOOT00 radio sources show positive evolution above the RLF break, while this is not the case for the SXDS objects. We have to note though, that these results might be affected by the simplistic spectral indices used and the number of high luminosity objects with photometric redshifts in the SXDS sample.

These results agree with previous studies, where it has been shown that low-luminosity radio sources in a low-frequency-selected radio sample evolve differently from FRII objects (e.g. Clewley & Jarvis 2004). In particular, Laing, Riley, & Longair (1983) found that objects at redshifts $z \gtrsim 0.2$ with luminosities at 178 MHz above the FRI/FRII break show strong density evolution, while for objects at $z < 0.1$ below the FRI/FRII break no signs of evolution are evident.

Table 4.4: Banded $V/V_{\rm max}$ test for various sub-samples in the TOOT00 sample, and for redshifts $z_0 > 0$ (**Column 3**), $z_0 > 1$ (**Column 4**) and $z_0 > 2$ (**Column 5**); the numbers in brackets give the number of objects in the sub-sample. **Column 1** shows different sub-samples that the mean banded V/V_{max} and associated error (based on Eqns 4.1, 4.3 & 4.2) was calculated for; **line 1** gives statistics for the whole TOOT00 sample; **line 2** gives statistics for Q & Q? objects; **line 3** gives statistics for Q objects; **line 4** gives the statistics for G & G? objects; **line 5** gives statistics for G objects; **line 6** gives the banded $< V/V_{\rm max} >$ for objects with radio luminosity at 151 MHz below the FRI/FRII break, $\log_{10}(L_{151\rm MHz}/[\rm WHz^{-1}sr^{-1}]) < 25$; **line 7** gives statistics for objects between the FRI/FRII and RLF breaks, $25 < \log_{10}(L_{151\rm MHz}/[\rm WHz^{-1}sr^{-1}]) < 26$; **line 8** gives statistics for objects with radio luminosity at 151 MHz above the RLF break, $\log_{10}(L_{151\rm MHz}/[\rm WHz^{-1}sr^{-1}) > 26$; and **line 9** gives the banded $< V/V_{\rm max} >$ for objects with radio luminosity at 151 MHz above $\log_{10}(L_{151\rm MHz}/[\rm WHz^{-1}sr^{-1}) > 27$.

	Sub-samples	$< \frac{V-V_{z_0=0}}{V_{\rm max}-V_{z_0=0}} >$ $z_0 > 0$	$< \frac{V-V_{z_0=1}}{V_{\rm max}-V_{z_0=1}} >$ $z > 1$	$< \frac{V-V_{z_0=2}}{V_{\rm max}-V_{z_0=2}} >$ $z > 2$
1	All TOOT00	0.56 ± 0.04 (47)	0.59 ± 0.06 (26)	0.58 ± 0.09 (10)
2	Q & Q?	0.66 ± 0.09 (10)	0.63 ± 0.10 (9)	0.66 ± 0.14 (4)
3	Q	0.62 ± 0.12 (6)	0.58 ± 0.13 (5)	1.00 ± 0.29 (1)
4	G & G?	0.54 ± 0.05 (37)	0.57 ± 0.07 (17)	0.52 ± 0.12 (6)
5	G	0.53 ± 0.05 (29)	0.51 ± 0.07 (11)	0.62 ± 0.14 (4)
6	$\log_{10}(L_{151}) < 25$	0.43 ± 0.11 (7)		
7	$25 < \log_{10}(L_{151}) < 26$	0.60 ± 0.08 (14)	0.82 ± 0.17 (3)	
8	$\log_{10}(L_{151}) > 26$	0.58 ± 0.06 (26)	0.56 ± 0.06 (23)	0.58 ± 0.09 (10)
9	$\log_{10}(L_{151}) > 27$	0.45 ± 0.11 (7)	0.40 ± 0.11 (7)	0.56 ± 0.17 (3)

Table 4.5: Banded $V/V_{\rm max}$ test for various sub-samples in the SXDS sample, and for redshifts $z_0 > 0$ (**Column 3**), $z_0 > 1$ (**Column 4**) and $z_0 > 2$ (**Column 5**); the numbers in brackets give the number of objects in the sub-sample. **Column 1** shows the sub-samples that the mean banded V/V_{max} and associated error (based on Eqns 4.1, 4.3 & 4.2) was calculated for; **line 1** gives statistics for the whole TOOT00 sample; **line 2** gives statistics for Q & Q? objects; **line 3** gives the $< V/V_{\rm max} >$ for Q objects; **line 4** gives statistics for G & G? objects; **line 5** gives statistics for G objects; **line 6** gives the banded $< V/V_{\rm max} >$ for objects with radio luminosity at 1.4 GHz below the FRI/FRII break, $\log_{10}(L_{1.4\rm GHz}/[\rm WHz^{-1}sr^{-1}]) < 24.3$; **line 7** gives statistics for objects between the FRI/FRII and RLF breaks, $24.3 < \log_{10}(L_{1.4\rm GHz}/[\rm WHz^{-1}sr^{-1}]) < 25.3$; **line 8** gives the banded $< V/V_{\rm max} >$ for objects with radio luminosity at 1.4 GHz above the RLF break, $\log_{10}(L_{1.4\rm GHz}/[\rm WHz^{-1}sr^{-1}]) > 25.3$; and **line 9** gives statistics for objects with radio luminosity at 1.4 GHz above $\log_{10}(L_{1.4\rm GHz}/[\rm WHz^{-1}sr^{-1}]) > 26.3$.

	Sub-samples	$< \frac{V-V_{z_0=0}}{V_{\rm max}-V_{z_0=0}} >$ $z_0 > 0$	$< \frac{V-V_{z_0=1}}{V_{\rm max}-V_{z_0=1}} >$ $z > 1$	$< \frac{V-V_{z_0=2}}{V_{\rm max}-V_{z_0=2}} >$ $z > 2$
1	All SXDS	0.50 ± 0.04 (37)	0.37 ± 0.06 (21)	0.26 ± 0.11 (7)
2	Q & Q?	0.47 ± 0.09 (10)	0.35 ± 0.10 (9)	0.20 ± 0.13 (5)
3	Q	0.49 ± 0.17 (3)	0.45 ± 0.17 (3)	0.29 ± 0.17 (3)
4	G & G?	0.51 ± 0.06 (27)	0.37 ± 0.08 (12)	0.41 ± 0.20 (2)
5	G	0.52 ± 0.07 (15)	0.12 ± 0.29 (1)	
6	$\log_{10}(L_{1.4}) < 24.3$	0.60 ± 0.06 (21)		
7	$24.3 < \log_{10}(L_{1.4}) < 25.3$	0.39 ± 0.09 (11)	0.32 ± 0.09 (10)	
8	$\log_{10}(L_{1.4}) > 25.3$	0.27 ± 0.13 (5)	0.22 ± 0.12 (5)	0.16 ± 0.17 (3)
9	$\log_{10}(L_{1.4}) > 26.3$	0.24 ± 0.29 (1)	0.21 ± 0.29 (1)	0.08 ± 0.29 (1)

Table 4.6: Results from the analysis on the 47 TOOT00 radio sources: **Column 1** shows the name of the object. **Column 2** gives the optical classification and **Column 3** the radio-optical classification (see Table 3.3). **Columns 4 & 5** give the redshift and type of redshift respectively; 's' denotes spectroscopic redshift, 'p-Kz' denotes photometric redshift calculated from the $K_{\rm W} - z$ relation of Willott et al. (2003; see Section 3.3.1 in Chapter 3). **Column 6** gives the maximum redshift the TOOT00 radio source would have given the flux density limit of the TOOT00 sample, 100 mJy at 151 MHz; the value of α shown in **Column 9** was used in the calculation. **Column 7** gives the base-10 logarithm of the radio luminosity at 151 MHz. **Column 8** gives the $V/V_{\rm max}$ values for the TOOT00 objects. **Column 9** gives the radio spectral index $\alpha^{\rm 151MHz}_{\rm 1.4GHz}$.

(1)	(2)	(3)	(4)	(5)	(6)	(7)	(8)	(9)
Name	OpCl	R-OpCl	z	type-z	$z_{\rm max}$	$\log_{10}($ $L_{\rm 151MHz}/$ $[{\rm WHz^{-1}sr^{-1}}])$	$V/V_{\rm max}$	$\alpha^{1.4}_{151}$
TOOT00_1140	G	FRI	0.911?	s	1.935	26.21	0.22	0.75
TOOT00_1099	G	FRI?	1.397?	s	1.730	26.21	0.67	1.01
TOOT00_1125	Q	FRII-Q	1.916	s	4.516	27.17	0.31	0.94
TOOT00_1143	G	FRI	0.438	s	0.470	24.87	0.83	1.32
TOOT00_1233	Q[a]	Q-F	1.244	s	1.301	25.66	0.91	0.34
TOOT00_1022	G	CSS	2.872	p-Kz	3.092	26.77	0.90	0.92
TOOT00_1204	G	FRI	0.6395	s	0.692	25.14	0.82	0.60
TOOT00_1235	Q	Q-F?	0.743	s	1.279	25.72	0.30	0.55
TOOT00_1224	G	CSS	3.438	p-Kz	4.597	27.07	0.71	0.79
TOOT00_1291	G	FRII?	0.917	p-Kz	1.223	25.78	0.54	0.83
TOOT00_1107	G	FRI	0.300	s	0.371	24.65	0.56	1.52
TOOT00_1180	G?	FRII?	1.810	s	2.132	26.44	0.76	1.01
TOOT00_1027	G	CSS	0.890	s	1.042	25.13	0.70	-0.73
TOOT00_1195	G	FRII	1.418	p-Kz	1.502	26.05	0.90	0.93
TOOT00_1069	Q	CSS-Q	2.300	s	2.300	26.76	1.00	1.49
TOOT00_1094	G	CSS	1.516?	s	5.569	27.43	0.16	1.00
TOOT00_1149	G	FRI	0.260	s	0.415	24.70	0.28	1.04
TOOT00_1298	G	FRI	1.287?	s	1.571	26.00	0.68	0.75
TOOT00_1200	G?	FRII	0.691	s	2.243	26.38	0.09	0.79
TOOT00_1215	G	FRI?	0.278	s	0.480	24.84	0.23	0.96
TOOT00_1240	G?	FRII	2.543?	s	3.795	26.89	0.59	1.29
TOOT00_1289	G	FRII	1.784?	s	2.360	26.54	0.63	1.00
TOOT00_1072	G	FRII	0.577	s	1.222	25.75	0.18	0.74
TOOT00_1134	G	FRI	0.311	s	0.941	25.52	0.06	0.87
TOOT00_1244	Q	Q-F?	1.358	s	1.526	25.92	0.80	0.62
TOOT00_1066	G	FRII	0.926?	s	0.926	25.50	1.00	0.87
TOOT00_1261	Q?	FRII-Q?	2.544	s	2.912	26.78	0.82	1.03
TOOT00_1252	G	FRII?	3.229	p-Kz	3.930	27.06	0.78	0.98
TOOT00_1214	Q?	FRII-Q?	3.081	s	3.081	26.80	1.00	0.98
TOOT00_1152	G	FRII	3.310	p-Kz	5.106	27.24	0.61	0.88
TOOT00_1129	Q?	FRII-Q?	1.860	s	5.110	27.21	0.26	0.84
TOOT00_1090	G	FRI	0.201	s	0.273	24.26	0.42	0.88
TOOT00_1267	G?	FRII	0.968	s	2.057	26.30	0.23	0.80
TOOT00_1188	G?	FRII	1.417	s	1.417	25.94	1.00	0.86
TOOT00_1196	G?	FRI?	1.662	p-Kz	1.662	26.64	1.00	> 2.11
TOOT00_1173	G	FRI	0.332	s	0.407	24.64	0.58	0.77
TOOT00_1228	G	CSS	1.135?	s	1.802	26.06	0.41	0.57
TOOT00_1034	G	FRI	0.580	s	1.270	25.76	0.16	0.66
TOOT00_1255	G	FRII?	0.582	s	0.672	25.12	0.70	0.64
TOOT00_1048	G?	FRII	1.943	s	4.778	27.23	0.30	0.94
TOOT00_1029	G	CSS	0.737	s	0.766	25.26	0.91	0.68
TOOT00_1115	G	FRI?	0.416	s	0.716	25.22	0.25	0.83
TOOT00_1132	G	FRI?	0.183	s	0.365	24.53	0.14	0.75
TOOT00_1250	Q	FRII?	1.350	s	2.321	26.44	0.38	0.85
TOOT00_1268	Q?	Q-F	2.015	s	2.287	26.17	0.81	0.34
TOOT00_1251	G?	FRII?	2.490	s	3.373	26.95	0.66	1.06
TOOT00_1203	G	FRII?	1.397	s	4.024	26.94	0.20	0.84

Table 4.7: Results from the analysis on the 37 SXDS radio sources: **Column 1** shows the name of the object. **Column 2** gives the optical classification (see Section 2.3.3) and **Column 3** the radio-optical classification (see Section 4.2). **Columns 4 & 5** give the redshift and type of redshift respectively; 's' denotes spectroscopic redshift and 'p-BC' stands for photometric redshift estimated from HyperZ (see Vardoulaki et al. 2008 for further discussion). **Column 6** gives the maximum redshift the SXDS radio source would have given the flux density limit of the SXDS sample, 2 mJy at 1.4 GHz; the value of α shown in **Column 9** was used in the calculation. **Column 7** gives the base-10 logarithm of the radio luminosity at 1.4 GHz. **Column 8** gives the $V/V_{\rm max}$ values for the SXDS objects. **Column 9** gives the radio spectral index from 1.4 GHz to 610 MHz or from 1.4 GHz to 325 MHz, which are marked with 'm'; estimated values are in brackets.

(1)	(2)	(3)	(4)	(5)	(6)	(7)	(8)	(9)
Name	OpCl	R-OpCl	z	type-z	$z_{\rm max}$	$\log_{10}($ $L_{1.4\rm GHz}/$ $[\rm WHz^{-1}sr^{-1}])$	$V/V_{\rm max}$	α
sxds_0001	G	FRI	0.626	s	2.814	25.04	0.05	1.03
sxds_0002	OQ	FRII	1.183	s	5.022	25.57	0.11	0.93
sxds_0003	OQ	FRII-Q?	2.433	s	9.083	26.39	0.24	1.17
sxds_0004	BL	COM-F	2.270	p-BC	7.212	25.38	0.26	0.34
sxds_0005	G?	CSS	1.610	p-BC	3.724	25.36	0.28	1.07
sxds_0006	G?	COM-F	1.882	p-BC	10.71	24.62	0.14	-0.65
sxds_0007	G?	FRII	1.325?	s	2.244	25.20	0.39	1.81
sxds_0008	SB	CSS	0.458	s	0.879	23.71	0.20	0.72
sxds_0009	Q	Q-F	3.570?	s	7.672	25.61	0.46	0.53
sxds_0010	G?	CSS?	1.400	p-BC	2.514	24.85	0.36	0.90
sxds_0011	G	FRI	0.647	s	1.322	24.15	0.20	(0.80)
sxds_0012	G	FRII	0.865	s	1.430	24.29	0.34	0.97
sxds_0013	Q	Q-F	2.713	s	5.400	24.96	0.44	0.08
sxds_0014	G?	COM-F	2.205	p-BC	5.413	24.51	0.32	-0.47
sxds_0015	G	FRI	0.344	s	0.542	23.31	0.30	1.23
sxds_0016	OQ	FRII-Q?	1.345?	s	2.082	24.73	0.45	1.04
sxds_0017	Q	FRII-Q	2.583	s	3.934	25.15	0.57	$0.68^{\rm m}$
sxds_0018	G	FRI	0.919	s	1.399	24.29	0.41	1.02
sxds_0019	G	FRI	0.694	s	1.019	23.88	0.41	(0.80)
sxds_0020	G?	FRI	1.135	p-BC	1.718	24.33	0.44	0.62
sxds_0021	G?	CSS	1.645	p-BC	2.421	24.80	0.52	0.87
sxds_0022	G	COM-F	0.248	s	0.355	22.76	0.37	0.40
sxds_0023	G	CSS	0.586	s	0.784	23.71	0.49	1.19
sxds_0024	G	FRI	0.516	s	0.663	23.55	0.53	1.30
sxds_0025	WQ	Q?-F	0.964	s	1.200	23.91	0.62	(0.40)
sxds_0026	G	FRI?	0.450	s	0.564	23.27	0.56	0.76
sxds_0027	OQ	Q?-F	1.595	p-BC	1.975	24.37	0.69	(0.40)
sxds_0028	G	COM-F	0.627?	s	0.728	23.45	0.69	0.46
sxds_0029	G?	COM-F	1.380	p-BC	1.603	24.12	0.75	0.27
sxds_0030	G	FRI?	0.535	s	0.594	23.31	0.77	0.71
sxds_0031	G?	COM-F	1.325	p-BC	1.670	24.15	0.64	0.24
sxds_0032	G	FRI	1.010	p-BC	1.078	24.13	0.87	1.41
sxds_0033	G	FRI	0.647	s	0.694	23.57	0.84	1.16
sxds_0034	OQ	CSS-Q?	1.095	s	1.163	24.00	0.88	0.72
sxds_0035	G?	COM-F	2.715	p-BC	2.951	24.19	0.89	-0.48
sxds_0036	G	COM-F	0.871	s	0.892	23.31	0.95	$<$ -0.77
sxds_0037	G?	COM-F	1.085	p-BC	1.100	23.83	0.97	(0.40)

4.5 Conclusions

This study focuses on the redshift distribution of the TOOT00 and the SXDS radio sources. Investigation of the probability for redshift spikes associated with large-scale structure, as well as simple testing for density evolution of the sample, lead to the following conclusions:

• Both TOOT00 and SXDS samples have redshift distributions that can be predicted well from the S^3-SEX simulation.

• The $z \sim 1.3$ redshift spike appears to be significant in the TOOT00 radio-source sample, and might be due to Large-Scale Structure.

• The $z \sim 0.65$ & 2.7 redshift spikes appear to be significant in the SXDS sample, and might be due to Large-Scale Structure.

• The TOOT00 radio sources show evolution with cosmological epoch from $z \sim 0.2$-3.6, where $< V/V_{\rm max} > \approx 0.8$ at $z \sim 3$, while the SXDS objects do not: $< V/V_{\rm max} > \approx 0.5$.

• Quasars in the TOOT00 sample display signs of evolution with distance ($< V/V_{\rm max} > \approx 0.7$), while galaxies do not appear to evolve so rapidly ($< V/V_{\rm max} > \approx 0.6$); any differences are barely significant.

• Both quasars and galaxies in the SXDS sample show no evolution with distance, since $< V/V_{\rm max} > \approx 0.5$.

• The lower radio luminosity radio-source population, here most directly probed by the SXDS objects, evolves less rapidly with cosmological distance than a higher radio luminosity population, here essentially the TOOT00 radio sources.

Appendix C

4.6 Results on the probability for redshift spikes in two samples of 100 S^3-SEX simulated sky areas equal to the TOOT00 and SXDS

This section presents detailed results from the calculation of the probability for redshift spikes in two samples of 100 almost independent simulations equal to the TOOT00 and the SXDS sky areas, respectively. Tables 4.8 & 4.9 present the minimum probability per redshift bin for redshift spikes in the 100-simulations given the S^3-SEX simulation, scaled to the TOOT00 and the SXDS sky areas respectively.

Table 4.8: : Minimum probability for redshift spikes in the 100-simulations with sky area equal to TOOT00 compared to the S^3-SEX simulation **Column 1** gives the number of the area. **Columns 2 & 3** give the minimum probability for a redshift spike(s) in 100 bins and the redshift respectively. **Columns 4 & 5** give the minimum probability for a redshift spike in 50 bins and the redshift spike(s) respectively. **Columns 6 & 7** give the minimum probability for a redshift spike in 20 bins and the redshift spike(s) respectively.

(1)	(2)	(3)	(4)	(5)	(6)	(7)
Number of area	MIN (prob) 100 bins	z_{100}	MIN (prob) 50 bins	z_{50}	MIN (prob) 20 bins	z_{20}
1	0.00004	1.275	0.00006	1.250	0.007	1.125
2	0.0003	4.275	0.001	4.250	0.008	4.375
3	0.00006	2.175	0.0001	2.150	0.016	0.125
4	0.004	0.075/3.775	0.016	3.750	0.063	3.875
5	0.001	4.025/4.625	0.001	4.650	0.002	4.625
6	0.001	3.225	0.003	4.350	0.008	4.375
7	0.0004	2.225	0.008	2.750	0.024	2.125
8	2E-09	2.175	1E-07	2.150	0.0006	2.125
9	0.001	1.625	0.002	1.650	0.024	2.125
10	2E-09	2.175	1E-07	2.150	0.0006	2.125
11	0.002	3.975	0.001	1.150	0.063	3.875
12	0.001	0.175	0.010	0.950	0.020	3.625
13	0.0006	2.125	0.002	3.650	0.020	3.625
14	0.002	3.975	0.005	2.050	0.024	2.125
15	0.002	4.325	0.003	2.850	0.008	4.375
16	1E-06	2.675	0.00004	2.650	0.00006	3.375
17	0.004	2.175	0.013	2.650	0.023	2.625
18	2E-09	2.175	1E-07	2.150	0.0006	2.125
19	0.0003	4.425	0.0003	4.450	0.008	4.375
20	0.001	3.125	0.009	3.150	0.041	0.625
21	0.020	3.125	0.044	3.350	0.098	3.125
22	0.003	3.825	0.008	3.850	0.018	0.875
23	0.002	4.325	0.003	4.350	0.008	4.375
24	0.002	3.975	0.012	3.950	0.063	3.875
25	0.0005	0.325	0.002	0.350	0.008	4.375
26	0.001	3.075	0.009	0.250	0.013	2.375
27	0.004	2.175	0.013	2.650	0.023	2.625
28	$<$ 1E-15	2.275	1E-14	2.250	3E-14	2.375
29	0.00002	1.525	0.0004	1.550	0.004	3.375
30	0.002	3.975	0.006	0.050	0.063	3.875
31	0.006	3.425	0.002	2.650	0.029	3.375
32	0.00003	2.075	0.001	3.750	0.005	3.125
33	0.0003	4.975	0.0007	4.950	0.002	4.875
34	0.001	4.075	0.004	4.050	0.032	4.125
35	8E-08	0.925	3E-06	0.950	0.006	2.625
36	0.0006	2.125	0.0007	2.150	0.063	3.875
37	0.0006	1.225	0.010	1.250	0.056	1.125
38	8E-08	0.925	3E-06	0.950	0.0002	0.875
39	1E-06	2.675	0.00004	2.650	0.0009	2.875
40	0.0003	4.825	0.0003	4.850	0.002	4.875
41	0.001	4.625	0.001	4.650	0.002	4.625
42	2E-09	2.175	1E-07	2.150	0.0006	2.125
43	0.004	3.525	0.001	3.550	0.002	3.625
44	2E-09	2.175	1E-07	2.150	0.0006	2.125
45	5E-07	2.175	0.00001	2.150	0.002	2.125
46	0.002	3.325	0.004	3.350	0.004	3.375
47	8E-05	4.575	0.0003	4.550	0.002	4.625
48	8E-05	4.525	0.0003	4.550	0.0006	2.125
49	0.0004	2.225	0.002	3.650	0.001	1.375
50	0.0003	4.275	0.001	4.250	0.008	4.375

Table 4.8: (continued)

(1)	(2)	(3)	(4)	(5)	(6)	(7)
Number of area	MIN (prob) 100 bins	z_{100}	MIN (prob) 50 bins	z_{50}	MIN (prob) 20 bins	z_{20}
51	0.004	1.775	0.022	1.750	0.047	1.875
52	0.001	2.975	0.002	2.950	0.018	2.875
53	0.00007	3.375	0.0003	3.350	0.004	3.375
54	0.001	4.075	0.004	4.050	0.002	4.125
55	0.001	4.025	0.004	4.050	0.002	4.125
56	0.0005	0.325	0.010	0.350	0.022	0.375
57	< 1E-15	1.475	< 1E-15	1.450	6E-15	1.375
58	0.00001	2.525	0.00002	2.550	0.002	4.625
59	0.001	4.125	0.003	1.950	0.032	4.125
60	0.002	0.275	0.009	0.250	0.063	3.875
61	0.00003	2.075	0.001	2.050	0.008	3.875
62	0.0003	4.275	0.001	4.250	0.008	4.375
63	0.001	4.075	0.003	2.850	0.018	2.875
64	0.0001	3.025	0.001	3.050	0.002	4.625
65	0.0003	4.425	0.0003	4.450	0.008	4.375
66	0.0004	2.225	0.002	2.250	0.064	2.125
67	0.0006	2.125	0.021	2.150	0.064	2.125
68	0.001	3.175	0.009	3.150	0.066	2.875
69	0.004	3.775	0.016	3.750	0.063	3.875
70	0.001	2.975	0.019	2.950	0.126	0.375/1.125
71	0.00001	2.525	0.00002	2.550	0.003	2.375
72	0.002	3.975	0.005	2.050	0.008	2.125
73	0.0003	4.275	0.001	4.250	0.0004	4.375
74	0.002	3.375	0.001	2.050	0.024	2.125
75	0.001	4.075	0.004	4.050	0.002	4.125
76	0.001	2.725	0.001	4.650	0.002	4.625
77	0.0003	2.075	0.005	2.050	0.008	2.125
78	0.003	1.275	0.002	1.250	0.063	3.875
79	0.001	4.125	0.010	4.150	0.032	4.125
80	0.00003	2.575	0.0007	4.950	0.002	4.875
81	0.0001	3.525	0.001	3.550	0.020	3.625
82	0.001	3.075	0.003	4.350	0.005	3.125
83	0.0003	4.975	0.0007	4.950	0.002	4.875
84	0.0003	2.075	0.005	2.050	0.005	3.125
85	0.004	1.775	0.022	1.750	0.047	1.875
86	0.002	4.325	0.003	4.350	0.008	4.375
87	0.001	1.925	0.003	4.350	0.008	4.375
88	0.0002	2.025	0.003	4.350	0.008	4.375
89	0.001	3.075	0.009	3.050	0.051	0.125
90	0.0008	2.425	0.0005	4.150	0.002	4.125
91	0.008	2.425	0.010	1.250	0.061	1.625
92	0.0003	4.975	0.0007	4.950	0.002	4.875
93	0.001	4.125	0.004	2.150	0.020	3.625
94	0.001	2.325	0.013	2.350	0.013	2.375
95	0.001	4.025/4.625	0.001	4.650	0.002	4.625
96	0.001	4.075	0.004	4.050	0.002	4.125
97	0.00003	2.575	0.0003	4.550	0.002	4.625/4.875
98	0.0006	2.125	0.0007	2.150	0.064	2.125
99	0.0001	0.775	0.005	0.750	0.007	0.875
100	0.00002	1.525	0.002	1.550	0.007	1.625

Table 4.9: Minimum probability for redshift spikes in the 100-simulations with sky area equal to SXDS compared to the S^3-SEX simulation: **Column 1** gives the number of the area. **Columns 2 & 3** give the minimum probability for a redshift spike(s) in 100 bins and the redshift respectively. **Columns 4 & 5** give the minimum probability for a redshift spike in 50 bins and the redshift spike(s) respectively. **Columns 6 & 7** give the minimum probability for a redshift spike in 20 bins and the redshift spike(s) respectively.

(1)	(2)	(3)	(4)	(5)	(6)	(7)
Number of area	MIN (prob) 100 bins	z_{100}	MIN (prob) 50 bins	z_{50}	MIN (prob) 20 bins	z_{20}
1	0.0009	3.125	0.143	4.050	0.002	3.125
2	0.002	4.125	0.148	4.150	0.057	4.125
3	0.001	0.524	0.305	0.350	0.032	1.875
4	0.0006	0.875	0.124	4.350	0.015	0.875
5	0.00005	2.025	0.180	3.850	0.043	2.125
6	0.007	2.025	0.266	0.150	0.043	2.125
7	0.0001	2.725	0.148	4.150	0.0007	2.625
8	0.0002	0.125	0.102	4.650	0.001	0.625
9	0.002	4.075	0.143	4.050	0.007	4.125
10	0.0003	3.525	0.223	3.550	0.020	3.625
11	0.002	2.675	0.266	0.150	0.012	0.375
12	0.0009	3.275	0.143	4.050	0.049	3.375
13	0.001	3.225	0.102	4.650	0.015	3.125
14	0.003	4.175	0.148	4.150	0.057	4.125
15	0.00002	0.325	0.136	4.450	0.009	3.375
16	0.0009	3.125	0.148	4.150	0.0151	3.125
17	0.0008	2.175	0.136	4.450	0.009	3.375
18	0.0009	3.125	0.143	4.050	0.004	0.375
19	0.0006	1.325	0.126	4.250	0.007	4.125
20	0.0003	3.525	0.136	4.450	0.002	3.625
21	0.0009	3.275	0.102	4.650	0.029	4.625
22	0.002	4.075	0.143	4.050	0.043	2.125
23	0.0003	3.675	0.066	4.750	0.011	4.875
24	0.0004	0.975	0.124	4.350	0.035	0.375
25	7E-06	1.925	0.126	4.250	0.0007	1.875
26	0.0009	3.275	0.136	4.450	0.015	2.625
27	0.00007	2.275	0.102	4.650	0.0003	2.375
28	0.001	1.125	0.148	4.150	0.008	1.125
29	0.0008	2.175	0.215	3.650	0.012	2.125
30	0.001	4.575	0.117	4.550	0.029	4.625
31	0.002	4.475	0.136	4.450	0.012	2.125
32	0.003	3.725	0.170	3.750	0.029	2.375
33	0.003	2.425	0.286	1.750	0.029	2.375
34	0.0002	1.125	0.180	3.850	0.051	1.375
35	0.001	2.825	0.117	4.550	0.026	2.875
36	0.0001	3.925	0.193	3.950	0.015	3.875
37	0.006	0.775	0.223	3.550	0.043	2.125
38	0.002	4.375	0.124	4.350	0.047	4.375
39	0.002	4.525	0.117	4.550	0.029	4.625
40	0.00001	2.575	0.124	4.350	0.003	2.625
41	0.002	0.575	0.193	3.950	0.058	2.625
42	0.002	4.375	0.124	4.350	0.0159	3.875
43	0.0001	1.875	0.193	3.950	0.054	1.125
44	0.0006	1.975	0.066	4.750	0.006	0.875
45	0.002	4.375	0.124	4.350	0.015	3.875
46	0.0004	4.725	0.066	4.750	0.029	4.625
47	0.004	2.525	0.193	3.950	0.015	2.625
48	2E-07	2.175	0.117	4.550	0.0001	2.125
49	0.00005	1.475	0.050	4.950	0.011	4.875
50	0.0002	2.575	0.170	3.750	0.058	2.625

Table 4.9: (continued)

(1)	(2)	(3)	(4)	(5)	(6)	(7)
Number of area	MIN (prob) 100 bins	z_{100}	MIN (prob) 50 bins	z_{50}	MIN (prob) 20 bins	z_{20}
51	0.002	4.125/4.475	0.136	4.450	0.047	4.375
52	0.002	4.375	0.124	4.350	0.035	0.375
53	0.002	4.375	0.124	4.350	0.020	3.625
54	0.001	0.225	0.148	4.150	0.009	3.375
55	0.0002	2.475	0.126	4.250	0.002	3.125
56	0.001	1.625	0.126	4.250	0.007	4.125
57	0.0005	3.425	0.263	3.450	0.035	0.875
58	0.001	4.625	0.102	4.650	0.015	0.875
59	0.00008	2.775	0.064	4.850	0.011	4.875
60	0.001	4.675	0.102	4.650	0.002	4.625
61	0.0001	3.775	0.170	3.750	0.002	3.875
62	0.0002	0.125	0.266	0.150	0.032	1.875
63	1E-06	2.375	0.102	4.650	0.00001	2.375
64	0.0007	3.075	0.296	3.150	0.015	3.125
65	0.0006	0.825	0.126	4.250	0.006	0.875
66	0.0003	3.525	0.102	4.650	0.002	4.625
67	1E-16	1.575	0.117	4.550	6E-11	1.625
68	0.001	4.675	0.102	4.650	0.002	4.625
69	0.001	4.625	0.102	4.650	0.007	2.375
70	0.00009	0.675	0.275	3.350	0.0121	0.625
71	7E-06	0.425	0.117	4.550	0.002	0.875
72	0.0008	2.275	0.124	4.350	0.001	2.375
73	0.001	2.875	0.126	4.250	0.007	4.125
74	0.001	2.825	0.136	4.450	0.009	3.375
75	0.003	4.175	0.148	4.150	0.057	4.125
76	0.0007	4.775	0.066	4.750	0.011	4.875
77	0.005	2.075	0.215	3.650	0.020	3.625
78	0.0008	0.025	0.124	4.350	0.002	3.875
79	0.005	3.975	0.193	3.950	0.096	3.875
80	9E-06	3.575	0.102	4.650	0.002	3.625
81	0.0002	4.975	0.050	4.950	0.009	3.375
82	0.002	4.075	0.143	4.050	0.007	4.125
83	0.0006	1.975	0.266	0.150	0.018	1.625
84	0.0002	0.125	0.266	0.150	0.024	0.125
85	0.00008	2.775	0.064	4.850	0.005	2.875
86	0.0007	2.225	0.117	4.550	0.012	2.125
87	0.00003	2.125	0.263	3.450	0.012	2.125
88	0.001	3.225	0.148	4.150	0.049	3.375
89	0.002	1.025	0.320	3.050	0.054	1.125
90	0.001	4.575	0.117	4.550	0.015	2.625
91	0.002	4.225	0.126	4.250	0.007	4.125
92	0.0007	4.775	0.066	4.750	0.011	4.875
93	0.0004	4.725	0.066	4.750	0.020	1.375
94	0.00009	0.825	0.170	3.750	0.015	0.875
95	0.002	4.325	0.117	4.550	0.029	4.625
96	0.0004	0.575	0.223	3.550	0.003	2.125
97	0.0006	4.825	0.064	4.850	0.011	4.875
98	0.0002	3.875	0.126	4.250	0.002	3.875
99	0.004	1.425	0.180	3.850	0.020	1.375
100	0.001	0.725	0.126	4.250	0.015	3.875

Chapter 5

The $K-z$ relation and the radio structure of the TOOT00 and the SXDS radio sources

Abstract

A near-infrared (K-band) study of the TOOT00 and SXDS radio-source samples is presented. Comparison to the $K-z$ relation of Willott et al. (2003) suggests that the TOOT00 radio sources obey the same $K-z$ relation defined by 3CRR/6CE/6C*/7CRS radio sources, with a few outliers, adding to similar examples identified before. The SXDS radio sources do not follow the $K-z$ relation so well, appearing to be significantly fainter than previous radio-source samples, like the 3CRR, 6CE, 6C* and 7CRS, at K. The mean K-corrected and passive-evolution-corrected luminosity at K for the TOOT00 sample is $L_{K-\mathrm{Ke}} \sim 4\ L^*_K$, excluding the 'bright at K' quasars in TOOT00. For the SXDS sample, again excluding quasars, $L_{K-\mathrm{Ke}} \sim 2\ L^*_K$, suggesting that the TOOT00 radio sources at a median redshift $z_{\mathrm{med}} \sim 1.25$ are 2-times more luminous at K than the $z_{\mathrm{med}} \simeq 1.1$ SXDS radio sources. The distribution of the TOOT00 and SXDS radio sources at K are different to each other and different from the local 6dF sample of radio sources, suggesting that they include different populations of objects. The FRI/FRII divide in radio luminosity seen at $z \ll 0.5$ is also obeyed at $z \sim 1$ for FRII objects in the TOOT00 and SXDS samples, but examples of FRI radio sources that are above the FRI/FRII break in radio luminosity exist in both samples. Finally, comparison of the SXDS with 6dF objects in the 1.4-GHz radio luminosity range $22 \lesssim \log_{10}(L_{1.4\mathrm{GHz}}/[\mathrm{WHz}^{-1}\mathrm{sr}^{-1}]) \lesssim 26$ shows that the three samples have similar luminosities at K, although there is a tail of low-K objects

at high redshift.

5.1 Introduction

It has been known for many decades that powerful radio galaxies follow a tight correlation between their apparent K-band magnitudes and redshift (Lilly & Longair 1984). The near-infrared (near-IR) K-band emission from radio sources typically originates from stellar light of the host galaxy (Best, Longair & Röttgering 1998; Simpson, Rawlings & Lacy 1999). Studies of the so-called $K-z$ relation for the 3CRR, 6CE, 6C* and 7CRS radio-source samples (e.g. Eales & Rawlings 1996; Jarvis et al. 2001c; Inskip et al. 2002; Willott et al. 2003) show a tight correlation of the observed near-IR magnitude with increasing redshift. These samples of radio sources cover 3 dex in radio luminosity over a wide range of redshifts ($0 < z < 3$). According to Willott et al. (2003), the $K-z$ relation that fits the above radio-source samples is consistent with a model in which the hosts of radio sources are, or mimic, a homogeneous stellar population that formed the bulk of their stars at high redshifts ($z > 5$) and evolved passively to the present day. On the other hand, it was stated that for example, 3CRR galaxies between redshifts $z = 0$ and $z = 1$ cannot be simply described by such a passively evolving model (e.g. Best, Longair & Röttgering 1998).

The best tool to study the space density of radio sources in co-moving volume is the radio luminosity function RLF (e.g. Willott et al. 2001b and references therein). This is often described as a broken power law (e.g. Kaiser & Best 2007a), with a characteristic luminosity at the break L^*. The break luminosity is close to, but seemingly above the luminosity separating the two FR classes (Fanaroff & Riley 1974), where FRI objects lie below the FRI/FRII break and FRII objects are found above the break (see also Kaiser & Best 2007a). It was found by Ledlow & Owen (1996) that the radio luminosity separating the two FR classes appears to depend on the optical luminosity of the host galaxy. In particular for radio sources at $z \lesssim 0.5$ the radio luminosity at the FRI/FRII break is $L_{1.4\mathrm{GHz}} \propto L_{\mathrm{opt}}^{1.65}$ (Ledlow & Owen 1996; Meier et al. 1998).

At high redshifts ($z \sim 1$), the most powerful radio sources are found to reside in rich environments (i.e. clusters of galaxies; e.g. Best, Longair & Röttgering 1998) with high R-band luminosity. For example, 3CRR radio sources reside in $\simeq 4L^*$ galaxies, while the lower luminosity 6CE and 7CRS objects typically inhabit hosts with luminosities of $\simeq 3L^*$ and $\simeq 2L^*$ respectively (McLure et al. 2004). Further study of these samples has revealed a correlation between radio luminosity and host luminosity that is suggestive of a correlation of both these

properties with black hole mass (e.g. Willott et al. 2003; McLure et al. 2004).

At lower redshifts radio sources are hosted in otherwise normal luminous (and massive) galaxies (Bahcall et al. 1997; Dunlop et al. 2003; Pagani et al. 2003) that are isolated or in small groups (Best 2000, and references therein) and are characterised by a conspicuous spheroidal component that becomes dominant in radio-loud quasars (RLQs). Furthermore, at $z \simeq 0.2$ radio galaxies and the hosts of RLQs, are all luminous galaxies with $L \gtrsim L^*$ at K (L^*_K) and have very similar luminosities (De Breuck et al. 2002). L^*_K, the luminosity at the break of the LF, depends on the sample and is different at different cosmic times.

Study of the bivariate radio/near-IR RLF by Mauch & Sadler (2007) on a local sample of radio galaxies spanning 6 dex in radio luminosity ($L_{1.4\mathrm{GHz}} \sim 10^{20}$-$10^{26}$ W Hz^{-1}) revealed that radio-loud AGN preferentially inhabit the brightest and hence the most massive host galaxies with $M_K > M^*_K$ (M^*_K being the luminosity at the LF break), which agrees with the findings of Best et al. (2005). In particular, the fraction of all galaxies which host a radio-loud AGN, $f_{\mathrm{radio-loud}}$, scales with luminosity at K as $f_{\mathrm{radio-loud}} \propto L_K^{2.1}$, which is indicative of a similarly strong scaling with stellar and hence black hole mass.

Although near-IR studies of low-frequency radio samples show a close relation between the K-band magnitude and redshift, there are reported offsets from the $K-z$ relation. The scatter in the $K-z$ relation may be due to a dependence of K magnitude on the radio luminosity, with the highest radio power sources inhabiting the most massive host galaxies (De Breuck et al. 2002). Another cause of this dispersion might be the fact that the K-band magnitude is measured at different apertures for different objects. Correction for that contribution has been applied when modelling the $K-z$ relation (e.g. Willott et al. 2003), which improves the fit but offsets still exist. On the other hand, Taylor et al. (1996) claim that the dispersion in the $K-z$ plane is not caused by aperture effects but is rather of nuclear nature, i.e. contribution of the central AGN to the K magnitude (see also Brookes et al. 2008).

At $z \sim 1$, there is observational evidence from studies of samples of radio galaxies that the contribution of AGN emission to the K-band emission is small (Brookes et al. 2008). The contribution by AGN emission to the K-band magnitude is $\lesssim 10\%$, as shown in 3CRR and in lower redshift radio galaxies (Simpson, Rawlings & Lacy 1999; Simpson, Ward, & Wall 2000), even in the most powerful radio sources. Furthermore, near-IR polarimetry observations by Leyshon & Eales (1998) indicate that scattered quasar light makes only a small contribution at near-IR wavelengths, even in sources where this contribution is important in the UV and optical. On the other hand, De Breuck et al. (2002) claim that since AGN emission can be extremely bright relative to the emission from the stellar population in the host galaxy, even

a small partially obscured, or scattered, contribution could have a significant influence on the total integrated K-band magnitude (also see Dunlop et al. 1993). If one removes the AGN contribution to the K-band magnitude, the objects tend to shift to fainter magnitudes in the $K-z$ diagram, as has been shown for local sample of radio sources (e.g. Simpson, Ward & Wall 2000).

Another source of the scatter at $K-z$ diagram with increasing redshift could be explained by emission-line contamination. The most-luminous sources at high redshift may be contaminated by the bright optical emission lines redshifted into the infrared (e.g. Eales & Rawlings 1993), which is particularly true for sources in radio flux-density limited samples. The strong correlation between low frequency radio luminosity and emission-line strength (e.g. Rawlings & Saunders 1991; Willott et al. 1999; Jarvis et al. 2001c) will increase the contribution to the measured K-band magnitudes from the emission-lines in the most radio luminous sources.

Emission line contribution to the K-band magnitudes can be significant at $z > 2$, when the strong Hα λ6563, [O III] λ5007 and [O II] λ3727 emission lines are redshifted into the K-band at $1.9 \gtrsim z \gtrsim 2.7$, $2.9 \gtrsim z \gtrsim 3.7$ and $4.2 \gtrsim z \gtrsim 5.2$, respectively (Eales & Rawlings 1993, 1996; Jarvis et al. 2001a).

The reported offsets from the $K-z$ relation indicate a connection of offset and flux-density limit (e.g. Willott et al. 2003). From the study of various radio samples, like the 3CRR (e.g. Simpson, Ward & Wall 2000; Taylor et al. 1996), 6CE (Rawlings, Eales & Lacy, 2001; see also Eales & Rawlings 1996; Inskip et al. 2002), 6C* (Jarvis et al. 2001a, b), 7CRS (Willott et al. 2003), and CENSORS (Brookes et al. 2006; 2008), a trend towards fainter magnitudes with increasing radio luminosity has been reported. The offset increases with decreasing flux density limit of the survey: the 6CE radio sources were found 0.3 mag fainter than the $K-z$ relation, the 6C* and 7CRS objects were ~ 0.5 mag fainter and the CENSORS radio sources were 0.6 mag fainter at high redshifts than expected.

The current study first examines the $K-z$ relation of the low-frequency 151-MHz selected TOOT00 radio sources (Vardoulaki et al. 2009; see also Chapter 3). The target is to see whether the tight correlation between K and z still stands and to look for differences with the $K-z$ relation of Willott et al. (2003). In order to investigate whether the correlation between K-band magnitude and redshift holds for a fainter (moderately high-frequency) radio-selected sample, the TOOT00 radio sources are compared to the SXDS sample (Vardoulaki et al. 2008; see also Chapter 2).

Section 5.2 is a description of the sample used in the analysis in Section 5.3, where the $K-z$ diagram is presented, as well as a further investigation of the near-IR properties of both

samples. A detailed discussion follows in Section 5.4, where the TOOT00 and SXDS radio sources are compared to a local sample of 6dF radio sources. The conclusions are presented in Section 5.6.

The convention for all spectral indices, α, is that flux density $S_\nu \propto \nu^{-\alpha}$, where ν is the observing frequency. A low-density, Λ-dominated Universe in which $H_0 = 70$ km s^{-1}Mpc^{-1}, $\Omega_{\rm M} = 0.3$ and $\Omega_\Lambda = 0.7$ is assumed throughout.

5.2 The Sample

Two samples of radio sources are presented here. The first sample includes the TOOT00 radio sources with a ∼85% spectroscopic completeness (40 out of 47 objects) and a median redshift of $z_{\rm med} \sim 1.25$, including photometric redshifts; all photometric redshifts that are used in the analysis were estimated from the $K - z$ relation of Willott et al. (2003; see Section 3.2). The TOOT00 radio sources were selected from the 7C survey to have a flux density limit of $\simeq$ 100 mJy at 151 MHz (see Vardoulaki et al. 2009; see also Section 3.2). The second sample, includes the 37 brightest radio sources from the SXDF (Simpson et al. 2006), namely SXDS radio sources, selected to be brighter than 2 mJy at 1.4 GHz (Vardoulaki et al. 2008; Section 2.2). This sample has a ∼65% spectroscopic completeness (24 out of 37 objects) and a median redshift $z_{\rm med} \simeq 1.1$, including photometric redshifts; all photometric redshifts that are used in the analysis were estimated from HyperZ (Bolzonella et al. 2000; also see Section 2.3.2).

Data for these samples include spectroscopic and photometric redshifts, optical and near-IR photometry, radio flux densities and maps, as well as mid-IR photometry for the SXDS only. The data are presented in Chapter 2 for the SXDS and Chapter 3 for TOOT00. Here an analysis on the near-IR K-band photometry is presented, as well as a comparison of the TOOT00 and SXDS $K-z$ relations to those obeyed by the 3CRR, 6CE, 6C* and 7CRS datasets (Laing, Riley & Longair 1983; Rawlings, Eales & Lacy 2001, Jarvis et al. 2001c and Willott et al. 2003, respectively).

Tables 5.1 & 5.2 give basic properties of the TOOT00 and SXDS radio sources used in the analysis, like the flux density and luminosity at MHz and GHz frequencies, the radio structure, the K-band magnitude measured from the near-IR imaging (see Section 3.2 & 2.2), the radio spectral index, and the luminosity at K (see Section 5.3).

Table 5.1: Basic properties of the 47 TOOT00 radio sources needed for analysis of the $K-z$ diagram. **Column 1** shows the name of the object and **Column 2** the redshift; 'Kz' denotes that the photometric redshift presented was estimated using the $K_{\rm W}-z$ relation (Eqn. 5.1; Section 5.3); a '?' shows uncertainty. **Columns 3 & 4** give the flux density at 151 MHz and 1.4 GHz respectively. **Column 5** gives the optical class (OpCl; see Section 3.3.1): Q stands for quasars, Q? denotes possible quasar, G? denotes possible galaxy and G denotes galaxy; 'a' denotes a broad-absorption-line QSO (BALQSO; see Section 2.6). **Column 6** gives the radio structure (see Section 3.3.2): CD stands for classical double, TJ for twin-jet, FD for fat double and COM for a compact radio source. **Column 7** gives the radio-optical classification (see Table 3.3): FRI-type and FRII-type as in Fanaroff & Riley classification (1979); FRII-Q denotes quasar with FRII radio structure; Q-F denotes quasar with flat radio spectral index; CSS stands for compact-steep-spectrum object; CSS-Q denotes quasar with steep radio spectral index; a '?' shows uncertainty. **Column 8** gives the K-band magnitude in the Vega magnitude system. **Column 9** gives the difference between K magnitude and the one calculated from the $K_{\rm W}-z$ relation, K-$K_{\rm W}$. **Column 10** gives the K-corrected and passive-evolution-corrected luminosity at K, $L_{K-{\rm Ke}}$, in units of L^*_K (see Section 5.3). **Column 11** gives the radio spectral index (see Section 3.3.2). **Columns 12 & 13** present the base-10 logarithm of the radio luminosity at 151 MHz and 1.4 GHz respectively.

(1)	(2)	(3)	(4)	(5)	(6)	(7)	(8)	(9)	(10)	(11)	(12)	(13)
Name	redshift	S_{151} (Jy)	$S_{1.4}$ (mJy)	OpCl	Radio structure	R-OpCl	$K_{\rm Vega}$ (mag)	ΔK (mag)	$L_{K-{\rm Ke}}$ $[L^*_K]$	$\alpha^{1.4}_{151}$	$\log_{10}(L_{151{\rm MHz}}/{\rm WHz^{-1}sr^{-1}})$	$\log_{10}(L_{1.4{\rm GHz}}/{\rm WHz^{-1}sr^{-1}})$
TOOT00_1140	0.911?	0.58	109.5	G	FD	FRI	17.0	0.19	3.79	0.75	26.21	25.49
TOOT00_1099	1.397?	0.17	17.9	G	TJ?	FRI?	16.5	1.50	14.14	1.01	26.21	25.23
TOOT00_1125	1.916	0.76	93.5	Q	CD	FRII-Q	15.6	2.97	60.04	0.94	27.17	26.26
TOOT00_1143	0.438	0.12	6.40	G	FD	FRI	16.0	-0.23	2.11	2.55	24.88	23.60
TOOT00_1233	1.244	0.11	51.2	Q[a]	COM?	Q-F	15.3	2.48	30.67	0.34	25.66	25.33
TOOT00_1022	2.872^{Kz}	0.12	15.6	G	COM	CSS	19.4	-0.10	3.78	0.92	26.78	25.89
TOOT00_1204	0.6395	0.12	31.3	G	FD	FRI	16.3	0.21	3.73	0.60	25.13	24.55
TOOT00_1235	0.743	0.34	99.3	Q	COM?	Q-F?	17.0	-0.20	2.59	0.55	25.72	25.19
TOOT00_1224	3.438^{Kz}	0.19	32.6	G	COM	CSS	19.7	-0.09	5.00	0.79	27.07	26.31
TOOT00_1291	0.917^{Kz}	0.20	31.6	G	CD?	FRII	17.3	-0.09	2.82	0.83	25.78	24.98
TOOT00_1107	0.300	0.17	5.70	G	TJ	FRI	18.1	-3.09	0.13	1.52	24.65	23.18
TOOT00_1180	1.810	0.15	15.8	G?	CD?	FRII?	18.3	0.17	4.51	1.01	26.44	25.46
TOOT00_1027	0.890	0.13	664.3	G	COM	CSS	19.5	-2.35	0.36	-0.73	25.13	25.84
TOOT00_1195	1.418^{Kz}	0.12	15.1	G	CD	FRII	18.1	-0.08	3.36	0.93	26.05	25.15
TOOT00_1069	2.300	0.10	3.60	Q	COM?	CSS-Q	> 20.3	-1.40	1.09	1.49	26.76	25.32
TOOT00_1094	1.516?	2.30	248.0	G	COM	CSS	18.3	-0.15	3.28	1.00	27.43	26.46
TOOT00_1149	0.260	0.30	29.5	G	TJ	FRI	14.6	0.12	2.62	1.04	24.70	23.69
TOOT00_1298	1.287?	0.16	30.4	G	TJ	FRI	17.3	0.54	5.37	0.75	26.00	25.28
TOOT00_1200	0.691	1.59	272.4	G?	CD	FRII	17.4	-0.74	1.56	0.79	26.38	25.61
TOOT00_1215	0.278	0.36	42.8	G	TJ?	FRI?	15.0	-0.14	1.97	0.96	24.84	23.91
TOOT00_1240	2.543?	0.13	7.40	G?	CD	FRII	18.9	-0.09	4.82	1.29	26.89	25.64
TOOT00_1289	1.784?	0.20	21.8	G	CD	FRII	17.8	0.64	6.97	1.00	26.54	25.58
TOOT00_1072	0.577	0.58	111.1	G	CD	FRII	15.7	0.61	6.97	0.74	25.75	25.03
TOOT00_1134	0.311	1.37	119.2	G	TJ	FRI	14.6	0.48	5.43	0.87	25.52	24.46
TOOT00_1244	1.358	0.13	32.4	Q	COM	Q-F?	18.8	-0.86	1.57	0.62	25.92	25.32
TOOT00_1066	0.926?	0.10	14.4	G	CD	FRII	18.0	-0.78	1.52	0.87	25.50	24.66
TOOT00_1261	2.544	0.14	14.2	Q?	CD	FRII-Q?	19.0	0.08	4.40	1.03	26.78	25.78
TOOT00_1252	3.229^{Kz}	0.16	18.0	G	CD?	FRII?	> 19.6	-0.10	4.30	0.98	27.06	26.11
TOOT00_1214	3.081	0.10	11.3	Q?	CD?	FRII-Q?	18.6	0.82	9.31	0.98	26.80	25.86
TOOT00_1152	3.310^{Kz}	0.27	38.3	G	CD	FRII	19.6	-0.05	4.72	0.88	27.24	26.40
TOOT00_1129	1.860	1.01	156.6	Q?	CD	FRII-Q?	20.2	-1.68	0.83	0.84	27.22	26.41
TOOT00_1090	0.201	0.20	27.9	G	FD	FRI	14.6	-0.41	1.71	0.88	24.26	23.40
TOOT00_1267	0.968	0.59	99.5	G?	CD	FRII	17.1	0.21	3.68	0.80	26.30	25.52
TOOT00_1188	1.417	0.10	14.7	G?	CD	FRII	18.3	-0.28	2.79	0.86	25.94	25.11
TOOT00_1196	1.662^{Kz}	0.10	< 0.9	G	FD?	FRI?	18.4	-0.09	4.60	> 2.11	26.64	24.59
TOOT00_1173	0.332	0.16	28.8	G	TJ	FRI	15.3	-0.09	2.09	0.77	24.64	23.89
TOOT00_1228	1.135?	0.28	79.1	G	COM	CSS	18.4	-0.79	1.46	0.57	26.06	25.51
TOOT00_1034	0.580	0.61	140.5	G	TJ	FRI	16.1	0.22	3.81	0.66	25.76	25.12
TOOT00_1255	0.582	0.14	33.8	G	CD?	FRII?	16.8	-0.47	2.02	0.64	25.12	24.50
TOOT00_1048	1.943	0.84	104.1	G?	CD	FRII	17.5	1.10	10.72	0.94	27.23	26.32
TOOT00_1029	0.737	0.11	24.1	G	COM?	CSS	15.9	0.89	7.21	0.68	25.26	24.60
TOOT00_1115	0.416	0.36	56.1	G	TJ?	FRI?	15.9	-0.23	2.02	0.83	25.22	24.42
TOOT00_1132	0.183	0.47	88.3	G	TJ?	FRI?	15.0	-1.01	1.07	0.75	24.53	23.80
TOOT00_1250	1.350	0.36	54.0	Q	CD?	FRII?	18.0	-0.07	3.22	0.85	26.44	25.62
TOOT00_1268	2.010	0.13	61.2	Q?	COM	Q-F?	17.6	1.06	10.42	0.34	26.16	25.84
TOOT00_1251	2.490	0.21	19.6	G?	CD	FRII	19.1	-0.06	3.75	1.06	26.95	25.92
TOOT00_1203	1.397	1.06	164.6	G	CD?	FRII?	17.4	0.60	6.17	0.84	26.94	26.13

Table 5.2: Basic properties of the 37 SXDS radio sources needed for analysis of the the $K-z$ diagram. **Column 1** shows the name of the object and **Column 2** the redshift; 'BC' denotes that the photometric redshift presented was estimated using HyperZ (see Section 2.3.2); a '?' shows uncertainty. **Column 3** gives the flux density at 610 MHz or at 325 MHz, marked with '325'; the character 's' shows that the flux densities of each component of the radio source have been added to calculate the whole flux density of the radio sources. **Column 4** gives the flux density at 1.4 GHz. **Column 5** gives the optical/IR classification (see Section 2.3.3): 'Q' stands for a quasar, 'OQ' for an obscured quasar, 'G?' for a possible galaxy, 'G' for a secure galaxy, 'SB' for a starburst, 'WQ' for a weak quasar and 'BL' for a BL Lac object. In the analysis (see Section 5.3) the OQ, WQ and BL are replaced by Q? and SB is replaced by G?. **Column 6** gives the radio classification (Section 2.2): CD stands for classical double, TJ for twin-jet, FD for fat double and COM for a compact radio source. **Column 7** gives the radio-optical classification (see Sec 2.2): FRI-type and FRII-type as in Fanaroff & Riley classification (1979); FRII-Q denotes quasar with FRII radio structure; Q-F denotes quasar with flat radio spectral index; CSS stands for compact-steep-spectrum object; COM-F denotes compact radio source with flat radio spectral index; a '?' denotes uncertainty. **Column 8** gives the K-band magnitude, where the magnitudes of the SXDS objects in Table 2.3 have been converted to the Vega magnitude system ($K_{\rm Vega} = K_{\rm AB}$ - 1.898; Hewett et al. 2006). **Column 9** gives the difference between K magnitude and the one calculated from the $K_{\rm W}-z$ relation (Eqn. 5.1; Section 5.3), K-$K_{\rm W}$. **Column 10** gives the K-corrected and passive-evolution-corrected luminosity at K, $L_{K-{\rm Ke}}$, in units of L^*_K (see Section 5.3). **Column 11** gives the radio spectral index 1.4 GHz to 610 MHz or from 1.4 GHz to 325 MHz, which are marked with 'm'; estimated values are in brackets. **Columns 12 & 13** present the base-10 logarithm of radio luminosity at 151 MHz and 1.4 GHz respectively; the radio spectral indices of each source were used in the calculations.

(1)	(2)	(3)	(4)	(5)	(6)	(7)	(8)	(9)	(10)	(11)	(12)	(13)
Name	redshift	$S_{325\rm MHz}$ (mJy)	$S_{1.4\rm GHz}$ (mJy)	Op/IR Type	Radio structure	R-OpCl	$K_{\rm Vega}$ (mag)	ΔK (mag)	$L_{K-{\rm Ke}}$ $[L^*_K]$	α	$\log_{10}(L_{151\rm MHz}/$ WHz^{-1}sr^{-1})	$\log_{10}(L_{1.4\rm GHz}/$ WHz^{-1}sr^{-1})
sxds_0001	0.626	194.4	82.50	G	TJ	FRI	16.59	-0.12	2.79	1.03	26.04	25.04
sxds_0002	1.183	135.0	62.11	OQ	CD	FRII	18.03	-0.34	2.21	0.93	26.47	25.57
sxds_0003	2.433	141.3	53.60	OQ	CD	FRII-Q?	18.99	0.01	4.09	1.17	27.52	26.39
sxds_0004	$2.270^{\rm BC}$	22.4	16.95	BL	COM-F	COM	19.51	-0.63	2.31	0.34	25.71	25.38
sxds_0005	$1.610^{\rm BC}$	38.8	16.01	G?	COM	CSS	18.67	-0.42	2.65	1.07	26.40	25.36
sxds_0006	$1.882^{\rm BC}$	7.0	12.02	G?	COM	COM-F	18.31	0.23	4.82	-0.65	23.99	24.61
sxds_0007	1.325?	$43.3^{\rm s}$	9.60	G?	CD	FRII	17.78	0.11	3.73	1.81	26.95	25.20
sxds_0008	0.458	16.6	9.15	SB	COM	CSS	16.34	-0.48	2.08	1.74	24.40	23.71
sxds_0009	3.570?	19.3^{325}	8.91	Q?	COM	Q-F	20.62	-0.94	2.58	$0.53^{\rm m}$	26.12	25.61
sxds_0010	$1.400^{\rm BC}$	17.1	8.12	G?	COM?	CSS?	19.22	-1.22	1.17	0.90	25.72	24.85
sxds_0011	0.647	13.3	10.90	G	TJ	FRI	16.17	0.37	4.35	(0.80)	24.92	24.15
sxds_0012	0.865	15.4	6.90	G	CD	FRII	17.21	-0.11	2.79	0.97	25.23	24.29
sxds_0013	2.713	6.7	6.25	Q	COM	Q-F	19.89	-0.69	2.11	0.08	25.03	24.96
sxds_0014	$2.205^{\rm BC}$	4.2	6.19	G?	COM	COM-F	19.33	-0.51	2.47	-0.47	24.06	24.51
sxds_0015	0.344	$17.0^{\rm s}$	6.10	G	FD	FRI	15.79	-0.50	1.40	1.23	24.50	23.31
sxds_0016	1.345?	$14.1^{\rm s}$	5.95	OQ	CD	FRII-Q?	20.16	-2.24	0.44	1.04	25.73	24.73
sxds_0017	2.583	13.5^{325}	4.97	Q	CD?	FRII-Q	19.74	-0.63	2.19	$0.68^{\rm m}$	25.81	25.15
sxds_0018	0.919	13.3	5.70	G	FD	FRI	16.98	0.23	3.79	1.02	25.28	24.29
sxds_0019	0.694	–	5.00	G	FD?	FRI	18.36	-1.69	0.65	(0.80)	24.65	23.88
sxds_0020	$1.135^{\rm BC}$	$8.5^{\rm s}$	5.10	G?	FD?	FRI	19.32	-0.71	0.63	0.62	24.94	24.34
sxds_0021	$1.645^{\rm BC}$	9.1	5.00	G?	COM	CSS	19.14	-0.84	1.77	0.87	25.64	24.80
sxds_0022	0.248	6.1	4.36	G	COM	COM-F	14.58	0.04	2.38	0.40	23.14	22.76
sxds_0023	0.586	11.3	4.20	G	COM	CSS	17.07	-0.73	1.59	1.19	24.86	23.71
sxds_0024	0.516	11.2	3.80	G	TJ	FRI	15.90	0.19	3.47	1.30	24.81	23.55
sxds_0025	0.964?	–	3.23	QW?	COM	Q?-F	19.70	-2.40	0.33	(0.40)	24.30	23.91
sxds_0026	0.450	6.4	3.40	G	TJ?	FRI?	15.76	0.07	2.84	0.76	24.00	23.27
sxds_0027	$1.595^{\rm BC}$	–	3.13	OQ?	COM	Q?-F?	18.82	-0.58	2.24	(0.40)	24.75	24.37
sxds_0028	0.627?	4.1	2.80	G	COM	COM-F	16.81	-0.34	2.20	2.29	23.90	23.45
sxds_0029	$1.380^{\rm BC}$	3.4	2.72	G?	COM	COM-F	18.73	-0.75	1.76	0.27	24.39	24.12
sxds_0030	0.535	4.6	2.56	G	TJ?	FRI?	16.54	-0.38	2.12	0.71	23.99	23.31
sxds_0031	$1.325^{\rm BC}$	3.9	3.20	G?	COM	COM-F	18.42	-0.52	2.07	0.24	24.38	24.15
sxds_0032	$1.010^{\rm BC}$	$7.7^{\rm s}$	2.39	G	FD?	FRI	18.61	-1.22	1.00	1.41	25.50	24.13
sxds_0033	0.647	6.3	2.40	G	TJ	FRI	16.51	0.03	3.19	1.16	24.69	23.57
sxds_0034	1.095	4.2	2.31	OQ	COM?	CSS-Q?	17.85	-0.31	2.24	0.72	24.69	23.99
sxds_0035	$2.715^{\rm BC}$	1.5	2.24	G?	COM	COM-F	19.97	-0.77	1.97	-0.48	23.73	24.19
sxds_0036	0.871	<1.1	2.09	G	COM	COM-F	16.81	0.29	4.10	<-0.77	22.56	23.31
sxds_0037	$1.085^{\rm BC}$	–	2.07	G?	COM	COM-F	18.70	-1.18	1.03	(0.40)	24.22	23.83

5.3 Analysis

Figure 5.1 presents the radio luminosity at 151 MHz, $L_{151\mathrm{MHz}}$, versus redshift z diagram for the 3CRR (Laing, Riley & Longair 1983), 6CE (Eales et al. 1997; Rawlings, Eales & Lacy 2001), 6C* (Jarvis et al. 2001c), 7CRS (Willott et al. 2001b; Willott et al. 2003), TOOT00 (Vardoulaki et al. 2009) and SXDS (Vardoulaki et al. 2008) radio sources; the radio luminosity $L_{151\mathrm{MHz}}$ of each of the SXDS objects was calculated using the radio spectral indices for each object shown in Table 5.2. Note that the radio spectral index of each SXDS object was calculated between 1.4 GHz and 610 or 325 MHz (see Table 5.2), meaning the calculation of $L_{151\mathrm{MHz}}$ is approximate. The flux density limits of various radio surveys are also shown: 3CRR, 6CE, 7CRS (12.4 Jy, 2.0 Jy and 0.5 Jy respectively; Willott et al. 2001a), TOOT00 (100 mJy), and SXDS (0.01 Jy at 151 MHz[1]; see Section 3.1). Note that many of the quasars in the 3CRR, 6CE and 7CRS samples are excluded from the plot. The line showing the flux density limit of the SXDS in Figure 5.1 is calculated using a typical steep-spectrum radio spectral index of 0.8, while the spectral indices of each object are used to calculate the luminosity of SXDS objects in Figure 5.1. As a result, objects with flat radio spectral index lie below than the apparent flux density limit of the survey, which is only appropriate for $\alpha \simeq 0.8$ objects.

The TOOT00 objects have median radio luminosity at 151 MHz of $\sim 1.2 \times 10^{26}$ W Hz^{-1} sr^{-1}, while for the SXDS the median value is lower, $\sim 6.4 \times 10^{24}$ W Hz^{-1} sr^{-1}. This suggests that at $z \sim 1$, the TOOT00 objects are radio-brighter than the SXDS radio sources by more than an order of magnitude.

The $K-z$ relation of Willott et al. (2003; hereafter $K_{\mathrm{W}}-z$) fits the 3CRR, 6CE, 6C* and 7CRS data sets, where the K magnitude is aperture and emission-line corrected:

$$K_{\mathrm{W}}(mag) = 17.37 + 4.53 \times (\log_{10} z) - 0.31 \times (\log_{10} z)^2, \tag{5.1}$$

where z is the redshift. Application of this relation should overestimate the value of z for the TOOT00 and SXDS objects, since it is aperture-corrected, whereas the K magnitudes for the TOOT00 and SXDS radio sources are not. We chose not to perform aperture corrections in our K magnitudes for three reasons: i) above redshift $z > 0.6$ aperture corrections are ~ 0.3 mag (Eales et al. 1997); ii) most of the objects have K-band magnitude measured at the same aperture, apart from some exceptions due to confusion by nearby object (see Table 3.1 and Section 3.6 for TOOT00; in the SXDS the same aperture was used – Section 2.3.2); iii) in order

[1] A typical steep spectrum radio spectral index $\alpha = 0.8$ is used to convert from the 2 mJy flux density limit at 1.4 GHz to 151 MHz.

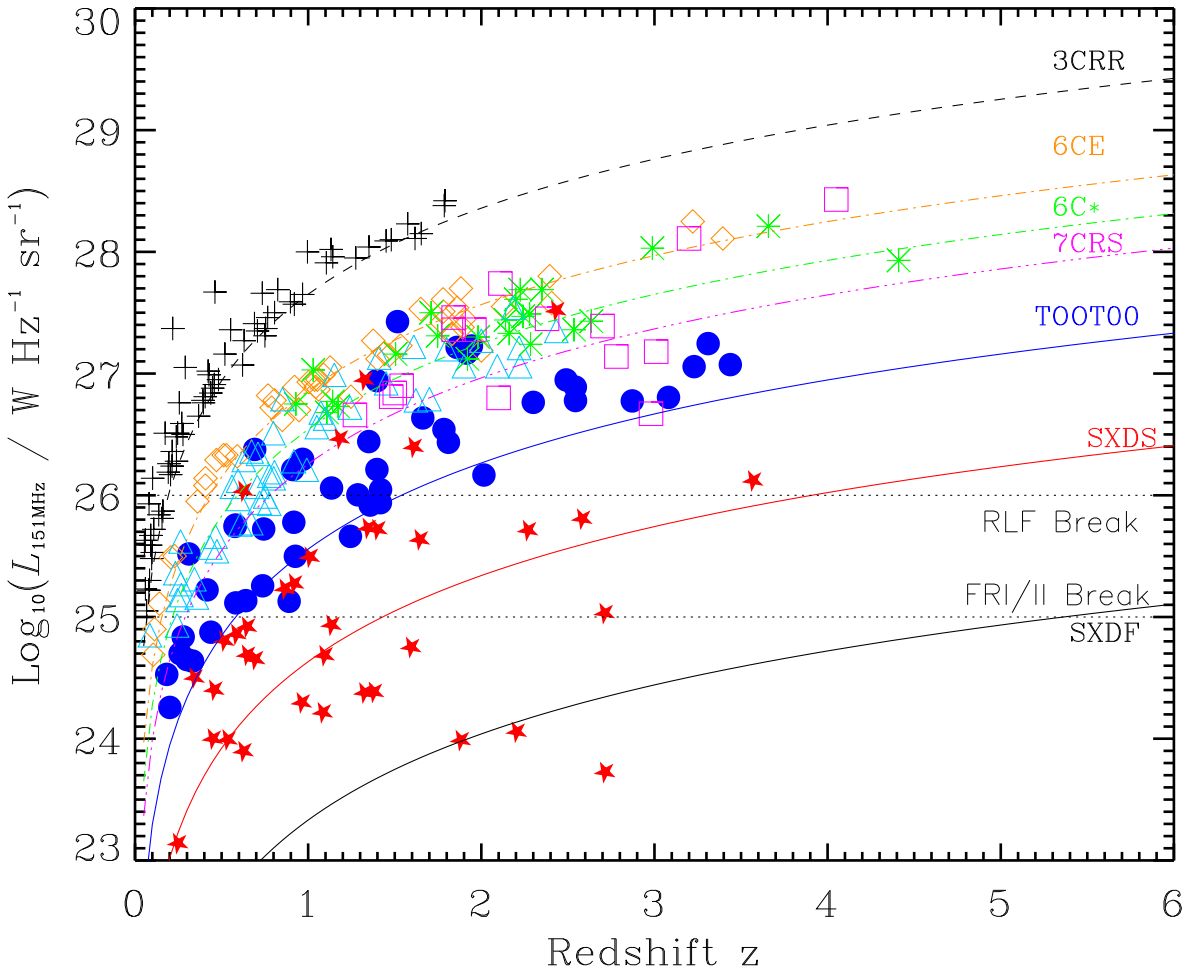

Figure 5.1: Radio luminosity at 151 MHz, $L_{151\mathrm{MHz}}$, versus redshift for the TOOT00 and the SXDS radio sources. Symbols: blue filled circles stand for TOOT00 and red filled stars denote SXDS objects. Also plotted for comparison are the 3CRR (black crosses), 6CE (orange diamonds), 6C* (green stars), 7CI-II (light-blue triangles) and 7CIII (pink boxes) samples (the data are taken from http://www.science.uottawa.ca/∼cwillott/kz/kz.html and they only include narrow-line galaxies; the same cosmology is used, as the one stated in Section 5.1, in the calculation of the radio luminosity). The flux density limits for all these surveys with their corresponding colour are also shown; the black solid line shows the flux density limit of the SXDS (100 μJy at 1.4 GHz). A typical spectral index of 0.8 was used to convert the flux density limits of the 3CRR, 6CE, 6C*, 7CRS, SXDS and SXDF to 151 MHz flux density; the flux limits are then respectively: 12.4, 2.0, 0.96–2.0, 0.5, 0.1, 0.012 and 0.0006 Jy. The horizontal dotted lines show the RLF and FRI/FRII breaks calculated from the Willott et al. (2003) and the Fanaroff & Riley (1974) values respectively using a typical steep-spectrum spectral index of 0.8. Note: the 3CRR sample is incomplete, since the provided list does not contain every radio galaxy at $z > 0.05$ as well as quasars. The 7CIII sample includes only narrow-line radio galaxies above $z > 1.2$.

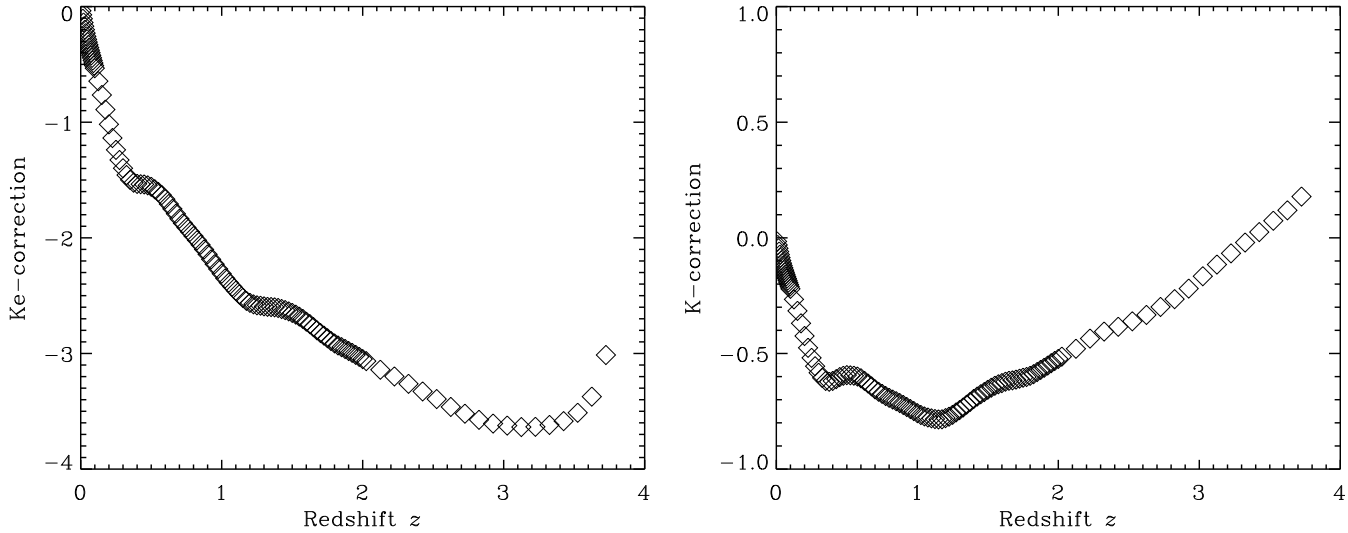

Figure 5.2: **a) Left:** K-correction and passive evolution correction, Ke-correction, for the K-band magnitude versus redshift z. **b) Right:** K-correction for the K-band magnitude versus redshift z. The data are produced using the code from Bruzual & Charlot (2003). Their code computes the spectral energy distributions of stellar populations at ages between 1×10^5 and 2×10^{10} yr at a resolution of 3 Å in the wavelength range from 3200-9500 Å for a wide range of metallicities. The cosmological parameters used in the calculation are: $H_0 = 71$ km s^{-1}Mpc^{-1}, $\Omega_{\rm M} = 0.27$, $\Omega_\Lambda = 0.71$, q_0 = -0.5950, $t_{univ} = 13.68$ Gyr and $z_{max} = 3.99$.

to correct the K magnitude for differences in aperture one needs typically to assume that there is no evolution of radio sources (e.g. Eales et al. 1997), which is certainly not the case (e.g. Best et al. 2005; Eales & Rawlings 1996).

As discussed in Willott et al. (2003), the best-fitting $K-z$ relation to the 3CRR, 6CE, 6C$*$ and 7CRS objects is close to the expected K-magnitude evolution of a galaxy of local luminosity 3 L^* which forms all of its stars in an instantaneous burst at $z_{\rm f} = 10$. In those calculations, the K magnitude was K-corrected, for the fact that absolute magnitudes in cosmology are affected by a shift of the spectrum in frequency, and also corrected for the effects of passive evolution, i.e. the dimming of objects from observed redshift to $z = 0$ (see Chapter 1 for more details). Figure 5.2–a gives the K-correction and passive-evolution correction at K (hereafter Ke-correction) in respect to redshift. It can be seen that these corrections are quite significant as the redshift increases, Figure 5.2–b the effects of K-correction at K alone can be seen. It is obvious that objects are much brighter than when the passive evolution correction is also applied.

For our analysis, we calculate the luminosity at K using three methods:
(1) $L_{K-{\rm Ke}}$ is the K-corrected and passive-evolution-corrected luminosity at K in L^*_K units, where the following equation was used to calculate the absolute magnitude at K, M_K:

$$M_K = K({\rm mag}) - 5 \times \log_{10}\left(\frac{D_L}{10{\rm pc}}\right) + 2.5 \times \log_{10}(1+z) - {\rm K}(z) - {\rm E}(z); \qquad (5.2)$$

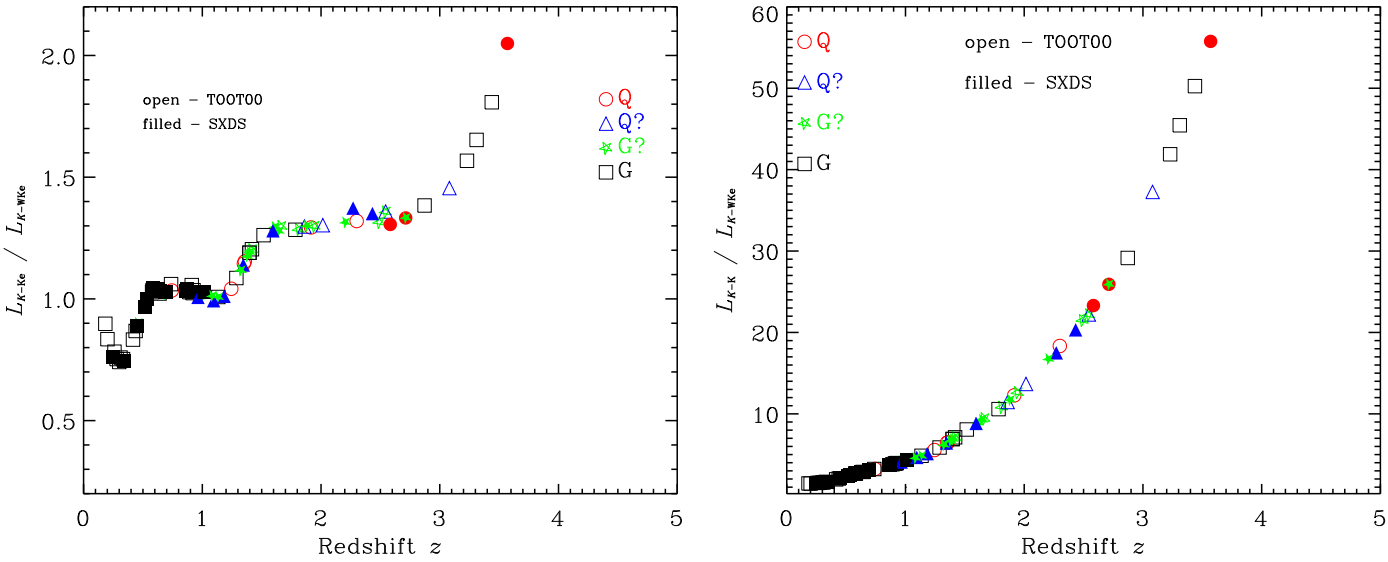

Figure 5.3: $L_{K-\mathrm{Ke}}/L_{K-\mathrm{WKe}}$ and $L_{K-\mathrm{K}}/L_{K-\mathrm{WKe}}$ vs z for the TOOT00 and the SXDS objects. Symbols indicate optical classification (see Section 3.3.1 & 2.3.3 for the TOOT00 and SXDS objects respectively): red circles denote Q objects, blue triangles stand for Q? (including WQ and BL), green stars denote G? (including SB) and black squares denote G objects; open symbols indicate TOOT00 objects and filled symbols denote SXDS radio sources. **a) Left:** Ratio of K-corrected and passive-evolution-corrected luminosity at K, $L_{K-\mathrm{Ke}}$, to the luminosity $L_{K-\mathrm{WKe}}$ calculated from Willott et al. (2003) versus redshift z. **b) Right:** Ratio of K-corrected luminosity at K, $L_{K-\mathrm{K}}$, to the luminosity $L_{K-\mathrm{WKe}}$ calculated from Willott et al. (2003) versus redshift z.

where K is the apparent magnitude at the K-band, D_L is the luminosity distance, K(z) is the K-correction and E(z) is the correction for passive evolution. The values for K-correction and passive evolution correction were generated using the Bruzual & Charlot (2003) code.

(2) $L_{K-\mathrm{K}}$ is the K-corrected luminosity at K in L^*_K units, calculated in the same way as (1) excluding the passive evolution corrections.

(3) $L_{K-\mathrm{WKe}}$ is the K-corrected and passive-evolution-corrected luminosity at K in L^*_K units, calculated using the $K_\mathrm{W}-z$ relation and the basic relation between luminosity and magnitude; the $K_\mathrm{W}-z$ fits a 3 L^* passively evolving galaxy model in which all stars are formed in an instantaneous burst at $z_\mathrm{f}=10$ (Willott et al. 2003).

Note that for the calculation of the luminosity at K, a typical M^*_K = -23.96 (Smith et al. 2009; value calculated for our adopted cosmology) was used. Values of the absolute magnitude and luminosity at K are presented in Tables 5.3 & 5.4 for the TOOT00 and the SXDS objects respectively.

Figure 5.3–a presents how the luminosity at K depends on redshift when K-corrections and passive evolution corrections are applied and Figure 5.3–b when only the K-correction is applied. In Figure 5.3–a the ratio $L_{K-\mathrm{Ke}}/L_{K-\mathrm{WKe}}$ is close to 1 around redshift $z=1$, but it increases at higher redshifts with a maximum of 2 for $z\sim3.6$. In Figure 5.3–b, the

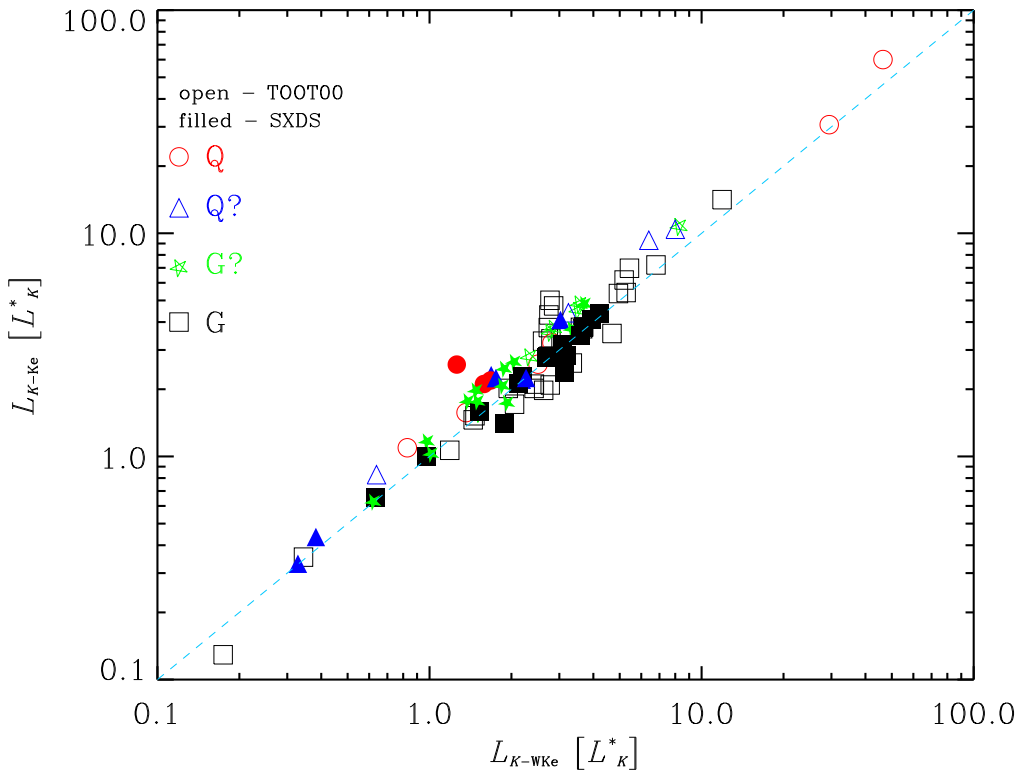

Figure 5.4: K-corrected and passive-evolution-corrected luminosity at K, $L_{K-\mathrm{Ke}}$, versus the K-corrected and passive-evolution-corrected luminosity at K calculated using the $K_\mathrm{W}-z$ relation, $L_{K-\mathrm{WKe}}$, both in L^*_K units. Symbols indicate optical classification as in Figure 5.3; open symbols indicate TOOT00 objects and filled symbols denote SXDS radio sources.

increase of the ratio $L_{K-\mathrm{K}}/L_{K-\mathrm{WKe}}$ is exponential, showing how significant the corrections for passive evolution are in the K-band luminosity. The fact that $L_{K-\mathrm{K}}$ is not corrected for passive evolution means that objects are seen brighter at higher redshifts due to them being younger in terms of their stellar populations.

The tail above redshift 2 in Figure 5.3–a can be explained by the fact that the Ke-correction in Figure 5.2 was calculated for $z_\mathrm{max} = 3.99$, whereas the $K_\mathrm{W} - z$ relation assumes formation at a redshift of $z_\mathrm{max} = 10$. The wiggles seen in Figure 5.3–a are explained by the fact that $L_{K-\mathrm{WKe}}$ is calculated from $K_\mathrm{W} - z$ is a best fit to data and is close to a 3 L^* elliptical galaxy. This is also shown in Figure 5.4, where objects causing those wiggles are found off the $L_{K-\mathrm{Ke}}$ = $L_{K-\mathrm{WKe}}$ line. Nevertheless, it is obvious that methods (1) and (3) give similar results, as expected, since they are both K-corrected and passive-evolution-corrected. Furthermore, the TOOT00 objects fit the $K_\mathrm{W} - z$ relation well, but tend to be fainter at higher redshifts $z \sim 1$ (see Figure 5.5). The SXDS objects are in general fainter, especially at high redshifts (see also Section 5.4.1). This implies that using the $K_\mathrm{W} - z$ relation as a guide to calculate the luminosity at K introduces errors, thus the $L_{K-\mathrm{Ke}}$ calculated by method (1) is going to be used in the further analysis.

Table 5.3: Luminosity at K for the 47 TOOT00 radio sources. **Column 1** shows the name of the object and **Column 2** the redshift; 'Kz' denotes that the 7 photometric redshifts were estimated from the $K_{\rm W} - z$ relation (Eqn. 5.1; Section 5.3); a '?' shows uncertainty. **Column 3** gives the K-corrected and passive-evolution-corrected absolute magnitude at K, $M_{K-{\rm Ke}}$. **Column 4** gives the K-corrected absolute magnitude at K, $M_{K-{\rm K}}$. **Column 5** gives the K-corrected and passive-evolution-corrected luminosity at K, $L_{K-{\rm Ke}}$, in L^*_K units. **Column 6** gives the K-corrected luminosity at K, $L_{K-{\rm K}}$, in L^*_K units. **Column 7** gives the K-corrected and passive-evolution-corrected luminosity at K, $L_{K-{\rm WKe}}$ in units of L^*_K, that was calculated from the $K_{\rm W} - z$ relation of Willott et al. (2003) that fits a 3 L^* passively evolving galaxy that formed all its stellar population at high redshift (see Section 5.3). For the calculation of absolute magnitude and luminosity at K, a typical M^*_K = -23.96 mag (Smith et al. 2009) was used.

(1)	(2)	(3)	(4)	(5)	(6)	(7)
Name	redshift	$M_{K-{\rm Ke}}$ (mag)	$M_{K-{\rm K}}$ (mag)	$L_{K-{\rm Ke}}$ $[L^*_K]$	$L_{K-{\rm K}}$ $[L^*_K]$	$L_{K-{\rm WKe}}$ $[L^*_K]$
TOOT00_1140	0.911?	-25.41	-26.83	3.79	14.01	3.58
TOOT00_1099	1.397?	-26.84	-28.75	14.14	82.13	11.88
TOOT00_1125	1.916	-28.41	-30.85	60.04	569.3	46.40
TOOT00_1143	0.438	-24.77	-25.71	2.11	4.99	2.43
TOOT00_1233	1.244	-27.68	-29.49	30.66	163.6	29.44
TOOT00_1022	2.872^{Kz}	-25.40	-28.71	3.78	79.60	2.73
TOOT00_1204	0.6395	-25.39	-26.51	3.73	10.47	3.65
TOOT00_1235	0.743	-24.99	-26.23	2.59	8.09	2.50
TOOT00_1224	3.438^{Kz}	-25.71	-29.32	5.01	139.2	2.77
TOOT00_1291	0.917^{Kz}	-25.08	-26.54	2.812	10.75	2.75
TOOT00_1107	0.300	-21.74	-22.55	0.13	0.27	0.17
TOOT00_1180	1.810	-25.60	-27.91	4.51	38.09	3.51
TOOT00_1027	0.890	-22.83	-24.25	0.35	1.31	0.34
TOOT00_1195	1.418^{Kz}	-25.28	-27.21	3.36	19.88	2.79
TOOT00_1069	2.300	-24.06	-26.91	1.09	15.19	0.83
TOOT00_1094	1.516?	-25.25	-27.27	3.28	21.02	2.60
TOOT00_1149	0.260	-25.01	-25.73	2.62	5.09	3.35
TOOT00_1298	1.287?	-25.78	-27.62	5.37	29.03	4.95
TOOT00_1200	0.691	-24.44	-25.62	1.56	4.63	1.52
TOOT00_1215	0.278	-24.70	-25.47	1.98	4.03	2.63
TOOT00_1240	2.543?	-25.67	-28.70	4.82	78.76	3.55
TOOT00_1289	1.784?	-26.07	-28.36	6.97	57.46	5.43
TOOT00_1072	0.577	-25.80	-26.83	5.43	14.01	5.28
TOOT00_1134	0.311	-25.34	-26.15	3.56	7.53	4.68
TOOT00_1244	1.358	-24.45	-26.33	1.57	8.86	1.36
TOOT00_1066	0.926	-24.42	-25.87	1.52	5.81	1.47
TOOT00_1261	2.544	-25.57	-28.60	4.40	71.92	3.24
TOOT00_1252	3.229^{Kz}	-25.54	-29.11	4.30	115.0	2.75
TOOT00_1214	3.081	-26.38	-29.90	9.31	238.2	6.39
TOOT00_1152	3.310^{Kz}	-25.65	-29.24	4.73	129.8	2.86
TOOT00_1129	1.860	-23.75	-26.12	0.83	7.31	0.64
TOOT00_1090	0.201	-24.54	-25.14	1.71	2.96	2.05
TOOT00_1267	0.968	-25.37	-26.89	3.68	14.92	3.64
TOOT00_1188	1.417	-25.07	-27.00	2.79	16.50	2.32
TOOT00_1196	1.662^{Kz}	-25.36	-27.51	3.60	26.16	2.77
TOOT00_1173	0.332	-24.76	-25.61	2.09	4.58	2.78
TOOT00_1228	1.135?	-24.37	-26.08	1.46	7.02	1.45
TOOT00_1034	0.580	-25.41	-26.44	3.81	9.84	3.69
TOOT00_1255	0.582	-24.72	-25.75	2.02	5.21	1.95
TOOT00_1048	1.943	-26.54	-29.01	10.72	104.3	8.26
TOOT00_1029	0.737	-26.10	-27.31	7.21	21.94	6.80
TOOT00_1115	0.416	-24.72	-25.65	2.02	4.73	2.42
TOOT00_1132	0.183	-24.03	-24.55	1.07	1.72	1.19
TOOT00_1250	1.350	-25.23	-27.11	3.23	18.17	2.82
TOOT00_1268	2.015	-26.50	-29.06	10.42	109.3	8.00
TOOT00_1251	2.490	-25.40	-28.43	3.75	61.31	2.85
TOOT00_1203	1.397	-25.94	-27.85	6.17	35.85	5.19

Table 5.4: Luminosity at K for the 37 SXDS radio sources. **Column 1** shows the name of the object and **Column 2** the redshift; 'BC' denotes that the 13 photometric redshifts were estimated from HyperZ (Bolzonella et al. 2000); a '?' shows uncertainty. **Column 3** gives the K-corrected and passive-evolution-corrected absolute magnitude at K, $M_{K-\mathrm{Ke}}$. **Column 4** gives the K-corrected absolute magnitude at K, $M_{K-\mathrm{K}}$. **Column 5** gives the K-corrected and passive-evolution-corrected luminosity at K, $L_{K-\mathrm{Ke}}$, in L^*_K units. **Column 6** gives the K-corrected luminosity at K, $L_{K-\mathrm{K}}$, in L^*_K units. **Column 7** gives the K-corrected and passive-evolution-corrected luminosity at K, $L_{K-\mathrm{WKe}}$ in units of L^*_K, that was calculated from the $K_\mathrm{W} - z$ relation of Willott et al. (2003) that fits a 3 L^* passively evolving galaxy that formed all its stellar population at high redshift (see Section 5.3). For the calculation of absolute magnitude and luminosity at K, a typical M^*_K = -23.96 mag (Smith et al. 2009) was used.

(1)	(2)	(3)	(4)	(5)	(6)	(7)
Name	redshift	$M_{K-\mathrm{Ke}}$ (mag)	$M_{K-\mathrm{K}}$ (mag)	$L_{K-\mathrm{Ke}}$ $[L^*_K]$	$L_{K-\mathrm{K}}$ $[L^*_K]$	$L_{K-\mathrm{WKe}}$ $[L^*_K]$
sxds_0001	0.626	-25.08	-26.17	2.79	7.60	2.68
sxds_0002	1.183	-24.82	-26.58	2.21	11.17	2.18
sxds_0003	2.433	-25.49	-28.44	4.09	61.53	3.03
sxds_0004	2.270^{BC}	-24.88	-27.64	2.31	29.48	1.69
sxds_0005	1.610^{BC}	-25.02	-27.12	2.65	18.27	2.04
sxds_0006	1.882^{BC}	-25.67	-28.06	4.82	43.55	3.71
sxds_0007	1.325?	-25.39	-27.26	3.73	20.72	3.33
sxds_0008	0.458	-24.57	-25.50	1.74	4.12	1.93
sxds_0009	3.570?	-24.99	-28.58	2.58	70.20	1.26
sxds_0010	1.400^{BC}	-24.13	-26.04	1.17	6.78	0.98
sxds_0011	0.647	-25.56	-26.68	4.35	12.21	4.20
sxds_0012	0.865	-25.08	-26.47	2.79	10.02	2.70
sxds_0013	2.713	-24.78	-28.00	2.11	41.05	1.58
sxds_0014	2.205^{BC}	-24.95	-27.71	2.47	31.50	1.88
sxds_0015	0.344	-24.33	-25.21	1.40	3.15	1.88
sxds_0016	1.345?	-23.06	-24.94	0.44	2.45	0.38
sxds_0017	2.583	-24.82	-27.94	2.19	39.07	1.68
sxds_0018	0.919	-25.41	-26.87	3.79	14.47	3.69
sxds_0019	0.694	-23.50	-24.68	0.65	1.93	0.63
sxds_0020	1.135^{BC}	-23.46	-25.16	0.63	3.01	0.62
sxds_0021	1.645^{BC}	-24.58	-26.74	1.77	12.84	1.38
sxds_0022	0.248	-24.91	-25.63	2.38	4.62	3.12
sxds_0023	0.586	-24.47	-25.50	1.60	4.12	1.53
sxds_0024	0.516	-25.32	-26.30	3.47	8.60	3.59
sxds_0025	0.964?	-22.76	-24.28	0.33	1.34	0.33
sxds_0026	0.450	-25.10	-26.03	2.84	6.72	3.20
sxds_0027	1.595^{BC}	-24.84	-26.94	2.24	15.48	1.75
sxds_0028	0.627?	-24.86	-25.95	2.29	6.24	2.20
sxds_0029	1.380^{BC}	-24.58	-26.47	1.76	10.07	1.50
sxds_0030	0.535	-24.78	-25.76	2.12	5.25	2.12
sxds_0031	1.325^{BC}	-24.76	-26.62	2.07	11.52	1.85
sxds_0032	1.010^{BC}	-23.96	-25.52	1.00	4.18	0.97
sxds_0033	0.647	-25.22	-26.34	3.19	8.95	3.08
sxds_0034	1.095	-24.84	-26.52	2.25	10.52	2.26
sxds_0035	2.715^{BC}	-24.70	-27.92	1.97	38.39	1.48
sxds_0036	0.871	-25.50	-26.88	4.10	14.69	3.93
sxds_0037	1.085^{BC}	-23.99	-25.64	1.03	4.67	1.01

5.4 Discussion

5.4.1 The $K-z$ diagram

Figure 5.5 presents the $K-z$ diagram (in the Vega magnitude system) for the 47 TOOT00 radio sources and the 37 SXDS[2] radio sources; 7 out of 47 TOOT00 objects, although plotted, were excluded from the $K-z$ fit since their photometric redshifts are estimated using the $K_{\rm W}-z$ relation (see Chapter 3). Previous redshift surveys of radio sources, like the 3CRR, 6CE, 6C* and 7CRS, are shown for comparison. There is a fairly good agreement with the $K_{\rm W}-z$ relation. The best linear fit on the TOOT00 sample is very similar to the $K_{\rm W}-z$ relation of Eqn. 5.1, although there is scatter, as can be seen in Figure 5.6. The two near-IR bright quasars in the TOOT00 sample below the $K_{\rm W}-z$ fit, TOOT00_1233 & TOOT00_1125, do not follow this relation. Note that quasars in the 3CRR and 6CE do not follow the $K_{\rm W}-z$ relation either, as can be seen by 3C22 that is plotted as an example. This can be attributed to light from the nucleus that is being observed at K, instead of the near-IR emission coming from the stellar population (e.g. objects 3C22 and 3C280, see Taylor et al. 1996); an expected result for quasars. TOOT00_1107[3] & TOOT00_1027 are other clear outliers, and these objects are genuinely faint in the K-band. Other examples of such faint at K objects do exist (e.g. 6C**0935+4348 & 6C**1009+4327, Cruz et al. 2007; 5C7.178, Willott et al. 2002, 2003), as can be seen in Figure 5.5. One explanation of underluminous outliers is the 'young galaxy' hypothesis (e.g. Willott et al. 2003; e.g. Jarvis, van Breukelen & Wilman 2005) – i.e. that the object is observed during an epoch at which it has yet to form much of its stars – but is unlikely to be the case here because of the relatively low redshifts of the objects. Another scenario is that fainter K magnitudes could be expected in any model in which powerful jets can, if only rarely, be associated with underluminous galaxies (Willott et al. 2003). Again, objects of the kind do exist (e.g. Vardoulaki et al. 2008). It is interesting that both TOOT00_1107 and TOOT00_1027 have unusual radio spectra: TOOT00_1107 is ultra-steep (like 6C**0935+4348 & 6C**1009+4327) at high frequency, flattening dramatically at low frequency, while TOOT00_1027 is a GPS source.

Figure 5.6 shows the difference between K magnitudes of the TOOT00 and SXDS samples and the ones calculated from the $K_{\rm W}-z$ relation, ΔK (see Tables 5.1 & 5.2), plotted against redshift. This gives another insight into the behaviour of the two samples. It is interesting that the two bright quasars in the TOOT00 sample, TOOT00_1125 & TOOT00_1233, are much

[2]The K magnitudes of the SXDS radio-source sample are converted from AB to Vega magnitudes using the relation $K_{\rm Vega} = K_{\rm AB}$ - 1.898 (e.g. Hewett et al. 2006; see Table 2.3 for the $K_{\rm AB}$ values).

[3]The fact that TOOT00_1107 is an outlier in all figures presented here could be explained by the uncertain ID of the object (see Section 3.6).

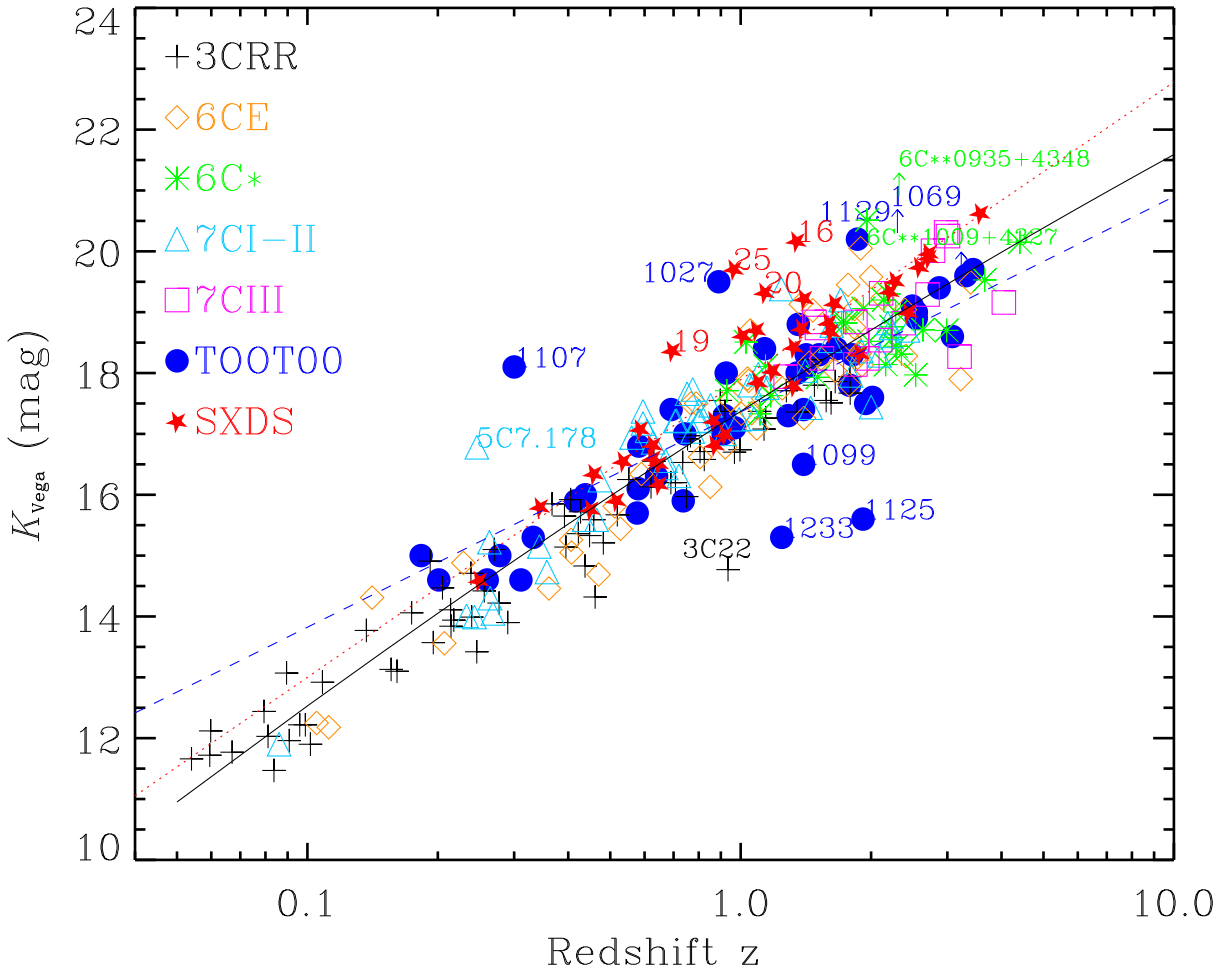

Figure 5.5: The $K-z$ diagram for the TOOT00 and the SXDS radio sources; both spectroscopic and photometric redshifts are shown (including 7 cases in TOOT00 where the redshift is estimated form the $K_{\rm W}-z$ relation). Symbols are the same as in Figure 5.1; the aperture-corrected K magnitude is used for the 3CRR, 6CE, 6C* and 7CRS samples. The solid black line is the $K_{\rm W}-z$ relation of Willott et al. (2003). The dashed blue line is the best-fit line for the TOOT00 radio sources excluding the 7 photometric points that were estimated using the $K_{\rm W}-z$ relation (see Table 5.1), and excluding all quasars: $K = 17.36 + 3.54 \times \log_{10}(z)$, where linear Pearson correlation coefficient is 0.75 and the Spearman's $\rho = 0.81$ with a $\gg 99.99\%$ probability for a correlation. The red dotted line is the best-fit line for the SXDS radio sources $K = 17.89 + 4.89 \times \log_{10}(z)$, where the linear Pearson correlation coefficient is 0.82 and the Spearman's $\rho = 0.87$ with a $\gg 99.99\%$ probability for a correlation. Note: TOOT00_1196 & TOOT00_1252 are plotted as limits (see Section 3.6 in Chapter 3). Also, the 3CRR sample is incomplete, since the provided list does not contain quasars; the 3C22 quasar is also plotted for comparison and labelled with its name (data taken from Rawlings et al. 1995 and Simpson, Rawlings & Lacy 1999). The 6CE sample plotted is incomplete as it includes only narrow-line radio galaxies (complete list in Rawlings, Eales & Lacy 2001). The 6C* sample plotted is incomplete as it includes only narrow-line radio galaxies (see Jarvis et al. 2001a). Objects 6C**0935+4358 and 6C**1009+4327 (Cruz et al. 2007) are also plotted since they are discussed in Section 5.4; they lie in the right-top part of the diagram. The 7CI-II sample plotted includes only narrow-line radio galaxies. The 7CIII sample plotted is incomplete as it includes only narrow-line radio galaxies above $z > 1.2$; a complete list of the 7CIII objects can be found in Lacy, Bunker & Ridgway (2000) and Willott et al. (2003).

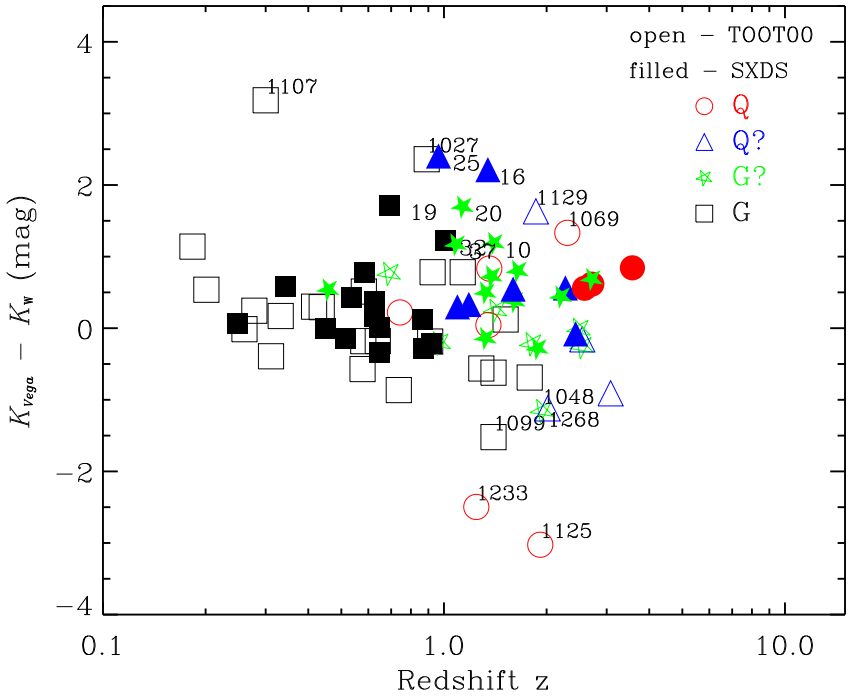

Figure 5.6: $K_{\rm Vega} - K_{\rm W}$ versus redshift for the TOOT00 and the SXDS radio sources; the 7 TOOT00 objects that their redshift was estimated using the $K_{\rm W} - z$ relation are excluded from the plot; the 13 SXDS objects with photometric redshift are included since their redshift is estimated with HyperZ. Symbols indicate optical classification as in Figure 5.3; open symbols denote TOOT00 radio sources and filled symbols stand for SXDS objects. Objects with $K_{\rm Vega} - K_{\rm WKe} <$ -1 and $K_{\rm Vega} - K_{\rm W} > 1$ are marked with their name.

brighter than the $K_{\rm W} - z$ predicts by ~ 3 orders of magnitude, suggesting a luminosity 15 times brighter at K than expected from a model of a 3 L^* passively evolving galaxy. Furthermore, TOOT00_1107 is ~ 3 orders of magnitude fainter, and thus ~ 0.06 times less luminous at K than a model of a 3 L^* passively evolving galaxy predicts. From Figure 5.6 can be seen that a galaxy G, TOOT00_1099, is unusually bright at K ($L_{K-{\rm Ke}} \sim 14\ L^*_K$). One explanation could be the uncertain spectroscopic redshift of the object (see Table 5.1), but the emission line in the optical spectrum is almost certainly [OII] (see Figure 3.10); another reason is that it is a brighter cluster galaxy (BCG) where objects are found to have luminosities $\sim 10\ L^*$ (e.g Collins et al. 2004).

Figure 5.7 presents a histogram of ΔK based on Figure 5.6. Objects for which their redshift is estimated, using the $K_{\rm W} - z$ relation, are excluded from the plot. Also spectroscopically confirmed quasars Q are excluded, because the K-band emission is probably contaminated with light from the nucleus. This histogram shows clearly that the SXDS radio sources are, in general, fainter at K than predicted by the $K_{\rm W} - z$ relation, especially at high redshifts. We calculate the two-sided Kolmogorov-Smirnov (K-S test; Press et al. 1993) statistic and associated probability to investigate whether the SXDS $K - z$ relation and $K_{\rm W} - z$ relation are

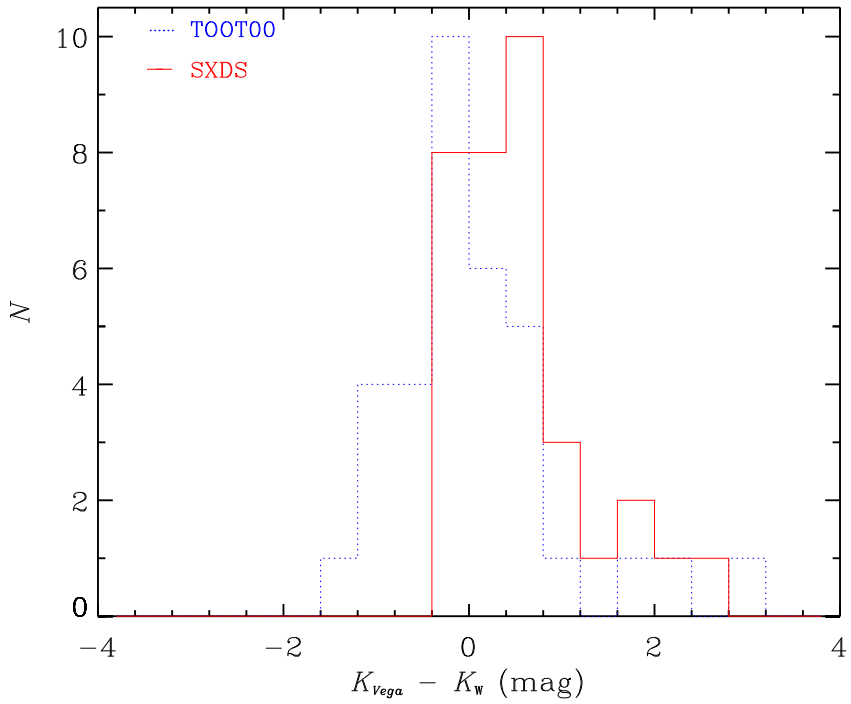

Figure 5.7: $K_{\rm Vega} - K_{\rm W}$ histogram for the TOOT00 and the SXDS radio sources. Objects that have their redshifts estimated using the $K_{\rm W} - z$ relation and quasars Q are excluded from the plot. The blue dotted line denotes TOOT00 objects and the red solid line stands for SXDS radio sources. The binning on the x-axis is 0.4.

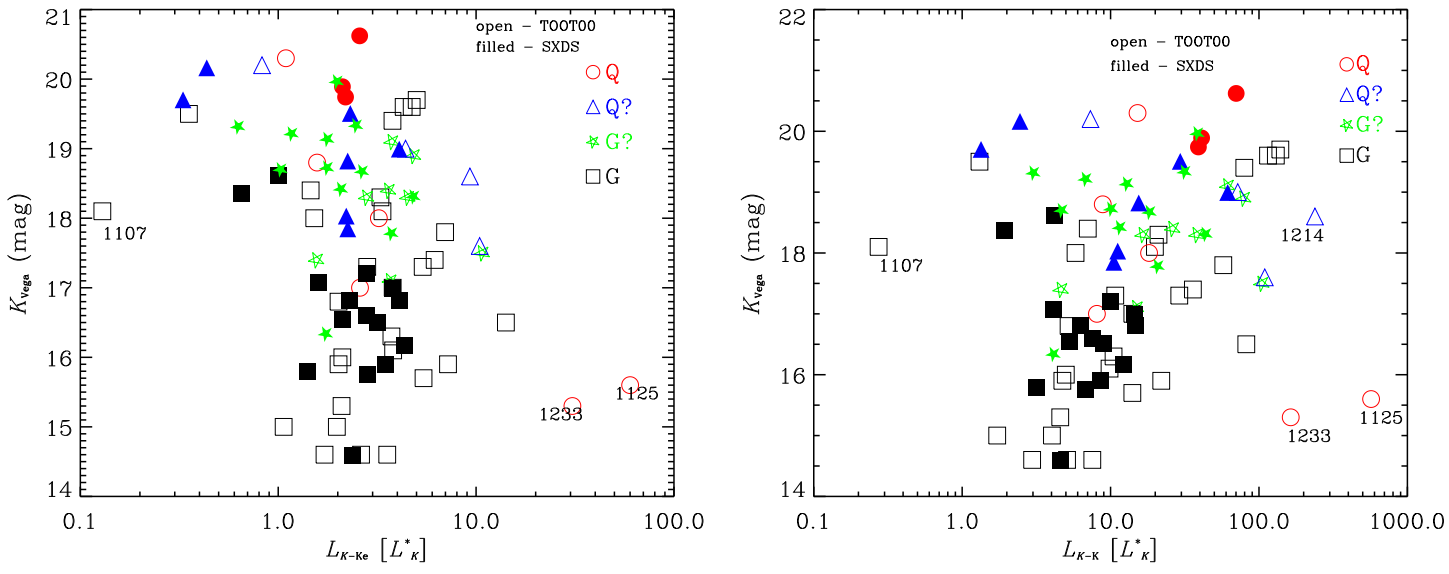

Figure 5.8: **a) Left**: K magnitude versus K-corrected and passive-evolution-corrected luminosity at K, $L_{K-{\rm Ke}}$, in L^*_K units for the TOOT00 and the SXDS radio sources. **b) Right**: K magnitude versus K-corrected luminosity at K, $L_{K-{\rm K}}$, in L^*_K units for the TOOT00 and the SXDS radio sources. In both plots symbols indicate optical classification as in Figure 5.3; open symbols denote TOOT00 objects and filled symbols stand for SXDS radio sources.

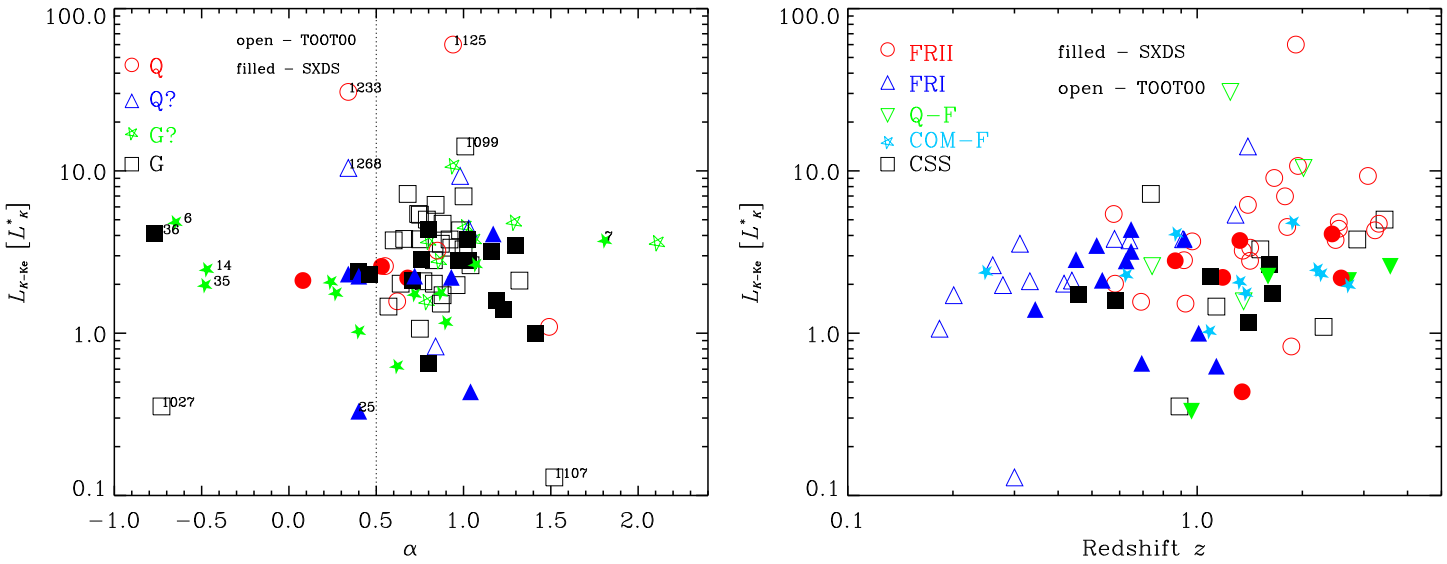

Figure 5.9: **a) Left**: K-corrected and passive-evolution-corrected luminosity at K, $L_{K-\mathrm{Ke}}$, in L^*_K units versus radio spectral index α for the TOOT00 and the SXDS radio sources. Symbols indicate optical classification as in Figure 5.3; open symbols denote TOOT00 objects and filled symbols stand for SXDS radio sources. The vertical dotted line at $\alpha = 0.5$ shows the conventional border between steep and flat-spectrum sources. **b) Right**: K-corrected and passive-evolution-corrected luminosity at K, $L_{K-\mathrm{Ke}}$, in L^*_K units versus redshift z for the TOOT00 and the SXDS radio sources. Symbols indicate radio-optical classification (see Tables 5.1 & 5.2): open symbols denote TOOT00 objects and filled symbols stand for SXDS radio sources; red circles denote FRII objects, blue triangles denote FRI radio sources, green upside-down triangles denote Q-F objects, blue stars denote COM-F radio sources and black squares denote CSS objects; open symbols denote TOOT00 objects and filled symbols stand for SXDS radio sources.

different distributions. The maximum deviation between the two is ~ 0.29 and the significance level of the K-S test is $\sim 6\%$. This result suggests that the SXDS $K-z$ and the $K_{\mathrm{W}}-z$ relations are different distributions. This verifies that the $K_{\mathrm{W}}-z$ relation does not describe well the relation of K magnitude with redshift in the SXDS objects. For the TOOT00 objects the maximum deviation between $K-z$ relation and $K_{\mathrm{W}}-z$ relation is ~ 0.09 and the associated probability is 99.88%, verifying that the TOOT00 radio sources can be described by the $K_{\mathrm{W}}-z$ relation that fits the 3CRR, 6CE, 6C* and 7CRS radio sources; objects that their redshift was estimated from the $K_{\mathrm{W}}-z$ relation and the two bright at K quasars were excluded from the test. A K-S test between the TOOT00 and SXDS $K-z$ relations shows that the two distributions are different, with maximum deviation of ~ 0.29 and probability $\sim 9\%$; quasars Q and objects with redshift from the $K_{\mathrm{W}}-z$ relation were excluded from the test.

From Figure 5.8–a we see that the K-band magnitude is weakly anti-correlated with the luminosity at K, especially in the SXDS radio sources. This correlation is driven by the

emergence, mainly in SXDS, of a population of faint ($K \gtrsim 19$ mag) radio galaxies at $z \sim 1$–2 (see Figure 5.5) that are significantly less luminous ($L_{K-\mathrm{Ke}} \ll 3L^*_K$) than low-$z$ radio galaxies. We note a high quasar fraction (~ 0.21) amongst this population, particularly significant when we see that in many cases their $L_{K-\mathrm{Ke}}$ is an upper limit to stellar luminosity.

For comparison, the K versus $L_{K-\mathrm{K}}$ plot is shown in Figure 5.8–b. The much bigger dispersion in $L_{K-\mathrm{K}}$ is obvious, showing in particular that faint at K objects are more luminous at K when passive evolution corrections are not applied.

Figure 5.9–a presents the comparison between luminosity at K, $L_{K-\mathrm{Ke}}$, and radio spectral index α. We do not see a particular correlation, as both flat- and steep-spectrum objects show cases of high- and low-$L_{K-\mathrm{Ke}}$ objects. For example very steep-spectrum objects, like TOOT00_1196 & sxds_0007 have $L_{K-\mathrm{Ke}} \gtrsim 4\ L^*_K$, but TOOT00_1007 has luminosity at K of $\lesssim 0.1\ L^*_K$. Very flat-spectrum objects, like sxds_0006 & sxds_0036 have $L_{K-\mathrm{Ke}} \gtrsim 4\ L^*_K$, while the very flat-spectrum radio galaxy TOOT00_1027 has $L_{K-\mathrm{Ke}} \lesssim 0.4\ L^*_K$.

In Figure 5.9–b the dependence of $L_{K-\mathrm{Ke}}$ on redshift z can be seen. For the TOOT00 radio sources, the median luminosity at K is $\sim 3.56\ L^*_K$, excluding the two bright at K quasars TOOT00_1125 & TOOT00_1233 for the reasons explained above; the mean $L_{K-\mathrm{Ke}} \sim 4\ L^*_K$. If we exclude all the outliers, the two bright at K quasars and the two faint at K TOOT00_1027 & TOOT00_1107, then the mean $L_{K-\mathrm{Ke}}$ is again $\sim 4\ L^*_K$. The SXDS radio sources have a median luminosity at K of $2.24\ L^*_K$, suggesting that SXDS objects belong to a different population of radio sources than the TOOT00 objects (see also Figure 5.7). Furthermore, they suggest that the TOOT00 radio sources at a median redshift of $z_{\mathrm{med}} \sim 1.25$ correspond to $\sim 4\ L^*_K$ host galaxies at redshift zero. Similarly, the SXDS radio sources at $z_{\mathrm{med}} \simeq 1.1$ correspond to $\sim 2\ L^*_K$ host galaxies at redshift zero. Thus the host of the TOOT00 radio sources are 2-times more luminous at K than the hosts of the SXDS objects implying, assuming K-band traces old stars, a corresponding fraction of ~ 2 difference in stellar masses.

5.4.2 Relation of K-band magnitude, radio luminosity and radio structure

Figures 5.10 & 5.11 show the relation between radio luminosity at 1.4 GHz and 151 MHz and the luminosity at K for the TOOT00 and the SXDS radio sources. The Ledlow & Owen (1996) radio-optical luminosity relationship, which has been argued to divide the FRIs and FRIIs, is also shown. It is interesting that all FRII objects lie above the plotted line, with the exception of TOOT00_1196 (see Figure 5.10–c), but there are some FRI objects above the line contrary to the Ledlow & Owen (1996) general result. FRI radio sources above the FRI/FRII break in the radio luminosity are known to exist (e.g. Heywood, Blundell & Rawlings 2007; Vardoulaki

et al. 2008). There is evidence (Heywood, Blundell & Rawlings 2007) that the division between FRI and FRII radio sources changes with z, where FRIs can exist above the traditional break luminosity at higher redshifts. This is probably caused by cosmic evolution in radio-source environments (e.g. Heywood, Blundell & Rawlings 2007) and is also likely to affect the lower-z population with $z \sim 0.5$. In both TOOT00 and SXDS samples there are examples of FRI objects at lower redshift that have radio luminosities well above the FRI/FRII break (e.g. TOOT00_1034 at $z = 0.580$; sxds_0001 at $z = 0.626$; see also Table 5.1 & Figure 5.11 for the TOOT00 sample and Table 5.2 & Figure 5.10 for SXDS the sample).

From Figure 5.10 we see a few objects with low $L_{K-\mathrm{Ke}}$ and $L_{1.4\mathrm{GHz}}$ values above the Ledlow & Owen (1996) line. There is no strong evidence for existence of these objects in this part of the Ledlow & Owen (1996) plot. This is confirmed by Mauch (priv. communication) in a local sample.

A histogram of the number of SXDS objects with redshift based on their radio-optical classification is shown in Figure 5.12–a. In Figure 5.12–b the similar histogram is shown for model predictions from the S^3-SEX simulation (Wilman et al. 2008) at the appropriate flux density limit of the SXDS, scaled down to a 0.0002-sr sky area (see Chapter 4 for more details on the simulation). The relevant histogram for the TOOT00 radio sources is presented in Figure 3.7 (see Section 3.4 in Chapter 3). It can be seen that above redshift $z \sim 1.2$ for the SXDS and $z \sim 1.4$ for the TOOT00 there are no FRI objects. Furthermore, the difference between the number high-$L_{1.4}$ and high-L_{151} objects seen in Figures 5.12–b & 3.7–b respectively, can be attributed to the fact that the S^3-SEX simulation is based on low-frequency selected samples and thus, perhaps slightly, underpredicts the high-z population at $L_{1.4\mathrm{GHz}}$ (see Section 4.3). Note that the few high-redshift CDs in SXDS are underpredicted and that lots of FDs that may be selected as FRIIs but are perhaps best associated with the low-L_{151} population. Finally, the S^3-SEX simulation predicts one radio-quiet-quasar (RQQ) below redshift $z = 1.5$ inside a 0.0002-sr sky area at a flux limit of 2 mJy at 1.4 GHz, and one GPS source. In the data there is a significant fraction of Q objects at high redshift ($\sim 30\%$ above $z = 2$). Unfortunately we have no spectral-index information for the simulated objects and thus we cannot compare the number of flat-spectrum QSOs seen in the data and in the S^3-SEX simulation.

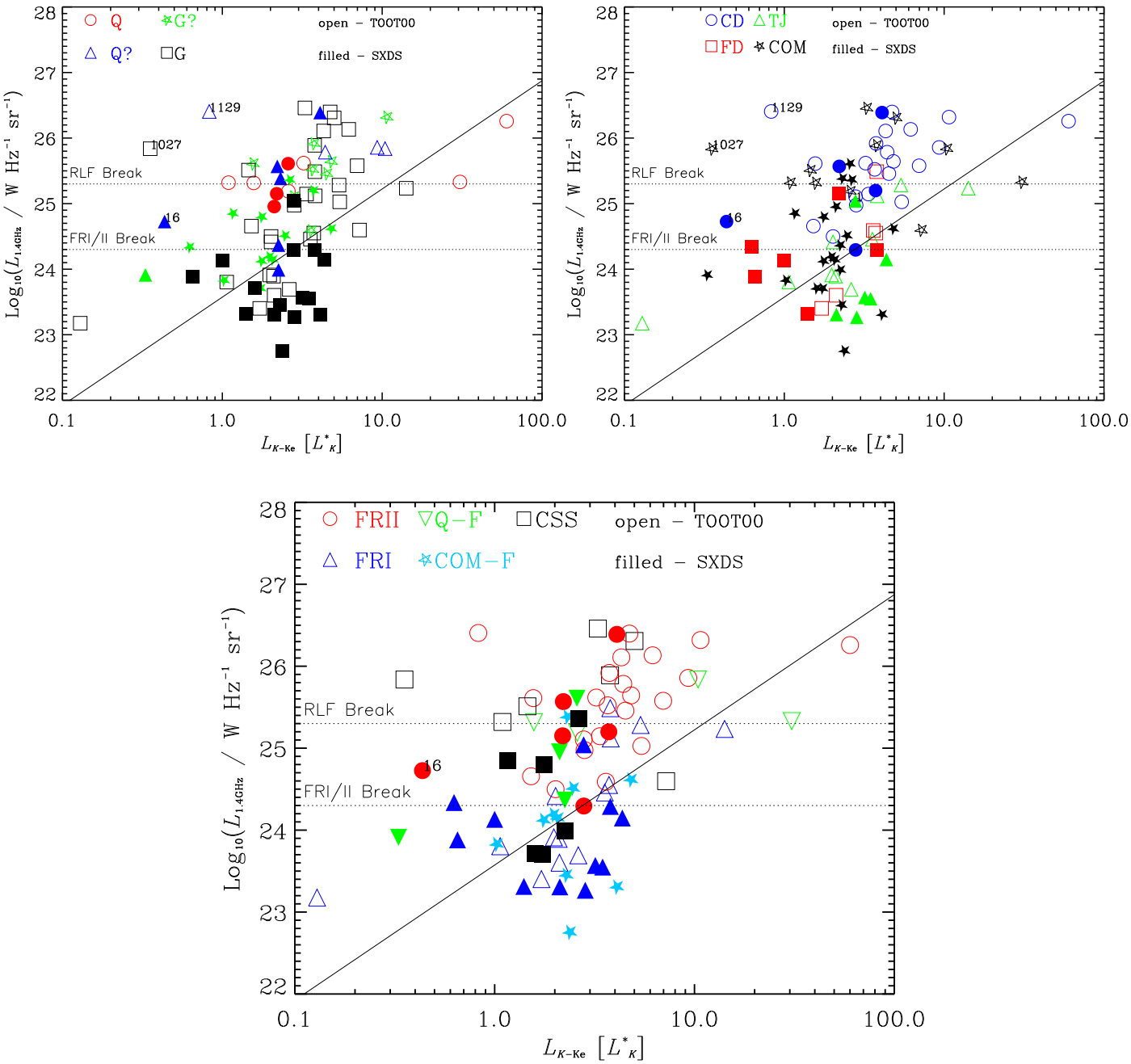

Figure 5.10: Radio luminosity at 1.4 GHz, $L_{1.4\mathrm{GHz}}$, versus K-corrected and passive-evolution-corrected luminosity at K, $L_{K-\mathrm{Ke}}$, in L^*_K units for the TOOT00 and the SXDS radio sources; open symbols denote TOOT00 objects and filled symbols stand for SXDS radio sources. **a) Top Left**: Symbols indicate optical classification as in Figure 5.3. **b) Top Right:** Symbols indicate radio classification (see Table 3.1 & Table 2.1 respectively): blue circles denote CD radio sources, red squares denote FD objects, green triangles denote TJ sources and black stars stand for COM radio sources. **c) Bottom**: Symbols indicate radio-optical classification as in Figure 5.9–b. In all plots, the black solid line is the Ledlow & Owen (1996; see also Meier et al. 1998; $\log_{10}(L_{1.4\mathrm{GHz}}) = 10.35 - 0.66 \times \mathrm{M}_{24.5}$) line $L_{1.4\mathrm{GHz}} \propto L_{\mathrm{opt}}^{1.65}$, converted for the luminosity at K assuming $\mathrm{M}_{\mathrm{opt}}$ = -22 mag (Ledlow & Owen 1996) and M_K = -23.96 mag (Smith et al. 2009). The horizontal lines show the RLF and FRI/FRII breaks calculated from the Willott et al. (2003) and the Fanaroff & Riley (1974) values respectively using a typical steep-spectrum spectral index of 0.8.

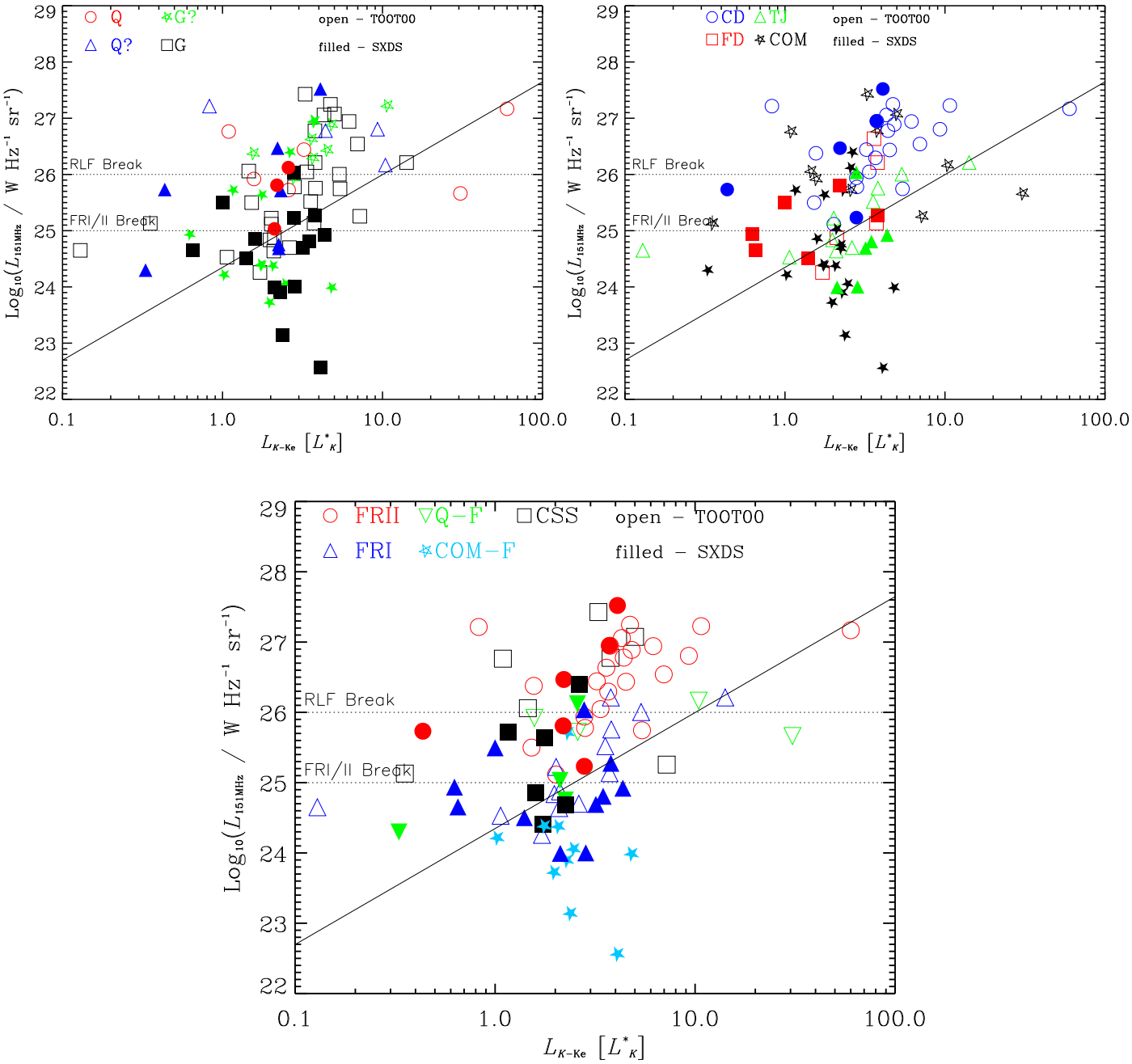

Figure 5.11: Radio luminosity at 151 MHz, $L_{151\mathrm{MHz}}$, versus $L_{K-\mathrm{Ke}}$ in L^*_K units for the TOOT00 and SXDS radio sources; open symbols denote TOOT00 objects and filled symbols stand for SXDS radio sources. **a) Top Left**: Symbols indicate optical classification as in Figure 5.3. **b) Top Right:** Symbols indicate radio classification as in Figure 5.10. **c) Bottom**: Symbols indicate radio-optical classification as in Figure 5.9. In all plots, the black solid line is the Ledlow & Owen (1996; see also Meier et al. 1998; $L_{1.4\mathrm{GHz}}$ = 10.35 - 0.66 × $\mathrm{M}_{24.5}$) line $L_{1.4\mathrm{GHz}} \propto L_{\mathrm{opt}}^{1.65}$, converted for the luminosity at K assuming $\mathrm{M}_{\mathrm{opt}}$ = -22 mag (Ledlow & Owen 1996) and M_K = -23.96 mag (Smith et al. 2009); a typical steep-spectrum radio spectral index of 0.8 was used to convert the luminosity at 1.4 GHz to 151 MHz. The horizontal lines show the RLF and FRI/FRII breaks calculated from the Willott et al. (2003) and the Fanaroff & Riley (1974) values respectively using a typical steep-spectrum spectral index of 0.8.

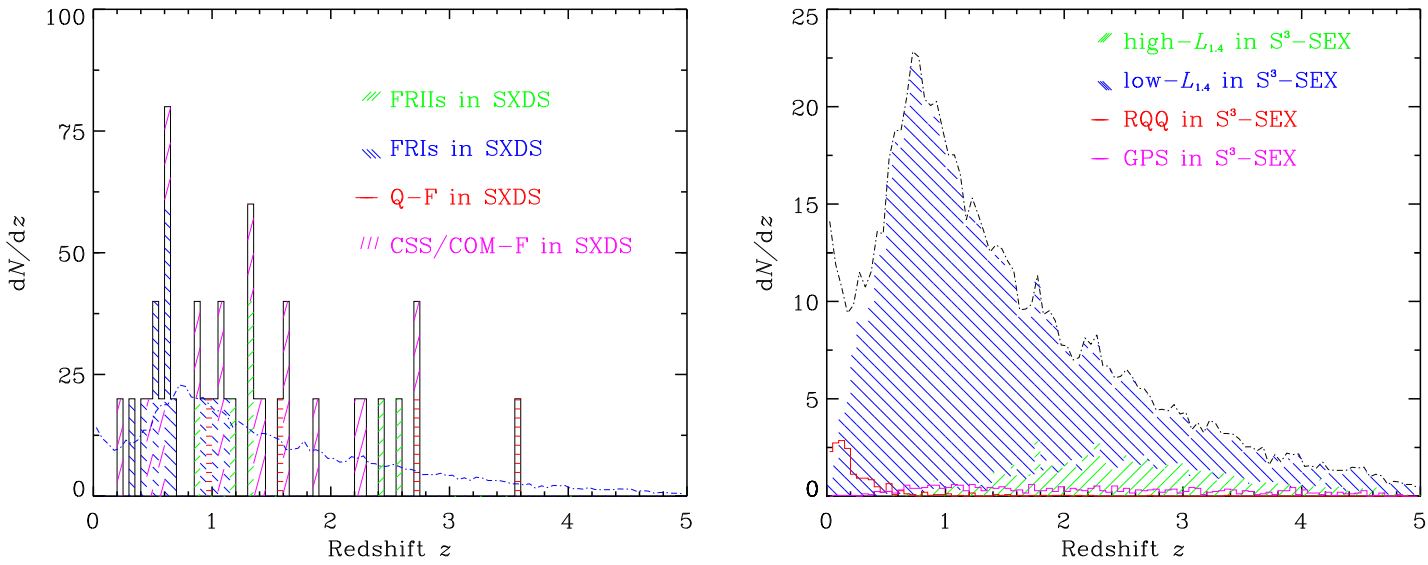

Figure 5.12: **a) Left:** Histogram of the redshift distribution for the 37 SXDS radio sources according to radio-optical class (see Table 5.2). The binning on the redshift axis is dz = 0.05. The green colour represents FRIIs, blue represents FRIs, red represents flat-spectrum quasars (Q-F) and purple represents CSS objects; the black histogram shows the TOOT00 distribution. FRIIs correspond to CD radio sources; FRIs correspond to FD and TJ; Q-F correspond to quasars with flat radio spectral index; Q-F? correspond to quasars with α close to the critical value 0.5 ($0.5 < \alpha < 0.7$); Compact Steep Spectrum (CSS) correspond to objects with steep radio spectral index ($\alpha > 0.7$) and compact radio structure; and CSS-Q correspond to quasars associated with a compact steep spectrum ($\alpha > 0.7$) object. The dotted-dashed blue line shows model predictions from the S^3-SEX simulation (Wilman et al. 2008) for an area of 0.1212 sr, which is scaled down to the SXDS area of 0.0002 sr; this is also shown on the right in black. **b) Right:** Model predictions from the S^3-SEX simulation for an area of 0.1212 sr, which is scaled down to the SXDS area of 0.0002 sr. The binning on the redshift axis is dz = 0.05. Objects are marked according to their radio source classification as stated in Wilman et al. (2008); blue denotes high-L_{151} objects, green denotes low-L_{151} objects, red denotes RQQ objects and purple stands for GPS sources in the S^3-SEX simulation; normal galaxies are not presented for clarity (see Chapter 3.4 for details on classification).

5.5 Comparison of the TOOT00 and the SXDS radio sources with the low-redshift 6dF radio sources

We compare the 47 TOOT00 radio sources with median redshift $z_{\rm med} \sim 1.25$, and the 37 SXDS radio sources with $z_{\rm med} \simeq 1.1$, to the 413 6dF radio sources dominated by AGN processes at a median redshift $z_{\rm med} = 0.0774$ (data from Mauch & Sadler 2007; see also Jones et al. 2004, for the 6dF galaxy survey). The selection criteria for the 6dF AGN are $S_{1.4\rm GHz} > 2.8$ mJy and $K < 12.75$ mag. In Figure 5.13 the radio luminosity at 1.4 GHz versus redshift diagram is presented. The median $L_{1.4\rm GHz}$ for the 6dF objects is $\sim 1.5 \times 10^{22}$ W Hz^{-1} sr^{-1}, which is more than 3 orders of magnitude fainter than the median radio luminosity of the TOOT00 objects and two orders of magnitude fainter that the SXDS radio sources.

Figure 5.14 presents the K-band magnitude of the TOOT00, SXDS and 6dF radio sources. The 6dF radio sources have a much fainter tail at K than predicted by the $K_{\rm W} - z$ at low redshifts, and get more faint at the low-redshift end of the sample.

The 6dF sample includes 6 FRIIs, 184 FRIs, 53 COM and 170 FD radio sources with a median radio spectral index of 0.55 between 1.4 GHz and 843 MHz. Figure 5.15–a presents the luminosity at K, $L_{K-\rm Ke}$ in L^*_K units, for the SXDS radio sources. For comparison, the 244 out of 413 6dF radio sources that are at a similar 1.4-GHz radio luminosity range ($22 \lesssim \log_{10}(L_{1.4\rm GHz}/[\rm WHz^{-1}sr^{-1}]) \lesssim 26$) are shown. This plot suggests that the 6dF radio sources at $z_{\rm med} \sim 0.1$ are not associated with the TOOT00 nor the SXDS radio-source populations, since no sub-L^* objects are found in the given luminosity that would explain a possible connection. Note that the two bright at K objects in the TOOT00 sample, TOOT00_1125 & TOOT00_1233, are both quasars and the K-band emission probably is not dominated by stellar light (see Chapter 3). The very low-$L_{K-\rm Ke}$ object, TOOT00_1107 (see also Chapter 3), is an unusually faint at K galaxy; we know that these objects exist although we do not fully understand them yet.

In Figures 5.10 & 5.11 we can see some FRI objects above the Ledlow & Owen line, which marks the divide between FRI and FRII radio sources at low redshifts (Ledlow & Owen 1996). In order to investigate whether there is evolution in the FRIs on this plane or if the Ledlow & Owen result is based on the failure to detect any FRIs in their local sample, we calculate the co-moving space density of FRIs between the FRI/FRII and RLF breaks, i.e. the quantity $\Sigma \frac{1}{V_{\rm max}}$, for the sky area of each survey (see Chapter 4). For the SXDS objects we get for the space density $\sim 2 \times 10^{-8}$ Mpc^{-3} at a median redshift $z_{\rm med} \approx 1.1$, while for the TOOT00 FRIs the space density is $\sim 3.8 \times 10^{-7}$ Mpc^{-3} at $z_{\rm med} \sim 1.25$. For our local sample of 6dF

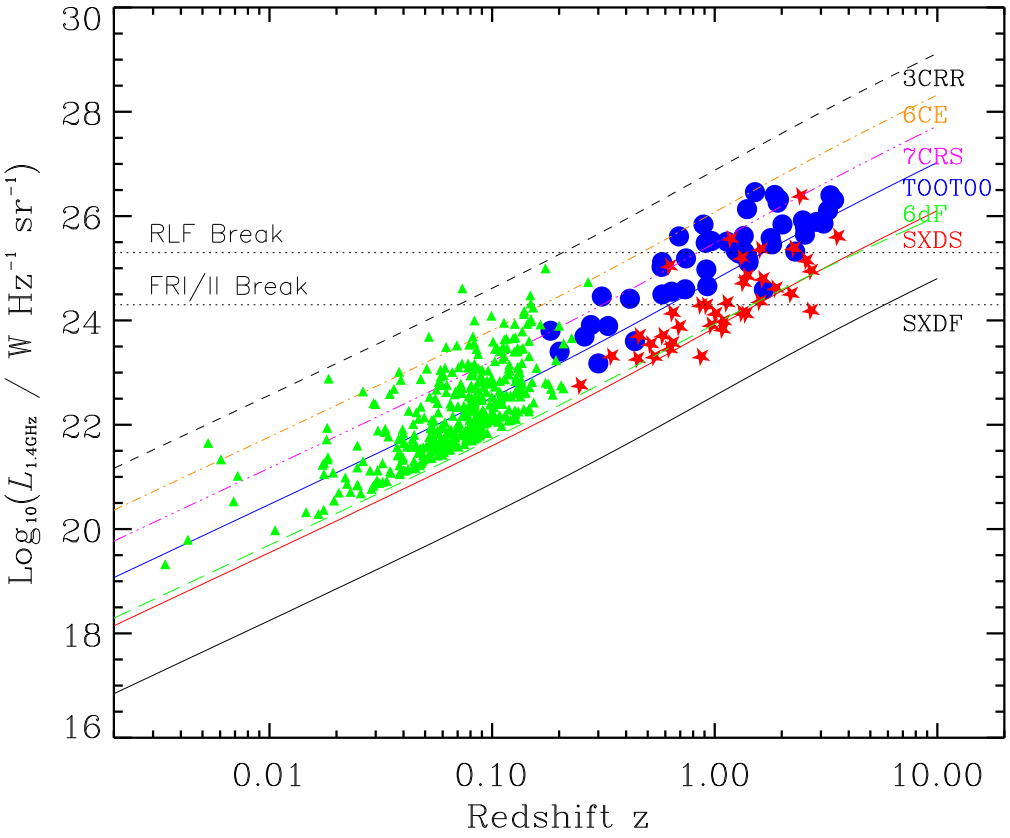

Figure 5.13: Radio luminosity at 1.4 GHz versus redshift for the 47 TOOT00, the 37 SXDS and 296 6dF radio sources. Symbols: filled blue circles denote TOOT00 objects, filled red stars stand for SXDS radio sources and filled green triangles denote 6dF objects. A radio spectral index of 0.55 was used to calculate the radio luminosity of the 6dF objects, whereas for the TOOT00 and the SXDS radio sources the spectral index of each object was used. A typical steep radio spectral index of 0.8 was used to convert the flux limits of the 3CRR, 6CE, 7CRS and TOOT00 surveys to 1.4 GHz; for the 6dF an $\alpha = 0.55$ was used. The flux density limits for the 3CRR, 6CE, 7CRS, TOOT00, 6dF, SXDS and SXDF are: 2.09, 0.33, 0.084, 0.017, 0.0028, 0.002 and 0.0001 Jy respectively. The horizontal lines show the RLF and FRI/FRII breaks calculated from the Willott et al. (2003) and the Fanaroff & Riley (1974) values respectively using a typical steep-spectrum radio spectral index of 0.8.

objects the space density at the relevant luminosity range is $\sim 2.4 \times 10^{-7}$ Mpc^{-3} (Mauch & Sadler 2007). These approximate values show that the space density of the TOOT00 objects at a median redshift of $z_{\rm med} \sim 1.25$ is not that different from the space density of the 6dF objects at $z_{\rm med} = 0.08$, suggesting no evolution for this range of radio luminosity between the FRI/FRII and RLF breaks.

Finally, in order to investigate whether any 6dF objects between the FRI/FRII and RLF breaks are missing due to their K magnitude upper limit, we compare the number of FRI TOOT00 and SXDS objects between those breaks with luminosity at K brighter than $L_{K-\rm lim}$ = 1.952 L^*_K. This value corresponds to K = 12.75 mag at the median redshift $z_{\rm med}$ = 0.08 of the 6dF objects. We find 1 SXDS object fainter than $L_{K-\rm lim}$ and 1 brighter, 0 TOOT00 objects fainter and 6 brighter than $L_{K-\rm lim}$, while for the 6dF sample there are 0 objects below

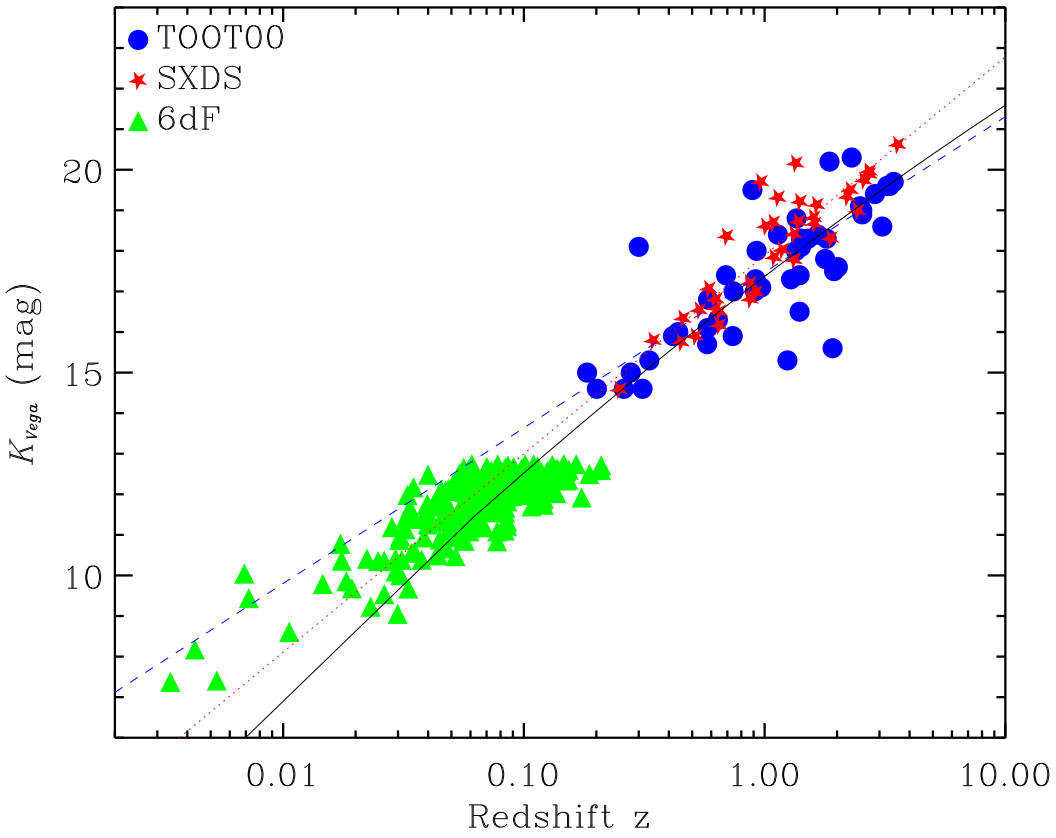

Figure 5.14: K magnitude (in the Vega magnitude system) versus redshift for the 47 TOOT00, 37 SXDS and 413 6dF radio sources. Symbols: filled blue circles denote TOOT00 objects, filled red stars stand for SXDS radio sources and filled green triangles denote 6dF objects. The black solid line is the $K_{\rm W} - z$ relation (Eqn. 5.1). The blue dashed line is the best-fit line for the TOOT00 objects, where the slope and intercept are 3.45 and 17.30 respectively; the Spearman's correlation coefficient is $\rho = 0.74$ with $\gg 99.99\%$ probability for a correlation; the 7 objects with photometric redshift estimated from the $K_{\rm W} - z$ relation were excluded from the fit; the two bright quasars, TOOT00_1125 & TOOT00_1235, were also excluded from the fit. The red dotted line is the best-fit line for the SXDS objects, where the slope and intercept are 4.89 and 17.89 respectively; the Spearman's correlation coefficient is $\rho = 0.88$ with $\gg 99.99\%$ probability for a correlation.

$L_{K-\rm lim}$ and 5 brighter than $L_{K-\rm lim}$. The fact that we do not detect any FRI TOOT00 objects between the FRI/FRII and RLF breaks fainter than $L_{K-\rm lim}$, while keeping in mind the 6dF result, suggests that the 6dF sample is complete to the K magnitude limit. Note that the one FRI SXDS object fainter than $L_{K-\rm lim}$ (sxds_0020) is a FD radio source.

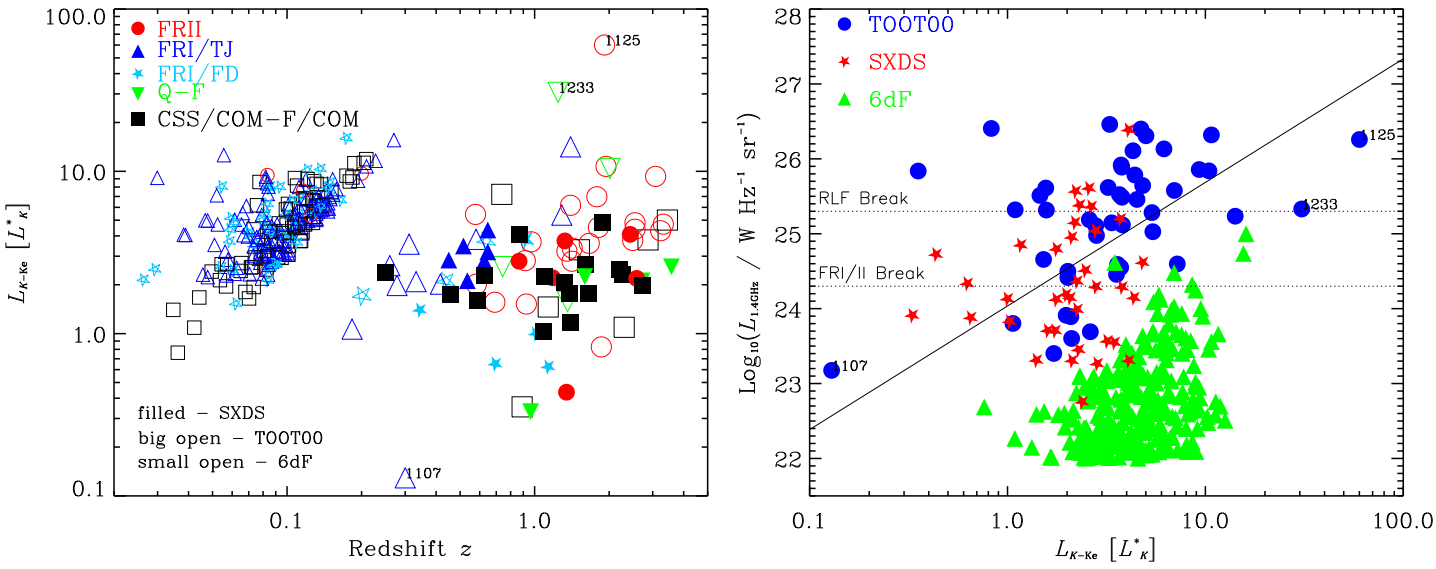

Figure 5.15: **a) Left:** K-corrected and passive-evolution-corrected luminosity at K, $L_{K-\mathrm{Ke}}$, in L^*_K units versus redshift z for the TOOT00, the SXDS and the 6dF radio sources; the 6dF objects have radio luminosity at 1.4 GHz in the range $22 \lesssim \log_{10}(L_{1.4\mathrm{GHz}}/[\mathrm{WHz}^{-1}\mathrm{sr}^{-1}]) \lesssim 26$. Symbols denote radio-optical classification, adjusted to the 6dF classification: red circles denote FRII radio sources; blue triangles denote FRI/TJ objects; light-blue stars denote FRI/FD objects; green upside-down triangles denote Q-F radio sources; black squares denote CSS/COM-F/COM objects; filled symbols show SXDS objects, big open symbols denote TOOT00 radio sources and small open symbols denote 6dF radio sources. **b) Right:** Radio luminosity at 1.4 GHz versus K-corrected and passive-evolution-corrected luminosity at K, $L_{K-\mathrm{Ke}}$, in L^*_K units for the TOOT00, the SXDS and the 6dF radio sources; the 6dF objects have radio luminosity at 1.4 GHz in the range $22 \lesssim \log_{10}(L_{1.4\mathrm{GHz}}/[\mathrm{WHz}^{-1}\mathrm{sr}^{-1}]) \lesssim 26$. Symbols are the same as in Figure 5.13.

5.6 Conclusions

Study of the $K-z$ relation of the TOOT00 and the SXDS radio sources reveals that these two samples include different types of radio sources at K, probably partly explained by the fact that the TOOT00 objects are selected at a low-frequency radio survey while the SXDS radio sources are high-frequency selected, and partially explained by the extra depth of SXDS being sufficient to probe different populations. The basic conclusions on the near-IR K-band study of these two samples are as follows:

• The TOOT00 radio sources approximately follow the $K_{\rm W}-z$ relation of Willott et al. (2003), and thus they can be described by a model of a $\sim 3\ L^*$ passively evolving galaxy that formed in an instantaneous burst at high redshift ($z_{\rm f}=10$); the median luminosity is actually $4\ L^*$. Some exceptions of bright quasars and faint radio galaxies do exist.

• There is a tight correlation between K-band magnitude and redshift for the SXDS high-frequency radio selected sample, but this relation deviates significantly from the $K_{\rm W}-z$ relation of Willott et al. (2003). The SXDS objects appear to be significantly fainter at K than other low-frequency selected radio-source samples, like the 3CRR, 6CE and 7CRS, with a median value of $\sim 2\ L^*$.

• Thus, the TOOT00 radio sources at a median redshift $z_{\rm med}\sim 1.25$ are 2-times more luminous at K than the $z_{\rm med}\simeq 1.1$ SXDS radio sources.

• The FRI/FRII divide in radio luminosity seen at $z\lesssim 0.5$ is also observed at $z\sim 1$ for FRII objects in the TOOT00 and SXDS samples, but examples of FRI radio sources that are above the FRI/FRII break in radio luminosity do exist. Comparison of the space density of the TOOT00 and SXDS FRI objects above the FRI/FRII break with the local 6dF FRI radio sources above the FRI/FRII break suggests that these objects exist at both high and low redshifts, but they are rare.

• Comparison of the $K-z$ diagram of TOOT00, SXDS and 6dF radio sources shows that they follow different distributions, and thus contain different mixes of objects in the near-IR K-band.

• In the 6dF we see objects at the same luminosity range as in the TOOT00 and the SXDS, although there is a tail of low-K objects at high redshift. We speculate these might be young dusty galaxies (Cruz et al. 2007).

Chapter 6

Accretion indicators and radio structure in the TOOT00 and the SXDS samples of radio sources

Abstract

Accretion indicator properties are presented for the 47 TOOT00 (151-MHz selected) radio sources described in Chapter 3, and the 37 SXDS (1.4-GHz selected) radio sources described in Chapter 2. A strong correlation is found between the [OII] narrow-emission-line luminosity $L_{[\mathrm{OII}]}$ and radio luminosity L_{rad}, where for the TOOT00 objects $L_{[\mathrm{OII}]} \propto L_{\mathrm{rad}}^{0.7\pm0.15}$, and for the SXDS objects $L_{[\mathrm{OII}]} \propto L_{\mathrm{rad}}^{0.6\pm0.17}$, implying consistent correlations in the two independent samples and in agreement with previous studies of radio-brighter samples; the normalisation in TOOT00 and SXDS is not significantly different from each other. A correlation is also found between $L_{[\mathrm{OII}]}$ and the 24 μm luminosity L_{24} for the SXDS radio sources, where $L_{[\mathrm{OII}]} \propto L_{24}^{0.8\pm0.17}$, implying a rough proportionality between L_{24} and L_{rad} in the sense that high-L_{rad} objects exhibit excess mid-infrared emission. Study of radio sources at 24 μm in the SXDS reveals that 30% of the quasar optical light is absorbed by the torus and re-emitted in the mid-IR, and study of a correlation between blueness and mid-IR excess implies $\sim 1\%$ gets scattered in the blue above and below the torus. Similar results are seen in TOOT00 if [OII] luminosity is used as a proxy for mid-IR excess. Finally, in both the TOOT00 and the SXDS radio-source samples, FRI objects above the traditional FRI/FRII break in the radio luminosity exist, while there are no FRII radio sources below that divide. This confirms previous suggestions (e.g. Heywood, Blundell & Rawlings 2007), that FRI sources can significantly exceed the FRI/FRII

divide at high-z (for TOOT00 $z_{\rm med} \sim 1.25$; for SXDS $z_{\rm med} \simeq 1.1$) perhaps because of cosmic evolution in radio-source environments.

6.1 Introduction

The unified active galactic nuclei (AGN) model consists of a super-massive black hole (SMBH; e.g. Rees 1984) that is surrounded by an optically thick and geometrically thin accretion disk, a hot corona and an opaque and obscuring torus of gas and dust (Antonucci 1993) that surrounds the central engine. This torus, if it is sufficiently optically thick, can prevent a distant observer from seeing events deep in its interior in regions very near to the black hole. The obscuration is likely to be most effective at optical, untraviolet (UV) and soft X-ray wavelengths, with the torus becoming less opaque at both longer and sorter wavelengths. Observations at the mid-infrared, and in particular at 24 μm, target regions close to the active nucleus without getting blocked by the torus.

The dominant accretion mechanism in a BH is accretion of cold gas. The formation of BH is quick in newly formed galaxies, with the hole radiating at the Eddington limit (Small & Blandford 1992). At later epochs, when supply of fuel is no longer plentiful, the holes accrete only intermittently at an average rate that is perhaps the same for all quasars. Cavaliere & Padovani (1989) suggested that objects exhibit re-current episodes of quasar activity. This 'duty cycle' (i.e. the fraction of the time that the system will be seen as an AGN), is quite small and in the range $f_{\rm BH} \simeq 10^{-4}$-$2{\times}10^{-3}$ (Haehnelt & Rees 1993).

Many authors adopt the idea of different black hole fuelling and triggering mechanisms for low- ($L_{1.4{\rm GHz}} \lesssim 5{\times}10^{25}$ W Hz^{-1}) and high-$L_{\rm rad}$ ($L_{1.4{\rm GHz}} > 5{\times}10^{25}$ W Hz^{-1}) AGN (e.g. Smolčić et al. 2009). The energetic output of the low-luminosity radio-loud AGN is in their radio jets ('radio mode'), while optically- or X-ray-selected AGN have a radiatively efficient nucleus ('quasar mode'). This is also reflected in the types of host galaxies with weak radio AGN being preferentially found in the most massive and evolved galaxies (even out to $z \sim 1$; e.g. Tasse et al. 2008). Recently, there has been evidence that low- and high-L_{151} radio sources are fundamentally distinct objects (e.g. Best 2009), implying that these objects are fuelled by a different mechanism. The low-luminosity radio sources are fuelled by accretion of hot gas from their surrounding X-ray haloes (e.g. Hardcastle, Evans & Croston 2007), while powerful radio sources are preferably triggered in major mergers following shortly after the phase of massive star formation at high redshifts (Tasse et al. 2008; Smolčić et al. 2009).

The difference between the two modes of AGN fuelling maybe distinct from that of the

two different radio morphological classes of radio-loud AGN (Fanaroff-Riley classes I and II; Fanaroff & Riley 1974), with the FR-dichotomy more closely associated with the environment and evolution of the radio sources (e.g. Best 2009).

Accretion in FRI objects occurs at a smaller rate, but also perhaps at lower efficiency than in standard accretion disks (e.g. Best et al. 2006; Allen et al. 2006), suggesting different accretion modes for these objects (e.g. Hardcastle, Evans & Croston 2007), i.e. accretion of hot gas associated with the host galaxy corona. There may, however, still be correlations between the luminosity of an FRII and the accretion rate (Cao & Rawlings 2004) and these might signify, or mimic, a common physical mechanism (in either accretion mode) powering the jet (Rawlings & Saunders 1991).

The powerful radio emission in both FRIs & FRIIs is thought to originate from relativistic jets expelled by the accretion disk around the SMBH (e.g. Urry & Padovani 1995). The strong correlation found between the radio luminosity and the accretion rate supports the notion that radio jets are directly coupled to the accretion disk (Rawlings & Saunders 1991; Wang, Ho & Staubert 2003).

Furthermore, is well known that emission-line luminosity and radio luminosity are strongly correlated (e.g. Rawlings & Saunders 1991). For example, Willott et al. (1999) found a strong positive correlation between emission-line luminosity of the narrow-line region and radio luminosity in 3CRR and 7CRS radio galaxies (for $H_0 = 50$ km s^{-1}Mpc^{-1}, $\Omega_{\rm M} = 1$ and $\Omega_\Lambda = 0$):

$$L_{\rm NLR} \propto L_{\rm 151MHz}^{0.79\pm0.04} \tag{6.1}$$

This correlation is not strongly connected to environmental effects, such as redshift z, linear size D and spectral index α, but the radio-source environment is believed to play a role in the scatter (e.g. Rawlings & Saunders 1991). Other factors contributing to the scatter about the mean emission-line/radio correlation include long-term time variability effects, since the light-travel time to the narrow-line region is much less than to the radio lobes; emission lines excited by means other than the radiation cone from the quasar, e.g. shocks, blazar beams and possibly starbursts; and use of emission-line ratios and, for some of the quasars, line equivalent widths (EW) to estimate emission-line strengths (e.g. Willott et al. 1999).

The positive correlation between the narrow-emission-line luminosity $L_{\rm NLR}$ and extended radio luminosity $L_{\rm rad}$ suggests a close relationship between accretion rate $\dot{M}$ and jet power $Q_{\rm jet}$ in FRII radio sources. Rawlings & Saunders (1991) found that jet power is almost proportional to the narrow-line luminosity, $Q \propto L_{\rm NLR}^{0.9\pm0.2}$; this almost proportionality extends over four orders

of magnitude, which rules out environmental effects as the cause of the correlation (e.g. Willott et al. 1999). According to Willott et al. (1999), the relationship between jet power and radio luminosity at 151 MHz, $L_{151\mathrm{MHz}}$, is given by $Q \simeq 3\times10^{38} L_{151\mathrm{MHz}}^{6/7}$W ($L_{151\mathrm{MHz}}$ is in units of 10^{28} W Hz^{-1} sr^{-1} and the normalisation is uncertain due to unknown physics like the composition of the jet). The almost linear relation between jet power and accretion rate indicates that the efficiency of this mechanism must have only a very weak dependence on the amount of accreting gas (Balmaverde, Baldi & Capetti 2008).

Traditionally, the [OIII] λ5007 emission-line luminosity has been taken as good tracer of the underlying ionizing continuum in radio-loud AGN. However, the [OIII] emission is anisotropic, with part of [OIII] being emitted in the obscured central regions (e.g. Tadhunter et al. 1998). On the other hand, the [OII] luminosities of the broad- and narrow-line radio galaxies are similar (Hes, Barthel & Fosbury 1993), thus it makes more sense to use the [OII] emission line as a comparison to radio luminosity.

The radio luminosity is also correlated to emission from broad lines. Jarvis et al. (2001c) found a relation between Lyα emission-line luminosity to radio luminosity at 151 MHz, where $L_{\mathrm{Ly}\alpha} \propto L_{151\mathrm{MHz}}^{1.49\pm0.25}$. This may be interpreted in the same way as in Willott et al. (1999), that the L_{NRL}–L_{rad} correlation is evidence for a close relationship between the accretion rate and the jet power of radio sources (Rawlings & Saunders 1991). Furthermore, Cao & Jiang (1999) have found an intrinsic correlation between the total luminosity of the broad-line region (BLR) and the bulk kinetic power of the relativistic jet, that confirms a connection between the relativistic jet and the accretion process: $Q \propto L_{\mathrm{BLR}}^{0.86\pm0.07}$.

Generally, on large (kpc to Mpc) scales the narrow-line luminosity is correlated to the kinetic luminosity from the radio lobes (e.g. Baum & Heckman 1989a, 1989b; Rawlings & Saunders 1991). On smaller scales, the relativistic jet in radio-loud objects is linked with the accretion disk (Celotti & Fabian 1993; Celotti, Padovani & Ghisellini 1997).

The origin of the FRI/FRII division, i.e. the observed differences in the properties of low- and high-power radio sources, lies near or in the central engine itself (e.g. Baum, Zirbel & O'Dea 1995; Kaiser & Best 2007a). Rees et al. (1982) suggest the possibility that FRI sources are produced when the central engine is fed at a lower accretion rate, while FRII sources are produced when the central engine is fed at a higher accretion rate. On that note, Wang, Ho & Staubert (2003) claim that the various subclasses of radio-loud AGNs – ranging from high-luminosity sources (flat-spectrum radio quasars and FRIIs) to low-luminosity sources (BL Lacs and FRIs) – can be viewed as a continuous sequence of varying accretion rate.

Brighter, more massive galaxies undergo the FRI/FRII transition at a significantly higher

radio luminosity than fainter galaxies: $L_{\rm radio}^{\rm break} \propto L_{\rm opt}^{1.65}$ (Meier et al. 1998; Ledlow & Owen 1996). The physical interpretation of these results is that both types of sources are produced by twin jets ejected from an engine in the centre of the galaxy. According to Kaiser & Best (2007a; 2007b), all radio sources start out with an FRII-type structure. Less powerful jets develop turbulent flows close to the core with an FRI-type radio structure. These sources dominate the radio luminosity function (RLF) at low radio luminosities. More powerful jets grow beyond the core region before the pressure in their lobes decreases too much. They retain their FRII-type structure and form the bulk of the population at the high luminosity end of the RLF.

Heywood, Blundell & Rawlings (2007) claim that high-power jets can give rise to both FRI and FRII morphologies depending on their environment (see also Kaiser & Best 2007a; 2007b). Their observations of $z \sim 1$ radio sources at 151 MHz, disprove the idea that FRI radio structures cannot be associated with a quasar (i.e. highly accreting black hole central engine). Although FRI type sources are observed with luminosities over a factor of 10 higher than the transitional FRI/FRII break, there are no FRII objects with luminosities significantly below the break (Heywood, Blundell & Rawlings 2007). This provides some evidence that the division between FRI and FRII radio sources changes with z, in the sense that FRIs can exist above the traditional break luminosity at higher redshifts. The obvious explanation for this (which is also therefore likely to affect the $z \sim 0.5$ population) is a systematic change in the environments of radio sources with cosmic epoch.

This chapter presents emission-line properties in connection to 24 μm data, radio luminosity and radio structure for two samples of radio sources: a) the TOOT00 objects selected at a low-radio-frequency (151 MHz) with median redshift $z_{\rm med} \sim 1.25$ (Chapter 3); and b) the SXDS radio sources selected at a high-frequency (1.4 GHz) with a median redshift $z_{\rm med} \simeq 1.1$ (Chapter 2). Section 6.2 describes how the emission-line luminosity is calculated used in Section 6.3. Section 6.3.1 presents a comparison of the radio to the emission-line luminosity. Section 6.3.2 presents investigation of the 24 μm data and [OII] emission-line luminosity as accretion indicators, following the discussion of Section 2.4.1 in Chapter 2. Finally, Section 6.3.3 presents how the different types of radio sources are connected to the emission-line and radio luminosity.

We use J2000.0 positions and the convention for all spectral indices, α, that flux density $S_\nu \propto \nu^{-\alpha}$, where ν is the observing frequency. We assume throughout a low-density, Λ-dominated Universe in which $H_0 = 70$ km s^{-1}Mpc^{-1}, $\Omega_{\rm M} = 0.3$ and $\Omega_\Lambda = 0.7$.

6.2 Analysis

We investigate the relation between the emission-line and radio luminosity at 1.4 GHz and 151 MHz in the SXDS and TOOT00 radio-source samples. The flux of the $[OII]_{\lambda 3727}$ emission line is used here, since it is the most frequently observed line in the optical in quasars and radio galaxies. In the case where the [OII] line is not present, or the spectrum displays a featureless continuum, the following approaches are taken:
(i) When the object is a quasar we measure the flux from the narrow core[1] of the most prominent broad emission line in the optical spectrum (e.g. Lyα, $[CIV]_{\lambda 1549}$, [CIII] or MgII emission line); in the case the emission line is narrow, we measure the whole flux.
(ii) When the object is a galaxy but there is no [OII] line, we measure the flux from another narrow emission line like [OIII].
(iii) For objects without emission lines in the optical spectrum, a rough estimate of a limit on the [OII] line flux was made as follows: a) for galaxies, i.e. in the case the continuum is clearly strong, we took a limit of ~ 10 Å which corresponds to lines clearly detectable in the spectrum of $z \sim 0.5$ ellipticals, observed with moderate S/N ratio; b) for fainter objects on which the origin of the continuum is unclear, we supply as a limit the flux of the brightest but probably spurious line-like feature in the spectrum adjacent to the estimated location (given the photometric redshift) or the bright expected narrow-line.
(iv) In the case of a featureless continuum where the [OII] line lies outside the optical spectrum due to the high redshift of the object, we use the Lyα line as reference and measure the flux as in (iii).
Following these measurements, the fluxes are converted to [OII] luminosity by applying average line ratios quoted by Willott et al. (1999) and Jarvis et al. (2001c); the ratios used are Lyα/[OII] = 5., CIV/Lyα = 0.07 (for linear size $D < 70$ kpc), CIV/Lyα = 0.14 (for $D > 70$ kpc), MgII/[OII] = 6.25, and [OIII]/[OII] = 3.

Tables 6.1 & 6.2 present the [OII] emission-line luminosity and radio luminosities at 151 MHz and 1.4 GHz for the TOOT00 and the SXDS samples respectively. The emission-line luminosity is used to investigate whether the known correlation between radio and emission-line luminosities is verified by the independent TOOT00 and SXDS radio-source samples. The correlations are presented in Figures 6.1, 6.2 & 6.3.

Note that we were able to calculate [OII] luminosities for only 28 out of 37 SXDS objects, due to lack of spectroscopy. For TOOT00, 45 out of 47 have a [OII] line measurement. Thus

[1] Use of a broad EW provides an upper limit on the narrow-emission-line strength (Francis et al. 1997; Francis et al. 1991).

[OII] luminosities are not complete for SXDS, adding a bias when comparing the two samples.

6.3 Discussion

6.3.1 Correlation of emission-line and radio luminosity

Figure 6.1 presents the [OII] line-luminosity, $L_{[\mathrm{OII}]}$ versus radio luminosity at 151 MHz (left plot) and 1.4 GHz (right plot). The known correlation between narrow emission-line luminosity and radio luminosity is well known (e.g. Willott et al. 1999; Rawlings & Saunders 1991), as shown in Eqn. 6.1 (Section 6.1). Here that correlation is verified for the TOOT00 and SXDS radio sources. The observed large scatter can be partially explained by the different emission lines and line-ratios used to calculate $L_{[\mathrm{OII}]}$. As discussed in Section 6.1, many other factors probably contribute to the scatter. The population of FRII TOOT00 object with high radio luminosity on the right of the best-fit line in Figure 6.3 is not unexpected since objects of the kind are also seen in the 7CRS sample (Willott et al. 1999).

The correlation between emission-line luminosity $L_{[\mathrm{OII}]}$ and 151-MHz radio luminosity $L_{151\mathrm{MHz}}$ of the TOOT00 radio sources presented in Figures 6.1, 6.2 & 6.3 is:

$$\log_{10}(L_{[\mathrm{OII}]}) = (17.98 \pm 0.76) + \log_{10}(L_{151\mathrm{MHz}}^{0.64\pm0.15}), \tag{6.2}$$

where $L_{[\mathrm{OII}]}$ is in units of [W] and the radio luminosity is in [W Hz^{-1} sr^{-1}] units. The correlation between emission-line luminosity and 1.4-GHz radio luminosity $L_{1.4\mathrm{GHz}}$ is:

$$\log_{10}(L_{[\mathrm{OII}]}) = (15.60 \pm 0.75) + \log_{10}(L_{1.4\mathrm{GHz}}^{0.76\pm0.15}). \tag{6.3}$$

In general we can write the correlation between emission-line luminosity and radio luminosity L_{rad} for the TOOT00 objects as:

$$L_{[\mathrm{OII}]} \propto L_{\mathrm{rad}}^{0.7\pm0.15}. \tag{6.4}$$

For the SXDS radio sources the correlation between emission-line and 151-MHz radio luminosity is:

$$\log_{10}(L_{[\mathrm{OII}]}) = (18.65 \pm 0.62) + \log_{10}(L_{151\mathrm{MHz}}^{0.63\pm0.17}), \tag{6.5}$$

while the correlation between emission-line and 1.4-GHz radio luminosity is:

$$\log_{10}(L_{[\mathrm{OII}]}) = (19.16 \pm 0.62) + \log_{10}(L_{1.4\mathrm{GHz}}^{0.63\pm0.17}). \tag{6.6}$$

In general we can write the correlation between emission-line luminosity and radio luminosity L_{rad} for the SXDS objects as:

$$L_{[\mathrm{OII}]} \propto L_{\mathrm{rad}}^{0.6\pm0.17}. \tag{6.7}$$

These relations are very close in slope to the one found by Willott et al. (1999) in Eqn. 6.1, and within the uncertainty assumed. It is important to note that these are completely independent samples.

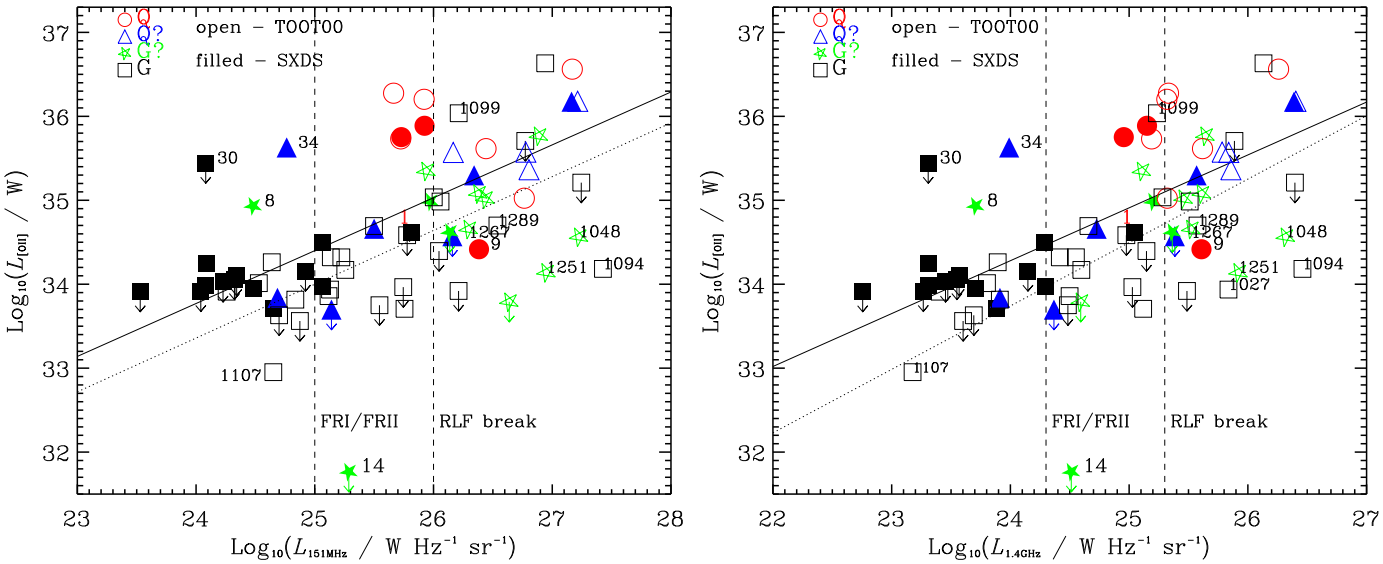

Figure 6.1: **a) Left**: $L_{[\mathrm{OII}]}$ vs $L_{151\mathrm{MHz}}$ for the TOOT00 and SXDS radio sources. Symbols indicate optical classification (see Table 2.1 in Chapter 2 for the SXDS objects and Table 3.3 in Chapter 3 for the TOOT00 objects): open symbols denote TOOT00 objects and filled symbols stand for SXDS radio sources; red circles denote Q objects; blue triangles denote Q? objects; green stars denote G?; black boxes denote G objects. The solid black line is the best-fit line for the SXDS radio sources, where the slope and intercept are 0.61 and 18.68 respectively; the Spearman correlation coefficient is $\rho = 0.479$ with a 98.71% probability for a correlation (upper limits were included in the calculation of ρ). Excluding sxds_0014, we get a slope and intercept of 0.63 and 18.65 respectively, and $\rho = 0.532$ with 99.33% probability for a correlation; we use this value for the analysis. The dotted black line is the best-fit line for the TOOT00 radio sources, where the slope and intercept of the fit are 0.64 and 17.98 respectively; the Spearman correlation coefficient is $\rho = 0.467$ with a 99.81% probability for a correlation (upper limits were included in the calculation of ρ). **b) Right**: $L_{[\mathrm{OII}]}$ vs $L_{1.4\mathrm{GHz}}$ for the TOOT00 and SXDS radio sources. Symbols are the same as in Figure 6.1–a; open symbols denote TOOT00 objects and filled symbols stand for SXDS radio sources. The solid black line is the best-fit line for the SXDS objects, where the slope and intercept are 0.61 and 19.16 respectively; the Spearman correlation coefficient is $\rho = 0.479$ with a 98.71% probability for a correlation. Excluding sxds_0014, we get a slope and intercept of 0.63 and 19.13 respectively, and $\rho = 0.532$ with 99.33% probability for a correlation; we use these value for the analysis. The dotted black line is the best-fit line for the TOOT00 objects, where the slope and intercept of the fit are 0.75 and 15.62 respectively; the Spearman correlation coefficient is $\rho = 0.586$ with a 99.98% probability for a correlation. In both plots, the vertical lines mark the FRI/FRII divide and RLF break in radio luminosity (a typical steep-spectrum radio spectral index of 0.8 was used to convert to our assumed cosmology). Objects marked with their name are discussed in the text. Note: only objects with detections are shown in the plots and included in the calculations. The Buckley-James method in the survival analysis (ASURV) statistics package (Lavalley et al. 1992) was used in the calculations of the best-fit line in order to account for the upper limits in the dependent variable.

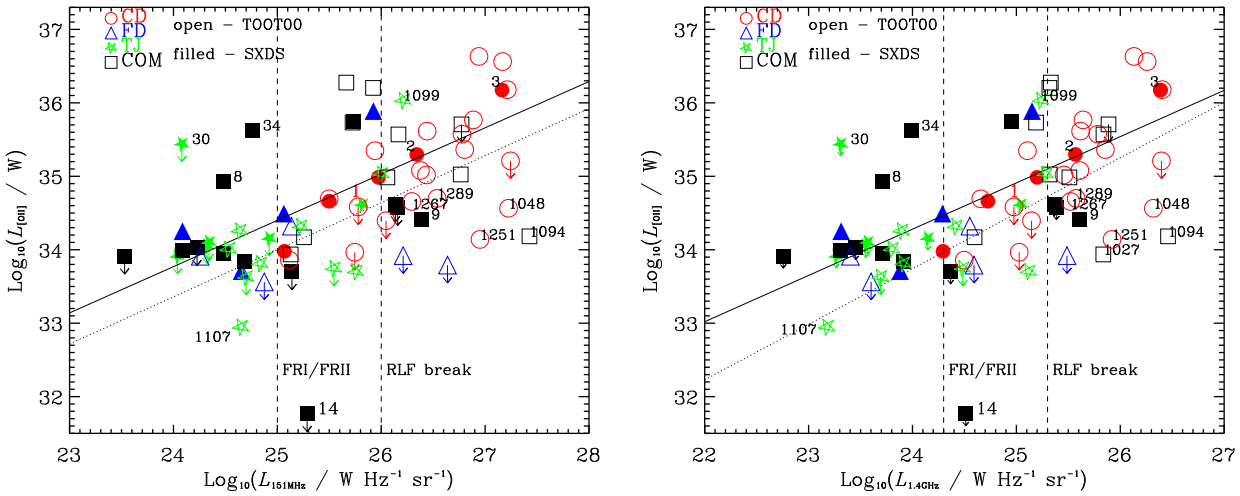

Figure 6.2: **Left**: $L_{[\mathrm{OII}]}$ vs $L_{151\mathrm{MHz}}$ for the TOOT00 and SXDS radio sources. Symbols indicate radio classification (see Table 2.1 in Chapter 2 for the SXDS objects & Table 3.1 in Chapter 3 for the TOOT00 objects): open symbols denote TOOT00 objects and filled symbols stand for SXDS radio sources; red circles denote CD objects, blue triangles denote FD radio sources, green stars denote TJ radio sources and black squares denote COM objects. The best-fit lines are the same as in Figure 6.1–a. **Right**: $L_{[\mathrm{OII}]}$ vs $L_{1.4\mathrm{GHz}}$ for the TOOT00 and SXDS radio sources. Symbols are the same as on the left plot. The best-fit lines are the same as in Figure 6.1–b. In both plots, the vertical lines mark the FRI/FRII divide and RLF break in radio luminosity (a typical steep-spectrum radio spectral index of 0.8 was used to convert to our assumed cosmology). Objects marked with their name are discussed in the text.

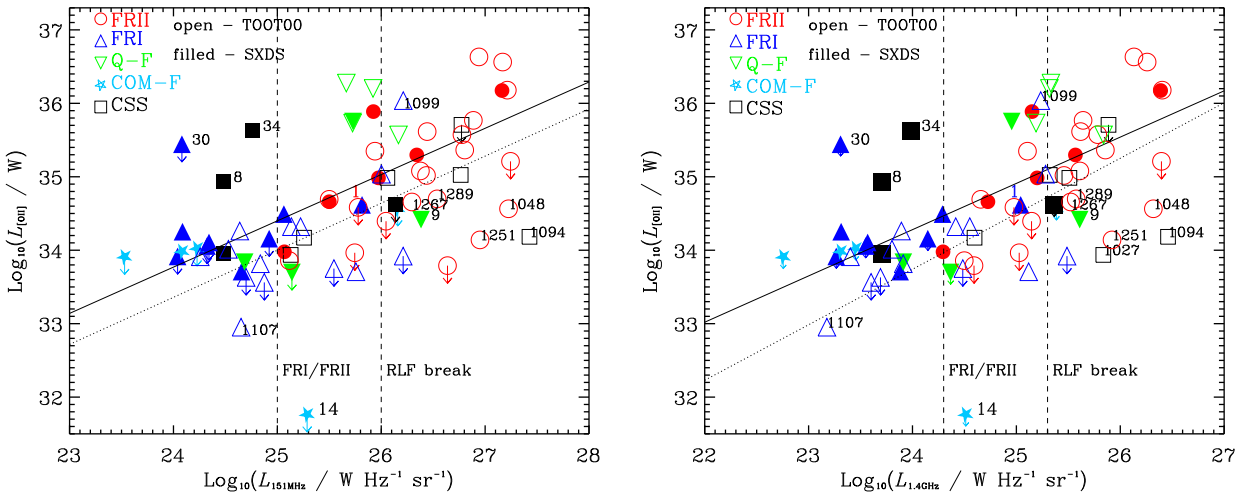

Figure 6.3: **Left**: $L_{[\mathrm{OII}]}$ vs $L_{151\mathrm{MHz}}$ for the TOOT00 and SXDS radio sources. Symbols indicate radio-optical classification (see Table 4.7 in Chapter 5 for the SXDS objects & Table 3.3 in Chapter 3 for the TOOT00 objects): open symbols denote TOOT00 objects and filled symbols stand for SXDS radio sources; red circles denote FRII objects, blue triangles denote FRI radio sources, green upside-down triangles denote Q-F objects, blue stars denote COM-F radio sources and black squares denote CSS objects. The best-fit lines are the same as in Figure 6.1–a. **Right**: $L_{[\mathrm{OII}]}$ vs $L_{1.4\mathrm{GHz}}$ for the TOOT00 and SXDS radio sources. Symbols are the same as on the left plot. The best-fit lines are the same as in Figure 6.1–b. In both plots, the vertical lines show the FRI/FRII divide and RLF break in radio luminosity (a typical steep-spectrum radio spectral index of 0.8 was used to convert to our assumed cosmology). Objects marked with their name are discussed in the text.

Table 6.1: Emission-line and radio-luminosities for the TOOT00 radio sources. **Column 1** gives the name of the object. **Column 2** gives the flux density of the most prominent emission line measured from the spectrum; a limit denotes estimation from the continuum and measurement of the EW of a line-like feature in the spectrum (see also Section 3.2). **Column 3** gives the base-10 logarithm of the [OII] emission line-luminosity, as measured from the spectrum of each object; in the case that [OII] was not present, the most prominent line was used in the calculations (as indicated in Table 3.4 in Chapter 3), where the flux was converted to [OII] luminosity as described in Section 6.2. Absence of measurement denotes lack of spectroscopic data. **Column 4** gives the name of the emission line used in the calculations; 'n' denotes measurement of a narrow line profile at FWHM using a Gaussian fit (see also Figure 3.4); a − is used when no spectroscopy is available. **Columns 5 & 6** give the base-10 logarithm of the luminosity at 151 MHz and 1.4 GHz respectively. **Column 7 & 8** give the blue excess (as in Eqn. 2.2, Chapter 2) and the mid-IR excess; the mid-IR excess was calculated from the extrapolated [OII] emission line luminosity, $L_{[\mathrm{OII}]-24}$, based on Eqn. 6.10 (Section 6.3.2). Note that values of $L_{[\mathrm{OII}]-24}$ are normalised to the mean $L_{[\mathrm{OII}]-24}$ of each sample. The rest luminosities at 4000 Å and 1 μm were calculated using photometric data of each object, from the U- to the K-band. When a data point was not available, the nearest photometric data point was used.

(1)	(2)	(3)	(4)	(5)	(6)	(7)	(8)
Name	S_{line} (10^{-19} W m^{-2})	$\log_{10}(L_{[\mathrm{OII}]}$ / [W])	Emission Line	$\log_{10}(L_{151\mathrm{MHz}}/$ [WHz^{-1}sr^{-1}])	$\log_{10}(L_{1.4\mathrm{GHz}}/$ [WHz^{-1}sr^{-1}])	$\log_{10}([\nu L]_{4000\mathrm{Å rest}}/$ $[\nu L]_{1\mu\mathrm{mrest}})$	$\log_{10}(L_{[\mathrm{OII}]-24}/$ $[\nu L]_{1\mu\mathrm{mrest}})$
TOOT00_1140	< 0.20	< 33.92	[OII]	26.21	25.49	-2.03	< -0.58
TOOT00_1099	9.10	36.04	[OII]	26.21	25.23	-1.21	0.41
TOOT00_1125	70.0	36.56	Lyα^{n}	27.17	26.26	1.10	0.54
TOOT00_1143	< 0.52	< 33.56	[OII]	24.88	23.60	-1.21	< -1.41
TOOT00_1233	4.20	36.28	CIII]	25.66	25.33	-0.12	0.27
TOOT00_1022	< 3.65	< 35.71	Lyα	26.78	25.89	-2.14	< -0.54
TOOT00_1204	1.20	34.32	[OII]	25.13	24.55	-0.91	-0.16
TOOT00_1235	21.4	35.73	[OII]	25.72	25.19	-1.12	1.10
TOOT00_1224	–	–		27.07	26.31	1.26	–
TOOT00_1291	< 0.91	< 34.58	[OII]	25.78	24.98	-1.56	< -0.05
TOOT00_1107	0.31	32.95	[OII]	24.65	23.18	-0.76	0.30
TOOT00_1180	2.30	35.02	Lyα^{n}	26.44	25.46	-1.01	-0.31
TOOT00_1027	0.22	33.94	[OII]	25.13	25.84	-1.83	0.55
TOOT00_1195	< 0.20	< 34.39	[OII]	26.05	25.15	-1.43	< -0.22
TOOT00_1069	1.30	35.02	Lyα^{n}	26.76	25.32	0.41	0.27
TOOT00_1094	0.65	34.18	MgII	27.43	26.46	-2.06	-0.85
TOOT00_1149	< 2.05	< 33.63	[OII]	24.70	23.69	-0.99	< -0.38
TOOT00_1298	1.11	35.04	[OII]	26.00	25.28	-2.03	-0.24
TOOT00_1200	5.70	35.08	[OII]	26.38	25.61	-0.20	0.82
TOOT00_1215	2.70	33.82	[OII]	24.84	23.91	-1.44	-0.10
TOOT00_1240	5.64	35.77	Lyα	26.89	25.64	0.62	0.83
TOOT00_1289	1.43	34.70	MgII	26.54	25.58	-2.16	-1.21
TOOT00_1072	< 0.68	< 33.97	[OII]	25.75	25.03	-1.60	< -0.53
TOOT00_1134	1.79	< 33.75	[OII]	25.52	24.46	-1.16	< -0.45
TOOT00_1244	10.0	36.20	CIV^{n}	25.92	25.32	1.22	1.78
TOOT00_1066	1.14	34.69	[OII]	25.50	24.66	-1.45	0.47
TOOT00_1261	3.60	35.57	Lyα^{n}	26.78	25.78	0.15	0.45
TOOT00_1252	–	–		27.06	26.11	-0.74	–
TOOT00_1214	1.14	35.36	Lyα^{n}	26.80	25.86	-0.59	-0.46
TOOT00_1152	< 0.83	< 35.21	Lyα	27.24	26.40	-1.42	< -0.97
TOOT00_1129	31.2	36.18	Lyα^{n}	27.22	26.41	-0.53	1.42
TOOT00_1090	7.00	33.91	[OII]	24.26	23.40	-0.80	0.02
TOOT00_1267	0.94	34.66	[OII]	26.30	25.52	-1.10	0.02
TOOT00_1188	1.80	35.35	[OII]	25.94	25.11	-0.64	0.46
TOOT00_1196	< 0.21	< 33.79	MgII	26.64	24.59	-1.14	< -1.25
TOOT00_1173	5.00	34.26	[OII]	24.64	23.89	-1.07	0.16
TOOT00_1228	1.35	34.99	[OII]	26.06	25.51	-0.89	0.61
TOOT00_1034	0.37	33.71	[OII]	25.76	25.12	-2.14	-0.58
TOOT00_1255	0.52	33.86	[OII]	25.12	24.50	-1.12	-0.15
TOOT00_1048	0.68	34.56	Lyα^{n}	27.23	26.32	-2.09	-1.58
TOOT00_1029	0.60	34.17	[OII]	25.26	24.60	-1.78	-0.61
TOOT00_1115	3.37	34.32	[OII]	25.22	24.42	-1.15	0.18
TOOT00_1132	10.9	34.01	[OII]	24.53	23.80	-0.45	0.40
TOOT00_1250	0.75	35.62	CIII]^{n}	26.44	25.62	-1.11	0.44
TOOT00_1268	6.30	35.57	Lyα^{n}	26.16	25.84	-1.24	-0.11
TOOT00_1251	0.14	34.14	Lyα^{n}	26.95	25.92	-1.77	-1.01
TOOT00_1203	35.8	36.63	[OII]	26.94	26.13	-0.89	1.24

Table 6.2: Emission-line and radio luminosities for the SXDS radio sources. **Column 1** gives the name of the object. **Column 2** gives the flux density of the most prominent emission line in the spectrum; a − denotes absence spectroscopic data; a limit shows that the flux of a line-like feature in the spectrum was measured (see Section 3.2); the character 'e' denotes that the value is an estimate, assuming the SED continuum at the expected wavelength given the redshift and a EW measurement from the spectrum, since the spectra were not flux calibrated (see Figure 2.7, Chapter 2). **Column 3** gives the base-10 logarithm of the [OII] emission-line luminosity, as measured from the spectrum of each object; in the case that [OII] was not present, the most prominent line was used in the calculations as indicated in **Column 4**, where the flux was converted to [OII] luminosity as described in Section 6.2; a − is used when no spectroscopy is available; the character 'e' denotes that the value is an estimate, assuming the SED continuum at the expected wavelength given the redshift and a EW measurement from the spectrum, since the spectra were not flux calibrated. **Columns 5 & 6** give the base-10 logarithm of the luminosity at 151 MHz and 1.4 GHz respectively. The luminosity at 151 MHz was calculated using the 1.4-GHz flux density of each object and a typical steep radio spectral index $\alpha = 0.8$; we don't use the radio spectral index of each object since it is not calculated between 1.4 GHz and 151 MHz and would introduce further uncertainties (see Chapter 2. **Columns 7 & 8** give the blue excess and mid-IR excess; the mid-IR excess was calculated from the extrapolated [OII] emission line luminosity, $L_{[\mathrm{OII}]-24}$, based on Eqn. 6.10 (Section 6.3.2). Note that values of $L_{[\mathrm{OII}]-24}$ are normalised to the mean $L_{[\mathrm{OII}]-24}$ of each sample. The rest luminosities at 4000 Å and 1 μm were calculated using photometric data of each object, from the B- to the K-band. When a data point was not available, the nearest photometric point was used.

(1)	(2)	(3)	(4)	(5)	(6)	(7)	(8)
Name	S_{line} (10^{-19} W m^{-2})	$\log_{10}(L_{[\mathrm{OII}]}$ / [W])	Emission Line	$\log_{10}(L_{151\mathrm{MHz}}$/ [WHz^{-1}sr^{-1}])	$\log_{10}(L_{1.4\mathrm{GHz}}$/ [WHz^{-1}sr^{-1}])	$\log_{10}([\nu L]_{4000\mathrm{\AA rest}}$/ $[\nu L]_{1\mu\mathrm{mrest}}$)	$\log_{10}(L_{[\mathrm{OII}]-24}$/ $[\nu L]_{1\mu\mathrm{mrest}}$)
sxds_0001	2.50	34.62	[OII]	25.82	25.04	-1.31	0.30
sxds_0002	2.50	35.30	[OII]	26.34	25.57	-1.06	0.56
sxds_0003	16.0	36.17	Lyα	27.16	26.39	-0.73	1.09
sxds_0004	$< 0.47^{e}$	$< 34.57^{e}$	Lyα	26.16	25.38	-1.32	< 0.14
sxds_0005	< 1.54	< 34.62	MgII	26.14	25.36	-0.69	< 0.42
sxds_0006	–	–		25.39	24.62	-1.27	–
sxds_0007	0.92	34.98	[OII]	25.97	25.20	-1.22	-0.03
sxds_0008	11.0	34.93	[OII]	24.48	23.71	-0.32	1.27
sxds_0009	0.11^{e}	34.42^{e}	Lyα	26.38	25.61	-1.81	-1.19
sxds_0010	–	–		25.63	24.85	-1.21	–
sxds_0011	< 0.80	< 34.16	[OII]	24.92	24.15	-1.12	< -0.34
sxds_0012	0.26	33.98	[OII]	25.07	24.29	-1.37	-0.74
sxds_0013	0.93	35.75	[OII]	25.73	24.96	-1.25	0.77
sxds_0014	$< 0.0008^{e}$	$< 31.77^{e}$	Lyα	25.29	24.51	-5.46	< -6.68
sxds_0015	4.50	34.25	[OII]	24.09	23.31	-0.41	0.77
sxds_0016	0.42	34.66	[OII]	25.50	24.73	-0.56	0.72
sxds_0017	1.00	35.89	CIV^{n}	25.92	25.15	-0.97	0.97
sxds_0018	0.73	34.49	[OII]	25.06	24.29	-1.13	-0.31
sxds_0019	0.24	33.71	[OII]	24.65	23.88	-0.80	0.15
sxds_0020	–	–		25.11	24.34	-0.41	–
sxds_0021	–	–		25.57	24.80	-0.56	–
sxds_0022	< 13.0	< 33.91	[OIII]	23.53	22.76	-0.78	< 0.16
sxds_0023	0.64	33.95	[OII]	24.48	23.71	-0.54	0.20
sxds_0024	< 1.10	< 34.06	[OII]	24.32	23.55	-0.93	< -0.20
sxds_0025	0.90	33.84	MgII	24.69	23.91	-0.39	0.79
sxds_0026	< 1.10	< 33.92	[OII]	24.04	23.27	-1.09	< -0.19
sxds_0027	< 0.03	< 33.70	[OII]	25.14	24.37	-1.81	< -1.07
sxds_0028	< 0.64	< 34.03	[OII]	24.23	23.45	-0.46	< 0.43
sxds_0029	–	–		24.90	24.12	-1.11	–
sxds_0030	$< 24.5^{e}$	$< 35.44^{e}$	[OII]	24.08	23.31	-1.03	< 1.10
sxds_0031	–	–		24.92	24.15	-1.36	–
sxds_0032	–	–		24.91	24.13	-0.92	–
sxds_0033	< 0.71	< 34.11	[OII]	24.34	23.57	-0.39	< 0.17
sxds_0034	6.50	35.63	[OII]	24.76	23.99	-0.30	1.51
sxds_0035	–	–		24.96	24.19	-1.14	–
sxds_0036	0.26	33.99	[OII]	24.08	23.31	-1.73	-0.77
sxds_0037	–	–		24.60	23.83	-1.64	–

6.3.2 Accretion indicators using 24 micron data

In Chapter 2 we showed that some of the SXDS radio sources have 24 μm excess emission which was quantified by the mid-IR excess (see Section 2.4.1). The connection of blueness and mid-IR excess is shown in Figure 6.4. This adopted model assumes that light from the nucleus with intrinsic optical luminosity $L_{\rm opt}$ is i) absorbed by dust and re-emitted in the mid-IR generating luminosity $[\nu L]_{10\mu{\rm mrest}}$ and ii) scattered, generating a contribution to luminosity $[\nu L]_{4000\mathring{\rm A}{\rm rest}}$:

$$[\nu L]_{4000\mathring{\rm A}{\rm rest}} = {\rm k}_1 \times [\nu L]_{1\mu{\rm mrest}} + {\rm k}_2 \times [\nu L]_{10\mu{\rm mrest}} \Rightarrow \tag{6.8}$$

$$\frac{[\nu L]_{4000\mathring{\rm A}{\rm rest}}}{[\nu L]_{1\mu{\rm mrest}}} = {\rm k}_1 + {\rm k}_2 \times \frac{[\nu L]_{10\mu{\rm mrest}}}{[\nu L]_{1\mu{\rm mrest}}} \tag{6.9}$$

Figure 6.4 presents results on a linear-linear fit based on Eqns 6.8 & 6.9. This approach gives similar results to the one presented in Chapter 2. The slope and intercept of Figure 6.4 give ${\rm k}_1 \sim 0.47$ and ${\rm k}_2 \sim 0.06$ (Eqn. 6.9), which agrees well with independent evidence for the properties of radio sources as we now argue. The value deduced for ${\rm k}_1$ is in line with the expectations of template spectra of galaxies which formed their stars at high redshift. Optical polarisation studies (e.g. Kishimoto et al. 2001) tell us that $[\nu L]_{4000\mathring{\rm A}{\rm rest}} \gtrsim 0.01\ [\nu L]_{\rm opt}$, which is consistent with our value of ${\rm k}_2$ given that QSO SED studies suggest $[\nu L]_{10\mu{\rm mrest}} \sim 0.3\ [\nu L]_{\rm opt}$ (Rowan-Robinson 1995), and $0.06 \times 0.3 \simeq 0.01$. We conclude that whenever nuclear accretion is significant in our sample of radio sources, dust in the torus absorbs 30% of the photons and dust above and below the torus scatters $\sim 1\%$ of the photons.

The fact that no 24 μm data are available for the TOOT00 sample is further restrictive for testing the model presented in Chapter 2 on the TOOT00 radio sources, so we focus initially on the SXDS dataset.

Figure 6.5 shows the correlation between [OII] emission-line luminosity and 24 μm luminosity for the SXDS sources. The relationship between the two quantities is:

$$\log_{10}(L_{\rm [OII]}) = (16.6 \pm 3.80) + \log_{10}(L_{24}^{0.79\pm0.17}), \tag{6.10}$$

where the $L_{\rm [OII]}$ is in units of [W] and L_{24} is in [W Hz^{-1} sr^{-1}] units. This correlation implies that emission from the NLR and mid-IR re-emitted light from the nucleus are connected, and supports the notion that AGN illumination of the circumnuclear dust is the primary heating

mechanism for the dust producing thermal mid-IR emission at 24 μm (see Dicken et al. 2008). Most high-$L_{[\mathrm{OII}]}$ SXDS objects show significant accretion, apart from one, sxds_0027, that has a rather faint optical spectrum lacking emission lines. One could speculate that this is a 'host obscured' quasar (Martínez-Sansigre et al. 2005) in which dust on the scale of the host galaxy extinguishes even the narrow emission lines. The scatter between $L_{[\mathrm{OII}]}$ and $L_{24\mu\mathrm{m}}$ can be explained by the points made in Section 6.1 on the emission-line/radio correlation, factors like different emission-line ratios used in the calculation of $L_{[\mathrm{OII}]}$ and variations in the covering factors of the line-emitting gas and the dust as presented to the central illuminating source.

From the correlation between radio luminosity and 24 μm luminosity in Figure 6.6, it is obvious that the high-radio luminosity objects have excess mid-IR emission, as noted in Section 6.1 (see also Smolčić et al. 2009; Tasse et al. 2008). The relationship between the two quantities is almost a proportionality:

$$L_{1.4\mathrm{GHz}} \propto L_{24}^{0.97\pm0.23} \tag{6.11}$$

From Eqn. 6.11 we conclude that radio luminosity, which is also an indicator of jet power Q (e.g. Rawlings & Saunders 1991), scales in proportion to the accretion rate. Furthermore, from Eqn. 6.10 is shown that the accretion rate increases with luminosity at 24 μm. It has been argued that the [OIII] λ5007 is a better indicator of accretion than the [OII] λ3727 line (Simpson 1998), but here we use [OII] since the [OIII] emission is probably anisotropic (Tadhunter et al. 1998). Since the [OII] emission line is an indicator of the the accretion rate (see Sec 6.1), we decided to use the [OII] emission line, as a proxy for the 24 μm data in Eqn. 2.1 based on Eqn. 6.10, to include [OII] and thus compare the TOOT00 and SXDS radio sources. The relevant values are presented in Tables 6.1 & 6.2. The relation to investigate is:

$$[\nu L]_{4000\mathring{\mathrm{A}}\mathrm{rest}} = \mathrm{l}_1 \times [\nu \mathrm{L}]_{1\mu\mathrm{mrest}} + \mathrm{l}_2 \times \mathrm{L}_{[\mathrm{OII}]-24} \Rightarrow \tag{6.12}$$

$$\frac{[\nu L]_{4000\mathring{\mathrm{A}}\mathrm{rest}}}{[\nu L]_{1\mu\mathrm{mrest}}} = \mathrm{l}_1 + \mathrm{l}_2 \times \frac{L_{[\mathrm{OII}]-24}}{[\nu L]_{1\mu\mathrm{mrest}}}, \tag{6.13}$$

where $L_{[\mathrm{OII}]-24}$ is the extrapolated [OII] luminosity from Eqn. 6.10.

Figure 6.7 presents the blue excess versus the extrapolated [OII] emission-line luminosity, $L_{[\mathrm{OII}]-24}$, for both TOOT00 and SXDS radio sources. Note that values of $L_{[\mathrm{OII}]-24}$ in these

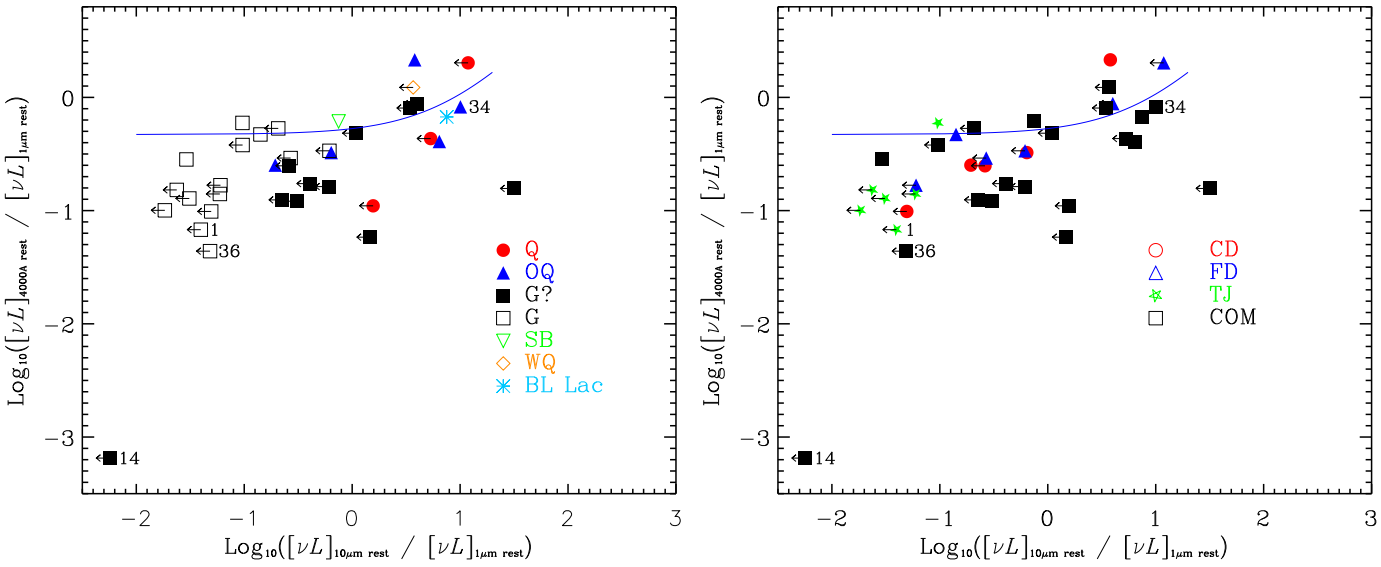

Figure 6.4: Blueness vs mid-IR excess for the SXDS radio sources. **a) Left**: Symbols indicate optical/IR classification as in Section 2.3.3: red filled circles for quasars 'Q', blue filled triangles for obscured quasars 'OQ', black filled squares for possible galaxies 'G?', black squares for secure galaxies 'G', green upside-down triangles for starbursts 'SB', orange diamonds for weak quasars 'WQ' and light-blue stars for 'BL Lac' objects. Note: this diagram is also presented in Chapter 2. **b) Right**: Symbols indicate radio-optical classification as in Figure 6.2. In both plots, the blue solid line is the best-fit line in a linear-linear plane where objects without detections were treated as limits: the slope and intercept are 0.06 and 0.47 respectively. 'SB', 'BL', 'Q' and 'WQ' were excluded from the fits (see Section 2.4.1 in Chapter 2). Schmitt's method (Schmitt 1985; ASURV) was used in these calculations.

plots are normalised to the mean $L_{[\mathrm{OII}]-24}$ of each sample for clarity. The outliers in Figure 6.7 are mostly TOOT00 objects: sources with blue SEDs end up on the top right of the plot, while red objects are found on the bottom. The one very red outlier in the SXDS sample, sxds_0014, is a very faint at blue object (see Figure 2.7 in Chapter 2). For the TOOT00 radio sources, we get $\mathrm{l}_1 = 0.15$ and $\mathrm{l}_2 \simeq 0.14$ (Figure 6.7 and Eqn. 6.13). For the SXDS radio sources we get $\mathrm{l}_1 = 0.16$ and $\mathrm{l}_2 = 0.03$ (Eqn. 6.13). These values show that for the SXDS sample, using the [OII] emission-line luminosity as a proxy for $L_{24\mu\mathrm{m}}$ gives similar results as in Figure 6.4, i.e. $\sim 1\%$ of light is scattered above and below the torus. For the TOOT00 the result is similar. Thus it is efficient to use [OII] as a proxy for 24 μm emission. We have to note that ASURV methods are not valid in the regime where most of the limit sources are at one end of the distribution.

6.3.3 Radio structures of the TOOT00 and the SXDS radio sources

Radio sources exhibit a variety of radio structures. The connection of emission-line luminosity and radio luminosity to the radio structure in the TOOT00 and the SXDS radio-source samples can be seen in Figures 6.2 & 6.3.

Both FRI and FRII objects combined span three dex in [OII] emission-line luminosity

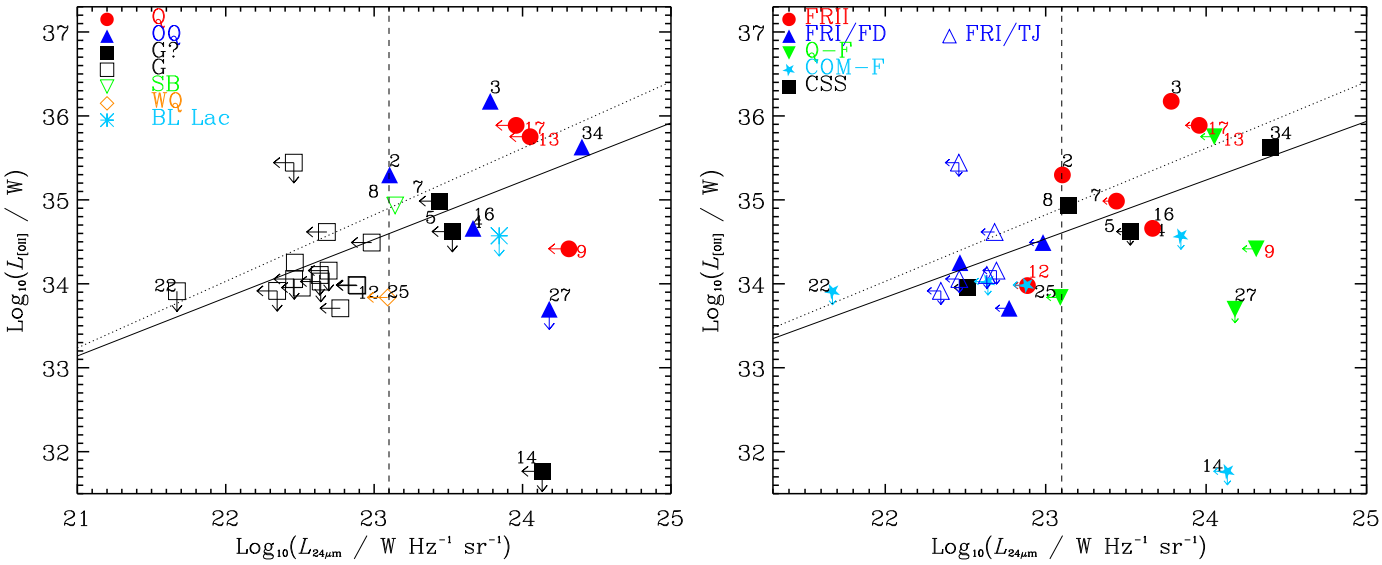

Figure 6.5: Emission-line luminosity $L_{[\mathrm{OII}]}$ versus 24-μm luminosity $L_{24\mu\mathrm{m}}$ for the SXDS radio sources. **a) Left**: Symbols indicate optical/IR classification as in Figure 6.4. **b) Right**: Symbols indicate radio-optical classification as in Figure 6.3; filled blue triangles denote FD objects and open blue triangles denote TJ radio sources. In both plots, the black solid line shows the best-fit line, where the slope and intercept are 0.69 and 18.57 respectively; excluded from the fit are SB and BL objects, as well as sxds_0014 and sxds_0027 due to their unusual nature (see notes on objects in Section 2.6). The black dotted line shows the best-fit line where the linear regression coefficients are calculated by Schmitt's method (Schmitt 1985) in the ASURV statistics package, in order to include upper limits in both independent and dependent variables; the slope and intercept are 0.79 and 16.58 respectively. The Spearman correlation coefficient is $\rho = 0.605$ with a 99.83% probability for a correlation; including all the upper limits gives $\rho = 0.528$ and probability 98.87%. The dashed vertical line denotes the limit of 'significant' accretion (see Section 6.3.2).

over the radio luminosity range $\sim 10^{24-28}$ W Hz^{-1} sr^{-1}, with the FRIIs having an order of magnitude higher emission-line luminosity than FRIs; this result agrees with previous studies on the emission-line/radio connection (Baum, Zirbel & O'Dea 1995). Thus FRII radio sources produce substantially more optical line emission than FRI objects. An exception seems to be TOOT00_1099, which is a galaxy with FRI radio structure, high radio luminosity at both 151 MHz and 1.4 GHz and bright optical emission-lines. In the SXDS sample, sxds_0001 and sxds_0020[2] are two examples that FRI objects do exist well above the FRI/FRII divide, despite the fact they have no signs of a QSO component that would explain their high radio luminosity value. FRI objects well above the FRI/FRII break in the radio luminosity above redshift $z \sim 1$ have been noted before (Heywood, Blundell & Rawlings 2007). FRI objects above the FRI/FRII break are present in both TOOT00 and SXDS samples, while there is absence of FRII objects below the FRI/FRII divide.

[2]sxds_0020 is not presented in Figures 6.2 & 6.3 due to absence of emission line measurement. The 1.4-GHz radio luminosity value can be seen in Table 6.2.

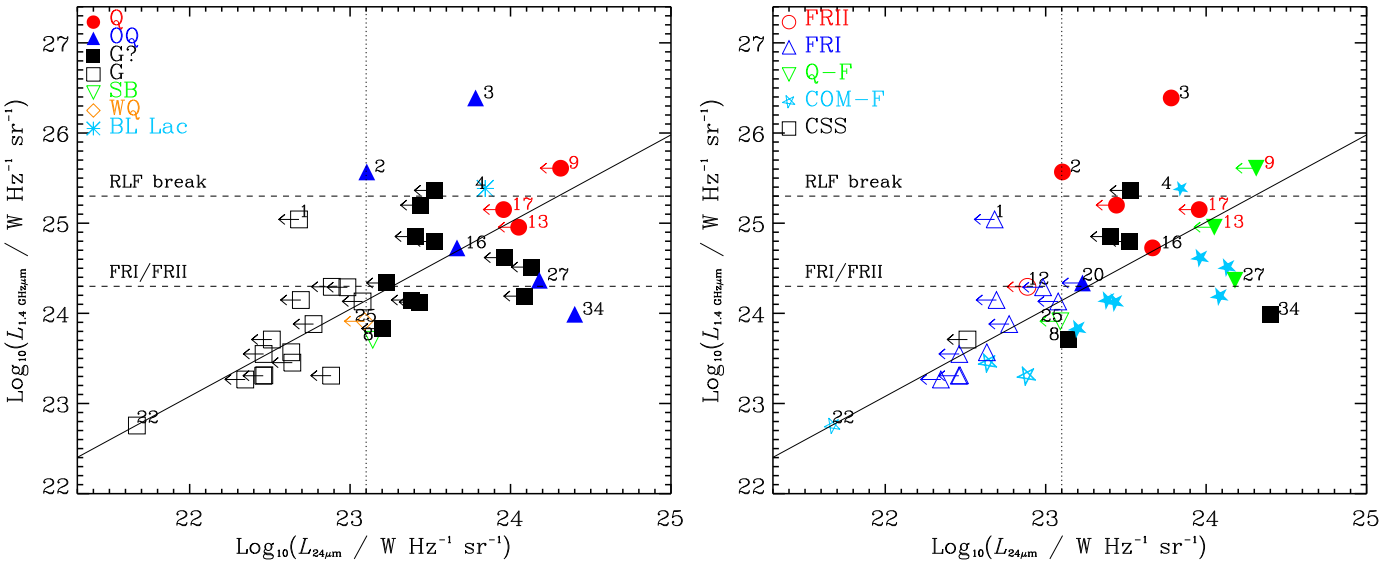

Figure 6.6: Radio luminosity $L_{1.4\mathrm{GHz}}$ versus 24-μm luminosity $L_{24\mu\mathrm{m}}$ for the SXDS radio sources. **a) Left**: Symbols indicate optical/IR classification as in Figure 6.4. **b) Right**: Symbols indicate radio-optical classification as in Figure 6.3; filled symbols indicate objects with 24 μm excess emission. In both plots the black solid line shows the best-fit line, where the slope and intercept are 0.97 and 1.81 respectively; the linear regression coefficients are calculated by Schmitt's method (ASURV), in order to include upper limits in both independent variable. The Spearman correlation coefficient is $\rho = 0.958$ with a 100% probability for a correlation. The dotted vertical line denotes the limit of 'significant' accretion (see Section 6.3.2). The horizontal lines show the FRI/FRII divide and RLF break in radio luminosity (a typical steep-spectrum radio spectral index of 0.8 was used to convert to our assumed cosmology).

Two SXDS objects that do not follow the emission-line/radio correlation are sxds_0008 and sxds_0034, which are below the FRI/FRII break in the radio luminosity with high emission-line luminosity values, and have CSS radio structures. Both objects have excess 24 μm emission, indicating that objects with low radio luminosity can have excess emission in the mid-IR that is connected to the high-excitation narrow lines in the spectrum of the objects (in sxds_0034; see Figure 2.7) or perhaps is connected to a starburst component (as in sxds_0008).

Furthermore, differences between FRI and FRII radio sources include 24 μm excess emission. In Figure 6.6–b can be seen that few FRIs show 24 μm accretion (e.g. sxds_0020), but most FRIIs (apart from sxds_0012) do.

6.4 Conclusions

This Chapter presents analysis on the [OII] emission-line and radio luminosity of the TOOT00 and SXDS radio sources. The 24 μm data of the SXDS sample are used to provide guidance on the connection between the [OII] emission-line and a more direct measure of accretion. Finally, the radio structures of both source-samples are investigated in connection to the above

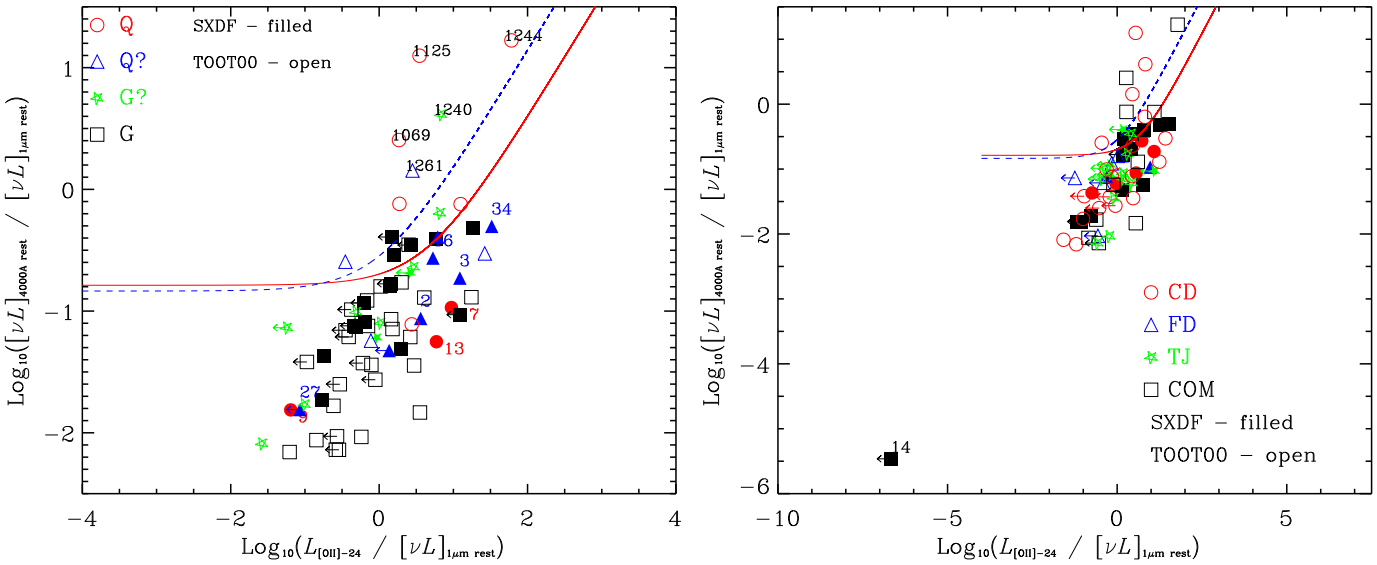

Figure 6.7: Blueness vs $L_{[\mathrm{OII}]-24}$ for the TOOT00 and the SXDS radio sources. **a) Left**: Symbols indicate optical classification as in Figure 6.1. Note that this plot excludes sxds_0014 for clarity; it can be seen on the right plot. **b) Right**: Symbols indicate radio classification as in Figure 6.2. In both plots the red solid line is the best-fit line in a linear-linear plane for the SXDS objects where objects without detections were not included in the calculations; also 'SB', 'BL', 'Q' and 'WQ' objects and sxds_0014 were excluded from the fit: the slope and intercept are 0.03 and 0.16 respectively. In both plots the blue dashed line is the best-fit line in the linear-linear plane for the TOOT00 objects where objects without detection were not included in the calculations; also 'Q' objects were excluded from the fit: the slope and intercept are 0.14 and 0.15 respectively. Schmitt's method (ASURV) was used in these calculations. Note: values on the x-axis were normalised to the mean value of each sample for presentation reasons.

analysis. The basic conclusions are the following:

• Both FRII and FRI objects span 3 dex in [OII] emission-line luminosity over the radio luminosity range 10^{24-28} W Hz^{-1} sr^{-1}, with the FRIIs having an order of magnitude higher emission-line luminosity than the FRIs.

• We get almost the same slope for the correlation between [OII] emission-line and radio luminosity as previous studies in two new totally-independent samples. The normalisation in TOOT00 and SXDS is also not significantly different from each other.

• The TOOT00 radio sources show an increased scatter in the $L_{[\mathrm{OII}]}$ - L_{rad} relation, suggesting a population of $z \sim 2$ radio sources with weak lines in the UV. We are possibly seeing more host obscured objects as we approach the RLF break.

• The mid-IR excess at 24 μm and the [OII] emission-line luminosity are correlated while some scatter is present, probably dominated by the emission-line ratios used in the calculation of [OII].

• The almost proportionality between radio luminosity at 1.4 GHz and 24 μm luminosity suggests that L_{rad} does trace accretion luminosity and $L_{[\mathrm{OII}]} \propto L_{\mathrm{rad}}^{0.7}$ may reflect imperfections in

$L_{[OII]}$-accretion luminosity scaling.

• In the SXDS sample, mid-IR 24 μm observations suggest that 30% of the light from the nucleus is absorbed by the torus and re-emitted in the mid-IR, while $\sim$ 1% of the light is scattered above and below the torus.

• Use of the [OII] emission line as a proxy for 24 μm emission as an indicator of accretion gives similar results for both SXDS and TOOT00 radio sources.

Chapter 7

Conclusions

This DPhil dissertation provides a better understanding of the faint radio-source population, using as tools radio, optical, near- and mid-IR observations of two independent samples of radio sources. The first sample, presented in Chapter 2, is the 37 high-frequency selected SXDS radio sources with flux densities at 1.4 GHz above 2 mJy, a spectroscopic completeness of 65% and a median redshift of $z_{\rm med} \simeq 1.1$, when including photometric redshifts estimated from HyperZ. The second sample, presented in Chapter 3, is the 47 low-frequency selected TOOT00 radio sources with flux densities at 151 MHz above 100 mJy, a spectroscopic completeness of 85% and a median redshift of $z_{\rm med} \sim 1.25$, when including photometric redshifts estimated from the $K_{\rm W} - z$ relation of Willott et al. (2003); this value is slightly higher than the $z \sim 1.1$ of the 6CE and 7CRS surveys.

Objects in both samples have been classified based on their optical, radio, and a combination of optical and radio properties. We have classified the SXDS radio sources as either quasars 'Q', obscured quasars 'OQ', possible galaxies 'G?', secure galaxies 'G', starbursts 'SB', weak quasars 'WQ' or BL Lac objects 'BL'. The TOOT00 radio sources were classified based on their optical properties as quasars 'Q', possible quasars 'Q?', possible galaxies 'G?' and galaxies 'G'. The radio classification places them in the classical-double 'CD', fat-double 'FD', twin-jet 'TJ' and compact 'COM' categories. Finally, the radio-optical classification combines radio and optical classes in: FRII, FRI, Q-F, COM-F, CSS objects.

Based on the optical classification of the SXDS objects, and taking into account the 24 μm excess, we find that objects 'Q', 'OQ' and 'G?' have significant nuclear accretion, since they obey $\log_{10}(L_{24\mu{\rm m}}/[{\rm WHz^{-1}sr^{-1}}]) > 23.1$ (or $[\lambda L]_{24\mu{\rm m}} > 10^{37.3}$ W). This value corresponds to $[\lambda L]_{24\mu{\rm m}} \geq 10^{-1.8} L_{Edd}$ for a black hole mass $M_{\rm BH} \geq 10^8 M_{\odot}$. Significant accretion is also nearly ubiquitous above the 'FRI/FRII' luminosity break, i.e. at redshift $z \gtrsim 1$ for objects in

the SXDS sample. The presence of significant accretion is linked to the radio luminosity $L_{\rm rad}$ (or radio structure) of the radio source at $z \sim 1$, just as it is at $z \sim 0.1$. Using the 24 μm excess as an indicator for significant accretion we find that the quasar-mode fraction, defined here as the fraction of objects with significant accretion rates to the total number of objects – and not as the number of sources with quasar-like optical spectra – is $\sim 0.5 \rightarrow 0.9$. There are counter examples like the low-accretion FRI sxds_0001, but they are rare. Similarly, based on the optical classification of the TOOT00 objects and their radio luminosity we find that the fraction of 'naked' quasars is $0.13 < f_{\rm q} < 0.25$ above the FRI/FRII break in the 151-MHz radio luminosity and below that break, the quasar fraction drops towards zero. These results are similar to the 3CRR, 6CE, 7CRS redshift surveys.

Furthermore, we compare the redshift distributions of the SXDS and the TOOT00 radio sources to a simulated distribution of radio sources from the SKADS Simulated Skies Semi-Empirical Extragalactic Database (S^3-SEX; Wilman et al. 2008), simulations extrapolated from the 3CRR/6CE/7CRS datasets. We find that the total number of TOOT00 objects and their distribution are consistent with the S^3-SEX simulation. For the SXDS sample, results are only broadly similar, which is not entirely surprising as S^3-SEX was built around low-frequency-selected redshift surveys and source counts, and it is expected to be less accurate at higher frequencies. Comparison of the SXDS with the S^3-SEX simulation, and with a sample of 100-simulated sky areas equal to the SXDS, suggests that the redshift spikes seen at $z \sim 0.65$ & 2.7 in the SXDS redshift distribution are significant and might be due to Large-Scale Structure. Similar comparison for the TOOT00 redshift distribution shows that the $z \sim 1.3$ redshift spike is significant and might be due to LSS.

We test for cosmic evolution in the SXDS and TOOT00 samples with the $V/V_{\rm max}$ test (Rowan-Robinson 1968; Schmidt 1968) and find that the SXDS radio sources do not evolve with redshift, since the mean $V/V_{\rm max} \approx 0.5$. On the contrary, the TOOT00 radio sources evolve with redshift since $V/V_{\rm max} \approx 0.6$, and ≈ 0.8 at redshifts $z \sim 3$. This suggests that the cosmic evolution of these two samples of radio sources is different.

Study of the $K - z$ relation of the TOOT00 and the SXDS radio sources reveals that these two samples include different types of radio sources at K. This can probably be partly explained by the fact that the TOOT00 objects are selected at a low-frequency radio survey. The SXDS radio sources are high-frequency selected, where the extra depth of SXDS being sufficient to probe different populations. The TOOT00 radio sources seem to follow the $K_{\rm W} - z$ relation that fits a 3 L^* passively-evolving galaxy that formed at redshift $z = 10$. The actual median luminosity at K is 4 L^*, while some exceptions of bright quasars and faint radio galaxies do

exist. The SXDS radio sources are in general fainter than the $K_{\rm W} - z$ relation, and the median luminosity at K is 2 L^*. Thus we find that the TOOT00 radio sources at a median redshift $z_{\rm med} \sim 1.25$ are 2-times more luminous at K than the $z_{\rm med} \simeq 1.1$ SXDS radio sources. Finally, comparison of the $K - z$ diagram of TOOT00, SXDS and 6dF radio sources shows that they are in the same K luminosity range, but low-K objects exist at high redshifts.

A very interesting result is that the FRI/FRII divide in radio luminosity seen at $z \lesssim 0.5$ is also observed at $z \sim 1$ for FRII objects in the TOOT00 and SXDS samples, but examples of FRI radio sources that are above the FRI/FRII break in radio luminosity do exist. Comparison of the space density of the TOOT00 and SXDS FRI objects above the FRI/FRII break with the local 6dF FRI radio sources above the FRI/FRII break suggests that these objects exist at both high and low redshifts, but they are rare. Furthermore, at $z \lesssim 1$ most of the 'FRI'-regime sources in SXDS have low accretion rates and $f_{\rm QM} \lesssim 0.1$, but one high-accretion-rate object (sxds_0034) does exist; this is an obscured 'radio-quiet quasar' which may have FRI-like jets.

Comparison of the [OII] emission-line luminosity and radio luminosity provides a correlation in both SXDS and TOOT00, seen in previous samples like the 7CRS (Willott et al. 1999): $L_{\rm [OII]} \propto L_{\rm rad}^{0.7}$. The almost proportionality between radio luminosity at 1.4 GHz and 24 μm luminosity suggests that $L_{\rm rad}$ does trace accretion luminosity and $L_{\rm [OII]} \propto L_{\rm rad}^{0.7}$ may reflect imperfections in $L_{\rm [OII]}$-accretion luminosity scaling.

Mid-IR 24 μm observations in the SXDS sample suggest that 30% of the light from the nucleus is absorbed by the torus and re-emitted in the mid-IR, while $\sim$ 1% of the light is scattered above and below the torus. Due to absence of 24 μm data for the TOOT00 sample, the [OII] emission-line luminosity is being used as a proxy for 24 μm emission, based on a correlation found between them, where $L_{\rm [OII]} \propto L_{24\mu{\rm m}}^{0.8\pm0.17}$. Similar results are shown in TOOT00 when this method is used.

We conclude that the study of the two independent SXDS and TOOT00 radio-source samples provides vital information on the nature of faint radio sources, but also gives some guidance for future research.

7.1 The future of radio astronomy

The future of radio astronomy looks very promising, with new surveys and new radio telescopes that aim to study wider sky areas than those observed before. Their goal is to find more radio sources based on deeper observations, better resolution, bigger area coverage and combined observations at other wavebands.

The Low-Frequency Array LOFAR (Röttgering et al. 2006), already in operation in the Netherlands with a UK involvement (e.g. Best et al. 2008), is designed to observe at low radio frequencies from 30 to 240 MHz. The goals are to improve radio observations at frequencies below 40 MHz, with simultaneous observations of large fields of view ($\sim$ 1000 deg^2), and low-frequency radio spectroscopy for studies of the epoch of reionization. At higher frequencies the target is to match optical, (sub-mm) and X-ray observing facilities (e.g. Röttgering 2006). LOFAR is important for studies of high-z radio galaxies, since low frequencies ($\sim$ 30 MHz) can be used to trace galaxies above the redshift of six, and it also aims to detect radio-loud AGN up to high redshifts. At high frequencies (e.g. 120 MHz) the goal is to gain reliable spectral indices and good positional information. Furthermore, LOFAR aims to study the cosmic star formation history without the effects of dust obscuration and probe galaxies with representative star-formation rate (SFR) for $z > 2$ similar to those in local galaxies ($\sim$ 10 M$_\odot$ yr^{-1}). This can be achieved by combination with sub-mm imaging (e.g. Scuba-2 and ALMA; Robson & Holland 2007 and Wootten & Thompson 2009, respectively), as well as far-infrared observations (e.g. Spitzer and Herschel; Lonsdale et al. 2003 and Latter et al. 2007, respectively). Sub-mm and far-IR studies promise to shed light to the understanding of the AGN population. Although LOFAR will be able to study the AGN population, one will always need optical and near-infrared spectroscopy for a secure redshift information.

In the near future, year 2020, the Square Kilometre Array (SKA; Jarvis & Rawlings 2004; Torres-Rodríguez & Cress 2007) will be able to observe both the radio-loud and radio-quiet AGN population up to redshifts of $z > 6$, including the epoch of reionization. The SKA proposal suggests that this new radio telescope will provide astronomers with a 3-dimensional view of the radio sky.

Although there is a current trend for observations at wavebands other than radio (e.g. X-rays), these are biased towards high accretion objects. Jets associated with low accretion can be revealed by radio observations. New generation radio telescopes, like the LOFAR and the SKA, promise to probe the faint radio-source population over all cosmic epochs.

Appendix D

D.1 Statistics

This section provides a sort description on the statistics used in the analysis.

D.1.1 Survival analysis statistical package – ASURV

(Lavalley et al. 1992) describes a powerful tool used for statistical analysis of data. The following methods are used in the analysis:

• The Buckley-James method calculates a regression with Kaplan-Meier residuals. It can treat several independent variables if the dependent variable contains only one kind of censoring (i.e., upper or lower limits). The task requires only that the censoring distribution about the fitted line is random. Of the three linear regression methods available in the ASURV package, this method is probably the most reliable.

• Schmitt's method calculates the binned two-dimensional Kaplan-Meier distribution and associated linear regression coefficients derived by Schmitt (1985). Schmitt's binned linear regression can treat mixed censoring including censoring in the independent variable, but can have only one independent variable. This task requires only that the censoring distribution about the fitted line is random.

• Spearman's correlation computes the generalised Spearman's rank order correlation coefficient between two variables. It can treat mixed censoring including censoring in the independent variable, but can have only one independent variable.

D.1.2 Poisson Probability

Poisson distribution is a discrete probability distribution that expresses the probability of a number of events occurring in a fixed period of time if these events occur with a known average

rate and independently of the time since the last event (see e.g. Barlow 2002). The Poisson distribution can also be used for the number of events in other specified intervals such as distance, area or volume.

If the expected number of occurrences in this interval is λ, then the probability that there are exactly k occurrences (k being a non-negative integer, $k = 0, 1, 2, ...$) is equal to:

$$f(k;\lambda) = \frac{\lambda^k e^{-\lambda}}{k!}, \tag{D.1}$$

where e is the base of the natural logarithm ($e = 2.71828...$); k is the number of occurrences of an event - the probability of which is given by the function; $k!$ is the factorial of k; and λ is a positive real number, equal to the expected number of occurrences during the given interval.

In the analysis we calculate (a) the probability for the number of objects to be greater than the data given the simulation (when the number of data is more than that of the simulation) or (b) the probability for the number of objects to be less than the data given the simulation (when the number of data is less than that of the simulation). As an example for case (a), consider the case where the observed number is 2 and the expected from the simulation is 1; then the Poisson probability to observe more than 2 objects is P(2;1) = $\sum$(P(i;1)), where i=2,... or P(2;1) = 1 - $\sum$(P(j;1)), where j=0,1,2. As an example for case (b), consider the case where the observed number is 0 and the expected from the simulation is 0.1; then the Poisson probability to observe more than 1 objects is P(1;0.1) = $\sum$(P(1;i)), where i=0,1.

D.1.3 Kolmogorov-Smirnov statistic

The K-S test gives the Kolmogorov-Smirnov statistic and associated probability that two arrays of data values are drawn from the same distribution (e.g. Press et al. 1993). The maximum deviation between the two distributions, $S_{N_1}(x)$ and $S_{N_1}(x)$ with data points N_1 and N_2, respectively, is:

$$D = \max|S_{N_1(x)} - S_{N_2(x)}|. \tag{D.2}$$

The significance level of D is given by:

$$\text{Probability}(D > \text{observed}) = Q_{\rm KS}\left(\left[\sqrt{N}_{\rm e} + 0.12 + 0.11/\sqrt{N}_{\rm e}\right] D\right), \tag{D.3}$$

where $Q_{\rm KS} = 2\sum_{j=1}^{\infty}(-1)^{j-1}e^{-2j^2\lambda^2}$ with limiting values $Q_{\rm KS}(0) = 1$ and $Q_{\rm KS}(\infty) = 0$; $N_{\rm e}$ is the effective number of data points, $N_{\rm e}\frac{N_1 N_2}{N_1+N_2}$.

Bibliography

[1] Alexander, P., Leahy, J. P., 1987, MNRAS, 225, 1

[2] Allen, S. W., Dunn, R. J. H., Fabian, A. C., Taylor, G. B., Reynolds, C. S., 2006, MNRAS, 372, 21

[3] Alonso-Herrero, A., Quillen, A. C., Rieke, G. H., Ivanov, V. D., Efstathiou, A., 2003, AJ, 126, 81

[4] da Angela, J., Shanks, T., Croom, S. M., Weilbacher, P., Brunner, R. J., Couch, W. J., Miller, L., Myers, A. D., Nichol, R. C., Pimbblet, K. A., de Propris, R., Richards, G. T., Ross, N. P., Schneider, D. P., Wake, D., 2008, MNRAS, 383, 565

[5] Aird, J., Nandra, K., Laird, E. S., Georgakakis, A., Ashby, M. L. N., Barmby, P., Coil, A. L., Huang, J.-S., Koekemoer, A. M., Steidel, C. C., Willmer, C. N. A., 2010, MNRAS, 401, 2531

[6] Antonucci, R., 1993, ARA&A, 31, 473

[7] Aretxaga, I., Hughes, D. H., Coppin, K., Mortier, A. M. J., Wagg, J., Dunlop, J. S., Chapin, E. L., Eales, S. A., Gaztanaga, E., Halpern, M. et al., 2007, MNRAS, 379, 1571

[8] Augusto, P., Wilkinson, P. N., Browne, I. W. A., 1998, MNRAS, 299, 1159

[9] Bahcall, J. N., Kirhakos, S., Saxe, D. H., Schneider, D. P., 1997, ApJ, 479, 642

[10] Balmaverde, B., Baldi, R. D., Capetti, A, 2008, A&A, 486, 119

[11] Barmby, P., Alonso-Herrero, A., Donley, J. L., Egami, E., Fazio, G. G., Georgakakis, A., Huang, J.-S., Laird, E. S., Miyazaki, S., Nandra, K., et al., 2006, ApJ, 642, 126

[12] Barthel, P. D., 1989, ApJ, 336, 606

[13] Baum, S. A., Zirbel, E. L., O'Dea, C. P., 1995, ApJ, 451, 88

[14] Baum, A. S., Heckman, T. M., 1989a, ApJ, 336, 681

[15] Baum, A. S., Heckman, T. M., 1989b, ApJ, 336, 702

[16] Bertin, E., Arnouts, S., 1996, AAPS, 117, 393

[17] Best, P. N., 2009, AN, 330, 184

[18] Best, P. N., LOFAR-UK Consortium, the, 2008, arXiv:0802.1186v1 [astro-ph]

[19] Best, P. N., Kaiser, C. R., Heckman, T. M., Kauffmann, G., 2006, MNRAS, 368, 67

[20] Best, P. N., Kauffmann, G., Heckman, T. M., Brinchmann, J., Charlot, S., Ivezić, Ž., White, S. D. M., 2005, MNRAS, 362, 25

[21] Best, P. N., Arts, J. N., Röttgering, H. J. A., Rengelink, R., Brookes, M. H., Wall, J., 2003, MNRAS, 346, 627

[22] Best, P. N., 2000, MNRAS, 317, 720

[23] Best, P. N., Longair, M. S., Röettgering, H. J. A., 1998, MNRAS, 295, 549

[24] Bird, J. C., Martini, P., Kaiser, C. R., 2008, ApJ, 676, 147

[25] Blandford, R. D., Znajek, R. L., 1977, MNRAS, 179, 433

[26] Blundell, K. M., Kuncic, Z., 2007, ApJ, 668, 103

[27] Blundell, K. M., Rawlings, S., 2001, ApJ, 562, 5

[28] Blundell, K. M., Rawlings, S., Willott, C. J., 1999, AJ, 117, 677

[29] Bolzonella, M., Miralles, J. M., Pello, R., 2000, A&A, 363, 476

[30] Brand, K., Rawlings, S., Hill, G. J., Lacy, M., Mitchell, E., Tufts, J., 2003, MNRAS, 344, 283

[31] van Breugel, W., De Breuck, C., Stanford, S. A., Stern, D., Rottgering, H., Miley, G., 1999, AJ, 518, L61

[32] van Breukelen, C., Cotter, G., Rawlings, S., Readhead, T., Bonfield, D., Clewley, L., Ivison, R., Jarvis, M., Simpson, C., Watson, M., 2007, MNRAS, 382, 971

[33] van Breukelen, C., Clewley, L., Bonfield, D. G., Rawlings, S., Jarvis, M. J., Barr, J. M., Foucaud, S., Almaini, O., Cirasuolo, M., Dalton, G., Dunlop, J. S., Edge, A. C., Hirst, P., McLure, R. J., Page, M. J., Sekiguchi, K., Simpson, C., Smail, I., Watson, M. G., 2006, MNRAS, 373, L26

[34] Brookes, M. H., Best, P. N., Peacock, J. A., Röttgering, H. J. A., Dunlop, J. S., 2008, MNRAS, 385, 1297

[35] Brookes, M. H., Best, P. N., Rengelink, R., Röttgering, H. J. A., 2006, MNRAS, 366, 1265

[36] Brookes, M., Best, P. N., 2004, proceedings of Multiwavelength AGN Surveys conference, 343

[37] Brown, M. J. I., Brand, K., Dey, A., Jannuzi, B. T., Cool, R., Le Floc'h, E., Kochanek, C. S., Armus, L., Bian, C., Higdon, J., Higdon, S., Papovich, C., Rieke, G., Rieke, M., Smith, J. D., Soifer, B. T., Weedman, D., 2006, ApJ, 638, 88

[38] Bruzual, A. G., Charlot, S., 2003, MNRAS, 344, 1000

[39] Bruzual A. G., Charlot, S., 1993, ApJ, 405, 538

[40] Calzetti, D., Armus, L., Bohlin, R. C., Kinney, A. L., Koornneef, J., Strorchi-Bergmann, T., 2000, ApJ, 533, 682

[41] Cao, X., Rawlings, S., 2004, MNRAS, 349, 1419

[42] Cao, X., Jiang, D. R., 1999, MNRAS, 307, 802

[43] Cavaliere, A., Padovani, P., 1989, ApJ, 340, 5

[44] Cimatti, A., di Serego Alighieri, S., Fosbury, R. A. E., 1993, Salvati, M., Taylor, D., 1993, MNRAS, 264, 421

[45] Celotti, A. C., Padovani, P., Ghisellini, G., 1997, MNRAS, 286, 415

[46] Celotti, A., Fabian, A. C., 1993, MNRAS, 264, 228

[47] Cleary, K., Lawrence, C. R., Marshall, J. A., Hao, L, Meier, D., 2007, AJ, 660, 117

[48] Clewley, L., Jarvis, M. J., 2004, MNRAS, 352, 909

[49] Cohen, A. S., Lane, W. M., Cotton, W. D., Kassim, N. E., Lazio, T. J. W., Perley, R. A., Condon, J. J., Erickson, W. C., 2007, AJ, 134, 1245

[50] Cohen, A. S., Röttgering, H. J. A., Kassim, N. E., Cotton, W. D., Perley, R. A., Wilman, R., Best, P., Pierre, M., Birkinshaw, M., Bremer, M., Zanichelli, A., 2003, ApJ, 591, 640

[51] Coleman, G. D., Wu, C. C., Weedman, D. W., 1980, ApJS , 43, 393

[52] Collins, Ch., Brough, S., Burke, D., Mann, R., Lynam, P., 2004, Ap&SS, 285, 51

[53] Combes, Boissé, Mazure & Blanchard, 2002, Galaxies and Cosmology, Springer

[54] Condon, J. J., Cotton, W. D., Yin, Q. F., Shupe, D. L., Storrie-Lombardi, L. J., Helou, G., Soifer, B. T., Werner, M. W., 2003, AJ, 125, 2411

[55] Condon, J. J., Cotton, W. D., Greisen, E. W., Yin, Q. F., Perley, R. A., Taylor, G. B., Broderick, J. J., 1998, AJ, 115, 1693

[56] Condon, J. J., 1984, ApJ, 287, 461 ??

[57] Cress, C. M., Helfand, D. J., Becker, R. H., Gregg, M. D., White, R. L., 1996, ApJ, 473, 7

[58] Croom, S. M., Richards, G. T., Shanks, T., Boyle, B. J., Strauss, M. A., Myers, A. D., Nichol, R. C., Pimbblet, K. A., Ross, N. P., Schneider, D. P., Sharp, R. G., Wake, D. A., 2009, MNRAS, in press

[59] Croom, S. M, Smith, R. J., Boyle, B. J., Shanks, T., Miller, L., Outram, P. J., Loaring, N. S., 2004, MNRAS, 349, 1397

[60] Cruz, M. J., Jarvis, M. J., Rawlings, S., Blundell, K. M., 2007, MNRAS, 375, 1349

[61] Croton, D. J., Springel, V., White, S. D. M., De Lucia, G., Frenk, C. S., Gao, L., Jenkins, A., Kauffmann, G., Navarro, J. F., Yoshida, N., 2006, MNRAS, 365, 11

[62] De Breuck, C., van Breugel, W., Stanford, S. A., Röttgering, H., Miley, G., Stern, D., 2002, AJ, 123, 637

[63] Dicken, D., Tadhunter, C., Axon, D., Morganti, R., Inskip, K. J., Holt, J., Delgado, R. González, Groves, B., 2009, ApJ, 694, 268

[64] Dunkley, J., Komatsu, E., Nolta, M. R., Spergel, D. N., Larson, D., Hinshaw, G., Page, L., Bennett, C. L., Gold, B., Jarosik, N., Weiland, J. L., Halpern, M., Hill, R. S., Kogut, A., Limon, M., Meyer, S. S., Tucker, G. S., Wollack, E., Wright, E. L., 2009, ApJS, 180, 306

[65] Dunlop, J. S., McLure, R. J., Kukula, M. J., Baum, S. A., ODea, C. P., Hughes, D. H., 2003, MNRAS, 340, 109

[66] Dunlop, J. S., Peacock, J. A., 1990, MNRAS, 247, 19

[67] Dunlop, J. S., Taylor, G. L., Hughes, D. H., Robson, E. I., 1993, MNRAS, 264, 455

[68] Eales, S., Rawlings, S., Law-Green, D., Cotter, G., Lacy, M., 1997, MNRAS, 291, 593

[69] Eales, S. A., Rawlings, S., 1996, ApJ, 460, 68

[70] Eales, S. A., Rawlings, S., 1993, AJ, 411, 67

[71] Elitzur, M., 2006, NewAR, 50, 728

[72] Emonts, B., Morganti, R., Oosterloo, T., van Gorkom, J., 2008, proceedings of "The Modern Radio Universe: From Planets to Dark Energy Conference", Manchester UK

[73] Fan, X., Strauss, M. A., Schneider, D. P., Becker, R. H., White, R. L., Haiman, Z., Gregg, M., Pentericci, L., et al., 2003, AJ, 125, 1649

[74] Fan, X., Narayanan, V. K., Lupton, R. H., Strauss, M. A., Knapp, G. R., Becker, R. H., White, R. L., Pentericci, L., Leggett, S. K., Haiman, Z., et al., 2001, AJ, 122, 2833

[75] Fanaroff, B. L., Riley, J. M., 1974, MNRAS, 167, 31

[76] Fazio, G. G., Hora, J. L., Willner, S. P., Stauffer, J. R., Ashby, M. L., Wang, Z., Tollestrup, E. V., Pipher, J. L., Forrest, W. J., McCreight, C. R., et al., 1998, SPIE, 3354, 1024

[77] Ferrarese, L., Merritt, D., 2000, ApJ, 539, 9

[78] Francis, P. J., Webster, R. L., Masci, F. J., Drinkwater, M. J., Peterson, B. A., 1997, ASPC, 113, 130

[79] Francis, P. J., Hewett, P. C., Foltz, C. B., Chaffee, F. H., Weymann, R. J., Morris, S. L., 1991, ApJ, 373, 465

[80] Fukuda, Y., Hayakawa, T., Ichihara, E., Inoue, K., Ishihara, K., Ishino, H., Itow, Y., Kajita, T., Kameda, J., Kasuga, S., et al. 1998, PhRvL, 81, 4279

[81] Furusawa, H., Kosugi, G., Akiyama, M., Takata, T., Sekiguchi, K., Furusawa, J., 2008, ASPC, 399, 131

[82] Geach, J. E., Simpson, C. J., Rawlings, S., Read, A. M., Watson, M., 2007, MNRAS, 381, 1369

[83] Gebhardt, K., Bender, R., Bower, G., Dressler, A., Faber, S. M., Filippenko, A. V., Green, R., Grillmair, C., Ho, L. C., Kormendy, J. et al., 2000, ApJ, 539, 13

[84] Gopal-Krishna, Wiita, P. J., 2001, ApJ, 560, 115

[85] Goto, T., 2007, MNRAS, 381, 187

[86] Granato, G. L., Danese, L., 1994, MNRAS, 268, 235

[87] Gunn, J., Weinberg, D., 1995, proceedings of the Wide Field Spectroscopy and the Distant Universe conference, Cambridge

[88] Haehnelt, M. G., Rees, M. J., 1993, MNRAS, 263, 168

[89] Hales, S. E. G., Riley, J. M., Waldram, E. M., Warner, P. J., Baldwin, J. E., 2007, MNRAS, 382, 1639

[90] Hambly, N. C., Collins, R. S., Cross, N. J. G., Mann, R. G., Read, M. A., Sutorius, E. T. W., Bond, I. A., Bryant, J., Emerson, J. P., Lawrence, A. et al. 2007, arXiv:0711.3593

[91] Hardcastle, M. J., Evans, D. A., Croston, J. H., 2007, MNRAS, 376, 1849

[92] Hawkins, E., Maddox, S., Cole, S., Lahav, O., Madgwick, D. S., Norberg, P., Peacock, J. A., Baldry, I. K., Baugh, C. M., Bland-Hawthorn, J. et al. 2003, MNRAS, 346, 78

[93] Hes, R., Barthel, P. D., Fosbury, R. A. E, 1993, Nature, 362,326

[94] Heywood, I., Blundell, K. M., Rawlings, S., 2007, MNRAS, 381, 1093

[95] Hill, G., Rawlings, S., 2003, NewAR, 47, 373

[96] Hill, G. J., Nicklas, H. E., MacQueen, P. J., Tejada, C., Cobos Duenas, F. J., Mitsch, W., 1998, Proc SPIE, 3355, 37

[97] Hill, G. J., Lilly, S. J., 1991, ApJ, 367, 1

[98] Hine, R. G., Longair, M. S., 1979, MNRAS, 188, 111

[99] Hewett, P. C., Warren, S. J., Leggett, S. K., Hodgkin, S. T., 2006, MNRAS, 367, 454

[100] Ho, L. C., 2002, ApJ, 564, 120

[101] Houck, J. R., Roellig, T. L., Van Cleve, J., Forrest, W. J., Herter, T. L., Lawrence, C. R., Matthews, K., Reitsema, H. J., Soifer, B. T., Watson, D. M., et al., 2004, SPIE, 5487, 62

[102] Howarth, I. D., 1983, MNRAS, 203, 301

[103] Howatt, R. S. et al., 2004, "The commissioning of and first results from the UIST imager spectrometer", In Proc Spie 5492, UV and Gamma-Ray Space Telescope Systems, eds. Hasinger G, Turner M.J.

[104] Hoyle, F., 1949, MNRAS, 109, 365

[105] Ibar, E., Ivison, R. J., Biggs, A. D., Lal, D. V., Best, P. N., Green, D. A., 2009, MNRAS, 397, 281

[106] Inskip, K., Best, P. N., Longair, M. S., MacKay, D. J. C., 2002, MNRAS, 329, 277

[107] Ivison, R. J., Greve, T. R., Dunlop, J. S., Peacock, J. A., Egami, E., Smail, Ian, Ibar, E., van Kampen, E., Aretxaga, I., Babbedge, T., Biggs, A. D., Blain, A. W., Chapman, S. C., Clements, D. L., Coppin, K., Farrah, D., Halpern, M., Hughes, D. H., Jarvis, M. J., Jenness, T., Jones, J. R., Mortier, A. M. J., Oliver, S., Papovich, C., Prez-Gonzlez, P. G., Pope, A., Rawlings, S., Rieke, G. H., Rowan-Robinson, M., Savage, R. S., Scott, D., Seigar, M., Serjeant, S., Simpson, C., Stevens, J. A., Vaccari, M., Wagg, J., Willott, C. J., 2007, MNRAS, 380, 199

[108] Jackson, C. A., Wall, J. V., 2001, ASPC, 227, 242

[109] Jackson, N., Rawlings, S., 1997, MNRAS, 286, 241

[110] Jannuzi, B., Elston, R., Schmidt, G. D., Smith, P. S., Stockman, H. S., 1995, AJ, 454, 111

[111] Jarvis, M. J., van Breukelen, C., Wilman, R. J., 2005, MNRAS, 358, L11

[112] Jarvis, M J., Rawlings, S., 2004, NewAR, 48, 1173

[113] Jarvis, M. J., Rawlings, S., Eales, S., Blundell, K. M., Bunker, A. J., Croft, S., McLure, R. J., Willott, C. J., 2001a, MNRAS, 326, 1585

[114] Jarvis, M. J., Rawlings, S., Eales, S., Blundell, K. M., Willott, C. J., 2001b, arXiv:astro-ph/0103364

[115] Jarvis, M. J., Rawlings, S., Lacy, M., Blundell, K. M., Bunker, A. J., Eales, S., Saunders, R., Spinrad, H., Stern, D., Willott, C. J., 2001c, MNRAS, 326, 1563

[116] Jarvis M. J., Rawlings S., Willott C. J., Blundell K. M., Eales S. A., Lacy M., 2001d, MNRAS, 327, 907

[117] Johnston, H., Hunstead, R., Sadler, E., Cotter, G., Morganti, R., 2004, IAUS, 222, 451

[118] Jones, D. H., Saunders, W., Colless, M., Read, M. A., Parker, Q. A., Watson, F. G., Campbell, L. A., Burkey, D., Mauch, T., Moore, L., Hartley, M., Cass, P., James, D., Russell, K., Fiegert, K., Dawe, J., Huchra, J., Jarrett, T., Lahav, O., Lucey, J., Mamon, G. A., Proust, D., Sadler, E. M., Wakamatsu, K., 2004, MNRAS, 355, 747

[119] Kaiser, C. R., Best, P. N., 2007a, MNRAS, 381, 1548

[120] Kaiser, C. R., Best, P. N., 2007b, hvcg conf, 222

[121] Kaiser, C. R., Alexander, P., 1997, MNRAS, 286, 215

[122] Kembhavi, Ajit K., Narlikar, Jayant V., 1999, Quasars and active galactic nuclei : an introduction, Cambridge University Press

[123] Kennicutt, R. C., 1998, ARA&A, 36, 189

[124] Kishimoto, M., Antonucci, R., Cimatti, A., Hurt, T., Dey, A., van Breugel, W., Spinrad, H., 2001, ApJ, 547, 667

[125] Koekemoer, A. M., O'Dea, C. P., Baum, S. A., 2003, PASA, 20, 147

[126] Kollmeier, J. A., Onken, C. A., Kochanek, C. S., Gould, A., Weinberg, D. H., Dietrich, M., Cool, R., Dey, A., Eisenstein, D. J., Jannuzi, B. T., et al. 2006, ApJ, 648, 128

[127] Kormendy, J., Richstone, D., 1995, ARA&A, 33, 581

[128] Krolik, J. H., 1999, Active Galactic Nuclei, Princeton Series is Astrophysics

[129] La Franca, F., Fiore, F., Comastri, A., Perola, G. C., Sacchi, N., Brusa, M., Cocchia, F., Feruglio, C., Matt, G., Vignali, C., et al., 2005, ApJ, 635, 864

[130] Lacy, M., Canalizo, G., Rawlings, S., Sajina, A., Gates, E. L., Storrie-Lombardi, L., Armus, L., 2004, AAS, 205, 1670

[131] Lacy, M., Bunker, A. J., Ridgway, S. E., 2000, AJ, 120, 68

[132] Laing, R.A., Riley, J.M., Longair, M.S., 1983, MNRAS, 204, 151

[133] Laing, R. A., Longair, M. S., Riley, J. M., Kibblewhite, E. J., Gunn, J. E., 1978, MNRAS, 184, 149

[134] Lavalley, M., Isobel, T., Feigelson, E., 1992, ASPC, 25, 245

[135] Lawrence, A., Warren, S. J., Almaini, O., Edge, A. C., Hambly, N. C., Jameson, R. F., Lucas, P., Casali, M., Adamson, A., Dye, S., et al., 2007, MNRAS, 379, 1599

[136] Ledlow, M. J., Owen, F. N., 1996, AJ, 112, 9

[137] Leyshon, G., Eales, S., 1998, MNRAS, 295, 10

[138] Liddle, A., 2004, An Introduction to Modern Cosmology, WILEY

[139] Lilly, S. J., Longair, M. S., 1984, MNRAS, 211, 833

[140] Liu, F. K., Wu, X-B., Cao, S. L., 2003, MNRAS, 340, 411

[141] Longair, M. S., 1966, Nature, 211, 949

[142] Lonsdale, C. J., Smith, H. E., Rowan-Robinson, M., Surace, J., Shupe, D., Xu, C., Oliver, S., Padgett, D., Fang, F., Conrow, T., et al., 2003, PASP, 115, 897

[143] Latter, W. B., NHSC, HSC Teams, 2007, AAS, 210, 110

[144] Lawrence, A., Warren, S. J., Almaini, O., Edge, A. C., Hambly, N. C., Jameson, R. F., Lucas, P., Casali, M., Adamson, A., Dye, S., Emerson, J. P., Foucaud, S., Hewett, P., Hirst, P., Hodgkin, S. T., Irwin, M. J., Lodieu, N., McMahon, R. G., Simpson, C., Smail, I., Mortlock, D., Folger, M., 2007, MNRAS, 379, 1599

[145] MacDonald, E. C., Allen, P., Dalton, G., Moustakas, L. A., Heymans, C., Edmondson, E., Blake, C., Clewley, L., Hammell, M. C., Olding, E. et al. 2004, MNRAS, 352, 1255

[146] Magorrian, J., 2006, MNRAS, 373, 425

[147] Magorrian, J., Trenaube, S., Richstone, D., Bender, R., Bower, G., Dressler, A., Faber, S. M., Gebhardt, K., Green, R., Grilmair, C. et al., 1998, AJ, 115, 2285

[148] Martínez-Sansigre, A., Rawlings, S., Garn, T., Green, D. A., Alexander, P., Klöckner, H. R., Riley, J. M., 2006, MNRAS, 373, 80

[149] Martínez-Sansigre, A., Rawlings, S., Lacy, M., Fadda, D., Marleau, F., R., Simpson, C., Willott, C. J., Jarvis, M. J., 2005, Nature, 436, 666

[150] Marulli, F., Bonoli, S., Branchini, E., Moscardini, L., Springel, V., 2008, agn8.conf, 21

[151] Mauch, T., Sadler, E. M., 2007, MNRAS, 375, 931

[152] Meier, D. L., Godon, P., Edgington, S., Payne, D. G., Lind, K. R., 1998, ASPC, 144, 51

[153] Merloni, A., Heinz, S., 2008, MNRAS, 388, 1011

[154] McGilchrist, M. M., Baldwin, J. E., Riley, J. M., Titterington, D. J., Waldram, E. M., Warner, P. J., 1990, MNRAS, 246, 110

[155] McLure, R. J. , Dunlop, J. S., 2004, MNRAS, 352, 1390

[156] McLure, R. J., Jarvis, M. J., 2004, MNRAS, 353, L45

[157] McLure, R. J., Willott, C. J., Jarvis, M. J., Rawlings, S., Hill, G. J., Mitchell, E., Dunlop, J. S., Wold, M., 2004, MNRAS, 351, 347

[158] McLure, R. J., Kukula, M. J., Dunlop, J. S., Baum, S. A., O'Dea, C. P., Hughes, D. H., 1999, MNRAS, 308, 377

[159] Miller, P., Rawlings, S., Saunders, R., 1993, MNRAS, 263, 425

[160] Mortier, A. M. J., Serjeant, S., Dunlop, J. S., Scott, S. E., Ade, P., Alexander, D., Almaini, O., Aretxaga, I., Baugh, C., Benson, A. J., et al., 2005, MNRAS, 363, 563

[161] Nolta, M. R., Wright, E. L., Page, L., Bennett, C. L., Halpern, M., Hinshaw, G., Jarosik, N., Kogut, A., Limon, M., Meyer, S. S., Spergel, D. N., Tucker, G. S., Wollack, E., 2004, ApJ, 608, 10

[162] Norman, C., Hasinger, G., Giacconi, R., Gilli, R., Kewley, L., Nonino, M., Rosati, P., Szokoly, G., Tozzi, P., Wang, J., Zheng, W., Zirm, A., Bergeron, J., Gilmozzi, R., Grogin, N., Koekemoer, A., Schreier, E., 2002, ApJ, 571, 218

[163] Obreschkow, D., Croton, D., DeLucia, G., Khochfar, S., Rawlings, S., 2009, ApJ, 698, 1467

[164] Ogle, P. M., Antonucci, R. R. J., Whysong, D., 2007, ASPC, 373, 578

[165] Ogle, P., Whysong, D., Antonucci, R., 2006, ApJ, 647, 161

[166] Owen, F. N., Laing, R. A., 1989, MNRAS, 238, 357

[167] Pagani, C., Falomo, R., Treves, A., 2003, ApJ, 596, 830

[168] Page, M. J., Lehmann, I., Boller, Th., Watson, M. G., Dwelly, T., Hess, S., Matute, I., Loaring, N. S., Rosen, S., Ziaeepour, H., et al., 2007, MNRAS, 378, 1335

[169] Paragi, Z., Frey, S., Fejes, I., Venturi, T., Porcas, R. W., Schilizzi, R. T., 2000, PASJ, 52, 983

[170] Parma, P., Murgia, M., de Ruiter, H. R., Fanti, R., 2002, NewAR, 46, 313

[171] Peacock, J. A., 1999, Cosmological Physics, Cambridge University Press

[172] Pierre, M., Valtchanov, L., Altieri, B., Andreon, S., Bolzonella, M., Bremer, M., Disseau, L., Dos Santos, S., Gandhi, P., Jean, C., et al., 2004, JCAP, 9, 11

[173] Press, W. H., Teukolsky, S. A., Vetterling, W. T., Flannery, B. P., Lloyd, C., Rees, P., 1993, Numerical Recipes, Cambridge U Press

[174] Rawlings, S., 2003, NewAR, 47, 397

[175] Rawlings, S. 2002, IAUS, 199, 34

[176] Rawlings, S., Eales, S. A., Lacy, M., 2001, MNRAS, 322, 523

[177] Rawlings, S., 2000, ASP Conference Series, 199

[178] Rawlings, S., Lacy, M., Sivia, D. S., Eales, S. A., 1995, MNRAS, 274, 428

[179] Rawlings, S., Saunders, R., 1991, Nature, 349, 138

[180] Rawlings, S., Eales, S., Warren, S., 1990, MNRAS, 243, 14

[181] Rees, M. J., 1984, ARA&A, 22, 471

[182] Rees, M. J., Begelman, M. C., Blandford, R. D., Phinney, E. S., 1982, Nature, 295, 17

[183] Rees, N., 1990, MNRAS, 244,233

[184] Richards, G. T., Hall, P. B., Vanden Berk, D. E., Strauss, M. A., Schneider, D. P., Weinstein, M. A., Reichard, T. A., York, D. G., Knapp, G. R., Fan, X., Ivezić, Ž., Brinkmann, J., Budavari, T., Csabai, I., Nichol, R. C., 2003, AJ, 126, 1131

[185] Richstone, D., Ajhar, E. A., Bender, R., Bower, G., Dressler, A., Faber, S. M., Filippenko, A. V., Gebhardt, K., Green, R., Ho, L. C., Kormendy, J., Lauer, T. R., Magorrian, J., Tremaine, S., 1998, Nature, 395, 14

[186] Rieke, G. H., Young, E. T., Engelbracht, C. W., Kelly, D. M., Low, F. J., Haller, E. E., Beeman, J. W., Gordon, K. D., Stansberry, J. A., Misselt, K. A., et al., 2004, ApJS, 154, 25

[187] Riley, J. M. W., Waldram, E. M., Riley, J. M., 1999, MNRAS, 306, 31

[188] Robson, I., Holland, W., 2007, ASPC, 375, 275

[189] Roche, et al., 2002, Proc Spie 4841 Instrument Design and Performance for Optical/IR Ground Based Telescopes, eds. M Iye & A.F. Moonwood

[190] Röttgering, H., 2007, AAS, 210, 6604

[191] Röttgering, H. J. A., Braun, R., Barthel, P. D., van Haarlem, M. P., Miley, G. K., Morganti, R., Snellen, I., Falcke, H., de Bruyn, A. G., Stappers, R. B., et al., 2006, proceedings of the conference "Cosmology, galaxy formation and astroparticle physics on the pathway to the SKA", Oxford

[192] Röttgering, H. J. A., 2006, AN, 327, 118

[193] Rowan-Robinson, M., 1995, MNRAS, 272, 737

[194] Shapiro, S. L., Teukolsky, S. A., 1983, Black holes, white dwarfs, and neutron stars: The physics of compact objects (New York: Wiley-Interscience)

[195] Sarazin, C. L., Koekemoer, A. M., Baum, S. A., O'Dea, C. P., Owen, F. N., Wise, M. W., 1999, ApJ, 510, 90

[196] Sawada-Satoh, S., Inoue, M., Shibata, K. M., Kameno, S., Migenes, V., Nakai, N., Diamond, P. J., 2000, PASJ, 52, 421

[197] Schechter, P., 1976, ApJ, 203, 297

[198] Schmitt, J. H. M. M., 1985, ApJ, 293, 178

[199] Schmidt, M. 1968, ApJ, 151, 393

[200] Schoenmakers, A. P., de Bruyn, A.G., Röttgering, H.J.A., van der Laan, H., Mack, K.-H., Kaiser, C.R.. 1999, astro − ph/9910448

[201] Sekiguchi, K., 2004, AAS, 205, 8105

[202] di Serego Alighieri, S., Cimatti, A., Fosbury, R. A. E., 1993, ApJ, 404, 584

[203] Serjeant, S., Rawlings, S., Lacy, M., McMahon, R, G., Lawrence, A., Rowan-Robinson, M., Mountain, M., 1998, MNRAS, 298, 321

[204] Sikora, M., Stawarz, Ł., Lasota, J.-P. 2007, ApJ, 658, 815

[205] Silverman, J. D., Green, P. J., Barkhouse, W. A., Kim, D.-W., Kim, M., Wilkes, B. J., Cameron, R. A., Hasinger, G., Jannuzi, B. T., Smith, M. G., Smith, P. S., Tananbaum, H., 2008, ApJ, 679, 118

[206] Simpson, C., Martínez-Sansigre, A., Rawlings, S., Ivison, R., Akiyama, M., Sekiguchi, K., Takata, T., Ueda, Y., Watson, M., 2006, MNRAS, 372, 741

[207] Simpson, C., Ward, M., Wall, J., 2000, MNRAS, 319, 963

[208] Simpson, C., Rawlings, S., Lacy, M., 1999, MNRAS, 306, 828

[209] Small, T. A., Blandford, R. D., 1992, MNRAS, 259, 725

[210] Smith, A. J., Loveday, J., Cross, N. J. G., 2009, MNRAS, tmp, 772

[211] Smolčić, V., Zamorani, G., Schinnerer, E., Bardelli, S., Bondi, M., Bîrzan, L., Carilli, C. L., Ciliegi, P., Elvis, M., Impey, C. D., Koekemoer, A. M., Merloni, A., Paglione, T., Salvato, M., Scodeggio, M., Scoville, N., Trump, J. R., 2009, ApJ, 696, 24

[212] Snellen, I. A. G., 2008, proceedings of the symposium "Approaching Micro-Arcsecond Resolution with VSOP-2: Astrophysics and Technology" (ISAS/JAXA, Sagamihara, Japan, 3-7 Dec 2007)

[213] Snellen, I., Best, P., 2003, NewAR, 47, 225

[214] Snellen, I. A. G., Schilizzi, R. T., van Langevelde, H. J., 2000, MNRAS, 319, 429

[215] Soria, R., Fabbiano, G., Graham, A. W., Baldi, A., Elvis, M., Jerjen, H., Pellegrini, S., Siemiginowska, A., 2006, ApJ, 640, 126

[216] Tabor, G., Binney, J., 1993, MNRAS, 263, 323

[217] Tadhunter, C. N., Morganti, R., Robinson, A., Dickson, R., Villar-Martin, M., Fosbury, R. A. E., 1998, MNRAS, 298, 1035

[218] Tadhunter, C. N., Scarrott, S. M., Draper, P., Rolph, C., 1992, MNRAS, 256, 53

[219] Tasse, C., Best, P. N., Röttgering, H., Le Borgne, D., 2008, A&A, 490, 893

[220] Tasse, C., Röttgering, H. J. A., Best, P. N., Cohen, A. S., PIerre, M, Wilman, R., 2007, A&A, 471, 1105

[221] Tasse, C., Cohen, A. S., Röttgering, H. J. A., Kassim, N. E., Pierre, M., Perley, R., Best, P., Birkinshaw, M., Bremer, M., Liang, H., 2006, A&A, 456, 791

[222] Taylor, G. L., Dunlop, J. S., Hughes, D. H., Robson, E. I., 1996, MNRAS, 283, 930

[223] Teerikorpi, P., 2004, A&A, 424, 73

[224] Torres-Rodrguez, A., Cress, C. M., 2007, MNRAS, 376, 1831

[225] Ueda, Y., Watson, M. G., Stewart, I. M., Akiyama, M., Schwope, A. D., Lamer, G., Ebrero, J., Carrera, F. J., Sekiguchi, K., Yamada, T., Simpson, C., Hasinger, G., Mateos, S., 2008, ApJS, 179, 124

[226] Ueda, Y., Akiyama, M., Ohta, K., Miyaji, T., 2003, ApJ, 598, 886

[227] Urry, C. M., Padovani, P., 1995, PASP, 107, 803

[228] Vardoulaki, E., Rawlings, S., Hill, G. J., Mauch, T., Inskip. K., Riley, J., Brand, K., Croft, S., Willott, C. J., 2009, MNRAS, in press

[229] Vardoulaki, E., Rawlings, S., Simpson, C., Ivison, R. J., Ibar, E., 2008, MNRAS, 387, 505

[230] Vardoulaki, E., Rawlings, S., Simpson, C., 2006, astro − ph/0609719

[231] Vardoulaki, E., Rawlings, S., Hill, G. J., Croft, S., Brand, B., Riley, J., Willott, C., 2006, AN, 327, 282

[232] Wall, J. V., Benn, C. R., Grueff, G., Vigotti, M., 1986, HiA, 7, 345

[233] Wang, J.-M., Ho, L. C., Staubert, R., 2003, A&A, 409, 887

[234] Watson, M. G., Pye, J. P., Denby, M., Osborne, J. P., Barret, D., Boller, Th., Brunner, H., Ceballos, M. T., Della Ceca, R., Fyfe, D. J., Lamer, G., Maccacaro, T., Michel, L., Motch, C., Pietsch, W., Saxton, R. D., Schröder, A. C., Stewart, I. M., Tedds, J. A., Webb, N., 2003, AN, 324, 89

[235] Weedman, D. W., Le Floc'h, E., Higdon, S. J. U., Higdon, J. L., Houck, J. R., 2006, ApJ, 638, 613

[236] Weisskopf, M. C., Brinkman, B., Canizares, C., Garmire, G., Murray, S., Van Speybroeck, L. P., 2002, PASP, 114, 1

[237] Willott, C. J., Rawlings, S., Jarvis, M. J., Blundell, K. M., 2003, MNRAS, 339, 173

[238] Willott, C.J., Rawlings, S., Blundell, K. M., Lacy, M., Hill, G. J., Scott, S. E., 2002, MNRAS, 335, 1120

[239] Willott, C. J., Rawlings, S., Blundell, K. M., 2001a, MNRAS, 324, 1

[240] Willott, C. J., Rawlings, S., Blundell, K. M., Lacy, M., Eales, S. A., 2001b, MNRAS, 322, 536

[241] Willott, C. J., Rawlings, S., Blundell, K. M., Lacy, M., 2000, MNRAS, 316, 449

[242] Willott, C. J., Rawlings, S., Blundell, K. M., Lacy, M., 1999, MNRAS, 309, 1017

[243] Willott, C. J., Rawlings, S., Blundell, K. M., Lacy, M., 1998, MNRAS, 300, 625

[244] Wilman, R. J., Miller, L., Jarvis, M. J., Mauch, T., Levrier, F., Abdalla, F. B., Rawlings, S., Kloeckner, H. -R., Obreschkow, D., Olteanu, D., Young, S., 2008, MNRAS, 388, 1335

[245] Windhorst, R. A., Miley, G. K., Owen, F. N., Kron, R. G., Koo, D. C., 1985, ApJ, 289, 494

[246] Wootten, A., Thompson, A. R., 2009, IEEE proceedings

[247] Yamada M., Fujita Y., 2001, ApJ, 553, 145

[248] Yu, Q., Tremaine, S., 2002, MNRAS, 335, 965